

Massachusetts Institute of Technology
University of Maryland
NASA Goddard Space Flight Center

MAGESTIC: Magnetically Enabled Structures Using Interacting Coils

NIAC Phase II Final Report

PI: Dr. Alvar Saenz-Otero, MIT Space Systems Lab

Co-I: Prof. Raymond Sedwick, UMD Space Power and Propulsion Lab
Dr. Carl Adams, NASA Goddard Space Flight Center

MIT Researchers: Gwendolyn V. Gettliffe
Maria de Soria-Santacruz
Brian Cohen
David Smart
Guillermo Bautista
Aaron Perez (Harvard)
Prof. Enrico Lorenzini
Prof. Manuel Martinez-Sanchez
Prof. David W. Miller
16.89 Spring 2013 Class

UMD Researchers: Allison Porter
Zachary Schwartz
Scott Kindl
Prof. Raymond Sedwick

NASA GSFC Researchers: Richard Wesenberg

Report compiled by Gwendolyn Gettliffe
3-6-2015

Contents

1.	Introduction	2
1.1.	Motivation.....	2
1.2.	Phase I Review	2
1.3.	Study Approach.....	4
1.4.	Scientific Principles Enabling HTS Structures.....	6
1.4.1.	Creation of Lorentz and Laplace forces.....	6
1.4.2.	Meissner Effect and Superconductors.....	7
1.4.3.	Space Environment	8
1.5.	Overview of Report.....	8
2.	Mission Applicability and Risks	9
3.	Selected Applications.....	9
4.	Magnetic Structures.....	14
4.1.	Overview	14
4.2.	Optimization of an Electromagnetic Spacecraft Boom.....	14
4.3.	Hardware Effort	18
4.4.	Stability Work.....	19
5.	Flexible Cooling System.....	19
6.	Future Work and Conclusions.....	21
Appendices		

1. Introduction

In our NIAC Phase I study [1], awarded September 2011, the MIT Space Systems Lab (MIT SSL) began investigating a new structural and mechanical technique aimed at reducing the mass and increasing the stowed-to-deployed ratio of spacecraft systems. This technique uses the magnetic fields from current passing through coils of high-temperature superconductors (HTSs) to support spacecraft structures and deploy them to operational configurations from their positions as stowed inside a launch vehicle fairing. These electromagnetic coils are tethered or hinged together in such a way that their motion in some directions or around some axes is constrained, as in Figure 1. Our Phase II study, awarded in Fall 2012, continued this work on electromagnetic structures, with an added focus on developing a new thermal system, investigating additional, non-structural electromagnet functions, and creating a maturation roadmap and plan for addressing barriers to feasibility of the technology. We now call the project MAGESTIC, or MAGnetically Enabled STructures using Interacting Coils.

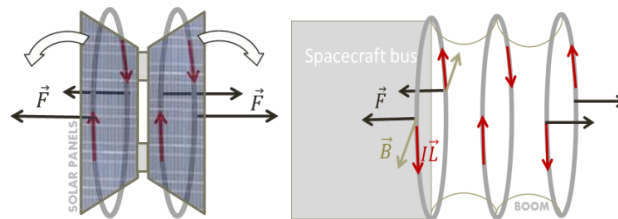


Figure 1: Example electromagnetic structural systems (hinged panels on left, tethered boom on right)

1.1. Motivation

The chief limiting factor in spacecraft design today is the prohibitively large launch cost per unit mass. Therefore, the reduction of spacecraft mass has been a primary design driver for the last several decades. The traditional approach to the reduction of spacecraft mass is the optimization of actuators and structures to use the minimum material required for support, deployment, and interconnection. Isogrid panels, aluminum or composites, and gas-filled inflatable beams all reduce the mass of material necessary to build a truss or otherwise apply surface forces to a spacecraft structure. We instead look at using electromagnetic body forces generated by HTSs to reduce the need for material, load-bearing support, and standoffs on spacecraft by maintaining spacing, stability, and position of elements with respect to one another.

HTS structures present an opportunity for significant mass savings over traditional options, especially in larger systems that require massive structural components. Electromagnetic body forces are used to move and position spacecraft elements in lieu of traditional structural components, such as telescoping beams, segmented masts and inflatables. HTS structures have less mass per characteristic length of the spacecraft than aluminum beams and therefore offer the performance benefits of larger structures while fitting into existing launch vehicle payload fairings. However, the major cost of using HTS structures is the need to cool them to low temperatures, which requires passive cooling structures like heatshields or active cooling subsystems like cryogenic heat pipes.

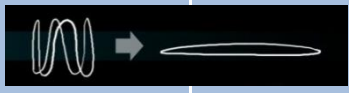


1.2. Phase I Review

In this section, we will describe our Phase I efforts: our goals, our progress, and the enabling principles and motivation for HTS structures. The three primary questions that we considered within our Phase I study are listed below along with the methods we used in Phase I and within the Phase II study to further address the questions:

1. **Can we use electromagnetic forces generated by and acting between high-temperature superconductor (HTS) current-carrying coils to move, unfold, and support parts of a spacecraft from its stowed position?**
 - Phase I includes modeling of coils and validation of models against analytical solutions.
 - Phase II includes refined modeling, structural stability analysis, and efforts at validating models using laboratory experiments.
2. **For what operations and system sizes does this technology represent an improvement over existing or in-development options?**
 - Phase I does a qualitative comparison of structural technologies and describes the trades that must be performed between subsystems with the selection of HTS structures.
 - Phase II includes performance and architectural trade space studies and optimization, feasibility analysis, thermal modeling and experiments, and deeper studies of a range of selected applications.
3. **What new mission capabilities does this technology enable?**
 - Phase I describes seven possible coil deployment and operational configurations, described in Table 1, including the identification of reconfiguration, deformation, and refocusing as operational possibilities.
 - Phase II focuses on identifying missions that can only be performed via the use of high-temperature superconducting electromagnetic structures as well as *ancillary capabilities* that an electromagnetic subsystem provides in addition to structural functions.

Coil configurations: HTS coils can repel, attract, and even shear. In combination with various boundary conditions, these operations lead to the seven functional coil configurations, depicted in Table 1, that we have identified in the course of our Phase I efforts: four (1-4, in blue) are for initial deployment and three (5-7, in green) are variants of the deployment configurations for shape flexibility during spacecraft operations. Table 1 describes the configurations and the spacecraft operations they could perform. These configurations will be capitalized when referred to.

Table 1: Seven potential functional coil configurations

Configuration	Phase	Description	Uses
1. Expand 	Deployment	A single, flexible HTS coil that is folded in its stowed position and uses its own magnetic field when current is run through it to Expand to flat shape	To deploy and hold taut the perimeters of large membranous or flexible structures
2. Inflate 	Deployment	A 3D structure is built with two or more repelling coils in a configuration that creates a space between the two, Inflating a structure (open to space or bounded by flexible walls or tethers)	To create a volume (such as a tank or toroidal perimeter) or to increase surface area (for solar cells)
3. Unfold 	Deployment	A series of coils embedded in or attached to a structure that is stowed folded and must be Unfolded to become operational (folds can be hinges, springs, or couplings)	To deploy long, flat structures (like solar panels) or to take advantage of mechanical resistance at folds to create variable angles

4. Separate	Deployment	Corollary of Inflate, in which two or more coils repel each other in series facing each other to Separate two parts of a spacecraft; tethered or membranous structure connecting	To put large, controllable distance between two sensitive parts of spacecraft (such as a nuclear reactor, astronauts, optics, thrusters)
5. Deform	Operational	Two or more coils embedded in parts of the structure act magnetically on each other to temporarily Deform or change the shape of the spacecraft	To reduce radar cross section (RCS) or adjust shape for avoidance of debris
6. Reconfigure	Operational	Corollary of Deform, except Reconfigured state is sustainable and lasting	To reduce drag profile or Reconfigure satellite for different ConOps
7. Refocus	Operational	Two or more coils adjust their magnetic state such that an antenna or mirror is Deformed to Refocus it. Orientation of coils dependent on original shape of mirror or antenna.	To change focus lengths of mirrors and gains of antennas by reforming or moving their dishes, mirrors, or horns to Refocus them on a new target

1.3. Study Approach

1. Describe and analyze mission functions which can be performed by an electromagnetic subsystem

Structural functions aren't the only functions that can be provided by an electromagnetic subsystem; we call functions and capabilities that are not necessarily structural capabilities *ancillary capabilities*. Ancillary capabilities can save size, weight, and/or power (SWAP) in systems requiring them because the electromagnetic subsystem is not only reducing the structural mass, but saving SWAP from other subsystems as well. Figure 2 provides a visualization of several different mass reduction techniques: reducing the parts (reducing the mass of a single subsystem), reducing the sum of the parts (same structural mass but it is saving mass from other subsystems), or doing both (lighter structures *and* ancillary capabilities provided).

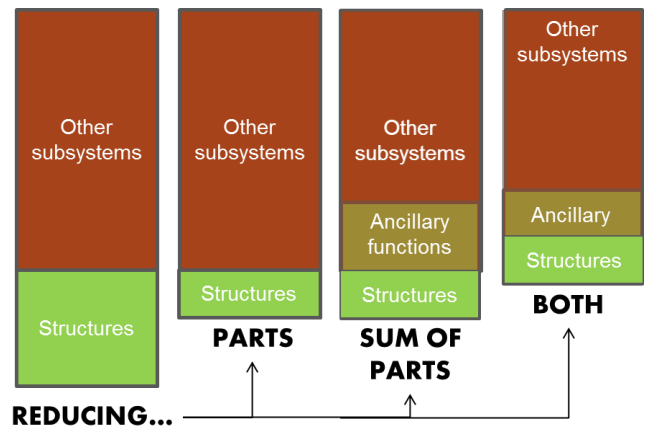


Figure 2: Visualization of approaches to reducing mass

Some of these ancillary capabilities or functions:

- Strong controllable magnetic field
- Contactless controllable actuation
- Lossless energy storage
- Low exported vibration/heat transfer because of the lack of or reduced amount of connective hardware

- Wireless power and/or data transfer (when operated with alternating current)
- Circular deployed/tensioned area
- Performs equivalently or better in cold environments because of the increased cooling capacity of the cryocoolers

2. *Refine and create models of actuation of single- and multi-coil systems*

This is a process that began in Phase I and is continuing to be developed past Phase II as work continues on stability and determining the conditions under which tethered electromagnetic booms are statically and dynamically stable. This work is discussed briefly in Section 4.4.

3. *Reduce risk and validate modeling via hardware proof-of-concepts*

Section 4.3 discusses our attempts to validate our numerical computer models with hardware experiments.

4. *Map multivariate space by performance based on models, functions, and other technologies*

This step of the approach morphed into an optimization problem, presented in Section 4.2 for a multi-coil, tethered electromagnetic boom structure.

5. *Assess utility for candidate applications, such as GEO magnetorquers, EMIC wave antennas, in-space assembly, and deployable sunshields*

Section 3 discusses the selected applications, chosen specifically as missions that fill a specific role and timeframe on our maturation roadmap in Figure 16 (near-term, building flight heritage; mid-term, a technology-enabled mission; far-term, a complex mission with many opportunities for interacting technology functions).

6. *Identify and evaluate risks and roadblocks to technology integration*

Risks are defined as identified issues that *might* present a barrier to all or some of our roadmap. They require additional analysis to determine whether they can be reduced or if they will become a roadblock. Roadblocks are identified issues that *do* present a barrier to some or all of our roadmap. Roadblocks can be addressed with Key Enabling Technologies, technologies that need to be developed before the technology is fully technically feasible and economically viable. Table 2 summarizes those risks, roadblocks, and Key Enabling Technologies that we have identified, separated into three functional/organizational categories: Electromagnets and Deployment (MIT/GSFC), Thermal Control (UMD), and Power Management and Control (not the focus of this study). Not all of these risks and roadblocks were tackled over the course of the study, but identifying them aids in future work directions.

Table 2: Identified risks, roadblocks, and Key Enabling Technologies

	Electromagnets & Deployment	Thermal Control	Power Mgmt & Control
Risks	<ul style="list-style-type: none"> • Uncompetitive performance/cost with other structural options • Instability of configuration • Disturbances (Cryocooler vibration, solar pressure, external mag. field) • Inability of single expanding coil to deform itself plus attached equipment 	<ul style="list-style-type: none"> • Power consumption of cooling system is prohibitively high • Twisting of cooling sheath as it inflates 	<ul style="list-style-type: none"> • Potential EMI negatively affecting other subsystems or vice versa • Distributing power across coils inefficient or prohibitive • Inadequate position accuracy and knowledge
Roadblocks	<ul style="list-style-type: none"> • Losses prohibitive in AC applications and rectangular tape 	<ul style="list-style-type: none"> • Cooling not available for flexible coil • Leakage of coolant if thermal hardware broken/pierced 	<ul style="list-style-type: none"> • Do not have controllers for connected coils or GEO desat • Orthogonalizing coils

Key Enabling Technologies	<ul style="list-style-type: none"> • Striated superconductors for lower AC losses • Twisting tape stacks to reduce perpendicular magnetic field • Self-reversible electromagnetic latches 	<ul style="list-style-type: none"> • Flexible cooler for flexible HTS • More power-efficient cryocoolers • Non-helical MLI sheath • Self-healing materials for puncture mitigation 	<ul style="list-style-type: none"> • Controller for desaturation in GEO magnetic field • Phasing for 2+ matched sets of magnets w/out cross-interaction • Controller for tethered or otherwise constrained magnets
----------------------------------	----------------------------------------------------------------------------------------------------------------------------------------------------------------------------------------------------------------------------	------------------------------------------------------------------------------------------------------------------------------------------------------------------------------------------------------------------------------	-----------------------------------------------------------------------------------------------------------------------------------------------------------------------------------------------------------------------------------------------------

1.4. Scientific Principles Enabling HTS Structures

HTS structures are enabled by the fundamental scientific principles of electromagnetism and the unique environment of space, as well as the developments made over the last several decades in manufacturing superconductors and controlling electromagnets onboard multi-system vehicles. The industry development is described in later sections; this section describes the underlying fundamental scientific principles that enable HTS structures, including:

1. The creation of Lorentz and Laplace forces via interaction of a magnetic field and current
2. The Meissner effect and superconductivity
3. Enabling characteristics of space environment (microgravity and vacuum)

1.4.1. Creation of Lorentz and Laplace forces

HTS structures operate using electromagnetic forces to push, pull, and move with respect to each other. Electromagnetic forces (called Lorentz or Laplace forces depending on whether the force is acting on a single charge or a current of charges respectively) result from the interaction of a magnetic field and a current.

A point charge q moving with velocity \mathbf{v} in external magnetic (\mathbf{B}) and electric (\mathbf{E}) fields experiences a Lorentz force \mathbf{F} , given by

$$\mathbf{F} = q[\mathbf{E} + (\mathbf{v} \times \mathbf{B})].$$

$q\mathbf{E}$ is the *electric* force, while $q\mathbf{v} \times \mathbf{B}$ is the *magnetic* force. The macroscopic force on a wire is the *magnetic* force and is called the Laplace force. It is generated by a magnetic field \mathbf{B} on a wire carrying current I (a stream of point charges) as follows:

$$\mathbf{F} = I \int d\boldsymbol{\ell} \times \mathbf{B}$$

In order to calculate the magnetic field \mathbf{B} for use in calculating the Laplace force on a wire or coil of wire, one can use the Biot-Savart law, which can be derived from Ampère's law and Gauss's law, to compute the resultant magnetic field vector \mathbf{B} at a position \mathbf{r} with respect to a steady current I .

$$\mathbf{B} = \frac{\mu_0}{4\pi} \int_C \frac{I d\boldsymbol{\ell} \times \mathbf{r}}{|\mathbf{r}|^3}$$

In our Phase I deployment modeling work, we calculate the magnetic field and the Laplace forces across a current-carrying wire over time by implementing the Biot-Savart law numerically, by discretizing current elements in order to determine the magnetic field generated by arbitrary configurations of rigid (meaning a fixed, non-changing shape) and flexible coils. Knowledge of the magnetic field at each point in space around a current-carrying wire allows us to then calculate the resultant force upon another current-carrying wire as a result of that magnetic field, which we can then use to determine the number of turns a coil needs or how much current it needs to carry in order to deploy a structure.

1.4.2. Meissner Effect and Superconductors

Superconductors enable HTS structures because they are able to generate much larger forces via their larger current carrying capacity, which increases the distance over which they can work for the same amount of mass.

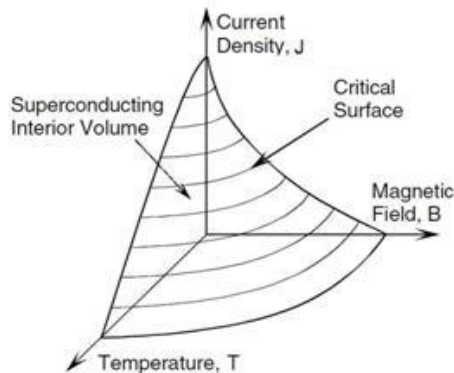


Figure 3. Critical Surface for Type II Superconductor [2]

Superconductors are materials that conduct electrical current perfectly below a critical temperature T_c ; superconductors have zero resistivity, with negligible quantities right around their T_c . Any current through them will persist significantly longer than through a non-superconductive material.

Superconductivity is characterized by **the Meissner effect**, the expulsion of an external magnetic field from a superconductor once cooled below its T_c during its transition to a superconducting state. Every superconductor has a critical temperature, external magnetic field strength, and current density above which superconductivity ceases, shown graphically in Figure 3.

High-temperature superconductors, or HTSs, are those superconductors with T_c s above 77K, or the boiling point of liquid nitrogen, enabling them to be

cooled to a superconducting state using LN2. The higher the T_c , the less it costs (in terms of power, storage, and consumables, for applications where a cryogen is not recycled) to do the cooling. HTS development and the subsequent development of HTS wire has led to a broad array of applications for superconductors, including long distance power transfer, electromagnets, and energy storage.

There are two types of superconductors; Type-I only exhibit the Meissner effect with one critical field strength above which superconductivity ceases. Type-II superconductors, which include all high-temperature superconductors as well as some low-temperature superconductors (LTSs) with T_c s too low to qualify as “high-temperature”, also exhibit a **“mixed-state” Meissner effect** that increases their critical magnetic fields and configuration stability and as such are often used in superconducting magnets in the form of coils of wire made with superconductor filaments embedded in support material less than a millimeter in diameter.

The “mixed” Meissner effect is different from the Meissner effect in that some magnetic field penetrates the superconductor through filaments of normal-state material and the material can support higher magnetic fields before superconductivity breaks down. There are thus two critical field strengths in Type II superconductors: beyond the first field strength, where superconductivity would cease completely in a Type I superconductor, a vortex (“mixed”) state exists in which some magnetic flux is allowed to penetrate the material while it continues superconducting. Beyond the second, higher critical field strength, superconductivity ceases. Small defects in the material can increase critical magnetic fields and contribute to the stability of the system by fixing vortex points, or filaments, through which magnetic flux can pass. This phenomenon is known as flux pinning and its use in docking or positioning has been the subject of work by Peck et al at Cornell University [4].

Type-II superconductors are the only type of superconductor used in wire. Many of these types of wire are made with HTSs to lower cooling costs, especially for non-magnetic applications. Some wire, however, especially that which is used in powerful electromagnets like those in the Large Hadron Collider, is made with LTSs that need to be kept much colder but can sustain much higher current densities than HTSs. For example, niobium–tin (Nb3Sn) has a T_c of 18.3K and can withstand magnetic field strengths up to 30 tesla (with a record current density of 2643 A/mm² at 12T and 4.2K) [5]. HTS wires do not have the same current densities and as a result, they cannot generate magnetic fields as high as LTSs. But, though pure HTS materials are just as brittle as LTS materials, HTSs are able to be constructed into flexible, durable wire. The flexibility of HTS wire enables the Expand configuration that we proposed earlier in this section for deployment of a single, folded and stowed coil into a large, flat, expanded coil.

Compared to standard, room-temperature conductors, HTS wires are able to create larger magnetic fields and sustain higher current densities, with little-to-no resistive losses through the wire (compared to high resistive losses in copper and aluminum). While room temperature conductor coils can be used to magnetically operate on each other, the Laplace forces able to be generated on each other are significantly lower than those that can be created with HTS coils, due to the lower magnetic field and current combination. HTS wire thus enables electromagnetic structures with multi-

meter separation between coils, which in turn enables larger vehicles and the performance benefits that accompany larger structures.

Whereas several decades ago, it was difficult for manufacturers to create HTS wire of any useful length, **HTS can now be created in lengths upwards of 1500m** [6], reducing the need for splices that result in resistive losses of power to heat.

Individual strands of tape-shaped (wide and thin) cable are multilayered with various substrates and insulators for mechanical strength and chemical stability while at the same time trying to maximize the current density of the wire. Figure 4 shows a cutaway view of an HTS wire.

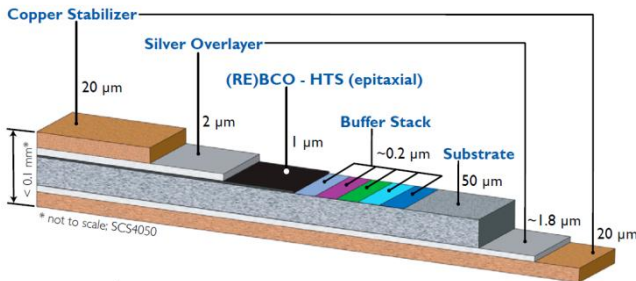


Figure 4: Cutaway view of a 2G HTS wire [3]

Roebel cables are a way of winding together individual wire strands to reduce AC losses due to self-field interaction with the current running through each strand, reducing the critical current I_c able to pass through that wire. When determining the configuration of turns in a coil or strands in a cable, it is especially important to consider how the self-field affects the I_c in each strand to optimize for the maximum current density in the coil cross-section possible.

SuperPower Inc, a subsidiary of Furukawa Electric Co., Ltd, manufactures a flexible “2G”, or second generation, HTS wire with a minimum bend diameter of 11mm at room temperature (and at least 25.4 mm at superconducting temperatures) and maximum hoop stress of 700 MPa before irreversible degradation of the critical current. Recent axial stress-strain measurements conducted at the Naval Research Laboratory on standard 4 mm wide SCS4050 production wire gave a yield stress for the wire of 970 MPa at 0.92% strain. [7] The 2G HTS wire can carry between 250 and 350 A/cm wire width (or 25 – 35 kA/cm² with a .1mm wire thickness) through 650m lengths (80-110A critical current with a 4mm wire width) [8].

1.4.3. Space Environment

On the ground, gravity and the need to cool superconductors in an otherwise room-temperature environment makes using electromagnets as actuators or continuous structural deployment difficult and not broadly useful. In the space environment, however, an electromagnet does not need an enormous magnetic field to actuate components, and there is no air transferring heat into the magnet by convection, making space a unique environment for the use of HTS structures.

The microgravity environment of space enables HTS structures because spacecraft elements can be actuated without overcoming gravitational forces. Thus, only small forces are needed to cause motion or actuation, reducing the necessary size and current of electromagnets used for such tasks compared to what would be needed, for instance, to repel a coil upwards on the Earth’s surface.

The vacuum of space is both beneficial and detrimental to the use of superconductors. If it can avoid radiated input from the sun or Earth or other bodies, a thermally isolated HTS subsystem can maintain superconducting temperatures without cryogenics. However, it is difficult to remove heat from the system in a vacuum if it cannot be isolated from conductive or radiating heat sources.

1.5. Overview of Report

This report is presented as a high-level summary and short excerpts from of a number of papers, reports, and presentations written and co-written by a number of contributors over the course of the two year NIAC Phase II study. The referenced papers, reports, and presentations are included as appendices on this paper and are referred to where appropriate (except for **Appendix 9**, which is relevant to all sections of this report and will therefore not be mentioned in every section).

Appendices:

1. **Mission Applicability and Risks**
– Richard Wesenberg, NASA Goddard Space Flight Center
2. **System Concept Development for Multifunctional Electromagnetically Actuated and Supported Space Structures** – IAC 2014 paper
– Gwendolyn V. Gettliffe, David W. Miller, MIT
3. **Design of a Space-borne Antenna for Controlled Removal of Energetic Van Allen Belt Protons**
– IEEE Aerospace 2014 paper
– Maria de Soria-Santacruz, Guillermo Bautista, Gwendolyn V. Gettliffe, Manuel Martinez-Sanchez, David W. Miller, MIT
4. **Tradespace Investigation of a Telescope Architecture for Next-generation Space Astronomy and Exploration**
– 16.89 Space Systems Engineering final report
– Giuseppe Cataldo, Mark Chodas, Pratik Davé, Atray Dixit, Sherrie Hall, Robert Harris, Dustin Hayhurst, Fernando Hicks, Chris Jewison, Ioana Josan-Drinceanu, Brandon Karlow, Bryan McCarthy, Andrew Owens, Eric Peters, Margaret Shaw, David Sternberg, Kathleen Voelbel, Marcus Wu, MIT
5. **Multi-Disciplinary Optimization of an Electromagnetic Spacecraft Boom**
– 16.888 Multi-Disciplinary Design Optimization final report
– Brian Cohen, Gwendolyn Gettliffe, Dave Smart, MIT
6. **MAGESTIC Hardware Testing**
– MIT Space Systems Lab Seminar
– Aaron Perez, Harvard, and Gwendolyn Gettliffe, MIT
7. **Introduction to Magnetic Boom Stability Analysis**
– Gwendolyn Gettliffe, MIT
8. **Thermal Enclosure Design and Testing Report**
– Allison Porter, Raymond Sedwick, UMD
9. **MAGESTIC Phase II Mid-Study Review Slidedecks**

2. Mission Applicability and Risks

Appendix 1 includes an overview of design considerations and potential risks for using HTS magnets for space applications, as well as some proposed future space missions and use cases and ways in which HTS structures or magnets could be used in those missions to accomplish some of their requirements or goals. It's important to identify these mission integration possibilities in order to establish opportunities to mature this technology as well as some of the pros and cons of the approach as compared to traditional approaches. Section 3 and its affiliated appendices focus on a few of these applications in particular for more detailed study.

3. Selected Applications

Four main applications were selected for more detailed analysis during the Phase II study. Three of them were selected as anchoring applications to provide a maturation pathway for superconducting technology in space and to represent a cross-section of potential multi-functional allocation to an electromagnetic structural subsystem: torque coils for satellites in geostationary orbit, a large deployed loop antenna for precipitation of protons out of the inner Van Allen belt with electromagnetic ion cyclotron (EMIC) waves, and a next generation space-based observatory with

electromagnetically deployed and formation flown elements. The fourth application is an electromagnetic asteroid tug for the redirection of ferromagnetic asteroids.

1. “Near-Term”: GEO Magnetorquers

Near-term spans the time period between now and five years from now with the goal of achieving TRL 5 for high-temperature superconducting electromagnets in orbit and proposing a demonstration mission for electromagnetic structures. The near-term is focused on building flight heritage and further maturation of HTS technology from Earth-based technology to a functioning system on orbit, and the anchoring application is geostationary orbit (GEO) magnetorquers. This application is addressed more in depth in **Appendix 2**, which is a 2014 International Astronautical Congress (IAC) paper on the three selected anchoring applications.

The most extensive use of electromagnets in space to date has been magnetorquers, coils of wire used to torque a spacecraft against the Earth’s geomagnetic field in order to dump momentum from the spacecraft’s attitude control components. With superconducting wire becoming cheaper, more flexible, and more manufacturable, the idea of using superconducting electromagnets for relative actuation of spacecraft and spacecraft elements became feasible.

The use of magnetorquers would save lifetime-limiting propellant for GEO satellites that would otherwise be used for desaturation, but magnetorquers are not currently used at geostationary orbit (GEO) for two reasons: the Earth’s geomagnetic field is very weak in GEO compared to Low Earth orbit (LEO) because the field strength decreases proportional to $1/R^3$ where R is the distance from the center of the Earth, and the geomagnetic field at GEO is very time variant, making it difficult to write controllers for desaturation of attitude control hardware. The use of HTS wire for GEO magnetorquers will address the weak magnetic field strength by greatly increasing the magnetic moment of the magnetorquer and thus the torque it can provide in the weaker field at GEO. The time-variant field can be addressed by more robust controllers, which are not the subject of this study.

Since no actuation functions are required of magnetorquers and the use of magnets as torque coils in space is very mature (albeit with regular conductors), this application would provide flight heritage for HTS magnets and cooling systems with relatively little engineering development compared to other, more complex applications for HTS magnets in space.

2. “Mid-Term”: EMIC Wave Antenna

Mid-term spans the time period between five and fifteen years from now with the goal of enabling or enhancing new mission concepts that have heretofore been impossible or infeasible. The mid-term is focused on addressing technical feasibility barriers, starting with those associated with the anchoring application of a large deployed spinning superconducting loop antenna. This application is summarized in the **Appendix 2** IAC paper (and excerpted below) and addressed in much greater detail in **Appendix 3**, which is a 2014 IEEE Aerospace Conference paper on the design of a space-based EMIC-wave emitting antenna for controlled removal of energetic Van Allen belt protons and discusses the EMIC-wave mission, the antenna design, and the predicted performance of the antenna.

The Van Allen belts are regions encircling the Earth in which the Earth’s geomagnetic field has trapped and concentrated energetic charged particles. The trapped particles come from cosmic rays, solar flares and storms, and other processes. There are two major Van Allen belts. The inner belt comprises electrons and protons; the outer belt comprises mainly electrons. Charged particles are not healthy for spacecraft or humans as they can cause unwanted single event effects in spacecraft electronics and damage DNA in human cells, leading to cancer or other health concerns. A method for “cleaning” the trapped particles out of the Van Allen belts would reduce the radiation dosage to current and future space missions.

It has been observed that ultra-low and very low frequency waves (ULF and VLF) can scatter particles that are trapped in helical paths around the Earth’s magnetic field lines into a pitch angle that causes precipitation into the upper atmosphere, freeing them from the Van Allen Belts. Electromagnetic ion cyclotron (EMIC) waves (with frequencies less than 10 Hz) can interact with both protons and electrons, making them a good option for reducing the trapped radiation in the inner Van Allen belt. A mission incorporating a large space-based antenna that could emit EMIC waves and begin precipitating inner belt protons would be both scientifically and economically valuable.

A very large (30 m diameter) magnetic loop antenna was chosen for this application because of its very small radiation resistance in plasma compared to a linear dipole antenna. To prevent large voltages from forming across a static AC coil due to its enormous self-inductance, a rotating DC coil was selected, which in the far field (5000 km or so away from the antenna) has a dipole component equivalent to two static orthogonal AC coils if the rotation rate of the coil matches the desired frequency of its signal. In order to radiate the power necessary to detect whether the EMIC wave technique works (25W with a 30 m diameter coil), high-temperature superconductors were selected. Additionally, a 30 m diameter antenna would not fit in a launch vehicle fairing and would need to be deployed somehow, likely via a combination of magnetic self-force, strain energy and inflation.

A scientific proof-of-concept mission of the EMIC-wave antenna is possible with a smaller (5 m diameter coil) that doesn't require deployment and can be rigid. However, demonstrating a flexible cooling and deployment system would be a big step towards creating a mission that could start removing radiation in measurable quantities.

3. "Far-Term": Commissioning of Large, In-Space Observatories

Far-term spans the time period beyond fifteen years from now with the goal of using electromagnetic capabilities to imagine revolutionary mission concepts, reinventing how we imagine large spacecraft. Missions in the far-term, including the anchoring application of a large space-based observatory, will not just be enabled by but also defined by their use of electromagnetic systems. Therefore, it will be important to focus in the far-term on addressing barriers to the integration and operation of sometimes several different electromagnetic subsystems with each other and the rest of the spacecraft. Figure 5 depicts a notional image of such a large and complex observatory.

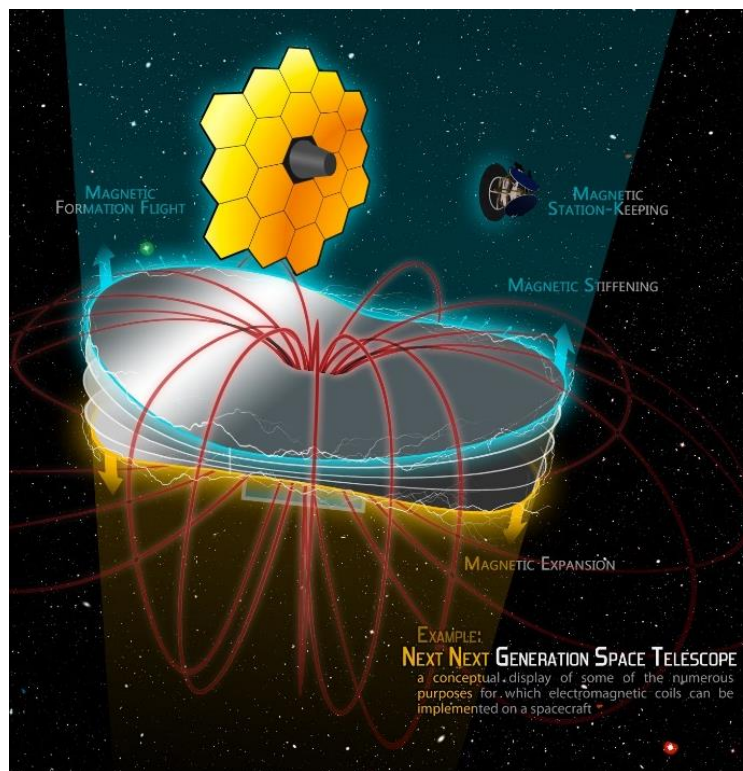


Figure 5: Notional depiction of a "Next Next Generation Space Telescope" incorporating many structural and ancillary electromagnetic functions

Analysis and discussion of several facets of this concept, including but not limited to sunshield/starshade separation and tensioning, positioning of optics, and formation flying a sunshield with respect to a primary mirror are presented in **Appendix 2**, and this anchoring application was the subject/inspiration for the large-scale architectural analysis and trade study for the assembly and servicing (including electromagnetic tugs) of large in-space observatories conducted in a Spring 2013 16.89 (Space Systems Engineering) graduate class at MIT, attached as **Appendix 3**. Originally, a more detailed case study was planned, using the James Webb Space Telescope (JWST), but the lack of public information on design specifics and requirements led us to pursue different facets of electromagnetic integration on a large observatory. Also, an analysis of customer needs revealed a movement away from monolithic deployment of observatories and towards assembly for future large observatories.

4. Magnetic Asteroid Tug

While gravitational asteroid tugs are frequently discussed for redirecting asteroids, the force that a gravitational tug is able to exert on an asteroid hinges on the mass of the spacecraft, which actively goes against the goal of minimizing mass to minimize cost, and also means that as fuel is expended, the force the tug exerts substantially decreases as well. The force exerted by an electromagnetic tug equipped with a large, superconducting electromagnetic coil, however, would not rely on mass explicitly, but rather electrical power and the size of the electromagnet. A magnetic tug is directly comparable to a gravitational tug, since both system concepts involve a vehicle that is not physically interacting with the asteroid but rather maintaining proximity and inducing some sort of force to pull the asteroid in a desired direction. For the same mass spacecraft, an electromagnetic tug could exert orders of magnitude more attractive force on the asteroid than a gravitational tug, depending upon the asteroid's magnetic and tumbling states.

The asteroid would need to be ferromagnetic and either not tumbling with an oriented magnetic dipole moment, or not already possessing an oriented magnetic dipole moment. A magnetic tug would be equipped with a strong directional HTS magnet that would either act to attract the magnet via its preexisting dipole moment or induce a time-variant alignment within the ferromagnetic core towards the HTS magnet. Further work is necessary to investigate how well the latter technique would work, but it is an application that is very much worth exploring in detail.

For a quick calculation of the ratio of force provided between magnetic and gravitational tugs of the same mass, we use the asteroid Vesta as an example and assume that it is not spinning and will be being tugged in a direction along its magnetic dipole moment, as well as that the minimum paleointensity at its surface is $2\mu\text{T}$, based on meteorites found on Earth that likely sample Vesta's crust [9]. We also assume that the coil (not including thermal system) is 5% of the magnetic tug's mass, and explore later how changing that percentage changes the force ratio. The distribution of mass (including power, propellant, and thermal systems) is not otherwise specified.

The gravitational force between an asteroid and a space craft is

$$F_g = \frac{GM_A M_{sc}}{d^2}$$

The magnetic force between two aligned magnetic dipoles (we are using the dipole approximation for the magnetic moment of the coil) is

$$F_m = \frac{3\mu_0 N_1 I_1 A_1 \mu_A}{2\pi d^4}$$

where N is the number of turns, A is the area of the coil, d is the distance from the center of the coil to the center of the asteroid, I is the current per turn, μ_0 is the vacuum permeability, or $4\pi * 10^{-7} \text{N/A}^2$, and μ_A is Vesta's magnetic dipole.

To determine Vesta's magnetic dipole from an assumed $2\mu\text{T}$ surface field and $r_{ast} \sim 260\text{km}$, we use the formula for magnetic field at a distance $R=r_{ast}$ along moment axis:

$$2\mu\text{T} = \frac{\mu_0}{4\pi} * \frac{2\mu_A}{(260\text{ km})^3}$$

$$\mu_A = 1.7576 * 10^{17} \text{Am}^2$$

The best approximation for Vesta's mass is

$$M_A = 2.591 * 10^{20} \text{kg}$$

We want the ratio x between the magnetic and gravitational forces

$$xF_g = F_m, \quad x = \frac{F_m}{F_g} = \frac{3\mu_0 N_1 I_1 A_1 \mu_A}{2\pi d^2 G M_A M_{sc}}$$

We've assumed the coil mass is

$$0.05M_{sc} = 2\pi r_{coil} N_1 * CSA * \rho_{HTS}$$

where CSA is wire cross-sectional area (m), and ρ_{HTS} is the density of the wire (kg/m^3).

$$A_1 = \pi r_{coil}^2$$

Rearranging the above equation for coil mass in terms of N and multiplying by A, we get

$$N_1 A_1 = N_1 \pi r_{coil}^2 = \frac{M_{SC} * r_{coil}}{40 * CSA * \rho_{HTS}}$$

Substituting what we know into the equation for the ratio x,

$$x = \frac{3\mu_0 I_1 \mu_A M_{SC} r_{coil}}{80 CSA * \rho_{HTS} \pi d^2 G M_A M_{SC}} = \frac{3\mu_0 I_1 \mu_A r_{coil}}{80 CSA * \rho_{HTS} \pi d^2 G M_A} = \frac{3\mu_0 I_1}{80 CSA \rho_{HTS} \pi G} * \frac{\mu_A r_{coil}}{d^2 M_A}$$

The first term, we'll call it Z, comprises constant terms (with a final unit of kg/A-m, to avoid writing out all the units below), so we can determine its value:

$$Z = \frac{3\mu_0 I_1}{80 CSA \rho_{HTS} \pi G} = \frac{3 * 4\pi * 10^{-7} * 150}{80 * 6 * 10^{-7} * 8583.33\pi * 6.67 * 10^{-11}} = (6.55013 * 10^6) \frac{kg}{Am}$$

We can begin inserting the properties of Vesta, which gives us

$$\frac{Z \mu_A}{M_A} = \frac{(6.55013 * 10^6) \frac{kg}{Am} * (1.7576 * 10^{17} Am^2)}{2.591 * 10^{20} kg} = 4443.27m$$

$$x = \frac{Z \mu_A r_{coil}}{d^2 M_A} = 4443.27m * \frac{r_{coil}}{d^2}$$

d depends largely on the optimal distance from the asteroid to both reduce plume impingement of the thrusters on the asteroid and use propellant the most efficiently, if the thrusters are not aligned with the vector of movement. This high-level calculation gives us an idea of how the ratio changes depending on how large we can make the coil and how closely we can operate to the asteroid. Clearly the larger radius the coil the better, the only drawback being that a larger coil would mean more mass dedicated to a thermal system (depending on where in the solar system the asteroid is located) and less to propellant, and deployment of that coil also becomes necessary when the radius exceeds that of the launch vehicle fairing. It's also worth noting that a larger force exerted on the asteroid allows it to be moved more quickly.

How does this ratio change if we devote more or less of the spacecraft mass to the naked coil? We can quickly see by multiplying Z by the multiplier between 5% and the desired mass percent. For example, if the coil is 50% of the mass of the spacecraft, $\frac{Z \mu_A}{M_A} = 10 * 4443.27m = 44432.7 m$.

It should be noted that this analysis *just* compares the relative forces, while an electromagnetic tug would *also* exert a gravitational force by virtue of its having mass, so at a given instant, an electromagnetic tug would exert $F_{tot} = F_G + F_{EM}$ force on the asteroid, or

$F_{tot} = F_G(1 + x)$, which is by necessity no less than F_G . This does not take into account fuel or mission lifetime and how including an EM coil might change those parameters, but it is clear that if an asteroid could possibly be or become magnetized, then an electromagnetic component to a tug would be a very useful option to explore.

4. Magnetic Structures

4.1. Overview

In our Phase I effort, we modelled some of the rigid body physics of deploying tethered, hinged, and loose electromagnetic coils and verified the dipole approximation for coils in the far-field. Our Phase II structural work was two-pronged: explore electromagnetic structures in the context of selected example missions (as previously mentioned) and example structures, and study the stability of magnetically supported structures after their deployment. This section and its associated appendices focus on 2+ coils tethered together coaxially (henceforth described as a “boom”) as depicted in Figure 6 and will describe a multi-objective, multidisciplinary optimization of the structure; the effort to validate our tethered deployment model; and the ongoing work in describing the conditions for stability of such a structure.

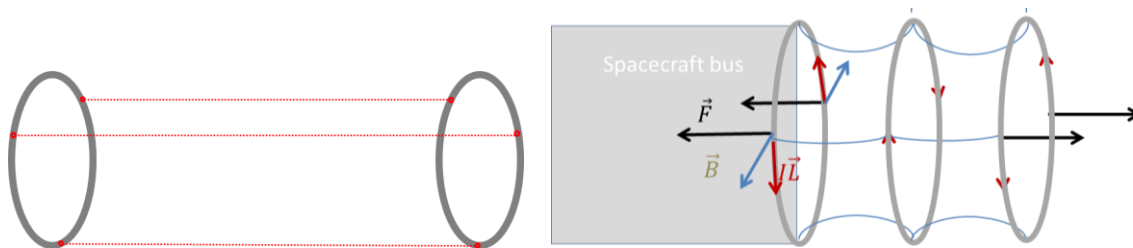


Figure 6: (a) Diagram of 3-tether spacing between two coils, (b) Three coil boom with slack tethers

4.2. Optimization of an Electromagnetic Spacecraft Boom

Appendix 4 presents a multi-disciplinary, multi-objective optimization of a multi-coil electromagnetic boom as depicted in Figure 6, using different optimizers, exploring single and multiple objectives (min(mass), min(power), and max(length)), and including information and suboptimization within multiple disciplines/subsystems (structural, thermal, and power). The design variables used and varied across were number of coils (2 to 5), coil radius of each of however many coils were in a design (from 0.1m to 4.5m) and number of turns in each coil in the design (1 to 250).

Table 3 gives the design variables, parameters, constraints and objectives within the scope of the electromagnetic boom design problem.

Table 3: Master table of design variables, parameters, constraints, and objectives

Design Variables	Variable	Symbol	Description	Upper Bound	Lower Bound	Nominal Initial Value	Unit
	Coil radius	R_{1-5}	Radius of the EM coils	4.5	0.1	1	meter
	# of coils	N_C	Number of coils in boom	5	2	2	-
	# of turns	$N_{T,1-5}$	Number of turns per coil	250	1	100	-
Parameters	Wire type	W	Brand of superconductor	-	-	SuperPower 2G HTS	-
	Boom length	L	End-to-end length of boom	-	-	50	meter
	Density of wire	ρ	Material density of the superconductor tape	-	-	8548.2	kg/m ³
	Solar constant	S	The flux of solar heat energy through a meter square area	-	-	1366	W/m ²
	Boom tension	t	Tension from end to end	-	-	50	μ N
	Wire width	w	Width of superconductor	-	-	4	mm
	# of tethers	N_t	Number of tethers connecting adjacent coils	-	-	3	-
	Payload mass	m_{PL}	Lump mass to be supported	-	-	25	kg
	Bus mass	m_{bus}	Lump mass at start of boom	-	-	1000	kg

Constraints	$T < T_c$	T_c, T	The temperature of each coil is less than critical temp. of the superconductor	-	-	-	Kelvin
	$M_{cryo} \leq 50kg$	M_{cryo}	The mass of each cryocooler is less than 50kg	-	-	-	kg
Objectives	Min(mass)	M	Want to minimize the total mass of the boom and supporting hardware	-	-	-	kg
	Min(power)	P	Want to minimize the power burden of the EM boom on the spacecraft	-	-	-	W
(optional)	Max(length)	L	Removes L as a parameter and instead tries to maximize the length of the boom	-	-	-	m

Figure 7 shows the design of experiments (DOE) that samples the space of potential designs and plots them against the two initial objective metrics of mass and power.

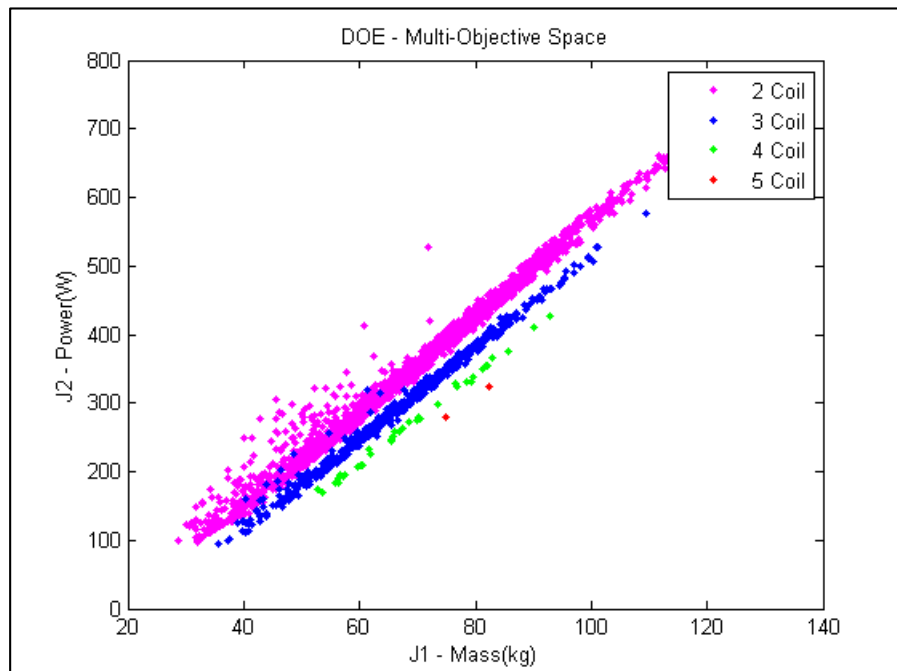


Figure 7: Multi-objective DOE

It was found and can be seen in Figure 8 that the Pareto front for the two-objective optimization of min(mass) and min(power) for an electromagnetic boom of the architecture described in this paper is very small because the two single objective utopia points are very close to each other. Mass and power are very coupled objectives (largely because cryocooler mass is a major part of the system mass and increases as cryocooler power increases), and computation involved in optimization could be reduced by eliminating one of the two and optimizing for just the other. It can be seen that a two coil system with a large number of turns tends to be Pareto optimal for the single or two objective optimization.

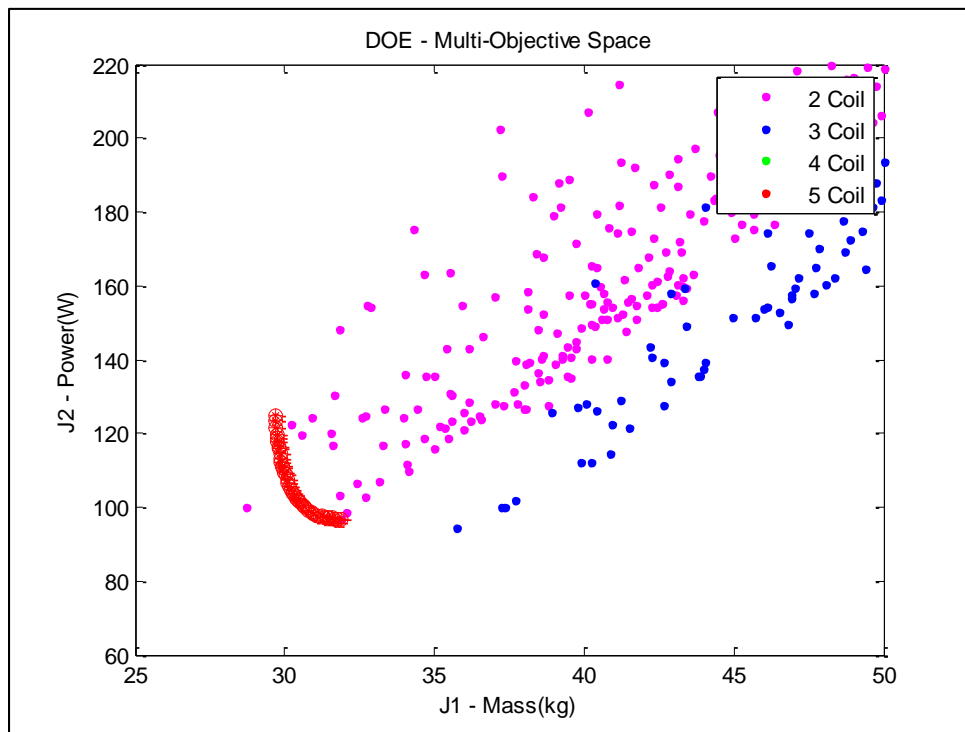


Figure 8: Two-objective Pareto frontier found using Adaptive Weighted Sums method

The tradespace is significantly expanded by adding the third objective, max(length), because with greater length comes by necessity greater mass and power. Figure 9 shows one view of a three dimensional plot of the DOE, highlighting non-dominated designs. The tradespace becomes more computationally expensive to produce because of its breadth, but the designs found in the Pareto front of a multiobjective problem involving length are much more diverse than the exclusively two-coil designs along the min(mass) and min(power) Pareto front.

Objective Space

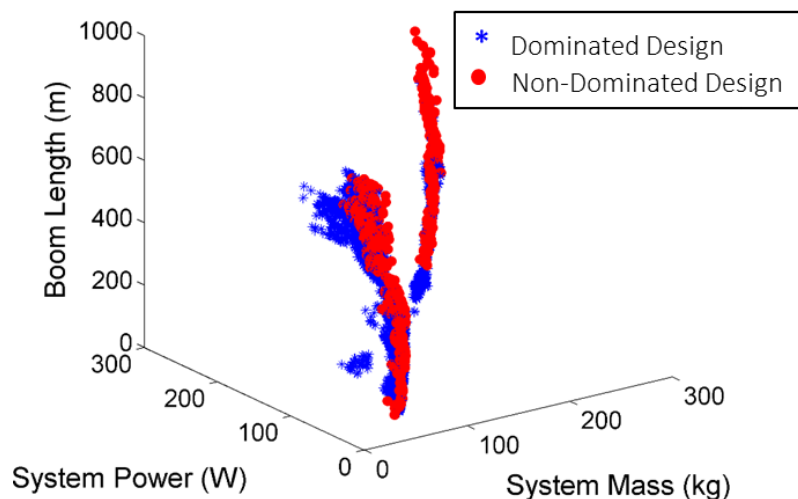


Figure 9: Three objective Pareto optimal designs

What is clear from Figure 9 is that there are two design families. To further explore the design architectures that have been arrived at, the non-dominated solutions are binned or categorized into families according to each major design variable: number of coils, coil radii, number of turns, and number of MLI layers. This filtering is presented in Figure 10:

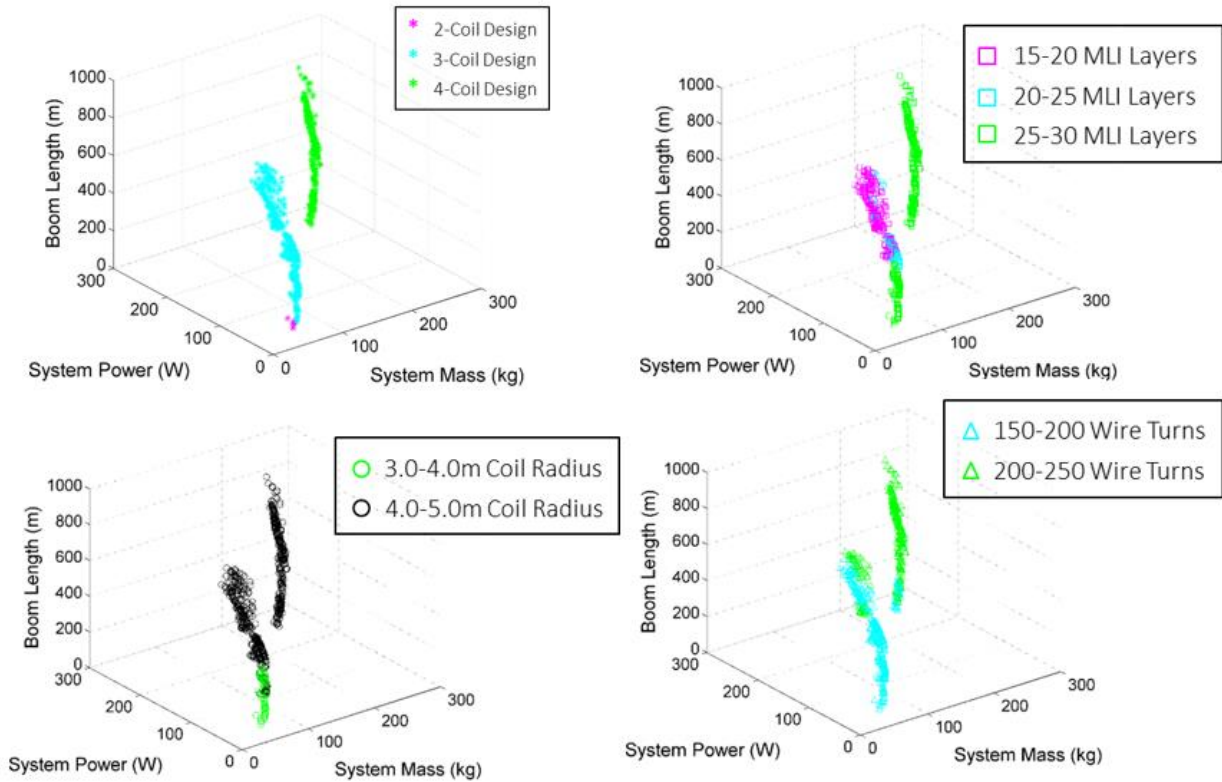


Figure 10: Two objective Pareto optimal design architectures

Future work to further improve this optimization includes the incorporation of dynamic stability conditions, which depend on multiple design variables and parameters and will more greatly constrain the design space, resulting in islands of infeasibility where designs do not satisfy the stability constraints. A comparison of the boom optimal mass versus length with other structural technologies like deployed trusses and inflatables will provide spacecraft designers with a clear picture of the mass savings possible with an electromagnetic structure. A possible fourth objective or additional constraint is cost, though it would be difficult to capture a cost function for such a low TRL technology.

4.3. Hardware Effort

An important risk-reduction measure for electromagnetic structures is hardware validation of the numerical models developed in the NIAC Phase I study and improved during the NIAC Phase II study. A couple of features of the model that are difficult to replicate in a ground laboratory environment are microgravity and moving superconducting coils. We simulate microgravity by installing coils on air carriages that float and approximate frictionless movement in the plane of a flat floor or table, but the cryogenic heatpipes developed for the cooling of superconducting coils in space would experience pooling due to gravity and thus not function properly if positioned axis perpendicular to the gravity vector, as in Figure 11.

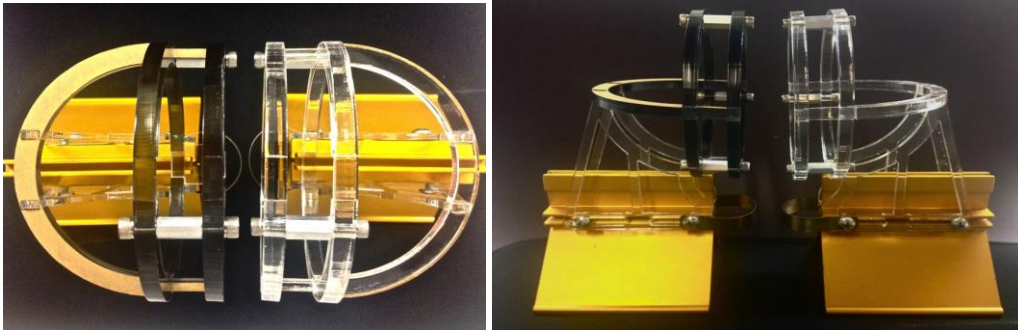


Figure 11: Acrylic coil holders for Separate deployment test on linear air track

As such, we decided to use resistive copper coils, as shown in Figure 12. This decision still fits the assumptions in the Phase I dynamic models, since the models account only for current and number of turns, so using copper coils allows us to experimentally test a (very small) portion of the low end of the (nondimensionalized) force range.



Material:	Copper magnet wire
Turns:	350
Inner Radius:	1.125 "
Outer Radius:	1.5 "
Voltage run:	~ 31.5 V
Current run:	~ 1.5 A

Figure 12: Copper coil as used in both Separate and Unfold deployment tests

It was quickly found that the available facilities were not adequate for the planned testing; the masses and inertias of the existing air carriages were too large for the relatively small forces between the copper coils to overcome. The setup for the unfold test is shown in Figure 13. **Appendix 6** gives an overview of the test setup and results. Future hardware validation could be done using the ground or ISS RINGS hardware (larger coils providing larger magnetic force).

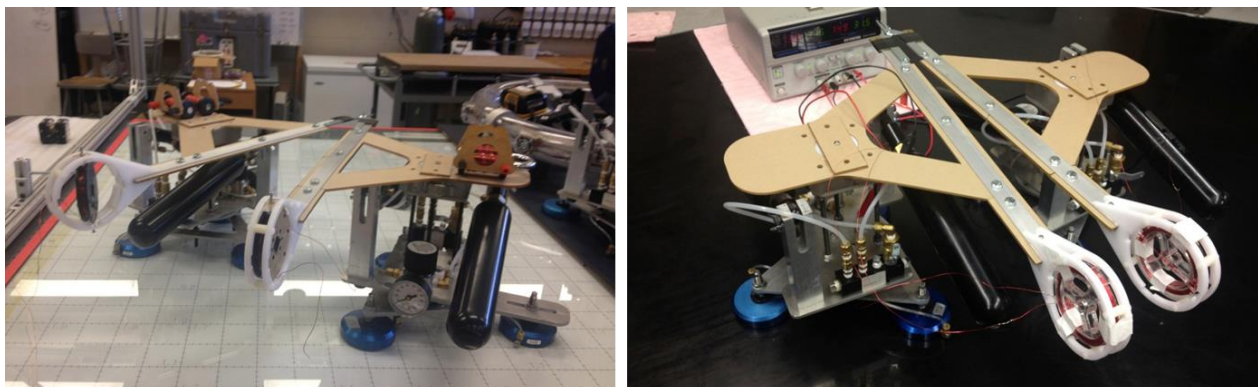


Figure 13: Unfold test setup using air carriages on glass table (left) and epoxy flat floor (right)

4.4. Stability Work

In the Phase I study, we modeled some of the initial deployment dynamics and equilibria of Separating and Unfolding coils. As part of the Phase II study and continuing on as the focus of a PhD dissertation to be completed in 2015, the static and dynamic stability of a multi-coil tethered boom around its equilibria are examined in detail, with the goals of being able to determine how much a given coil design can be perturbed from an equilibrium before becoming unstable and being able to assess the probability of certain designs to be stable within a certain range of perturbations. Stability of repelling coils is important to almost all of the structural functions identified for electromagnetic coils, and therefore our focus turned to this subject during the course of the study. **Appendix 7** presents the nomenclature of stability and some simple investigations of equilibria as a precursor to the more in-depth analysis to be included in the dissertation and delivered to NIAC as supplementary content to this report upon completion.

5. Flexible Cooling System

One of the major identified key enabling technologies for electromagnetic space structures was a thermal system capable of cooling the superconductors below their critical temperatures as well as deploying from a condensed stowed position within a launch vehicle. **Appendix 8** presents the full investigation by the University of Maryland Space Power and Propulsion Laboratory into the feasibility of designing and constructing a thermal enclosure capable of deploying in space for the operation of a large superconducting coil. The investigation was broken up into two primary components. The first part was an examination of the structure and deployment method. The second part was an examination of the thermal performance in order to evaluate the ability to maintain a superconducting coil at temperatures below the critical temperature of the superconductor.

The initial concept presented in the Phase II proposal was that of a flexible heatpipe with a bellows-like enclosure that would be deployed via magnetic self-force on the coil contained within, but it was quickly decided that another method of cooling would be necessary and that the thermal system would need to provide deployment force as well, since motion from the coil force alone would be impeded by the mechanical resistance to deformation of the thermal enclosure. After investigating different thermal management technologies, the use of a cryocooler to chill liquid nitrogen circulated as a vapor in a thin walled structure was chosen. The thin walled structure would house the superconducting coil in the core and be thermally insulated from incident radiation using a multi-layer insulation (MLI) blanket.

For each portion of the thermal enclosure, an analytical approach and experimental results are described. Multiple test articles were produced and analyzed, including a straight cylindrical segment for deployment force testing and toroids of varying major radii. The majority of the thermal testing involved the cooling of a torus with a major diameter of 1.85 m in a custom vacuum chamber.

The two primary test articles (straight cylinder and large torus) consisted of the same structural and thermally insulative components. Compression springs in the core of the enclosure used to produce a deployment force as well as internal structure for the vapor containment layers. The springs extended straight axially to span the distance between polyvinyl chloride (PVC) cuffs. The use of springs added a structural component that was still high flexible and capable of being stowed compactly inside a launch vehicle payload fairing.

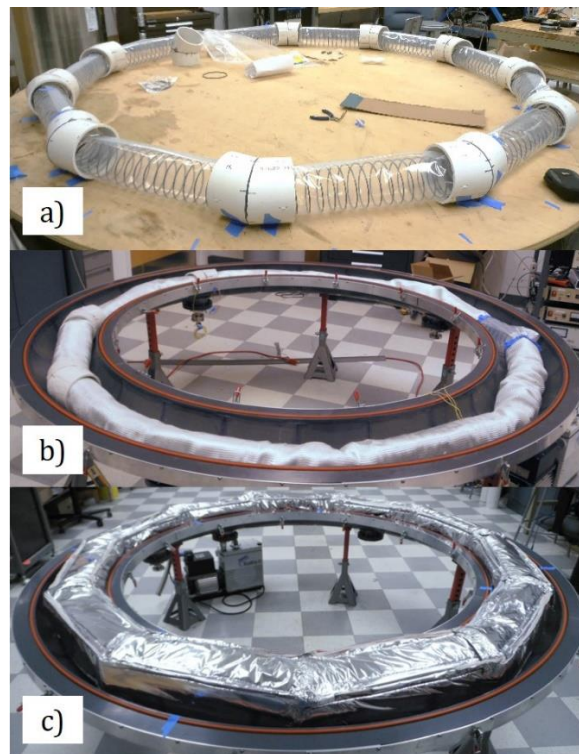


Figure 14: Lab-scale toroidal enclosure a) structure, b) vapor containment layers added, c) final test article with MLI

A double layer of plastic was reinforced using a biaxial fiberglass sleeve. For the large torus, both the fiberglass and plastic layers were a continuous pieces around the circumference, terminating at end caps that also acted as the inlet and outlet for the chilled nitrogen vapor. Panels of MLI blankets were applied to the outside of the PVC cuffs to provide passive thermal shielding from incident radiation. The MLI panels were not attached to each other along the length of a joint-to-joint segment, allowing the panels to extend outward and not affect the stowage size. This concept was an improvement on previous use of metal bellows for flexible cryogenic heat pipes in space missions which were heavy and lacked the ability to bend and collapse in the same way as can a thin-walled containment structure.

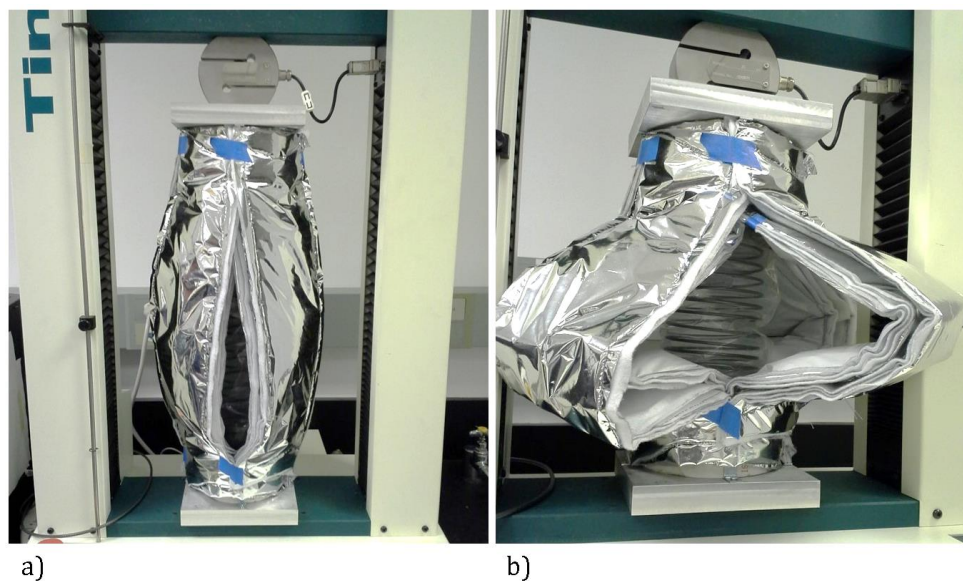


Figure 15: Deployment force test a) at the start of compression, b) near full compression

The force for deployment was found to be dominated by the spring with some contribution from the MLI and plastic layers. The motion of the straight segment was primarily linear for slow deployment rates. The same structure and material layers were included in a full torus enclosure and thermally tested in a vacuum chamber to investigate the ability to obtain sufficiently low temperatures for superconducting coil operation. The poor performance of the

insulative material and high vacuum chamber pressure resulted in much higher temperatures and heat transfer rates than what an expected on-orbit system would experience. However, analysis has shown that if the insulative material properties matched empirically derived values for conditions in high vacuum, the rate of heat extraction using forced nitrogen vapor flow would be sufficient given the capabilities of commercially available cryocoolers. The thin walled structure would be capable of stowing compactly for delivery to orbit and being deployed prior to operation using primarily spring force.

6. Future Work and Conclusions

This report concludes the work being conducted under the MAGESTIC NIAC Phase II, save for where it continues as graduate student dissertation work. Initially, we divided the barriers to feasibility that we wished to address into three categories: Power/Thermal, Dynamics/Control, and Integration (before we later recategorized the focus groups as Power Management and Control, Thermal, and Electromagnets and Deployment). As expected, the areas that demanded our focus were not necessarily the ones we initially predicted. In the following sections, the barriers to feasibility that were mentioned in the proposal are listed, with the one(s) that were focused on bolded and discussed.

Power/Thermal:

- **Cost: Complex power and thermal control, generation and management**
- *Cost:* Thermal vacuum chamber testing expenses
- *Performance:* Power for HTS operations needing to be taken from other subsystems
- **Key technology:** Low-power rigid and **flexible cryogenic heatpipes**
- *Performance:* Lower power cryocoolers

The primary focus of UMD during this study was the development of a flexible and deployable thermal enclosure and heat removal system, and despite some changes from the original bellows-like concept, a very innovative system was designed, though the limits of the laboratory environment have come to bear upon it. Cryocoolers still remain the most massive and power-hungry elements of the electromagnetic system.

Dynamics/Control:

- **Performance: Coil dynamics**
- **Performance: Stability of configuration**
- *Performance:* Position accuracy and knowledge
- *Performance:* Disturbances (Cryocooler vibration, solar pressure)

Coil dynamics and stability became a major focus in the second half of the study, when it was realized that a lack of stability conditions for electromagnetically supported and tethered structures could undermine the rest of the work if there proved to be instability that was uncorrectable by changes in boom design parameters or changes in connective hardware like tethers and attachment points. It is work that is continuing beyond the auspices of this study and will hopefully provide added support for the conclusions and ideas set forth in this and our Phase I report.

Integration:

- *Cost:* Cost may be uncompetitive with other structural options
- **Performance: Performance may be uncompetitive in multi-subsystem tradespace**
- *Performance:* Potential EMI, negatively affecting other subsystems on board or vice versa
- **Development Time: Technology roadmap may be too linear to allow missions to use less complex HTS structures as flight hardware prior to completion**

The performance and tradespace issue was taken up in two different studies – the multi-disciplinary optimization in **Appendix 5**, and the architectural tradestudy of large telescopes and their modularity and assembly in **Appendix 4**. More work needs to be done on detailed structural comparison to other structural technologies, but as was found in the

optimization study, it's difficult to really analyze structural performance without a stability or stiffness constraint, so it is our hope that further progress on the stability work will provide the tools to work more on such comparative studies.

The decision to focus on anchoring near-, mid-, and far-term applications drastically improved the technology roadmap, presented in its revised form below in Figure 16, allowing parallel development of tasks farther down the pipeline while gaining flight heritage and integration experience in earlier steps. Each of these applications still has fruitful analysis left to be done and would benefit from study in the context of an actual mission program.

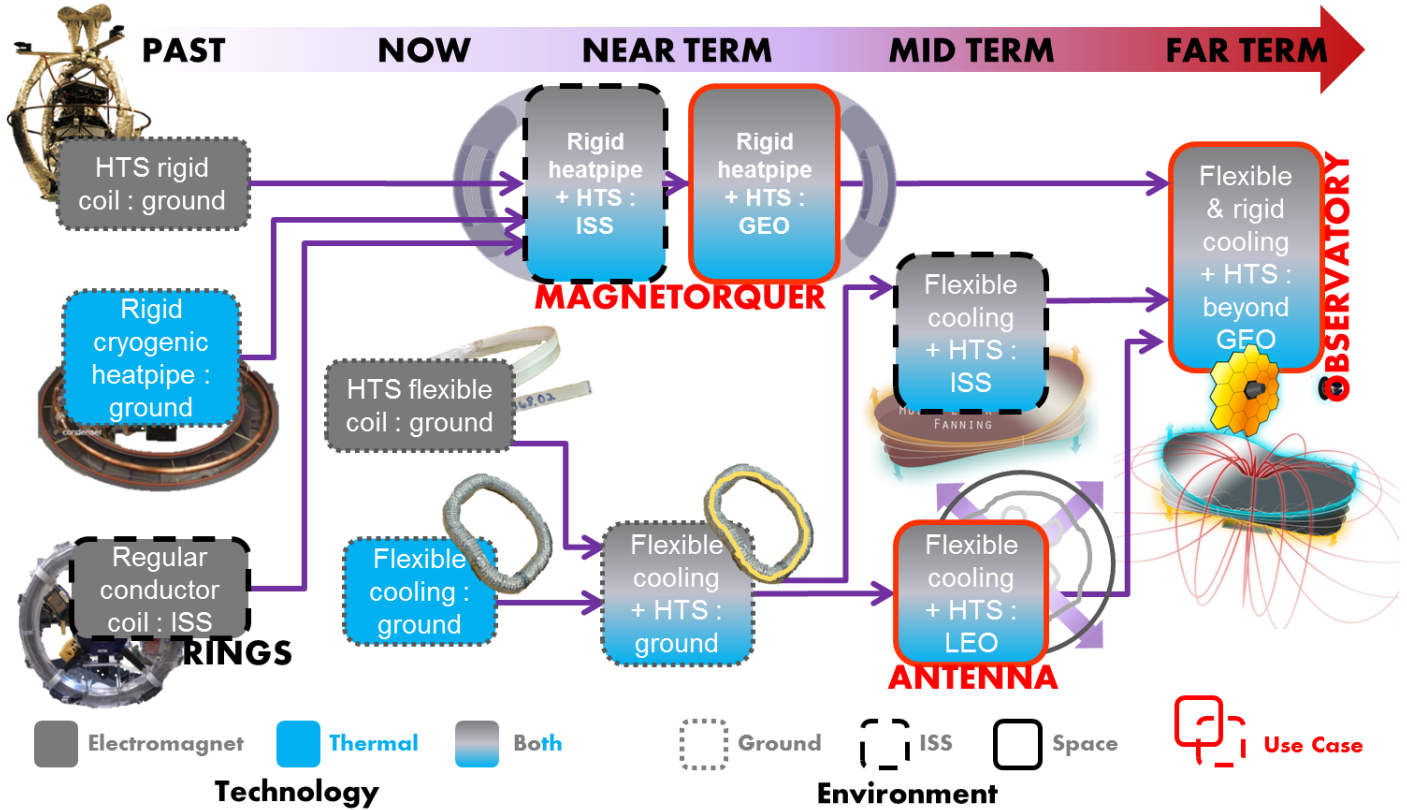


Figure 16: Revised technology roadmap featuring anchoring applications

REFERENCES

- [1] Gettliffe, G.V., Inamdar, N., Masterson, R., and Miller, D.W., "High-Temperature Superconductors as Electromagnetic Deployment and Support Structures in Spacecraft," NASA Innovative Advanced Concepts Phase I Final Report, October 2012.
- [2] <http://www.lhc-closer.es>, "Superconductivity in Short," [Online]. Available: <http://www.lhccloser.es/php/index.php?i=1&s=4&p=8&e=0>. [Accessed 21 May 2012].
- [3] SuperPower Inc., "SuperPower®2G HTS Wire Specifications," [Online]. Available: http://www.superpowerinc.com/system/files/SP_2G+Wire+Spec+Sheet_for+web_2012FEC_v2_0.pdf.
- [4] Sedwick, R. and Kwon, D., *Cryogenic Heat Pipe for Cooling High Temperature Superconductors with Application to Electromagnetic Formation Flight Satellites*, Massachusetts Institute of Technology, 2009.
- [5] Bruker Daltonics, "Record current with powder-in-tube superconductor," 2008.
- [6] Selvamanickam, V., "Coated Conductors: From R&D to Manufacturing to Commercial Applications," in *Superconductivity Centennial Conference*, Den Haag, the Netherlands, 2011.
- [7] Llambes, J., and Hazelton, D., "Advantages of Second-Generation High Temperature Superconductors for Pulsed Power Applications," in *Pulsed Power Conference*, Washington, DC, 2009.
- [8] SuperPower Inc., "SuperPower®2G HTS Wire Specifications," [Online]. Available: http://www.superpowerinc.com/system/files/SP_2G+Wire+Spec+Sheet_for+web_2012FEC_v2_0.pdf.
- [9] Fu, R.R., Weiss, B.P., Shuster, D.L., et al, "An ancient core dynamo on Vesta," *Science*, 338, 238 (2012).

Appendix 1: Mission Applicability and Risks

Mission Applicability and Risks

Rick Wesenberg, NASA Goddard Spaceflight Center

High-temperature superconductor (HTS)-based magnetics can function to configure structures or move spacecraft elements in space without requiring stiff interconnecting structure. This has some distinct advantages for space missions. The magnetic field scale, that is, magnetic field strength and shape at a specified distance, is a specification pertaining to a spaceflight application that determines the position and force/torque upon a spacecraft element. The magnetic hardware that generates the magnetic field has a number of design and operational characteristics that must be considered, including form, mass, magnetic field-induced stresses, temperature control, quenching, susceptibility to the space environment and safety. In space, support of HTS magnetics requires that key enabling technologies, such as thermal control, be at an appropriate technology readiness level (TRL).

Primary Structural and Ancillary Functions

The functions that could be implemented in-space include expansion and contraction, inflation and deflation, folding and unfolding, separation, deformation, reconfiguration and focus. The functions are conceptually depicted in Figure 1 and described in Table 1.

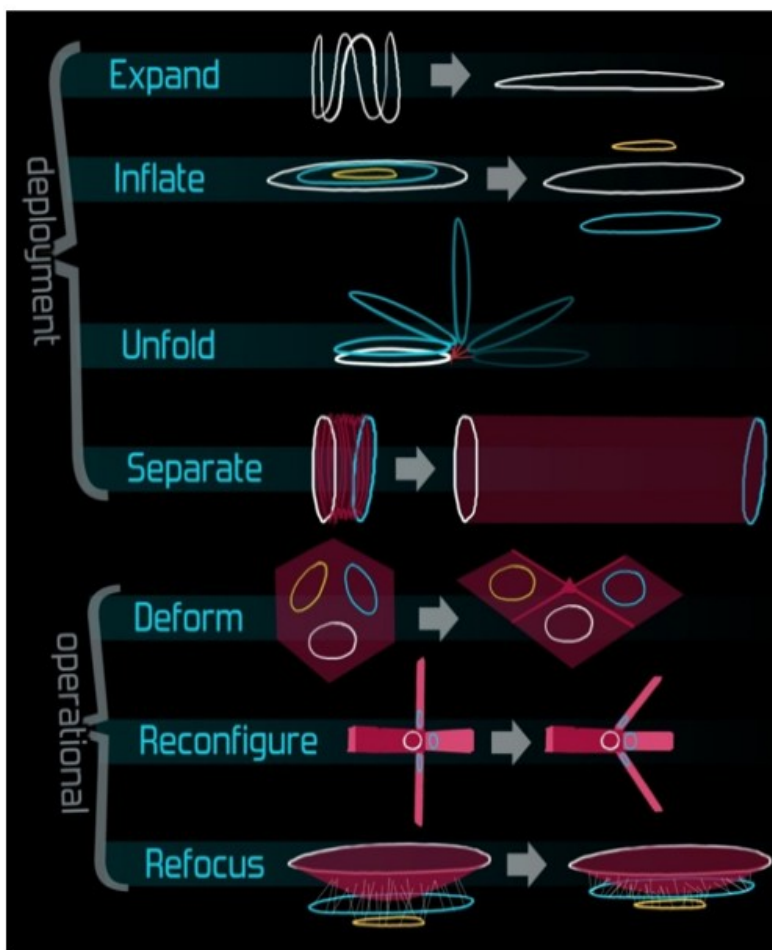


Figure 1: Functions that could be implemented in space using HTS magnetics.

Configuration	Description	Uses
1. Expand	A single, flexible HTS coil that is folded in its stowed position and uses its own magnetic field when current is run through it to expand to flat shape	To deploy and hold taut the perimeters of large membranous or flexible structures
2. Inflate	A 3D structure is built with two or more repelling coils in a configuration that creates a space between the two, inflating a structure (bounded by flexible walls or tethers)	To create a volume (such as a tank or toroidal perimeter) or to increase surface area (for solar cells)
3. Unfold	A series of coils embedded in or attached to a structure that is stowed folded and must be unfolded to become operational (folds can be hinges, springs, or couplings)	To deploy long, flat structures (like solar panels) or to take advantage of mechanical resistance at folds to create variable angles
4. Separate	Corollary of Inflate, in which two or more coils repel each other in series facing each other to separate two parts of a spacecraft; tethered or membranous structure connecting	To put large, controllable distance between two sensitive parts of spacecraft (such as a nuclear reactor, astronauts, optics, thrusters)
5. Deform	Two or more coils embedded in parts of the structure act magnetically on each other to temporarily deform or change the shape of the spacecraft	To reduce radar cross section (RCS) or adjust shape for avoidance of debris
6. Reconfigure	Corollary of Deform, except Reconfigured state is sustainable and lasting	To reduce drag profile or reconfigure satellite for different ConOps
7. Refocus	Two or more coils adjust their magnetic state such that an antenna or mirror is deformed to refocus it. Orientation of coils dependent on original shape of mirror or antenna.	To change focus lengths of mirrors and gains of antennas by reforming or moving their dishes, mirrors, or horns to Refocus them on a new target

Table I: Descriptions and uses for electromagnetic structural configurations

Electromagnet Forms

The geometry of the electromagnet or form is chosen to achieve a magnetic field with a particular intensity and shape over an application-specific characteristic distance. The pancake and solenoid form are the most developed because they can provide an intense field at a distance, as well as a uniform field within a solenoid's bore for applications which require such uniformity. These forms are common in particle accelerators, fusion research, medical devices, motors, maglev trains, and various industrial applications.

Pancake Form

The pancake form is characterized by a short coil stack height (in the along-axis direction) and a large radius in the cross-axis directions (height \ll radius). Since the central axis field decreases as radius grows,

$$B_x = \frac{\mu_0 IR}{4\pi(x^2 + R^2)^{3/2}} \oint ds = \frac{\mu_0 IR^2}{2(x^2 + R^2)^{3/2}}$$

B_x being the magnetic field strength along the x axis, if the center of the coil is $x=0$, R is the radius of the coil, I is the effective current (in amps, multiplied by the number of turns) and μ_0 is the vacuum permeability, or $4\pi * 10^{-7} N/A^2$.

A pancake coil has a weaker field strength along its axis than a solenoidal coil of the same effective current, but it has a larger cross section across which the field acts in the same direction, and can be useful in applications with limited dimension in height or which require coils of a larger radius for an optical pathway or other similar spatially-wide application.

Solenoid Form

The solenoid form is characterized by a tall coil stack height (which often means many turns of wire, though not necessarily more than would be found in a pancake coil since pancake coils are often wound significantly in the radial

direction) and small radius, or height \gg radius. The field at the center and along the central axis of a solenoid is stronger than that of a pancake coil of the same effective current but larger radius. Solenoids keep the field more uniform within the bore of the magnet, but there is a narrower cross section across which this field operates in the same direction.

Other forms

Space based structural applications will require a field intensity similar to that which exists in low-Earth orbit, of predictable shape that is stable over time. The environmental forces encountered will be weak: micro-gravitational, solar pressure, environmental magnetic fields and forces generated by differential heating of the structure due to solar and planetary insolation. The windings could be laid down with interesting geometries. For example, coils wound on a loose spiral on a plane, cone, ellipse or hyperbola could be optimal depending upon the application. This work primarily focuses on pancake coils, but further work could explore the interesting field shapes and resultant trajectories or actuations that could be implemented with different winding geometries.

For instance, a thought that was briefly explored but not focused on in the MAGESTIC NIAC Phase I work was the concept of etching or otherwise constructing concentric HTS rings across the surface of a flexible membrane in order to create a curved surface when adjacent rings are run with different direction currents.

HTS Design Considerations for Space Applications

HTS magnets are at the forefront of accelerator, fusion reactor and ground power distribution design. Space applications are at an early stage of development. The design tutorials developed for the US Particle Accelerator School [4] and "Case Studies in Superconducting Magnets: Design and Operational Issues" by Iwasa [3] are particularly useful. These tutorials are aimed at systems that provide uniform and intense magnetic field (1-15 Tesla) over lengths on the order of centimeters. The space systems considered herein will require magnetic field intensities of on the order of a Gauss (1/10000 Tesla) over 10's of meters, a very different scale of field strength from most ground applications of superconductors, which attempt to achieve high fields within the bore of the magnet. [Kwon SM, 50 Gauss at the core of the EMFF vehicle at $\frac{1}{2}$ max current]

Critical Temperature, Magnetic Field Intensity and Critical Current

There are two categories of superconductors: type 1 or low-temperature superconductors (LTS) and type 2 or high temperature superconductors (HTS). Type 1 superconductors are metallic elements and transition to superconducting state at liquid helium temperatures. They are diamagnetic up to a characteristic magnetic field density. Type 1 behavior is described by Bardeen-Cooper-Schrieffer (BCS) theory [1]. Type 2 superconductor materials may consist of one, two or many chemical elements. Type 2 superconductors are diamagnetic depending upon the temperature, current density in the conductor, and magnetic field intensity (see Figure 2). Type 2 superconductors have two characteristic critical magnetic field intensities, H_{c1} and H_{c2} , where $H_{c1} < H_{c2}$. Type 2 can be diamagnetic at magnetic field intensities less than H_{c1} , in a mixed state between H_{c1} and H_{c2} , and non-superconducting above H_{c2} . Type 2 behavior is described by Ginsburg, Landau, Abrikosov, Gorkov (GLAG) theory [2]. Type 2 critical temperatures range from about 10 K to more than 100 K. Many materials have been found to exhibit high-temperature superconducting behavior, but few have other material properties conducive to the commercial production of HTS cable [3].

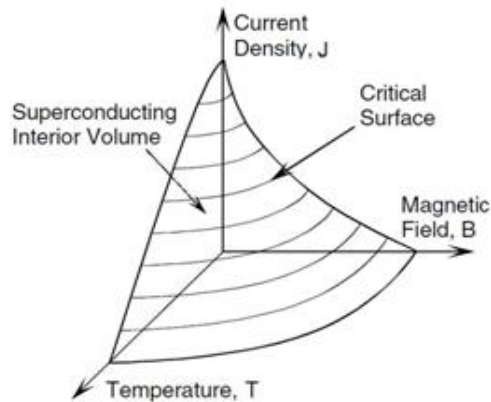


Fig. 2: Critical surface for high-temperature superconductor [1]

Operating Temperature

HTS systems can operate at higher temperatures (>20 K) than type 1 superconductors [4], and have much more performance margin (robust) when operated below their critical temperature as can be seen in Figure 2. While some HTS magnets can operate at liquid nitrogen temperatures, generally colder is better with the trade-off being feasibility, robustness, mass and power versus operating temperature.

Thermal Control

HTS magnets and cabling must be maintained below their critical temperature for the desired maximum field intensity at the position of the cable and the maximum desired current density. Some cable designs include a cryogen path inside the cable. The approach pursued in this work uses a flexible cryogenic sleeve to surround the HTS conductor. The cryogen employed will depend on the required operating temperature. A wide variety of space qualified cryocooling equipment exists. Large scale sterling heat pumps have been space qualified for converting heat to power.

Multi-Electromagnet Interaction

The magnetic field intensity is a critical factor in the state of an HTS superconductor. Configurations that use more than one HTS magnet and where there are other magnetic field sources, man-made or environmental, must be taken into account. Note that HTS can be fully superconducting, in a mixed state, and non-superconducting depending upon magnetic field intensity, critical current and temperature. The design must comport with the critical surface of the HTS material using appropriate margin for variation in the operating conditions of the system. For instance, it's also important to note that the rated critical current of a length of HTS wire is an upper bound on the critical current of the actual magnet system once wound; the critical current of the magnet is always somewhat lower than the critical current of the wire, all other conditions remaining equal. This is because of turn-to-turn interactions, the bending of the wire, how carefully the wire is handled during manufacturing of the system, and other factors which all reduce the critical current of the magnet. It is difficult to predict how much lower the critical current of a magnet will be than its wire. Therefore, it is wise to operate with a fair amount of margin in the design of the magnet to insure that the required magnetic fields for an application can be reached.

Quenching

HTS magnets are much less susceptible to quenching than Type 1 superconductors. This is because they have a higher critical temperature and because of the small safety margin due to the mixed Meissner effect that Type II superconductors exhibit. If a section of a Type I superconductor slightly heats when operating near its critical surface, thus breaching it, it quenches immediately from full operation. If a section of an HTS coil warms slightly, it goes into a mixed state. Resistance increases, but if it is cooled before the critical surface is breached, it returns to a superconducting state. The mixed state gives the system some warning to redirect magnetic energy elsewhere if quenching is inevitable. However, both types of superconductor quench immediately if any section of their wire breaches the critical surface. Unlike Type 1 superconductors, local heating due to high energy particles colliding with HTS superconductors do not appear to cause failures[3]. HTS system operating temperature should be colder than the critical surface to provide margin.

Magnetically Induced Stress

Many thousands of materials have been shown to exhibit high-temperature superconducting, but only a few are suitable for the production of HTS conductors and cables. Fewer yet are in commercial production [4]. They tend to be combinations of several chemical elements with material characteristics similar to ceramics that are then engineered as tapes or cables. Compact HTS coils carrying high currents that produce high intensity magnetic fields for accelerators can produce high local magnetic stresses. HTS conductors sheathed with stainless steel or copper have been designed for that environment [3]. However, space applications to develop large-scale but low intensity magnetic fields may be able to avoid the high magnetic stress and thus the mass of the sheathing. The sheathing does provide some quench risk reduction; should the system quench, the copper sheathing on the SuperPower 2G HTS wire gives the system about 1 second to redirect the magnetic energy that is being converted to heat to a location that can handle that much heat energy. However, given the lack of convective cooling and mass restraints on heat sinks in space, this amount of quench “protection” may not be worthwhile if the chosen method for quench protection is operation well below the critical surface. This would be an active trade in any space system using HTS magnets.

HTS System Failure Modes

The failure modes of the HTS magnet components are being vetted as ground applications are developed and deployed. There would be significant differences between ground and space system designs, and space systems have not been developed to the level required level to establish system level failure modes and effects.

Availability and Cost

Availability of HTS tapes and cables is limited at present and the cost is high because of the difficulty and cost of fabrication. Investment to service commercial applications, such as power distribution, will reduce this problem. Custom conductors and cables as required for space applications may remain scarce and costly because low demand does not make investment production of such items economically feasible.

Environmental Susceptibilities of HTS

Radiation Hardness

HTS superconducting magnets designed for accelerators and fusion reactors must survive high neutron fluxes for many years. These designs typically do include some shielding. The flux levels expected in most space applications are much less (neutrons, electrons and charged particles). However, the materials, components and sensors used to fabricate a space HTS magnetic system will still need to be radiation qualified for the mission environment. The hardness of control electronics and power supplies is a concern but no different than for other system electronics.

Vibration and Shock

HTS magnets for ground applications are very robust with respect to vibration, shock and mechanical stress. The HTS material itself is usually brittle, so that it is subject to magnetic stress, vibration and shock unless the conductor/cable is designed to mitigate these effects. The configurations required for space applications that provide low intensity fields at a distance may be somewhat less robust and much lower mass. These designs will require qualification in the same way as other spacecraft mechanical and structural components.

Micrometeorite Damage

HTS magnets for ground application are very robust with respect to penetration because of their sheathing. The configurations required for space applications that provide low intensity fields at a distance may be more susceptible because lower magnetic field stress may obviate the need for massive sheathing. If a micrometeorite penetrated and damaged the HTS conductor, that section may enter a resistive state causing the magnet to quench. This may be an area of concern, depending on the micrometeorite flux and the shielding due to surrounding structure and the configuration of the HTS coil. The HTS component would have to be armored to mitigate micrometeorite damage depending upon the shielding from surrounding structure. The cooling system of an HTS coil must also anticipate and compensate such impacts and/or punctures.

Materials degradation

Materials degradation for HTS magnetic systems is a concern, but no more so than for any space system. The HTS components themselves should be stable over time but other materials used for the HTS cable are at issue. Materials compatibility within a particular system design will require close attention.

Thermal Cycle/Shock

HTS materials tend to be brittle and may be more subject to thermal cycle and shock than more familiar metal alloys. Though designed for a cryogenic environment, there may be a limitation on the number of temperature cycles beyond some threshold temperature maximum and minimum depending on the HTS material.

Contamination Control

HTS magnets are not susceptible to contamination but may be sources of contamination in space. The magnetic stress to which the HTS coil is subjected may cause rubbing and shaking producing particles. The coil structure and materials may be a source of volatiles or may trap them in the windings complicating bakeout. Protocols will have to be developed to clean the HTS conductors, bake them out and encapsulate them when required. These protocols will be similar to those required for motor and transformer windings which have similar issues.

Hazards and Safety Considerations

Hazards to Humans

Direct exposure of the whole body to static magnetic fields below 2T is not directly harmful to human beings. However, movement in high fields can cause nausea and disorientation. Exposure of limbs of up to 8T is acceptable. High fields may displace implanted medical devices made of metal, and may upset pacemakers and similar devices. Metal objects can be propelled with extreme force in the vicinity of high magnetic fields, causing injury [17][18][19]. Space based HTS magnetic systems may require keep-out cages in areas where the magnetic field intensity present a risk to human EVA activity.

Hazards to Equipment

The residual and background magnetic fields on spacecraft are usually minimized to improve the performance of sensors such as magnetometers. Magnetometers are used for attitude sensing with respect to known, stable environmental magnetic fields surrounding planets and as science instruments. The magnetic field intensity close to an HTS magnet may cause loose metallic objects to suddenly accelerate with sufficient force to cause damage to equipment. Structure could be subjected to high magnetic field induced stress. High magnetic fields can damage some data storage media and could upset inductors and some mechanisms. Current could be induced in conducting loops (some types of antennas) that spin thereby cutting the magnetic field.

Handling

An HTS magnetic system does not present a high static magnetic field hazard until it is powered on. In the off state, risks are similar to other space-borne mechanical and electrical systems. In the on-state, operational safety is at issue.

Operational Safety

While on, HTS magnetic systems will generate high static magnetic fields, will require generation of and will host large electrical currents that can present a hazard to humans. The fields generated can disrupt medical devices imbedded in the human body. The rapid acceleration of metallic objects may cause penetration of space suits and other critical equipment. Blunt trauma and penetration of the human body could occur. The area around the magnet where high fields are generated may have to be caged for safety.

Future Missions and Potential HTS Uses/Benefits

In this section, the application of HTS magnetics to space missions is examined from a systems engineering perspective in the classical sense, an attempt "to shorten the time lags between scientific discoveries and their applications, and between the appearance of human needs and the production of new systems to satisfy these needs [Hall, 1962]." The objective is to identify potential advantages and risk issues with the application of HTS magnets in space.

Approach and Objectives

Public documents on existing space missions and proposed missions and their timeframes were reviewed identifying key mission driving requirement(s) and possible roles for HTS and potential benefits. The synergy with other developing technologies was considered as well as the development of collaborating technologies required to apply HTS magnetics. From these analyses we established a set of use cases. The timeframe for each mission was classified as near-term or within five years, mid-term or more than 5 but within 15 years, and beyond 15 years. The missions studied are summarized in Table II.

Mission	Agency	Time Frame (years)			Driving Requirement	Form ¹	Potential HTS Application
		< 5	5 - 15	> 15			
JWST	NASA	•			Uniform Low temperature	P	Thermal shield deployment & shape maintenance
OpTIIX	NASA	•			In-space robotic telescope assembly	P	Fine grained angular & linear momentum control
RBR	USAF		•		Generation of EMIC waves	P	Large, rotating multi-turned coil in Earth orbit
Euclid	ESA		•		Thermal stability to preserve alignment	P	Solar Array/thermal shield deployment
NASA	WFIRST		•		Thermal stability to preserve alignment	P	Solar Array/thermal shield deployment
Asteroid Capture	NASA		•		Angular/linear momentum control	P	Controlling position and angular momentum of asteroid without grappling or bagging
LISA	NASA		•		Relative position and attitude of 3 SC formation	P	Fine grained angular & linear momentum control of robotic maintenance SC
NEAT	NASA		•		2 SC telescope configuration & reconfiguration	P S	Fine grained angular & linear momentum control of 2 SC
IXO	NASA		•		Post-launch, expands 12.1 m to place instruments at focus	S	Embedded HTS mechanism to support stray light cover expansion
ATLAST	NASA		•		Thermal stability to preserve alignment	P	Solar Array/thermal shield deployment
Assembly at Libration Point	NASA			•	Robotic assembly of sub-assemblies	P	Fine grained angular & linear momentum control for assembly
Starshade	NASA			•	Deployment and shape maintenance of starshades	P	Deployment and edge shape mechanisms
Telescope arrays	NASA			•	Robotic tending to sustain and maintain	P S	Fine grained angular & linear momentum control of robotic maintenance SC
Magnetic Shielding	NASA			•	Deployment and positioning of magnetic shield components	P S	Fine grained angular & linear momentum control for robotic assembly; structural support

¹ P=Pancake, S=Solenoid, P|S=Pancake or Solenoid

Table II: Summary of case studies of existing and proposed space missions.

Based on Table II, potential uses in-space for HTS magnetics are captured in the following uses cases:

1. The **deployment and shape maintenance** of an extended surface such as a thermal shield, star shade, solar array or solar sail;
2. **Fine grained attitude and position control** of a group of associated elements such as a constellation of spacecraft, between non-interconnected elements of an observatory, of a swarm of assembly robots, cargo and astronauts in EVA around a spacecraft or space station;
3. **Angular and or linear momentum control** of objects without the use of grapple, nets or bags; objects such as asteroids, cargo and EVA astronauts (particularly during an emergency);
4. **Expanding metering structures with/without light shields** employed on structures that are compressed for launch but expand in space.
5. The **modulation of the charged particle fluxes** in a magnetosphere or to shield a spacecraft or space station.

The use of HTS magnetics for charged particle shielding is deemed out-of-scope for this study.

Use Case 1: Deployment and shape maintenance

An in-space facility (e.g. observatory, space station or depot facility) is launched and located either in LEO, GEO, a Libration point, or deep space. Deployment and shape maintenance of a large shaped surface is required. Typical applications:

- A thermal shield that is approximately the same size as the facility. The driving requirements for the thermal shield are the wavelengths to be shielded, the temperature across the facility must be ($< TBR$ Kelvin), and the maximum temperature gradient ($< TBR$ kelvin/m). Depending upon the requirements, the number of layers, coatings and the accuracy and precision of the thermal shield shape may complicate the thermal shield design. Thermal shields are common elements of observatories that have an optical bench requiring temperature control. The complexity of the thermal shield increases with shield effectiveness, maximum acceptable thermal gradient, shield size, mass, testability and deployment approach. The JWST thermal shield is unusually complex because of the low optical bench temperature required and the thermal shield size.
- A flexible solar array (TBR sq meters) must be deployed to provide power. The shape and flatness of the array and temperature must be $< TBR$ Kelvin to achieve desired power output. Flexible solar arrays are often used on modern spacecraft. They can be used for deep space low-thrust engines by sizing them to account for reduced solar insolation and degradation at end-of-mission. Deep space missions may require very large solar arrays.
- A star shade used as an occulter, usually circular with a diameter of TBR meters that must be deployed on a separate spacecraft a long distance from the rest of a stellar coronagraph. The shape, particularly the shape of the edge of the occulter must typically remain within TBR mm of the theoretical ideal shape.
- A solar sail must deploy to provide thrust and/or torque/trim to a spacecraft or space station. The required thrust is TBR Nt/sq m and the sail mass density must be no more that TBR gm/sq m. A solar sail could be deployed using HTS magnetics alone together with shaped memory materials. It may be possible in the future to use a material with photo-voltaic properties to initialize the HTS magnetics.

There may be a point where the size of the deployed area may necessarily make using traditional mechanisms too complex, massive, untestable and unreliable. HTS may conceivably provide a way to do deploy large surface arrays where the mass and general complexity would scale linearly with size.

Use Case 2: Fine grained attitude and position control

An observatory consisting of several spacecraft operating together or alternatively, a structure (e.g. space station, observing array or large deep-space exploratory vehicle) consisting of modules that must be assembled is launched and located either in LEO, GEO, a libration point, or deep space. Typical applications include:

- The control and maintenance of the relative attitude and position control of spacecraft in formation or non-contacting parts of an observatory at short distances from each other. The relative attitude shall be within TBD arc sec, each axis, of the desired attitude. The spacecraft must stay within a distance of $X \pm \Delta x$ of each other
- Assembly of modules of a structure in a self-assembly mode or using assembly robots. The relative location must be maintained to within TBD mm, each axis, of the desired location. Force and torque at assembly points must be controlled within specified limits.
- The attitude control of a single spacecraft using magnetics in the presence of a weak or intermittent natural magnetic field (e.g. magnetosphere).

Linear momentum control is traditionally provided by thrusters. Angular momentum control may be provided by thrusters, torque wheels and magnetics in various combinations. For example, when a predictable natural magnetic field of sufficient strength is present, magnetics may be used for angular momentum control or with torque wheels; the magnetics can be used to de-saturate the wheels. When a predictable natural magnetic field of sufficient strength *not* is present, thrusters may be used for angular momentum control or with torque wheels; the thrusters can be used to de-saturate the wheels. If a predictable artificial magnetic field of sufficient strength could be provided with a local area; magnetics could be used within that area for linear and angular momentum control within the artificial field or in combination with thrusters or torque wheels. This would be particularly useful for assemblages of elements in space, for example, spacecraft formation, assembly robots or self-assembling modules, and observatories that consist of several pieces flying in formation. The proposed ESA Near Earth Astrometric Telescope (NEAT) mission consists of a telescope

and the focal plane separated by 40m flying in formation. The telescope moves around the focal plane to point providing whole sky coverage in 20 days. Fine control is required for wave front metrology. The traditional approach would be to use booms, or to use two formation flying spacecraft each with a portion of the observatory using thrusters and wheels for position and attitude control. With HTS, a master slave configuration can be envisioned. The master portion could include a complete ACS system including thrusters, while the slave portion may require only non-HTS magnetics, or wheels and use the HTS field to de saturate the wheels and provide distance control. Eliminating thrusters on the slave portion would be a significant reduction in cost, complexity and mass. Similar optimizations could be done with self-assembling modules or assembly robots. No thrusters would mean no expendables and, if low-thrust would otherwise be employed, a large power sub-system would not be needed. HTS magnetic torque rods could increase the distance over which the robots or self-assembling modules could function. HTS magnetic torque rods could eliminate the need for thrusters and mission-life limiting expendables where the natural magnetic fields are too weak.

Use Case 3: Angular and or linear momentum control

An in-space facility (e.g. observatory, space station or assembly point) is launched and located either in LEO, GEO, a libration point, or deep space. There is a need to stop and reorient a tumbling object (e.g. module, astronaut, observatory, space debris, or asteroid) near the facility. The concept is to use an HTS magnetic field to control the angular and/or linear momentum control of a tumbling object without grappling; a space tug. The object's tumbling must be damped by the imposed HTS field. The tumbling must respond to the imposed damping field naturally, by design, or by imposition of a magnetic field axis. Consider a mission to capture and redirect a 7-10 m diameter asteroid into a stable orbit using a robotic spacecraft. The most recent mission concept envisions a single spacecraft with a deployable "capture bag. Depending on the composition of the asteroid, the impinging field may be sufficient to de-tumble the asteroid. If the asteroid is non-magnetic, robot magnetic stanchions or harpoons could be attached. The facility that produces the HTS field could then slowly and predictably damp the rotation of the asteroid. This approach could be used in concert with solar pressure by changing the surface albedo of the asteroid in an appropriate way. The same basic HTS concept would work by design with assembly modules, docking vessels and astronaut EVAs. While HTS magnets are now being deployed for accelerators, fusion research and medical devices, they have not been used in space. The time required to qualify an HTS magnetic system for spaceflight for this application is on-the-order of 5-10 years.

Another concept for asteroid mitigation missions that would not necessarily require detumbling the asteroid is a magnetic asteroid tug. The asteroid would need to be ferromagnetic and either not tumbling with an oriented magnetic dipole moment, or not already possessing an oriented magnetic dipole moment. A magnetic tug would be equipped with a strong directional HTS magnet that would either act to attract the magnet via its preexisting dipole moment or induce a time-variant alignment within the ferromagnetic core towards the HTS magnet.

A magnetic tug is directly comparable to a gravitational tug, since both system concepts involve a vehicle that is not physically interacting with the asteroid but rather maintaining proximity and inducing some sort of force to pull the asteroid in a desired direction.

Use Case 4: Expanding metering structures with/without light shields

An observatory with an expanding or telescoping section is launched and located either in LEO, GEO, a Libration point, or deep space. The telescoping section or metering section must be covered with an expanding stray light shield that must not bind, tear or develop more than TBR holes all smaller than TBR mm after expanding/contracting TBR times. The reliability must be TBR or better. Expanding booms based on shaped memory elements (e.g. springs or thermally activated materials) are used for this application today. HTS could extend these designs, enabling larger structures that could actively re-align after deployment. An HTS-only boom design without tension or shaped memory materials may reduce the risk of binding or damaging the light shield. The HTS magnet system could be turned-on during re-configuration or re-alignment and then turn-off to avoid affecting instruments sensitive to varying magnetic fields.

Use Case 5: Modulation of the intensity of charged particles

This use case is described further in Appendices 2 and 3, but a spinning, DC, TBR m diameter magnetic loop antenna emitting ULF or VLF waves can be used to change the paths of charged particles around the Earth's geomagnetic field lines such that they precipitate out into the Earth's upper atmosphere at the end of their arc instead of bouncing back along the field line. In order to precipitate out electrons specifically, Whistler waves (frequencies in the kHz range) can be used; electromagnetic ion cyclotron (EMIC) waves with frequencies less than 10Hz can be used for both protons and electrons. Radiated power of TBR W is needed to precipitate a noticeable amount of radiation, TBR coils radiating TBR W being required to actually reduce the proton population completely in TBR years.

Pros and cons

The advantages, disadvantages and risks to each application is summarized in Table III below. Since all of the components for a space based HTS system are in an early phase of development (TRL < 3), low-risk means that a prototype with similar function exists and has been shown to function and perform as required; medium-risk means that a prototype is in development and there is no reason to expect that the component will not function and perform as required; and high-risk means no prototype exists or a prototype does exist but *has not* functioned or performed as required.

	Deployment and shape maintenance	Fine grained attitude and position control	Angular and linear momentum control	Expanding metering structures with light	Modulation of charged particle flux
Pros	<p>HTS could be integrated within the deployed material eliminating the need for a complex support structure.</p> <p>Reduced structure would reduce the mass of the system employing a deployed shield.</p> <p>Passive cooling may be possible providing a very simple deployment mechanism and supporting thermal control.</p> <p>Simple deployment system with few and testable failure modes (in principle)</p> <p>Not subject to thermal gradients that cause alignment to fluctuate over time. In principle, very stable.</p> <p>Dynamically reconfigurable (if used without permanent locking mechanism)</p>	<p>Fine grained attitude control using non-superconducting magnetics has been available for decades. Very low technical risk.</p> <p>Assembly robots and cargo would not require thrusters and associated expendable propellant; no refueling.</p> <p>Lower mass than long extended booms and less subject to failure (in principle).</p> <p>Not subject to thermal gradients that cause alignment to fluctuate over time. In principle, very stable.</p> <p>Does not use expendable propellant. Does not contaminate near-by space.</p>	<p>Simpler and safer way (compared to capture bags and lassos) to de-tumble and/or re-direct an asteroid or other uncontrolled mass.</p> <p>Can be applied to fragile masses so as to minimize breakup of the mass, preserving the mass and maintaining safety of operations.</p> <p>Re-usable. A bag or lasso may be one-time use.</p> <p>Simple safety system for capturing and collecting EVA astronauts that are incapacitated.</p> <p>Simpler and safer way to dock vehicles in space.</p> <p>Much faster than using albedo and light pressure to modify an objects motion. Does not require application of albedo changing material</p> <p>Does not use expendable propellant. Does not contaminate near-by space.</p>	<p>Not subject to thermal gradients that cause alignment to fluctuate over time. In principle, very stable.</p> <p>Feasible for metering structures 10's of meters in length. Can be sized to correct for some perturbing forces.</p> <p>Simple deployment system with few and testable failure modes (in principle)</p> <p>Reduced structure would reduce the mass of the system.</p> <p>Reliability should, in principle, be higher than for equivalent mechanism.</p> <p>In principle, capable of multiple deployment/retraction cycles without concern for bearing wear and other mechanism reliability issues.</p>	<p>HTS current capacity required for EMIC wave emission at desired amplitude</p> <p>HTS flexible enough to stow in launch vehicle fairing</p> <p>HTS coil experiences radial tensioning, maintaining circular shape</p>
Cons	<p>Cost, mass and power for the HTS magnetic field generation system.</p> <p>Residual magnetic field (when HTS is off) could upset some sensors and other systems.</p> <p>Loss of current and/or thermal control over a portion of the HTS magnet may cause quenching that may result damage to the HTS magnet.</p> <p>Fine spacing control of the layers of a deployed material, critical for thermal shields and similar applications, has not been demonstrated.</p> <p>Use in an external magnetic field like the Earth's geomagnetic field effects a magnetic torque on the magnet.</p> <p>Stable structural designs are much fewer (if any) than traditional configurations due to instability of repelling magnets</p>	<p>Cost, mass and power for the HTS magnetic field generation system.</p> <p>Residual magnetic field (when HTS is off) could upset some sensors and other systems.</p> <p>Loss of current and/or thermal control over a portion of the HTS magnet may cause quenching that may result damage to the HTS magnet.</p> <p>Use in an external magnetic field like the Earth's geomagnetic field effects a magnetic torque on the magnet.</p> <p>Use in an external magnetic field like the Earth's geomagnetic field effects a magnetic torque on the magnet.</p>	<p>Cost, mass and power for the HTS magnetic field generation system.</p> <p>Residual magnetic field (when HTS is off) could upset some sensors and other systems.</p> <p>Loss of current and/or thermal control over a portion of the HTS magnet may cause quenching that may result damage to the HTS magnet.</p> <p>Procedures for the magnetic capture and control of masses has not been demonstrated. Safety of operations implications.</p> <p>Requires that the object to be controlled have a magnetic axis that can be excited by the imposed magnetic field. A natural object may not have a usable axis and imposition of one using harpoons or other means may be</p>	<p>Cost, mass and power for the HTS magnetic field generation system.</p> <p>Residual magnetic field (when HTS is off) could upset some sensors and other systems.</p> <p>Loss of current and/or thermal control over a portion of the HTS magnet may cause quenching that may result damage to the HTS magnet.</p> <p>Spinning of antenna may make an active cooling system not function due to centripetal acceleration of coolant outwards</p>	<p>Cost, mass and power for the HTS magnetic field generation system.</p> <p>Strong DC field may upset some sensors and other systems.</p> <p>Loss of current and/or thermal control over a portion of the HTS magnet may cause quenching that may result damage to the HTS magnet.</p> <p>Spinning of antenna may make an active cooling system not function due to centripetal acceleration of coolant outwards</p>
Risks	<p>Space application oriented HTS wire cables and related technology do not develop because there is not enough call for it and thus insufficient funds to support development.</p> <p>Performance of HTS system is hard to predict due to damage to the HTS material during manufacturing, launch and from micrometeorite damage.</p> <p>Failure modes of HTS systems for space application are not understood and vetted. It is difficult to predict HTS system lifetime.</p> <p>Some HTS materials with otherwise desirable performance qualities prove too brittle to survive the launch environment and/or limit lifetime on off or warm cool cycles.</p> <p>HTS cables and wire designed for ground applications are suitable for space application but use a material that cannot survive in a particular space environment.</p> <p>No stable configurations of tethered electromagnetic coils in space may exist.</p> <p>Methods for current maintenance have been demonstrated but the systems may not be applicable to space application.</p>	<p>Space application oriented HTS wire cables and related technology do not develop because there is not enough call for it and thus insufficient funds to support development.</p> <p>Performance of HTS system is hard to predict due to damage to the HTS material during manufacturing, launch and from micrometeorite damage.</p> <p>Failure modes of HTS systems for space application are not understood and vetted. It is difficult to predict HTS system lifetime.</p> <p>Some HTS materials with otherwise desirable performance qualities prove too brittle to survive the launch environment and/or limit lifetime on off or warm cool cycles.</p> <p>HTS cables and wire designed for ground applications are suitable for space application but use a material that cannot survive in a particular space environment.</p> <p>No stable configurations of tethered electromagnetic coils in space may exist.</p> <p>Methods for current maintenance have been demonstrated but the systems may not be applicable to space application.</p>	<p>Space application oriented HTS wire cables and related technology do not develop because there is not enough call for it and thus insufficient funds to support development.</p> <p>Performance of HTS system is hard to predict due to damage to the HTS material during manufacturing, launch and from micrometeorite damage.</p> <p>Failure modes of HTS systems for space application are not understood and vetted. It is difficult to predict HTS system lifetime.</p> <p>Some HTS materials with otherwise desirable performance qualities prove too brittle to survive the launch environment and/or limit lifetime on off or warm cool cycles.</p> <p>HTS cables and wire designed for ground applications are suitable for space application but use a material that cannot survive in a particular space environment.</p> <p>No stable configurations of tethered electromagnetic coils in space may exist.</p> <p>Methods for current maintenance have been demonstrated but the systems may not be applicable to space application.</p>	<p>Space application oriented HTS wire cables and related technology do not develop because there is not enough call for it and thus insufficient funds to support development.</p> <p>Performance of HTS system is hard to predict due to damage to the HTS material during manufacturing, launch and from micrometeorite damage.</p> <p>Failure modes of HTS systems for space application are not understood and vetted. It is difficult to predict HTS system lifetime.</p> <p>Some HTS materials with otherwise desirable performance qualities prove too brittle to survive the launch environment and/or limit lifetime on off or warm cool cycles.</p> <p>HTS cables and wire designed for ground applications are suitable for space application but use a material that cannot survive in a particular space environment.</p> <p>No stable configurations of tethered electromagnetic coils in space may exist.</p> <p>Methods for current maintenance have been demonstrated but the systems may not be applicable to space application.</p>	<p>Space application oriented HTS wire cables and related technology do not develop because there is not enough call for it and thus insufficient funds to support development.</p> <p>Performance of HTS system is hard to predict due to damage to the HTS material during manufacturing, launch and from micrometeorite damage.</p> <p>Failure modes of HTS systems for space application are not understood and vetted. It is difficult to predict HTS system lifetime.</p> <p>Some HTS materials with otherwise desirable performance qualities prove too brittle to survive the launch environment and/or limit lifetime on off or warm cool cycles.</p> <p>HTS cables and wire designed for ground applications are suitable for space application but use a material that cannot survive in a particular space environment.</p> <p>No stable configurations of tethered electromagnetic coils in space may exist.</p> <p>Methods for current maintenance have been demonstrated but the systems may not be applicable to space application.</p>

Legend
Low Risk
Medium Risk
High Risk

Table III: Pros, cons, and risks of HTS implementation in various use cases.

References

References

1. Bardeen, J., Cooper, L. N., Schrieffer, J. R., "Theory of Superconductivity", *Physical Review*, 108 5 1957.
2. GLAG reference.
3. Iwasa, Yukikazu, "Case Studies in Superconducting Magnets: Design and Operational Issues", 2nd Ed., Springer 2009.
4. Ramesh, G., "High Temperature Superconductor (HTS) Magnet R&D and Designs", *US Particle Accelerator School, University of California-Santa Barbara, June 23-27, 2003*.
5. <http://www.lhc-closer.es>, "Superconductivity in Short," [Online]. URL: <http://www.lhc-closer.es/php/index.php?i=1&s=4&p=8&e=0>. [cited 10 September 2014].
6. P. Seibelhaus, J. Decker, "James Webb Space Telescope: Project Overview", *IEEE A&E Systems Magazine*, July 2007.
7. "Super-tough sunshield to fly on the James Webb Space Telescope", *Defense & Aerospace Business* (Dec 10, 2008).
8. "Northrup Grumman Completes Fabrication of Sunshield Deployment Flight Structure for JWST", *Space Daily*, December 13, 2011.
9. Stockman, P. "James Webb Space Telescope", November 15, 2002.
10. "New Worlds, New Horizons in Astronomy and Astrophysics", NAP, 2010.
11. Carpenter et. al., "OpTIX: An ISS-based Testbed Paving the Roadmap toward an Next Generation, Large Aperture UV/Optical Space Telescope", *UV Astronomy: HST and Beyond Conference*, 2012.
12. Postman, M., "Advanced Technology Large-Aperture Space Telescope (ATLAST): A Technology Roadmap To The Next Decade", NASA, 2009.
13. Lawson, P. R., "Exoplanet Exploration Program Technology Plan Appendix: 2012", JPL Document D-77698, 2013.
14. Bock, J et. al, "CMB Technology Roadmap for the NASA Inflation Probe", *NASA Physics of the Cosmos Analysis Group*, 2011.
15. Crooke, J., Gunderson, J., Hagopian, J. Levine, M., "Developing a NASA Strategy for the Verification of Large Space Telescope Observatories", *Procof SPIE*, 6271, 2006.
16. Levine, M., Soummer, R., "Overview of Technologies for Direct Optical Imaging of Exoplanets", JPL, March 2009.
17. "NASA Occupational Health Program Procedures w/change 2 (5/17/2013)", NPR 1800.1C, paragraph 4.17.3.8.
18. "ICNIRP Guidelines: On limits of exposure to static magnetic fields", *Health Physics* 96(4), 2009.
19. "Static Magnetic Fields Quick Reference Sheet", WWW.AIHA.ORG, 2014.

Appendix 2: System Concept Development for Multifunctional Electromagnetically Actuated and Supported Space Structures

IAC-14- D1.2.2
SYSTEM CONCEPT DEVELOPMENT FOR MULTIFUNCTIONAL ELECTROMAGNETICALLY ACTUATED
AND SUPPORTED SPACE STRUCTURES

Gwendolyn V. Gettliffe

Massachusetts Institute of Technology, United States, gvg@mit.edu

Prof. David W. Miller

Massachusetts Institute of Technology, United States, millerd@mit.edu

Spacecraft designers have long been faced by two contradicting objectives: reduce spacecraft mass to minimize prohibitive launch costs while simultaneously making structures as dimensionally large as possible to maximize their performance. This research will pursue mass minimization via tradespace exploration and concept maturation for a new electromagnetic structural subsystem that also performs other spacecraft bus and payload functions. With the support of consecutive Phase I and Phase II grants from the NASA Innovative Advanced Concepts (NIAC) program, we are investigating the use of interacting high-temperature superconducting electromagnets for actuation, positioning, and support of large space structures. Our goal is to determine the feasibility and viability of electromagnetic space structures, and our assessment is grounded in this paper by analysis of three specific mission applications: torque coils for satellites in geostationary orbit, a large deployed loop antenna for precipitation of protons out of the inner Van Allen belt with electromagnetic ion cyclotron (EMIC) waves, and a next generation space-based observatory with electromagnetically deployed and formation flown elements. These mission applications were selected to provide a maturation pathway for superconducting technology in space and to represent a cross-section of potential multi-functional allocation to the electromagnetic structure subsystem.

I. INTRODUCTION

The environment and logistics of getting to space present many challenges to spacecraft designers. The enormous cost per unit mass to launch a spacecraft is so high that reducing both the dry and the wet mass of the spacecraft are key design objectives. At the same time, making the spacecraft dimensionally larger to reap the performance benefits of large spacecraft is a competing objective.

The competing objectives of mass minimization and size maximization can be captured in a general sense by an objective minimizing the linear or areal density of a structure (the mass per unit length or area). A structural technology that can reduce the density of a structure would enable larger structures for the same mass as a traditional structure and the same size structures for less mass. The two structural approaches to a lower-density spacecraft are to create a lower density structural material or system (inflatables, composites, isogrids, and tensegrity structures all pursue this approach) or to have the structural subsystem perform additional, or “ancillary” functions generally allocated to other subsystems, thus eliminating the need and the mass of additional hardware to provide those ancillary functions and capabilities.

This research combines both of the aforementioned approaches and proposes an electromagnetic subsystem that performs structural functions as well as some of the duties of other traditional spacecraft subsystems. Some

unique capabilities also exist that can only be performed by an electromagnetic subsystem. We specifically look at superconducting electromagnets and the advantages that high-temperature superconductors (HTS) offer.

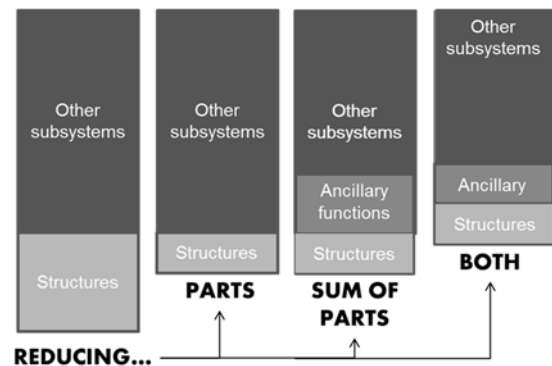


Fig. I: Visualization of approaches to reducing the mass of a space system.

Fig. I displays generalized approaches to reducing spacecraft mass: reducing the “parts” (for instance decreasing the mass of the structural subsystem, which is on average 20% of spacecraft dry mass [1]), reducing the “sum of the parts” (having one subsystem perform ancillary functions), or reducing both (decreasing subsystem mass while also having it perform ancillary functions). The end goal of this research is to determine which of these three approaches electromagnetic structures are capable of providing.

In this paper, we focus on the structural capabilities of an electromagnetic subsystem but also introduce and discuss “ancillary” capabilities of such a subsystem. After broadly discussing these capabilities, we discuss them in the context of three selected applications that were selected to provide a maturation pathway for superconducting technology in space and to represent a cross-section of potential multi-functional allocation to the electromagnetic structure subsystem: torque coils for satellites in geostationary orbit, a large deployed loop antenna for precipitation of protons out of the inner Van Allen belt with electromagnetic ion cyclotron (EMIC) waves, and a next generation space-based observatory with electromagnetically deployed and formation flown elements.

II. BACKGROUND

The most extensive use of electromagnets in space to date has been magnetorquers, coils of wire used to torque a spacecraft against the Earth’s geomagnetic field in order to dump momentum from the spacecraft’s attitude control components (discussed in more detail in Section IV.I). With superconducting wire becoming cheaper, more flexible, and more manufacturable, the idea of using superconducting electromagnets for relative actuation of spacecraft and spacecraft elements became feasible.

Electromagnetic formation flight (EMFF) [2, 3, 4, 5, 6] is a concept that would use three orthogonal superconducting coils per vehicle to provide a fully steerable electromagnetic dipole that can actuate against the field from another such vehicle and dipole. A two-vehicle (3 degree-of-freedom each), liquid nitrogen-cooled air table testbed was created in 2003 by the MIT Space Systems Lab (MIT SSL) [3] to test the EMFF concept and develop controllers for such a system. Fig. II shows one of the two testbed vehicles with subsystem labels. For reference, the diameter of the coils is 0.9m.

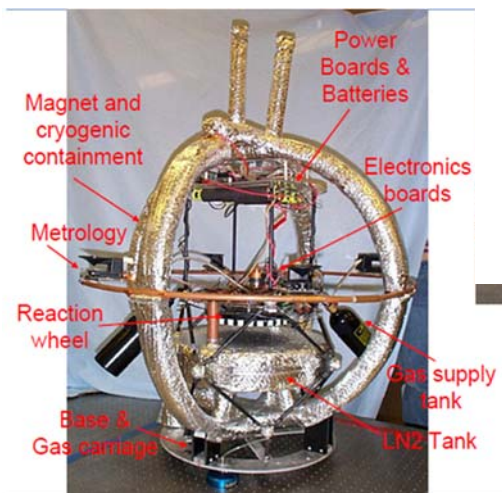


Fig. II: MIT SSL 3DOF EMFF testbed [3].

A microgravity EMFF testbed run by the University of Maryland and MIT SSL began operation on the International Space Station (ISS) in 2013-2014, called the Resonant Inductive Near-field Generation System (RINGS). RINGS used aluminium coils instead of superconducting coils and was limited to one coil per vehicle instead of three, using the thrusters of the Synchronized Position Hold Engage and Reorient Experimental Satellites (SPHERES) for steering of the vehicles’ electromagnetic dipoles. Since the governing equations of electromagnetic force are not specific to the type of wire (as discussed further in the next section), both the air-table testbed and the RINGS testbed contribute to the maturation of the EMFF concept. Fig. III shows one of the RINGS attached to a SPHERES unit on an air table.



Fig. III: A SPHERE outfitted with RINGS hardware in laboratory [7].

Electromagnetic tensioning of membranous or hollow structures has been proposed on multiple occasions, such as Zubrin’s “magsail” concept in which a large plasma wind sail is supported using a flexible HTS perimeter to magnetically repel itself into a flat circle and keep the sail under tension. For the initial deployment of such a sail, Zubrin ultimately settled upon a non-magnetic rotating boom system to deploy the sail via centrifugal force, citing “reliable deployment” as a key issue for magsails [8]. A NIAC study by Powell et al [9] discussed a “magnetically inflated cable” system for large space structures: flexible cables made of high-temperature superconducting wire expanding themselves magnetically, serving simultaneously as actuators, perimeter support, and standoff structures.

The applications discussed in this paper include a myriad of electromagnet configurations, from single,

rigid coils as in magnetorquers to flexible coils; tethered coils to free-flying coils.

III. ELECTROMAGNETIC CAPABILITIES

III.I Fundamentals

Electromagnets and electromagnetic structures as spacecraft components are enabled by the fundamental physical principles of electromagnetism, superconductivity, and the unique features of the space environment. This section briefly describes the underlying principles that enable HTS structures, including:

1. The generation of Laplace forces via interaction of a magnetic field and current
2. Superconductivity
3. Enabling characteristics of the space environment (microgravity and vacuum)

Laplace Forces

The resultant magnetic field at any point \vec{r} from a current-carrying wire can be described by the Biot-Savart law, integrating over the wire length (or coil circumference) where I is a constant current and μ_0 is the magnetic constant, $4\pi \times 10^{-7} \text{ N/A}^2$:

$$\vec{B}_i = \frac{\mu_0}{4\pi} \int_{\text{coil } i} \frac{I d\vec{l}_i \times \vec{r}_{ji}}{r_{ij}^3} \quad [1]$$

The force on another current-carrying wire placed in the magnetic field of the first one is called the Laplace force and is described by the cross product of the second wire's current segments with the field of the first wire, integrated over the second wire or coil:

$$\vec{F}_{ij} = I_j \int_{\text{coil } j} d\vec{l}_j \times \vec{B}_i \quad [2]$$

Parallel currents cause attractive forces while opposite currents cause repulsive forces.

Superconductivity

Superconductors are materials that conduct electrical current losslessly when isothermalized below a critical temperature T_c . Superconductors have zero resistivity, with negligible quantities when approaching their T_c . Every superconductor has a critical temperature, external magnetic field strength, and current density above which superconductivity ceases, as shown graphically as the "critical surface" in Fig. IV. The highest potential current density (while still remaining in the superconducting state) can be reached when the temperature and magnetic field are their lowest (though absolute zero is not quite possible) and so on for each of the three parameters. Superconductors enable HTS structures because they are able to generate much larger forces than regular conductor magnets can generate. The

larger forces are due to the superconductor's much larger current carrying capacity when superconducting, which translates to a larger distance over which superconductors can act upon each other for the same amount of mass. [7]

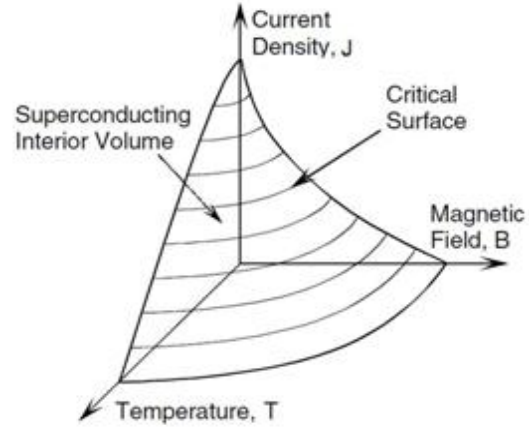


Fig. IV: Critical surface for high-temperature superconductor [10].

High-temperature superconductors, or HTSs, are those superconductors with T_c s above 77K, the boiling point of liquid nitrogen (LN2), enabling LN2 to be used as a coolant. The higher a superconductor's T_c , the less cooling it costs (in terms of power, storage, and consumables, for applications where a cryogen is not recycled).

III.II Structural

We consider structural capabilities in this work to be functions that traditionally fall to the structural subsystem to perform, such as deployment, support, and operational actuation functions. Electromagnetic coils can repel, attract, and even shear with respect to one another when energized, providing the forces and torques required for structural motion and support. Fig. V shows seven structural functions that can be accomplished by electromagnetic coils depending on their boundary conditions, whether the coils are rigid or flexible (a flexible coil's self-field exerts a force upon itself to flatten and tension the coil into a circular shape), and whether the functions are executed at the initial deployment of a structure or at a point later in the operational lifetime (respectively referred to as either the "deployment" or "operational" phase).

Table I (from Gettliffe 2012 [7]) describes the configurations shown in Fig. V and some of their potential uses on a spacecraft.

Configuration	Description	Uses
1. Expand	A single, flexible HTS coil that is folded in its stowed position and uses its own magnetic field when current is run through it to expand to flat shape	To deploy and hold taut the perimeters of large membranous or flexible structures
2. Inflate	A 3D structure is built with two or more repelling coils in a configuration that creates a space between the two, inflating a structure (bounded by flexible walls or tethers)	To create a volume (such as a tank or toroidal perimeter) or to increase surface area (for solar cells)
3. Unfold	A series of coils embedded in or attached to a structure that is stowed folded and must be unfolded to become operational (folds can be hinges, springs, or couplings)	To deploy long, flat structures (like solar panels) or to take advantage of mechanical resistance at folds to create variable angles
4. Separate	Corollary of Inflate, in which two or more coils repel each other in series facing each other to separate two parts of a spacecraft; tethered or membranous structure connecting	To put large, controllable distance between two sensitive parts of spacecraft (such as a nuclear reactor, astronauts, optics, thrusters)
5. Deform	Two or more coils embedded in parts of the structure act magnetically on each other to temporarily deform or change the shape of the spacecraft	To reduce radar cross section (RCS) or adjust shape for avoidance of debris
6. Reconfigure	Corollary of Deform, except Reconfigured state is sustainable and lasting	To reduce drag profile or reconfigure satellite for different ConOps
7. Refocus	Two or more coils adjust their magnetic state such that an antenna or mirror is deformed to refocus it. Orientation of coils dependent on original shape of mirror or antenna.	To change focus lengths of mirrors and gains of antennas by reforming or moving their dishes, mirrors, or horns to Refocus them on a new target

Table I: Descriptions and uses for electromagnetic structural configurations

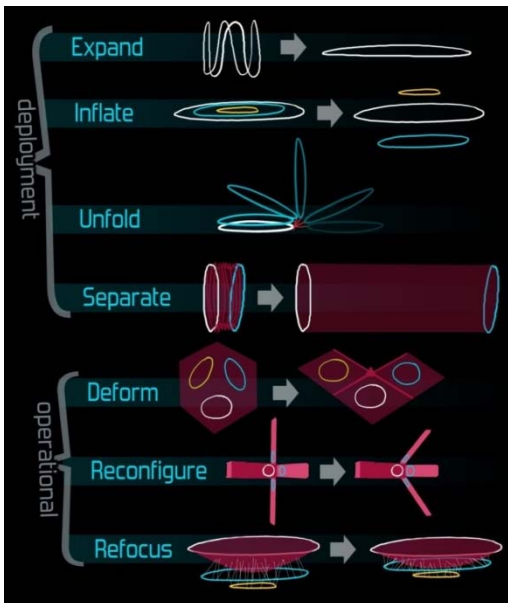


Fig. V: Electromagnetic structural functions and configurations [7].

III.III Ancillary

As described previously, ancillary capabilities or functions are those qualities that electromagnets naturally possess or provide which would normally be allocated to a (non-structural) subsystem or which will save mass from another subsystem. We will discuss here some ancillary capabilities of superconducting electromagnetic coils in particular.

Strong controllable electric and magnetic field: Superconducting electromagnets can carry large currents, translating to powerful magnetic (and electric) fields. Because the current is controllable, the field strengths are easily controllable as well (unlike with permanent magnets). For applications that require transmitting a signal (like an antenna) or perhaps deflecting particles (as in active radiation protection), such a field would be desired.

Naturally circular deployed area and/or tensioned perimeter: A flexible current-carrying loop or coil, when folded, experiences magnetic forces due to the interaction of its current with its own magnetic field such that it expands and is tensioned into a flat, circular shape. There are some stowed configurations of such a flexible coil that will end up in a non-circular shape, such as a figure-8, but with planning, a large circular area with natural

tensioning can be deployed from a stowed configuration. The self-force of such a flexible coil becomes weak at large sizes, so magnetic deployment can also be combined with strain energy or inflation to fully overcome any material resistance to deployment.

Consumable-free controllable actuation w.r.t non-contacting elements: Motion of spacecraft or spacecraft elements relative to one another is generally either a one-time only occurrence (pyrotechnics), requires motors and other connective hardware, or thrusters, which use up propellant. With electromagnetic formation flight, spacecraft can move with respect to one another without touching and without consumables (only electrical power). Electromagnets can also provide an external torque on the spacecraft when interacting with an external magnetic field such as the Earth's geomagnetic field.

Lossless energy storage: Superconductors, when below their superconducting critical temperature, operate without resistive losses. Energy in an electromagnetic coil persists indefinitely (save for small losses in non-superconducting elements of the circuit if any exist), making superconducting magnetic energy storage (SMES) a possible alternative to batteries. The lossless nature of superconductors also means that superconducting magnets are very low-power compared to non-superconducting magnets (though this difference is made up at least in part by the power requirements of cryocoolers if such devices are needed to bring superconductors below their critical temperature.

Performs as well or better in cold environs: Superconductors can handle a larger amplitude current at lower temperatures, meaning that for missions to outer planets or cryogenic missions, a superconducting electromagnet can store more energy and produce a stronger field if desired.

Low exported vibration and heat transfer: Electromagnetically-supported structures (which have mostly empty space between them instead of solid structures) minimize the conductive pathways between spacecraft elements, enabling better thermal and vibrational isolation for sensitive components. If the structures are formation flying (having no connective hardware), then heat transfer is completely limited to radiation.

Wireless power and/or data transfer: Exposure to a changing magnetic field induces a current in wire, which allows to power to be transferred wirelessly from coil to coil, as well as data if it is encoded within the signal.

In the following section's discussion of selected applications, these ancillary capabilities will be referred to and their role in the application discussed.

IV. SELECTED APPLICATIONS

In order to mature electromagnetic space systems, we have established a three-tier roadmap, each tier anchored by a selected application that further advances and proves electromagnet use in space. The tiers are near-term, mid-term, and far-term.

Near-term spans the time period between now and five years from now with the goal of achieving TRL 5 for high-temperature superconducting electromagnets in orbit and proposing a demonstration mission for electromagnetic structures. The near-term is focused on building flight heritage and further maturation of the technology from Earth-based concept to a functioning system on orbit, and the anchoring application is geostationary orbit (GEO) magnetorquers.

Mid-term spans the time period between five and fifteen years from now with the goal of enabling or enhancing new mission concepts that have heretofore been impossible or infeasible. The mid-term is focused on addressing technical feasibility barriers, starting with those associated with the anchoring application of a large deployed superconducting antenna.

Far-term spans the time period beyond fifteen years from now with the goal of using electromagnetic capabilities to imagine revolutionary mission concepts, reinventing how we imagine large spacecraft. Missions in the far-term, including the anchoring application of a large space-based observatory, will not just be enabled by but also defined by their use of electromagnetic systems. Therefore, it will be important to focus in the far-term on addressing barriers to the integration and operation of sometimes several different electromagnetic subsystems with each other and the rest of the spacecraft.

IV.I Near-term: GEO Magnetorquer

Spacecraft in low-Earth orbit (LEO) typically use reaction wheels or control moment gyros (CMGs) for attitude control and magnetic torque coils, or magnetorquers, to desaturate their wheels or gyros by causing an external torque to act on the spacecraft (the magnetic torque induced by the interaction of the Earth's geomagnetic field with the magnetorquer). In GEO, spacecraft generally require the use of thrusters (also used for stationkeeping) for the desaturation of their reaction wheels and/or CMGs because the Earth's geomagnetic field is significantly weaker at GEO than at LEO. GEO satellites are typically lifetime-limited by their propellant, and so a consumable-free desaturation method like magnetorquers would be hugely beneficial to GEO spacecraft lifetimes.

A quick way to approximate the strength of the Earth's geomagnetic field at a distance r from the center of the Earth is via the first-order dipole Earth model, wherein the field strength B falls off proportional to $\frac{1}{r^3}$, or:

$$|B| = B_0 \left(\frac{R_E}{R}\right)^3 \sqrt{1 + 3 \cos^2 \theta} \quad [3]$$

where B_0 is the mean strength of the geomagnetic field on Earth's surface, 3.12×10^{-5} T, R_E is the radius of the earth, and θ is the azimuth measured from the north magnetic pole. For comparison, the magnetic field strength at 42164 km from the center of the Earth (GEO) is 251.7 times weaker than the magnetic field strength at 6678.1km from the Earth's center (a 300km altitude orbit, LEO).

In addition to the weakness of the field at GEO, one thing the first-order Earth dipole model does not capture is the time-variance of the field at GEO, due to the interaction of the solar wind's interaction with the magnetosphere. Because the Earth dipole model does not capture this time-variance, it can only reliably be used to describe geomagnetic field strength out to about three Earth radii from the Earth's center [11].

We are focusing on one of these two barriers to the use of magnetorquers for desaturation at GEO; the issue of weak field strength can potentially be resolved via the use of superconductors. Prediction of the field strength over time is an active field of research for space weather scientists, and there exist several models for the geomagnetic and magnetospheric fields over time [11, 12, 13]. Another way of compensating for the uncertainty of the field is to design robust controllers for magnetorquers at GEO that can compensate for a lack of precise knowledge of the geomagnetic field strength at that location and time.

Magnetic torque τ on a current-carrying coil with magnetic moment μ in an external magnetic field B is determined by

$$\tau = \mu \times B \quad [4]$$

We can see from Eqn. 4 that the magnitude of magnetic torque is the product of the magnetic field strength and the strength of the magnetic moment of the coil; the same torque can be induced from a weak magnetic moment in a strong external field as can be induced by a strong magnetic moment in a weak external field. Since we cannot increase the field strength at GEO, we can instead increase the magnitude of the magnetic moment.

The magnetic moment μ of an air-cored current-carrying coil of area A , turns N , and current I is as follows:

$$\mu = NI\vec{A} \quad [5]$$

where the direction of \vec{A} is normal to the area enclosed by the coil, such that the current I is flowing counter-clockwise around \vec{A} . According to Desiderio et al [14], 3000-4000 Am^2 is a good estimate for the magnetic dipole moment needed from a torque coil for continuous magnetic momentum unloading for an average GEO spacecraft. A large magnetic moment can be provided with a) a large area, b) lots of turns, or c) a high current. Superconducting magnetorquers provide the latter.

Magnetorquers used on LEO spacecraft are typically wound with copper wire and are one of two form factors: large area, flat, air-cored coils (often wound around the perimeter of one of the spacecraft sides or solar arrays) or small area, tall, iron-cored coils (often called torque rods, with several placed orthogonally inside the spacecraft to provide desaturation in all axes). Ferromagnetic cores provide a stronger magnetic dipole than air cores because the core acts to concentrate the magnetic field lines, but torque rods are typically reserved for spacecraft with larger mass budgets, due to the large mass of iron cores. In this paper, we focus on large area, flat, air-cored torque coils wound with high-temperature superconducting (HTS) wire, but it would not be impossible to create an iron-cored HTS-wound torque rod.

Fig. VI shows for a given area of coil how many ampere-turns ($I * N$) are required to produce magnetic dipole strengths of 3000, 3500, and 4000 Am^2 :

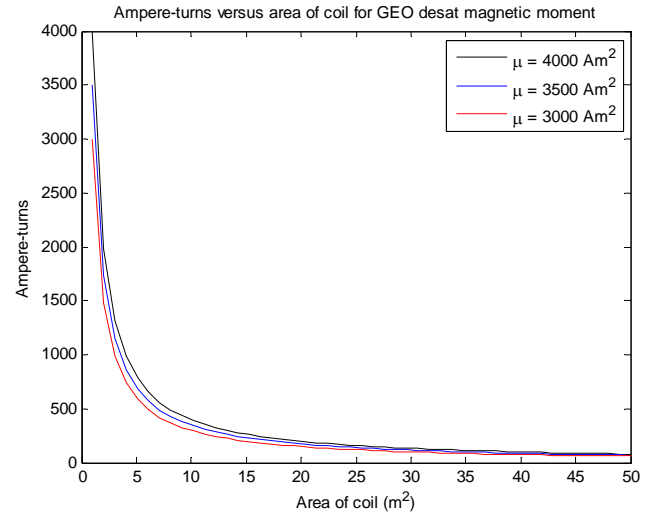


Fig. VI: Ampere-turns versus area of coil required for several example magnetic moments.

The knee in the curve is around $5m^2$ – larger areas do not save that many ampere-turns. $5m^2$ is also a reasonable area to assume that a GEO spacecraft can accommodate, so we will use $5m^2$ as our example coil

area going forward. Fig. VII assumes that the wire is carrying 150A (the critical current for the commercially available 6mm wide SuperPower HTS wire [15]) and shows how many turns would then be required for the same magnetic dipole strengths as in Figure VI.

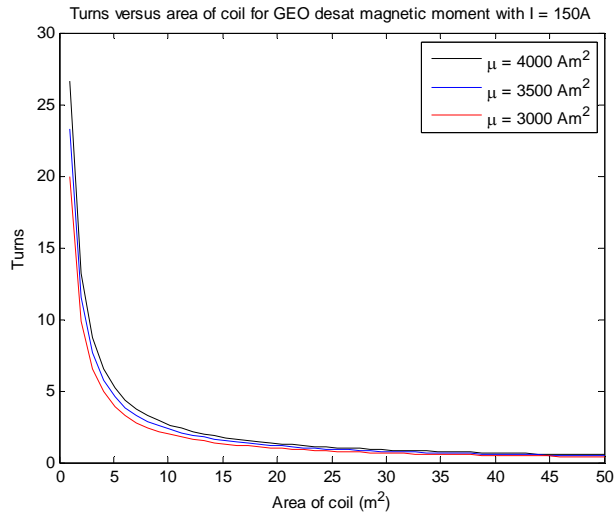


Fig. VII: Turns versus area of coil required for several example magnetic moments.

Fig VII shows that for $5m^2$, the number of turns with a current of 150A is roughly 5 turns. The mass of a 150A coil (using the density of the 6mm Superpower HTS wire) is shown versus the coil area in Fig. VIII.

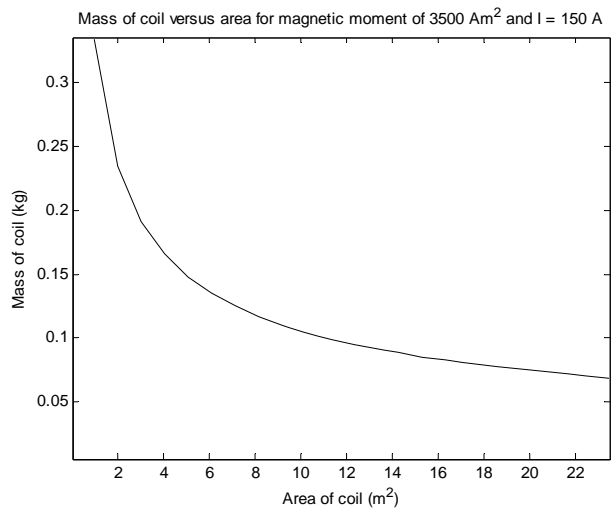


Fig. VIII: Mass versus area of coil required for a magnetic moment of $3500 Am^2$.

A mass of 0.14kg for a magnet capable of providing $3500Am^2$ is very low. Note that this value does not account for the hardware required to cool the coil to 77K with liquid nitrogen, which will add significantly to the

mass. Comparing a single turn coil of copper and one of HTS wire, both coils of the same mass and wire area, the HTS coil provides a magnetic dipole moment two orders of magnitude larger than that of the copper coil.

The copper versus HTS comparison is not just about mass of the coil, however, or many-turn copper magnetorquers would be used regularly at GEO. Even with heavy coils, the propellant savings would be still likely be worth the tradeoff. One of the defining characteristics of a superconductor is that when it is cooled below its superconducting temperature, the wire is virtually lossless. This allows a high-amperage current to pass through an HTS wire without melting it or losing any energy to heat. In contrast, copper is resistive and some of the electrical energy passed through it is converted to heat. Too many turns of copper (and no convection in the vacuum of space) would eventually heat a copper coil to its melting point. So, while a massive copper coil could theoretically provide the needed magnetic moment, it would require additional cooling hardware as well to evacuate the emitted heat, making adding extra propellant to the spacecraft the more reasonable of the two options for desaturation. Both HTS and copper coils requiring additional thermal hardware at GEO makes the choice between the two magnetorquer options simple.

Further work includes an analysis of how much propellant would be “saved” by using magnetorquers on a GEO spacecraft as well as a more detailed thermal comparison of HTS and copper magnetorquers.

IV.II Mid-term: EMIC Wave Antenna

The Van Allen belts are regions encircling the Earth in which the Earth’s geomagnetic field has trapped and concentrated energetic charged particles. The trapped particles come from cosmic rays, solar flares and storms, and other processes. There are two major Van Allen belts. The inner belt, which encompasses the equatorial region roughly between 0.2 and 2 Earth radii from the Earth’s surface (1,000-6,000 km altitude), comprises electrons and protons; the outer belt spans 3 to 10 Earth radii from the Earth’s surface (13,000-60,000 km) and comprises mainly electrons [16].

Charged particles are not healthy for spacecraft or humans as they can cause unwanted single event effects in spacecraft electronics and damage DNA in human cells, leading to cancer or other health concerns. Spacecraft in high LEO or highly elliptical orbits pass through the inner belt and are thus exposed to high dosages of radiation. Geostationary orbit is 35,786 km in altitude, so satellites in GEO are also constantly exposed to the particles trapped in the outer belt. A method for “cleaning” the trapped particles out of the Van Allen

belts would reduce the radiation dosage to current and future space missions.

The charged particles in the Van Allen belts travel in helical paths around the geomagnetic field lines and “bounce” back and forth along the lines, reversing directions at “mirror points” along the field line where the angle, or “pitch angle”, between the helical path and the field line is 90 degrees. If the mirror points occur in atmosphere dense enough that the charged particles collide with atmospheric particles, then the charged particles are absorbed by the atmosphere and are no longer trapped. Particles with mirror points at low altitudes (and thus will precipitate into the atmosphere within a few cycles) have pitch angles that fall inside an altitude-defined “loss cone” around the field line during the middle of a bounce [17]. Particles with equatorial pitch angles outside of the loss cone stay trapped around the field line unless an external influence such as interaction with a plasma wave “scatters” their pitch angle into the loss cone.

It has been observed that ultra-low and very low frequency waves (ULF and VLF) can scatter trapped particles into the loss cone, freeing them from the Van Allen Belts. Whistler waves (with frequencies of kHz) interact with electrons, while electromagnetic ion cyclotron (EMIC) waves (with frequencies less than 10 Hz) can interact with both protons and electrons, making them a good option for reducing the trapped radiation in the inner Van Allen belt [18]. A mission incorporating a large space-based antenna that could emit EMIC waves and begin precipitating inner belt protons would be both scientifically and economically valuable. This section will briefly discuss how superconducting electromagnets contribute to and enable the EMIC wave mission; for more in-depth analysis of the EMIC wave mission, antenna design and performance, see de Soria 2014 [18]. The following discussion includes a brief summary of the findings from the aforementioned paper.

A very large (30 m diameter) magnetic loop antenna was chosen for this application because of its very small radiation resistance in plasma compared to a linear dipole antenna. To prevent large voltages from forming across a static AC coil due to its enormous self-inductance, a rotating DC coil was selected, which in the far field (5000 km or so away from the antenna) has a dipole component equivalent to two static orthogonal AC coils if the rotation rate of the coil matches the desired frequency of its signal.

In order to radiate the power necessary to detect whether the EMIC wave technique works (25W with a 30 m diameter coil), high-temperature superconductors were selected. Cooling superconductors to colder temperatures increases their performance, as previously stated, but then the cryocoolers necessary to achieve such

temperatures demand more power and mass, so there is always a trade between power, mass, and performance when working with superconductors in space.

Additionally, a 30 m diameter antenna would not fit in a launch vehicle fairing and would need to be deployed somehow, likely via a combination of magnetic self-force, strain energy and inflation. Centrifugal force would not be ideal in the case of this antenna because it would mean inducing acceleration and motion around a different axis (normal to the plane of the coil) than the antenna should spin, which would stiffen it against efforts to spin it up around the correct axis (in the plane of the coil).

To date, only rigid heat pipes for the isothermalization of superconducting coils have been created [3]. A rigid heat pipe would not work for a coil large enough to need to be folded or otherwise stowed within a launch vehicle. In light of the difficulties of deployment and cooling, as part of our NIAC Phase II study, the University of Maryland Space Power and Propulsion Lab is developing a flexible vapour-cooling system for cooling superconducting coils to cryogenic temperatures. In addition, the cooling system uses strain energy (a compressed spring around the exterior of the tube) and inflation pressure (from the vapour) to assist deployment of a flexible coil.

A scientific proof-of-concept mission of the EMIC-wave antenna is possible with a smaller (5 m diameter coil) that doesn’t require deployment and can be rigid. However, demonstrating a flexible cooling and deployment system would be a big step towards creating a mission that could start removing radiation in measurable quantities.

IV.III Far-term: Observatory

Space-based observatories are by necessity complex and precise structures. Each successive observatory has increasingly stringent requirements and the observatory’s designers accommodate these requirements with often unique structures and solutions. Fig. IX depicts a notional “Next Next Generation Space Telescope” that incorporates many of the structural and ancillary capabilities mentioned in Section III.

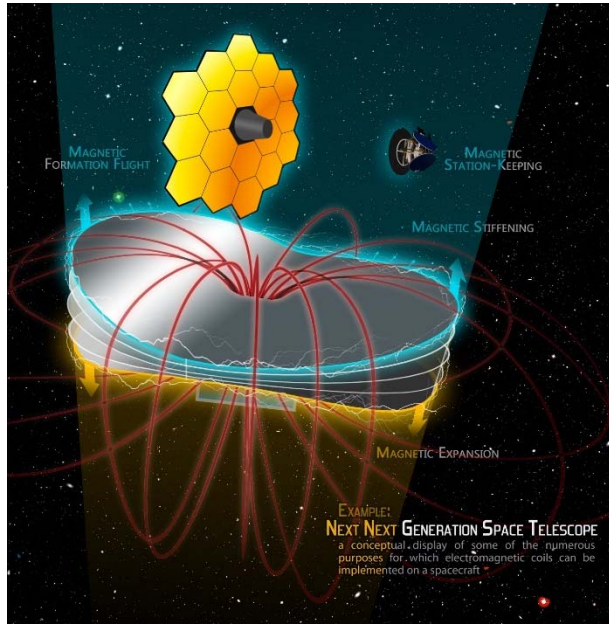


Fig. IX: Notional depiction of a “Next Next Generation Space Telescope” incorporating many structural and ancillary electromagnetic functions. [7]

Some of the uses incorporated in this futuristic observatory (or other variants upon it) are:

Sunshield/starshade separation and tensioning: Sunshields are structures found in cryogenic telescopes such as the James Webb Space Telescope (JWST) which has instruments that must be kept at cryogenic temperatures in order to observe in infrared. Fig. X shows a multi-layered sunshield where superconducting coils around the perimeter of the layers are tensioning the layers radially as well as repelling against each other to fan the layers apart. Referring back to the structural configurations shown in Fig. V, the sunshield depicted in Fig. X includes both Expand and Separate.

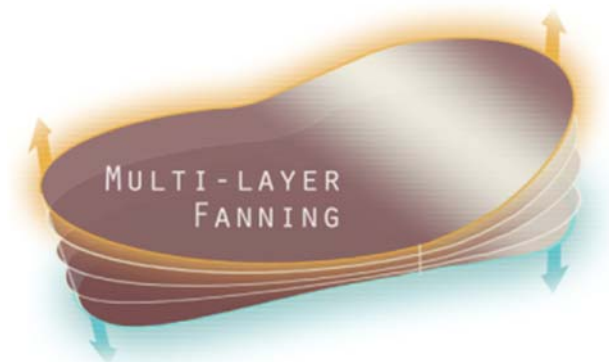


Fig. X: Electromagnetically tensioned multi-layer sunshield for a cryogenic telescope.

In a telescope wherein some of the spacecraft is kept at cryogenic temperatures, the ancillary capability of a superconducting magnet to perform better in cold environments could also be leveraged.

For an occulting telescope like the proposed New Worlds Observer [19], a starshade might be used – an enormous flower-like membranous structure positioned great distances away from the telescope itself in order to occult a star and allow for study of a planetary system around said star. A starshade is also a structure that could benefit from electromagnetic perimeter tensioning or deployment.

Positioning of optics: Fig. IX shows a telescope in which multiple parts of the spacecraft are formation flying with each other without any physical contact. In particular, formation flying the secondary mirror with respect to the primary mirror eliminates the obscuration of a tower joining the two as well as takes advantage of the thermal and vibration isolation ancillary capabilities.

Using an example of a telescope positioned at GEO, we can explore how strong the magnetic dipoles on each of the primary and secondary mirrors would need to be to provide the required force to keep the two optics aligned. We assume a primary mirror mass of 100,000 kg (could also include the rest of the spacecraft) and a secondary mirror mass of 5,000 kg. The distance between the two is 150 m. The center of mass of the two-body system is along the orbit, aligned with the origin of the coordinate system seen in Fig. XI below.

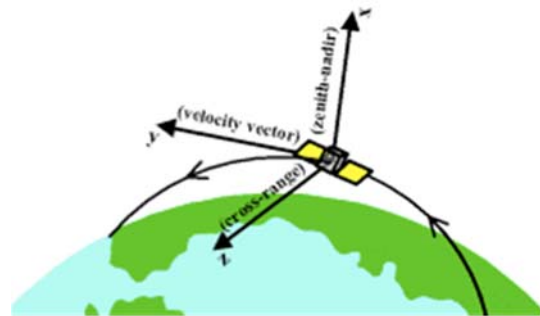


Fig. XI: Coordinate system of formation flying optics example. [20]

We would like to know the positions of the primary and secondary mirrors with respect to the center of mass of the system. Fig. XII shows the positions x_p and x_s of the primary and secondary mirrors respectively and the basic parameters of the problem.

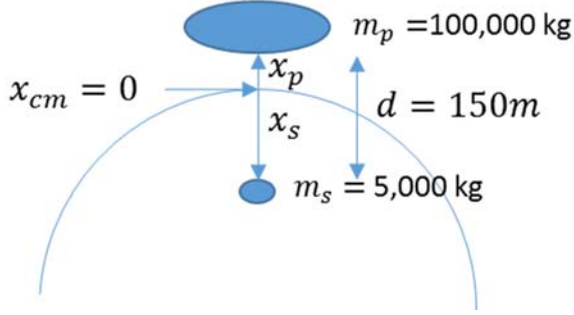


Fig. XII: Orientation of primary and secondary mirrors if they are separated in the x direction.

We are assuming a nominal orbit with no active orbit control, a spherical Earth (no J2 perturbation), and no drag, magnetic or solar pressure perturbations. The frame origin/center of mass is in a circular orbit and rotates about the z-axis once per orbit.

The center of mass of the system is at

$$\frac{m_p x_p + m_s x_s}{m_p + m_s} = x_{cm} = 0 \quad [6]$$

so solving for x_p and x_s ,

$$x_p = \frac{m_s}{m_p + m_s} d = 7.14m \quad [7]$$

$$x_s = -\frac{m_p}{m_p + m_s} d = -142.86m \quad [8]$$

Change x to y or z for cases where the mirrors are separated in those directions.

Considering the Hill's frame where n is the orbital rate = 7.29×10^{-5} rad/s (GEO) and a_x , a_y , and a_z are accelerations:

$$\begin{aligned} \ddot{x} - 2n\dot{y} - 3n^2x &= a_x \\ \ddot{y} + 2n\dot{x} &= a_y \\ \ddot{z} + n^2z &= a_z \end{aligned} \quad [9]$$

If the mirrors are separated in x direction:

$$\begin{aligned} \ddot{x} = \ddot{y} = \ddot{z} = \dot{x} = \dot{y} = \dot{z} = x = y = z = 0 \\ a_{x,s} = -3n^2x_s = 3n^2 \left(\frac{m_p}{m_p + m_s} d \right) \end{aligned} \quad [10]$$

$$\begin{aligned} F_{x,s} = m_s a_{x,s} = 3n^2 \left(\frac{m_p m_s}{m_p + m_s} d \right) = -F_{x,p} \\ = 0.0114 \text{ N (attraction)} \end{aligned}$$

If mirrors are separated in z direction:

$$\begin{aligned} \ddot{x} = \ddot{y} = \ddot{z} = \dot{x} = \dot{y} = \dot{z} = x = y = z = 0 \\ a_{z,s} = n^2 z_s = -n^2 \left(\frac{m_p}{m_p + m_s} d \right) \end{aligned} \quad [11]$$

$$\begin{aligned} F_{z,s} = m_s a_{z,s} = -n^2 \left(\frac{m_p m_s}{m_p + m_s} d \right) = -F_{z,p} \\ = -0.0038 \text{ N (repulsion)} \end{aligned}$$

If mirrors are separated in y direction:

$$\begin{aligned} \ddot{x} = \ddot{y} = \ddot{z} = \dot{x} = \dot{y} = \dot{z} = x = y = z = 0 \\ a_{y,s} = 0 = F_{y,s} = F_{y,p} \end{aligned} \quad [12]$$

We can see that separation in the x direction requires twice the force of separation in the z direction, but the x direction requires attraction while z requires repulsion. Magnetic attraction is inherently more stable than repulsion, but it's likely that the orientation will depend on the mission objectives. We see that there is no force required to keep the mirrors the desired distance apart when they are aligned along the velocity vector, which comes as no surprise.

The separation forces in x and z are small. We want to determine how large and/or massive the magnets attached to the formation flying mirrors would need to be in order to achieve these forces.

When the coils are in the "far-field", meaning at least 10 coil radii apart, they can be approximated as magnetic dipoles, for which the force between two parallel coils in repulsion or attraction is

$$|F| = \frac{3\mu_0\mu_1\mu_2}{2\pi d^4} \quad [13]$$

where is $\mu_0 = 4\pi * 10^{-7}$ N/A² as mentioned before and the magnetic moments of the two coils are $\mu_{1,2}$. Assuming that the two coils have the same magnetic moment $\mu_1 = \mu_2 = \mu_{12}$, we get that

$$|F| = \frac{6*10^{-7} * \mu_{12}^2}{d^4} \quad [14]$$

Inserting the material density and dimensions of SuperPower wire and solving for the magnetic moment in terms of the mass and radius of a coil, we get that the force of a SuperPower HTS-wound magnet is roughly

$$F_{SP} \sim \frac{128.3(MR)^2}{d^4} \quad [15]$$

where M is the mass of a single coil in kg and R is the radius of the coils in meters. Combining Eqns 10, 11, and 15, we get

$$(MR)_x = \sqrt{\frac{0.0114*150^4}{128.3}} = 212.09 \text{ kg-m} \quad [16]$$

$$(MR)_z = \sqrt{\frac{0.0038*150^4}{128.3}} = 122.45 \text{ kg-m} \quad [17]$$

We can see that the larger the coil on each of the optical elements can be, the less massive the magnet ends up being, making it clear that increasing the radius of the coil if possible is beneficial to the mass budget (but the maximum radius may be capped by launch vehicle parameters or other environmental constraints.)

This analysis is valid for other formation flying elements, not just optical elements.

Formation flying sunshield with respect to primary mirror: Another possible advantage of formation flying within an observatory with a sunshield or something similarly large is that the orientation of the parts can be adjusted over time.

JWST’s nominal lifetime is limited by its propellant supply. Barring another unexpected failure, the mission finishes when it runs out of fuel. The propellant is used for two purposes after the spacecraft reaches its operational destination of the Earth-Sun L2 point: stationkeeping in its halo orbit around the L2 point, and desaturation of its reaction wheels. The reaction wheels on JWST saturate because of a net solar radiation pressure torque resulting from a center of pressure – center of mass offset on the spacecraft. Because JWST’s sunshield is firmly attached to its primary mirror assembly, over the course of its orbit the offset varies but is not persistently zero. Figure XIII shows how disconnecting the optical assembly from the sunshield of our futuristic telescope and formation flying them allows for translational momentum exchange.



Fig. XIII: Reducing the center of pressure-center of mass offset of a cryogenic telescope at L2

By doing this, one is essentially “trimming” the sunshield over the course of the orbit to minimize the CoP-CoM offset and therefore use less propellant for desaturation of the telescope.

Enumerating the propellant that could be saved by such a technique is a task for future work.

V. CONCLUSIONS

The roadmap that we have established gives us clear applications and example problems to approach with an electromagnetic subsystem, and the selected applications provide context for the more general goal of reducing spacecraft mass. The work presented herein indicates Each of the selected applications show enough promise and potential benefit to stakeholders in each mission type that the goals of the near-, mid-, and far-term construct can be accomplished: mature the technology by building flight heritage of superconductors in general through low-risk applications (via GEO HTS magnetorquers), enable a valuable new mission in order to overcome technical feasibility concerns (such as the deployment, spinning, and radiation of a large EMIC-wave antenna), and finally completely reenvisioning large, complex, and unique missions (like space-based observatories), moving away from the monolithic form-factor that has been a staple of spacecraft design for years and starting to blur the lines of the traditional subsystem structure.

VI. REFERENCES

- [1] Wertz, J. R., *Space Mission Engineering: The New SMAD*, Microcosm Press, 2011.
- [2] Kwon, D., "Electromagnetic Formation Flight of Satellite Arrays", SM Thesis, Aeronautics and Astronautics Dept., Massachusetts Institute of Technology, Cambridge, MA, 2005.
- [3] Kwon, D., "Cryogenic Heat Pipe for Cooling High Temperature Superconductors with Application to Electromagnetic Formation Flight Satellites," Ph.D. Dissertation, Aeronautics and Astronautics Dept., Massachusetts Institute of Technology, Cambridge, MA, 2009.
- [4] Kong, E., "Spacecraft Formation Flight Exploiting Potential Fields," Ph.D. Dissertation, Aeronautics and Astronautics Dept., Massachusetts Institute of Technology, Cambridge, MA, 2002.
- [5] Schweighart, S., "Electromagnetic Formation Flight Dipole Solution Planning," Ph.D. Dissertation, Aeronautics and Astronautics Dept., Massachusetts Institute of Technology, Cambridge, MA, 2005.
- [6] Sakaguchi, A., "Micro-Electromagnetic Formation Flight of Satellite Systems," SM Thesis, Aeronautics and Astronautics Dept., Massachusetts Institute of Technology, Cambridge, MA, 2007.
- [7] Gettliffe, G.V., "High-Temperature Superconductors as Electromagnetic Deployment and Support Structures in Spacecraft," SM Thesis, Aeronautics and Astronautics Dept., Massachusetts Institute of Technology, Cambridge, MA, 2013.
- [8] Zubrin, R., "NIAC Study of the Magnetic Sail," NASA Institute of Advanced Concepts, 1999.
- [9] Powell, J., Maise, G., Paniagua, J., and Rather, J., "Magnetically Inflated Cable (MIC) System for Large Scale Space Structures," NASA Institute of Advanced Concepts, 2006.
- [10] <http://www.lhc-closer.es>, "Superconductivity in Short," [Online]. URL: <http://www.lhc-closer.es/php/index.php?i=1&s=4&p=8&e=0>. [cited 10 September 2014].
- [11] Tsyganenko, N., "Modeling the Earth's Magnetosphere Using Spacecraft Magnetometer Data," [Online]. URL: <http://geo.phys.spbu.ru/~tsyganenko/modeling.html>. [cited 10 September 2014].
- [12] Finlay, C., "International Geomagnetic Reference Field," [Online]. URL: <http://www.ngdc.noaa.gov/IAGA/vmod/igrf.html>. [cited 10 September 2014].
- [13] Olson, W.P., Pfitzer, K.A. and Mroz, G.J., "Modeling the Magnetospheric Magnetic Field," *Quantitative Modeling of Magnetospheric Processes*, edited by W.P. Olson, Vol. 21, American Geophysical Union, Washington, D. C., 1979.
- [14] Desiderio, D., Lovera, M., Pautonnier, S., and Draï, R., "Magnetic momentum management for a geostationary satellite platform," *47th IEEE Conference on Decision and Control*, IEEE, Cancun, Mexico, 2008.
- [15] SuperPower Inc., "SuperPower®2G HTS Wire Specifications," [Online]. URL: http://www.superpower-inc.com/system/files/SP_2G+Wire+Spec+Sheet_for+web_2012FE_C_v2_0.pdf. [cited 10 September 2014].
- [16] "Van Allen radiation belt." *Encyclopaedia Britannica Online Academic Edition*. Encyclopædia Britannica Inc., 2014. [Online]. URL: <http://www.britannica.com/EBchecked/topic/622563/Van-Allen-radiation-belt>. [cited 10 September 2014].
- [17] Reyes, R., "Charged Particle Motion," Southwest Research Institute, [Online]. URL: <http://pluto.space.swri.edu/image/glossary/pitch.html>. [cited 10 September 2014].
- [18] de Soria-Santacruz, M., Bautista, G., Gettliffe, G.V., Martinez-Sanchez, M., and Miller, D.W., "Design of a Spaceborne Antenna for Controlled Removal of Energetic Van Allen Belt Protons," *IEEE Aerospace Conference*, Big Sky, Montana, March 2014.
- [19] "Starshades," New Worlds Observer, [Online]. URL: <http://newworlds.colorado.edu/starshade/index.htm>. [cited 10 September 2014].
- [20] Kong, E.M.C., "Minimum Energy Trajectories for Techsat 21 Earth Orbiting Clusters," *Space 2001 Conference & Exposition, Albuquerque NM, 2001*. Presentation. [Online]. URL: http://ocw.mit.edu/courses/aeronautics-and-astronautics/16-851-satellite-engineering-fall-2003/lecture-notes/l12_ff2_resizing.pdf. [cited 10 September 2014].

Appendix 3: Design of a Space-borne Antenna for Controlled Removal of Energetic Van Allen Belt Protons

Design of a Space-borne Antenna for Controlled Removal of Energetic Van Allen Belt Protons

Maria de Soria-Santacruz, Guillermo Bautista, Gwendolyn V. Gettliffe, Manuel Martinez-Sanchez, David W. Miller
 Massachusetts Institute of Technology
 77 Massachusetts Avenue, Cambridge, MA 02139
 617-838-4944, 678-640-2189, 617-253-6799, 617-253-5613, 617-253-3288
 mdesoria@mit.edu, gbau@mit.edu, gvg@mit.edu, mmart@mit.edu, millerd@mit.edu

Some sections of this paper have been omitted for appearance in the MAGESTIC NIAC Phase II report. This is noted under the relevant headings, and those sections can be read in the full IEEE publication.

Abstract— The energetic protons trapped in the inner Van Allen belt pose a risk to humans and spacecraft operating in Low Earth Orbit (LEO). These particles come from cosmic rays, solar storms and other processes, and they are a hindrance to development of space technologies. The Radiation Belt Remediation (RBR) idea has been proposed as a way to solve this problem through Very/Ultra Low Frequency (VLF/ULF) transmissions in the magnetosphere capable of inducing pitch angle scattering of the hazardous particles and precipitating them into the atmosphere. Whistler-type emissions (VLF band, tens of kHz) have been extensively studied for precipitation of energetic trapped electrons, but much less work has been devoted to the controlled removal of inner belt protons. The latter would require the man-made radiation of Electromagnetic Ion Cyclotron (EMIC) waves into the magnetosphere (ULF band, less than 10 Hz), the frequency of which is close to the cyclotron frequency of the trapped protons. In this paper we first identify the space-borne transmitter capable of radiating EMIC waves, and we estimate its radiation impedance and radiation pattern. The selected antenna configuration consists of a DC rotating coil, which is equivalent to two AC phased-orthogonal coils but with negligible self-inductance. The radiation resistance of these magnetic dipoles is very small. For this reason, we propose a design based on superconductors and multiple turn arrangements. One of the most challenging aspects of using superconductors in space is their cooling system. This paper presents a preliminary thermal and mechanical design of a superconducting coil antenna capable of radiating EMIC waves into the magnetosphere. The coil is composed of high temperature superconducting tapes (HTS), which have to be kept below 77 K. Active thermal control and the use of cryogenics are therefore required to reject the heat coming from environmental sources. This preliminary design is next used to calculate the power radiated from the antenna, its radiation pattern and its effect on the energetic proton population of the inner Van Allen belt. The feasibility of the remediation concept, as well as a scientific mission scaled down to detectability of the precipitating fluxes are finally addressed at the end of the paper.

TABLE OF CONTENTS

1. INTRODUCTION	1
2. RADIATION OF EMIC WAVES FROM A SPACE-BORNE TRANSMITTER	2
3. ELECTRICAL, MECHANICAL AND THERMAL IMPLICATIONS	4

4. THE SCIENCE AND FEASIBILITY OF THE REMEDIATION CONCEPT.....	9
5. SCALING DOWN TO DETECTABILITY: A SCIENTIFIC MISSION	11
6. SUMMARY	12
ACKNOWLEDGEMENTS.....	14
REFERENCES.....	14
BIOGRAPHY	16

1. INTRODUCTION

The inner Van Allen radiation belt that surrounds the Earth is a concentration of high-energy charged particles originating from cosmic rays, solar storms, and other processes. These particles can rapidly damage electronics, solar panels and other components of the space systems crossing the inner belt region, therefore limiting the capabilities of Low Earth Orbit (LEO) missions [3], [4]. Shielding against radiation is extremely expensive and even with hardening measures the reliability of space systems is limited by degradation caused by these energetic particles. Observations and modeling, however, show that naturally generated Ultra-low and Very-low frequency (ULF/VLF) waves can change the momentum of the energetic trapped particles by a mechanism called pitch angle scattering, which causes a portion of them to get lost into the atmosphere [1], [2], [20], [26]. These observations show that whistler waves (typically tens of kHz) can induce precipitation of energetic trapped electrons, while Electromagnetic Ion Cyclotron (EMIC) waves (typically less than 10 Hz) are capable of interacting with both energetic electrons and protons. This fact suggests that, if power requirements allow, it could be possible to have human control over the stable inner belt proton population by artificially radiating EMIC waves from space-based transmitters, thus protecting the orbiting systems from energetic particles' injections [39], [40]. EMIC waves are naturally generated by a cyclotron instability of ring current ions located at $L > 3$, where the L parameter or L -shell corresponds to the geomagnetic field line that crosses the magnetic equator at the corresponding number of Earth's radii. Consequently, the precipitation of MeV protons at lower L -shells requires artificial injection of EMIC waves into the inner zone. Initial research efforts on controlled removal techniques (commonly referred as remediation) [18], [19], [22] have targeted the energetic trapped electrons because they are the dominant product of high-altitude

nuclear explosions (HANEs) [8], [29], [30]; a space test of an electric dipole antenna aiming at testing the capability of whistler waves to interact with radiation belt electrons is ready to be launched in the near future [41]. It is well known, however, that geomagnetic storms cause large-scale injections of both protons and electrons into the Earth's magnetosphere. The naturally occurring radiation belts contain both kinds of particles with similar deleterious effects, which represent by themselves a large hazard to spacecraft over a vast volume of space. For this reason, the interaction between inner belt protons and man-made EMIC waves from space-based antennas is an unexplored solution to the radiation environment that should be investigated given its relevance to the engineering and scientific communities.

Two options exist to radiate ULF/VLF waves into the magnetosphere, which are ground-based and space-based transmitters. While ground based transmitters have been used to test the concept of remediation in the whistler band [17], [19], the radiation of EMIC waves from ground is much more complicated due to their very low frequency. Magnetospheric coupling of EMIC waves would require multi-km horizontal linear antennas, which are very inefficient because the ground is a very good conductor and cancels out the antenna potential and radiated fields [10]. In the EMIC band, space-borne transmitters are preferred to ground-based antennas because they avoid inefficiencies associated with ionospheric coupling and ground effects. Additionally, space-based concepts are more flexible than ground-based ones, which operate at a fixed frequency, with no directional control and cannot be moved. Flexibility is especially important in the development of proof-of-concept or scientific missions that may enable testing specific parts of the remediation ideas.

In this paper we attempt to reveal the engineering implications of a space-borne antenna capable of radiating EMIC waves with the purpose of inducing controlled precipitation of very energetic (20 to 300 MeV) radiation belt protons. More specifically, the following sections discuss potential transmitter configurations capable of radiating EMIC waves, the effect of the plasma on the antenna radiation characteristics, and the electrical, mechanical and thermal implications of such arrangements. The feasibility of the remediation idea is also addressed at the end of the paper, as well as a preliminary characterization of a scientific mission scaled down to detectability of the proton precipitating fluxes.

2. RADIATION OF EMIC WAVES FROM A SPACE-BORNE TRANSMITTER

The plasma that surrounds a space-borne transmitter strongly modifies its radiation characteristics compared to vacuum; plasmas are dispersive, or in other words, the wavelength is a function of the direction of propagation of the wave. Fig. 1 represents the equivalent circuit of a space-based antenna (or antenna-sheath-plasma system) operating at ULF/VLF

frequencies. The physical antenna is enclosed in the green box and consists of an AC source, a resistor that accounts for ohmic losses, and the self-reactance. In the case of a linear antenna, the accumulation of charge on its surface also involves the formation of a thick oscillatory sheath around the transmitter, which is due to the different response time of protons and electrons to the fields generated by the antenna [9], [37], [43]; the sheath is a region of non-neutrality that shields the fields generated by the source and limits their coupling to the plasma. The fourth component is the plasma impedance connected to the antenna; the real part of this impedance is the radiation resistance responsible for radiation, while the wave energy is stored as reactive power due to the radiation reactance (imaginary part). Sheath and plasma impedances are enclosed in the pink box of Fig. 1, which represents the effect of the plasma. High system performance requires large radiation resistance and minimization of any system reactance. In this section we focus on the effect of the plasma on the radiation, while Section 3 discusses the physical antenna in the green box.

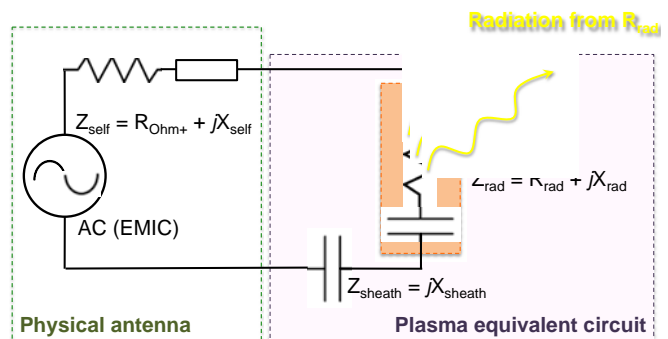


Figure 1 – Antenna-plasma system

The radiation of EMIC waves from space-based antennas is more complex than the higher frequencies of whistlers. In the case of a linear dipole, the sheath around it is very thick, and so its capacitance dominates. The radiation resistance of an electric dipole immersed in a magnetoplasma was derived by Balmain [5] under the quasi-static approximation, which is valid in our case and whenever the gradient distances are relatively small. According to his model, an inductor of 1 H would be required to compensate for the sheath capacitance of an 80-meter electric dipole operating at 10 kHz (whistler band). On the other hand, for the EMIC regime, the same system would require an inductor of 2 MH for circuit compensation [39]. The associated capacitive reactance in the EMIC band is extremely high even for a multi-km transmitter, to the point that it is not realistically feasible to use a linear dipole antenna to radiate these very low frequency waves.

A hopeful solution to this problem has been identified, which consists of a DC rotating coil operating as an EMIC transmitter. As we will see in Section 3, a plasma sheath will most likely appear around an static AC coil due to its excessive self-inductance introduced by the large dimensions and circulating current required by the system.

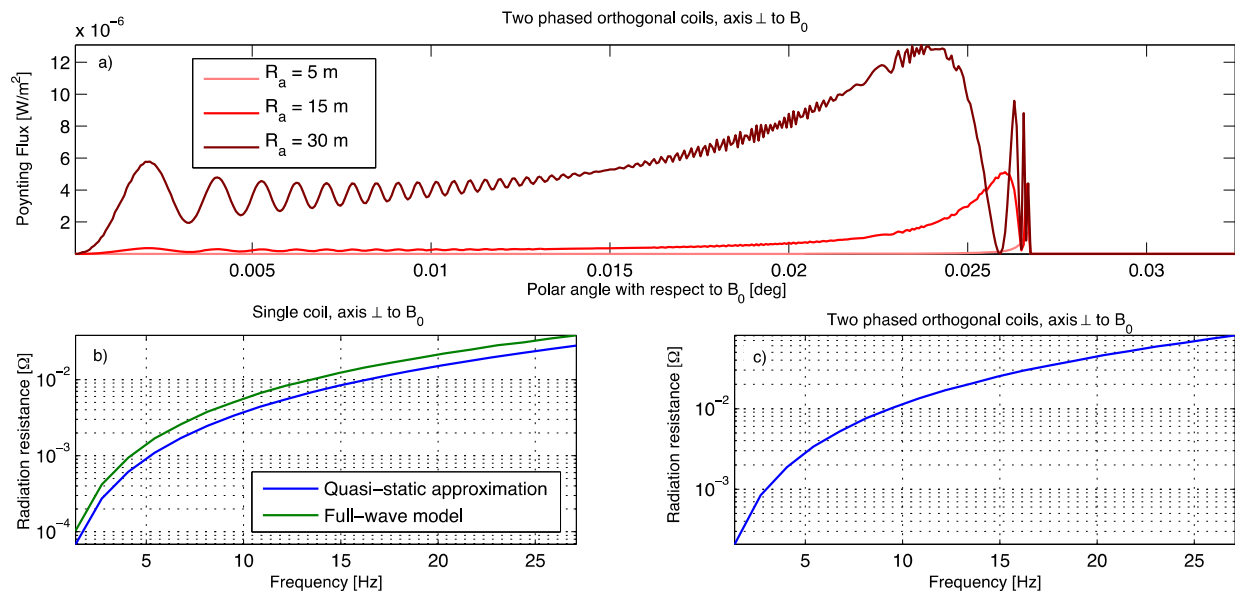


Figure 2 – (a) Poynting flux from two-phased orthogonal coils with axes perpendicular to the Earth's magnetic field. (b) Comparison between the radiation resistance of a single coil ($R_a = 15$ m) from the full-wave and Bell and Wang [6] models. (c) Radiation resistance versus frequency for two-phased orthogonal coils with $R_a = 15$ m.

This inductance translates into huge voltages across the coil and the potential for sheath formation. For this reason, instead of an alternate current circulating around a static coil, we propose a direct current driven around a rotating coil. The current is DC, thus the only reactance that remains is the one associated with the plasma currents, which is small and will not be discussed here. The radiation energy eventually comes from the kinetic energy of the rotating antenna. Both DC and AC options, however, can be equivalently modeled in terms of radiation characteristics, since the dipole component of the rotating DC antenna is equivalent to two AC static orthogonal coils. Laboratory experiments developed at the UCLA Large Plasma Device (LAPD) tested a phased orthogonal two-loop antenna immersed in a magnetized plasma [15], [21] and they showed that they are capable of radiating very low frequency waves in the Alfvén regime.

Table 1. Environmental and antenna parameters

Antenna location	$L = 1.5$, equatorial
Distance to the observation point (far-field)	5000 km
Plasma density, n_0	$3.05 \cdot 10^4 \text{ cm}^{-3}$
Geomagnetic field, B_0	$0.89 \cdot 10^{-5} \text{ T}$
Plasma composition	Electron-proton
Antenna current	300 A
# turns, N_{turn}	106
Wire radius	0.5 mm

Following the approach presented in de Soria-Santacruz [38] for a linear antenna, we have developed a full-wave linear model of the far-field radiation pattern of two-phased orthogonal coils immersed in a magnetoplasma and operating in the EMIC band. The plasma is assumed cold, consisting of

electrons and protons. The fields from the two-coil configuration are simply the composition of the fields from the two individual coils, one displaced 90° in space and time with respect to the other. Fig. 2(a) presents the Poynting flux from the two-phased orthogonal coil configuration for the parameters detailed in Table 1, a frequency of 2 Hz and for three different loop radii, R_a . The radiation pattern in the figure is equivalent to that of a DC rotating coil with symmetry axis always perpendicular to the Earth's magnetic field, B_0 . Our calculations show that the perpendicular axis orientation is preferred in terms of radiation efficiency because the Poynting flux is up to eight orders of magnitude larger compared to the parallel case. For this reason, the antenna axis should always remain perpendicular with respect to the Earth's magnetic field lines. By definition, power flows in the direction of the group velocity, which is almost perpendicular to the phase velocity direction. In the figure we observe that the power propagates very close to field-aligned, in a small cone around the magnetic direction defined by the resonance cone of EMIC waves [39], while the corresponding wave number vectors are almost perpendicular. This Poynting flux is characteristic of any space-borne transmitter in the EMIC band, which is controlled by the surrounding plasma environment. This pattern will generate short but strong wave-particle interactions, as we will see in Section 4. In addition, we observe that increasing the loop radius has the effect of filling up the resonance cone, while the power concentrates on the surface of the cone for the smaller radius values. This happens because larger R_a couples to larger wavelengths, i.e. smaller wave number vectors and more field-aligned group velocity according to the dispersion surface of EMIC waves.

The radiated power and the radiation resistance can be found by integrating the Poynting flux in Fig. 2(a) over a spherical

shell around the antenna. Bell and Wang [6], [45] developed a quasi-static analytical approximation of the radiation resistance of a small filamentary ULF/VLF loop antenna immersed in a magnetoplasma. According to their expressions, the radiation resistance of magnetic dipoles scales with the cube of the loop radius and the square of the frequency. Fig. 2(b) compares the radiation resistance from Bell and Wang with the solution of our full-wave model applied to a single perpendicular coil for the parameters in Table 1, where it can be observed that the quasi-static approximation is in very good agreement with our simulation. Similarly, Fig. 2(c) shows the radiation resistance of the two orthogonal coil configuration calculated with the full-wave model, which presents the same trends as the results for a single coil antenna, with the exception that the values of the resistance are slightly higher, but by no more than a factor of 3.

Nevertheless, the radiation resistance of coil antennas is several orders of magnitude smaller than the one of linear dipoles. For this reason, we require the use of superconductors and multiple turn arrangements to increase the radiated power, which are described in the next section.

3. ELECTRICAL, MECHANICAL AND THERMAL IMPLICATIONS

Based on the plasma response above, space-borne magnetic dipoles are the best candidates to radiate EMIC waves in the magnetosphere. The most promising solution involves a DC rotating coil, as we will see below. This section analyzes the green box in Fig. 1, i.e. the physical antenna. More specifically, we discuss the electrical, mechanical and thermal implications of such a transmitter, including a preliminary sizing of a superconducting coil antenna, its thermal control system and an estimation of its performance. The remediation of the inner Van Allen belt requires a huge amount of radiated power. For this reason, in this section we derive the engineering implications for the largest coil dimensions that can be reasonably launched, while a scientific mission scaled down to detectability of the precipitating fluxes is presented in Section 5.

Electrical Considerations: A DC Rotating Coil Antenna

The superconducting coil structure under consideration has a very large self-inductance due to the high currents circulating around it. This self-inductance is the reason why we require a DC rotating coil instead of a static AC antenna. The self-inductance of a coil transmitter operating in AC, L_{ind} , is given by

$$L_{ind} = \frac{N_{turn}^2 \mu_0 \pi R_a^2}{H} \quad (1)$$

where N_{turn} is the number of turns, R_a is the radius of the coil, $H = N_{turn} \cdot (t + l)$ is the total thickness of the coil, and t and l are the superconducting wire and Kapton insulation

thicknesses, respectively (detailed in the following sections). Taking $N_{turn} = 106$, $R_a = 15$ m and $H = 0.021$ m, this gives $L_{ind} \approx 470$ H, which is indeed very large. In an AC system, this inductance would have to be compensated in order to increase the antenna efficiency, and in such a way to reduce the voltage drop across the coil. But is this compensation possible? A conceivable circuit for this purpose would have a capacitor in series with the coil inductance. The resulting voltage across terminals would tend to zero at the circuit resonance ($C = 1/(\omega^2 L_{ind})$), which is the purpose of compensation. The voltage at resonance across the loop (and across the capacitor), however, would be around 10 kV for a single turn loop operating at 300 A, unacceptable in terms of arcing and sheath formation. This result shows that not even a sequential compensation of every loop in the coil antenna seems feasible. The non-linear effects generated by this voltage drop are outside the scope of this paper, but we believe that it will attract charged particles and generate a plasma sheath around it.

The solution to the problem above involves a DC rotating coil. The rotation rate would have to match the desired wave frequency, which is unacceptably high in the case of whistler waves but reasonable in the EMIC regime (< 2 Hz). The dipole component of this current distribution is equivalent to two AC static orthogonal coils, as described in the previous section. The engineering implications of a rotating coil for radiation of EMIC waves are being analyzed here for the first time and should be addressed in more detail in the future work given its relevance to the controlled removal of energetic Van Allen belt protons. The following sections analyze the mechanical and thermal implications of such a concept, which involves superconductor technology and therefore active control of the antenna temperature.

HTS Performance Characterization

As stated earlier, magnetic loops have a very small radiation resistance, which requires the use of superconducting wires combined with multiple-turn arrangements in order to increase the radiated power and minimize the ohmic losses.

The nature of superconducting materials can be characterized with three critical variables: temperature, current density, and self-generated magnetic field. Every superconductor generates a magnetic field that limits its ability to transport current, and in addition, at lower temperatures, this ability is greatly enhanced by the increased levels of intrinsic pinning in the material. Together, these three variables form what is known as the critical surface for a superconductor, where the material borders on undergoing a process known as quenching, whereby said material transitions to a resistive state. This process can be brought about by raising the superconductor above its critical temperature, critical current density or critical magnetic field.

There are two identifiable categories of superconducting materials: Low Temperature Superconductors (LTS) and

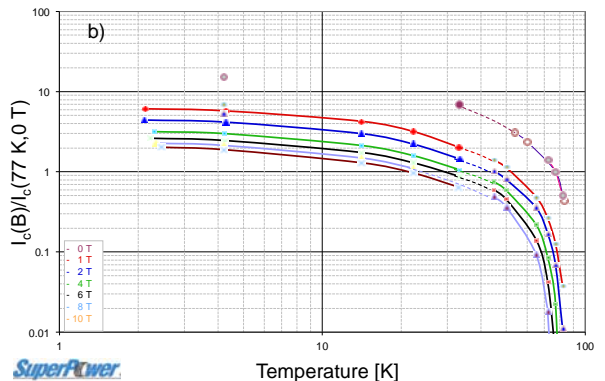
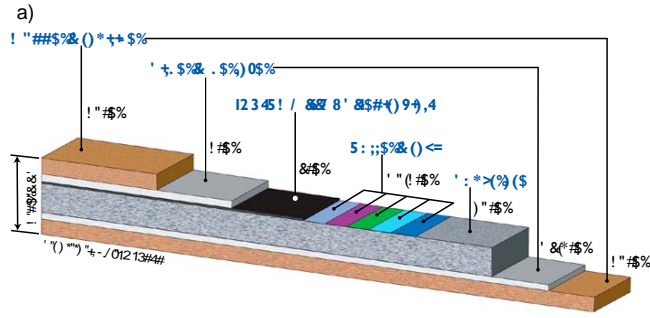


Figure 3 – (a) SuperPower (RE)BCO-based 2G HTS tape [16]. (b) Critical current as a function of temperature for different values of applied perpendicular magnetic field.

High Temperature Superconductors (HTS). LTS are characterized by very low critical temperatures, but also very high critical current densities and magnetic fields; usually, their critical temperatures hover around 10 K. HTS have critical temperatures above 77 K, and until recently much lower critical current densities and critical magnetic fields. However, a new second generation (2G) of HTS materials have critical current densities even higher than that of LTS materials in some cases, while still maintaining high critical temperatures. HTS wires are produced in the form of flexible tapes, much easier to pack and manipulate than the brittle LTS designs. Additionally, HTS tapes can be cooled down below their critical temperature with corresponding increase in critical current density.

Even for HTS, the antenna has to be kept below 77 K, which requires active thermal control means. The use of LTS would translate into very large input power requirements, to the point that it is unfeasible to use LTS for space applications. For this reason, the transmitter design presented below builds upon high temperature superconducting materials.

HTS have been used and proposed for different space applications. The Variable Specific Impulse Magnetoplasma Rocket (VASIMR) [31] uses HTS technology to generate magnetic nozzles and confine plasma plumes. Other uses involve torque coils to de-saturate reaction wheels or control moment gyros, or Electromagnetic Formation Flight (EMFF). EMFF uses electromagnets coupled with reaction wheels to provide a propellant-less method for formation flight propulsion. More specifically, Kwon [23] characterized the performance of HTS wires for EMFF applications; in a later work [24], he studied consumable-free methods of maintaining isothermalization of a large HTS coil, which will be referenced throughout this paper.

Preliminary Sizing— In this section we describe the dimensions and composition of HTS materials and we set the preliminary sizing of the coil that will be used as a reference in the following sections. The total wire length is a flexible parameter, only limited by the total mass and the torques on the antenna. Most of the analyses this section consider a reference wire length of 10 km, but other values are explored

in Section 5 when analyzing a potential scientific mission. A reference coil radius is taken to be 15 meters due to deployment considerations based on standard launch vehicle fairing dimensions; in doing that, we are assuming that we have a working deployment strategy. This strategy is currently being addressed in the Space Systems Laboratory at MIT, which is based on flexible deployment concepts as discussed later. The sensitivity of the loop performance to the coil radius is also analyzed in the following sections. From the wire length and coil radius, the number of turns can be easily calculated as follows

$$N_{turn} = \frac{l_{wire}}{2\pi R_a} \quad (2)$$

where l_{wire} and R_a are the wire length and antenna radius, respectively. For $l_{wire} = 10$ km and $R_a = 15$ m, then $N_{turn} \approx 106$ turns.

The mass and dimensions of the HTS tape are taken from SuperPower dimensions [16]. Commercially available HTS tapes vary in width from 4 to 12 mm. Unless otherwise specified, we consider a width of 12 mm and thickness of 0.1 mm of the whole tape as given by SuperPower, which is capable of carrying the largest amount of current (300 A). The mass density and proportion of the different layers in Fig. 3(a) are summarized in Table 2.

Table 2. Mass density and area proportionality factors of SuperPower (RE)BCO-based 2G HTS tape

	Mass Density, ρ_x [kg/m ³]	Area Proportionality Factor, λ_x
Copper	9080	40%
(RE)BCO	6300	1%
Silver	10490	3.8%
Hastelloy C-276	8890	50%
LaMnO ₃	6570	0.05%
MgO	3580	0.05%
Y ₂ O ₃	5010	0.05%
Al ₂ O ₃	3590	0.05%

The mass of wire can therefore be estimated as follows

$$\begin{aligned}
m_{\text{tape}} = & l_{\text{wire}} dt (\lambda_{\text{Cu}} \rho_{\text{Cu}} + \lambda_{(\text{RE})\text{BCO}} \rho_{(\text{RE})\text{BCO}} \\
& + \lambda_{\text{Ag}} \rho_{\text{Ag}} + \lambda_{\text{C276}} \rho_{\text{C276}} + \lambda_{\text{LaMnO}_3} \rho_{\text{LaMnO}_3} \\
& + \lambda_{\text{MgO}} \rho_{\text{MgO}} + \lambda_{\text{Y}_2\text{O}_3} \rho_{\text{Y}_2\text{O}_3} + \lambda_{\text{Al}_2\text{O}_3} \rho_{\text{Al}_2\text{O}_3})
\end{aligned} \quad (3)$$

where d and t are the tape width and thickness, respectively.

The nominal coil and tape dimensions described above together with the corresponding mass estimates are summarized in Table 3.

Table 3. Nominal sizing of the HTS tape coil

Tape length, l_{wire} [km]	10
Coil radius, R_a [m]	15
# turns, N_{turns}	106
Tape width, d [mm]	12
Total tape thickness, t [mm]	0.1
Superconductor thickness, t_{sup} [μm]	1
Total tape mass, m_{tape} [kg]	103

Critical Variables— In this section we characterize the critical surface of the HTS tapes described above, and analyze its dependency on the number of turns of the coil.

The current density in an HTS tape is more sensitive to the magnetic field perpendicular to the tape's surface than to the parallel field [34]. The perpendicular magnetic field will therefore determine the critical surface of the superconductor. Additionally, the critical current density of HTS tapes dramatically increases with decreasing temperature below 77 K, which starts to saturate at around 20 K. For this reason, it is strongly desired to operate below the nominal 77 K, since small temperature reductions produce large performance improvements. This trend is presented in Fig. 3(b), taken from SuperPower specifications.

In order to construct the critical surface as a function of the number of turns, we must first develop a model for the magnetic fields generated by the coil. In this study, the tapes are approximated as line currents stacked on top of each other. The magnetic field generated by a line current, I , at a distance r can be estimated as follows

$$B = \frac{\mu_0 * I}{2\pi r} \quad (4)$$

In addition to the tapes of thickness $t = 0.1$ mm, the stack also consists of layers of Kapton insulation (with thickness $l = 0.1$ mm) in between each turn [24]. Each tape sees the magnetic field induced by the neighboring wires in the stack. The wires that see the maximum field are the ones at the end of the stack, where all the contributions add up. For a stack with N_{turn} turns, the maximum parallel magnetic field is given by

$$B_{\parallel \text{max}} = \frac{\mu_0}{2\pi} \sum_{j=2}^{N_{\text{turn}}} \frac{I_j}{(j-1)(t+l)} \quad (5)$$

We have already established, however, that it is the perpendicular magnetic field that dominates the coil behavior. In this case, due to the large radius of curvature of the loop, the contributions to the perpendicular field are all assumed to be local, which can then be modeled by taking an equivalent circular cross section with the same area as the tape stack

$$r_{\text{eq}} = \sqrt{\frac{d * N_{\text{turn}}(t+l)}{\pi}} \quad (6)$$

where $d = 12$ mm is the tape width. It then follows that the maximum perpendicular field is

$$B_{\perp \text{max}} = \frac{\mu_0 * N_{\text{turn}} * I}{2\pi r_{\text{eq}}} = \sqrt{\frac{N_{\text{turn}}}{\pi}} * \frac{\mu_0 * I}{4\sqrt{d(t+l)}} \quad (7)$$

Using these relationships to find the induced fields in the coil, together with the critical parameters for a single tape made available by SuperPower, we can construct the critical surface of the HTS coil, which is presented in Fig. 4. The stack dimensions are as described previously, with N_{turn} allowed to vary freely, and three temperature curves selected for analysis: 20 K, 50 K, and 77 K. The perpendicular field in Fig. 4(a) dominates the coil behavior, while the parallel field in Fig. 4(b) remains subcritical. The critical current of a 100-turn coil at 50 K increases by more than a factor of 2 compared to the case at 77 K, and by a factor of 3 when operating at 20 K. These results reaffirm the importance of working at low temperatures.

Quench Failsafe System— A superconductor quenches when it goes from having no resistance (superconducting state) to being resistive (normal state). This change can be generated by exceeding the critical magnetic field inside the superconductor, or by causing too large of a change of field (which generates eddy currents and heating), or a combination of both. The quenching process is accompanied by an increase in the rate of volumetric generation of heat, which may damage the transmitter. The copper in the HTS tape by SuperPower is a risk mitigation technique, designed to protect the wire in the event of a quench. At the critical temperature of the HTS wire, the copper is much less conductive than the superconductor. If quenching happens, the temperature will rise, the superconductor will become resistive and the current will flow through the copper instead. This copper layer must be able to absorb all the stored magnetic energy, which is given by

$$E_M = \frac{L_{\text{ind}} * I^2}{2} \quad (8)$$

where L_{ind} is the self-inductance of the coil given by equation (1). The copper must be able to absorb the stored magnetic energy, or in other words

$$E_M = \frac{L_{\text{ind}} * I^2}{2} = m_{\text{Cu}} \int_{T_0}^{T_{\text{melt}}} c_{p,\text{Cu}}(T) dT \quad (9)$$

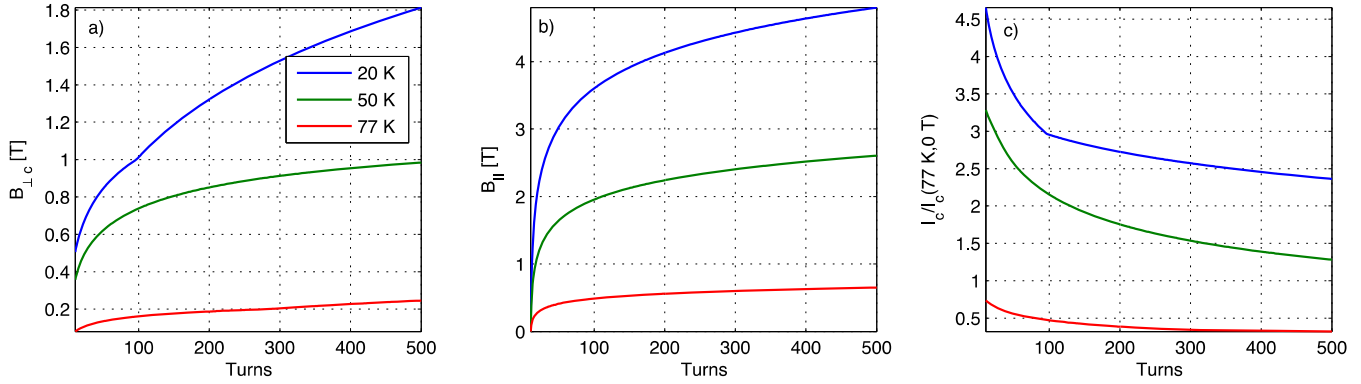


Figure 4 – (a) Critical perpendicular magnetic field, (b) parallel magnetic field, and (c) critical current (I_c normalized to $I_c(77\text{K}, 0\text{T})$) as a function of number of turns.

The mass of copper, m_{Cu} , can then be expressed as follows

$$m_{Cu} = \frac{E_M}{\int_{T_0}^{T_{melt}} c_{p,Cu}(T) dT} \quad (10)$$

where $c_{p,Cu}(T)$ is the copper specific heat at constant pressure, T_0 is the operating temperature of the superconductor and T_{melt} is the copper melting temperature. Typically, $T_{melt} = 1375.8\text{ K}$, and $c_{p,Cu}(T)$ is taken from tables [27], [46].

For the coil in Table 3 with a Kapton insulation of $l = 0.1\text{ mm}$, operation at $T_0 = 77\text{ K}$, $I_c/I_c(77\text{ K}, 0\text{ T}) = 0.5$ and $I_c(77\text{ K}, 0\text{ T}, 12\text{ mm}) = 300\text{ A}$, we can say that the current I is $0.5 \cdot 300 = 150\text{ A}$. As stated previously, the inductance L_{ind} is approximately 470 H . The magnetic energy stored by the coil $E_m(77\text{ K})$ is therefore 5 MJ , and the required copper mass $m_{Cu}(77\text{ K})$ is approximately 10 kg .

For the same dimensions of the coil, the mass of the copper in the HTS tape can be found as follows

$$m_{Cu} = l_{wire} dt \lambda_{Cu} \rho_{Cu} \approx 43.6\text{ kg} \quad (11)$$

that is, the mass of copper in the HTS tape arrangement has a safety factor greater than 4 when operating at 77 K . However, as seen in the description of the critical variables, it is desirable to operate at lower temperatures since they represent a dramatic increase in current density. At $T_0 = 50\text{ K}$, the ratio $I_c/I_c(77\text{ K}, 0\text{ T})$ is equal to 2, and therefore $E_m(77\text{ K})$ becomes 85 MJ , a 17-fold increase which results in a required copper mass $m_{Cu}(77\text{ K}) = 156\text{ kg}$. Similarly, at $T_0 = 20\text{ K}$, the copper mass required to absorb the stored magnetic energy equals $m_{Cu}(20\text{ K}) = 350\text{ kg}$. A possibility could be to accept more risk in the mission by keeping the SuperPower proportions of copper and relying on the thermal subsystem to cool down the superconductor. This option will be considered in the following sections.

In the case of low temperature superconductors (LTS), the copper involved to absorb the magnetic energy stored in our system would be several hundreds of tons, out of realm of what can be reasonably launched into space. Quenching management and thermal control are the main reasons why LTS are not used for space applications. On the ground, however, LTS are commonly used to generate large magnetic

fields. One example of ground-based application is the CERN Large Hadron Collider (LHC) in Switzerland, which is the world's most powerful particle accelerator and consists of a 27-km ring of superconducting magnets. The LHC has enough copper to provide 1 s to dump heat away from the magnet; after that, the local hot-spot would overheat and eventually melt (L. Bottura, CERN Division LHC, personal communication, May 2013). The purpose of the copper is to provide a reaction time, but in a LTS high current density application it will never be enough to absorb the magnetic energy. In order to do that, LTS ground systems make sure that the quench propagates to the whole system so that the complete mass (heat capacity) absorbs the magnetic energy (converted to heat through Joule heating). Another option used on the ground consists of extracting the energy from the system by dumping the circuit on an external resistance. All this complexity makes LTS unfeasible for space applications. For these reasons, our design is based on HTS superconductors, which have manageable quenching and thermal requirements.

Cooling Requirements and Thermal Control

One of the most challenging aspects of using superconductors in space is the design of the cooling system. The antenna will be subjected to environmental thermal loads from the Sun and the Earth.

This section is available in the full IEEE version of this paper.

Dynamics and deployment of the DC rotating coil

The DC coil is rotating at the EMIC frequencies. In addition, we showed that the coil axis should remain close to perpendicular to the Earth's magnetic field since it maximizes the radiated power. This configuration is illustrated in Fig. 5.

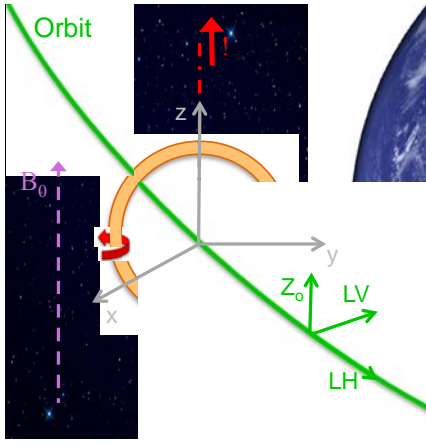


Figure 5 – Orientation and rotation that maximizes the power radiated from the antenna.

Three main torques will be acting on the coil: gyroscopic, magnetic and gravity gradient torques. The gyroscopic torque, τ_{gyro} , appears from the transformation between inertial and body-axes frames; it is therefore an internal torque and does not change the angular momentum in the inertial frame, but it does in the orbital frame. This torque tends to align the orbital angular velocity, Ω_{orbit} , with the coil's spin rate, ω , and it is stable when spinning around a major axis of inertia. An approximation to the worst-case gyroscopic torque is then

$$\tau_{gyro}|_{max} = \Omega_{orbit}\omega I_r \quad (32)$$

where $I_r = M \cdot R_a^2$ is the coil's polar inertia, and M is the total mass of the antenna. For an equatorial orbit at $L = 1.5$ then $\Omega_{orbit} = 6.75 \cdot 10^{-4}$ rad/s. Taking $\omega = 3.15$ rad/s (0.5 Hz), $M = 350$ kg (for a wire length of 10 km, including HTS and thermal system) and $R_a = 15$ m, this gives a gyroscopic torque of $\tau_{gyro}|_{max} = 165$ N·m.

Another relevant torque is the magnetic torque, τ_{mag} , which can be calculated as follows

$$\vec{\tau}_{mag} = \vec{\mu} \times \vec{B}_0 \quad (33)$$

where $\mu = N_{turn} \cdot I \pi R_a^2$ is the magnetic moment of the coil with direction given by the right-hand rule. The effect of this torque is to align the magnetic moment of the antenna, normal to the coil surface, with the external magnetic field direction. The zero-torque configuration, however, will not give any sort of radiation. The worst-case magnetic torque can be approximated as follows

$$\tau_{mag}|_{max} = N_{turn} I \pi R_a^2 B_0 \quad (34)$$

Taking $B_0 = 8 \cdot 10^{-6}$ T, $I = 300$ A, $N_{turn} = 106$ and $R_a = 15$ m, we get a magnetic torque equal to $\tau_{mag}|_{max} = 180$ N·m.

Finally, the gravity gradient torque, τ_{gg} , tends to align the coil's axis of smaller inertia with the vertical direction towards the Earth's center. This torque has a complex form, but a worst-case approximation can be calculated as follows

$$\tau_{gg}|_{max} = 3\Omega_{orbit}^2 I_r \quad (35)$$

which equals $\tau_{gg}|_{max} = 0.1$ N·m for the values considered above and is negligible compared to the gyroscopic and magnetic torques.

The gyroscopic and magnetic effects represent the main contribution to the torque. The gyroscopic torque cancels for $\Omega_{orbit} \parallel \omega$, and it is stable when spinning around a major axis of inertia; this configuration, however, corresponds to maximum magnetic torque, which also impacts the dynamics of the coil. Additionally, we would like to spin the coil as represented in Fig. 5, since it provides the largest radiated power.

We believe that the solution to the dynamics problem described above involves a coil rotating as shown in Fig. 5, but with the spacecraft subsystems distributed on both sides of the coil such that the body becomes a major-axis spinner. This change of inertia would provide a much larger gyroscopic stability compared to the perturbations introduced by the magnetic torque. A spinning disc would be an equivalent representation of our distributed system in terms of inertia, which is gyroscopically stable even in the presence of dissipation.

Our preliminary calculations consider the dynamics of this spinning disc, which is a major-axis spinner with z-body axis perpendicular to the orbital plane. The Earth's magnetic dipole field is assumed aligned with the normal to the orbit, which is considered equatorial. The magnetic torque is therefore along the y-body axis, and it is approximately constant. For a body acted by constant magnetic torque, τ_{magY} , perpendicular to the angular momentum, \vec{H} , as an initial condition, it can be shown that the magnitude of this angular momentum is conserved on average, and that the vector \vec{H} precesses describing a small cone if the spin rate is sufficiently large. A criteria for \vec{H} precession stability is given by [42]

$$\omega > \frac{2}{I_z} \sqrt{\tau_{magY} I_y} \quad (36)$$

which depends on the ratio $\sqrt{I_y}/I_z$. Consider a magnetic torque of magnitude $\tau_{magY} = 180$ N·m as calculated above, and a distributed system with $I_y = 10^4$ kg·m² and $I_z/I_y = 1.9$; then the minimum spin rate for stability would be $\omega > 0.14$ rad/s (0.02 Hz). Similarly, for $I_z/I_y = 1.2$, this minimum spin rate is $\omega > 0.22$ rad/s (0.03 Hz). In other words, for a frequency of $\omega = 3.14$ rad/s (0.5 Hz), the ratio of inertias should be $I_z/I_y > 0.08$, which seems a feasible design. Our frequency will therefore set the configuration of the distributed system, that is, the length of the trusses and location of the spacecraft subsystems.

For unbalanced initial conditions, our results show that the effect of the magnetic torque just adds a small forced precession to the free gyroscopic precession of the antenna, and that these cones are small and stable as far as the spin

velocity is larger than the minimum value described above. What is more, dissipation of the excess kinetic energy with time will end up damping any free precession imposed by unbalanced initial conditions, and will bring the major-axis spinner to a circular precession of the angular momentum introduced by the external magnetic torque. The maximum semi-amplitude of the final circular precession can be estimated as follows

$$v_{max} \approx \frac{\tau_{mag} \gamma}{\omega^2 (I_z - I_y)} \quad [rad] \quad (37)$$

which is a small angle. For $I_z/I_y = 1.9$ and a frequency of 0.5 Hz, then $v_{max} = 0.1^\circ$, that is, a very small precession.

Overall, the orientation preferred in terms of science is also favorable in terms of dynamics. The stable solution, however, implies a transformation of the system into a major-axis spinner, which could be achieved by distributing the spacecraft subsystems around the coil. A detailed analysis of the dynamics of the antenna is needed to determine the design of the spacecraft structure, which should be addressed in future studies.

Deployment and support of a 15-meter radius coil (or larger) in space is a challenging endeavor. Given the maximum takeoff weight of a launch vehicle, reducing the mass of deployment and support infrastructure allows a larger coil to be launched, increasing the radiated power of the antenna. The 15 meter radius assumed in this paper was predicated on a 15 meter payload fairing length, assuming the worst case scenario of rigid members connecting the spacecraft bus at the center of the coil to the perimeter of the coil. The dynamical analysis presented above indicates the unlikelihood of this configuration given the need to spin around a major axis of inertia; it is far more likely that the connections between the spacecraft bus and the antenna will be flexible rather than rigid. As such, we will examine deployment methods extensible to coils larger than 15 meters as well. Potential deployment methods include motorized actuation of rigid components (as mentioned above), magnetic Lorentz forces, pressurized inflation of a hollow structure, and spin (centrifugal).

When electrical current is run through a closed loop (or coil) of wire, the magnetic field generated by each infinitesimal length along the wire creates a Lorentz force on every other length along the wire such that if the loop was not closed, the wire would straighten itself. The force upon a segment due to the magnetic field of another segment is dependent on the angles of the segments with respect to each other, the force going to zero as the angle goes to zero (meaning that the segments are aligned) and as the distance between the two goes to infinity. Since the loop is closed, the shape of a wire (ignoring material resistance) goes to circular and flat since that configuration represents the farthest distance and the shallowest angle that each segment can be from every other. This circular coil configuration fortuitously happens to be the configuration desired for use as an antenna. The circularizing effect is especially useful for tensioning a large and otherwise

flexible coil, and, depending on the number of turns and inertia of the coil, can be used to actuate a stowed (folded but not plastically deformed) coil outwards towards the final circular configuration. Another circularizing technology is gaseous inflation of a closed tube. The forced vapor cooling system under work by the University of Maryland [28] adds the capability for inflation deployment to the system and, like the magnetic self-force, is a natural byproduct of hardware already in place for another purpose (cooling). Spin deployment also extends a structure out radially, but we do not want to spin around the axisymmetric radius in the antenna application, so it is less applicable in the deployment of the antenna. The centrifugal force resulting from the spinning of the antenna does, however, have the tendency to pull the circular rotating coil into an oblong coil widest in the direction perpendicular to the spin axis. This deformation must be countered by either inflation or magnetic circularizing forces in order to keep the coil from becoming increasingly elongated to the point of collapse due to the spin forces.

Due to the small minimum diameter of curvature of the SuperPower 2G HTS wire, 11 mm, the wire can be bundled fairly tightly within the payload fairing without plastic deformation at their folds. With >100 turns in the coil, the outer turns in a fold will be nowhere near the minimum curvature so long as the inner turns remain above the threshold. The greater limit to the fold radius will be making sure that the outer and inner turns do not become misaligned and disconnected by going from a folded and stowed configuration to a flat and tensioned one. Both deployment and circularization will be simulated in great detail in future work, with attention paid in particular to coil and stowage design.

Coil Performance Estimation

In the following we calculate the performance of a DC rotating coil in terms of radiation efficiency, that is, input to useful output (radiated) power.

This section is available in the full IEEE version of this paper.

4. THE SCIENCE AND FEASIBILITY OF THE REMEDIATION CONCEPT

In the absence of waves, trapped energetic particles perform three adiabatic motions: gyro-motion around the magnetic lines, bouncing motion along these lines, and drift motion around the Earth. The effect of waves adds to their adiabatic motion as follows

$$\dot{\vec{p}} = q \left[\vec{E}^w + \frac{\vec{p}}{\gamma m} \times (\vec{B}^w + \vec{B}_0) \right] \quad (41)$$

where p is the particle's momentum, γ is the relativistic factor, q is the particle's charge, m is its mass, B_0 is the Earth's magnetic field, and E^w and B^w are the electric and magnetic fields of the wave, respectively. The wave fields are calculated from the analysis in Section 2. In that section we

also showed that the spreading of EMIC waves across field lines is very small. The antenna illuminates a very narrow region of space, which is confined along geomagnetic field lines. Additionally, energetic inner belt protons drift very rapidly around the Earth, which can take less than a minute. Energetic protons, therefore, drift through the illuminated region in a fraction of their gyroperiod, where they are instantly scattered by the waves.

Energetic trapped particles bounce back and forth along the Earth's magnetic field lines. The pitch angle of the particle, α , is the angle between their velocity vector and the direction of the field lines. If we define B_a as the magnetic field intensity at the border of the sensible atmosphere (~ 100 km), particles with $\alpha < \alpha_{lc} = 1/\sin[(B/B_a)^{1/2}]$ will be removed from the trapped configuration by collisions in the atmosphere [44]. The pitch angle α_{lc} is referred as the bounce loss cone of the particles. It can be shown that the magnetic wave force dominates the interaction between energetic protons and EMIC waves, which does not modify the energy of the particles but is capable of introducing pitch angle scattering and precipitation of energetic protons. Therefore, EMIC waves have the capability of changing the momentum of energetic trapped protons such as they fall into their loss cone and are lost into the atmosphere.

Proton natural residence times range from less than a year to more than 4000 years, and they are a function of the L -shell and particles' energy. Inner belt proton losses are dominated by slowing down due to excitation and ionization of O, N, He and H neutral atoms at different altitudes [12]. From now on, we call *remediation* to the fact of reducing the natural residence time of the shorted-lived proton energies in our range (20 MeV) by a factor of 10 (therefore also of the higher energy particles), which allows us to determine the power required to remediate the proton radiation belt.

Test particle simulations of the non-linear equations of motion (equation (41)) [39] are used to determine the precipitation fluxes at the edge of the loss cone resulting from the short non-gyroaveraged interactions described above, which determine the detectability requirements of a particle instrument onboard a scientific spacecraft, as we will see in Section 5. This formulation is also used to estimate pitch angle diffusion coefficients of energetic inner belt protons interacting with oblique EMIC waves. Test particle simulations, however, are very computationally intensive and cannot provide the time evolution of the distribution or the particles' lifetimes. For this reason, diffusion coefficients estimated from test particle

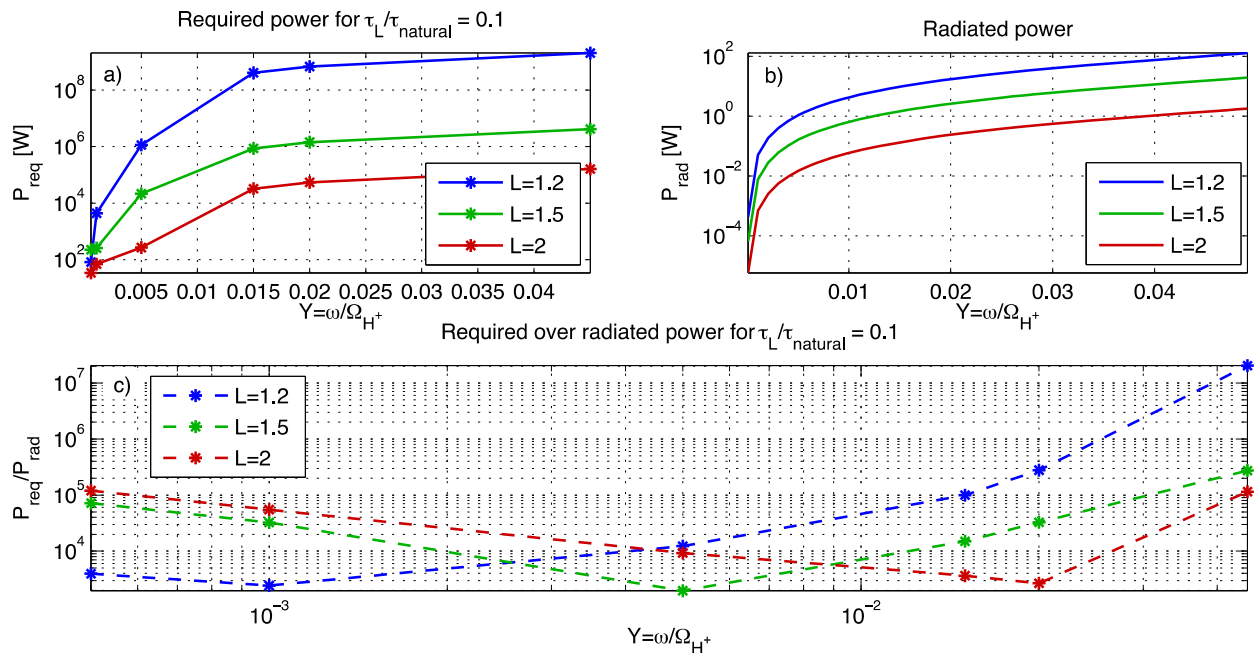


Figure 7 – (a) Power required to reduce the residence time of 20 MeV protons by a factor of 10 as a function of normalized frequency. (b) Radiated power from the coil in Table 3 and $T_c = 77$ K as a function of normalized frequency. (c) Ratio of required to radiated power as a function of normalized frequency.

simulations are used to solve the pitch angle diffusion (Fokker-Planck) equation. This approach is CPU-efficient and it is applied to calculate the time evolution of the distribution function of energetic protons as well as the particles' lifetime. The detailed formulation is outside the scope of this paper and will be addressed in a future publication, which is under preparation.

The simulations above show that the diffusion rates and particles' lifetime improve with decreasing frequency, while the power radiated from a loop antenna scales with the square of the frequency. Fig. 7 analyzes this frequency tradeoff between the power required for *remediation* of the thin L -shell thickness illuminated by the transmitter and the power radiated from this transmitter. The plots are for three different L -shells and represented as a function of normalized

frequency, $Y = \omega/\Omega_{H^+}$, where Ω_{H^+} is the proton cyclotron frequency at the equator given by $\Omega_{H^+} = qB_0/m$. Fig. 7(a) plots the power required, while Figure Fig. 7(b) shows the radiated power as a function of normalized frequency, where the radiated power is the one from a coil given by the dimensions in Table 3 and for $T_c = 77$ K. If we reduce the temperature to $T_c = 20$ K, then the current density increases by a factor of 3 (Fig. 5) and the radiated power by a factor of 9. Finally, Fig. 7(c) plots the ratio between required to radiated power, both through the same cross-sectional area. We can refer to the inverse of this ratio as *remediation efficiency*, i.e. $\eta_{rem} = P_{rad}/P_{req}$. In this plot, we observe that there is a desirable frequency of operation where this ratio is minimum, which is L -shell dependent. At $L = 1.5$ and operating at a frequency of 0.5 Hz ($Y = 0.005$), we would need 2400 spacecraft to reduce the lifetime of the energetic protons by a factor of 10 in a thin layer of thickness 200 m in the inner belt. Similarly, this number will be 115 spacecraft for operation at 50 K, or 60 spacecraft at 20 K. If we want to remediate the entire belt, however, we have to place approximately these many spacecraft every couple hundred meters for more than 5000 km along the equator. In other words, millions of antennas are required to clean up the inner belt region from energetic protons, which is out of the realm of what can be reasonably put into orbit.

Overall, the combination of small radiation and remediation efficiencies obviates the possibility of a controlled removal of the energetic proton population trapped in the inner Van Allen belt. This being said, the topics of study of this paper are of great interest to the scientific and engineering communities. The demonstration of large-scale superconducting structures in space will have a strong impact on future missions, with a broad range of applications. Additionally, it would be useful to test the science models developed and maybe discover unknown unknowns that may impact the science. For these reasons, the next section outlines a potential scientific mission that would allow us to explore and understand some of the still partially unsolved problems addressed in this manuscript.

5. SCALING DOWN TO DETECTABILITY: A SCIENTIFIC MISSION

Above we showed that it is not engineeringly feasible to remediate the Van Allen proton belt by radiating EMIC waves from space-based antennas. A scaled down scientific mission, however, would allow us to test the science involved, and will offer an opportunity for maturation of some key technologies like deployment of large-scale structures, demonstration of HTS superconductor technology or the development of new low temperature cryocoolers for space applications. There are many scientific missions that could be architected from these points; in what follows, however, we focus on testing the science involved in the concept of remediation.

The characteristic times for wave-particle interaction are all much shorter than the orbital period. Additionally, the interaction will be mostly local, close to the spacecraft. For these reasons, we believe that an on board particle instrument could detect the proton precipitation induced by the antenna. The initial precipitating fluxes at the edge of the loss cone set the detectability of the scattering induced by the transmitter. The lifetime of the entire proton population was determined by the first eigenmode of its decay, which is very slow. The initial precipitating fluxes through the loss cone, however, correspond to higher decay modes. These higher modes have much stronger fluxes through the loss cone, which could be detected by a particle instrument. The NOAA Polar Orbiting Environmental Satellites (POES) carry several of these instruments included in the Space Environment Monitor (SEM-2) instrument package. The Medium Energy Proton and Electron Detector (MEPED) in SEM-2 has two solid-state energetic particle telescopes capable of monitoring protons in six energy bands from 30 keV to 6.9 MeV. The difference between the two proton telescopes onboard the POES spacecraft is their orientation; the 0° -pointing detectors have their field-of-view (FOV) centered along the local zenith and pointing outward, while the 90° detectors are approximately perpendicular to the former. Both detectors have an aperture of $\pm 15^\circ$. These satellites are capable of determining the edge of the loss cone at the spacecraft and selecting only the measurements that fall within this cone [25], [32].

In our case, an orbit close to the equator, say at $L = 1.5$, would maximize the residence time around the same magnetic lines in the core of the inner belt, therefore allowing us to have many observations. Consequently, the mission lifetime could be kept short, limited by the cost of radiation hardening. We expect to detect the particles streaming towards the spacecraft after they interact with the waves not very far from the antenna. For this reason, the FOV of the particle telescope should be centered around the direction of the geomagnetic field lines with an aperture angle close to the edge of the loss cone of the particles. Similarly to POES, the loss cone should be determined at the location of the spacecraft, and the sensor should be capable of detecting proton energies of at least tens of MeV.

Based on POES data of precipitating proton fluxes from the field aligned detector [11], [13], we have set the detectability threshold to $10^2 \text{ cm}^{-2}\text{sr}^{-1}\text{s}^{-1}$, which is above the background proton precipitation in most of the cases. We believe that this is a conservative threshold because POES is only capable of measuring energies below 6.9 MeV; energies above 20 MeV will therefore correspond to lower background precipitating fluxes. Additionally, the transmitted signal should be modulated, which will also create a pattern in the precipitation signature, thus making its detection easier.

Using our test-particle code, we next calculate the induced proton precipitation at the edge of the loss cone, which is used to determine the radiated power required to reach a precipitated flux above the threshold value mentioned above.

An equatorial orbit in the core of the inner belt ($L = 1.5$) is used in our calculations, and the precipitation is computed very close to the antenna since the detectable scattering will happen near the spacecraft. In what follows we analyze three different coil radii: $R_a = 15$ m, $R_a = 5$ m and $R_a = 2.5$ m. A radius of 2.5 m would fit into the launch vehicle without requiring any special folding. On the other hand, the 5 m and 15 m designs assume that we have a working deployment strategy, which is currently being studied in the Space Systems Laboratory at MIT.

Fig. 8 shows the fluxes as a result of the local interaction between energetic protons and EMIC waves radiated from the antenna. A frequency of 0.5 Hz has been considered in the plot. The scientific mission, however, would ideally be capable of sweeping a broad range of frequencies to test the models developed in this study, though engineering for this capability may introduce difficulties which ultimately minimize the range of potential frequencies which may be sampled. Fig. 8(a) shows the directional flux of protons integrated over three energy ranges for the 15 m radius case. The dashed black line corresponds to the loss cone angle in our calculations. We clearly observe that the loss cone partially fills up as a result of the interaction. The plot is for a total wave power of 25 W, which is what is required to

detect precipitating protons with energies >20 MeV according to Fig. 8(b) (the dashed black line in this plot indicates the threshold value). As expected, the fluxes corresponding to the higher energy ranges are smaller, and therefore require more radiated power to enable their detection. Similarly, for the other radii values, we require 3.3 W for $R_a = 5$ m to detect energetic proton fluxes of energies >20 MeV, or 0.9 W for $R_a = 2.5$ m. It must be noted that the different antenna radii affect regions of different total cross-sectional area, the larger the antenna the larger the affected area; in terms of detectability, however, this is not a relevant issue.

The next step consists of determining the dimensions, mass and power requirements of a DC rotating coil antenna capable of radiating the amount of power calculated above. We would like to operate at superconducting temperatures of 50 K or higher, which allow us to use efficient and reliable space-rated cryocoolers. Based on the models developed in Section 3, Table 6 summarizes the radiated power, mass and input power of the coil required to satisfy the detectability threshold. The table analyzes the three different radii, each one requiring a different number of turns (or total wire length) to generate a detectable effect. Additionally, the table also displays the values considering a

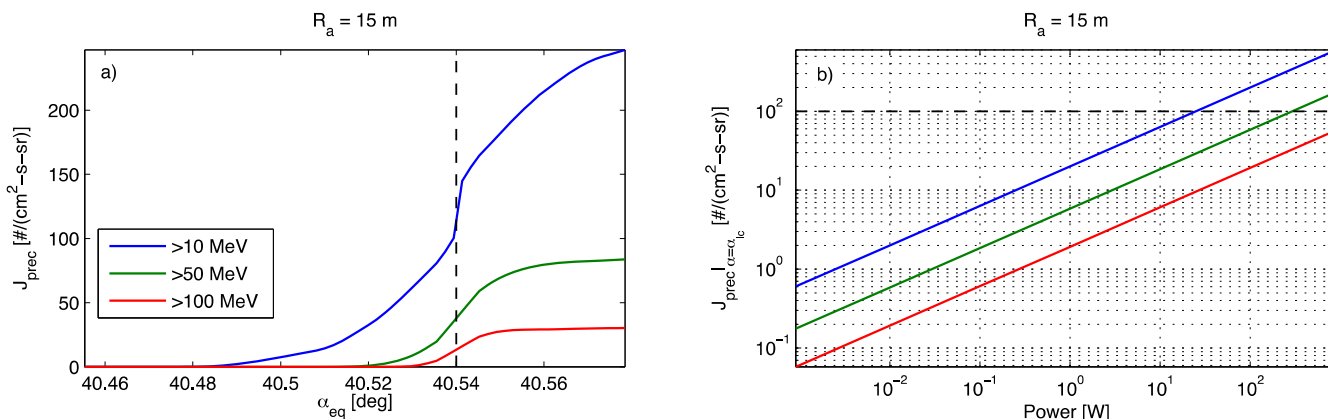


Figure 8 – (a) Directional proton flux for an antenna of $R_a = 15$ m and a radiated power of 2.4 W. (b) Precipitated proton flux at the edge of the loss cone as a function of radiated power for an antenna of $R_a = 15$ m.

50% margin in mass and thermal load, that is, an input power sized to remove 1.5 times more heat than expected.

Table 6. Scientific mission mass and power estimates

	$R_a = 15$ m		$R_a = 5$ m		$R_a = 2.5$ m	
	0%	50%	0%	50%	0%	50%
T_c [K]	50					
# cryos	1					
# turns	255		583		1050	
m_{tape} [kg]	262	393	200	300	180	270
$m_{thermal}$ [kg]	365	546	191	286	136	204
M [kg]	627	940	391	586	316	474
P_{in} [W]	156	207	79	106	58	76

The smaller radius case ($R_a = 2.5$ m) would be the most logical choice for a mission with the purpose of testing the interaction with energetic inner belt protons, since it is capable of generating a detectable scattering on the particles, it does not need to be deployed, and it is the lightest and least power consuming of all the options. In case we want to test the deployment of large-scale structures at the same time, then a larger antenna radius could be used. We suggest, however, separating the two objectives (detection and deployment) into two different scientific missions, thus reducing the risk and complexity of the spacecraft.

6. SUMMARY

In this paper we have characterized a space-borne antenna capable of radiating Electromagnetic Ion Cyclotron (EMIC)

waves with the purpose of inducing controlled precipitation of hazardous Van Allen belt protons. We have shown that a DC rotating coil transmitter is the best candidate to radiate these waves into space, which solves the problem associated with the large self-inductance that appears for AC operation. In terms of radiation, however, the DC rotating idea is equivalent to two static AC orthogonal coils. This radiation maximizes when the axis of the coil (normal to the coil surface) is perpendicular to the Earth's magnetic field direction, although we have shown that the radiation resistance is not very sensitive to angles around this orientation. In order to remain in this preferred orientation, and for equatorial orbits, the angular velocity of the coil has to be parallel to the orbit's angular velocity such as the axis of the coil is close to perpendicular to the external magnetic field. We have shown that this configuration is also favorable in terms of dynamics, which involves, however, the distribution of the spacecraft subsystems on both sides of the coil such that the body becomes a major-axis spinner. This change of inertia provides a much larger gyroscopic stability compared to the perturbations introduced by the magnetic torque.

The small radiation resistance of magnetic dipoles requires the use of superconductors, multiple turn arrangements and large coil radius. High Temperature Superconducting tapes have been selected for this application, since they can work at relatively high temperatures and they are much easier to pack and manipulate than the brittle Low Temperature Superconductor (LTS) designs. Additionally, HTS can be cooled down below their critical temperature with corresponding increase in critical current density. Moreover, the critical current density of HTS tapes dramatically increases with decreasing temperature below 77 K; for this reason, it is strongly desired to operate below the nominal 77 K, since small temperature reductions produce large performance improvements. For the HTS design of SuperPower, we have characterized the performance of the superconductor as a function of the number of turns of the coil, and analyzed the passive and active thermal control required to keep the wire at operating conditions. More specifically, we have selected 30 layers of Multilayer Insulator (MLI) together with Quartz over Silver Optical Solar Reflector (OSR) coating. For the active thermal control, we have adopted a hybrid cooling approach consisting of a flexible forced vapor system enclosing the coil to ensure isothermalization, and Stirling-cycle cryocoolers to extract the heat from the vapor. The use of passive heat pipes has been ruled out due to their stiffness, which will hinder the deployment of a flexible structure. Cryocoolers for temperatures below 50 K have been successfully used in space, and they are efficient and reliable. On the other hand, operation below 20 K, which is desirable in terms of critical current, requires heavy and power demanding cryocoolers like the ones developed by the Jet Propulsion Laboratory (JPL) for the Planck spacecraft. We have estimated that an antenna of 15 m radius operating at 20 K can radiate 6.4 W and requires 940 W of input power, which corresponds to a radiation efficiency of $\eta_{\text{rad}} = 0.7\%$. For operation at 50 K, the

antenna radiates 3.3 W but requires 100 W of input power, i.e. $\eta_{\text{rad}} = 3.3\%$. A clear tradeoff exists between radiated power and radiation efficiency: the larger the radiated power the colder the temperature of the superconductor, which requires power demanding cryocoolers and reduces the antenna radiation efficiency.

Using simulations of the interaction between waves and energetic trapped protons we have estimated the power required to remediate the inner Van Allen belt region, where remediation has been defined as the capability of reducing the natural residence time of the longer-lived particles by a factor of 10. We have shown that the combination of small radiation and remediation efficiencies obviates the possibility of a controlled removal of the energetic proton population trapped in the inner Van Allen belt. A scientific mission scaled down to detectability of the precipitating fluxes, however, would allow us to test the science involved in the concept of remediation, and will offer an opportunity for maturation of some key technologies. An orbit close to the equator at $L = 1.5$ would be ideal for this mission, since it maximizes the residence time in the inner belt, therefore allowing us to have many observations; the mission lifetime could be kept short, limited by the cost of radiation hardening. An onboard particle telescope could detect the particles streaming towards the spacecraft after they interact with the waves not very far from the antenna. For this reason, the field-of-view of the particle telescope should be centered around the direction of the geomagnetic field lines with an aperture angle close to the edge of the loss cone of the particles. Based on measurements from the Medium Energy Proton and Electron Detector (MEPED) onboard the NOAA Polar Orbiting Environmental Satellites (POES), we have determined that a minimum proton precipitating flux of $10^2 \text{ cm}^{-2}\text{sr}^{-1}\text{s}^{-1}$ is required for detection, which is above the background precipitation level. The radiated power required to generate this flux has been calculated for three different coil radii of 15, 5 and 2.5 meters. A radius of 2.5 m would fit into the launch vehicle without requiring any special folding; on the other hand, the 5 m and 15 m designs assume that we have a working deployment strategy, which is currently being studied in the Space Systems Laboratory at MIT. The 15 m radius has to radiate 25 W to generate detectable precipitation, while the 2.5 m radius only needs 0.9 W of radiated power. The different antenna radii affect regions of space of different total cross-sectional area; for this reason, the larger radius has to radiate more power to induce detectable precipitation. Finally, we have also calculated the mass and input power of these antenna designs. The smaller radius case (2.5 m) seems the most logical choice for a mission with the purpose of testing the interaction with energetic inner belt protons, since it is capable of generating a detectable scattering on the particles, it does not need to be deployed, and it is the lightest (316-474 kg) and least power consuming (56-76 W) of all the options.

ACKNOWLEDGEMENTS

The authors would like to thank Prof. Lorenzini from the University of Padova for his work on the dynamics of the antenna, as well as Prof. Sedwick at the University of Maryland for his research on active thermal control.

REFERENCES

- [1] B. Abel and R. M. Thorne, "Electron scattering loss in Earth's inner magnetosphere 1. Dominant physical processes," *J. Geophys. Res.*, vol. 103, no. A2, pp. 2385-2396, 1998.
- [2] J. M. Albert, "Analysis of quasi-linear diffusion coefficients," *J. Geophys. Res.*, vol. 104, no. A2, pp. 2429-2441, 1999.
- [3] D. N. Baker, "The occurrence of operational anomalies in spacecraft and their relationship to space weather," *IEEE Trans. Plasma Sci.*, vol. 28, no. 6, pp. 2007-2016, Dec. 2000.
- [4] D. N. Baker, "Satellite anomalies due to space storms," in *Space Storms and Space Weather Hazards*, vol. 38, I. A. Daglis, Ed. Dordrecht, The Netherlands: Kluwer Academic, 2001, pp. 285-311.
- [5] K. Balmain, "The impedance of a short dipole antenna in a magnetoplasma," *IEEE Trans. Antennas Propag.*, vol. 12, no. 5, pp. 605-617, Sep. 1964.
- [6] T. F. Bell and T. Wang, "Radiation resistance of a small filamentary loop antenna in a cold multicomponent magnetoplasma," *IEEE Trans. Antennas Propag.*, vol. 19, no. 4, pp. 517-522, Jul. 1971.
- [7] P. Bhandari, M. Prina, R. C. Bowman Jr., C. Paine, D. Pearson, and A. Nash, "Sorpton coolers using a continuous cycle to produce 20 K for the Planck flight mission," *Cryogenics*, vol. 44, no. 6, pp. 395-401, 2004.
- [8] W. L. Brown and J. D. Gabbe, "The electron distribution in the Earth's radiation belts during July 1962 as measured Telstar," *J. Geophys. Res.*, vol. 68, no. 3, pp. 607-618, 1963.
- [9] T. W. Chevalier, U. S. Inan, and T. F. Bell, "Fluid simulation of the collisionless plasma sheath surrounding an electric dipole antenna in the inner magnetosphere," *Radio Sci.*, vol. 45, p. 1010, 2010.
- [10] M. B. Cohen, "ELF/VLF phased array generation via frequency-matched steering of a continuous HF ionospheric heating beam," Ph.D. dissertation, Dept. of Electrical Engineering, Stanford Univ., Stanford, CA, 2009.
- [11] N. P. Dmitrieva, A. G. Yahnin, T. V. Miroshnikova, and I. V. Despirak, "Precipitation of Energetic Protons at High Latitudes: Dependence on the Interplanetary Magnetic Field," *Cosmic Res.*, vol. 37, no. 4, pp. 317-325, 1999.
- [12] A. Dragt, M. Austin, and R. White, "Cosmic ray and solar proton albedo neutron decay injection," *J. Geophys. Res.*, vol. 71, no. 5, pp. 1293-1304, 1966.
- [13] M. J. Engebreston, M. R. Kessard, J. Bortnik, J. C. Green, R. B. Horne, D. L. Detrick, A. T. Weatherwax, J. Manninen, N. J. Petit, J. L. Posch, et al., "Pc1-Pc2 waves and energetic particle precipitation during and after magnetic storms: Superposed epoch analysis and case studies," *J. Geophys. Res.: Space Phys.*, vol. 113, no. A1, 2008.
- [14] D. G. Gilmore, *Satellite thermal Control Handbook*, El Segundo, CA: Aerospace Corporation Press, 1994.
- [15] A. Gigliotti, W. Gekelman, P. Pribyl, S. Vicena, A. Karavaev, X. Shao, A. Sharma, and D. Papadopoulos, "Generation of polarized shear Alfvén waves by a rotating magnetic field source," *Phys. Plasmas*, vol. 16, p. 092106, 2009.
- [16] D. W. Hazelton, "2G HTS Conductors at SuperPower", in *Low Temperature High Field Superconductor Workshop*, Napa, CA, Nov. 2012.
- [17] W. L. Imhof, J. B. Reagan, H. D. Voss, E. E. Gaines, D. W. Datlowe, J. Mabilia, R. A. Helliwell, U. S. Inan, J. Katsufarakis, and R. G. Joiner, "Direct observation of radiation belt electrons precipitated by the controlled injection of VLF signals from a ground-based transmitter," *J. Geophys. Res.*, vol. 10, pp. 361-364, 1983.
- [18] U. S. Inan, T. F. Bell, and J. Bortnik, "Controlled precipitation of radiation belt electrons," *J. Geophys. Res.*, vol. 108, no. A5, p. SMP6-1, 2003.
- [19] U. S. Inan, H. C. Chang, and R. A. Helliwell, "Electron precipitation zones around major ground-based VLF signal sources," *J. Geophys. Res.*, vol. 89, no. A5, pp. 2891-2906, May 1984.
- [20] V. K. Jordanova, C. J. Farrugia, R. M. Thorne, G. V. Khazanov, G. D. Reeves, and M. F. Thomsen, "Modeling ring current proton precipitation by electromagnetic ion cyclotron waves during the May 14-16, 1997 storm," *J. Geophys. Res.*, vol. 106, no. A1, pp. 7-22, 2001.
- [21] A. V. Karavaev, N. A. Gumerov, K. Papadopoulos, X. Shao, A. S. Sharma, W. Gekelman, Y. Wang, B. Van Compernelle, P. Pribyl, and S. Vincena, "Generation of shear Alfvén waves by a rotating magnetic field source: Three-dimensional simulations," *Phys. Plasmas*, vol. 18, p. 032113, 2011.
- [22] P. Kulkarni, U. S. Inan, and T. F. Bell, "Energetic electron precipitation induced by space based VLF

- transmitters,” *J. Geophys. Res.*, vol. 113, no. A12, p. 9203, 2008.
- [23] D. W. Kwon, “Electromagnetic Formation Flight of Satellite Arrays,” M.S. thesis, Dept. of Aeronautics and Astronautics, Mass. Inst. Technol., Cambridge, MA, 2005.
- [24] D. W. Kwon, “Cryogenic heat pipe for cooling high temperature superconductors with application to Electromagnetic Formation Flight satellites,” Ph.D. thesis, Dept. of Aeronautics and Astronautics, Mass. Inst. Technol., Cambridge, MA, 2009.
- [25] M. M. Lam, R. B. Horne, N. P. Meredith, S. A. Glauert, T. Moffat-Griffin, and J. C. Green, “Origin of energetic electron precipitation > 30 keV into the atmosphere,” *J. Geophys. Res.: Space Phys.*, vol. 115, no. A4, 2010.
- [26] T. M. Loto’aniu, R. M. Thorne, B. J. Fraser, and D. Summers, “Estimating relativistic electron pitch angle scattering rates using properties of the electromagnetic ion cyclotron wave spectrum,” *J. Geophys. Res.*, vol. 111, no. A4, 2006.
- [27] G. Manfreda, “Review of ROXIE’s Material Properties Database for Quench Simulation,” Magnets, Superconductors and Cryostats, TE-MS, Internal Note 2011-24, 2011.
- [28] D. W. Miller, “Mid-term report to the NASA Shared Services Center (NSSC),” Massachusetts Institute of Technology, Cambridge, MA, 2013.
- [29] F. S. Mozer, D. D. Elliott, J. D. Mihalov, G. A. Paulikas, A. L. Vampola, and S. C. Freden, Preliminary analysis of the fluxes and spectrums of trapped particles after the nuclear test of July 9, 1962,” *J. Geophys. Res.*, vol. 68, no. 3, pp. 641–649, 1963.
- [30] G. F. Pieper, “A second radiation belt from the July 9, 1962, nuclear detonation,” *J. Geophys. Res.*, vol. 68, no. 3, pp. 651–655, 1963.
- [31] C. M. Rey, W. C. Hoffman Jr., F. R. Chang-Diaz, A. V. Ilin, A. J. Petro, D. S. Winter, H. Mukai, and S. W. Schwensterly, “Design and fabrication of an HTS magnet for the VASIMR experiment,” *IEEE Trans. Appl. Supercond.*, vol. 12, no. 1, pp. 993-996, 2002.
- [32] C. J. Rodger, T. Raita, M. A. Clilverd, A. Seppälä, S. Dietrich, N. R. Thomson, and T. Ulich, “Observations of relativistic electron precipitation from the radiation belts driven by EMIC waves,” *Geophys. Res. Lett.*, vol. 35, 2008.
- [33] R. G. Ross Jr. and R. F. Boyle, “An overview of NASA space cryocooler programs-2006,” Jet Propulsion Laboratory, National Aeronautics and Space Administration, Pasadena, CA, 2006.
- [34] V. Selvamanickam, Y. Yao, Y. Chen, T. Shi, Y. Liu, N. D. Khatri, J. Liu, C. Lei, E. Galstyan, and G. Majkic, “The low-temperature, high-magnetic-field critical current characteristics of Zr-aded (Gd, Y) Ba₂Cu₃O_x superconducting tapes,” *Supercond. Sci. Technol.*, vol. 25, no. 12, p. 125, 2012.
- [35] K. Shirley, S. Banks, R. Boyle, and R. Unger, “Design and Qualification of the AMS-02 Flight Cryocoolers,” in *Space Cryogenics Workshop*, Colorado Springs, CO, 2005.
- [36] R. Siegel and J. Howell, *Thermal radiation heat transfer*, 4th ed. New York, NY: Taylor and Francis, 2002, sec. 8.2.
- [37] P. Song, B. W. Reinisch, V. Paznukhov, G. Sales, D. Cooke, J. N. Tu, X. Huang, K. Bibl, and I. Galkin, “High-voltage antenna-plasma interaction in whistler wave transmission: Plasma sheath effects,” *J. Geophys. Res.*, vol. 112, no. A3, 2007.
- [38] M. de Soria-Santacruz, “Radiation of VLF/ELF waves from a magnetospheric tether,” M.S. thesis, Dept. of Aeronautics and Astronautics, Mass. Inst. Technol., Cambridge, MA, 2011.
- [39] M. de Soria-Santacruz and M. Martinez-Sanchez, “Electromagnetic Ion Cyclotron waves for Radiation Belt Remediation applications”, *IEEE Trans. Plasma Sci.*, 2013. doi: 10.1109/TPS.2013.2260181.
- [40] M. de Soria-Santacruz, K. G. Orlova, M. Martinez-Sanchez, and Y. Y. Shprits, “Scattering rates of inner belt protons by EMIC waves: A comparison between test particle and diffusion simulations,” *Geophys. Res. Lett.*, vol. 40, no. 18, pp. 4793-4797, 2013.
- [41] G. Spanjers, J. Winter, D. Cohen, A. Adler, J. Guarnieri, M. Tolliver, G. Ginet, B. Dichter, and J. Summers, “The AFRL Demonstration and Science Experiments (DSX) for DoD space capability in the MEO,” in *IEEE Aerospace Conference*, Big Sky, MA, 2006.
- [42] W. T. Thomson, *Introduction to space dynamics*, Mineola, NY: Dover Publications Inc., 1986.
- [43] J. Tu, P. Song, and B. W. Reinisch, “Plasma sheath structures around a radio frequency antenna,” *J. Geophys. Res.*, vol. 113, no. A7, 2008.
- [44] M. Walt, *Introduction to geomagnetically trapped radiation*. Cambridge, UK: Cambridge Univ. Press, 2005.
- [45] T. N. C. Wang and T. F. Bell, “VLF/ELF input impedance of an arbitrarily oriented loop antenna in a cold collisionless multicomponent magnetoplasma,” *IEEE Trans. Antennas Propag.*, vol. 20, no. 3, pp. 394-398, May 1972.
- [46] G. K. White and S. J. Collocott, *Heat capacity of reference materials, Cu and W*. American Chemical

Society and the American Institute of Physics for the National Bureau of Standards, 1984.

BIOGRAPHY

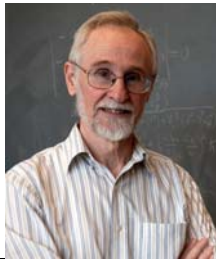


***Maria de Soria-Santacruz** received her S.B. in Aerospace Engineering from the Polytechnic University of Catalonia, Spain, in 2009, and the S.M. degree in the same field from MIT in 2011. She is currently a Ph.D. candidate in the Department of Aeronautics and Astronautics at MIT.*

Her current research interests include space systems, space weather, plasma waves, and magnetospheric physics.

Guillermo

Gwen



***Manuel Martínez-Sánchez** is a professor of Aeronautics and Astronautics at MIT. He obtained his Engineer's diploma from the Universidad Politécnica of Madrid, and his doctorate from MIT. His area of research is space propulsion, with extension to space physics and other applications of plasma science.*



***David W. Miller** is a Professor and Director of the Space Systems Laboratory in the Department of Aeronautics at MIT. His research focus is in dynamics, controls and systems engineering as applied to distributed satellite systems and precision optical telescopes. He has developed a series of ground testbed and Shuttle flight facilities for the*

conduct of research into dynamic modeling and control synthesis for precision optical systems.

Appendix 4: Tradespace Investigation of a Telescope Architecture for Next-generation Space Astronomy and Exploration

Tradespace Investigation of a Telescope Architecture for Next-generation Space Astronomy and Exploration

Giuseppe Cataldo, Mark Chodas, Pratik Davé, Atray Dixit, Sherrie Hall, Robert Harris, Dustin Hayhurst, Fernando Hicks, Chris Jewison, Ioana Josan-Drinceanu, Brandon Karlow, Bryan McCarthy, Andrew Owens, Eric Peters, Margaret Shaw, David Sternberg, Kathleen Voelbel, Marcus Wu

Prof. David Miller, Prof. Alessandro Golkar, Prof. Kerri Cahoy, Dr. Rebecca Masterson, Gwendolyn Gettliffe

May 2014

SSL # 13-14

Tradespace Investigation of a Telescope Architecture for Next-generation Space Astronomy and Exploration

Giuseppe Cataldo, Mark Chodas, Pratik Davé, Atray Dixit, Sherrie Hall, Robert Harris, Dustin Hayhurst, Fernando Hicks, Chris Jewison, Ioana Josan-Drinceanu, Brandon Karlow, Bryan McCarthy, Andrew Owens, Eric Peters, Margaret Shaw, David Sternberg, Kathleen Voelbel, Marcus Wu

Prof. David Miller, Prof. Alessandro Golkar, Prof. Kerri Cahoy, Dr. Rebecca Masterson, Gwendolyn Gettliffe

May 2014

SSL # 13-14

This work is based on the unaltered text of the final report by the 16.89 Spring 2013 class.

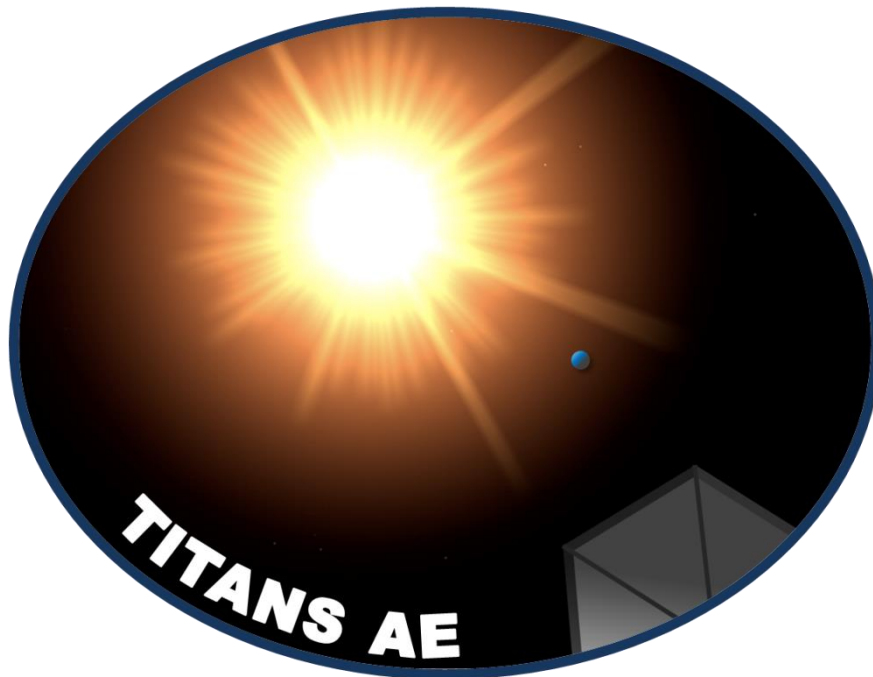
TITANS AE

Tradespace Investigation of a Telescope Architecture for Next-generation Space Astronomy and Exploration

May 2013

Department of Aeronautics and Astronautics

Massachusetts Institute of Technology



Students: Giuseppe Cataldo, Mark Chodas, Pratik Davé, Atray Dixit, Sherrie Hall, Robert Harris, Dustin Hayhurst, Fernando Hicks, Chris Jewison, Ioana Josan-Drinceanu, Brandon Karlow, Bryan McCarthy, Andrew Owens, Eric Peters, Margaret Shaw, David Sternberg, Kathleen Voelbel, Marcus Wu

Instructors:

Prof. David Miller, Prof. Alessandro Golkar, Prof. Kerri Cahoy, Dr. Rebecca Masterson, Gwendolyn Gettliffe

ACKNOWLEDGEMENTS

The authors would like to thank Professor David Miller, Professor Alessandro Golkar, Professor Kerri Cahoy, Dr. Rebecca Masterson, and Gwen Gettliffe for their guidance on this project thus far, as well as Tupper Hyde, Harley Thronson, Marc Postman, Lee Feinberg, Dan Lester, Howard MacEwen, and Swati Mohan for their helpful input.

TABLE OF CONTENTS

1 EXECUTIVE SUMMARY	16
1.1 Stakeholder Analysis	17
1.2 Technical Requirements and Assumptions.....	17
1.3 Architectural Decisions.....	18
1.3.1 Communications Architecture	18
1.3.2 Modularity.....	18
1.3.3 Location of Servicing.....	18
1.3.4 Frequency of Servicing	19
1.3.5 Assembly and Servicing Technique.....	19
1.3.6 Segmentation of Primary Mirror.....	19
1.3.7 Primary Mirror Segment Support Method	19
1.4 Trade Metrics	19
1.4.1 Cost	19
1.4.2 Utility to Science.....	19
1.4.3 Failed Downtime.....	20
1.4.4 Servicing Margin.....	20
1.5 Model Structure and Results	20
1.6 Conclusions	23
2 INTRODUCTION.....	24
3 TELESCOPE STAKEHOLDER ANALYSIS	25
3.1 Stakeholder Analysis	25
3.2 Requirements Definition.....	28
3.2.1 Science Goals.....	28
3.2.2 Model Goals.....	30
3.3 Architectural Assumptions.....	31
3.3.1 Operate at Sun-Earth L2	31
3.3.2 16.8-meter-diameter primary mirror	31
3.3.3 On-orbit assembly is necessary	31
3.3.4 Segmented primary mirror	31
3.3.5 Launch in 2028, Phase A in 2020, Technologies be TRL 6 by 2020.....	31
3.3.6 Lifetime of 40 years	31
3.3.7 Autonomous servicing, no human servicing.....	31
3.3.8 Scheduled servicing	31
3.3.9 No servicing of optical surfaces, only instruments and engineering components	32
3.3.10 No formation-flying coronagraph	32
3.3.11 Federated Satellite System (FSS) considered as a downlink architecture	32
4 ARCHITECTURAL ENUMERATION	33
4.1 Historical Analysis of Past Missions.....	33
4.2 Function and Form Mapping.....	34
4.3 Architectural Decisions.....	37
4.3.1 Communications Type	37
4.3.2 Modularity.....	40
4.3.3 Location of Servicing.....	44
4.3.4 Frequency of Servicing	45
4.3.5 On-Orbit Assembly/Servicing Technique.....	46
4.3.6 Segmentation of Primary Mirror	48
4.3.7 Primary Mirror Segment Support Method	50

5	Metrics and Model Description	53
5.1	Model Overview	53
5.2	Trade Metrics Descriptions.....	55
5.2.1	Utility to Science.....	55
5.2.2	Serviceability – The Specific Servicing Margin	56
5.2.3	Failed Downtime.....	58
5.2.4	Cost	59
5.3	Code Module Descriptions	61
5.3.1	Design Structure Matrix.....	61
5.3.2	Component Family Database	61
5.3.3	Subsystem Modules	63
5.3.4	Operations Module.....	129
5.3.5	Trade Metrics Calculation.....	135
6	MODEL VALIDATION	145
7	RESULTS AND ANALYSIS	147
7.1	Tradespace Exploration and Analysis.....	147
7.1.1	2-D visualization of tradespace: normalized Utility to Science vs. normalized Lifecycle Costs	148
7.1.2	3-D Visualization of Tradespaces	155
7.2	Interactions and Main Effects.....	159
7.2.1	Science Utility.....	159
7.2.2	Cost	161
7.2.3	Servicing Margin.....	162
7.2.4	Downtime.....	166
7.3	Tradespace Characterization.....	169
7.3.1	Principle Component Analysis (PCA)	169
7.3.2	Hierarchical Clustering	171
7.4	Sensitivity Analysis	174
7.4.1	Assumptions.....	174
7.4.2	Sensitivity of Trade Metrics to Assumptions.....	175
8	FUTURE WORK	185
8.1	Next steps to increase the validity of the model.....	185
8.2	Next steps for tradespace exploration	186
9	CONCLUSION	188
	APPENDIX A: VARIABLE LIST	189
	APPENDIX B: STAKEHOLDER QUESTIONS AND ANSWERS.....	195
	APPENDIX C: COMPONENTS DATABASE.....	204
	APPENDIX D: STRUCTURAL DSM.....	205
	APPENDIX E: THERMAL DSM.....	206
	APPENDIX F: DATA DSM	207
	APPENDIX G: POWER DSM.....	208
	APPENDIX H: OPTICAL DSM.....	209

APPENDIX I: DESCRIPTION OF ATLAST REQUIREMENTS AND THEIR IMPLICATIONS.....	210
APPENDIX J: FORMS AND FUNCTIONS FOR HISTORICAL MISSIONS.....	212
APPENDIX K: PROPOSED METHODOLOGY FOR CALCULATING INSTRUMENT-LEVEL SCIENCE VALUE.....	215
REFERENCES	223

LIST OF FIGURES

Figure 1: Needs of major stakeholders, organized as by inputs and outputs.....	27
Figure 2: Resolvable exoplanets as a function of mirror diameter.....	32
Figure 3: Reduced Architectural Decisions and Forms for Each Subsystem.....	35
Figure 4: LTA Architectural Decisions and Forms.....	36
Figure 5: Large Ground-Based Antennas of the Deep Space Network.....	37
Figure 6: Iridium satellite constellation for global communications.....	38
Figure 7: Visualization of FSS network and an individual satellite	39
Figure 8: Satellite to Ground Laser Communications.....	40
Figure 9: Notional trade between the number of modules in a satellite and the lifecycle cost (red), which is the sum of the costs incurred during the servicing (blue) and the development and launch phases.	41
Figure 10: Modularity breakdown tree.....	42
Figure 11: Reliability of the Hubble Space Telescope as a function of time since last servicing mission. Note the significant decline in reliability as time goes on.....	44
Figure 12: L1 Orbit Trajectory Used for Servicing (LOTUS), one of the orbits under consideration for servicing operations at a greater proximity to Earth.	45
Figure 13: (a) The JWST deployment sequence (mirror only) (b) The ATLAST stowed and deployed configurations.....	47
Figure 14: DARPA’s Phoenix project. Artist’s concept of the servicer/tender (or tug) assembling a space structure.....	47
Figure 15: Notional packing and assembly scenario for a highly structurally-segmented primary-mirror architecture.....	49
Figure 16: Architectural options selected for exploration in the primary mirror segmentation decision...50	50
Figure 17: Notional packing of segments into payload fairings of various heights and diameters (sizes are to scale).	50
Figure 18: The Herschel telescope primary mirror with ribbed backstructure.....	51
Figure 19: Surface-Parallel vs. Surface-Normal Actuation Techniques	52
Figure 20: N ² diagram showing interactions between code modules in the MATLAB model.....	54
Figure 21: Discovery efficiency for selected Hubble instruments	55
Figure 22: Tentative ATLAST Science Instruments and their FOV.....	67
Figure 23: Communication system inputs (left) and outputs (right)	68

Figure 24: The communication system design and sizing process, adapted for the context of this class ...	71
Figure 25: The communication systems architecture considered for the scope of this class	72
Figure 26: The orbit of TITANS AE in STK – at Sun-Earth L2.....	73
Figure 27: Alternate view of the orbit	73
Figure 28: STK scenario showing the Goldstone DSN site and the Iridium and TDRSS networks	75
Figure 29: E_b/N_0 values for different coding methods and BER desired values	81
Figure 30: The DSN trade: the increase in daily data volume (Gbits/day) versus the antenna size (meters)	83
Figure 31: The TDRSS trade: the increase in daily data volume (Gbits/day) versus the antenna size (meters).....	83
Figure 32: The laser communications trade: the increase in daily data volume (Gbits/day) versus the optical telescope size (m)	84
Figure 33: Avionics subsystem inputs (left) and outputs (right).....	89
Figure 34: Typical Avionics subsystem for satellite systems	90
Figure 35: ΔV Requirements for Transfers Between Various SE-L2 and EM-L2 Orbits.....	93
Figure 36: Zernike modes, which describe how a wavefront is distorted by a specific aberration2.....	112
Figure 37: Ithaco E Reaction Wheel PSD	113
Figure 38: Simplified Visualization of Surface-Parallel vs. Surface-Normal Configurations in the FEM107	
Figure 39: Primary Mirror Mesh for the FEM of the 16.8-m, 36-segment, $f/1.5$ Telescope, where (a) is a top-down view and (b) is a side view with the focal point.....	108
Figure 40: Raft Segmentation in the FEM where red shows surface-parallel connection between rafts and blue shows backstructure connection within rafts. Shown for three segmentations where (a) is the JWST-style fold, (b) the 12-segment, and (c) the 6-segment.	109
Figure 41: Normal Modes for the Primary Mirror where (a) is the undeflected mirror, (b) is the 6.09 Hz, 1 st , saddle bending mode and (c) is the 13.06 Hz, 7 th bending mode	110
Figure 42: Sample module definitions matrix with three modules	115
Figure 43: Fault tree diagram for the Structures and Mechanisms component failures that lead to system failure, where the numbers represent the corresponding row/component number in the Component DB shown in Appendix C.....	120
Figure 44: State diagram for the Attitude and Determination Control subsystem. Five different states were identified which lead to mission failure	124
Figure 45: State probabilities as a function of time. The time span was fixed to 10 years, because this could be the longest time interval without servicing. Since significant technology advancements may	

occur in such a long period of time, this type of analysis can be rerun for the remaining 30 years of the telescope’s lifetime by ensuring the failure rate values are updated.	127
Figure 46: Probability of failure for the subsystems affected by mission risk over a time span of 10 years, which is the longest time interval that could exist between servicing missions.....	128
Figure 47: Code structure diagram for the operations module.....	130
Figure 48: Comparison of cost model output to actual space telescope programs.....	144
Figure 49: Pareto front solutions (in red) for tradespace bounded by cost and utility to science.....	148
Figure 50: 2-D view of Filtered 3-D tradespace of “Pareto Optimal” solutions for the space telescope bounded by utility to science and cost.....	149
Figure 51: “Pareto Optimal” subset solutions closest to the utopia point (Cluster 1) on the filtered tradespace bounded by utility to science and cost, dominated by solutions with “7-1-1” architectural vectors.	150
Figure 52: Polar plot indicating frequency of occurrence for every alternative in each architectural decision for Pareto Optimal solutions. ML: Modularity, SL: Servicing Location, SF: Servicing Frequency, CA: Communications Architecture, PMA: Primary Mirror Actuation, AST: Assembly/Servicing Technique, SSPM: Structural Segmentation Primary Mirror Gray circle of radius 1 represents expected radius of any architecture decision if it is not associated with Pareto solutions.....	151
Figure 53: Polar plot array illustrating dominant architectural alternatives in every identified cluster. ...	152
Figure 54: Pareto trace of solutions across different tradespaces defined by combinations of various trade metrics with a fixed bound of cost.	154
Figure 55: 3-D tradespace of the space telescope bounded by cost, utility to science and failed downtime.	155
Figure 56: 3-D tradespace of the space telescope bounded by cost, utility to science, and service margin.	156
Figure 57: 3-D tradespace of the space telescope bounded by cost, utility to science and failed downtime, with “Pareto Optimal” solutions highlighted in red.	157
Figure 58: Filtered 3-D tradespace of “Pareto Optimal” solutions for the space telescope bounded by cost, utility to science and failed downtime.....	158
Figure 59: Main effects plot for Science Utility.....	159
Figure 60: Interaction Plot for Science Utility	160
Figure 61: Main effects plot for Cost	161
Figure 62: Interaction Plot for Cost.....	162
Figure 63: Tornado Chart of Component MTBF Delta Values.....	176
Figure 64: Tornado Chart of Reliability Delta Values	177
Figure 65: Crossover Percentages for Component MTBF variations	178

Figure 66: Modularity composition of architectures with higher costs at MTBF 50% 179

Figure 67: Crossover Percentages for Reliability Threshold variations 181

Figure 68: CDF of Cost varying Reliability Threshold (Comparing distributions) 182

Figure 69: CDF of Percent Change in Cost varying Reliability Threshold (comparing architectures)..... 183

Figure 70: Pareto Movement of Baseline Frontier 184

LIST OF TABLES

Table I: Assumptions derived from the ATLAST requirements, stakeholder analysis, and model complexity reduction.....	18
Table II: List of surveyed stakeholders	25
Table III: List of mission goals from stakeholder analysis	29
Table IV: ATLAST key optical performance requirements	30
Table V: List of goals for TITANS AE model based on stakeholder analysis	30
Table VI: Description of the 7 levels of the modularity architectural decision	43
Table VII: Component Family DB variable names organized by subsystem	61
Table VIII: Calculation of probability of no instrument failure.....	64
Table IX: Summary of Hubble instrument mass, power, and volume	65
Table X: Summary of instrument mass, power, and volume for TITANS AE model.....	66
Table XI: Communication system design process	72
Table XII: Iridium satellites considered for link access calculations.....	74
Table XIII: TDRSS satellites considered for link access calculations.....	74
Table XIV: The main parameters for the link budget	75
Table XV: Typical communication losses and their values	77
Table XVI: Parabolic antenna characteristics	78
Table XVII: Horn antenna characteristics.....	78
Table XVIII: Array antenna characteristics	79
Table XIX: DSN transmit and receive frequency range	80
Table XX: The link budget for the high gain antenna downlink case.....	80
Table XXI: The link budget for the low gain antenna downlink case	81
Table XXII: Summary of TITANS AE communication design	84
Table XXIII: ΔV requirements for various transfer trajectories	93
Table XXIV: Performance characteristics for various thrusters'	93
Table XXV: Values for pressurization system variables	94

Table XXVI: Power consumption and efficiencies for selected thrusters 95

Table XXVII: Summary of component families per thermal block..... 101

Table XXVIII: Number of primary-mirror actuators for mirror support architectural decision. 104

Table XXIX: Jitter analysis results* 114

Table XXX: Launch vehicle properties and cost estimates 141

Table XXXI: TITANS AE model validation against HST and JWST 145

1 EXECUTIVE SUMMARY

NASA has been engaged in a number of space missions aimed to further our understanding of the universe through the development and deployment of space telescopes such as Hubble, Herschel, Spitzer, Chandra, and Kepler, as well as the James Webb Space Telescope (JWST) currently under construction. Such instruments cover a large band of the electromagnetic spectrum, from the X-ray to the infrared, providing valuable information on a number of phenomena of interest to the entire scientific community. The 2010 Decadal Survey for Astronomy and Astrophysics calls for a medium-scale space mission that will hunt exoplanets in a wide field as an attempt to find stellar systems similar to this solar system and Earth-like planets. The Wide-Field InfraRed Survey Telescope (WFIRST) would be the candidate for this type of mission, which would play a preparatory role in the development of a large-scale space-based mission intended to image Earth-like planets in the habitable zones of nearby stars and study their atmospheres. Thus, a telescope for imaging and spectroscopy of exoplanets from the ultra-violet to near infra-red spectra will be one of the top-priority areas in the 2020 decade.

In order to lay the bases for this endeavor, NASA has commissioned the Massachusetts Institute of Technology's Space Systems Laboratory to perform a tradespace exploration analysis for a large, segmented telescope, referred to as a Large Telescope Array (LTA), with the capabilities necessary to achieve the above-mentioned scientific objectives. Specifically, this task involves the identification of a set of architectural decisions, which, once made, define an architecture that can be assessed based upon quantitative metrics (e.g., cost, mass, complexity, risk, performance, serviceability, assemble-ability). By varying the architectural decisions, a family of architectures can be compared, via these metrics, to identify the attributes that are common to the better performing architectures. To accomplish this task, then, the following questions were answered:

- 1. Who are the stakeholders and what are their needs and desires?*
The stakeholders are scientific organizations, high-tech companies, and universities interested in a tradespace study for a next-generation telescope capable of opening new horizons to science and stimulate the development of new technologies.
- 2. Based on the results of this stakeholder analysis, are there any assumptions that need to be taken into account and that would limit the scope of such a tradespace analysis?*
The assumptions were made based on the stakeholder needs and desires, the technical requirements of similar technologies, and the necessity to keep the scope of this project at a level manageable by a one-semester graduate course.
- 3. What are the technical requirements to build an LTA?*
Derived from NASA's Advanced-Technology Large-Aperture Space Telescope (ATLAST) concept, the requirements are: a 16.8-m-diameter primary mirror, operation at Sun-Earth Lagrangian Point 2, on-orbit assembly, launch in 2028, technology readiness level (TRL) 6 by 2020.
- 4. What architectural decisions can be made?*
The following seven were selected: communications architectures, modularity, location of servicing, frequency of servicing, assembly and servicing technique, primary mirror segmentation, and primary mirror segment support method.
- 5. What metrics can be employed to evaluate such architectures?*
The following four metrics were chosen: cost, utility to science, failed downtime, and servicing margin.

6. *What are the best-performing architectures resulting from a Pareto-front analysis?*

The Pareto-optimal solutions are represented by those which generate high utility to science at low cost.

The ultimate goal of the project was to develop a model that would take as inputs the assumptions, enumerate the architectural decisions, and develop a tradespace characterized by the selected trade metrics. The model would also determine how requirements affect architectural choices and examine the interactions between the different subsystems of the LTA. The following sections will illustrate the main steps taken during this process, leaving an exhaustive description of all their details to the dedicated sections of the present report.

1.1 Stakeholder Analysis

The following groups have been interested in similar architectural trade studies and were our points of contact throughout the project:

- NASA Goddard Space Flight Center (GSFC)
- NASA Headquarters (HQ)
- The Jet Propulsion Laboratory (JPL)
- The Space Telescope Science Institute (STScI)
- ITT (formerly Kodak)
- MIT
- Skoltech

Such a diverse set of stakeholders provided a broad range of perspectives on the key assumptions and technical requirements needed to define our architectures. They were asked questions related to mission goals, budget and cost models, mirror and detector technologies, data management, launch vehicle options, and inclusion of other potential stakeholders. All this information became the basis for the enumeration and downselection of our architectural decisions.

1.2 Technical Requirements and Assumptions

The technical requirements for our telescope architectures are derived directly from NASA's Advanced-Technology Large-Aperture Space Telescope (ATLAST) concept. The decision to use ATLAST as a starting point was made because it presented several similarities with the case discussed in this report. In particular, ATLAST is a concept for a space-based optical telescope with a 16.8-meter-diameter primary mirror meant to achieve the scientific objectives discussed above. This was a choice of the MIT team, who remains aware that other similar concepts were explored in the past.

Assumptions used in the model were derived from three main areas: the results of the stakeholder analysis, the requirements for ATLAST, and the need to keep the scope of the tradespace analysis limited to what can be achieved within the time frame of a one-semester graduate course. The assumptions provided a clear definition of the scope of the problem, which made the process of enumerating the various architectures more efficient and manageable from a computational perspective. The assumptions are summarized in Table I.

Table I: Assumptions derived from the ATLAST requirements, stakeholder analysis, and model complexity reduction

ATLAST requirements	16.8-m segmented primary mirror
	On-orbit assembly
	Operation at Sun-Earth Lagrangian Point 2
	Launch in 2028
	Technology at TRL 6 by 2020
Stakeholder analysis	40-year lifetime
	Serviceability required
	Implementation of a Federated Satellite System (FSS)
Model complexity reduction	Scheduled servicing
	No mirror replacement
	Included coronagraph

1.3 Architectural Decisions

In order to enumerate all possible architectures, a total of seven architectural decisions were selected. They are described below.

1.3.1 Communications Architecture

Data gathered by the LTA will need to be transferred to Earth for processing and utilization by the scientific community. In addition, specific commands may have to be sent to the LTA in order for it to accomplish correction maneuvers or accomplish certain tasks. Efficient communications systems are thus essential to mission success and will have to maintain optimal communications quality and high data volume rates within cost constraints. Among several options, the following architectures were selected:

- Direct radio using either the Track and Data Relay Satellite System (TDRSSS) or the Deep Space Network (DSN)
- Laser communications
- Federated Satellite System (FSS) – exploiting the potential of underutilized space commodities by trading and sharing previously inefficiently allocated and unused resource commodities that are available in space assets at any given time

1.3.2 Modularity

It is the level at which components are grouped into physically separate, easily replaced modules with simple interfaces, from level 1 (no modularity) to level 7 (all instruments bus components divided into separate modules). It is important to note that the scientific instruments and engineering components are modularized separately, and therefore the modularity level does not correspond directly to the number of modules. A more complete description of the modularity architectural decision is provided in the body of this report.

1.3.3 Location of Servicing

All servicing is assumed to be robotic and four different locations were identified: Sun-Earth L2 (SE-L2), Earth-Moon L2 (EM-L2), Earth-Moon L1 Orbit Trajectory Used for Servicing

(LOTUS), and Low Earth Orbit (LEO). Each location of servicing has its own challenges affecting ΔV requirements, propellant mass, launch cost, latency of communications, and total downtime for servicing.

1.3.4 Frequency of Servicing

This indicates a scheduled evaluation for replacement or improvement of failed parts or instruments every 3, 5, or 10 years.

1.3.5 Assembly and Servicing Technique

Three methods for assembling and servicing the LTA were identified:

- Self-assembly using self-deployment mechanisms and robotic arms (e.g., JWST)
- Independent tugs or tenders (e.g., DARPA Phoenix Project)
- Formation flying (e.g., SWARM robotics)

1.3.6 Segmentation of Primary Mirror

It represents the characterizing permutations of how the primary mirror could be segmented for launch packing efficiency and ease of on-orbit operations.

1.3.7 Primary Mirror Segment Support Method

The precision of the shape of the primary mirror plays a critical role in obtaining high-resolution images from a space-borne telescope. Given its large diameter, the mirror cannot be thick; therefore, a back-structure made of trusses or ribs needs to be employed to maintain the precise shape of each mirror segment, as well as its positioning with respect to the other surrounding segments. Three methods were chosen to support this function:

- **Surface-normal:** a rigid support of mirror segments using backplane structure
- **Surface-parallel:** relative positioning of mirror segments without backplane structure
- **Hybrid:** a combination of both surface-normal and surface-parallel actuation

1.4 Trade Metrics

The above architectures were evaluated against each other by means of four system-level trade metrics, which allow quantifying the variations in cost, risk, and performance among the different architectures.

1.4.1 Cost

It is the lifecycle cost of the designed telescope. It includes flight system development (based on Stahl 2005 paper, the Unmanned Space vehicle Cost Model 8th edition - USCM8, and NASA Instrument Cost Model - NICM), launch (based on historical and projected launch vehicle costs), assembly, and servicing (Baldearra 2007).

1.4.2 Utility to Science

Utility to science reflects the lifecycle science output of the telescope. It is defined as the discovery efficiency of each individual instrument integrated over instrument lifetime

(Baldesarra 2007). Instruments are assumed to gain utility with time and the telescope utility to science will increase as more advanced instruments are added.

1.4.3 Failed Downtime

The failed downtime is defined as the time during which no science can be done due to the failure of a component, and thus is a measure of the technical risk involved in the mission. Although downtime will also occur during the Assembly/Transit Phase and Servicing Phase of operations, this downtime is a part of normal telescope operations and thus is not a measure of the risk of a particular architecture.

1.4.4 Servicing Margin

It is a measure of the ease with which the telescope can be serviced. Serviceability is reported as a cost margin (the difference between the lifecycle cost of a repair and a replacement case mission architecture) per kilogram serviced over mission lifetime (Baldesarra 2007). Subsystem-level metrics were also developed to evaluate variations of each of the subsystems the telescope is composed of for all the different architectures. Complexity, mass, power, volume, and lifetime are metrics common to all subsystems; however, metrics specific to each subsystem were also identified and will be discussed more in detail in this report.

1.5 Model Structure and Results

In order to enumerate and characterize telescope architectures within the tradespace, a MATLAB code was developed to take inputs for architectural decisions and parameters based upon assumptions, generate a telescope architecture, simulate that architecture over the entire lifecycle, and characterize the architecture using the trade metrics described above. This code consists of three primary sections: the Architecture Generator, the Lifecycle Simulator, and the Trade Metric Characterizer.

The Architecture Generator consists of nine sub-functions, which map to nine systems within space telescope design (Optics, Communications, ADCS, Avionics, Propulsion, Power, Thermal, Structures, and Systems). The code executes these sub-functions in order, and uses the architectural decisions to generate a telescope architecture consisting of a set of components from a given component database. The architecture indicates which components are used, how many of them are present, and how they are grouped into modules; the component database supplies data such as component mass and Mean Time Between Failures (MTBF).

The Lifecycle Simulator performs a simulation of telescope operations over the assumed lifetime of 40 years, from launch to decommissioning. This simulation models the week-by-week operation of the telescope, including the Assembly, Science Gathering, and Servicing operational phases. During operations, the utility to science of the telescope is calculated for each time step and a random number generator is used along with MTBF data and operational time of telescope components to simulate random failures within the component set. When a time step corresponding to a scheduled servicing mission is reached, servicing is performed. This involves upgrading instruments and replacing modules as needed as well as calculating the serviced mass and servicing downtime. Scientific operations only resume once the servicing downtime is complete; there is no utility to science during servicing. In order to account for the stochastic nature of the random component failures, this simulation is repeated 10 times and the results are

averaged for each architecture. The outputs of the simulation are a time vector of utility to science and the amount of mass serviced during each servicing mission.

Finally, the Trade Metric Characterizer takes the outputs of the Lifecycle Simulator as well as characteristics of the generated architecture and uses them to calculate the four primary trade metrics: Cost, Utility to Science, Serviceability, and Risk. For each architecture, these results (and other metrics of interest) are saved with the architectural vector for later identification. The code is executed for every combination of the architectural decisions in order to enumerate the entire tradespace, and the results are plotted for analysis.

Discussion of Results

Results generated by the model illustrate several dependencies and trends among metrics. It will be seen that utility to science mainly depends on both servicing frequency and servicing location while upgrading the instruments often and minimizing the failed downtime. Cost is instead mostly affected by modularity level and servicing frequency with architectures requiring a large serviced mass being most expensive. Servicing frequency will be shown to have the largest effects on failed downtime since architectures with infrequent servicing are expected to experience more failures, which lead to lengthy downtimes. Finally, serviceability most strongly depends on modularity, servicing frequency, and assembly/servicing technique. Indeed, architectures with strong modularity which are serviced often and with cheap servicing techniques exhibit the lowest cost per unit serviced mass. A sensitivity analysis was also performed in terms of reliability threshold and mean times between failures. Results show that utility to science is the sole trade metric that is significantly affected by changes in such parameters.

The 2-D tradespace representation in Figure I illustrates the interactions between three different trade metrics. Points closest to the utopia point are considered “Pareto Optimal” and are highlighted in red. The utopia point has the lowest cost, highest utility to science, and highest servicing margin. Conversely, the so-called “bad” designs are characterized by high cost, low utility to science, and low servicing margin. In Figure 51I, clusters of architectural point solutions can clearly be seen on the tradespace, with a high concentration of points in the region with low utility to science and increasing cost. Clusters of larger points are seen closer towards the utopia point, reflective of designs with increasingly lower costs, higher utility to science, and higher servicing margin.

An analysis of the points directly reveals that the subset of “Pareto Optimal” solutions is dominated by the “7-1-1” architectural vector elements. “7-1-1” represents the identification numbers of the assigned alternative for the first three architectural decisions in order: the highest modularity level possible of 7, Sun-Earth L2 as the servicing location, and a servicing frequency of 3 years. A modularity level of 7 would constitute the combination of highest instrument modularity and spacecraft bus modularity. A servicing location at SE-L2 will ensure that the space telescope never experiences downtime, thereby providing the highest utility to science. A servicing frequency of 3 years also ensures that onboard instruments and component families remain in pristine operating condition throughout their mission lifecycles. These reasons thus collectively explain why solutions with the “7-1-1” architectural vector would be dominant in the “Pareto Optimal” subset closest to the utopia point.

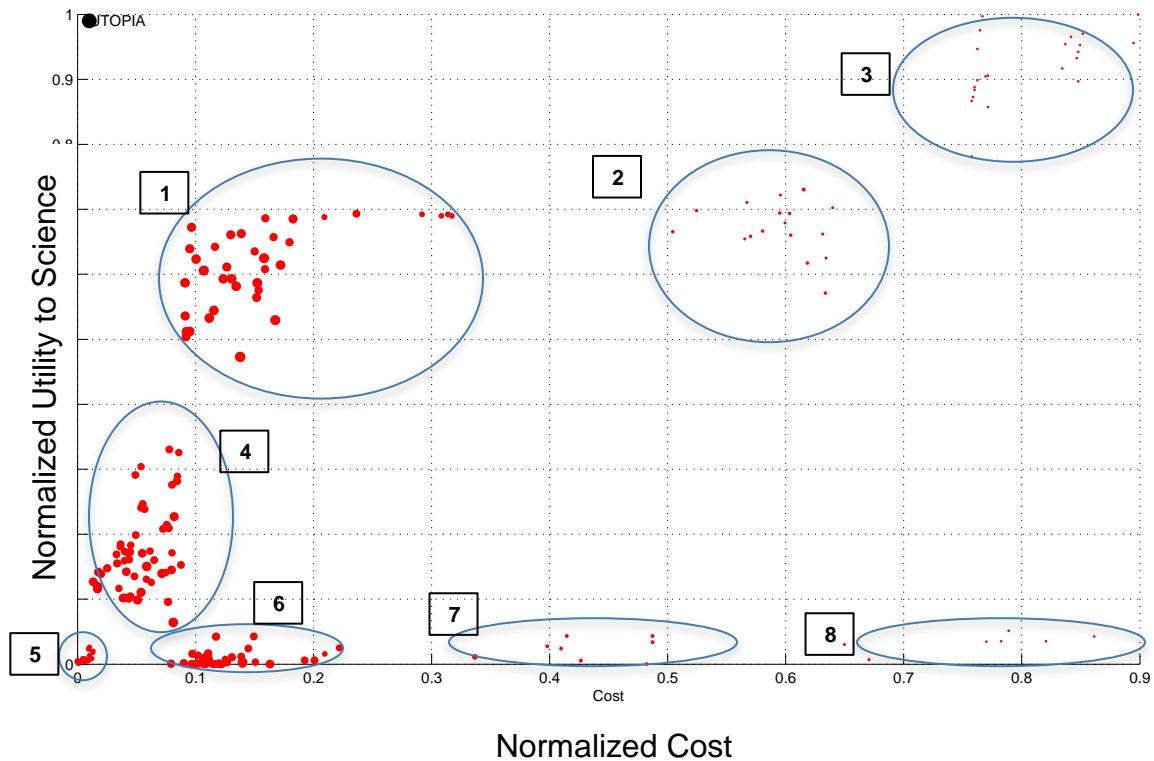


Figure 11: 2-D tradespace of “Pareto Optimal” solutions for the LTA, bounded by normalized utility to science and cost.

In Clusters 2 and 3, the dominant architectural alternatives are still the Sun-Earth L2 servicing location and a servicing frequency of once every 3 years (“X-1-1”). However, modularity is no longer as dominant in this cluster. In fact, lower levels of modularity become more prominent, and this results in increased cost due to higher launch costs required for high launch masses of instrument packages instead of individual components. As such, the solutions of Clusters 2 and 3 are located just to the right of Cluster 1 and in a region with higher normalized cost.

The architectural alternatives of Level 7 modularity, servicing location at LEO, and servicing frequency of one every 10 years dominate the solutions in Cluster 4 (“7-3-3”). Modularity Level 4 is also prominent, thus accounting for the presence of “4-3-3” solutions amongst the majority of “7-3-3” solutions. Cluster 4 is located below and to the left of Cluster 1 because servicing at LEO is a lot cheaper, but it also incurs higher downtime. Also, servicing the telescope once every 10 years means that there is a higher probability that certain instruments or components could fail without being replaced for long periods. This results in a loss of utility to science. Cluster 5 is almost similar to Cluster 4 (“7-3-3”), except that it reveals some alternatives for other architectural decisions have become more prominent. “4-3-3” points are also present in this cluster. These alternatives are laser communications architecture, surface-normal primary mirror actuation, assembly and servicing with tugs and 36 mirror segments. Cluster 6 has modularity level 7, servicing location at LEO, and servicing frequency of once every 3 years as the dominant architectural alternatives (“7-3-1”). While it might be cheaper to service at LEO, a much higher

frequency of servicing would result in higher total launch costs for the space telescope across its mission lifecycle. As such, the solutions in this cluster would have a higher normalized cost and they are located to the right of Clusters 4 and 5.

Finally, Clusters 7 and 8 are generally characterized by modularity levels 2 and 3, servicing location at LEO and servicing frequency of once every 3 years as the dominant architectural alternatives (“2/3-3-1”). Lower levels of modularity, near-Earth servicing location and high frequency of servicing collectively imply that large instrument packages or component families are being taken out and replaced frequently during its mission lifecycle. The high frequency of servicing drives the normalized costs up, while servicing a minimally modular spacecraft means that downtime will be a common occurrence, leading to lower utility to science. As such, these solutions are located in the region of increasing costs and low utility to science.

Through analyzing the clusters of solutions in the tradespace of “Pareto Optimal” points, it is evident that the architectural decisions of modularity, servicing location and servicing frequency have huge leverage on the spatial distribution of solutions in the utility-cost space. Higher modularity, servicing at its SE-L2 operating location, and high servicing frequency generally drive solutions towards the utopia point. Low modularity will generally drive solutions towards the high cost end while servicing at LEO or at a lower frequency will drive solutions towards the low-cost/low-utility end.

1.6 Conclusions

The analysis presented in this report will show that servicing frequency, servicing location, and modularity are the most important decisions when architecting a space telescope, while the other four architectural decisions affect the trade metrics in minor ways. In addition, the model developed will serve as a preliminary tool for the stakeholders with which it will be possible to explore the tradespace of large telescope architectures to perform unprecedented science. Several sources of uncertainty remain in the existing model, but the further steps that can be taken to improve its fidelity will be briefly described at the end of this report to allow for follow-on developments.

2 INTRODUCTION

Humanity's endeavor to further its scientific understanding of the celestial heavens has led to the creation and evolution of increasingly powerful and complex space telescopes. Space telescopes provide a view of the solar system, galaxy, and universe unobstructed by Earth's atmosphere and have profoundly changed the way people view space. In an effort to further advance space telescope capability and achieve the accompanying scientific understanding, the Massachusetts Institute of Technology (MIT), specifically, course 16.89 Space Systems Engineering, explored the tradespace of architectural enumerations encompassed within the design of an ultraviolet-optical-infrared (UVOIR) space telescope located at Sun-Earth Lagrangian Point Two (SE-L2). SE-L2 presents several advantages as an operating location for a UVOIR telescope such as a thermally stable environment and an orbit that allows the telescope to maintain a constant orientation with respect to all of the primary sources of heat and light. The main disadvantages associated with SE-L2 are caused by its relatively large distance from Earth, which marginalizes the effectiveness of real-time telerobotics because of latency and increases the cost of communications, launch, and servicing. Course 16.89 believes that, for this UVOIR application, the strengths of this operating location outweigh its weaknesses and therefore decided to explore the family of opportunities associated with SE-L2.

This course used appropriate performance and system metrics to quantify the effectiveness of the aforementioned architectures and create a Pareto front of viable architectures. Evaluating the designs along the Pareto front allowed the course to characterize and group architectures and present these group-types to stakeholders for the selection of an optimal space telescope according to stakeholder requirements and resources. This course also developed sensitivity analysis, which allowed for a greater understanding of how architectural decisions affect the performance of the satellite. Segmentation, modularity, assembly, autonomy, and servicing were key aspects of this multidimensional analysis given the 16.8-meter class size and location of the telescope. Within the respective operating environment and for a spacecraft of similar characteristics, this model will allow stakeholders to predict the long-term operational effectiveness of different space telescope architectures and capture the synergistic effects of combining various architectural decisions into a spacecraft design.

The following sections step through the aforesaid analysis and design efforts conducted in 16.89 beginning with Section III, which explicitly performs the stakeholder analysis and articulates the requirements of the mission. Section IV gives an overview of past designs and expands upon the architecture enumerations pertinent to this project, while Section V presents the methods and metrics by which those architectures will be evaluated and the system metrics which will be balanced and optimized in the creation of this space telescope. Section VI will present the model validation of this project and Section VII will discuss the results and analyses of the project. Finally, Section VIII will explore the future work opportunities of this project, while Section IX will present the conclusions and recommendations drawn from this project.

3 TELESCOPE STAKEHOLDER ANALYSIS

3.1 Stakeholder Analysis

A stakeholder analysis was performed to determine what the specific needs and desires are of relevant stakeholders at this stage of telescope design. This analysis also helped to define areas of interest for the TITANS AE trade study, as well as what applications stakeholders might seek to use this model for in the future. A set of questions on telescope performance, architecture, and cost was sent to various stakeholders around the country. Potential stakeholders with an interest in programs of this kind include:

- NASA Goddard Space Flight Center (GSFC)
- NASA Headquarters (HQ)
- The Jet Propulsion Laboratory (JPL)
- The Space Telescope Science Institute (STScI)
- ITT (formerly Kodak)
- MIT
- Skoltech
- The European Space Agency (ESA)
- Other international universities and space agencies
- The National Reconnaissance Office (NRO)
- Department of Defense (DoD)
- Other governmental organizations

The stakeholder responses were compiled into a set of assumptions and requirements. The list of stakeholders from outside MIT who responded to the questionnaire is shown in Table II. An effort was made to include a diverse set of stakeholders to represent a wide spectrum of views on the goals of our trade study. The stakeholder questions and answers are listed in Appendix B.

Table II: List of surveyed stakeholders

Stakeholder	Organization
Dan Lester	University of Texas
Lee Feinberg	NASA GSFC
Swati Mohan	JPL
Tupper Hyde	NASA HQ

The stakeholder answers to the questionnaire helped scope the model in a number of ways. The responses helped set the scientific goals of the mission, the timeframe of the mission, the size of the primary mirror, and the operating location. These responses also gave an indication of the range of opinions on different facets of our architecture. The stakeholders were adamant that the next-generation large space telescope should be a UVOIR telescope that primarily investigates exoplanets. Additionally, the stakeholders were consistent in their desire for a very serviceable telescope to achieve both a long lifetime and enable instrument replacement. There were some areas in which the stakeholders differed. The recommended primary mirror diameter ranged from 16 m to 30+ m. Also, the stakeholders disagreed on the magnitude of the available budget, ranging from < \$5B to \$15B. In instances where stakeholders differed, reasonable assumptions

were made that combined the stakeholder input with modeling constraints to arrive at sensible assumptions.

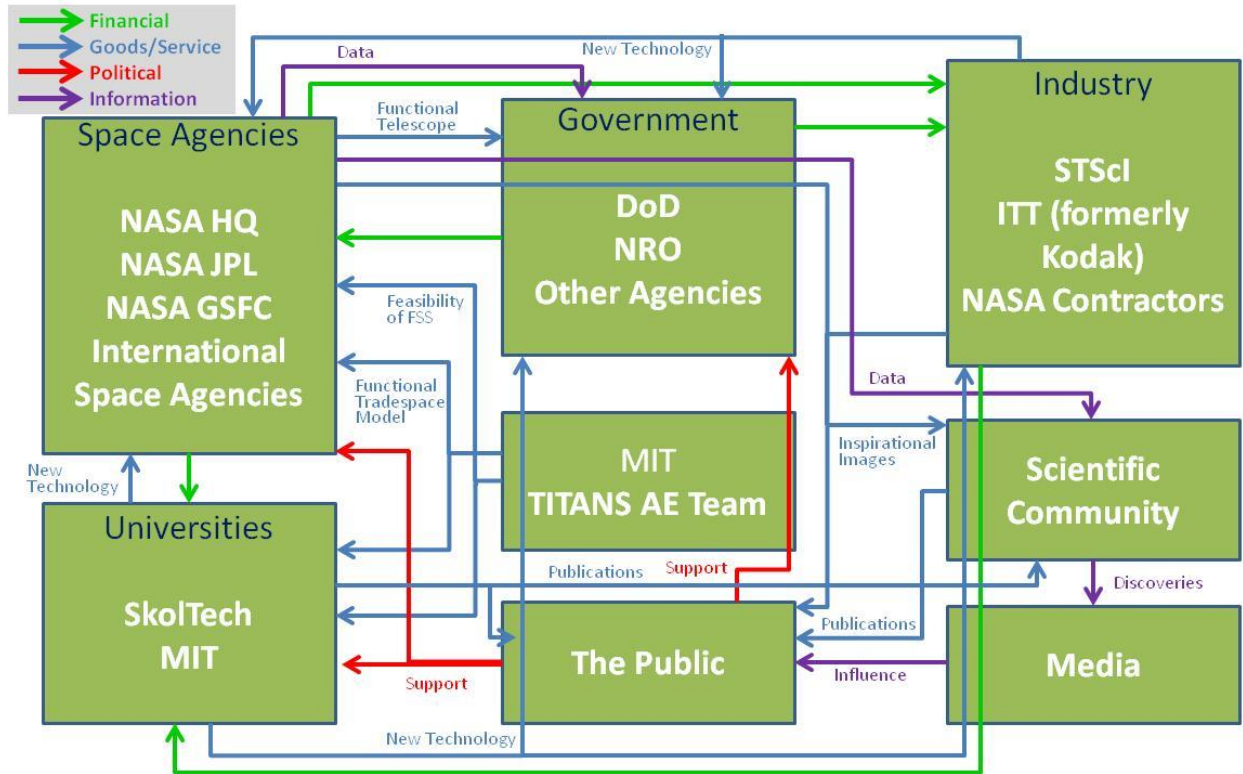


Figure 2: Map of stakeholder needs

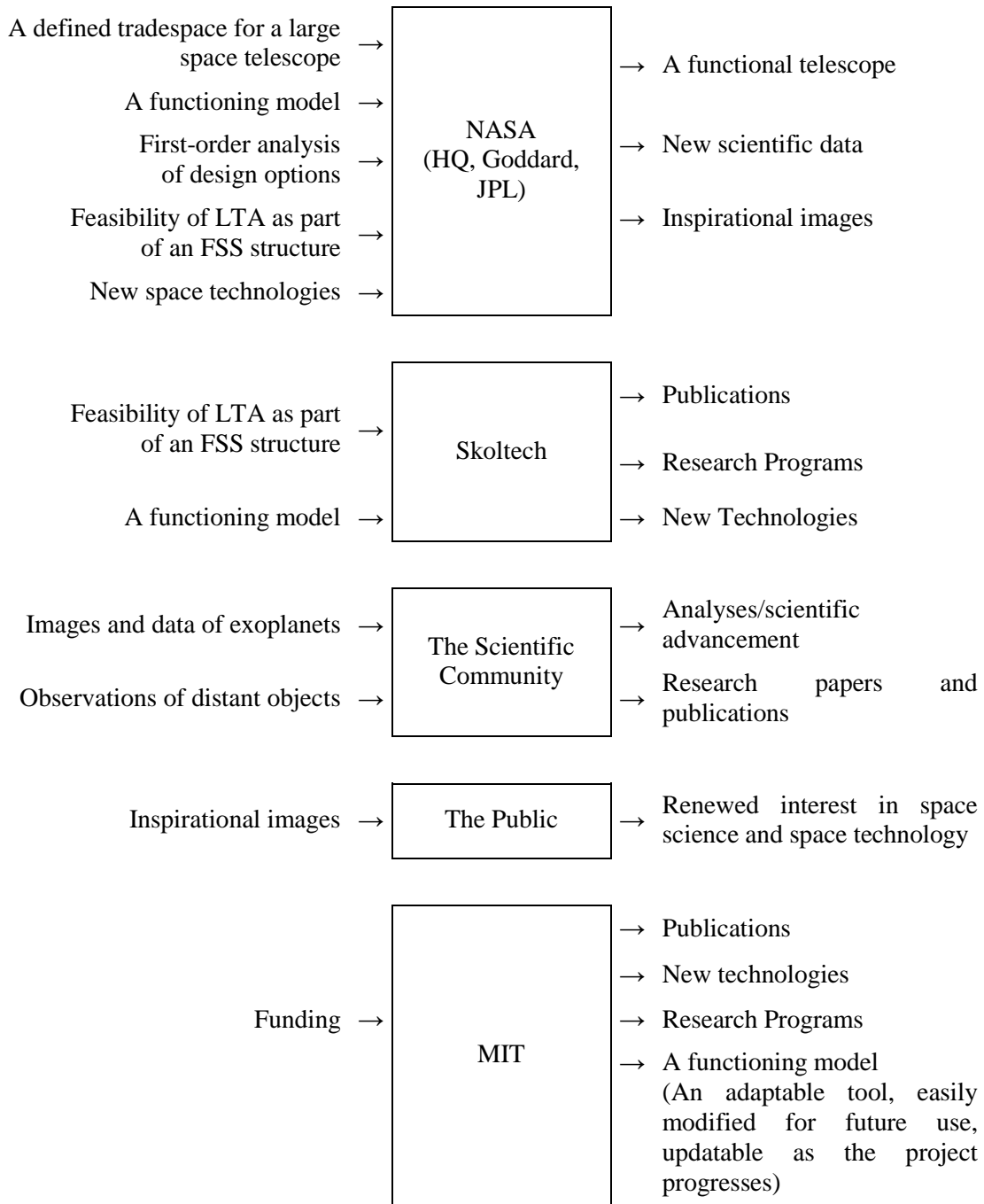


Figure 3: Needs of major stakeholders, organized as by inputs and outputs

As understanding of individual stakeholder desires came into focus, a list of high-level stakeholder groups was constructed, and the basic needs of those stakeholders identified. The needs and the interactions between all stakeholders are shown in Figure 2. For the high-level groups, these needs are displayed as inputs and outputs for each group in Figure 3. Understanding and organizing these needs enabled identification of what MIT’s primary outputs to stakeholders should be (see last block in Figure 3). Specific to the TITANS AE team, this identified the primary output to be a functioning model that may be used throughout future telescope development.

Of particular interest to NASA and Skoltech is including the concept of using Federated Satellite Systems (FSS) in the tradespace as major architectural decision. Using FSS, the final LTA would share processing power and access time with other satellites in its system, creating more efficient allocation of spacecraft resources. FSS use would be a sweeping paradigm shift in spacecraft technology and communications, and thus a key consideration for any new, long-term spacecraft design¹.

3.2 Requirements Definition

In order to identify requirements for the overall telescope design and the tradespace model that apply directly to the scope of this project, two stakeholder needs area were analyzed in detail – goals for data provided to the scientific community and goals for the model itself to make it functional for future use. These areas specifically have been chosen for further analysis because the TITANS AE team is fulfilling the need for a tradespace model, and the mission of the telescope will directly inform the potential telescope architectures explored by the model. Thus, the goals of the model itself and the science goals that affect model design are the needs areas that drive requirements for the TITANS AE project. The model must also incorporate the stakeholder-specified potential for FSS architectures, which will be taken into account directly as an architectural option.

3.2.1 Science Goals

To first understand the potential scientific objectives for a new large-scale space telescope, as well as which objectives are concurrent with needs of NASA and the larger scientific community, a study was conducted through review of the 2010-2020 decadal survey of astronomy and astrophysics². This survey represents a clear summary of the highest priority needs in terms of data for the scientific community and science drivers behind potential NASA missions. The first priority space-based medium-scale mission in the decadal survey is a New Worlds Technology Development Program. That is, laying the groundwork and beginning to explore possible technologies for an exoplanet-imaging telescope whose critical development would take place in the 2020-2030 decade. The main goal for such a telescope mission would be to image Earth-like planets in the habitable zones of nearby stars and provide insight on their atmospheres. It would rely on knowledge obtained from the Kepler and Wide Field InfraRed Survey Telescope (WFIRST) exoplanet finders for observable target selection. Such a mission would require understanding of zodiacal light (light scattered by dust around a star) levels around potential target stars and the ability to distinguish rocky planets through this light.

The first priority large-scale space mission from this decadal survey is the WFIRST telescope, designed to measure a wide field and detect exoplanets using near-infrared detection. WFIRST would determine the range of orbital parameters that permit an Earth-like planet to exist, which will help define the optical requirements necessary to resolve exoplanets. It is now likely that a recently donated National Reconnaissance Office (NRO) telescope will be repurposed to accomplish these goals³. The James Webb Space Telescope (JWST), though not ranked in this decadal survey, is recognized as an important mission in the near-infrared spectrum that will investigate the origins of planetary systems and the universe. The science goals of understanding the origins of the universe, galaxies, stars, and planets are still recognized as high-priority in this survey, and will likely still be of interest in the next decade.

From the rankings in this survey, a telescope for imaging and spectroscopy of exoplanets is in line to become the first priority large-scale space mission of the 2020 decade. This would build on the current New Worlds Technology Development Program, and serve as a logical next step following the WFIRST/repurposed telescope mission. Furthermore, the description of the program discussed here fits the timeline of this project, enhancing the impression that exoplanet studies should be one of this mission’s primary goals. Such a mission calls for observational capabilities in the visible-to-ultraviolet wavelength regimes. If this project is also to complement the mission of JWST, this new telescope will require the additional ability to make observations in the near-infrared spectrum and observe distant objects such as galaxies in early formation.

Based on review of the decadal survey, the main science objectives for the telescope are defined in Table III. These objectives, defined here as goals, are high-level mission requirements that apply to the final telescope design and correspond with stakeholder needs for science for this project.

Table III: List of mission goals from stakeholder analysis

Goal 1	To observe known Earth-like exoplanets in the habitable zones of their stars at UVOIR wavelengths
Goal 2	To analyze the atmospheres of these exoplanets through spectroscopy and obtain a clearer assessment of their potential to sustain life
Goal 3	To observe distant objects such as forming galaxies and solar systems in order to understand the origins and formation processes of these far-field objects

These science goals are similar to those of the Advanced Technology Large-Aperture Space Telescope (ATLAST). ATLAST was a NASA study performed several years ago that looked at the design of a large, next-generation UVOIR telescope primarily designed to determine if an exoplanet can harbor life⁴. Basing the key performance requirements on those from ATLAST means that the telescope being investigated will achieve the goals stated in Table III. These optical performance attributes are far more stringent than what has previously been achieved on Hubble and JWST. Based on stakeholder recommendations and desires, the technical requirements for the ATLAST optics are used as a baseline for this study. These hardware specific requirements are listed in Table IV.

Table IV: ATLAST key optical performance requirements⁵

Requirement Name	Minimum Requirement	Target Requirement	Science Drivers
Optical Bandwidth	0.2 – 2.5 μm	0.11 – 2.5 μm	Solar system exploration
Aperture Size	16.8 m		
Angular Resolution	6 – 12 mas	3.5 mas	
Field of View	5 arcmin		Extragalactic star formation
Pointing Stability	1 mas		Exoplanet characterization, life detection
Spectroscopic Resolution	300	120000	Extragalactic star formation
Contrast	1e+07	1e+10	Exoplanet characterization, life detection
Inner Working Angle	50 -100 mas	40 -50 mas	Exoplanet characterization, life detection
Wavefront Error	37 nm	0.07 nm	Exoplanet characterization, life detection
Wavefront Stability	10 nm	0.07 nm	Exoplanet characterization, life detection
Uninterrupted Observation Time	2 hours		
Operational Efficiency	90%		

Definitions of these technical requirements and descriptions of how they are considered in the model may be found in Appendix I.

3.2.2 Model Goals

Based on stakeholder needs for the TITANS AE model itself, the main goal of this project is to produce a tool that characterizes the tradespace for a large UVOIR telescope design, and not down-select to any single architecture. This tool must be flexible for future use and robust to major changes in the telescope architectural tradespace. Understanding this, the goals specific to the TITANS AE project are listed in Table V.

Table V: List of goals for TITANS AE model based on stakeholder analysis

Goal 1	To create a robust model that generates a fully enumerated tradespace for a large scale space telescope
Goal 2	The model shall be flexible and modular, such that it may be adapted to the telescope technical requirements desired by the user
Goal 3	The model shall provide data presented in a manner that will assist the user in determining what architecture characteristics are optimal for their needs, without down-selecting or defining an “optimal”
Goal 4	The model code shall be developed such that new trade metrics or variables may be added to suit future user needs without altering the fundamental model structure

3.3 Architectural Assumptions

To simplify the architecture development process, several assumptions have been made:

3.3.1 Operate at Sun-Earth L2

This is the location currently proposed for both JWST⁶ and ATLAST⁴. Sun-Earth L2 is a benign environment where the main heat and stray light inputs are always on one side of the telescope, simplifying design. Other operational locations that were considered and could be analyzed in future studies are Low Earth Orbit (LEO), Earth-Moon L2 and Earth-trailing.

3.3.2 16.8-meter-diameter primary mirror

This size is significantly larger than anything previously flown and on par with the largest size considered for the ATLAST design⁴. A 16.8-m mirror provides unprecedented light gathering and resolution capabilities enabling new science. Future studies may look at the science capabilities of even bigger mirrors in the 20–30-m range, comparable with future ground telescope mirror sizes.

3.3.3 On-orbit assembly is necessary

A 16.8-m mirror is significantly larger than any current or planned launch vehicle fairing. Therefore, on-orbit assembly will be required, chiefly for the primary mirror. Novel folding and packing schemes were not looked into.

3.3.4 Segmented primary mirror

The primary mirror must be composed of smaller hexagonal segments, as there is no current infrastructure that would allow the construction of a 16.8-meter monolithic mirror.

3.3.5 Launch in 2028, Phase A in 2020, Technologies be TRL 6 by 2020

These dates represent the next available slot for a large astrophysics mission. JWST will be operational, freeing up funds for the next large telescope.

3.3.6 Lifetime of 40 years

Lifetime is a main driver of lifecycle science value. A 40-year lifetime will allow this telescope's capabilities to be fully utilized before a presumably more capable telescope surpasses it. Lifetime is a significant driver of cost as well. Future studies can look at the effects of varying lifetime.

3.3.7 Autonomous servicing, no human servicing

The lifetime assumption drives the need to service the telescope as no space system has ever lasted 40 years on its own. Servicing also provides an opportunity to upgrade the instrument suite and enable the science output of the telescope to continue to increase over its lifetime. Human servicing capability in 2028 and beyond is highly uncertain and the technology for robotic servicing was assumed to be available and economically advantageous by 2028.

3.3.8 Scheduled servicing

Scheduled servicing, as opposed to on-demand servicing, simplifies the design and costing process since the interval between servicing and the number of servicing missions is known.

Additionally, the long travel times to Sun-Earth L2 mean that on-demand servicing would result in large downtimes.

3.3.9 No servicing of optical surfaces, only instruments and engineering components

Serviceability will be limited to instruments and engineering components as servicing mirrors introduce alignment and contamination concerns that would place strict constraints on the servicer. Additionally, optical services are unlikely to need servicing.

3.3.10 No formation-flying coronagraph

An external, formation-flying coronagraph was proposed for ATLAST⁴, but that architecture is neglected as it introduces unnecessary complexity in the form of another spacecraft design.

3.3.11 Federated Satellite System (FSS) considered as a downlink architecture

The FSS downlink architecture introduces multiple satellite-to-satellite links in the downlink chain. This pseudo-constellation allows data to be continuously transmitted from the telescope to the ground without concern for ground station line of sight. This capability potentially can reduce the mass and power of the communications and command and data handling subsystems.

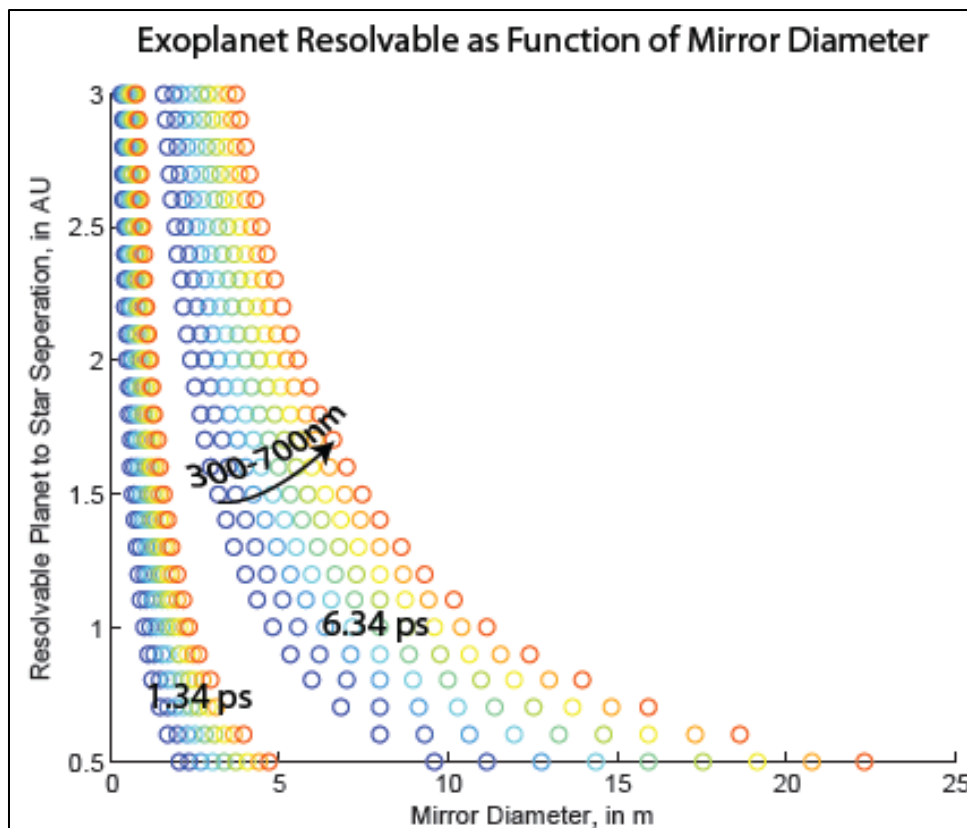


Figure 4: Resolvable exoplanets as a function of mirror diameter

4 ARCHITECTURAL ENUMERATION

4.1 Historical Analysis of Past Missions

Previous architectures can be described as a set of functions and forms developed to address various aspects of established science requirements. Functions are defined as the actions for which each system is created, and forms are the shapes, configurations, arrangements, or layouts that are implemented to achieve the system functions. The study of past forms and functions in previous architectures allowed the team to analyze past telescopes and space systems to gain insights into how different subsystems interact, how the science requirements lead to architectural decisions, and how to determine which architectural decisions were the most important to include in tradespace analysis. Consequently, the analysis of past designs facilitated the determination of a set of functions that each subsystem team needed to address. This analysis also determined sets of forms corresponding to each of these functions for each mission, since the previous missions provided a historical basis for scoping possible forms to study.

The example missions of the Hubble Space Telescope, James Webb Space Telescope, and Kepler Telescope were chosen because they span the tradespace of the current project goals and science requirements. Additionally, the Iridium Constellation was chosen to provide a basis for different communication architectures to analyze the Federated Satellite System concept. Specifically, the past missions permitted the analysis to incorporate several aspects of the different systems including: primary mirrors of various segmentation levels, wavelengths of study, and number of spacecraft in the systems. These telescopes and space systems also spanned a range of launch dates and revealed the progression in scientific and technical capabilities. The aim of the team analysis was the primary subsystem-related functions and forms for these four selected missions.

The result was a mapping of various forms to each analyzed subsystem function, which were then mapped to the architectural decisions. A list of these forms and functions for each of the historical missions can be found in Appendix J. Each subsystem team analyzed all of the historical missions to gather as much information about their respective subsystems and their implementation aboard these spacecraft as possible. In particular, each team focused on determining the methodology by which each historical mission's subsystems were designed and engineered to then determine a suite of forms and functions that historically were deemed the optimal designs and architectures. For example, the Structures and Mechanisms subsystem analyzed all four of the historical missions to determine the functional role of the Structures and Mechanisms subsystem for each mission, as well as how the structure was built for each mission and which mechanisms were selected to enable to spacecraft to perform their respective missions. Subsequently, the Structures and Mechanisms subsystem team was able to determine that the primary Structures and Mechanisms functions for the four analyzed missions were: protecting, supporting, pointing, preventing jitter, deploying, stowing, interfacing, access providing, and on-orbit assembling. These primary functions were then broken down into several additional sub-functions as required to fully define the various spacecraft architectures. The form by which each of the missions provides these functions was then listed on the row corresponding to each function. In this way, similarities between the missions could be determined. The architectural decisions arose from these functions, whereby the forms enabled the telescope to achieve the demands set forth by the architectural decisions.

4.2 Function and Form Mapping

The historical missions have several very similar functions that can be attributed to the missions' overall goal of collecting images of distant objects. With these sets of forms and functions, the teams were able to determine the most applicable functions with sample forms to be applied to the 16.8-m-total-width hexagonal-segment primary mirror telescope of the project. In addition, the forms allowed the teams to begin the determination of metrics to resolve differences between various architectural decisions as they are analyzed by an automated code. These metrics are quantitative in that they are based on relevant calculations. Additionally, the decisions themselves stem from the functions that must be performed by each subsystem, meaning that the architectural decisions made by each subsystem must be able to accomplish all of the respective functions as analyzed in the historical study. Figure 5 shows the top architectural decisions, functions, and forms for each subsystem as determined by observing which forms and functions best describe each subsystem across the different historical missions.

Figure 6 presents architectural decisions with their associated forms across all of the subsystems for the LTA project. The historical missions allowed these seven architectural decisions to be determined as those that provide a basis that spans the possible LTA architectures. These decisions, therefore, represent the most crucial design decisions that most greatly affect the overall design of the telescope. The historical examination was necessary for the LTA analysis team to both narrow the architectural decision list to these seven, as well as to populate the table with the appropriate forms for each decision. By studying the historical missions, the team was able to select forms that are applicable to the LTA while providing a set of forms that fully describe the types of methods for instantiating each of the architectural decisions. Therefore, the historical analysis proved to help scope the LTA project by defining the possible space of forms to be analyzed in the team's code.

ID	Architectural Decisions	Function	Possible Forms				
Systems 1	Location of Servicing	Provide an effectively servicable/upgradable system	Humans/Robots at Earth-Sun L2	Humans/Robots at LEO or MEO			
Systems 5	Science Instrumentation Modularity		Fully Integrated (No Servicing)	Sub-system modularity	Component modularity		
Systems 6	Optical Pathway Modularity		Fully Integrated (No Servicing)	Sub-system modularity	Component modularity		
Systems 7	Engineering Equipment Modularity		Fully Integrated (No Servicing)	Sub-system modularity	Component modularity		
Comm 1	Communications Type	Provide a communications link with ground	DSN	Laser			
Comm 2	Relay Type		FSS	Direct			
Comm 3	Processing Architecture		Centralized, hierarchic	Centralized, Non-hierarchic	Distributed, hierarchic	Distributed, Non-hierarchic	
Propulsion 1	Propulsion Type	Maintain orbit (station keeping) and move system to new location if needed	Pulsed chemical thrusters	Constant-fire electric thruster	None		
Structures 1	Jitter Prevention Method	Prevent jitter	Electromagnetic	Fluid	Mechanical	None	
Structures 2	Primary Mirror Articulation Method	Provide mirror structural support	Surface parallel	Surface normal	Both		
Structures 3	On-orbit Assembly Technique	Assemble telescope structure	Robotic Arm(s)	Mechanical Tug(s)	Electromagnetic Tug(s)	Swarm Robotics	Deployment (unfolding)
Thermal 1	Insulation from Sun, Earth	Insulate spacecraft from Sun, Earth	No sun-shield	Sun-shield			
Thermal 2	Cooling instrument and/or detectors	Maintain instrument temperature within operational range	Purely passive thermal design	Thermo-electric cooler	Cryocooler	Cryogenic dewar	
Thermal 3	Controlling temperature of optics, bus and other subsystems	Maintain temperature of bus and subsystems within operational range	Purely passive thermal design	Active thermal components			
Science 1	Telescope/Optical Train Architecture	Collect and focus light	Fully Unified Telescope Structure	Fully Distributed Telescope Architecture	Unified Primary, Detached Secondary, Detached Science Instruments	Unified Primary, Detached Secondary, Attached Science Instruments	Hybrid (e.g., Center of Primary Mirror Fixed, Outer Segments free-flying)
Science 2	Instrument/Optical Bench Architecture	Detect light and make observations	Multiple Primary Instruments with or without Secondary Science Payloads	Single Primary Instrument and Secondary Science Payloads			
Science 3	Coronagraph	Observe and characterize Earth-like exoplanets	Occultation disk (separate)	Coronagraphy built into optical train (Lyot-TR6)	Optical vortex coronagraph	No hardware Coronagraphy element	

Figure 5: Reduced architectural decisions and forms for each subsystem

Architectural Decisions	Possible Alternatives						
Servicing Location	Earth-Sun L2	Earth-Moon L2	LEO	LOTUS			
Servicing Frequency	Every 3 years	Every 5 years	Every 10 years				
Modularity Level	Level 1 (no modularity)	Level 2	Level 3	Level 4	Level 5	Level 6	Level 7
Communications Architecture	Direct, DSN	Direct, Laser	TDRS	FSS (LEO)			
Primary Mirror Actuation	Surface Parallel Actuators	Surface Normal Actuators	Both Surface Normal and Parallel Actuators				
Assembly/Servicing Technique	Self-Assembling (Use of Robotic Arms with Unfolding)	Tug	Swarm Robotics/Formation Flying				
Structural segmentation of Primary Mirror	36 Segments, 1 Mirror Each for 36 Structural Segments Total	6 Symmetric Segments (6 Mirrors Each) for 6 Structural Segments Total	1 Center Segment and 6 Symmetric Segments (4 Mirrors Each) for 7 Structural Segments Total	6 Symmetric Inner Segments (3 Mirrors Each) and 6 Symmetric Outer Segments (3 Mirrors Each) for 12 Structural Segments Total	Assymmetric (1 Central Segment and 2 Identical "Chord" Segments) for 3 Structural Segments Total		

Figure 6: LTA architectural decisions and forms

4.3 Architectural Decisions

4.3.1 Communications Type

Efficient communications are critical to the successful execution of space missions and architectural frameworks for space exploration. As operating a space telescope at L2 presents unprecedented challenges in maintaining optimal communications quality and high data volume rates within cost constraints, a number of existing and emergent technologies are being considered as prime candidates for the primary communications architecture. Existing technologies considered for architectural enumeration comprise radio-frequency (RF) communication platforms such as the Deep Space Network (DSN), Tracking and Data Relay Satellite System (TDRSS), and Federated Satellite Systems (FSS). An emergent technology is direct FSO (Free-Space Optical) or laser communications, which may eventually evolve to become the dominant option for space communications in future.

Radio-Frequency communications have long been the primary medium for space communications. Commonly used to provide communications support to interplanetary spacecraft missions, the DSN consists of a worldwide network of large antennas and communication facilities located in three locations spaced equally along the Earth's circumference: Goldstone, California; Madrid, Spain; and Canberra, Australia. These facilities contain extensive data processing platforms and several antennas varying from 11 to 70 meters in diameter. A distant spacecraft leveraging the DSN for communications support can thus potentially remain in contact with at least one site. With necessary infrastructure already in place and high reliability in its usage history, the DSN can provide the two-way communications link for guidance, control, telemetry, and scientific data transmission for the space telescope. Furthermore, telecommunications is continuously evolving to meet growing demands in data quality and quantity for commercial, military, and space applications. As such, using the DSN can provide flexibility to the space telescope in adapting to changing mission requirements over the system lifecycle.



Figure 7: Large ground-based antennas of the Deep Space Network⁷

The TDRSS is also a RF communications platform and it is a network of communication satellites and ground stations, where each satellite within the network is defined as a TDRSS. It has provided reliable communications support to existing spacecraft such as the Hubble Space Telescope and International Space Station, and is continuously being expanded with more planned launches of new data and relay satellites to manage increasing data rates and volumes. Also, its usage of the S-, Ku-, and Ka-bands will enable higher bandwidth communications for multi-spectral science instruments and reduce their susceptibilities to radio interference. With existing infrastructure to accommodate multiple users and achieve notable success in many state-

of-the-art applications, the TDRSS also presents an effective and practical communications architecture option for the space telescope. An existing TDRSS is the Iridium satellite constellation, which is a large group of Earth-pointing satellites providing voice and data coverage to satellite phones and other integrated transceivers over the Earth's entire surface.



Figure 8: Iridium satellite constellation for global communications⁸

While the DSN and TDRSS offer more direct communication paths between the spacecraft and ground stations, the FSS provides additional routing and relay capabilities for the space telescope. As such, the space telescope can operate as part of an infrastructure of an FSS architectural concept. The FSS is an emergent concept that leverages opportunistic cloud computing and which can potentially “increase the sustainability, cost effectiveness, robustness, and reliability of space-based assets, and hedge demand uncertainty while creating in-orbit markets of space resources.”⁹ The FSS concept is based on distributed satellite systems, where spacecraft within the federated network share unused space resources such as link capacity, storage capacity and data processing time. With the availability of communications resources already in orbit, designing the space telescope as part of an FSS can significantly reduce infrastructure costs and immediately achieve compliance with existing space communication regulations.

Providing the option for data relay through the FSS can influence further design decisions of the space telescope such as the onboard data storage capacity, antenna power, system reliability and complexity. For storage capacity, direct communications via the DSN or TDRSS will require significant onboard data storage since the communications link window has been stated to be approximately 4 hours per day and it is necessary to preserve all recorded science information throughout its mission lifecycle. Being part of an FSS, however, can allow data recorded outside the link window to be transmitted via cross-links to other federated satellites for storage before rerouting back to Earth, thus reducing the need for large data storage platforms.

With the FSS, antenna power may be reduced since the only transmission destinations are nearby satellites. While compensation for path loss may be required, power overheads for the space telescope can be significantly reduced if there is no need to overcome atmospheric attenuation. Despite its possible benefits, the FSS may also pose problems to system reliability since it is a concept still in its stages of developmental infancy. Without the presence of an existing or robust FSS in operation, there exists technical and bureaucratic obstacles involved in establishing a new

FSS and this incurs significant risk and uncertainty associated with its communications performance.

Complexity of the system is also increased with the FSS since efficient routing protocols and resource scheduling among the space telescope and other satellites will be required. Satellites that are FSS suppliers, i.e., satellites that receive, process, and transmit data from FSS customers will most likely have increased power, mass, and volume requirements. Increased usage may also negatively impact the lifetime of the communications sub-system. Nonetheless, the FSS is a concept that is achievable within current technological means, and designing the space telescope as part of the FSS to leverage on existing communication capabilities is a valuable option that should be seriously considered within the design tradespace.



Figure 9: Visualization of FSS network and an individual satelliteError! Bookmark not defined.

The final option for communications architecture is direct FSO or laser communications. Laser communications recently surfaced as a prospective alternative to RF communications with the successful application of the SILEX (Semiconductor-Laser Inter-satellite Link Experiment) communications payload onboard the Artemis satellite owned by the European Space Agency (ESA).¹⁰ With NASA's recent launch of the Laser Communications Relay Demonstration (LCRD) mission, laser communications offer potential improvements in terms of larger bandwidth, higher data capacity, lower power consumption, more compact equipment, greater security and higher immunity from electronic interference. At equivalent data rates, laser communications may also be implemented with lower mass for greater capability, which will circumvent the requirements for high antenna masses and heavy feed systems archetypal of RF communications. As such, laser communications may be feasible if there is a regular and sufficient period of time during which the space telescope remains within direct line of sight with ground stations.



Figure 10: Satellite-to-ground laser communications¹¹

There is also a remote possibility where laser communications can be deployed for inter-satellite data relay similar to FSS operations. Optical communications offer the potential of operating at unprecedentedly high data rates because optical frequencies allow the use of very narrow transmit beams, which can produce high received signal levels with comparatively small antenna packages¹².

However, infrastructures for relay-centric laser communications are currently under-developed. A general concern for laser communications would be its reliability and usage history as compared to RF communications. While laser communications have been validated for terrestrial systems, near-Earth and deep space applications are still in their infancy stages. For relay-centric laser communications to be possible, other laser-based satellites must first be deployed before a laser-based space telescope can begin providing value to stakeholders. As such, it is unlikely that current knowledge and infrastructure available during the early-phase design timeframe of the space telescope will enable relay-centric laser communications to become a worthwhile option. Therefore, only direct and not relay-based laser communications architecture will be considered within the design tradespace.

With differing performance specifications, complexity, implementation costs and scope of application, the selection of DSN, TDRSS, FSS or direct laser as the primary communications system will be an imperative architectural decision in the design of the space telescope. As the cost and complexity of integrating, launching, and deploying a communication system is contingent upon the form and capability, the choice of communication systems will be a key architectural design driver.

4.3.2 Modularity

The modularity of the telescope – defined as the extent to which components are grouped into physically separate, easily replaced modules with simple interfaces – plays a large role in the cost of the telescope. The number of modules impacts the cost of the telescope in two opposing ways. First, a higher number of modules will result in a higher development and launch cost due to an increased engineering effort to define and package modules as well as increased total mass and volume from module encapsulation materials and interface components. Second, a higher number of modules will result in decreased servicing costs; as the number of modules increases, the number of components per module decreases, therefore lowering the number of components that must be replaced to rectify a single component failure. Another way to consider the benefit

of increased modularity would be to think of wasted component time – if a single component within a module fails that component must be replaced, and therefore functional components within that module will also be replaced, even though they have not failed. As the number of components in a module decreases, the amount of useful component time that is lost due to a module replacement after a single component failure also decreases, thus it is more cost-effective for servicing to have more modules. This cost-effectiveness is magnified if modules are created by combining items with similar failure rates and will be discussed later. The combination of these two effects – low development/launch costs and high servicing costs for a small number of modules, high development/launch costs and low servicing costs for a large number of modules – is expected to produce a lifecycle cost curve with high costs at either end of the spectrum and low lifecycle costs at an intermediate number of modules. This trend is depicted notionally in Figure 11. It is important to note that this figure is not based upon any data; it was simply created to illustrate the trends in development/launch, servicing, and lifecycle costs with regard to the number of modules and to enable this discussion of the trade between the number of modules and lifecycle cost.

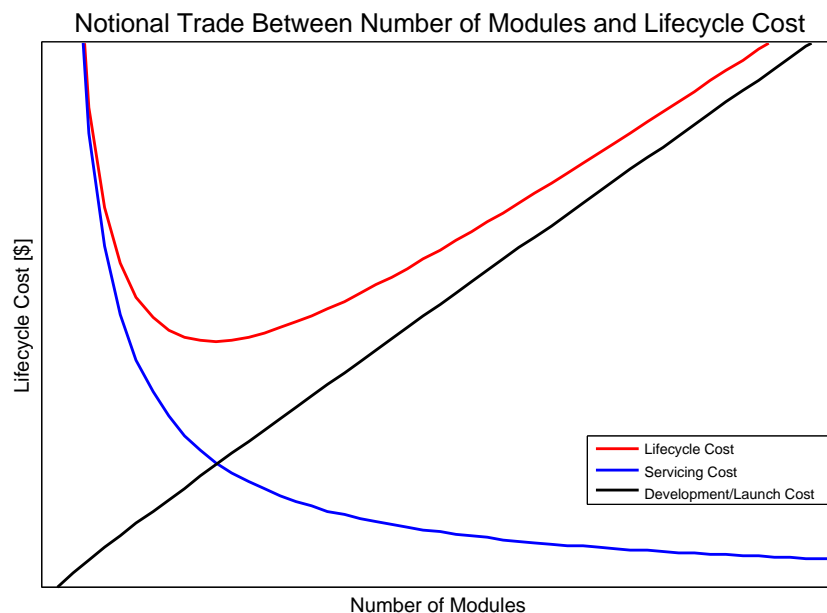


Figure 11: Notional trade between the number of modules in a satellite and the lifecycle cost (red), which is the sum of the costs incurred during the servicing (blue) and the development and launch phases. For the purposes of this analysis, all other factors in cost are assumed to be held constant.

The motivation behind the use of modules in telescope design is to enable servicing, where servicing is defined for our purposes as the action of removing one module and replacing it with another, newer one. Servicing serves two purposes. First, servicing missions can replace failed or unreliable components within the telescope to allow continued operation and extend mission lifetime. This includes the replenishment of consumables such as coolant or fuel. Second, servicing allows for component or instrument upgrades over the mission lifetime. This second purpose is of particular importance to scientific missions, since it allows space telescopes to take advantage of the advancement of instrument technology on Earth¹⁴. Instrument discovery efficiency increases over time, following a power law described in Baldesarra 2007¹³; servicing

gives space telescopes the capability to replace older instruments with newer ones that have higher discovery efficiencies. In this way, each servicing mission that upgrades an instrument will increase the overall utility to science of the telescope.

In order to capture these two separate purposes of servicing as they affect modularity decisions, the science instruments (the “instrument package”) are considered separately from the engineering components (the “spacecraft bus”). This is accomplished by defining a modularity breakdown tree, as shown in Figure 12. In this tree, the overall telescope (top level) is broken down into three branches representing three sections of the telescope: Permanent Infrastructure, which contains telescope components that are not expected to fail within the 40-year lifetime of the telescope, such as the primary mirror and the structural backbone; Instrument package, which contains the scientific instruments; and Spacecraft Bus, which contains the engineering components required to enable the telescope’s mission. Gray boxes indicate items that cannot be serviced without replacing the entire telescope.

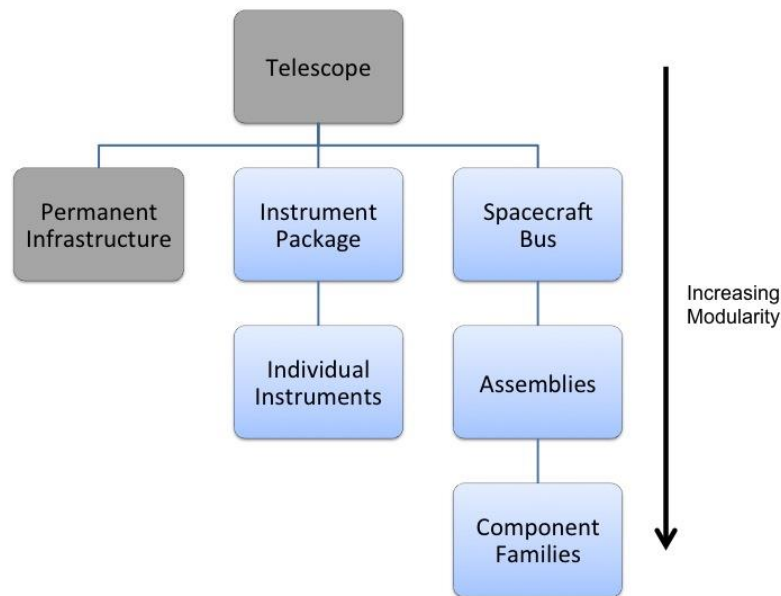


Figure 12: Modularity breakdown tree. This diagram defines the divisions within the telescope that are used to separate components before they are grouped into modules. Each branch of the tree can be modularized at different levels; the number of modules produced increases as one moves further down the branches. Gray boxes indicate permanent infrastructure that cannot be replaced without replacement of the full satellite; this includes components that are expected not to fail, such as the primary mirror and the structural backbone of the telescope.

The Instrument Package and Spacecraft Bus can both independently be broken down further. The second level of Instrument Package modularity involves the separation of individual instruments into their own independent modules. The second level of Spacecraft Bus modularity involves the grouping of components into assemblies for module encapsulation; the third level of Spacecraft Bus modularity involves the grouping of components into component families for encapsulation, meaning that multiple instances of the same component are grouped into the same module. For

the second level of Spacecraft Bus modularity, assemblies (which are encapsulated to create modules) are defined by grouping components within the architecture according to Design Structure Matrix (DSM) connections and Mean Time Between Failures (MTBF) values. In addition, the assembly/servicing technique informs module definitions – a self-assembling architecture adds a robotic arm for every ten modules, and all architectures include Universal Docking Ports (UDPs) in each module except for formation flying architectures, which have electromagnetic (EM) coils (these decisions are described further in the Assembly/Servicing Technique section). Where possible, components with similar MTBF values are grouped in the same module; this is to take advantage of the effect described in the first paragraph of this section. By grouping components with similar MTBF values, the components within a module are projected to fail at approximately the same time. Therefore, when one component fails, it is likely that the other components within that module are near failure and the amount of useful component time lost when a module is replaced is minimized. The full enumeration of all combinations of the levels of each branch of the tree generate 7 discrete modularity levels, described in Table VI. It is important to note that as a result of the separation of the modularity of the instrument package and the modularity of the spacecraft bus, the magnitude of the modularity trade metric does *not* correspond to the number of modules in the telescope. The modularity levels are labeled 1 through 7 simply for identification purposes. The number of modules at a given modularity level may fluctuate depending upon other architectural decisions, but the number of modules in a given architecture are saved for analysis later.

Table VI: Description of the 7 levels of the modularity architectural decision

Modularity Level	Description
1	Full Telescope (No Modularity)
2	Permanent Infrastructure Instrument Package Spacecraft Bus
3	Permanent Infrastructure Instrument Package Spacecraft Bus Assemblies
4	Permanent Infrastructure Instrument Package Spacecraft Bus Component Families
5	Permanent Infrastructure Individual Instruments Spacecraft Bus
6	Permanent Infrastructure Individual Instruments Spacecraft Bus Assemblies
7	Permanent Infrastructure Individual Instruments Spacecraft Bus Component Families

4.3.3 Location of Servicing

The telescope towards which this analysis is directed represents a substantial investment and is expected to provide significant scientific return for a lifetime of approximately 40 years. Since the probability of an event resulting in complete or partial loss of scientific capability increases significantly as time goes on (as illustrated by data from the Hubble Space Telescope, Figure 13) a 40-year lifetime strongly implies the need for servicing in order to repair and replace components¹⁴. In addition, servicing allows the telescope to maintain scientific relevance by upgrading instruments to take advantage of advancements in instrument technology.

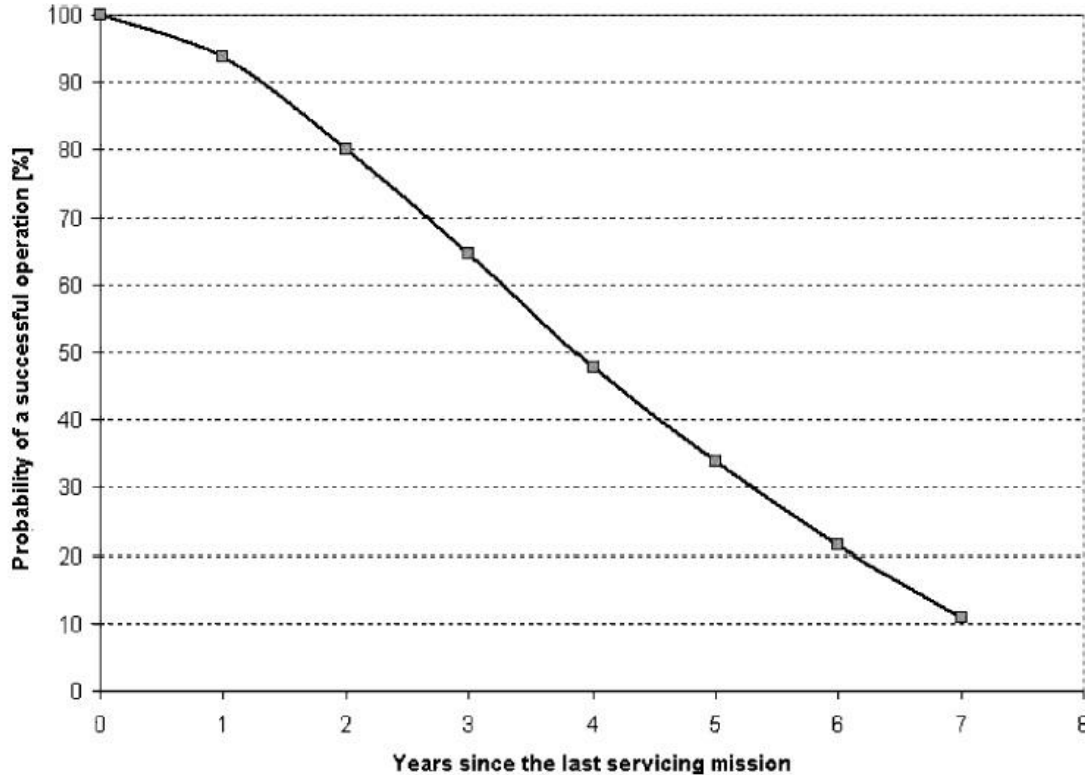


Figure 13: Reliability of the Hubble Space Telescope as a function of time since last servicing mission. Note the significant decline in reliability as time goes on¹⁵.

As mentioned previously, all servicing is assumed to be robotic. Four servicing locations have been identified: Sun-Earth L2 (in-situ servicing), Earth-Moon L2, L1 Orbit Trajectory Used for Servicing (LOTUS – see Figure 14), and Low Earth Orbit. Each servicing location has a different ΔV requirement to move the telescope into place for servicing operations, which incurs a launch cost from propellant mass. This launch cost, associated with the telescope itself, is higher for servicing locations closer to Earth, as the telescope must travel farther on its own. However, the launch cost for servicing (the cost to launch replacement parts) will decrease as the servicing location moves closer to Earth. For this model, the servicers are assumed to launch on a schedule so that they arrive at the servicing location; therefore, the transit time of the telescope must be included in the calculation of total servicing downtime but not the transit time of the servicers. Since transit time is time during which science cannot be done, the telescope architectures with longer transit downtimes due to moving to and from the servicing location are expected to exhibit a lower utility to science. In summary, the location of servicing primarily

affects the cost of the telescope itself via propellant mass, the launch cost of replacement parts during servicing, and the overall downtime and utility to science of the telescope.

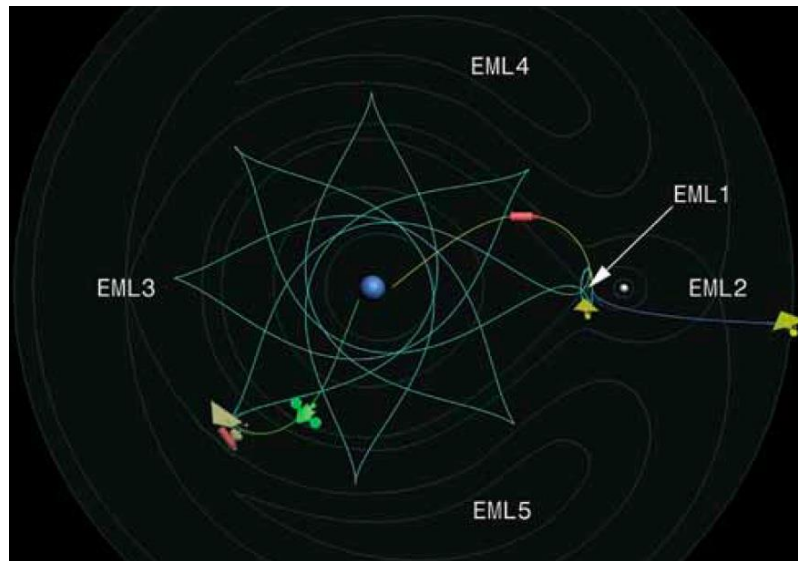


Figure 14: L1 Orbit Trajectory Used for Servicing (LOTUS), one of the orbits under consideration for servicing operations at a greater proximity to Earth. The Earth-Moon system is shown, with green lines indicating the proposed orbital paths of the telescope during servicing operations¹⁵.

4.3.4 Frequency of Servicing

As mentioned before, the servicing of the telescope is assumed to be on a regularly scheduled basis rather than on-demand. The frequency of servicing missions is therefore an architectural decision, and servicing missions may be sent every 3, 5, or 10 years. These values were chosen to represent short, medium, and long inter-servicing periods. 3 years was selected as the minimum because this is estimated to be approximately the time required to prepare and execute a servicing mission; 10 years was selected as the maximum due to the significant increase in instrument technology expected in a 10-year period – estimated to be an approximately 25x increase in discovery efficiency¹³ – as well as the increased risk of mission failure as the duration between missions increases (see Figure 13). The servicing schedule determines a minimum threshold for the MTBF of component families on the spacecraft – that is, components must be selected or set up in redundant systems such that they are expected to last at least the time between servicing missions.

The assumption of scheduled servicing as opposed to on-demand servicing was made to reduce model complexity and maintain the scope of this project at a level which could be completed in a one-semester graduate level class. Incorporation of on-demand servicing into the model would have increased model complexity in several ways. First, it would have required the implementation of some form of decision tree or decision rules analysis, which requires the definition of decision threshold values. For example, a parameter would have to be created to indicate what circumstances trigger a servicing mission. In addition, the inclusion of on-demand servicing as an option effectively triples the tradespace by adding the architectural decision of servicing architecture: on-demand, scheduled, or hybrid (on-demand or scheduled, whichever

triggers servicing first); one method to mitigate this would be to simply assume a different servicing architecture, but that would again be an assumption that must be justified. In addition, model parameters would have to be created to describe the duration of servicing mission development, and servicer transit time would need to be incorporated into the model. Currently, since servicing is scheduled, it is assumed that servicers are launched in such a way that they arrive at the servicing location at the start of scheduled servicing. Finally, there is a certain degree of risk associated with programmatic uncertainty – it is more difficult to organize and fund a servicing campaign that is not regularly scheduled – and this uncertainty would need to be factored into the mission risk analysis.

However, the differences between on-demand and scheduled servicing have been investigated for individual architectures by Baldesarra, who investigated the lifecycle effects of servicing on a particular telescope for both on-demand and scheduled servicing cases.¹³ His thesis determined that on-demand servicing has the potential to increase the utility to science of a given architecture for roughly the same cost.¹³ This makes sense, as on-demand servicing mitigates the problem of long periods of downtime between servicing missions in the event of a component failure. The longest possible downtime is the time it takes to prepare and launch a servicing mission and for that mission to reach the servicing location. Since downtime is time in the telescope's lifetime that has no utility to science, the more downtime a telescope has the lower its utility to science will be. The incorporation of on-demand servicing as an option within the model has the potential to raise the utility to science of certain architectures, or (if servicing architecture were incorporated as an architectural decision) to produce new families of architectures with higher utility to science, but at the cost of a more complex model. This option is further discussed in the future work section.

4.3.5 On-Orbit Assembly/Serviceing Technique

Central to this investigation is the evaluation of different methods of on-orbit assembly and servicing of large space structures. At the architectural level, the methods of assembly and servicing are grouped into three families or classes: self-assembly/servicing, tugs, and formation flying. Based on the results of the study, the telescope architectures will be grouped into these classes and compared to predict which of the three techniques performs the best in terms of cost, serviceability, utility to science and risk/schedule as discussed in later sections of the paper.

The self-assembly/servicing method involves only a single spacecraft, encompassing the telescope and supporting systems. The spacecraft is “folded” into one launch vehicle and uses deployment mechanisms to unfold or assemble various appendages once on orbit. This method is therefore very similar to JWST¹⁶ and ATLAST¹⁷, which both rely heavily upon complex deployment schemes. Shown in Figure 15 are the deployment methods for both JWST and ATLAST. If the size of the primary mirror prohibits folding into the selected launch vehicle, this technique requires the use of robotic arms that would access and assemble mirror segments stored in a stack below the spacecraft bus. To facilitate servicing, these robotic arms would also be able to remove and discard failing component modules and install new modules upon the docking of a new cargo shipment.

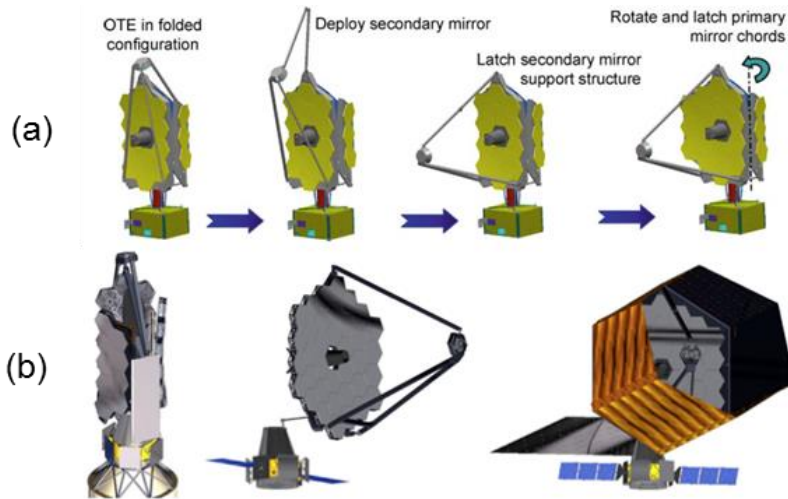


Figure 15: (a) The JWST deployment sequence (mirror only)¹⁶ (b) The ATLAST stowed and deployed configurations¹⁷

The tug technique¹⁸ involves one or multiple assembler/servicer spacecraft in addition to the main spacecraft containing the telescope and bus. This method allows for the telescope to be launched in several pieces, possibly on several smaller launch vehicles. There can be either one primary tug responsible for assembling the whole system, or several dedicated tugs, each with their own role. The tug(s) would be fully functioning spacecraft with robotic arms or docking ports. Once in orbit, the tug(s) would gather and assemble the mirror segments into the primary mirror, attach the secondary mirror and its support structure, and connect the spacecraft bus appropriately. After assembly, the tug(s) would dock to the main spacecraft and potentially add functionality in actuation and sensing. The tug(s) would also be able to service the telescope by replacing faulty components upon the arrival of new cargo. The tug(s) in this method are akin to the servicer/tender that harvests components from satellites in the geostationary graveyard orbit in DARPA's Phoenix program, shown in Figure 16¹⁹. Note that the cost or the complexities associated with designing the servicer/tenders is not accounted for in the system cost. This cost is regarded as too difficult to model without a baseline or previous mission to model after and is outside the scope of this model, so this aspect of the technique will not be captured in the architecture enumeration and analysis.

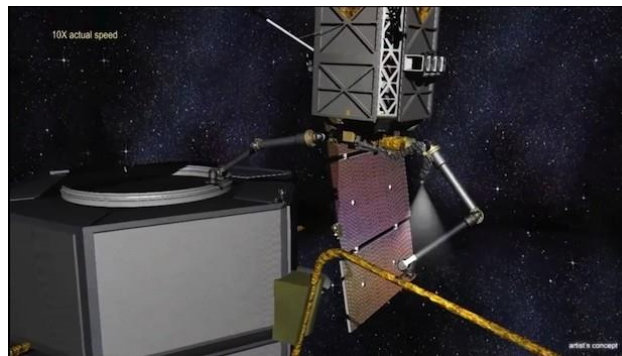


Figure 16: DARPA's Phoenix project. Artist's concept of the servicer/tender (or tug) assembling a space structure¹⁹

The formation flying technique requires the telescope and bus to be composed of several smaller modules that each has an attitude determination and control subsystem (ADCS). For example, the spacecraft bus, sun shield, primary mirror, secondary mirror, and science instruments would self-assemble by formation flying and then docking to form the completed telescope. This technique will employ electromagnetic formation flying that utilizes superconducting coils on each module to actuate against each other²⁰. Having non-contacting servicing and assembly provides added autonomy and flexibility, but will also require stiffer requirements on individual modules. Using the electromagnetic option also removes the need for a propulsion system and fuel in each and every module, as all that is needed is the electromagnetic coils. With this technique, the individual modules would be able to be replaced or serviced individually without impacting the rest of the system. However, if further modularization were required for consumables or short-lifetime components, the spacecraft bus would act as the servicing spacecraft and would require robotic arms. This technique is the riskiest of the options as it involves several stand-alone spacecraft, which increases the probability of a failure that requires servicing, because there are many more subsystems and components. It also uses lower technology readiness level (TRL) components to achieve electromagnetic formation flying, which are inherently riskier.

As one can see from the drastically different architectures described above, the architectural decision of the on-orbit assembly/servicing technique is necessary to include in the investigation. This decision has implications to every subsystem. The structures subsystems vary in each choice from a single, continuous structure to multiple, modular structures. The propulsion and ADCS subsystems play different roles, as do the distribution of communications and avionics. If this architectural decision were not included, the tradespace of the study would be significantly decreased.

4.3.6 Segmentation of Primary Mirror

As previously noted, the immense scale of the observatory envisioned in this study will necessitate some degree of on-orbit assembly and/or deployment to reach an operational configuration. Although the method of assembly, deployment and servicing is treated separately (architecture decision 6), some consideration of the type and configuration of components to be assembled or deployed is merited. Architectures containing a large number of independent components simplify launch considerations such as packing at the cost of increased complexity and risk in on-orbit initialization (and vice versa). Additionally, architectures may consider the degree of symmetry in the selected number of segments. Architectures with a high degree of symmetry will simplify assembly and increase reliability, but may complicate the design and/or manufacturing, particularly if bus or support functions are included within the separate segments (as opposed to located in a single primary bus segment).

The architectural trade described here is mostly clearly observable in the primary mirror element of the observatory. At one extreme, the primary mirror may be launched with the minimum number of structural components, which still permit the assembly to fit in the payload fairing. This option corresponds to a “chord segment” architecture not unlike that in use for JWST (Figure 15)¹⁶. At the other extreme, the number of structural components is equal to the number

of mirror segments.* Such a scenario envisions a higher degree of on-orbit assembly (Figure 17).²¹

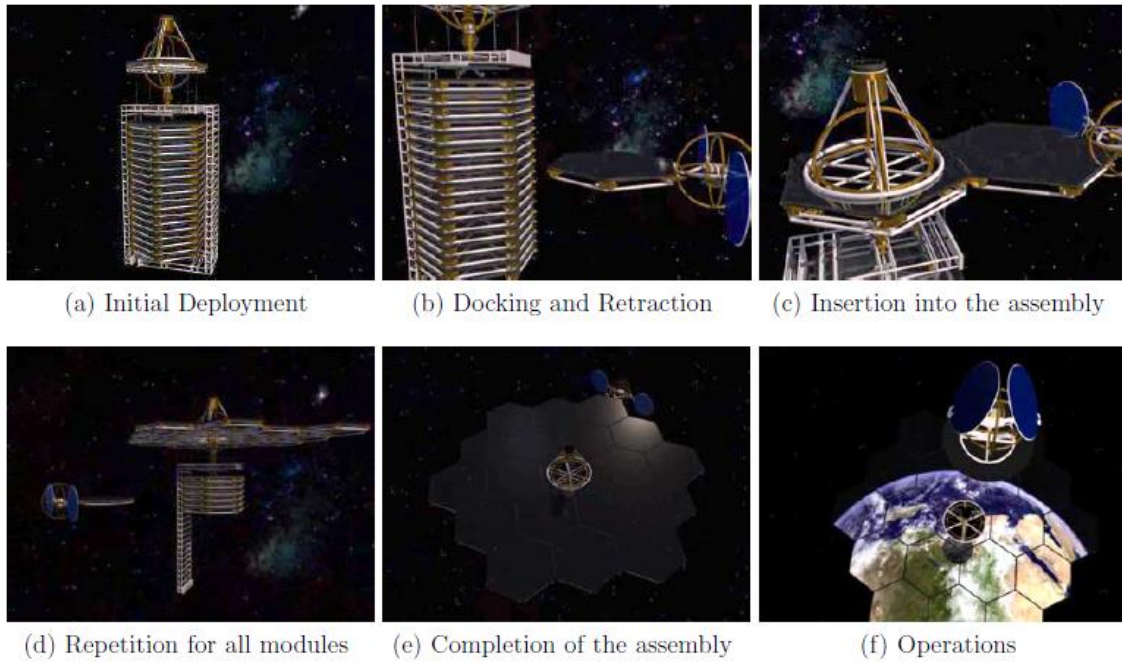


Figure 17: Notional packing and assembly scenario for a highly structurally-segmented primary-mirror architecture.²¹

Between these extremes, a variety of alternative segmentation concepts exist which have not been extensively explored in previous literature. Each offers a compromise between the launch- and packing-optimized high-segmentation approach and the on-orbit assembly- and deployment-optimized “chord segmentation” approach. For the purposes of this investigation, three 6-fold symmetric concepts were selected which provide a range of structural segment counts, dimensions, and volumes (Figure 18).

* Included in the requirements derived from the ATLAST telescope concept baseline is an assumption that three rings of 2.4 m mirrors will be used in the primary mirror architecture. See Appendix I for a detailed treatment of the ATLAST requirements and their implications. In a more general sense, the size and number of mirror segments is itself an important design consideration, but will not be addressed in the architectural trades treated here.

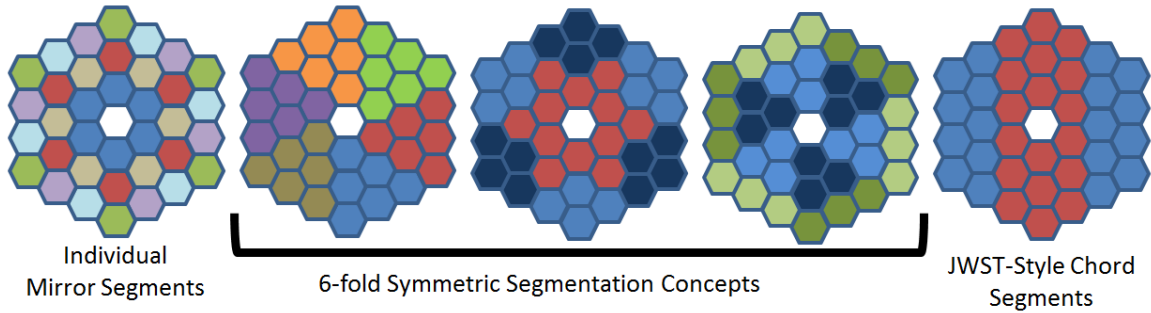


Figure 18: Architectural options selected for exploration in the primary mirror segmentation decision.

From an on-orbit assembly perspective, the complexity of the assembly operation is closely related to the total number of observatory segments to be deployed, the number of operations which must be conducted to deploy them, and the number of unique operations which must be developed to complete the assembly operation. The symmetry of the observatory segments as well as the number of segments thus heavily drive the degree of complexity of the overall assembly operation. By contrast, from a launch payload sizing and packing perspective, the dimensions and volumes of the segments are the most important factors to consider (Figure 19).

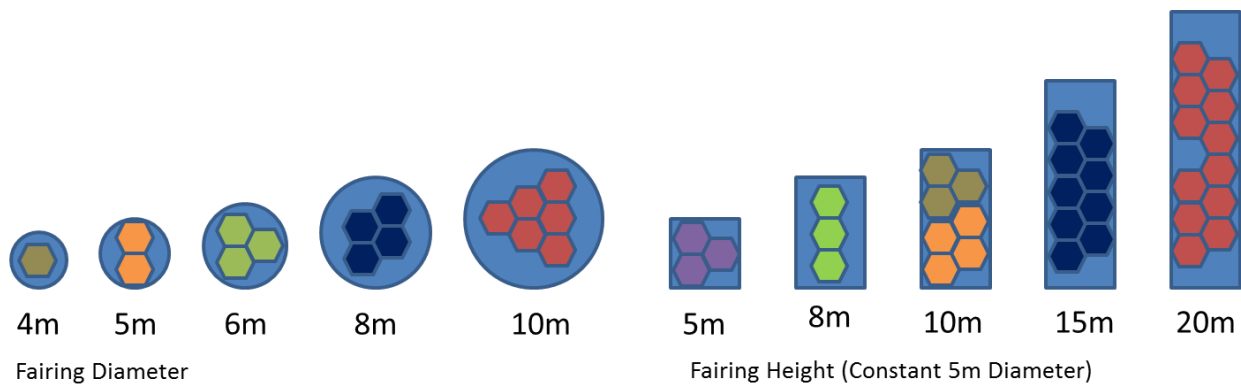


Figure 19: Notional packing of segments into payload fairings of various heights and diameters (sizes are to scale).

More efficient packing of structural segments becomes possible where individual structural segments are allowed to deform to meet the constraints of a given payload fairing. Such an approach would represent a hybrid between the segmentation/assembly and deployment models for telescope construction, where individual segments deploy, and are then assembled into the macro-structure of the observatory. Because these specific variations between segmentation and deployment tread heavily into the design space (as opposed to the architecture space under consideration here), they are not further addressed in this report.

4.3.7 Primary Mirror Segment Support Method

A critical part of obtaining high-resolution images from a space telescope is the precision of the shape of the primary mirror. While a precise shape can be maintained by making the mirror very thick, such a mirror would be too massive to launch, and in the case of a 16.8-meter mirror, too

large for any launch vehicle. Thus, other support methods have been developed. Typically, a large mirror is supported through a backstructure which contacts the back side of the mirror by pins at a discrete number of points. These pins can apply forces to the mirror to accurately articulate its shape. Because these pins are normal to the surface of the mirror, this technique is known as surface-normal actuation. The backstructure is typically made of trusses or ribs²², as shown in Figure 20.



Figure 20: The Herschel telescope primary mirror with ribbed backstructure²³

In the case of a segmented primary mirror, not only does each of the segments have to maintain an extremely precise shape, but each segment must also maintain a precise positioning with respect to each of the surrounding segments. Thus, a key architectural decision for the development of the next large space telescope is the primary mirror segment support method. For the purposes of this trade study, the three support methods being investigated are surface-normal, surface-parallel, and a combination of both surface-normal and surface-parallel. Each of these alternatives will be evaluated according to the metrics of utility to science, serviceability, downtime, and cost, which are described in the Trade Metrics Descriptions and Trade Metrics Calculation sections.

In the surface-normal support method, each of the mirror segments is supported directly by a backstructure that links all of the segments. This structure positions the segments relative to each other. In the surface-parallel support method, each of the segments is only relatively positioned. This positioning is done through actuators parallel to the surface of the mirror and between each of the segments. This method removes the need for the backstructure and could simplify assembly and servicing techniques; however, it does increase complexity. The final alternative is a combination of the first two. Figure 21 shows a diagram of surface-normal and surface-parallel techniques for connecting two mirror segments. The entire backstructure is not pictured in the surface-normal diagram.

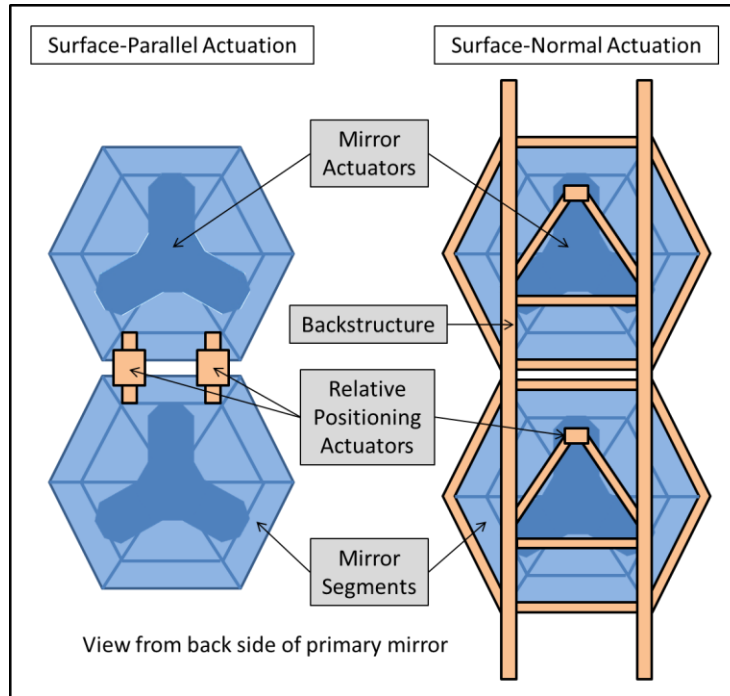


Figure 21: Surface-Parallel vs. Surface-Normal actuation techniques

This architectural decision is important to the investigation for several reasons. Each of the alternatives in this decision is needed to appropriately cover the tradespace. In the past, only surface-normal support techniques have been utilized. However, strictly surface-parallel actuation between segments is an alternative, which could significantly change the structure, assembly technique, and servicing technique of the primary mirror if determined to be more effective with respect to the metrics.

5 METRICS AND MODEL DESCRIPTION

The following sections go into detail regarding the inputs, outputs, and internal processes of the space telescope architecture model developed for this paper. First will be an overview of the layout of the model, followed by detailed descriptions of the trade metrics and the MATLAB code modules that make up the simulation environment.

5.1 Model Overview

The modeling and simulation environment of this project has been implemented in the form of MATLAB code modules that are run in ordered succession by an overarching *Main* wrapper that structures variables, defines constants, provides variable interfaces, and collects results. A detailed list of the code modules and variables tracked throughout the model can be found in Appendix A.

The first set of code modules (*Design Constants*, *Components DB and DSMs*, and *Design Vector*) are all contained within the *Main* wrapper. The *Design Constants* module sets values to important constants that are used throughout the other code modules. The *Components DB and Components DSMs* module captures component family data from Excel workbook files for use within the code. The *Design Vector* module enumerates the full modeling tradespace of architectures by expanding all of the possible combinations of the seven architectural decisions, as found in Section 4.3. Each architecture is captured within a common global variable structure (initialized in the *Main* wrapper as a *struct* data-type) known as an ‘LTA’ within the code, short for *Large Telescope Architecture*, which is gradually built upon as the design matures through the remaining code modules.

Once the LTAs have been enumerated, the *Main* wrapper iterates through each individual LTA and sends it through the subsystem code modules (in order: *Optics*, *Communications*, *ACS*, *Avionics*, *Propulsion*, *Power*, *Thermal*, and *Structures*), resulting in an architectural design, or a set of selected quantities of component families distributed into defined spacecraft modules. Each architectural design is then sent through the *Systems* code module, which computes the system complexity. Once this is completed, each architectural design is sent through the *Operations* code module, which performs Monte Carlo simulations of the spacecraft’s mission. Finally, the *Trade Metrics* code module receives the architectural designs and quantifies desired output metrics for later use in analyzing and evaluating all of the architecture designs against each other. The specific trade metrics (utility to science, serviceability, downtime, and cost) will be discussed further in Section 5.2.

The flow of information and variables between each module can be seen in the N^2 diagram in Figure 22, where the inputs for a given code module can be found in that module’s column, and the outputs of that code module can be found in the module’s row. Each code module will take the specified inputs and internally use subsystem, operations, and system-level models to compute the subsystem metrics required by other modules. The internal computations of each code module are described in detail in Section 5.3.

Design Constants					reliability_req			mirror_diam mirror_temp_range P_earth2telescope reliability_req shield_efficiency total_mass_estimate			lifetime_req	lifetime_req rep_segments segment_diam unique_prescr
	Components DB and DSMs		compPowerAvgCol massCol volCol	massCol				compPowerAvgCol massCol MTBFCol volCol	compPowerAvgCol compPowerPeakCol massCol MTBFCol volCol OverallDSM	DataDSM OpticalDSM OverallDSM PowerDSM StructuralDSM ThermalDSM TRLCol	massCol MTBFCol	compPowerPeakCol dimCol massCol MTBFCol volCol
		Design Vector		comm_arch	a_s_technique comm_arch servicing_freq	servicing_loc servicing_freq	servicing_freq	servicing_freq	a_s_technique comm_arch mirror_segmentation mirror_support modularity_level		a_s_technique modularity_level servicing_freq	mirror_segmentation modularity_level servicing_freq servicing_loc
			Optics				optics_avg_power_req	optics_power_diss optics_temp_range optics_v	optics_components optics_m optics_v		discovery_efficiency_inst_a discovery_efficiency_inst_b discovery_efficiency_inst_c discovery_efficiency_inst_d	
				Comm			comm_avg_power_req comm_peak_frequency comm_peak_length comm_peak_power	comm_power_diss comm_temp_range comm_v	comm_components comm_m comm_v			
					ACS		acs_avg_power_req	acs_avg_power_req acs_temp_range acs_v	acs_components acs_m acs_v			acs_m
					Avionics		avionics_avg_power_req	avionics_power_diss avionics_temp_range avionics_v	avionics_components avionics_m avionics_v			
						Propulsion	prop_avg_power_req	prop_power_diss prop_temp_range prop_v_nd	prop_components prop_m_nd prop_v_nd		prop_svc_time	
							Power	power_array_area power_avg_power_diss power_m power_m_nd power_temp_range power_v power_v_nd	power_components power_m_nd power_v_nd			
								Thermal	power_m [updated] power_v [updated] thermal_components thermal_m thermal_v			thermal_m
									Structures	overall_components	module_definitions overall_components	comm_m [updated] power_m [updated] overall_components prop_v structures_m sys_mass sys_vol
										Systems		sys_complexity
											Operations	MC_results.mean_m_serv_vec p_util_science time
												Trade Metrics

Figure 22: N² diagram showing interactions between code modules in the MATLAB model

One very important thing to take away from the N^2 diagram is that the model described in this paper does not have feedback loops, and therefore design decisions cascade through the model without any optimization between subsystems. This is justified in that the model is only meant to perform a first-order architecture evaluation and generate all possible designs, not only those that are optimal. With this in mind, simplifying assumptions regarding computations were made where possible. It is important to note that the order of the subsystem code modules was specifically designed in order to intuitively arrange the necessary inputs and outputs of each subsystem and minimize the number of assumptions to make, thereby simplifying the code and eliminating feedback loops. The code is expandable if feedback loops are desired in the future for more detailed design.

5.2 Trade Metrics Descriptions

5.2.1 Utility to Science

Utility to science reflects the lifecycle science output of the telescope. It quantifies the expected value to the scientific community. There are several methods of quantifying an instrument's utility including productivity rate (the rate that images are taken), number of papers, or discovery efficiency (field of view multiplied by throughput).

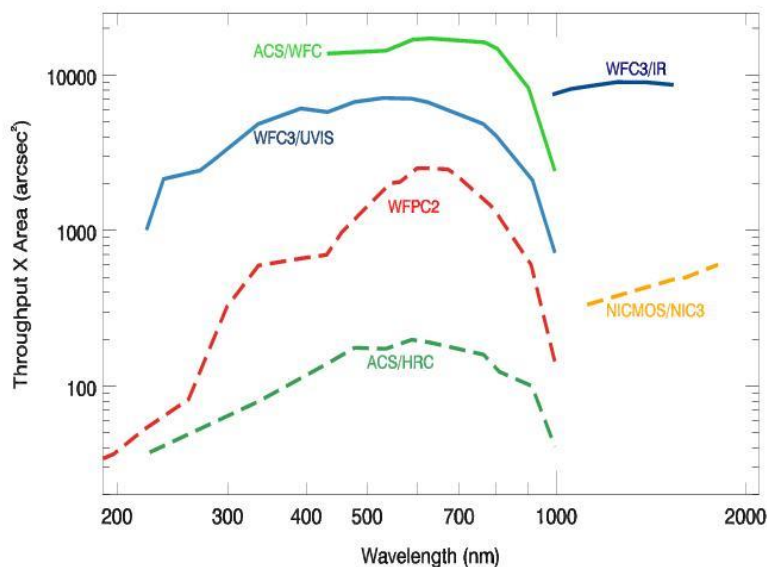


Figure 23: Discovery efficiency for selected Hubble instruments²⁴

This model for science utility will use discovery efficiency with an exponential improvement over time, similar to the model in Baldessara.¹³ The discovery efficiency for HST instruments is shown in Figure 23.

The two architectural decisions that most directly affect utility to science are servicing location and servicing frequency. Servicing frequency limits the maximum possible rate at which new instruments can be added to the telescope and therefore the maximum rate of increase of utility to science. Additionally, broken components that may have degraded the utility to science can only be fixed during a servicing mission, so more frequent servicing missions help limit the

downtime of the telescope. Servicing location determines the downtime per servicing mission which represents times in which it is impossible to perform science with the telescope.

In this model, utility to science can only be used to compare among telescope architectures. It cannot be used to compare with other telescopes as it has not been calibrated against existing telescopes.

5.2.2 Specific Servicing Margin

The serviceability of a telescope is defined as the ease with which telescope hardware can be changed after the start of the mission, either to replace or repair damaged components or to upgrade telescope systems that have become obsolete. This may be considered as the capability to achieve some benefit at a cost – a more serviceable architecture will have the capability to achieve more repair and upgrade benefits for a lower lifecycle cost. In order to quantify the serviceability of architectures in the tradespace, this report defines the specific servicing margin $\Delta\$_{serv}$: the number dollars of budget margin per kilogram of serviced mass for each servicing mission. Effectively, the specific servicing margin is a measure of how much money can be spent per kilogram of replacement parts for a given servicing mission before it becomes more cost-effective to simply replace the entire satellite rather than service it.

Ideally, a model of serviceability would be able to estimate the cost of each servicing mission in order to develop an estimate of the lifecycle cost of servicing for a given architecture. However, space telescope servicing and the technology that supports it are relatively new and are still subject to uncertainty that makes it difficult, if not impossible, to directly model the cost of servicing missions with confidence.¹³ Portions of the cost, such as the cost of replacement component development and the launch cost for the mass of replacement components, can be modeled. However, a valid model of the cost of a robotic servicer is beyond the scope of this project due to the wide variety and technological immaturity of robotic servicing architectures. Lacking a valid servicer cost model, any attempt to include the cost of servicers in the lifecycle cost would reduce the validity of the model output. Therefore, a more creative approach must be taken to measure the serviceability of a given architecture. Specifically, a metric must be used which does not require an estimate of the cost of each servicing mission. Hence, the specific servicing margin is defined and is calculated and utilized as described below.

Baldesarra has implemented a method that avoids the estimation of servicer costs.¹³ Instead of attempting to estimate the cost of servicing missions directly, the model instead calculates the lifecycle cost of each telescope architecture without including the cost of servicers (both development and launch cost). These lifecycle costs are used to compute the servicing margin, defined as the difference in lifecycle cost between the architecture and a baseline, “non-servicing” case

$$\Delta\$_{serv} = C_b - C$$

Eq. 1

where C_b is the baseline cost for a given architecture, C is a given architecture’s lifecycle cost not including servicers, and $\Delta\$_{serv}$ is the servicing margin. All units are in dollars. The baseline cost for each architecture is defined as the lifecycle cost (not including servicers) of the

architecture with modularity level 1 and all other architectural decisions (servicing location, servicing frequency, communications architecture, primary mirror actuation, assembly/servicing technique, and mirror support method) the same. Thus, the only difference between a given architecture and its baseline case is the modularity level. For example, an architecture represented by the architectural vector [4 1 1 1 1 1] (where the first element is the modularity level) would use for its servicing margin calculation a baseline architecture with the architectural vector [1 1 1 1 1 1]. It is important to note that, while these baseline costs do not include the cost of the servicers – due to the uncertainty in this value described above – they do include the development and launch cost of the replacement parts, as this value can be determined with the same validity as the value of the original cost of the telescope. Thus, costs that can be confidently modeled are included in the lifecycle cost, and costs that cannot (specifically, the cost of servicers) are not.

The baseline architecture is analogous to what Baldesarra called the “replacement case”¹³ With modularity level 1, at each servicing mission the only options are to replace the entire telescope or to not take any action. Replacement of the entire telescope is a cost that can be modeled with confidence, as it effectively consists of repeating the development and launch of the telescope. There is no servicer; the new telescope simply replaces the old one. Therefore, the lifecycle cost of a baseline architecture is a value which can be reported with the same degree of confidence as the initial telescope development and launch costs; there are no additional sources of uncertainty. Using this baseline value, the telescopes that are serviceable – that is, architectures with modularity levels 2 through 7 that are capable of replacing a part of the telescope without replacing the whole – can be compared to each other by calculating the servicing margin described above. The servicing margin is a measure of the amount of money that can be spent on servicing over the entire telescope lifetime before it becomes more expensive to service the telescope than to simply replace it.

However, this margin alone does not capture all aspects of servicing. Some telescope architectures may require more servicing than others, either by requiring more replacement parts or more servicing missions. Two metrics are used to capture this aspect: serviced mass and the number of servicing missions. Serviced mass is defined as the mass the modules that are replaced at each servicing mission. It is assumed for the purposes of this model that a module is replaced with another module of identical mass. For each servicing mission in the lifecycle simulation, the mass of each replaced module is known and can be used to calculate the total serviced mass in that mission. The mean of the total serviced mass across all missions is then calculated as a representative value for the amount of mass serviced in a typical mission for the architecture being analyzed. Additionally, during the lifecycle simulation the number of executed servicing missions is counted. It should be noted here that, while the mission lifetime is known and one of the architectural decisions is the frequency of servicing, it is not as accurate to simply pre-calculate the number of servicing missions that occur for a given architecture. Servicing missions only execute in the lifecycle simulation if servicing is required (i.e. if a component has failed or is below the reliability threshold, or if an instrument has become obsolete), so there is potential for one architecture to have fewer servicing missions than another even if they have the same frequency of servicing. Therefore, the number of servicing missions for a given architecture is determined in the lifecycle simulation rather than before it based upon the architectural decisions.

These three metrics – the servicing margin, the mean serviced mass, and the number of servicing missions – are combined to produce the specific servicing margin using the equation

$$\overline{\Delta\$}_{serv} = \frac{\Delta\$_{serv}}{m_{serv} \times n} \quad \text{Eq. 2}$$

where $\Delta\$_{serv}$ is the servicing margin in dollars, m_{serv} is the mean serviced mass in kilograms, n is the number of servicing missions, and $\overline{\Delta\$}_{serv}$ is the specific servicing margin in dollars per kilogram per mission. A higher specific servicing margin indicates that more money is available to service for the amount of servicing which occurs; therefore architectures with higher specific servicing margins are considered more serviceable.

As previously stated, the specific servicing margin is a measure of how much money can be spent per kilogram of replacement parts in a given servicing mission before it becomes more cost-effective to replace the telescope than to service it. This can be thought of as analogous to the amount of money that can be spent on servicers, and the metric is reported with the intent of informing stakeholders and mission planners of the budget available to spend on servicing. Specific servicer architectures can be considered independently, and once the cost of a given servicer architecture is estimated the specific servicing margin metric can be used to filter the telescope architecture tradespace to only those architectures for which servicing would be cost-effective. Conversely, the specific servicing margin of a given telescope architecture could be used to set an upper bound on the cost of a servicer, and based on mission-specific data mission planners can use this metric as an aid to decide whether it is feasible to develop a servicer within that budget.

In addition, two interesting artifacts appear in this metric. The first is the fact that, by definition, telescope architectures with modularity level 1 will have a specific servicing margin of 0. This makes sense, as an architecture with modularity level 1 is the non-modular case: it cannot be serviced – it can only be replaced. Therefore, no servicing occurs on these architectures, and the entire budget is spent on non-servicing items. This is the reason that the modularity level 1 family of architectures was chosen as the servicing margin baseline. More interestingly, the definition of this metric provides for the possibility that some architectures may have a negative specific servicing margin. These architectures are those for which it is in fact more expensive to develop and launch the telescope and replacement parts than it is to simply launch a new telescope when components fail, even before servicing costs are factored in. For these architectures, it is always more cost-effective to utilize modularity level 1 and build a non-serviceable telescope which is simply replaced when components fail. In both cases, the specific servicing margin accurately reflects the serviceability of the telescope architecture.

5.2.3 Failed Downtime

The failed downtime is defined as the time during which no science can be done due to the failure of a component. Downtime will also occur during the Assembly/Transit Phase and Servicing Phase of operations, but this downtime is a part of normal telescope operations and thus is not a measure of the risk of a particular architecture. Failure of individual components or subsystems could impact the scientific operations of the telescope, degrading the utility to science of the overall system either partially or completely. Different components will have a

different magnitude of effect; the effect of component failures on utility to science and their representation in this model are described further in the Code Module Description of Operations in the Metrics and Model Description Section. Failed downtime is used as a measure of the risk of a telescope architecture using the assumption that higher risk architectures will experience more failed downtime over the course of a telescope's mission lifetime. Thus, a telescope with more failed downtime is considered a riskier telescope than one with less failed downtime. Failed downtime is reported as a fraction of total mission lifetime.

5.2.4 Cost

The final trade metric is cost. In order to allow a true comparison of the costs associated with each different architecture, the entire lifecycle should be considered. For that reason, cost will be determined in terms of various phases of the space telescope project for each architecture. The phases are flight system development, launch, and on-orbit assembly and servicing. The on-orbit assembly and servicing costs are not estimated. Instead, the costs for a baseline concept in which there is no assembly or servicing are estimated. Then, costs for each mission are estimated without the assembly or servicing costs. The difference between the baseline cost and the cost for each mission is then reported for each decision vector. It is clear that the statistically based models presented here may not provide a highly accurate estimate for the absolute cost of the each design architecture. Rather, the relative costs with respect to the baseline mission cost will be the primary consideration. The goal is to help determine which of the design architectures are more attractive from a cost standpoint rather than to provide a reliable absolute cost estimate.

5.2.4.1 Flight System Development

Flight system development is defined here as the design, manufacture, test, and operation of the space telescope system. Several models for flight system development currently exist, and three are being used here. These existing models will be drawn upon in estimating a cost for each architecture. Each of these existing models provides a cost estimate for a portion of the total flight system cost, therefore, the cost estimate output from each will be summed to determine the total flight system cost.

The Stahl Ground-Based Telescope Model is a parametric cost model. It predicts the cost to produce an optical telescope assembly, which consists of the primary mirror, secondary mirror, auxiliary optics, and support structure.²⁵ The Unmanned Spacecraft Cost Model (USCM8) was developed by Tecolote Research for the US Air Force, Space and Missile Systems Center.²⁶ The model provides cost-estimating relationships for non-recurring and recurring cost for large spacecraft buses, including the development, ground equipment, launch operations and orbital support, and communications payload. The non-recurring costs included are design and development, manufacturing, and test of one spacecraft, and acquisition of peculiar support equipment.²⁶ Recurring costs include fabrication, manufacturing, integration, assembly, and test of the spacecraft.²⁶ The final flight system development model is the NASA Instrument Cost Model (NICM). This model provides cost estimating relationships for several different types of instrumentation.²⁶

The three cost models presented for the flight system development each capture a portion of the total cost. These models complement each other and will be summed to provide an estimate for the entire space telescope.

In addition to the architecture decisions captured by the models above, the complexity discussed in the structures subsystem metrics section will have an influence on the cost. To account for this influence, a complexity multiplier is applied to the cost estimate. This multiplier is applied to the non-recurring costs for the space telescope system bus and program overhead. These are the efforts that are directly impacted by the complexity of the design. Complexity is discussed in Section 5.3.3.9.

5.2.4.2 Launch

Launch costs will be estimated using historical launch costs as estimates for future costs from different launch vehicle providers. Launch costs are calculated for both the initial space telescope system launch and the subsequent servicing launches. The initial launch costs are determined based on the mass, volume, and largest dimension of the payload. A particular space telescope assembly must fall within the acceptable ranges for all of these characteristics for a given rocket, otherwise a larger rocket is required. Inflation will also have an effect on the dollars spent for a given launch in the time frame of the proposed space telescope system. The launch cost for the servicing missions, which take place over the 40-year life of the space telescope assembly, are discounted back to the year of launch in 2013 dollars using an assumed annual interest rate of 2.01%. A slight departure for the servicing launch costs involves the volume and largest dimension for each of the servicing payload. These values are not calculated in this model, therefore, only the masses of the service payloads are considered when calculating servicing launch costs. Each design architecture will be associated with a launcher type required as well as the number of launches required based on its mass and volume.

5.2.4.3 Assembly and Servicing

The models for each phase of the space telescope project described above are based on inputs from the subsystem modules. To avoid introducing unnecessary uncertainty into the model, the servicing and on-orbit assembly portions of the mission cost are not estimated. However, as mentioned above, the launch costs for the servicing missions as well as the cost of the replacement components deployed during servicing are being accounted for. These replacement component costs are estimated as a fraction of the original space telescope system cost allocated based on the mass fraction of those components over the mass of the entire system. For example, if 10% of the mass of a given space telescope system is to be replaced, the cost of those components are calculated as 10% of the cost of the original space telescope system.

Based on the inputs from the subsystems, the integrated cost model, composed of each of the individual cost models described above, will provide a lifecycle cost minus the cost of assembly and servicing for each architecture. These assembly and servicing costs are defined as the cost of developing, building, and deploying any object (e.g., tugs, servicer spacecraft) that are not a part of the space telescope system itself. The architectures will be compared based on the funds available for servicing by subtracting the cost of a serviceable telescope from a non-serviceable telescope which requires no assembly. For further details on the Servicing portion of the cost, see the Serviceability discussion below. The cost estimates and the remaining system metrics below can be used to evaluate each of the design architectures.

5.3 Code Module Descriptions

5.3.1 Design Structure Matrix

In order to determine the metrics such as mass, power, and volume for the telescope, two Excel documents were created: a Design Structure Matrix (DSM) and a Components Database (Components DB). These two documents, included as Appendices C through H, are read into MATLAB for the analysis of different architectures in the tradespace. The MATLAB code uses a standardized set of variables, listed in Table VII, across subsystems to capture the various metrics based on the Components DB, thereby allowing ease of use and information transfer.

Table VII: Component Family DB variable names organized by subsystem

	Average Power	Peak Power	Mass	Volume	TRL	Lifetime	Nominal Failure Probability
Structures	struct_avg_pwr	struct_peak_pwr	sruct_mass	sruct_vol	struct_trl	sruct_lifetime	sruct_p_fail
Science/Optics	Science_nominal_power	Science_peak_power	Science_mass	Science_volume	Science_trl	Science_instrument_nominal_lifetime	Science_p_fail
						Science_optical_train_lifetime	
Communications	comm_avg_pwr	comm_peak_pwr	comm_mass	comm_vol	comm_trl	comm_lifetime	comm_p_fail
Avionics	avionics_avg_pwr	avionics_peak_pwr	avionics_mass	avionics_vol	avionics_trl	avionics_lifetime	avionics_p_fail
Thermal	therm_avg_pwr	therm_peak_pwr	therm_mass	therm_vol	therm_trl	therm_lifetime	therm_p_fail
Propulsion	prop_avg_pwr	prop_peak_pwr	prop_mass	prop_vol	prop_trl	prop_lifetime	prop_p_fail
Power	power_avg_pwr	power_peak_pwr	power_mass	power_vol	power_trl	power_lifetime	power_p_fail

The DSM lists high-level components that will be included in the final telescope. The interfaces between these components include optical, thermal, data, power, and structural, and are enumerated in a format for ease of MATLAB utilization. The DSM is structured so that each of these interface types are listed on individual Excel sheets. The component families are listed across the first row and column to create an N^2 matrix. To accurately sum the interfaces, which are listed as a 1 for an existing interface or a 0 for no interface between two component families at the intersection of a row and column, the resulting matrix is lower triangular. To ensure that the matrix is lower triangular and remove the possibility for human error, the DSM reader MATLAB function forces any upper triangular values to become lower triangular values. The main diagonal is kept as zeros since component families do not interact with themselves, and duplication of interfaces would occur if the matrix were to be fully populated. By keeping the DSM lower triangular, each column can be summed to determine the total interfaces of each component family. Each subsystem adds their component families to the DSM. The MATLAB function sums the DSMs to create an overall interface DSM that defines whether any two components share an interface with any of the five interface types. By grouping component families by subsystem, the interaction between different subsystem component families throughout the telescope can be observed.

5.3.2 Component Family Database

The Component Family DB comprises the complete list of component families for the entire telescope that are included in the DSM. In this manner, each component family is fully described in the Component Family DB so that its interfaces can be recorded in the DSM. Specifically, the database contains for each component a best estimate for its mass, volume, cost, average power required, peak power required, design life, and nominal probability of failure. The Mean Time Between Failures (MTBF) is also computed directly in this spreadsheet based on the design life

and nominal probability of failure, as will be explained in greater detail in Section 5.3.3.8.18. Component families cannot contain specific individual components within each component family. Alternatively, the component family database contains values that are representative of the components within that particular family. In situations where widely varying properties can describe a family, that family can be broken into separate families, of which only one would be used in a particular architecture. Additionally, there are instances where one type of component may be used in widely differing roles, such as a deployment device for a solar panel versus deployment device for an antenna, or where one type of component family is used in very different places within the telescope, such as thermostatic heaters for different components. In these cases, splitting the component families into multiple sub-families allows the code to select the proper number of components for use in different modules of high modularity spacecraft architectures. The added granularity afforded by splitting component families allows for increased accuracy in the model. The DSM also reflects these component family splits, with both families' interfaces listed. Using this component family database, modularity decisions and system mass, volume, and power analyses may be conducted. Just as with the DSM, each subsystem contributes its section to the Components DB, which is kept updated as an Excel spreadsheet that is read into MATLAB each time the main code is run.

In each subsystem code module, the requirements and architectural decision vector dictate which of the component families should be used for a given architecture from the Components DB and incorporated into the architecture for analysis. These component families are recorded by each subsystem in a subsystem specific vector that is passed from module to module. This vector represents integer numbers of each component family that is incorporated into a particular architecture for each particular subsystem. Consequently, this vector is the same length as the number of rows in the Components DB and as the number of rows and columns in the DSM. The vector is used to determine many of the component centric metrics, since the resulting dot product between this component family vector with the DSM is used to determine the complexity of the system, and the dot product between this component family vector with columns in the Components DB is used to determine metrics such as power, volume, and mass. For example, the dot product of the component family vector with the mass column from the Components DB multiplies each component family mass by the number of that particular component family incorporated in the LTA. Summing the resultant provides the mass for that particular subsystem. In this manner, several metrics can be determined, as will be explained in later sections. The Structures and Mechanisms subsystem's code is run as the last subsystem code in order to perform telescope level calculations that require the sum of all components, such as the complete system mass. Consequently, the individual subsystems' values are incorporated into the Structures and Mechanisms code before being sent to the systems level analytics.

In order to determine how varying inputs to the model affects the output trade metrics, a sensitivity analysis was run. Two loops were included in the Main_Servicing.m function for conducting the sensitivity analysis, including a loop for running several cases of a MTBF multiplication factor. The MTBF multiplication factor was run at values of 0.50, 0.85, 0.90, 0.95, and 1.05 to see how varying the mean time between failures for every component family affects the outputs, since the MTBF values greatly affect how servicing missions are performed. All datasets are combined for the sensitivity analysis. The coding structure enables this sensitivity analysis by incorporating this factor in the initialization of the MTBF values, which occurs when

the Components Family DB is read into the LTA MATLAB structure array. A full description of the sensitivity analysis is discussed in Section 7.4.

5.3.3 Subsystem Modules

The code structure uses a series of subsystem modules as initial building blocks that construct the *LTA* structure of variables used to find the Trade Metrics. The following subsystem descriptions include both calculations used in Excel for the Components Data Base and MATLAB code modules. Each of the MATLAB modules is run through the *Main.m* function. Design options derived from the architectural decisions are specified in the *LTA* structure, which is fed into each of the subsystem modules in order. Each module adds to the MATLAB structure, and it is taken in by the next subsystem.

5.3.3.1 Science/Optics Subsystem Module

The Science/Optics subsystem is responsible for calculation of variables pertaining to the optical train and instrument package. The primary outputs from this module are the telescope discovery efficiency, which is found in the MATLAB code module and used for the “Utility to Science” trade metric, as well as the MTBF, power, mass, and volume estimates of the instruments, which appear in the Components Data Base using Excel. Secondary outputs that are required for other subsystem module calculations, such as power dissipation, data rate, and operational temperature range, are also generated in the MATLAB code. The assumptions made to perform the analyses from this module are as follows:

- There will be five instruments total: four optical instruments, plus fine guidance sensors (FGS)
- Mass, Power, Volume, and Temperature range of instruments is based on values for Hubble Space Telescope instruments
- All instruments have equal reliability
- Power dissipation is 20%, the standard used in spacecraft first-order estimations
- Data rate estimates are based on JWST instrument data rate
- Performance analysis used in Baldesarra, 2007¹³ can be applied to this system

5.3.3.1.1 Lifetime/MTBF

Instrument lifetime has been determined based on empirical analysis of past space-based telescope instruments and instrument packages. A list was compiled of every space telescope either currently in operation, or whose total operational mission length was ever planned to last longer than ten years. This data set was selected because it encompasses historical failure rates on long-duration telescope missions, as well as data from systems with the most advanced current optical technology. Ten years was chosen as the minimum intended mission length for the data set because it is the maximum time between servicing missions considered for TITANS AE, and thus the minimum time that any given component must last for the telescope to remain in continuous operation with the least amount servicing for potential repairs. Any problem involving direct compromise of instrument function, but not loss of the entire spacecraft, was classified as a failure in this analysis, even if the actual cause was in another subsystem directly related to instrument function (i.e., thermal systems). This extension beyond actual instrument hardware failure allowed all cases of instrument loss to be recorded, and captured the possibility of shorts in instrument-specific electronics in later full-system risk analysis.

For each relevant telescope, the number of instruments and number of instrument failures over the total mission lifetime was recorded. An estimate for the probability that no instrument will have failed by end-of-life on a future long-duration telescope mission was then calculated in two ways. In the first method, an overall probability (total probability of success) was determined by tallying the total number of instrument failures and dividing it by the total number of instruments ever flown on any of the relevant missions. The second method found the average probability of no failure (average probability of success) by dividing the number of failures by the total number of instruments in each instrument package in the data set. A full summary of this process is shown in Table VIII. The more conservative of the two probability values was selected for use in MTBF calculations, as indicated by the highlighted block in the table. This value represents a first-order estimate for the reliability of a space telescope optical instrument at the end of that telescope’s anticipated mission duration.

Table VIII: Calculation of probability of no instrument failure

Telescope	Number of Instruments	Number of Failures	Failure Type	Time Before Failure (years)	Mission Length/Time in orbit (years)	Probability of Success
HEAO 3	3	0			11	1
AGILE	3	0			6	1
Fermi	2	0			5	1
Granat	7	0			10	1
INTEGRAL	4	0			10	1
Swift	3	0			8	1
BeppoSAX	11	1			7	0.909091
			MECS power supply	1		
Chandra	4	0			14	1
Rossi	3	0			16	1
Suzaku	4	1			8	0.75
			thermal coolant leaked	0.1		
XMM-Newton	6	0			13	1
COROT	1	0			6	1
Hubble	15	3			23	0.8
			NICMOS thermal failure	8		
			STIS power failure	7		
			ADCS electronics issue	4		
Kepler	1	0			4	1
MOST	1	0			10	1
Herschel	3	0			4	1

Spitzer	3	0			10	1
Odin	2	0			12	1
Plank	2	0			4	1
IBEX	2	0			4.5	1
PAMELA	1	0			7	1
SAMPEX	4	0			12	1
Totals	85	5	---	---	---	---
Total Probability of Success						0.941176
Average Probability of Success						0.975413

The reliability estimate was used to determine an expected MTBF (in years) for each instrument by using the equation

$$MTBF = -t / \ln(R)$$

Eq. 3

Where R is the estimated reliability at the end of instrument life and t is the expected lifetime in years. For the purposes of this model, t is set to 40 years. Since at this stage of development no instruments have been selected and detailed instrument characteristics remain rough approximations, each instrument is assumed to have the same reliability. As the project progresses, the trade space for the entire system design narrows, and instrument design is known, the reliability numbers for individual instruments may be changed in the Components Data Base to improve model fidelity.

This calculation was originally coded as a sub-function in the MATLAB code, but was later incorporated into the Components Data Base in Excel, and extended to the MTBF calculations for each subsystem component. Using the Components Data Base method was found to be more efficient for overall code structure and helped shorten total model runtime. If later use of this model involves modifications in which calculation in MATLAB is more efficient, the sub-function may still be found in the Optics/Science module code comments.

5.3.3.1.2 Mass, Power, Volume

Instrument mass, power, and volume were determined based on empirical analysis of past space-based telescope instruments and instrument packages.

Table IX: Summary of Hubble instrument mass, power, and volume

Instrument	Type/Function	Mass (kg)	Power (Watts)	Volume (m ³)
High Speed Photometer	Photometer	300	~20	2.00
Goddard High Resolution Spectrograph	Spectrograph	~200	~20	~1.25
WFC3	Wide Field Camera	400	~80	1.78
FGS	Guidance, Astrometry	217	19	1.24
STIS	Spectrograph	374	~80	1.78
COS	Spectrograph	40	62	~1.25

NICMOS	NI Camera and Spectrometer	370	~80	1.74
FOS	Camera	329	130	1.78

Based on design requirement, telescope functionality was grouped into four instrument classes. Hubble references were used to assign approximate mass, power, and volume estimates according to instrument type/function. These numbers represent a rough instrument of the instrument payload for the telescope. While the instrument packages can be serviced, none of the architectural decisions explicitly alters specific set of instruments that is selected. Future work can examine the trades involved in how the science requirements translate into a set of science instruments and the associated changes in mass, power, and volume.

Table X: Summary of instrument mass, power, and volume for TITANS AE model

Instrument	Type/Function	Mass (kg)	Power (Watts)	Volume (m ³)
Instrument A	Wide Field of View, Low Spectral Resolution, NUV-VIS-VISNIR, Partially coronagraphic	500	90	1.25
Instrument B	Non-Imaging, Medium/High Spectral Resolution, FUV-NUV-VIS, Non coronagraphic	500	90	1.78
Fine Guidance Sensors	Orientation navigation	300	45	1.25
Instrument C	Imaging, Low/Medium Spectral Resolution, VISNIR-NIR-ExtNIR, coronagraphic	500	90	1.25
Totals	Camera	1800	315	5.5

5.3.3.1.3 Optical Performance

Because the current set of architectural decisions and assumptions hold much of the optical train design constant across the tradespace, overall optical performance will not vary substantially across the architectures under analysis. In general, optical performance is closely associated with the total collection area of the observatory primary mirror, the degree of wavefront control and stability, the degree of control over stray light entering the optical pathway and finally, the wavelength range and reflectivity permitted by the mirror coatings. By utilizing the ATLAST design requirements as a baseline, the total collection area, wavefront control parameters, and wavelength ranges were standardized across all architectures. (A detailed treatment of the ATLAST requirements and their implications can be found in Appendix I) Additionally, the selection of a James Webb-style sunshield design (based on engineering considerations) results in a uniform degree of stray light suppression performance across all architectures as well. Jitter and pointing stability do vary to a limited extent with the choice of mirror actuation and primary mirror segmentation. These are specifically addressed separately in the structures code module. As the “optics” module lies upstream from the structures module and feedback loops have been

deliberately suppressed in the code design, any implications derived from the jitter analysis are ultimately addressed in the trade metrics modules at the code terminus. As a result optical performance is initialized here as a constant modifier within the instrument performance module. A more detailed proposal for how optical performance might be addressed in future cases where architectural decisions substantially affect this metric can be found in Appendix K.

5.3.3.1.4 Data Collection/Science/Instrument Performance

Overall science output and performance is heavily dependent on the number and quality of instruments incorporated into the observatory architecture. This proposal uses the ATLAST science instrument set as a baseline for comparison and analysis (Figure 24).

Telescope	TMA Focal Plane Instruments				Cass Focal Plane Instruments		
	Vis/NIR Wide-field Imager	Vis/NIR Multi-Object Spectrograph	Vis/NIR IFU	FGS (FOV per FGS unit)	UV IFU & Spectrograph	Starlight Suppression	Exoplanet Imager & Spectrograph
8-m, 9.2-m	8x8 arcmin	4x4 arcmin	2x2 arcmin	3x3 arcmin	30 arcsec	Internal Coronagraph or Starshade Sensor	~10 arcsec
16.8-m	4x4 arcmin	3x3 arcmin	1x1 arcmin	~1x3 arcmin	15 arcsec		~10 arcsec

Figure 24: Tentative ATLAST science instruments and their FOV²⁷

This instrument set was devised by the key stakeholders at NASA, who are also, by virtue of experience and access, best positioned to determine the most useful instruments from a scientific perspective for a given telescope architecture. It is reasonable therefore to assume for our purposes that this selection of instruments represents an optimal balance of resources for each scientific function (otherwise, that instrument would have been given more FOV or more of those instruments would have been added in place of another instrument). As the scope of the architecture tradespace primarily analyzes the engineering and performance – rather than scientific goals – of a 16.8-meter class telescope implementation, this assumption does not substantially alter our analysis, provided the utility is assessed in a relative and normalized fashion.

For the purposes of the TITANS AE architectural model, the functions represented in the ATLAST instrument proposal were packaged into four instrument ‘boxes’ for the purposes of future assembly, operations and servicing calculations. Each is initialized with a baseline utility value of 10. Accompanying these baseline utilities is an additional value – the utility degradation rate – reflecting the decay in science utility as a result of radiation damage on orbit. Historical values derived from monitoring of Hubble instruments suggest a rate of approximately 1% a year to be in the appropriate range.^{28,29} These variables are later employed by the utility-to-science trade metric module to evaluate telescope performance against a variety of architectural decisions.

A more detailed proposal for how instrument performance might be addressed in future cases where architectural decisions substantially affect this metric can be found in Appendix K.

5.3.3.2 Communication Subsystem Module

5.3.3.2.1 Communication Subsystem Metrics

The communications module receives inputs from the design vector and other subsystems, i.e., Optics, and produces outputs for use by subsystems, i.e., Power, Thermal, Structures and Systems. The majority of the communications module outputs are calculated via the Satellite Communications Design Process (described in the following section). The communications module outputs required by the Systems module and to calculate the system metrics are calculated separately. The communications module will have the following inputs and outputs, illustrated in Figure 25.

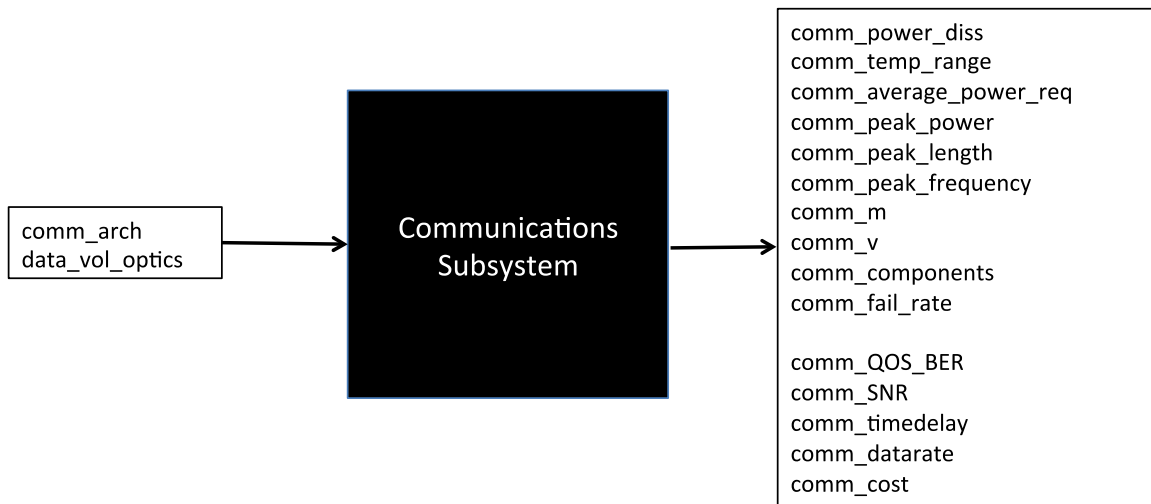


Figure 25: Communication system inputs (left) and outputs (right)

5.3.3.2.1.1 SNR (Signal to Noise Ratio)

The SNR is a basic subsystem metric for assessing communications systems and it is defined as the power ratio of the signal to background noise and it can be calculated at both the transmitting and receiving ends of a communications channel. The signal power will be equivalent to the power of the antennas onboard the space telescope and the relevant values can be tabulated for the high-gain, low-gain, and omni-directional forms after the communications architecture has been finalized. Assumptions will have to be made about the power of cosmic or galactic noise at the telescope's orbit position. High SNRs at both transmitting and receiving ends represent a stable and efficient communications channel, while low SNRs will indicate the need for higher antenna power or more electronic filters. SNR is constrained to have a minimum performance value in the communications module but the SNR value is also used as an input to systems metrics.

5.3.3.2.1.2 BER (Bit Error Rate)

Like SNR, BER is also a basic subsystem metric for any communications system. Since digital transmission is ubiquitous in satellite communications, the BER will determine the reliability of the communications channel established as it computes the number of bits in error divided by the number of the received bits in a data stream that may be altered due to noise, interference, distortion or bit synchronization errors. This metric can be used to assess the reliability of cross-links between satellites or satellite-Earth channels characteristic of FSS and TDRSS respectively,

or that of laser and RF communications. Choosing the appropriate communications architecture or relay type and making the right design choices by selecting high-power antennas, reliable modulation schemes and error correction codes can minimize BER. Assumptions will have to be made for the parameters required in calculation.

The equation for BER is below:

$$BER \approx \frac{1}{m} \operatorname{erfc} \left(\sqrt{\frac{E_b}{N_0}} \sin \left(\frac{\pi}{M} \right) \right)$$

Eq. 4

where N_0 is the noise power spectral density, the M-ary PSK modulation scheme encodes $m=2^M$ bits per symbol.

5.3.3.2.1.3 Power Requirements

Power requirements will be used to assess the architectural choices for the communications subsystem as there is always an operational need to regulate power consumption and power budgets may influence the choice of antenna sizes, communications relay and technology. Power will also impact other subsystems as it imposes constraints on the overall power supply and power dissipated by communications infrastructure will contribute significantly to the thermal characteristics of the space telescope. Power can implicitly be calculated through supply voltages and currents from the avionics or via other means such as the link budget equation.

5.3.3.2.1.4 Mass and Volume

Due to the considerable costs of launching a unit weight of load, mass and volume of the communications infrastructure are key considerations for determining the communications type, relay type and final design choices. RF communications require large antennas and heavy feed systems while laser communications may have more compact and lightweight equipment at the same performance level. They can be calculated through dimensions and densities of available communications infrastructure and adjustments may be made to accommodate the space telescope scenario with the appropriate assumptions justified.

5.3.3.2.1.5 Lifetime/MTBF

The predicted lifetime will be a key metric for evaluating the architectural choices, as the large amount of electrical equipment and distribution networks onboard the space telescope have to maintain a high level of reliability through the mission lifecycle. The lifetime of the communications sub-system can be predicted through calculating parameters such as probability of failure and average lifetime for a single or network of components. The communications subsystem is also assumed to be serviceable so that its predicted lifetime metrics do not necessarily have to meet or exceed the in-service lifetime of the entire system. The failure rate of the communications subsystem can thus be calculated via the multiplicative sum of communications components operating in a casual chain, and therefore variable across architectures.

5.3.3.2.1.6 Delay

Calculation of time delays in communications is vital if there are time and cost constraints for direct linkage between a spacecraft and relevant ground control stations. As space

communications entail the exchange of data over vast distances in space, communication channels established between L2 and Earth or other intermediary relay satellites are susceptible to electromagnetic interference and obstruction caused by objects in near-Earth orbits. Both architectural and design choices in communications technology, relay mechanisms and routing protocols have different measures of impact on the time delay experienced during data transmission. Typically, delay should be minimized within the constraints of cost and availability of technology so as to increase overall value and reliability of the communications system in the space telescope.

For example, to perform the delay calculations for the FSS option, the delays in uplink and downlink transmissions in the FSS system (assumed to be RF-based in this study) can be defined as functions of the distance between nodes and the processing time of each node. More specifically, the processing delays can be divided into transmission time, buffering delays, switching delays and data processing time.³⁰ Likewise, propagation delays can be divided into inter-satellite link delays (in-plane and cross-plane) and uplink/downlink delays with the ground station.

The number of supplier nodes in the FSS network greatly changes the delay; due to orbital alignment, the delay varies with time. For the purposes of this study, a model of the FSS constellation will be developed using documented assumptions (quantity and locations) and will be used as the baseline for communications performance. The model will be developed using Systems Tool Kit (STK).

The processing delays per node will be assumed to be uniform for all FSS suppliers and this delay will be a function of the link access time, data to be transmitted to ground and assumption on the processing speed. The processing speed of each FSS supplier node will be estimated using specification sheets of comparable satellite systems.

$$Propagation_Delay = \frac{d}{c}$$

Eq. 5

where d is distance and c is speed of light.

$$Processing_Delay = \frac{Vol_data_ground}{Processing_speed}$$

Eq. 6

5.3.3.2.2 Communications Design Process

Satellite Communications Design is an iterative process that involves defining the communication mission architecture, specifying the payload architecture, performing the link analysis, designing the payload, estimating impact to key metrics and updating parameters to achieve performance that meets requirements and meets the system level constraints. The design process for the communications module will follow the steps illustrated in Figure 26.

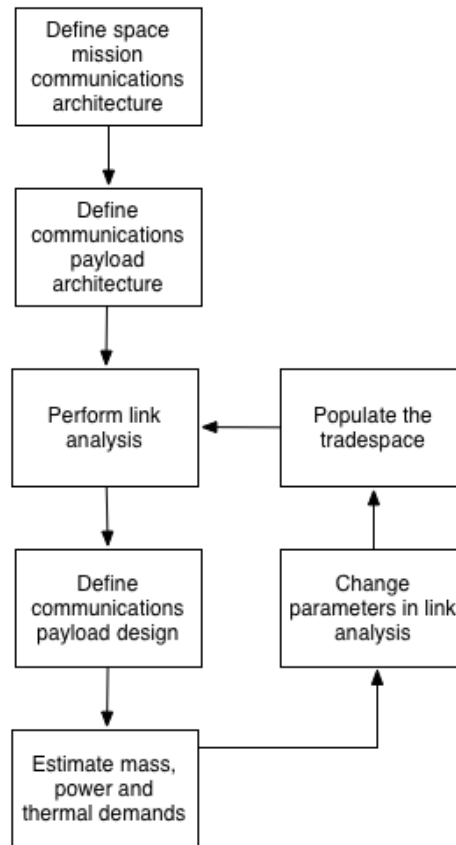


Figure 26: The communication system design and sizing process³⁰, adapted for the context of this class

The first two steps in the process outlined above involve making architectural decisions. One of the most important decisions for the communications module is fixed for the purposes of this study and that is the orbit and location of the telescope, Sun-Earth L2. It is also pre-determined that the Earth ground stations will be stationary. The ground stations considered are part of the DSN, detailed in the following section.

The first block in Figure 26, define space mission communications architecture, is the step in which the high-level communications architecture is determined. For this study, four options have been considered, which are DSN, TDRSS, FSS and direct laser as dictated by the “Communications Architecture” value in the design vector. The communications module calculations will vary according to the communications architecture.

The “Communications Architecture” impacts the second block in Figure 26, define communications payload architecture. For example, the communications payload for the RF-based communications systems varies greatly from the payload for the direct laser communications system. Furthermore, the payload systems for DSN, TDRSS and FSS have differing processing and transmission requirements, which will be analyzed separately in the following.

The way the communication system design was approached is the illustrated in Table XI.

Table XI: Communication system design process

Step	Step action
1	The system composition was identified – main components (ex. Antennas), other components (filters, amplifiers, modulation units, etc.)
2	STK scenarios were setup. The main goals were to visualize the telescope link to the ground directly, via LEO satellites and GEO satellites and compute the access times
3	Perform link budget calculations for a point design (i.e. having selected an antenna type and dimensions, calculate the maximum allowable downlink data rate for the link to be closed); also determine other relevant parameters for the design (antenna mass, volume, number of antennas, required power etc.)
4	Generalize the results of the link budget analysis – considering a variable antenna size, investigate how the communication subsystem design would scale with this variation
5	Write the MATLAB code for the communication subsystem in the cases analyzed in STK

Step 1 – Identify communication subsystem components

The architecture of the onboard communication system is outlined in Figure 27.

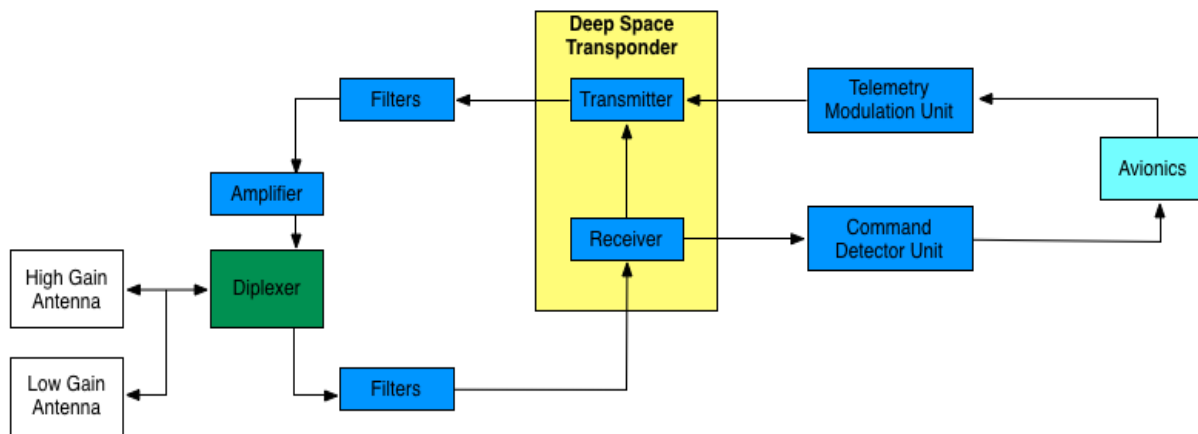


Figure 27: The communication systems architecture considered for the scope of this class³¹

Step 2 – Setup the STK scenario for the mission and calculate access times

Using STK, the orbit for the telescope is illustrated in Figure 28 and Figure 29:

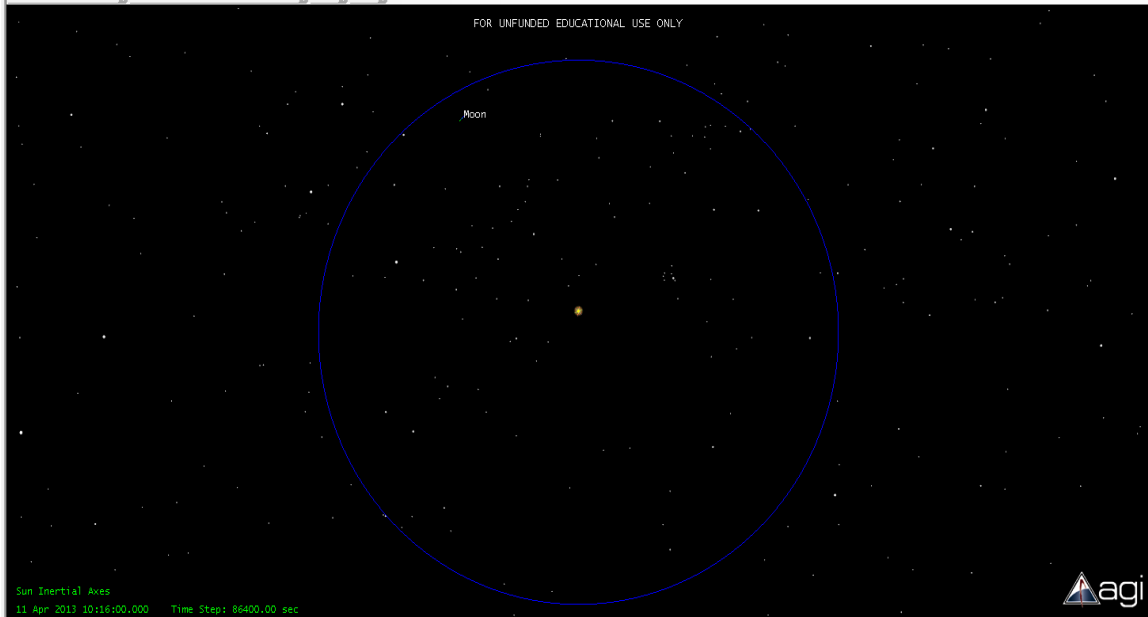


Figure 28: The orbit of TITANS AE in STK – at Sun-Earth L2

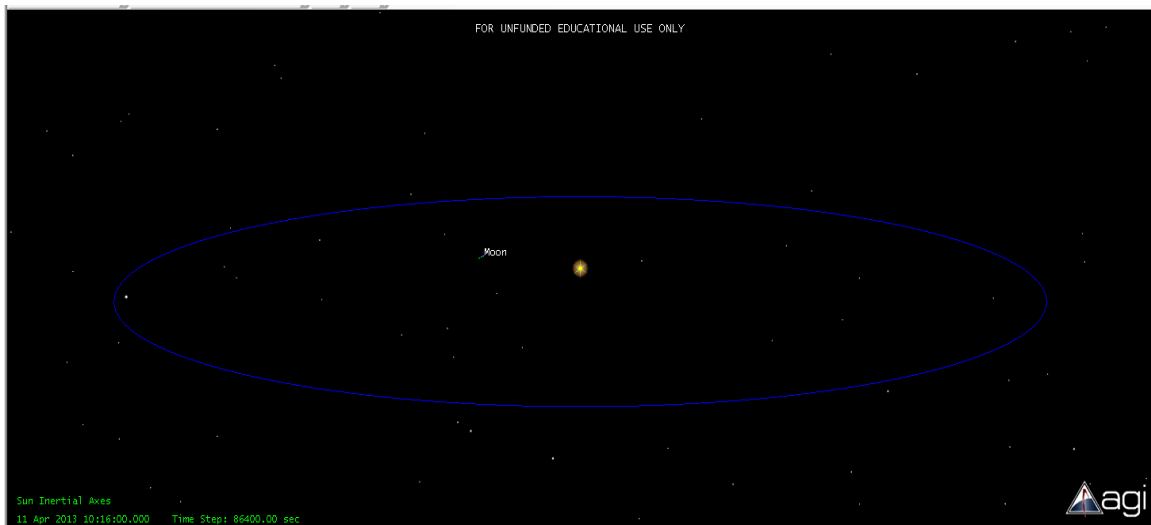


Figure 29: Alternate view of the orbit

The DSN considered is composed out of the following three ground stations:

- a) Goldstone Deep Space Network Communication Complex – Barstow, California, USA
- b) Robledo de Chavela – Madrid, Spain
- c) Tidbinbilla – Australia

The scenarios investigated are:

- a) Telescope direct communication with the DSN
- b) Telescope communication with the Iridium satellites (LEO) to DSN
- c) Telescope communication with the TDRSS satellites (GEO) to DSN
- d) Free space optical (FSO) communications (laser).

In cases b), c) and d) only the first part of the communication link has been analyzed, since it is the one relevant to the satellite communications architecture sizing.

Direct DSN:

The assumptions made are that the telescope communicates directly with the DSN ground stations. The average access time is 7.4 hours a day, with the three DSN stations. In order to have some margin here, the average access time was considered to be 4 hours a day with the DSN stations, due to additional scheduling factors (ex. Communication with the ISS and other satellites) that may limit the connection time. The STK computed access time was considered to be the best case, and the realistic value of this time will be considered as 4 hours.

LEO:

The satellite constellation considered was Iridium. The problem with this assumption is that the main antennas of Iridium are pointing towards Earth, and in order to establish a high-data rate connection with L2 they would have to point towards L2. However, Iridium also has omnidirectional S-band antennas, which can be used as a contingency scenario, because their gain is low and the supported data rate is also low. The Iridium satellites considered for the link access time calculations are shown in Table XII.

A better assumption would be to consider a LEO satellite network with two antennas: one pointing towards L2 so the telescope can communicate with it, at a high data rate (so a parabolic antenna would be desired), and another antenna pointing towards the Earth, so data collected by the previous antenna can be relayed to the Earth. This would entail a new communication satellite network to be designed, built, and launched for LEO, which translates into an entirely new program, which is considered unfeasible for the scope of this project. Therefore, the LEO case is considered a contingency scenario.

Table XII: Iridium satellites considered for link access calculations

Satellite name	Access time from telescope to satellite
Iridium_13_24840	14 access/day, each of 1.1 hours
Iridium_22_24907	
Iridium_24_25105	

TDRSS:

TITANS AE can see the TDRSS satellites 24 hours a day, so in theory this would be the access time. However, due to the reasons mentioned above, a more realistic value is 4 hours a day. The TDRSS satellites considered for the link access calculations are shown in Table XIII.

Table XIII: TDRSS satellites considered for link access calculations

Satellite name	Access time from telescope to satellite
TDRS3_19548	24 hour access
TDRS5_21639	
TDRS7_23613	

The Iridium and TDRSS constellations are illustrated in Figure 30.

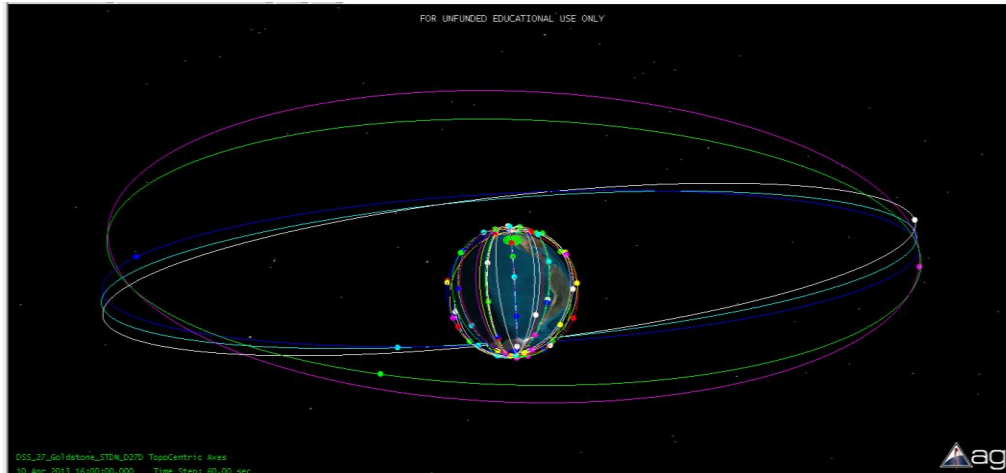


Figure 30: STK scenario with the Goldstone DSN site and the Iridium & TDRSS networks

Step 3 – Link budget calculations

The main process of this step is the link budget design. For this, a few definitions are necessary:

- Satellite Ground Terminal (SGT) – the satellite terminal on the ground, may be large or small, fixed or mobile
- Uplink – the link from the SGT to the satellite
- Downlink – the link from the satellite to the SGT
- Link budget – a quantitative analysis of a communication link, used to assess whether a link is closed (meets requirements) or open (does not meet requirements) and facilitate design.

The main parameters for the link budget are presented in Table XIV.

Table XIV: The main parameters for the link budget³²

Parameter	Unit	Definition
P_T	dBW	Transmit power
G_T	dBi	Transmit antenna gain relative to isotropic
EIRP	dBW	Effective Isotropic Radiated Power
L_P	dB	Free space loss
L_M	dB	Miscellaneous losses
L_R	dB	Losses due to rain
L_A	dB	Losses due to atmospheric effects
G_R	dBi	Receive antenna gain relative to isotropic
T	dBK	Temperature in degrees Kelvin
G/T	dB/K	Figure of Merit
C	dBW	Receiver carrier power
N	dBW	Noise power
C/N	dB	Carrier-to-noise ratio
B	dBHz	Signal bandwidth
S/N	dB	Signal-to-noise power ratio
R	dBHz	Data rate
k	dbW/K*Hz	Boltzmann's constant
E_b/N_0	dB	Energy per information bit to noise power density ratio

The link budget may be expressed in terms of carrier-to-noise (C/N) ratio as:

$$\frac{C}{N} \cong \frac{S}{N} = \frac{E_b}{N_0} = \frac{P_T G_T G_R}{L_A L_R L_M L_P k T B}$$

Eq. 7

It may be decomposed into uplink (UL) and downlink (DL) link budgets.

Since the uplink is mainly used for telecommands, the data rate that has to be supported by this link is small and therefore closing this link will not be as challenging as closing the downlink, in which the science data has to be downloaded and therefore will necessitate a high data rate. Therefore, for the purposes of this analysis, the link budget will focus on the downlink part.

For simplification purposes, the carrier-to-noise ratio was considered to be approximately equal with the signal-to-noise ratio (S/N).

The free space loss is given by the following formula

$$L_P = \left(\frac{\lambda}{4 \cdot \pi \cdot \text{range}} \right)^2$$

Eq. 8

where λ is the wavelength (meters) and the range is the path length (meters).

The antenna gain is dependent on the directivity of the beam, for the simplification purposes in this analysis it was assumed (in the first iteration), that the antenna is a parabolic dish, whose gain is given by the following formula

$$G = 10 \log \left[\varepsilon \left(\frac{\pi D}{\lambda} \right)^2 \right] \text{ (dBi)}$$

Eq. 9

where ε is the antenna efficiency (usually equal to 0.55), D is the diameter of the aperture in meters and λ is the wavelength ($c = f \lambda$).

EIRP is the effective isotropic radiated power of the transmitter

$$10 \log(EIRP) = 10 \log(P_T G_T) = 10 \log(P_T) + 10 \log(G_T) \text{ (dBW)}$$

Eq. 10

The noise power can be expressed as

$$P = \frac{hfB}{e^{kT} - 1}$$

Eq. 11

where $h = 6.62 \cdot 10^{-34} \text{ Js}$ (Planck's constant), $k = 1.38 \cdot 10^{-23} \text{ J/}^\circ\text{K}$, B is the receiver bandwidth, P is the noise power.

When $hf/kT \ll 1$, the formula above can be simplified and the receiver noise power is

$$P = kTB = N_0 B \text{ (W)}$$

$$P_N = GkTB \text{ (W)}$$

Eq. 12

Typical losses that affect the communications link are summarized in Table XV:

Table XV: Typical communication losses and their values

Loss	Value (dB)
Quantization	0.25
Differential encoding	0.2
Filtering	0.5
Adjacent channel interface	1
Interleaving	1
TOTAL:	2.95

The total value for typical losses is considered to be 3 dB. A margin of another 3 dB was added to give a losses value of 6 dB, which has been considered in the link budget as the miscellaneous losses.

The link analysis or link design for the communications module is performed by a set of interrelated equations used to close the link while maintaining an acceptable level of link performance. The communications module is constrained to have a link margin of greater than or equal to 3 dB and a Signal-to-Noise ratio of 5/10 (-3 dB) or better. These values were selected based on traditional performance standards.³⁰

The link analysis takes as one parameter the transmit power required. In combination with the transmit distance (determined by the communications architecture), the antenna type and size can be determined. From there, estimates of mass and volume can be provided for the antenna. Power, mass and volume for the non-antenna communications components will be estimated using specification sheets for comparable systems.

The different antenna types considered are parabolic, horn and array. The helix antenna will not be considered because of its low frequency application spectrum.³⁰

The equations for the antennas described above are presented in Table XVITable XVII, and Table XVIII:

Table XVI: Parabolic antenna characteristics³⁰

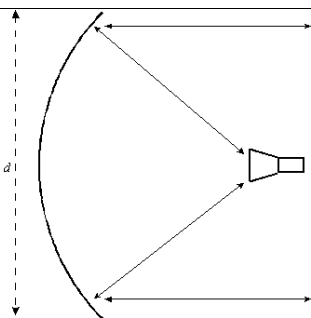
Antenna type	Parabolic reflector
Antenna model	
Beam type	Conical
Typical max gain (dBi)	15-65
Peak gain	$17.8 + 20 \log d + 20 \log f$ ($\epsilon = 0.55$)
Half-power beamwidth (deg)	$21 / (fd)$
Size (m)	D
Mass (kg)	10-30

Table XVII: Horn antenna characteristics³⁰

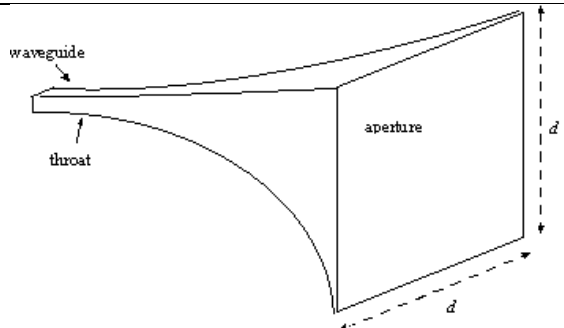
Antenna type	Horn
Antenna model	
Beam type	Conical
Typical max gain (dBi)	5-20
Peak gain	$20 \log (\pi d / \lambda) - 2.8$ ($\epsilon = 0.52$)
Half-power beamwidth (deg)	$225 / (\pi d / \lambda)$
Size (m)	D
Mass (kg)	1-2

Table XVIII: Array antenna characteristics³⁰

Antenna type	Array
Antenna model	
Beam type	Conical (scanning)
Typical max gain (dBi)	5-20
Peak gain	$10 \log (A/\lambda^2) + 8$
Half-power beamwidth (deg)	-
Size (m)	A
Mass (kg)	20-40

To simplify the design, two antenna types have been considered:

- i) Parabolic antenna – for the high gain communications. For redundancy purposes, the telescope will have two high-gain antennas, only one of them being powered at a time so that the overall power draw for the communication system will not be impacted by the built-in redundancy in the communication system
- ii) Patch antenna – for low gain communications. There will also be two antennas of this type, with only one of them being powered on at a time.

For the optical communication, TITANS AE will have two telescopes and two corresponding stabilizer units. Each DSN complex consists of at least four deep space stations equipped with ultrasensitive receiving systems and large parabolic dish antennas. There are:

- One 34-meter (111-foot) diameter High Efficiency antenna
- One 34-meter Beam Waveguide antenna (Three at the Goldstone Complex and two in Madrid)
- One 26-meter (85-foot) antenna
- One 70-meter (230-foot) antenna³³

The best antenna that could be used is the 70-meter antenna, which would give the highest value for the antenna gain. However, in order to ensure a conservative design, it will be assumed that the antenna that is available for communications with TITANS AE is the 34-meter antenna.

The power range for transmission from the DSN antenna is from 16 W to 400 kW. The maximum transmission power is considered to be of 200 kW. The frequencies are separate for Transmit (Earth to Space) and Receive (Space to Earth) and are shown in Table XIX.

Table XIX: DSN transmit and receive frequency range

	Transmit	Receive
S-Band	2110-2120 MHz	2290-2300 MHz
X-Band	7145-7190 MHz	8400-8450 MHz
Ka-Band	34200-34700 MHz	31800-32300 MHz

The transmission frequencies have been chosen to be 34.7 GHz for transmission and 32.3 GHz for reception for the high gain antennas onboard the telescope. For the contingency scenario, the reception frequency is 2.2 GHz (S-band). The link budget was done for the high-gain downlink case and the low-gain downlink case, considered a set antenna size. The link budget main parameters for the high gain case are illustrated in Table XX.

The link budgets for the downlink high and low gain cases are illustrated in the following tables. They represent the core of the communications system design, from which further generalization was done in the following sections.

Table XX: The link budget for the high gain antenna downlink case

Parameter	Unit	Value	Comments
Antenna elevation angle	degrees	30	Assumed high to minimize scattering from buildings or tall mountains
Maximum transmission range	km	1503178.873	L2 distance is 1.5 million km, taking into account the elevation angle this value was calculated
Frequency	GHz	32.3	Chosen from Table XIX
Wavelength	m	0.0093	$\lambda = c/f$
Path loss	dB	-246.2	Eq. 8 $8L_P = \left(\frac{\lambda}{4\pi \cdot \text{range}}\right)^2$ Eq. 8
Telescope antenna diameter	m	3.5	Chosen as a point design
Gain of the telescope antenna	dBi	58.9	Parabolic antenna
Gain of the ground antenna	dBi	84.9	Assumed 34-m diameter, parabolic
Noise temperature	K	225	Antenna assumed to be shaded from the Sun, to minimize Sun radiation interactions
Telescope antenna radiated power	W	20	Input power to the transmission system is assumed to be 200W, the yield of this is considered 10%
Required E_b/N_0	dB	12	Corresponds to a BER = 10^{-8} (see Figure 31, the coding method selected was QPSK because this is the most commonly used coding technique in satellite communications ³⁴)
Data rate	bps	50M	Arbitrarily chosen
Margin	dB	14.6	Link closed

The link budget main parameters for the low gain case are illustrated in Table XXI.

Table XXI: The link budget for the low gain antenna downlink case

Parameter	Unit	Value	Comments
Antenna elevation angle	degrees	30	Assumed high to minimize scattering from buildings or tall mountains
Maximum transmission range	km	1503178.873	L2 distance is 1.5 million km, taking into account the elevation angle this value was calculated
Frequency	GHz	2.2	Chosen from Table XIX
Wavelength	m	0.136363636	$\lambda = c/f$
Path loss	dB	-222.9	Eq. 8
Telescope antenna diameter	m	1.25	Chosen as a point design, patch antenna
Gain of the telescope antenna	dBi	10	Parabolic antenna
Gain of the ground antenna	dBi	61.55461367	Assumed 34m diameter, parabolic, at the corresponding S-band wavelength
Noise temperature	K	175	Antenna assumed to be shaded from the Sun, to minimize Sun radiation interactions
Telescope antenna radiated power	W	5	Input power to the transmission system is assumed to be 50W, the yield of this is considered 10%
Required E_b/N_0	dB	9.6	Corresponds to a BER = 10^{-8} (see see Figure 31 the coding method selected was QPSK because this is the most commonly used coding technique in satellite communications ³⁴
Data rate	bps	16k	Arbitrarily chosen
Margin	dB	7.24	Link closed

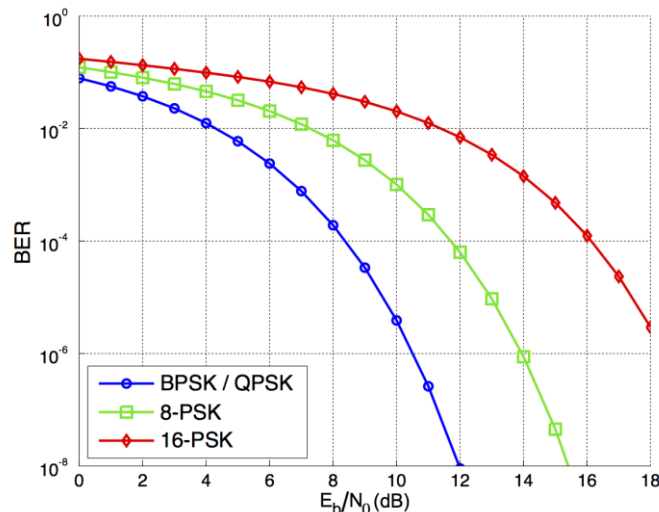


Figure 31: E_b/N_0 values for different coding methods and BER desired values

The laser communication is a novel communication technology, that allows a low satellite transmission power and a low transmit telescope dimensions, in the order of cm. It can also sustain high volumes of data. The problem is that it is cut off by cloudy conditions, therefore, to achieve 99% reliability in the reception link, 9 ground stations are used.³⁵

The mass and volume necessary to be accommodated aboard the telescope are about 5 times less than those needed for RF communications³⁵, but the laser beam has to be very accurately pointed toward the receiving station's direction. In order for this pointing accuracy to not impact the ADCS system, MIT Lincoln Labs have developed an extra stabilizer, which can help improve the telescope's pointing accuracy (The telescope is the optical transmission unit, different from TITANS AE). However, the TRL level for this technology is currently low.

The main mathematical relations describing the laser communications are presented in the following.

$$E_{ph} = \frac{hc}{\lambda} \tag{Eq. 13}$$

where E_{ph} is the energy per photon, h is Planck's constant, c is the speed of light and λ is the wavelength. Usually this is 1550 nm.

The energy per pulse can then be written as

$$E_{pulse} = n_s \cdot E_{ph} \cdot q_e \tag{Eq. 14}$$

where n_s is the number of photons in a pulse and q_e is the quantum efficiency, equal to 0.8.

The laser communication has $M = 16$ modulation levels (also called 16-PPM – 16 pulse position modulation).

The received power can be then expressed as

$$P_{received} = E_{pulse} \cdot \frac{R_b}{M} \tag{Eq. 15}$$

For the laser communication, the link budget main parameters are illustrated in Table XXII.

Step 4 - Generalize the results of the link budget analysis

MATLAB code was written to investigate how the daily data rate (for 4 hours of contact time) would scale with the TITANS AE antenna size.

The results are illustrated in the following plots.

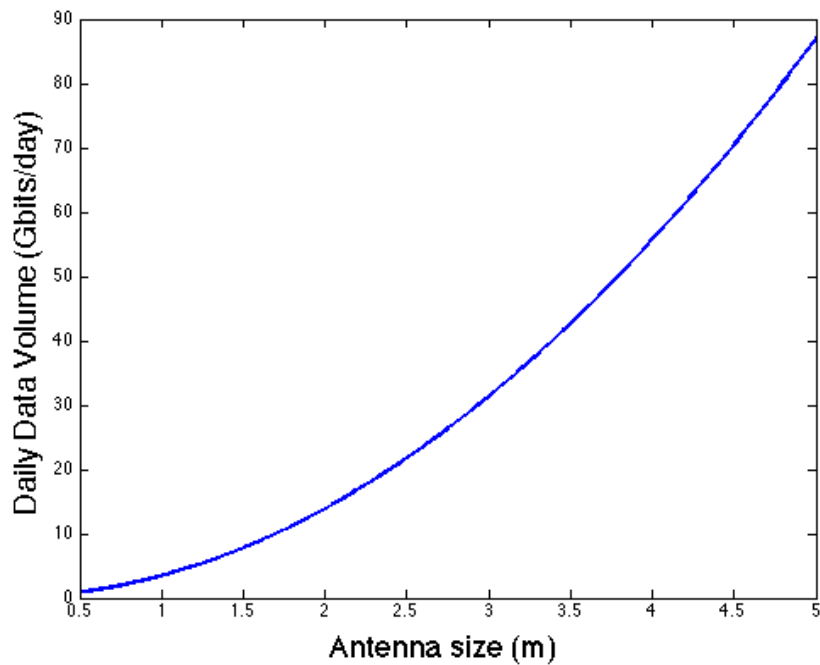


Figure 32: The DSN trade: the increase in daily data volume (Gbits/day) versus the antenna size (meters)

The maximum value of the daily data volume is at 5 m of antenna size, and is of 305 Gbits/day.

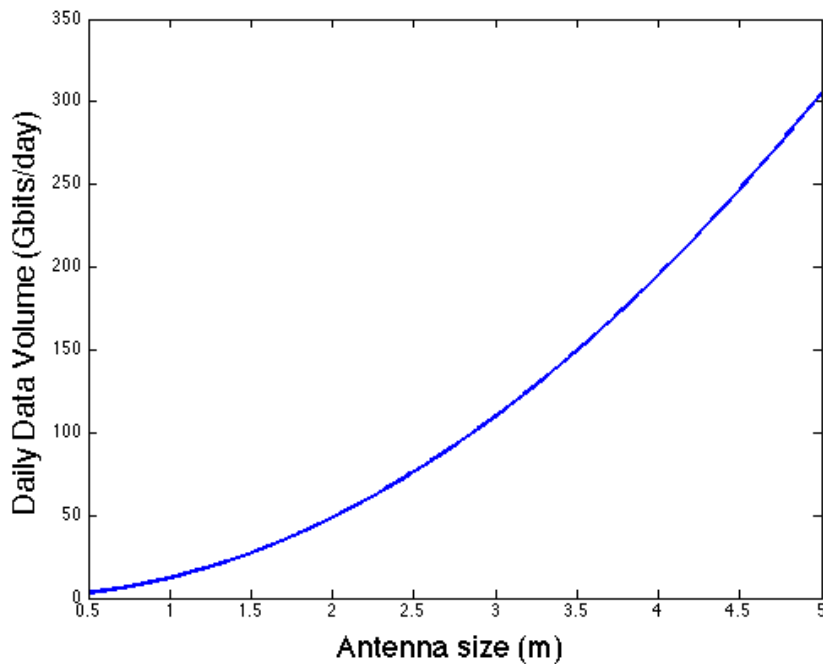


Figure 33: The TDRSS trade: the increase in daily data volume (Gbits/day) versus the antenna size (meters)

The maximum value of the daily data rate is at 5 m of antenna size, and is of 87 Gbits/day.

For both the DSN and TDRSS cases, the antenna size was varied from 0.5 to 5 meters, in increments of 0.01 m. There is an option to have deployable parabolic antennas (Harris) but it this option was not considered for this project.

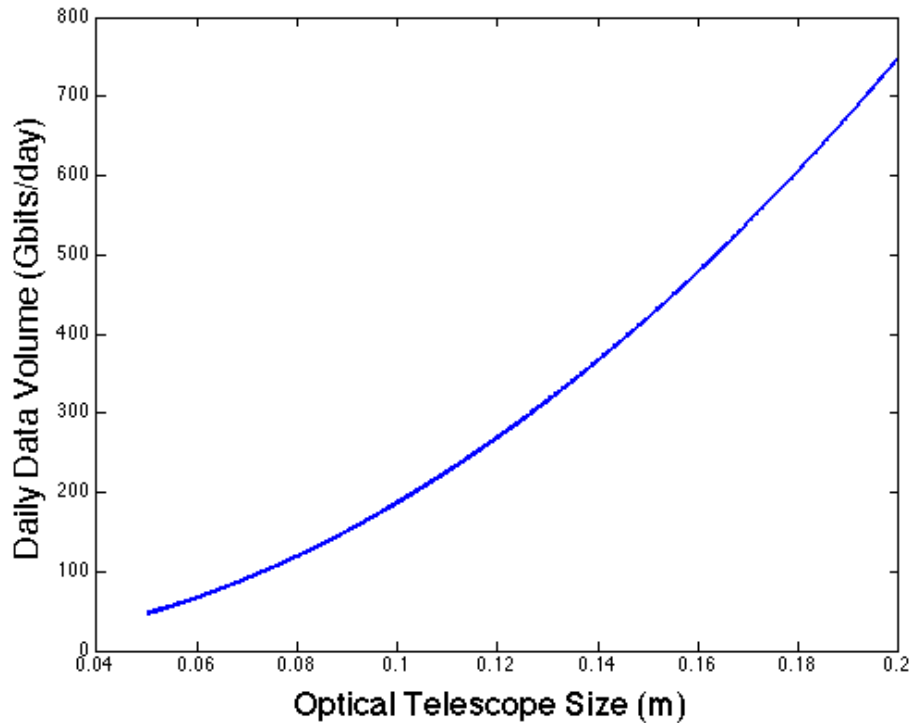


Figure 34: The laser communications trade: the increase in daily data volume (Gbits/day) versus the optical telescope size (m)

The maximum daily data rate is of 748.3 Gbits/day, and it corresponds to an optical telescope size of 0.2 m. The antenna size was varied from 0.04 m to 0.2 m.

Step 5 - Write the MATLAB code for the communication subsystem in the cases analyzed in STK
 The MATLAB code for the communications subsystem was hardcoded to include the values determined in the link budgets above for DSN, TDRSS and laser communications.

5.3.3.2.3 Conclusions, recommendations and future work

In conclusion, the options for TITANS AE communications are shown in Table XXII below.

Table XXII: Summary of TITANS AE communication design

Communication type	Gain value	Number of antennas	Band	Communication architecture
Telemetry and telecommand	Low	2	S	LEO (FSS)
Science data	High	2	Ka	TDRSS Laser

In conclusion, based on the results illustrated in Table XXII above, the best options for TITANS AE are as follows:

1. Laser communications – this is the best communication system option because of the advantages it offers: a low weight and power requirement and capability of sending a high data volume. These outweigh the limitations the weather effects may have on this technology
2. Direct DSN – this is the next best communication system option because TITANS AE is located at ESL2 (Sun-Earth Lagrange point 2), the distance from it to the Earth is 1.5 million km. The receiving antenna on the Earth is a DSN 34meter antenna, thus having a big gain and helping close the communication link.
3. TDRSS – this option is following DSN because, although the distance is shorter by 35786 km the receiving antenna aboard the TDRSS satellite is 4.9 meters, so it does not help closing the link as much as the 34 meter antenna on the ground does. So the shorter distance does not compensate the gain lost due to the smaller antenna.
4. LEO (or FSS) – if the FSS is considered to be in LEO (other options are possible too, and should be further explored), the antennas of satellites in LEO usually point towards the Earth and cannot sustain a high data rate communication link to L2. The omnidirectional antennas onboard these satellites would have to be used, which leads to a very small gain and data rate. Due to these considerations, this option is regarded as the contingency case.

As mentioned before, a future work point is to consider other satellite constellations as part of the FSS communication architecture. For example, FSS can include satellites that have highly elliptical orbits so that they can link at their apogees the telescope at L2 and at their perigee other communication satellites in LEO or even a DSN ground station. FSS is considered to be a very promising concept, and all of its aspects should be exploited when analyzing the communication system design in order to come up with novel architectural options.

5.3.3.3 Attitude Determination and Control System (ADCS) Subsystem Module

In the context of this project, the primary tasks of the attitude determination and control subsystem (ADCS) are to provide attitude control and stability to the satellite and provide sufficient slew rate and course pointing accuracy to the science instruments on the space telescope. In creating the ADCS model that would accomplish these tasks for this space telescope, much of the work was done without active feedback from other modules given the location of the ADCS module in the N² diagram. As a result, some assumptions needed to be made to create an effective ADCS. The primary assumption was that the mass and inertia of this space telescope would be on the same order of magnitude as the mass and inertia of the Advanced Technology Large Aperture Space Telescope (ATLAST) design. Given this assumption, the ADCS was designed such that the torqueing, slew rate, and momentum storage capabilities were on par with the capabilities of the ATLAST design. If this space telescope is created such that it has substantially greater mass or inertia, but that mass or inertia are not an order of magnitude greater than what was assumed, the space telescope will still operate effectively but with a lower slew rate.

While the momentum wheels and star tracker were modeled using established commercial off the shelf parts, the solar sail will be a custom made part. Therefore, in modeling the solar sail in the module code, the volume, mass, and power requirements of the solar sail are estimates, which are based on the design features of other custom-made solar sails. These estimates are adjusted based on the varying sizes and mission requirements of the comparison solar sails.

5.3.3.3.1 Pointing Control and Actuation

The ADCS for this space telescope will use momentum wheels to achieve attitude pointing and stability because of the hardware robustness, flight heritage and proven performance, and the lack of plume impingement associated with this ADCS component. In conjunction with the momentum wheels, this spacecraft will also utilize a solar sail to minimize the distance between the spacecraft center of gravity and the center point of the solar pressure from the sun. Since the only significant external disturbance torque present at SE-L2 is solar pressure, the solar sail will reduce the momentum wheel sizing requirements by an order of magnitude. The relatively small pointing requirement of 1 milliarcsecond (mas) will require the ADCS to have a star tracker and a fine guidance system (FGS) capable of actuating the telescope to that level of accuracy once the momentum wheels have achieved a less accurate pointing accuracy on the order of 0.1 degrees.

While this project explores a family of architectures rather than a single point design, certain components can be used in modeling the characteristics and requirements of a spacecraft. For this space telescope, the Honeywell HR16 Momentum Wheel (100 N-m-s variant) will be useful in modeling the ADCS of the spacecraft. The solar sail will be a customized solution with a two-axis gimbal attached to the boom connecting the spacecraft bus to the solar sail. This two-axis gimbal will allow for solar pressure torque modulation and allow the ADCS to dump the momentum from the momentum wheels without using propellant. The Ball Aerospace CT-633 Stellar Attitude Sensor will be used to model the star tracker on this space telescope.

Using this design architecture, the equations used to determine ADCS module outputs may be developed. These equations with their accompanying explanations are shown below.

The data rate required by the ADCS from Avionics subsystem will not constrain the capability of the Avionics subsystem because the computing requirements of the ADCS will be relatively constant, will not require a significant amount of memory for the inertial measurement unit (IMU) data, and will have allocated software and hardware specifically designed for the ADCS purpose. For the same reason, the data volume required by the ADCS will not be an issue of concern. Furthermore, the data throughput resulting from the images collected by the telescope will be orders of magnitude greater than the data throughput resulting from the ADCS. The required equations are shown below. Examples of support software include Kalman filter, Extended Kalman filter, noise filter, and mixer.

$$D_{Total} = (D_{mw})(N_{mw}) + (D_{ss})(N_{ss}) + (D_{st})(N_{st}) + (ssw) \quad \text{Eq. 16}$$

$$V_D = (D_{Total})(t_d) \quad \text{Eq. 17}$$

D_{Total} represents the total data rate of the ADCS, D_{mw} , D_{ss} , and D_{st} represent the data rate of the momentum wheels, solar sail, and star tracker, respectively. N_{mw} , N_{ss} , and N_{st} represent the number of momentum wheels, solar sails, and star trackers, respectively. ssw represents the support software data rate requirements. V_D represents the total data volume and t_d represents the time over which IMU data is collected.

As stated above, the ADCS will not require any propulsion to be used for momentum dumping. However, if solar pressure modulation will not be allowed or is infeasible, the following equations can be used. Given that nine of the aforesaid momentum wheels would allow the spacecraft to operate for approximately 11 days before reaching momentum saturation and the pointing time requirement for the telescope is only two hours, the frequency of momentum dumps may be arbitrarily selected between 4 to 8 days and still allow a significant margin of error both for pointing time requirements and for momentum wheel saturation. In order to determine the rate at which momentum builds up in the wheels, the following equation may be used.

$$T_{sp} = \left(\frac{F_s}{c}\right) A_s (1 + q) \cos(i)L \quad \text{Eq. 18}$$

Let T_{sp} represent the solar torque, F_s represent the solar constant, c represent the speed of light, A_s represent the area of the satellite exposed to sunlight, q represent the reflectance factor, i represent the angle of incidence to the Sun, and L represent the distance between the center of gravity of the spacecraft and the center of the solar pressure. It may be assumed that the solar constant at SE-L2 is $1296W/m^2$, the speed of light is 3×10^8 m/s, the surface area is between 1000 and 1500 m^2 , the reflectance factor is 0.6, and angle of incidence is 0 degrees, and the distance between the center of gravity of the spacecraft and the center of the solar pressure is less than 0.1 meter. The following equation can be used to determine the amount of momentum build up between momentum dumps.

$$M_T = T_{sp}t_m \quad \text{Eq. 19}$$

Let M_T represent the total momentum and t_m represent the time between momentum dumps.

The operating temperature of the momentum wheels is between -30 and 70 degrees Celsius. The operating temperature of the star tracker(s) is between 0 and 30 degrees Celsius. The operating temperature of the solar sail is between -150 and 110 degrees Celsius.

The power dissipation of the ADCS will be the power required multiplied by some factor of inefficiency as represented in the equation below.

$$P_D = \eta(P_u) \quad \text{Eq. 20}$$

Let P_D represent the power dissipation of the ADCS, let η represent the factor of inefficiency of the ADCS, and let P_u represent the power usage of the ADCS. The vast majority of power usage within the ADCS will be used by the momentum wheels. The equations below represent the worst case scenarios for steady state and peak power usage, respectively.

$$P_{uss} = (22\text{Watts})(N_{mw}) + (25\text{Watts})(N_{ss}) + (9\text{Watts})(N_{st}) \quad \text{Eq. 21}$$

$$P_{up} = (195\text{Watts})(N_{mw}) + (P_{pss})(N_{ss}) + (P_{pst})(N_{st}) \quad \text{Eq. 22}$$

Let P_{uss} represent the overall steady state power usage of the ADCS, let P_{up} represent the overall peak power usage of the ADCS, let P_{pss} represent the peak power usage of the solar sail, and let P_{pst} represent the peak power usage of the star tracker.

The momentum wheels are designed to last for over 15 years which is 5 years longer than the servicing option with the lowest frequency. Solar sails can be produced with incredibly low mass and volume, the star tracker(s) are relatively small and light weight, and the FGS will be integrated with the telescope hardware. Therefore, the momentum wheels will dominate the mass a volume requirements of the ADCS. The equations below represent these requirements.

$$M_M = (12\text{kg})(N_{mw}) + (20\text{kg})(N_{ss}) + (5.5\text{kg})(N_{st}) \quad \text{Eq. 23}$$

$$V_V = \pi \left(\frac{.351}{2} \right)^2 (.178)(N_{mw}) + (.125\text{m}^3)(N_{ss}) + (.002025\text{m}^3)(N_{st}) \quad \text{Eq. 24}$$

Let M_M represent the total mass of the ADCS and let V_V represent the total volume of the ADCS. Since the telescope architecture tradespace does not encompass an option with multiple non-physically connected segments in operational use and the lifetime of the components far exceeds the longest servicing period, the architectural choices will not have a dynamic impact on the design of the ADCS. As a result, the Pareto front could be characterized largely without the use of the ADCS module. However, the ADCS module does provide comprehensiveness and continuity in the model.

5.3.3.4 Avionics Subsystem Module

The avionics subsystem serves as the backbone for the data interface among all subsystems; it collects, processes, and stores data from the subsystems, schedules tasks, and transmits commands to the subsystems. The avionics subsystem is also responsible for formatting, packing

and unpacking data to/from the ground stations. The largest drivers of the avionics subsystem are the data rate/volume expected from optics, the communications architecture, and the assembly servicing technique. The science data from optics is the largest contributor to the processing and storage demands of the avionics system while in operation. The assembly/servicing technique could have a significant impact on the avionics system during assembly or servicing phases of operation, especially in the case of robotic arms or swarm robotics, which will be intensive from a processing and scheduling standpoint.

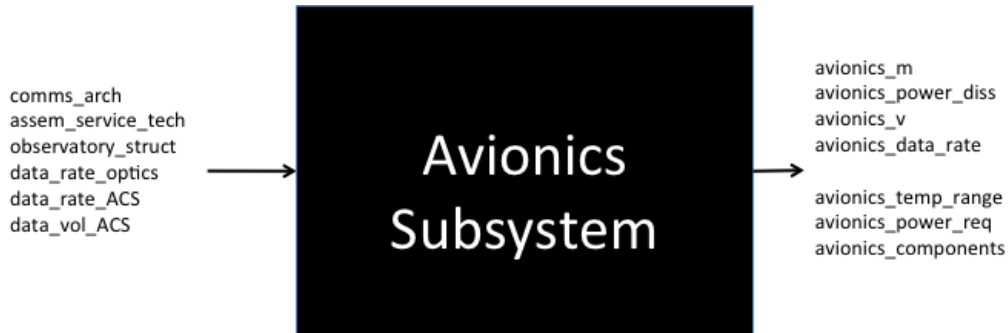


Figure 35: Avionics subsystem inputs (left) and outputs (right)

The majority of the avionics subsystem outputs (see Figure 35) are highly dependent on the selection of technology for each component. Advances in electronics have demonstrated that in less than a decade, data storage capacities, for example, have increased dramatically while form factors have decreased dramatically. As such, the approach for quantifying the avionics outputs will be to leverage the specifications of avionics components used in comparable systems or that have been space qualified by other means.

A typical avionics subsystem is depicted below in Figure 36. Using this diagram and documentation for the Hubble Avionics subsystem, the avionics components in the model are the Central Processing Unit (CPU), Random Access Memory (RAM), Data Management Unit (DMU), Data Interface Unit (DIU) and Power Converter Unit (PCU). The main computer in the model is based off of the specifications for the Hubble Advanced Computer which is 20 times faster, 36% lighter and has 6 times more memory than the DF-224/coprocessor combination that was initially launched with Hubble and developed in the 1970's.³⁶ Maxwell's Synchronous Dynamic RAM (SDRAM) is used for the volatile memory in the model as it represents one of the latest technologies in its class.^{37,38} The DMU and DIU are architecturally the same as Hubble. The DMU controls the central clock, interfaces with the DIUs and the CPU, whereas the DIUs are the data interface with the other subsystems.³⁹ The PCU essentially consists of a number of DC-DC converters that step down a common voltage supply provided by the solar panels to a series of lower voltage levels suitable for various avionics components as specified by their voltage-current operation requirements. The PCU specifications used in the model are based on the TDK: Lambda PXD Series of radiation-hardened DC-DC converters, which have been chosen as candidate component choices for a number of satellite-based science instruments.⁴⁰

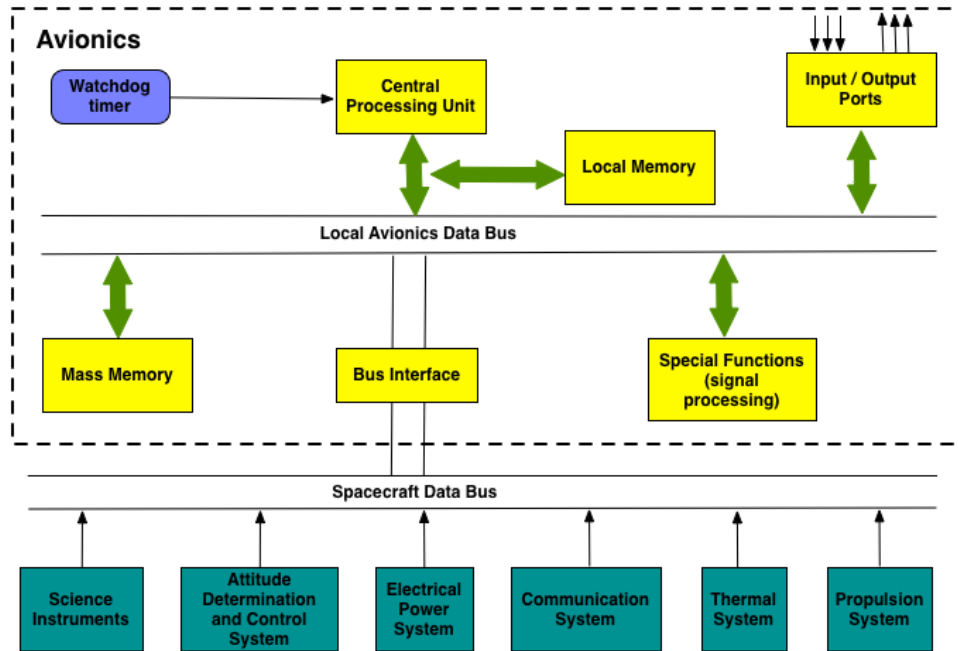


Figure 36: Typical Avionics subsystem for satellite systems⁴¹

The architecture of the avionics subsystem remains the same throughout all of the architectural decisions, i.e., data and physical connections are constant, but the quantity of each component changes in accordance with processing, memory, and reliability requirements. Redundancy is a common practice with avionics components; for example, the Hubble DIU is composed of two complete units where each unit is capable of performing all of the required functions.

The following sections briefly describe the key outputs of the avionics subsystem to other modules in the model.

5.3.3.4.1 Processing Speed

Processing speed represents the amount of data that a computer system can process in a given amount of time. Processing speed can play an important role in determining the amount of science data that can be collected, how that data is processed, and whether the data is processed on the satellite or on the ground. The amount of processing speed that a computer has impacts its ability to do onboard processing tasks that can improve the effectiveness of the satellite. Specifically, satellites can use onboard processing to overcome rain attenuation, utilize more efficient encoding, modulation, and multiplexing schemes, reduce the bit error rate, accelerate internet related throughput, mitigate problems associated with transmission delay, and allow the use of smaller aperture user antennas.

The communications architecture, on-orbit assembly and servicing technique, and the primary mirror actuation method will all have dynamic impacts on the processing requirements of the satellite. Using a Federated Satellite System, increasing the autonomy of the satellite, and increasing the number and complexity of tasks the satellite is expected to perform are all aspects of the design that will levy greater demands on the processing capability of the onboard computer.

Furthermore, the effective processing speed of a computer is dependent upon several aspects of the onboard computing system including clock speed of the central processing unit, front side bus speed, back side bus speed, the amount of random access memory, the amount of cache memory, how the data protocols are set up, how well the software has been optimized, the temperature of the computer, and what information the computer is expected to process. For this reason, establishing a closed-form solution for the required computing capability will not be feasible. Extensive design analysis, experience, and intuition are all required to determine the processing requirements of a satellite.

5.3.3.4.2 Mass and Volume

Similar to the communications subsystem, mass and volume of all avionics will affect the form and architecture of the space telescope. This should be lightweight and compact without any compromise in its value or performance. They are estimated via dimension ranges of electronics subsystems onboard existing spacecraft.

5.3.3.4.3 Power

Power requirements of satellite avionics components such as microprocessors, memory and other electronic equipment are generally similar to that of Hubble or James Webb space telescopes. An estimation or extrapolation may be derived from them since their overall function and purpose are equivalent. A more accurate method would be to use peak and average voltage and current ratings obtained from component datasheets of potential avionics components. The overall power consumption for the avionics subsystem is simply the sum of the power consumptions of individual components. As every component has its own power efficiency rating, power loss and dissipation is expected. The overall power dissipation for the avionics subsystem is then the sum of the power losses of individual components.

5.3.3.4.4 MTBF

This metric will be similar to that used in the communication subsystem. The lifetime of the avionics subsystem can be predicted through calculating parameters such as probability of failure and average lifetime for a single or network of electronic components. These values may be available in component datasheets of existing avionics systems. The avionics subsystem is also assumed to be serviceable so that its predicted lifetime metrics do not necessarily have to meet or exceed the in-service lifetime of the entire system. The failure rate of the communications subsystem can thus be calculated via the multiplicative sum of communications components operating in a casual chain.

5.3.3.5 *Propulsion Subsystem Module*

The propulsion system must carry enough fuel to correct for orbital disturbances over the lifetime of the mission (station-keeping) as well as allow for servicing missions to be conducted. From an operational standpoint, there are two servicing decisions being traded: in-situ servicing and servicing at a lower orbit. For the latter case, enough propellant must be carried to allow for round-trip travel from Sun-Earth L2 to the servicing orbit multiplied by the desired number of servicing missions. For the former case, it is useful to calculate the amount of propellant required to transport a robotic servicing probe to Sun-Earth L2 to facilitate a cost comparison between the two servicing options.

5.3.3.5.1 Assumptions

Several assumptions were made in order to minimize the complexity of the propulsion system calculations. For the various servicing locations, transit times were referenced directly from texts. This eliminated the need to calculate transit times from Sun-Earth L2 to the various servicing orbits for each of the propulsion systems under consideration. Furthermore, this also eliminated the need to consider the thrust capabilities of individual models within the engine families under consideration.

5.3.3.5.2 Lifetime

This metric is set by the Operations team. There are three critical inputs: mission duration, which impacts the amount of propellant required for station-keeping maneuvers; servicing location, which determines whether extra propellant will be required for servicing; and servicing frequency, which will determine the amount of propellant required for servicing, given that servicing does not occur in-situ.

5.3.3.5.3 Mass and Volume

The propulsion system mass will be calculated as a fraction of the entire satellite mass, as the fuel required to achieve a specific velocity change (ΔV) increases as the spacecraft mass increases. The required ΔV for the mission is influenced by two factors: station-keeping and servicing. For spacecraft in halo orbits around the Sun-Earth L2 point, it is recommended that a ΔV of 4 m/s per year be allocated for station-keeping²⁶. The total ΔV required for station-keeping is then simply 4 (m/s)/year multiplied by the number of years in service.

$$\Delta V_{stationkeeping} = n_{years\ in\ service} \times 4 \quad \text{Eq. 25}$$

The ΔV required for servicing missions varies based on the servicing option specified in the design vector. For in-situ servicing, zero additional ΔV capability is required on the spacecraft. However, propellant is still required for the transit of the servicing probe from a parking orbit around Earth to the L2 location. This has been calculated for the transit of the James Webb Space Telescope beginning from a 250 km parking orbit, and will therefore be hard-coded into the module.⁴²

$$\Delta V_{probe} = 3.21 \times 10^3 \quad \text{Eq. 26}$$

For the case where the telescope is brought closer to Earth for servicing, a separate method for finding the required ΔV must be employed. It has been shown that transfers between a halo orbit around the Sun-Earth L2 point to a halo orbit around the Earth-Moon L2 point can be accomplished with little ΔV – between 0 m/s to 20 m/s, depending on the initial and final orbital radii.⁴³ Other studies have shown that transfers from Sun-Earth L2 to lunar orbit and to geosynchronous Earth orbits are possible, along with the required ΔV and transit times.⁴⁴

Figure 37 and Table XXIII summarize the ΔV requirements and transit times for several transfer trajectories.

Earth-Moon Az [km]	Sun-Earth Az [km]	ΔV [m/sec]	Earth-Moon Az [km]	Sun-Earth Az [km]	ΔV [m/sec]
16,000	113,000	17.9	16,000	111,000	0
18,000	133,000	10.6	18,000	142,000	0
20,000	161,000	11.0	19,000	140,000	0
22,000	115,000	7.5	22,000	126,000	0
24,000	124,000	4.2	24,000	130,000	0
26,000	129,000	0.9	26,000	131,000	0
28,000	154,000	1.4	28,000	155,000	0
30,000	155,000	2.8	30,000	157,000	0

Figure 37: ΔV requirements for transfers between various SE-L2 and EM-L2 orbits⁴³

Table XXIII: ΔV requirements for various transfer trajectories

Trajectory	ΔV (m/s)	Transit Time (days)	Reference
LEO to SE-L2	3210	63	Catrysse
SE-L2 to Lunar Circular	1200	101	Truesdale
SE-L2 to GEO	5000	109	Truesdale

With the ΔV s known, the non-dimensionalized propellant mass (as a fraction of the total spacecraft mass) can be calculated as

$$\frac{m_{\text{propellant}}}{m_{\text{total}}} = 1 - e^{-\Delta V/c} \tag{Eq. 27}$$

where c is the thruster exhaust velocity. Since the propulsion module is independently trading the performance of chemical and electric propulsion systems, the propellant mass calculation is performed for three characteristic thrusters. For station-keeping and orbital maneuvering, a monopropellant hydrazine thruster is the preferred engine, while arcjets and Hall Effect thrusters are candidate electric propulsion solutions.^{45,46}

Table XXIV: Performance characteristics for various thrusters^{45,46}

Thruster	Isp (sec)	Propellant	Reference
Monopropellant Hydrazine	230	N ₂ H ₄	Sutton
Arcjet	1000	H ₂	Lozano
Hall Effect	1800	Xe	Lozano

The volume of the propulsion system is determined by the propellant mass fraction and propulsion system type. For the chemical propulsion design option, hydrazine is used as the propellant and has a density of 1011 kg/m³. Additionally, a tank containing a pressurized inert

gas (likely helium) will be needed to provide the desired mass flow rate of hydrazine. The specific volume (per unit spacecraft mass) can then be calculated as:

$$V_{chem} = \frac{m_{prop}}{\rho_{N_2H_4}}$$

$$v_{chem} = V_{chem}/m_{total} = \frac{1}{\rho_{N_2H_4}} \left(\frac{m_{prop}}{m_{total}} \right)$$

Eq. 28

For the pressurization system:

$$\frac{m_{gas}}{m_{total}} = \frac{p_p v_{chem}}{RT_0} \left(\frac{\gamma}{1 - p_g/p_0} \right)$$

Eq. 29

where p_p is the pressure in the propellant tank, v_{chem} is the specific volume of the propellant tank, p_g is the final pressure in the gas tank, and p_0 is the initial pressure in the gas tank. Values for the aforementioned variables were collected from Tables 6-3 of Sutton⁴⁵, and are summarized below in Table XXV.

Table XXV: Values for pressurization system variables

Variable	Value
P_p	1 atm (101 kPa)
P_g	1 atm (101 kPa)
P_0	3600 psi (2.5 MPa)

The total mass fraction for the chemical propulsion system is therefore the sum of the propellant specific mass and the pressurization system specific mass.

$$\frac{m_{chem}}{m_{tot}} = \frac{m_{propellant}}{m_{total}} + \frac{m_{gas}}{m_{total}}$$

Eq. 30

For the electric propulsion design case, if one assumes a particular exhaust gas, with a molar mass of M_{gas} and a tank pressure of P , then the specific volume (per unit spacecraft mass) can be calculated from the ideal gas law as:

$$PV = m \left(\frac{\mathcal{R}}{M_{gas}} \right) T$$

$$v_{elec} = \frac{\left(\frac{m_{prop} R_{spec} T}{P} \right)}{m_{total}} = \left(\frac{m_{prop}}{m_{total}} \right) \left(\frac{\mathcal{R} T}{M_{gas} P} \right)$$

Eq. 31

5.3.3.5.4 Power and Thermal

Values for average power consumption and efficiency for each thruster were taken from Table 19-7 of Wertz³⁰, and are replicated in Table XXVI below. No power data was found for the monopropellant hydrazine thruster. It was assumed that since the propellant is gas-pressurized and undergoes catalytic decomposition, power would only be needed to actuate the flow valves, which is negligible compared to the power required by electric propulsion systems.

Table XXVI: Power consumption and efficiencies for selected thrusters

Thruster Architecture	Power Required (W)	Efficiency
Monopropellant Hydrazine	0	0.9
Arcjet	1000	0.4
Hall	1000	0.5

Average power dissipated was calculated based on the thruster efficiency and the input power, per the equation below

$$P_{dissipated} = (1 - \eta) \times P_{input}$$

Eq. 32

5.3.3.6 Power Subsystem Module

The electrical power system generates, stores, regulates, and distributes electrical power to instruments and other subsystems. Electrical power is vital for the operation of the whole spacecraft. If there is a fault in the power system, all the other systems are lost including the mission. Challenges for the power system include maximizing efficiency, safety, reliability, and radiation tolerance. Providing a solution with minimal mass, volume, thermal characteristics, and costs is of extreme importance. The power subsystem analysis relies on several important informed assumptions. These suppositions build upon several operational aspects of the telescope. For future explorations and research these assumptions will have to be revised to make sure the model is still accurate. A list of the assumptions made for the power system is presented:

- The telescope will operate in a halo orbit around Sun-Earth L2, the spacecraft will orbit around this point at a radius much bigger than the Earth. This position is very benign for the power system since it guarantees a constant solar flux with no eclipses, the large radius of the orbit also ensures the antumbra of the Earth does not obstruct solar flux

reaching the solar panels. This advantage simplifies the solar array design along with the power storage unit (batteries).

- One of the architectural decisions is modularity. It was decided to model the power system as one module always. Its importance and size govern this decision. It is illogical to replace each individual solar cell when all of them will have the same level of degradation; same logic applies to the batteries. Power distribution systems will reside in each spacecraft module; this will allow servicing them in each segment, where they will be grouped with components that have similar failure rates. The power distribution scheme will be similar to a decentralized power architecture.
- For this study all the spacecraft subsystems will be considered as a constant power demand system except for communications. Uploading and downloading data to the telescope will have a very profound effect on the peak power demands and therefore on the battery capacity. This implies that the communications system is the only one that has an effect on the battery sizing. To be more accurate, a small fraction (10%) of the total power demanded by the subsystems is stored on the batteries as a safety measure. Parameters of the communications system that affect the battery design are peak power demand, frequency of download, and download time. State of the art lithium-ion batteries will be evaluated for this study.
- Solar arrays analysis is simplified due to the advantageous orbit of the spacecraft. The sun always points in the same direction during operation and there are no eclipses. Following these characteristics the solar panels are fixed within the spacecraft and do not rotate or track the sun. Educated predictions on the performance of triple junction GaAs solar cells for 2020 are used on the model.
- Besides power generation and storage, electricity has to flow to every subsystem that needs it. Distribution takes an important role on the whole system design. Since the specific electrical requirements of each subsystem are not known, the model relies on a general factor based on the total power generated. The factor is derived from averaging previous space missions, specifically the distribution mass per watt. This factor is the one with the most uncertainty on the power model. Further work and research can be done to model the distribution system with better accuracy.

Due to our trade study architecture with no feedback loops, the power system is responsible for generating an estimate of the mass and volume for the spacecraft taking into account each system electrical requirements. The structures and thermal subsystems (located lower on the N^2 diagram than power) will require a way to calculate the mass and volume needed for the power system once the electrical power equations have been solved. The best approach is to use a non-dimensionalized volume and mass factor with units of kg/watts and m^3 /watts respectively. The solution will provide the most accurate results based on the total power requirements of the spacecraft.

The following metrics will evaluate the performance of the electrical power system.

5.3.3.6.1 Power and Power generation

Generating enough power for all the subsystems is a vital element in the design. Power scheduling is also included in this metric (only communications subsystem is taken into account for power budget). To calculate the total power, all the power requirements of the subsystems are added together plus the power required to charge the batteries.

$$TotalPower = (Power_{Subsystems} + BatteryChargingPower)$$

Eq. 33

The power allocated to the batteries is based on the assumption that communications will happen few times a day, and not on a regular schedule. Therefore it is assumed that the battery has to be charged each day, giving 24 hours of allowable charging time. The battery power required is listed in Eq. 36, and it is derived from the communications peak power demand requirements. The next step is to calculate the array's specific power. This is a factor that takes into account the amount of solar flux available at the operation point, the efficiency of the solar cells used and the degradation by radiation at the end of life,⁴⁷

$$ArraySpecificPower = SolarFluxL2 * ArrayEfficiency(1 - Degradation)^{ServicingPeriod}$$

Eq. 34

Using this factor the total solar array area needed is calculated as follows:

$$Area_{Array} = \frac{TotalPower}{ArraySpecificPower}$$

Eq. 35

As mentioned previously solar flux will be constant, batteries are only needed for peak power demands. The only system that has considerable peak power demands is the communication subsystem. A safety margin will be added to the battery capacity in order to accommodate unplanned peak demands. The servicing frequency drives the Depth of Discharge (DOD) for the energy storage system. A relationship of DOD and number of cycles is calculated from SMAD.⁴⁷ Using this relationship, an allowable DOD is calculated from number of cycles required:

$$BatteryCapacity = (1 + (1 - DOD))(PeakPower * PeakPowerTime * PeakPowerFrequency)$$

Eq. 36

5.3.3.6.2 Lifetime/MTBF

Few systems really dictate the lifetime of the mission, power is the most obvious one. Being able to generate the necessary power for the required time generates constraints in the power generation scheme and size. This metric will measure the power generating performance of the system at the beginning and end of life. The system will be designed to be replaced with a predetermined servicing frequency. Servicing frequency will act as the lifetime of the whole system due to inherent degradation.

5.3.3.6.3 Mass

The mass of the power system will be dependent on the amount of power needed. The solar array plus all the necessary power switches, distribution systems, batteries, harness overhead, and different voltage buses will account for the total mass of the system. The total mass is calculated

by adding the solar array mass, the energy storage unit mass, and the overhead mass. These are the main divisions of the power system.

$$TotalMass = ArrayMass + BatteryMass + OverheadMass \quad \text{Eq. 37}$$

Array mass is calculated using a specific mass factor extracted from SMAD⁴⁷ also taking into account the inherent degradation and the lifetime of the system. State-of-the-art triple-junction Gallium-Indium cells will be considered for this study.

$$ArrayMass = \frac{SpecificMass * PowerRequired}{(1 - Degradation)^{Servicing Period}} \quad \text{Eq. 38}$$

A similar approach is used to calculate the battery mass, using Lithium-Ion cells.

$$BatteryMass = \frac{Capacity}{SpecificEnergy} \quad \text{Eq. 39}$$

The mass of power switches, distribution systems, and harness overhead are difficult to calculate without going into a detailed component design, which is out of scope of this study. A standard factor will be used taking into account the solar array mass. Previous space missions have provided information that suggests that the overhead mass is proportional to the power required by the spacecraft and therefore the solar array mass. The overhead mass factor is extrapolated from SMAD data.

$$OverheadMass = ArrayMass * OverheadMassFactor \quad \text{Eq. 40}$$

5.3.3.6.4 Volume

The volume of the power system will be dependent on the amount of power needed. The solar array plus all the necessary power switches, distribution systems, modularity overhead and different voltage buses will account for the total volume of the system. The available volume is calculated in the same fashion as the mass metric.

The total volume of the system is divided by the array, batteries, and overhead parts.

$$TotalVolume = ArrayVolume + BatteryVolume + OverheadVolume \quad \text{Eq. 41}$$

The array volume is calculated by multiplying the array area by the array thickness. Thickness is derived from SMAD information.

$$ArrayVolume = ArrayArea * ArrayThickness \quad \text{Eq. 42}$$

Similar to the mass metric, the volume of the energy storage system is calculated using a power density factor taken from SMAD.

$$BatteryVolume = Capacity * PowerDensity \quad \text{Eq. 43}$$

Following the mass metric, the overhead volume is derived using an overhead volume factor, extrapolated from previous space missions.⁴⁷

$$OverheadVolume = TotalPower * OverheadVolumeFactor \quad \text{Eq. 44}$$

5.3.3.7 Thermal Subsystem Module

In order to control the temperatures of the many critical subsystems on the spacecraft, paths for heat transfer will need to be designed in or around the assemblies throughout the space telescope. Different thermal control concepts will provide varying degrees of thermal balance, where thermal control mechanisms must be selected to maintain a component within its operating temperature range. Thermal balance is dictated by the following equation:

$$Q_{abs} + Q_{diss} + Q_{design} = A_r \epsilon \sigma T^4 = Q_{emit} \quad \text{Eq. 45}$$

where Q_{abs} is the heat energy absorbed from the environment, Q_{diss} is the internal heat energy from dissipated power loads, Q_{design} is the heat energy that is put in or taken out of the system by design (by a thermal control mechanism), A_r is the radiative surface area, ϵ is the emissivity, σ is the Stefan-Boltzmann constant, and T is the desired operating temperature. Typically, this equation is used to compute a temperature for a given thermal design; this model does the opposite by computing how much energy must be applied or removed in order given a desired operating temperature. Also, thermal modeling typically performs this calculation over a range of environmental absorption and internal power load conditions; however, this model assumes these conditions to be constant.

For this paper, the spacecraft's thermal control was designed separately for three thermal-evaluation blocks: (1) the Optics block, which is chiefly focused on controlling the temperature of the primary mirror; (2) the Instruments block, which contains three instruments to be kept at room temperature and one IR instrument to be kept near 60 K; and (3) the Bus block, which focuses on the electronics associated with the ADCS, avionics, communications, power, and

propulsion subsystems. The differences in how each thermal-evaluation block is handled within the thermal subsystem module code are shown in **Table XXVII**.

The heat energy absorbed by each thermal block is dictated by the following equation:

$$Q_{abs} = SA_p\alpha \quad \text{Eq. 46}$$

where S is the absorbed flux from the environment (assumed in this case to only be from the sun), A_p is the external surface area projected towards the flux source, and α is the absorptivity. The Optics block and the Instruments block area assumed to be behind a thermal shield, blocking the absorbed flux from the sun at a designed efficiency. For this project, this shield efficiency was assumed to be 80%. For several reasons (primarily thermal isolation), the Bus block is not assumed to be behind the thermal shield. However, the Bus block is assumed to be marginally shielded by the solar-cell arrays. Thus, a shielding efficiency of 50% is assumed for reduction of solar flux on the Bus block.

The internal heat energy from dissipated power loads for each thermal block is computed by the following equation:

$$Q_{int} = \sum [(1 - eff)P]_{subsys} \quad \text{Eq. 47}$$

where eff is the energy conversion efficiency of a given subsystem, and P is the average power draw of that subsystem. These values are summed up for each subsystem present per block. The Optics block is assumed to have zero power draw, the Instruments block adds up the power draw of each instrument, and the Bus block adds up the power draw from the ADCS, avionics, communications, power, and propulsion subsystems.

The desired operating temperature of a given thermal block is selected by first determining the restrictive operating temperature range for a given thermal block. This is done by selecting the highest minimum threshold from all of the subsystems within the block as the minimum restrictive operating temperature, and the lowest maximum threshold as the maximum restrictive operating temperature. For the Optics block, the mirrors are assumed to be operated near room temperature (between 22 and 24 degrees Celsius), just as Hubble's mirrors are. The Instruments block only considers the single cryogenic instrument's temperature range, assuming that the other instruments thermal control will be eclipsed by the cryocooling for the IR instrument. The Bus block considers the operating temperature ranges from the ADCS, avionics, communications, power, and propulsion subsystems. Now, an all-encompassing operating temperature range has been established for all of the components/subsystems within the thermal block. The desired operating temperature is simply the average value of this restrictive range. An additional estimation is made for the radiative surface area, A_r , and the surface area projected towards solar flux, A_p , of each thermal block. These surface areas are estimated using the volume of each subsystem, where each subsystem is modeled as a cube. In the case of the Bus block, the propulsion subsystem (dominated by the propellant tanks) is not considered in the area calculations.

Each thermal block contains one heating mechanism, one cooling mechanism, and a package of thermal sensors. **Table XXVII** displays the heating and cooling mechanisms per thermal block. Because this thermal model does not evaluate performance over a range of variable conditions, either a heating mechanism is selected for thermal balance, or a cooling mechanism. In other words, the model does not account for a thermal block requiring both heating and cooling needs. The quantity of a heating or cooling mechanism is determined to satisfy the requirement set by solving for Q_{design} in Eq. 45.

The Instruments and Bus blocks are modeled to have a variable quantity of thermal blankets for insulation and shielding. Thermal blankets are employed on the entire surface area of the Instruments block, and any surface area of the Bus block not used for an external radiator. In total, there are 11 thermal component families that can be selected for a given spacecraft architecture design: 3 heating mechanisms, 3 cooling mechanisms, 3 suites of thermal sensors, and 2 thermal blankets. See the Components Database in Appendix C to see individual properties of each thermal component family.

Table XXVII: Summary of Thermal-evaluation Blocks and Assumptions

	Optics Block	Instruments Block	Bus Block
Contents	Primary mirror and optical train to instruments	3 Instruments at Room Temperature, 1 Instrument at 60 K	Electronics from ACS, Comm, Avionics, Power, and Propulsion
Heating Mechanism	Thermostatic Heater(s)	Thermostatic Heater(s)	Thermostatic Heater(s)
Cooling Mechanism	Thermoelectric Cooler(s)	Cryocooler(s)	Heatpipes + Radiator
# of Thermal Sensors	150	50	75
Thermal Blankets	--	Yes	Yes
Absorptivity	0.06 (gold coating)	0.05 (thermal blanket)	0.05 (thermal blanket)
Emissivity	0.02 (gold coating)	0.02 (thermal blanket)	0.02 (thermal blanket)
Solar Shielding	80% shielded by thermal shield	80% shielded by thermal shield	50% absorbed by solar-cell arrays

The mass, power, volume, and lifetime performance metrics have been selected as most relevant to the thermal considerations of a next-generation space telescope design. Each metric will dictate the cost and certain design and development choices for the overall spacecraft, and will thus be used to determine and compare the values of varying architectures within the tradespace. The main resources for estimating the values of these metrics and other properties of the thermal control mechanisms (e.g., emissivity and absorptivity of the thermal blankets) are the *Spacecraft Thermal Control Handbook* by Gilmore⁴⁸ and Donabedian⁴⁹, along with parameterization from previous space telescope designs^{50,51} and currently available technologies⁵². Validation of the thermal subsystem code module was performed by comparing mass and power output metrics to true values for the Hubble Space Telescope and the James Webb Space Telescope.

5.3.3.7.1 Mass

Different thermal control concepts will contribute varying ranges of mass to the overall spacecraft, though it is not as simple as claiming passive components to be less massive than active components. For instance, a network of heat pipes leading to external radiators (passive) could be more or less massive than a thermal fluid loop (active) depending on the size, quantity, and degree to which components need cooling. However, because this model has been

simplified to only consider a single heating mechanism or cooling mechanism in order to satisfy the thermal balance, mass is not traded over various thermal design concepts. Instead, it is simply summed up over the selected number of components, by the following equation:

$$mass_{total} = \sum_{i=1}^{n_{components}} (mass_i)$$

Eq. 48

The mass of individual thermal component families is catalogued in the Components Database, which can be seen in Appendix C.

5.3.3.7.2 Volume

Similar to mass, different thermal control concepts will demand varying ranges of volume from the overall spacecraft. The total volume of the thermal subsystem is computed by adding up the selected number of components, by the following equation:

$$volume_{total} = \sum_{i=1}^{n_{components}} (volume_i)$$

Eq. 49

The stowed volume of individual thermal component families is catalogued in the Components Database, which can be seen in Appendix C.

5.3.3.7.3 Power

Power is another performance metric that is dependent on the types of thermal control components that will be used to maintain thermal stability for all components. Most active thermal control components, such as thermo-electric coolers, pumped fluid loops, and heaters, require power to operate, while passive thermal control components do not. The total average power draw of the thermal subsystem is computed by adding up the selected number of components, by the following equation:

$$power_{total} = \sum_{i=1}^{n_{components}} (power_i)$$

Eq. 50

The average power draw of individual thermal component families is catalogued in the Components Database, which can be seen in Appendix C.

5.3.3.7.4 Lifetime/MTBF

The lifetime metric is of particular interest to the overall mission of the space telescope, as the lifetime of thermal components will directly affect the lifetime of the on-board instruments. The mass, volume, and power metrics are directly affected by the reliability requirement (design constant) of the spacecraft architecture, where redundant units of a component family are designed into the spacecraft in order to satisfy the minimum reliability threshold, increasing the total mass, volume, and power of the thermal subsystem. The lifetimes of individual thermal component families is catalogued in the Components Database, which can be seen in Appendix C. The Mean Times Between Failures (MTBF) of individual thermal component families is derived using the following equation:

$$MTBF = \frac{-lifetime}{\ln(reliability)}$$

Eq. 51

The reliability of individual thermal component families is also catalogued in the Components Database.

5.3.3.8 *Structures and Mechanisms Subsystem Module*

The Structures and Mechanisms team is responsible for analyzing the structural components of the telescope and the mechanisms that actively modify the shape or performance of the structural elements. Consequently, the team is generally responsible for giving the telescope its overall shape and support, from integration into the launch vehicle through launch and transit to its operating orbit, to its assembly, operation, and periodic servicing.

For the telescope on which the MIT team is conducting a tradespace analysis, the Structures and Mechanisms team has developed a suite of MATLAB functions that analyzes the metrics of: the level of jitter of the primary mirror; the mass, volume, and power of all structures and mechanisms; and the precision of assembly in assembling the structure for operation. Additionally, the telescope is divided into modules according to the aforementioned modularity metric. These metric functions are subsequently incorporated into the system level analysis MATLAB scripts in order to automate the analysis of the full tradespace for the telescope. This tradespace is fed a series of trades from each subsystem, and the Structures and Mechanisms team has generated a collection of trades that are analyzed by the Structures and Mechanisms metrics in the full code. Therefore, with these metrics, architectural decisions can be evaluated in a Pareto front analysis at the full system level.

5.3.3.8.1 Structures and Mechanisms Code Description through Assumption and Component Selection

The Structures and Mechanisms subsystem has a wide array of possible components from which to incorporate into the overall components vector for the telescope. The architectural decisions guide the determination of the structural components and the mechanisms required to operate the telescope. The Components Family DB contains the full properties of each of these components and the values assigned for each parameter. Though hardcoded in the database, they can easily be changed from their values, which have been determined through analysis of historical components and structures, if more accurate data are provided in the tradespace study.

5.3.3.8.2 Mirror Actuation

The mirror support decision constitutes one of the driving architectural decisions for the Structures and Mechanisms subsystem because of the number of components that are added to fully actuate the mirror. The mirror can be actuated with surface-normal actuators, surface-parallel actuators, or a combination thereof, with surface-parallel actuators having a TRL value of 5 (as opposed to flight-proven TRL 9 surface-normal actuators) because they have not yet flown on large space missions. Table XXVIII shows the number of these actuators that are employed to shape the primary mirror based on the mirror support architectural decision chosen for a particular iteration.

Table XXVIII: Number of primary-mirror actuators for mirror support architectural decision

	Surface-Normal Decision	Surface-Parallel Decision	Combination Decision
Surface-Normal Actuators	252	0	144
Surface-Parallel Actuators	0	306	168
Total	252	306	312

As can be seen in this figure, the total number of actuators is least for the surface-normal decision, but highest for the decision to incorporate both surface-normal and surface-parallel. Importantly, a backstructure element is added for each mirror segment in both the surface-normal and combination architectural decision cases in order to provide a structure against which the surface-normal components could actuate. In the surface-normal case, seven degrees of freedom are achieved per mirror segment with the total number of actuators representing seven surface-normal actuators for each of 36 mirror segments. In the surface-parallel case, three actuators are used at each of 84 mirror segment boundaries, one actuator is used on the back of each mirror segment for segment curvature, and an additional actuator is given to the 18 segments on the outer ring because of the decreased number of segment neighbors. In the combination case, four surface-normal actuators are placed at each mirror segment, and two surface-parallel actuators are placed at each of the 84 mirror segment boundaries. In this manner, it is believed that full 7-degree-of-freedom motion can be attained by any mirror segment. These placements can easily be modified to incorporate better placement data to improve the model.

5.3.3.8.3 Secondary Mirror

Secondary mirror components are added to complete the optical train. A single mirror segment with a back frame element is used to represent the secondary mirror, and three bus structure elements are added in order to represent the booms that hold the secondary mirror in place. The mirror segmentation architectural decision also affects the support of the secondary mirror, so additional surface-normal and surface-parallel actuators are added to provide action to the secondary. It is believed that full seven degree-of-freedom is achieved using the coded numbers of each: seven surface-normal, 18 surface-parallel, and a combination of six surface-normal and six surface-parallel actuators for the three mirror support decisions, respectively. Again, it is trivial to modify these values as additional information regarding mirror support with surface-parallel actuators is included in the model analysis.

5.3.3.8.4 Communications Structure and Mechanisms

The communication architecture decision affects the number of gimbals, antenna deployment devices, and added bus structure mass in the Structures and Mechanisms code. The number of gimbals is incremented by two in each decision to account for the requirement that each antenna will need to be pointed in different directions than the optical direction of the telescope to allow for communications to occur. Additionally, the number of antenna deployment devices is incremented by two in order to deploy the antennas when the telescope is operational. To account for the increased structural support for the larger antennas required for all

communication types relative to laser communications, an added bus structure element is added to represent the added mass of this structural support.

5.3.3.8.5 Solar Array Gimbals

Gimbals are added not only for the antennas required for communications, but also for the solar panels. It is assumed that one gimbal is required for every kilowatt of generation power. These gimbals are added to allow the solar panels to track the sun for optimum power generation capability while the telescope is pointed in a different direction. Additionally, these added gimbals increase the jitter during operation, so a damper is added to the telescope architecture for each.

5.3.3.8.6 Jitter Control Devices

Determining the type of jitter control device to employ is based on the level of jitter as output from the separate jitter calculation code. A telescope was analyzed to determine the fundamental frequencies of the mirror and the wavefront error that is expected. Using these values, the jitter function generates a value for jitter to be used in the Structures and Mechanisms code. This value then determines the type of damper to be used, either magnetic isolation devices for jitter values less than 0.5, active dampers for jitter values above 1.5, or viscoelastic devices for all other jitter values. These three types of dampers are used because they represent three of the most common types of dampers used on spacecraft; their effective jitter ranges can be easily adjusted in the code in order to specify certain types or part numbers of each. Since the jitter is caused primarily by reaction wheels and gimbals, one damper of the jitter-level-determined type is added for each reaction wheel and gimbal included in the telescope.

5.3.3.8.7 Modularity Level Overhead Mass

The modularity decision is crucial in determining the overhead mass required for increasing the number of modules into which the telescope is divided. To obtain the mass overhead itself, the number of additional mass units, each 100 kg, was to be determined. By analyzing the increasing surface area cubes within an initially cubic structure, following the pattern of $8^{\text{number of cubings}}$ (1, 8, 64, etc.), with the *number of cubings* representing the number of times each cube was divided into eight cubes of identical volume, it was determined that the increase in surface area follows the following equation:

$$Mass_{added} = 6x^{\frac{1}{3}}$$

Eq. 52

In this equation, $Mass_{added}$ represents the added number of mass elements added for the x number of modules. By determining the mass overhead after the modularity creation script is run, it is possible to adjust the mass overhead to each particular architecture. Eq. 52 was derived from comparing the ratio of surface area to volume, which means that it represents a square/cubed law. Therefore, the added mass is hardcoded into the code for each modularity level, though it is possible to add a more continuous and module size dependent model in the future.

5.3.3.8.8 Assembly and Servicing Components

The assembly/servicing technique architectural decision causes a large variability in the number of components due to the method selected for aggregating the modules together. In order to assemble the telescope with the first technique, the use of telescope robotic arms, it is assumed

that 1 arm is able to maneuver 10 modules, and each module includes 2 docking ports. Therefore, the number of arms is 1/10 the number of modules that are created in the module creation function. Additionally, it is assumed that all docking ports are of the same size and load-bearing capacity. With these assumptions, the number of docking ports is twice the number of modules. In the second technique, the use of a separate servicer tug, arms also are used on the telescope to assist, and each module requires 2 docking ports. However, it is assumed that there is 1 arm per 20 modules because of the added capabilities of the tug itself. In the third technique, the use of self-assembling modules which maneuver with electromagnetic coils, it is required that each module be able to maneuver in all 6 degrees of freedom. Therefore, each module is equipped with 3 electromagnetic coils, which when assembled would be mounted orthogonal to one another. Additionally, it is again assumed that each module is equipped with 2 docking ports. Regardless of the number of docking ports, the numbers of power and communication interfaces are equal to the number of docking ports, since each docking port must be associated with both communications and data transfer capabilities. The code is able to add additional granularity, should it be required, because the modularity level can affect these current multiplication factors in determining the number of components per module. To cope with future changes, this section is already coded in a way that will allow separate component selection laws to be implemented for the seven different modularity levels.

5.3.3.8.9 Light Protection

A light shield is included to provide light protection for the optical train and instruments. The ATLAST light shield offers a baseline for the properties of the light shield.⁵³ The other method of light protection, a tubular baffle, is encoded in the Structures and Mechanisms code, though it is not incorporated into this model. The design parameters for the baffle are obtained by scaling the Hubble Space Telescope's baffle by the increased radius of the LTA design.⁵⁴ The specific mass, volume, and other properties are listed in the Components Family DB. Therefore, the analysis code is able to adjust as needed to an additional architectural design choice in future iterations of the code. The analysis team has made the assumption for the current analysis that only the light shield will be incorporated.

5.3.3.8.10 Structures and Mechanisms Subsystem Metrics

The Structures and Mechanisms subsystem metrics are determined once all of the structural components have been selected. Using the Components Family DB, it is possible to determine the mass and volume of the subsystem directly by summing the dot product of the structures components vector with the respective column from the database. The average and peak power of the Structures and Mechanisms subsystem, however, adds the power required to operate the Communication subsystem's antenna gimbals to the structures specific component power requirements because of the validation method chosen: since the Hubble Space Telescope included the mass of the gimbals in the Communication subsystem, the mass is treated as a Communications property, but the power is treated as a Structures and Mechanisms property because it is from a Structures and Mechanisms component family.⁵⁴

5.3.3.8.11 Finalizing Module Definitions

The last operation conducted by the Structures and Mechanisms subsystem is to call the module creation function. Though called once before to determine the number of modules in the subsystem code, it must be called again to place the components added to the telescope after the initial call into module. These added components include the bus structure overhead based on

modularity level, robotic arms, docking ports, electromagnetic coils for assembly and servicing, and docking port data and power transfer units. Once these components are placed into their proper modules according to modularity level, this information is passed to the Systems function.

5.3.3.8.12 Finite Element Model

Accurate imaging through a space-based telescope requires very accurate pointing of the optical telescope assembly. Any oscillations in the primary mirror will cause wavefront error and therefore limit the science output. Thus, the amount of jitter that the mirror experiences due to reaction wheels, thrusters, or other active components on the spacecraft bus is important to quantify. In order to quantify this behavior, a finite element model (FEM) of the system must be created to analyze how vibrations in one area of the spacecraft affect motion in another area through a normal modes analysis.

5.3.3.8.12.1 *Creating the Model of the Telescope*

In this modeling scenario, it is important to simplify the model to a level of abstraction that will be relatively constant between the different architectures, but be able to differentiate between all combinations of the segmentation of the primary mirror and primary mirror actuation method architectural decisions. At this stage in the trade study, the structural design of the telescope bus has not been developed, so the 36-segment, 16.8-m mirror must remain the primary focus of the model. The bus is modeled as a concentrated point mass representing the sum of subsystem masses. The effective response of the reaction wheel set accounting for damping comes out of this bus node. This is the disturbance input to the jitter analysis. The model also takes the primary mirror actuation method and the segmentation of the primary mirror as inputs. In general, these inputs affect the FEM according to the diagram in Figure 38.

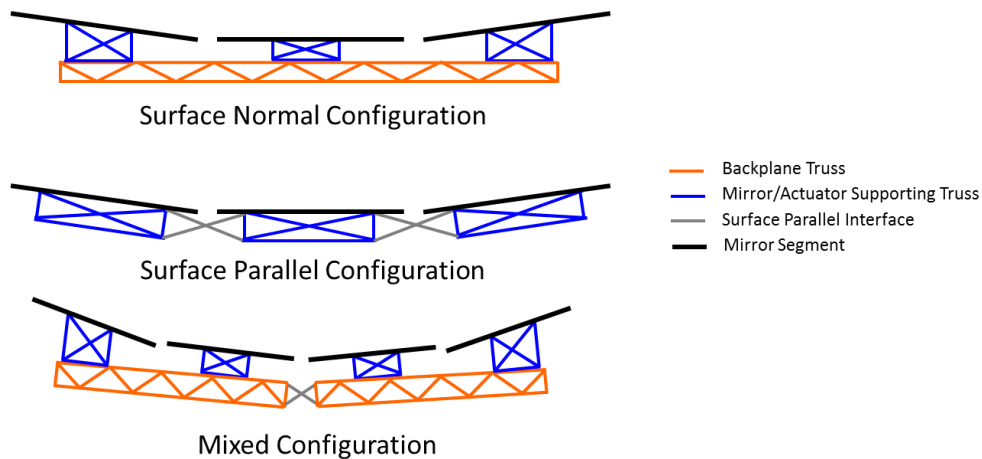


Figure 38: Simplified visualization of surface-parallel vs. surface-normal configurations in the FEM

The mixed configuration assumes that each major segment, or raft, from the segmentation of the primary mirror architectural decision will use surface-normal actuation internally, but surface-parallel actuation is used between rafts. The trusses in Figure 38 show a visualization of the layout of connections only, and do not reflect actual truss structural members. Not all segments or mirrors are pictured in these diagrams for simplicity. To simplify the model, each segment of the mirror is considered to include and represent the mass and stiffness of a primary mirror

segment, its actuators and its individual backstructure. The connections between segments represent the overall backstructure stiffness and vary based on the architecture decision to be more or less stiff.

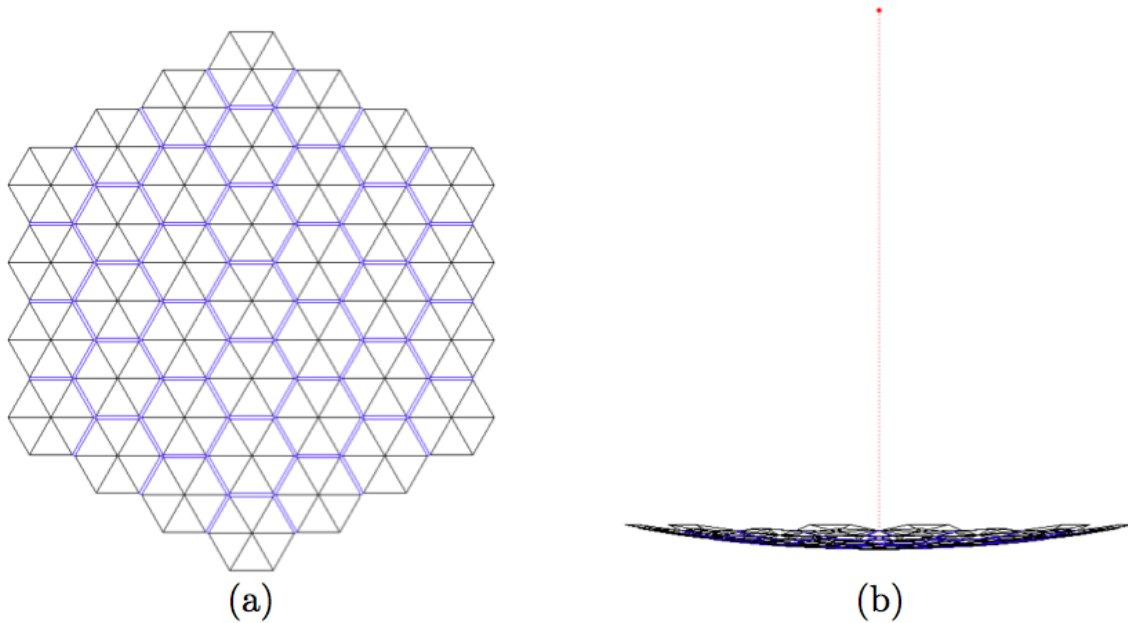


Figure 39: Primary mirror mesh for the FEM of the 16.8-m, 36-segment, $f/1.5$ telescope, where (a) is a top-down view and (b) is a side view with the focal point

The primary mirror is divided into 259 nodes or grid points in the mesh. One node is placed at the center of the segment and one node at each corner. These nodes are connected in a series of triangle and quadrilateral mesh elements with corners at the grid points. The final mesh of the mirror is shown in Figure 39, where the black lines show edges of triangle elements and the blue lines show edges of quadrilateral elements. The connection to the bus node is not shown, although the bus is connected with rigid bars to the edges of the first ring in the shown mesh. Shown in Figure 39, each grid point is also displaced vertically corresponding to the telescope's $f\#$ of 1.5. The quadrilateral elements represent the connection between segments and their properties change depending on the architectural decisions. For example, a surface-normal configuration would have a uniform higher stiffness for all of these quadrilateral elements, while a surface-parallel configuration would have a uniform lower stiffness for all of these elements. In the mixed case, the edges between rafts are considered lower stiffness while internal connections within a raft are considered higher stiffness. See Figure 40, for a depiction of these mixed cases, where red represents the surface-parallel, lower-stiffness interface and the blue represents the backstructure, higher-stiffness interface.

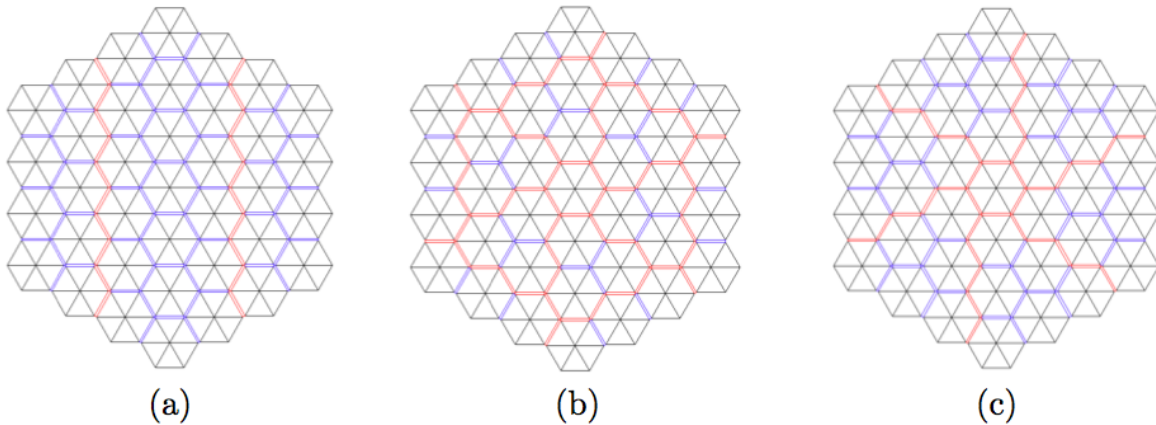


Figure 40: Raft segmentation in the FEM where red shows surface-parallel connection between rafts and blue shows backstructure connection within rafts. Shown for three segmentations where (a) is the JWST-style fold, (b) the 12-segment, and (c) the 6-segment.

5.3.3.8.12.2 Implementation and Output of the Model

The development and coding of this model, mesh and normal modes analysis uses a combination of MATLAB functions and NASTRAN finite element analysis software. The MATLAB functions are used to generate the grid points, elements and material properties for a particular architecture. NASTRAN requires this information to be input in different “cards,” along with information on what type of analysis to perform. These cards each need to be written to a data text file before sending to NASTRAN. NASTRAN is executed from the MATLAB function and runs the normal modes analysis on the inputted cards. NASTRAN returns a large text file of output that includes mass properties, normal mode frequencies, and mode shapes for all six degrees of freedom at each node in the model. This text file is subsequently parsed to return a diagonal matrix of natural frequencies and a dense matrix of mode shapes. These matrices are computed for each of the architectural decision options: surface-normal, surface-parallel, and five mixed cases corresponding to the segmentation of the primary mirror options. These seven matrices are output to the jitter calculation code discussed in the next section.

5.3.3.8.12.3 Validation of Results

An important aspect of running this analysis is the verification that the outputted results accurately predict the natural frequencies and mode shapes of the particular architecture. To discuss this, comparisons between previous FEM model outputs and mode shapes must be shown to reasonably match. Scott Uebelhart⁵⁵ analyzed a similar space telescope with hexagonal segments in his PhD thesis and saw a first mode of the primary mirror behave as a saddle bending mode at 6.15 Hz. Shown in Figure 41, the model used in the analysis outputs the first saddle bending mode at 6.09 Hz. Also, Rebecca Masterson, in an analysis of an interferometer, reports first bending modes of the mirrors to occur at 5.99 Hz.⁵⁶ The remaining modes in the model behave similar to increasing order Zernike polynomials as expected. While this only validates the surface-normal case, due to the lack of information one must assume that the other architecture choices will be correct modifications of this validated model. As expected, architectures with more surface-parallel interfaces tend to react to lower frequency responses. In addition it is important that the model represents an appropriate mass when compared with the telescopes in the architecture enumeration. The average total system mass across all of the

architectures in a full enumeration is 13,982 kg compared to the FEM model average output of 14,379 kg. With a difference of less than 3% from the computed average, it can be said that the model accurately represents the average architecture mass.

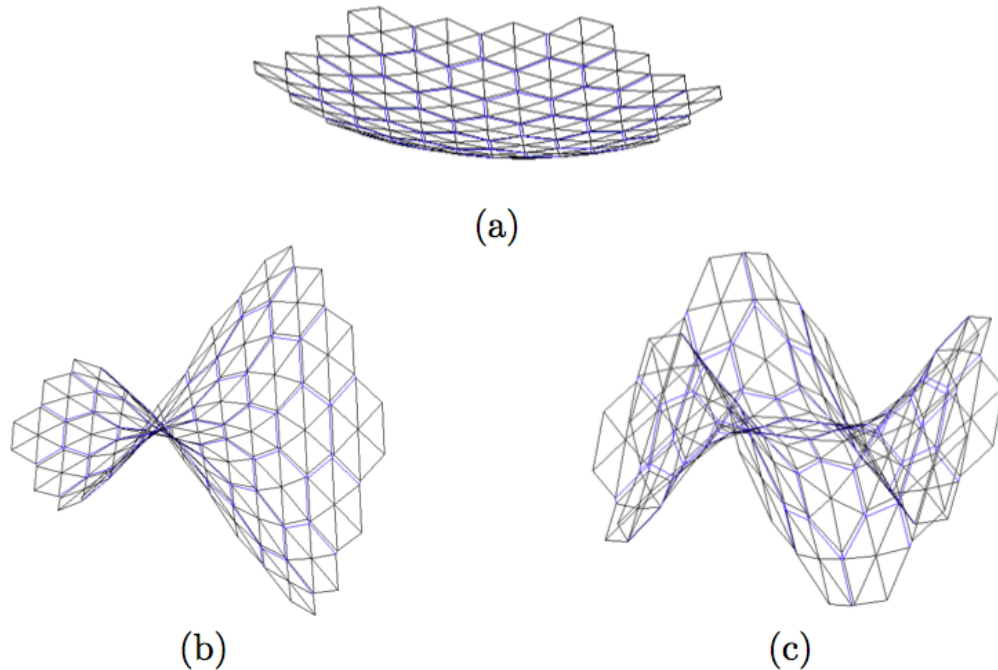


Figure 41: Normal modes for the primary mirror where (a) is the undeflected mirror, (b) is the 6.09 Hz, 1st, saddle bending mode and (c) is the 13.06 Hz, 7th bending mode

5.3.3.8.13 Jitter

The jitter analysis was done in a similar manner as that of Rebecca Masterson⁵⁶. The first step in the jitter analysis was to create a Finite Element Model (FEM) to represent the telescope, described in the previous section. Once this FEM was created, there were three important steps to complete the analysis: creation of a transfer function for the system from the disturbance input to the performance outputs, modeling of the disturbance input, and propagation of the disturbance input through the transfer function to calculate the performance outputs.

5.3.3.8.13.1 Creation of the Transfer Function

The normal modes analysis described in the previous section determined the modal frequencies and shapes of the FEM. NASTRAN outputted Ω , a diagonal matrix of natural frequencies, and Φ , which is a matrix containing the mode shapes, for each mirror support and mirror segmentation method, according to the various architectural decisions. These matrices were used to create a state-space model in MATLAB according to Eq. 53 and Eq. 54:

$$\begin{Bmatrix} \dot{q} \\ \ddot{q} \end{Bmatrix} = \begin{bmatrix} 0 & I \\ -\Omega^2 & -2Z\Omega \end{bmatrix} \begin{Bmatrix} q \\ \dot{q} \end{Bmatrix} + \begin{bmatrix} 0 \\ \Phi^T B_{\hat{x}\omega} \end{bmatrix} \omega = A \begin{Bmatrix} q \\ \dot{q} \end{Bmatrix} + B\omega \quad \text{Eq. 53}$$

$$z = [C_{z\hat{x}}\Phi \quad 0] \begin{Bmatrix} q \\ \dot{q} \end{Bmatrix} = C \begin{Bmatrix} q \\ \dot{q} \end{Bmatrix} \quad \text{Eq. 54}$$

where q are modal coordinates, Z is a diagonal matrix of damping ratios, $B_{\hat{x}\omega}$ is a mapping matrix between the disturbance forces and the physical degrees of freedom, ω is the disturbance input, z is the performance output, and $C_{z\hat{x}}$ is a mapping matrix from physical states to the output.

The matrix Z was set to 0.001 along the diagonal, according to Masterson's thesis⁵⁶. The matrix $B_{\hat{x}\omega}$ was set to all zeros with ones along the diagonal of the final six rows, meaning that the six degrees of freedom of the disturbance input map to the six degrees of freedom on the single bus node. Finally, the matrix $C_{z\hat{x}}$ was calculated using the function `zernikes2_hex.m`, taken from code used in an analysis done for the Modular Optical Space Telescope (MOST), which was an MIT Space Systems Laboratory project to develop a parameterized model for large space telescopes.⁵⁷ The function `zernikes2_hex.m` takes in each of the grid points used in the FEM, along with the diameter of the mirror, and, using Zernike polynomials 3-48, composes the matrix $C_{z\hat{x}}$. Several of these Zernike polynomials are pictured in Figure 42.

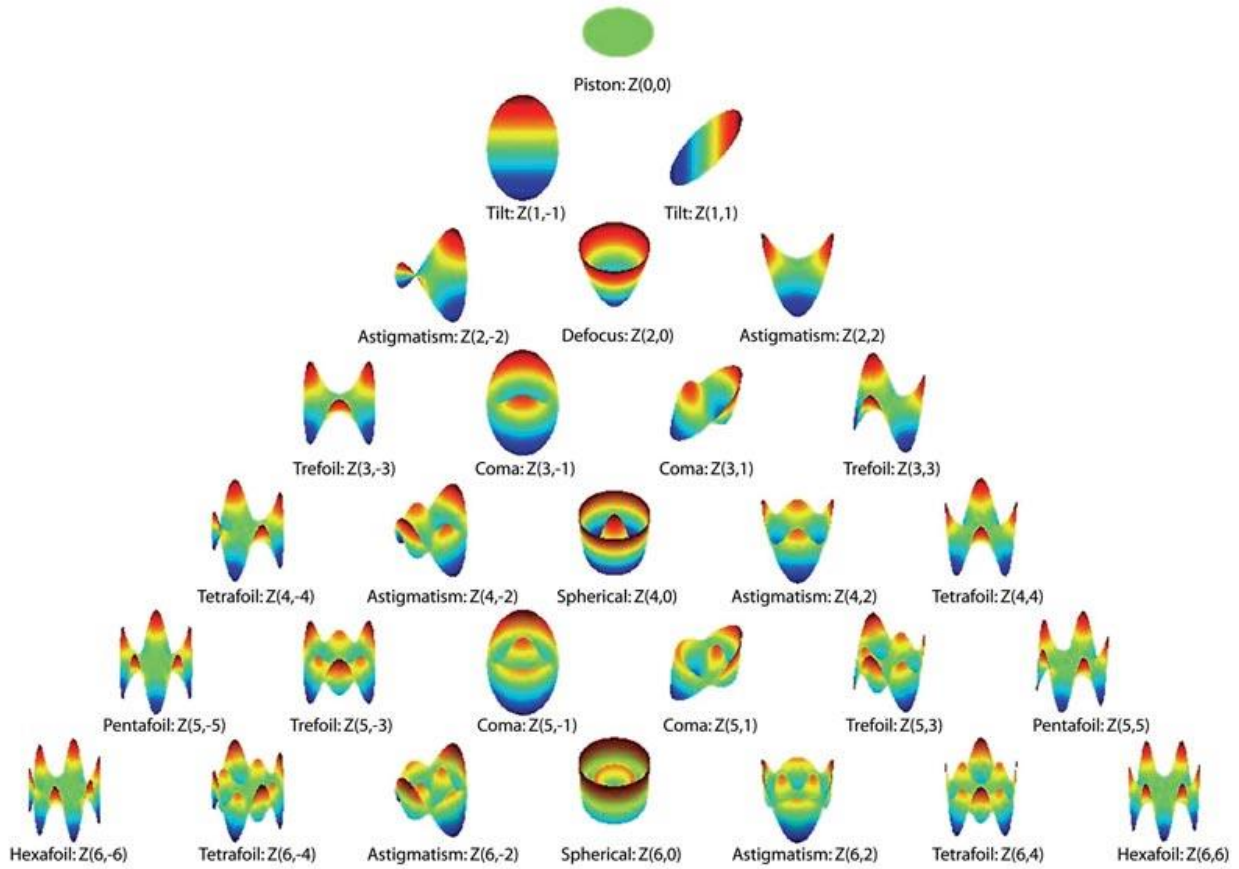


Figure 42: Zernike modes, which describe how a wavefront is distorted by a specific aberration⁵⁸

Matrices A , B , and C , given in Eq. 53 and Eq. 54, are typically combined according to Eq. 55 to generate a transfer function, $G_{z\omega}$.

$$G_{z\omega}(s) = C(sI - A)^{-1}B \quad \text{Eq. 55}$$

For the purposes of this analysis, transfer functions were calculated using a function called *qbode.m*, which was written by Etienne Balmes in 1992. The function calculates the transfer function of the system from each input to each output at each frequency in a frequency vector. This frequency vector was generated using the function *freq_gen.m*, written by Homero Gutierrez.

5.3.3.8.13.2 Modeling of the Disturbance Input

The model was subjected to a single source of vibration for the analysis—a set of reaction wheels located at the single bus node. The reaction wheel assembly is typically considered the dominant disturbance source, which, for the purposes of this study, was modeled according to parameters taken from Ithaco E Reaction Wheel data in Masterson’s Master’s Thesis.⁵⁹ The reaction wheel disturbance Power Spectral Density (PSD) was calculated using the function

psd_rwa_dist.m, written by Gutierrez and modified by Olivier de Weck in 1998. Inputs to the function include parameters taken from Gutierrez’s PhD Thesis⁶⁰: nominal reaction wheel speed of 1500 RPM, variation in reaction wheel speed of 1500 RPM, uniform wheel speed distribution, Euler angles from the spacecraft axes to wheel axes, and the type of reaction wheel model. This function outputs the PSD shown in Figure 43.

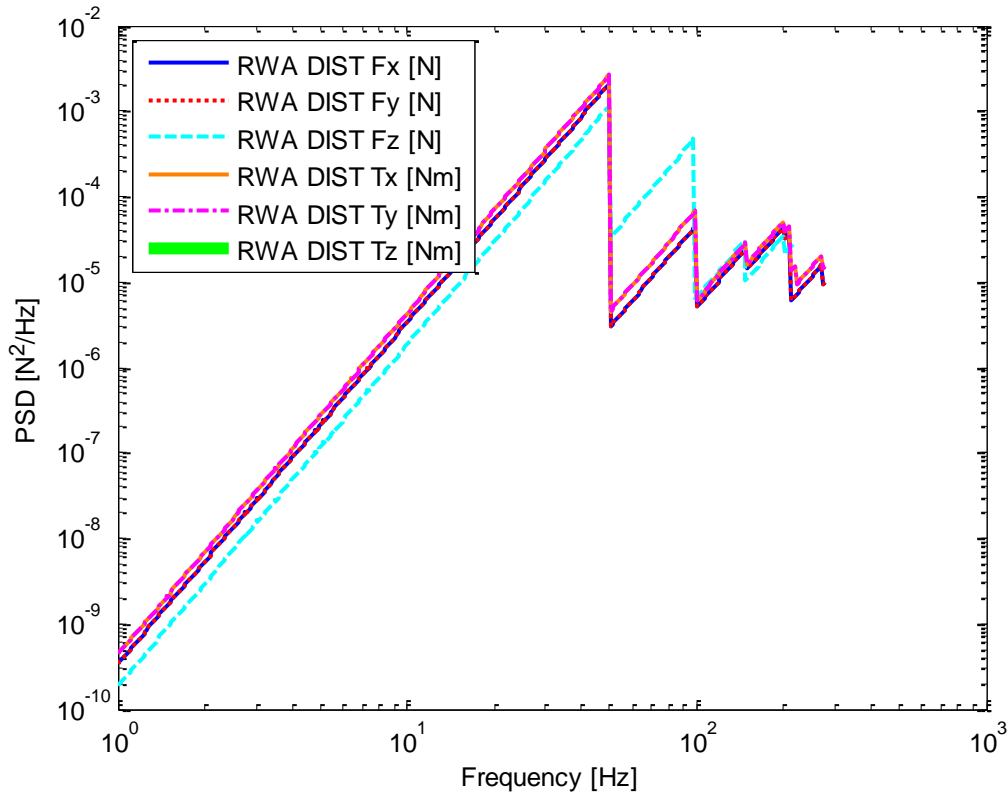


Figure 43: Ithaco E reaction wheel PSD

This figure shows the expected “sawtooth” pattern as seen in Gutierrez⁶⁰.

5.3.3.8.13.3 Calculating the Performance Output

With the transfer functions at each frequency and the reaction wheel PSD, $S_{\omega\omega}$, the PSD of the output signal is calculated according to Eq. 56

$$S_{zz} = G_{z\omega} S_{\omega\omega} G_{z\omega}^H \quad \text{Eq. 56}$$

where $()^H$ is the matrix Hermitian. The output signal PSD, S_{zz} , is then integrated over all frequencies to get the output covariance matrix, Σ_z , as shown in Eq. 57.

$$\Sigma_z = \int_{-\infty}^{\infty} S_{zz}(\omega) d\omega \quad \text{Eq. 57}$$

where the diagonal elements of the covariance matrix are the performance variances. This process was taken from Masterson's thesis⁵⁶. Finally, the root-sum-square of the performance variances gives wavefront error, in meters.

5.3.3.8.13.4 Results

The requirement on wavefront error, taken from the ATLAST optical performance requirements given in Section 3.2, is 37 nm, with a goal of 0.07 nm. Thus, the output is expected to be near that range. The results for each case are shown in Table XXIX.

Table XXIX: Jitter analysis results*

Primary Mirror Segment Support Method	Structural Segmentation of the Primary Mirror	Wavefront Error [nm]
Surface-normal	36 individual segments	2.12
Surface-parallel	36 individual segments	0.39
Mixed	3 "ring" segments	0.60
Mixed	6 symmetric segments	0.51
Mixed	7 segments (1 large, 6 small)	1.99
Mixed	12 segments	0.45
Mixed	3 JWST-style segments	1.89

*These results are subject to an unknown scaling error suspected to be due to unit mismatch which could not be resolved before the writing of this report. However, comparisons between results are still valid.

These results make sense when compared against each other. The surface-normal segment support method, with its more rigid backplane, translates the jitter through the structure more than the flexible surface-parallel support method, which performs the best. Likewise, the cases in which the primary mirror is divided into many smaller segments perform more similar to the surface-parallel support method than do the cases with only a few segments, such as the JWST-style segments.

According to these results, wavefront error is approximately proportional to the stiffness of the structure. This may be due to the fact that most of the energy from the reaction wheel

disturbances is concentrated at high frequencies, and most of the structural modes with high energy are at lower frequencies. With less stiffness, these structural modes drop in frequency, so the wavefront error scales appropriately.

The calculations were done offline and these results are implemented in the model using a simple switch-case architecture based on the primary mirror segment support method and the structural segmentation of the primary mirror.

5.3.3.8.14 Module Creation Code

As described in Section 4.3.2, the architectural decision about modularity presents seven options: modularity levels 1-7. This section describes how these seven levels were implemented in the code.

The module creation code takes in the overall components and MTBF columns of the component database, the DSM, and the architectural decisions of modularity level and assembly/servicing technique. The output is an $m \times n$ matrix containing the module definitions, where m is the number of modules and n is the number of component families in the component database. Therefore, each column represents a module. A sample module definitions matrix is shown in Figure 44.

$$\begin{array}{c}
 m = 3 \\
 \overbrace{\hspace{1.5cm}} \\
 \left[\begin{array}{ccc}
 5 & 0 & 0 \\
 0 & 3 & 1 \\
 0 & 4 & 0 \\
 3 & 1 & 0
 \end{array} \right. \\
 n = 4
 \end{array}$$

Figure 44: Sample module definitions matrix with three modules

In this example, module one contains five instances of component one, zero instances of component two, zero instances of component three, and three instances of component four. Similarly, module three only contains one instance of component two. The module creation code utilizes a switch-case architecture to create the appropriate module definitions matrix depending on the modularity level.

Modularity level 1 is the full telescope (no modularity). Thus, the module definitions matrix for level 1 only has a single column, and that column is simply equal to the overall components column in the component database.

Modularity level 2 is the permanent infrastructure, the instrument package, and the spacecraft bus. Permanent infrastructure components include the bus structure and any instances of the light shield, primary mirror baffle, and secondary mirror segments, which are all placed into module one. All of the instruments are placed into module two, and every component that has not already been dealt with is placed into module three.

Modularity level 3 is the permanent infrastructure, the instrument package, and spacecraft bus assemblies. The permanent infrastructure and instrument package modules are dealt with the same as in modularity level 2. The bus assemblies are broken out according to the following rule: components with connections in the DSM and similar MTBFs are put in the same module (with the exceptions of propulsion components, thermal bus components, thermal optical components, and thermal instrument components, which are placed in their own modules). The code begins by working across each row of the DSM, placing connected components into the same module and components with similar MTBFs in the same module, and placing components into a new module when they have no connections or similar MTBFs as any component already placed in another module. Currently, the code checks to see if the difference in MTBFs between any two components is less than one, effectively checking if they are equal. In the future, this should be modified to be a more meaningful number.

Modularity level 4 is the permanent infrastructure, the instrument package, and spacecraft bus component families. The permanent infrastructure and instrument package modules are dealt with the same as in modularity level 2. Then for each component family not already dealt with, a new module is created.

Modularity levels 5, 6, and 7 are divided the exact same way as modularity levels 2, 3, and 4, respectively, with the only difference being that the four instruments broken out into their own modules for levels 5, 6, and 7.

The final step for each modularity level is to add the appropriate number of assembly/servicing components to each module. Two UDPs are added to each module in every case. One robotic arm is added for every ten modules for each case besides formation flying; in that case, three electromagnetic coils are added to each module.

5.3.3.8.15 Mass

The mass of the structure and mechanisms within the telescope acts as one of the most tractable metrics, since the mass of the system must be kept low for cost, number of required launches, ground operations, and many other areas of the telescope's lifespan.^{18,59} The mass is also crucial to determine the inertia of the assembled telescope, which subsequently drives the attitude determination and control design for the spacecraft. Consequently, the mass of the system must be analyzed as one of the key values to be determined by the Structures and Mechanisms team.

To determine the mass of a particular architecture of both the Structures and Mechanisms subsystem mass and the entire telescope mass, two areas of the telescope must be massed and summed: the bus and connecting or supporting structures, as well as the mechanisms aboard the telescope themselves.

The mass of the Structures and Mechanisms subsystem is determined based on the number of components that are selected from the Components Family DB. Given the number of each component as listed in the structures component vector, a dot product with the mass column from the Components Family DB provides the total subsystem mass. This subsystem mass is then added with the masses of the other subsystems to determine the overall telescope's mass, as described in Eq. 58:

$$LTA.sys_mass = \left(LTA.optics_m + LTA.comm_m + LTA.acs_m + LTA.avionics_m + LTA.thermal_m \right. \\ \left. + LTA.structures_m + LTA.power_m + (LTA.structures_pow_avg \times LTA.power_m_nd) \right) \\ + (1 + LTA.prop_m_nd)$$

Eq. 58

In this equation, *LTA.sys_mass* is the total system volume in cubic meters, *LTA.optics_m* is the total Optics subsystem mass, *LTA.acs_m* is the total ADCS subsystem mass, *LTA.avionics_m* is the total Avionics subsystem mass, *LTA.thermal_m* is the total Thermal subsystem mass, *LTA.structures_m* is the total Structures and Mechanisms subsystem mass, *LTA.power_m* is the total Power subsystem mass, *LTA.structures_pow_avg* is the average power used by the Structures and Mechanisms subsystem in Watts, *LTA.power_m_nd* is the Power subsystem's nondimensional value in kilograms per Watt, and *LTA.prop_m_nd* is the Propulsion subsystem nondimensional parameter for propellant mass fraction per unit system mass.

Because the Structures and Mechanisms coding module is the last subsystem module to be run and there are no feedback loops, non-dimensional values for both Power and Propulsion are used to determine the overall mass of the telescope. As can be seen in the above equation, the masses for all subsystems are added, though there are two non-standard mass terms. The Power and Propulsion subsystems have provided to the Structures and Mechanisms subsystem non-dimensional values to be used in determining mass. The power-based non-dimensional value is used to determine the added mass of power management and distribution electronics and wiring harnesses required to power the various mechanisms that are used by the Structures and Mechanisms subsystem. The propulsion-based non-dimensional value, however, is used in determining the required propellant mass; as the propulsion system is required to move the telescope in its entirety, the total propellant mass cannot be determined until all other components have been determined. Therefore, the mass of required propellant is added to the system mass with the use of a non-dimensional value as calculated by the Propulsion subsystem. To account for these mass effects in both the Power and Propulsion subsystems, their respective values are updated immediately following this system mass calculation. Additionally, the Components Family DB is updated to reflect the mass of the propellant that is used in each iteration for use in other sections of the code.

Additionally, the validation process led to a change in the way that antenna gimbals are treated in the code. The mass of the gimbals required to operate the communication antennas have been incorporated not to the Structures and Mechanisms subsystem mass, but to that of the Communications subsystem. Though these components are added to the Structures and Mechanisms component vector, their mass properties are added to the Communication subsystem to aid in the validation process, since Hubble Space Telescope values combined gimbal and telescope mass together within the Communications subsystem.⁵⁴

5.3.3.8.16 Volume

Due to the constraint of the limit on launch volume imposed by the launch vehicles' fairings, only architectures that can be packed into launchable units may be deemed feasible architectures. Naturally, the fewer launches required, the less cost in launching the telescope's components. Therefore, the volume of each architecture must be determined in order to ensure that each architecture can meet this launch constraint. This volume metric, however, is opposed by the

complexity metric. For example, although the packed volume of one architecture may be less than another, the complexity of the resulting on-orbit assembly may render the less voluminous architecture less desirable overall.

To determine the volume of a particular architecture for both the Structures and Mechanisms subsystem and the entire telescope, the volume of the stowed configuration must be analyzed. This stowed configuration is determined in the Structures and Mechanisms coding module in a manner much like the calculation of system mass. To determine the total volume, the following simplified equation is executed:

$$LTA.sys_vol = \left(LTA.optics_v + LTA.comm_v + LTA.acs_v + LTA.avionics_v + LTA.thermal_v \right. \\ \left. + LTA.structures_v + LTA.power_v + (LTA.structures_pow_avg \times LTA.power_v_nd) \right) \\ + (LTA.sys_mass \times LTA.prop_v_nd)$$

Eq. 59

In this equation, *LTA.sys_vol* is the total system volume in cubic meters, *LTA.optics_v* is the total Optics subsystem volume, *LTA.acs_v* is the total ADCS subsystem volume, *LTA.avionics_v* is the total Avionics subsystem volume, *LTA.thermal_v* is the total Thermal subsystem volume, *LTA.structures_v* is the total Structures and Mechanisms subsystem volume, *LTA.power_v* is the total Power subsystem volume, *LTA.structures_pow_avg* is the average power used by the Structures and Mechanisms subsystem in Watts, *LTA.power_v_nd* is the Power subsystem's non-dimensional value in cubic meters per Watt, *LTA.sys_mass* is the total system mass, and *LTA.prop_v_nd* is the Propulsion subsystem non-dimensional parameter in cubic meters per kilogram. Just as in the system mass calculation, non-dimensional parameters are used by both the Power and Propulsion subsystems in determining the total volume of the telescope. Like the mass-based non-dimensional values, these values are necessary because the Structures and Mechanisms subsystem determines its components after the Power and Propulsion subsystems. They allow the system volume to be determined, and both the Power and Propulsion subsystem volumes are then immediately updated following this equation.

Additionally, just as with the determination of the system mass, the volume of the gimbals required to operate the communication antennas have been incorporated not to the Structures and Mechanisms subsystem volume, but to that of the Communications subsystem. Though these components are included in the Structures and Mechanisms component vector, their volume properties are added to the Communication subsystem to aid in the validation process, since Hubble Space Telescope values combined gimbal and telescope volume together as part of the Communications subsystem.⁵⁴

5.3.3.8.17 Power

The power of the Structures and Mechanisms subsystem is closely coupled with the Power subsystem, since the Power subsystem is responsible for generating, regulating, and distributing electricity throughout the telescope. In order to reduce the size and mass of solar panels, the power demands of all mechanisms must be kept low; the power metric allows the team to compare different architectures based on the power required to operate all components at both average and peak levels.

While the structure of the telescope itself does not have any power demands, there are mechanisms of the Structures and Mechanisms subsystem that levy power demands on the power management and distribution system. The trade decisions made at high systems levels, such as the modularity of the system, has a substantial effect on the total mechanism-required power of the telescope. Deployment mechanisms, such as high temperature superconductors, frangibolts, or burn wires significantly affect the peak power, but not the average power, because these large powered mechanisms are operated for only a few, short duration periods during the telescope's operational phases. The average power, however, is dominated by the mirror segment actuators during image collection. The following equations are used in determining the power required of the power generation system:

$$LTA.sys_pow_avg = \sum_{i=1}^N LTA.overall_components(i) \times LTA.compPowerAvgCol(i) \quad \text{Eq. 60}$$

$$LTA.sys_pow_peak = \left(\frac{LTA.sys_mass}{LTA.power_m_nd} \right) + LTA.structures_pow_peak \quad \text{Eq. 61}$$

In these equations, $LTA.sys_pow_avg$ is the total average system power in Watts, $LTA.overall_components$ is the vector of all telescope components, $LTA.compPowerAvgCol$ is the vector of the average required power in Watts for each component family as listed in the Components Family DB, $LTA.sys_pow_peak$ is the total peak power for the system in Watts, $LTA.sys_mass$ is the total system mass in kilograms, $LTA.power_m_nd$ is the Power subsystem non-dimensional parameter in kilograms per Watt, and $LTA.structures_pow_peak$ is the peak power required by the Structures and Mechanisms subsystem in Watts. The bounds for the summand range from the first to the N^{th} component.

As can be seen, the Components Family DB is used in determining the average power for the telescope, and the non-dimensional parameter from the Power subsystem is used in determining the peak power of the telescope, since this non-dimensional parameter takes into account the duty cycling of upstream components. With these values of peak and average power, it is possible to determine the mass of the associated solar arrays and the power management and distribution system required to supply sufficient power. This mass calculation is conducted as part of the system mass calculation.

5.3.3.8.18 Lifetime/MTBF

Because the mechanisms of the Structures and Mechanisms subsystem have much shorter MTBFs than the spacecraft structure itself, the focus of the lifetime/MTBF analysis for this subsystem will be on the mechanisms rather than the structure itself. The permanent infrastructure – mostly structural components such as the mirror backframe, bus structure, secondary boom, and light shield – will not be able to fail in the analysis as their lifetimes are orders of magnitudes higher than the other components. Depending on the architecture selected, the MTBF of the appropriate components will be retrieved from the Components DB shown in Appendix C. After parsing the data from the database, the MTBF will be output in a predefined data structure to the operations module. The MTBF that are stored in the database are estimated

based on typical component family MTBFs and do not represent precise numbers, only estimates. In the operations module, these MTBFs are used to compute component reliabilities in the Monte Carlo simulation to determine if a component fails during operation. The fault tree diagram shown in Figure 45 shows which component failures lead to system failure. When any of these conditions are met, the telescope will fail and the utility to science will drop to zero until the next servicing mission.

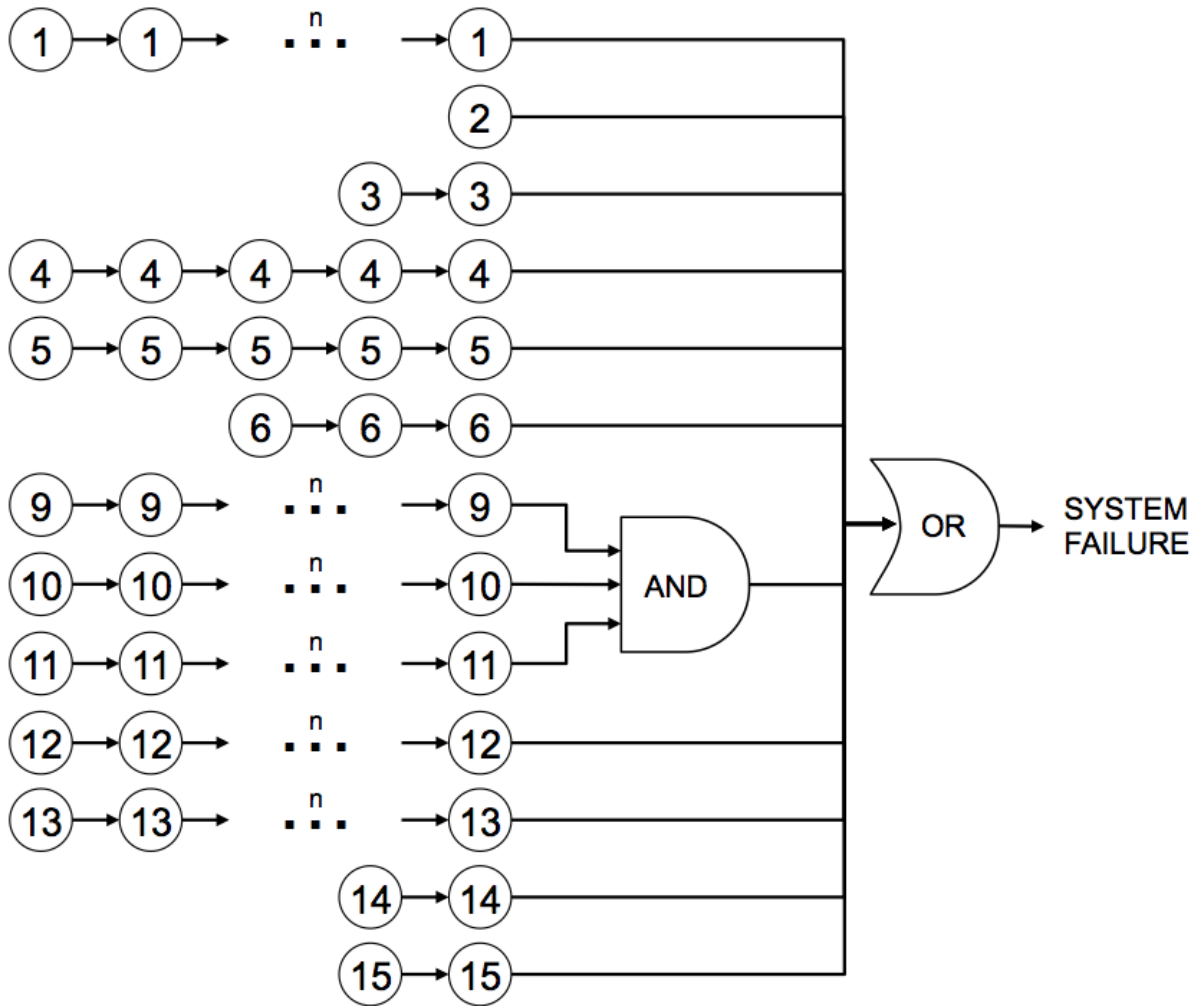


Figure 45: Fault tree diagram for the Structures and Mechanisms component failures that lead to system failure, where the numbers represent the corresponding row/component number in the Component DB shown in Appendix C.

As shown in the fault tree diagram in Figure 45, different components lead to system failure in various ways. Some components can only cause system failure if all of them fail. These are depicted with an ellipsis (e.g., components 1, 9, 10, 11, 12, and 13). Others can cause system failure if a specific number of them fail. For example, components 2, 3 and 4 require 1, 2 and 5 failures respectively. Components that only cause system failure when other components have also failed are grouped with an AND gate (e.g., components 9, 10, and 11). Components that will

cause system failure by themselves are linked together with an OR gate leading to system failure as are most in the fault tree.

The numbers in the fault tree diagram represent the components from the Component DB located in Appendix C. For example, robotic arms are component 1, electromagnetic coils are component 2, and docking ports are component 3. All robotic arms (component 1) need to fail before mission failure, as the design assumption is that all assembly/servicing maneuvers are able to be carried out by a single arm and others are included in the design for redundancy and ease of operation. One electromagnetic coil failure will cause that particular module to be unserviceable, since there are no robotic arms in those architectures in which electromagnetic coils are employed. Two docking port failures as well as the corresponding data and power interface failures (components 3, 14, and 15) are required to fail because all modules have two docking ports, so data and power could theoretically be routed to the module in two ways. Five failures of primary mirrors and surface-normal actuators (components 4 and 5) are assumed to degrade science utility to a level corresponding to mission failure. Alongside this five-mirror failure requirement, three surface-parallel actuators (component 6) would affect six mirror segments and thus drop the science utility below the threshold again. All vibrational dampers (components 9, 10, and 11) are required to fail before system failure. Nonetheless, in the Monte Carlo simulation, the utility to science parameter is scaled down for each failure of a component affecting science utility (e.g. mirrors, actuators, and dampers). Components in the primary infrastructure of the telescope are not included in the fault tree and are assumed to function for the full 40-year lifetime of the satellite.

5.3.3.9 Systems Module

5.3.3.9.1 Complexity

The computation of a structural complexity metric for the telescope architecture has been developed by Sinha and the MIT Phoenix Team.^{61,62} The architectural study employs a simplified structural complexity metric because it has been shown to be a predictor of development cost across several types of complex systems.⁶¹ This complexity metric was chosen because of its ability to be applied to a wide array of systems covering a broad spectrum of both complexity and function. Specifically, its use in determining the complexity of a highly fractionated architecture for the DARPA Phoenix Project was a key benchmark, since the LTA will be comprised most likely of several modules, not dissimilar from Phoenix satlets. The structural complexity metric used in the cost analysis contains three complexity factors:

$$C = C_1 + C_2 C_3 = (\sum_{i=1}^n \alpha_i) + (\sum_{i=1}^n \sum_{j=1}^n \beta_{ij} A_{ij})(\gamma E(A)) \quad \text{Eq. 62}$$

In this equation, C_1 represents the complexity due to the number and flight readiness of the components, C_2 represents the complexity due to pair-wise component interactions, and C_3 represents the complexity due to the topology of the system architecture and the associated complexity of system integration.⁶¹ These three complexity terms are determined with the following equation with variable values from the DSM and the Components DB:

$$C(n, m, A) = (\sum_{i=1}^n \alpha_i) + [\sum_{i=1}^n \sum_{j=1}^n \beta_{ij} A_{ij}] (\gamma E(A))$$

Eq. 63

In Eq. 62, n is the number of components, m is the number of interfaces, A is the Design Structural Matrix (DSM), α is a function of Technology Readiness Level (TRL) as described by Eq. 63, β is the complexity of each connection between pairs of components, γ is $1/n$, and $E(A)$ is the graph energy of the DSM, which is the sum of the singular values of the DSM as determined using the “svd” command in MATLAB.⁶¹ In the complexity analysis, higher values of β were given to components that have greater software and integration effort required when they are present in the system. The values of the β terms are currently based upon those from the DARPA Phoenix Project⁶², though in the future, further iteration should occur to determine the proper values. The addition of an optical-type interface is necessary for the telescope architecture, whereas in Phoenix no such interfaces existed.

$$\alpha = 9 \left(\frac{TRL_{max} - TRL}{TRL_{max} - TRL_{min}} \right)$$

Eq. 64

The structural complexity metric for each subsystem is included in the cost metric, since it is an input to the development cost. Sinha has shown that a power law relationship exists between complexity (X) and development cost (Y), as denoted in Eq. 65. Sinha demonstrated the wide applicability of this approach for both terrestrial and space applications, including those in development stages.⁶¹

$$Y = aX^b.$$

Eq. 65

Because the team is architecting, not designing, systems that fulfill the given high-level requirements, component families are included in the DSM and Components DB instead of specific components. There is no resultant specific design, but rather an estimate of the performance of the telescope system based on representative components for each component family. For this reason, the DSM and Components DB are constructed at a higher level with rather generalized representations of each subsystem that go into enough design detail necessary to distinguish between different architectures. Consequently, the application of these complexity relationships is novel and unique to this project. The values of β have been adjusted to reflect the complexity of integrating different groups of subsystem components.

5.3.3.9.2 Risk Analysis

The complexity of the mission discussed in this report in terms of mission objectives, design and manufacturing, test and verification, operations and maintenance requires a risk analysis in order to study the impact of failures on mission capability, as well as understand how to best use the available resources to maximize mission success. If something does not work as planned or a failure occurs, the entire mission could be lost along with large amounts of money, time, and effort. It becomes thus imperative to invest in such resources to protect against anomalies very early in the design process. By so doing, a risk analysis becomes an integral component throughout this process and will guide the designer in his choices and decisions.

In order to quantify the concept of risk, risk is defined as the product of the probability of a negative event occurring and its impact.⁴⁷ A risk analysis, therefore, encompasses a measure of the impact of the negative event, which can span from reduced performance to total mission failure. Two types of risk exist in practice: mission risk and programmatic risk. The former, also known as technical failure risk, has an impact on the total return from the mission and can be thought of as the amount of mission objectives that would be lost if the negative event occurred. In the case discussed here, the utility to science would be negatively affected by a mission failure as no data could be collected and no discoveries would be made. The latter type of risk, also known as implementation risk or management failure risk, affects budgets and reserves of several resources; its impact is translated into the amount of margin used to recover from the negative event. Programmatic risk plays an important role before operations begin, that is during the design and development stages of the mission when schedules slippages are likely, budget variations might occur because of political or leadership changes, engineering resources may not be adequate, etc. Both types of risk have been addressed in this study and will be presented in detail in this section.

5.3.3.9.2.1 Mission Risk

Whenever the overall return of the mission under consideration is affected by the timing of when a failure occurs, an Expected Productivity Analysis (EPA) is deemed appropriate to study technical failure risks.⁶³ This applies to all missions returning data of some sort throughout time and for which the more data the more successful the mission. This is certainly the case of space telescopes but also robotic missions returning scientific data. As opposed to this, if the most important requirement for mission success is that the end goal be met, then the timing of when a failure occurs does not matter. Such is the case of sample return missions, human spaceflight missions, or commercial satellites needing to operate for a certain number of years to fulfill contract requirements. Under these circumstances, a Probabilistic Risk Assessment (PRA) would be used, because the probability of meeting that specific end goal is what ought to be optimized.⁴⁷ Given the context of the mission described in this report, i.e., a large telescope array collecting and returning data to Earth, an extensive discussion of EPA will be carried out and numerical results will be presented.

By definition, the expected productivity of a system is the product of the probability of being in each functional state and the productivity in that state, summed over all states and all time. Here, this is to be considered as the expected value of the utility-to-science function over the entire mission lifetime. The expected productivity is calculated by following three steps:

1. Estimation of the probability of being in each state at each time
2. Estimation of the productivity in each state
3. Combination of the two previous steps to obtain the expected value of the total productivity by the end of mission life

The first step is based on a Markov model applied to each subsystem under the hypothesis that the future states of the subsystems depend only on the current state and not on any previous state. To clarify this assumption, which does apply to the case discussed in this report, if the subsystem under consideration fails if at least 2 actuators fail, it is irrelevant whether the subsystem started with 6 actuators and 4 have already failed, or if the subsystem started with only 2. The conclusion remains the same, that is, from now on the subsystem has remained with only 2 actuators and either one can fail at a given rate. In order to determine the probability of being in

any state at any time, one needs to define the possible states in which a subsystem can be and how it would transition from one state to the next. This can be accomplished by generating a state diagram, where each state is represented by a node and the transitions by the different interconnections among nodes. Transitions occur because components fail; therefore, each transition is associated with the failure rate of the component causing the system to vary its state. As an example, Figure 46 illustrates the state diagram of the Attitude and Determination Control subsystem (ADCS), here modeled with 9 momentum wheels (mw), 1 star tracker (st), and 1 solar sail (ss).

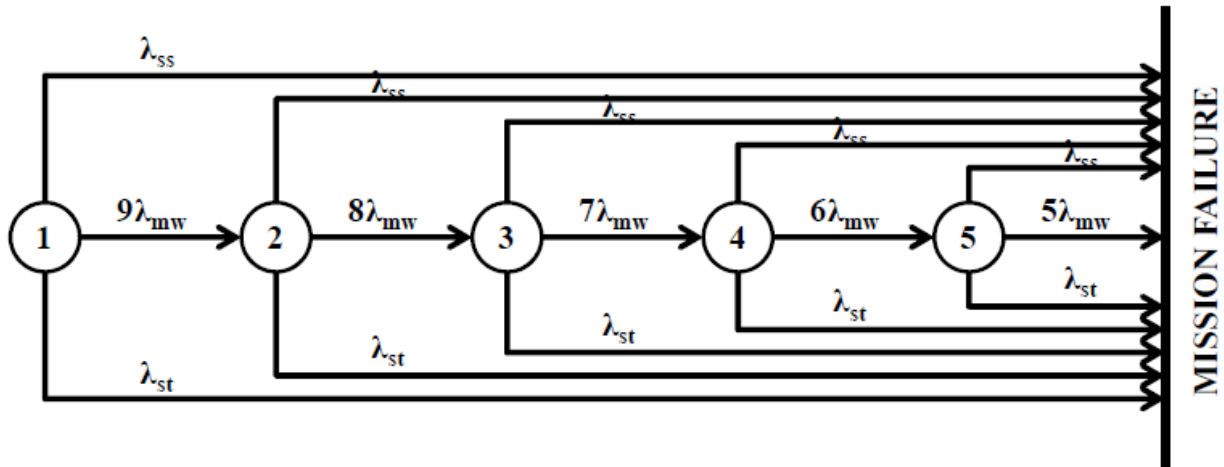


Figure 46: State diagram for the Attitude and Determination Control subsystem. Five different states were identified which lead to mission failure

In order to determine the failure rates (or alternatively, the Mean Time Between Failures – MTBF – defined as the inverse of the failure rates) needed to perform the analysis mentioned above, the following approach was adopted. Reliability values were estimated for all components based either on data available in the literature⁴⁷ or assumptions made to extrapolate the values of technology readiness levels (TRL) in the next decade for all components requiring substantial technology development. The following equation was used:

$$\lambda = \frac{1}{MTBF} = \frac{-\ln R}{\Delta t} \quad \text{Eq. 66}$$

where R is the reliability estimated at time Δt . The time span is equal to 40 years if the component being considered is assumed to never fail over the mission lifetime, otherwise it is set to values corresponding to the duration of operations before servicing, that is, 3, 5, or 10 years. The transitions are represented through the transition matrix, $[A]$, which is needed to solve the following system of first-order linear differential equations:

$$\dot{P}(t) = [A] \cdot P(t) \quad \text{Eq. 67}$$

where $\dot{P}(t)$ is the time rate of change of the state probability vector, $P(t)$. The elements of the transition matrix correspond to a different state and are determined by looking at what enters and

exits each node. As an example, for the case shown in Figure 46, the transition matrix would be as follows:

$$\begin{bmatrix} -(9\lambda_{mw} + \lambda_{ss} + \lambda_{st}) & 0 & 0 & 0 & 0 \\ 9\lambda_{mw} & -(7\lambda_{mw} + \lambda_{ss} + \lambda_{st}) & 0 & 0 & 0 \\ 0 & 8\lambda_{mw} & -(7\lambda_{mw} + \lambda_{ss} + \lambda_{st}) & 0 & 0 \\ 0 & 0 & 7\lambda_{mw} & -(6\lambda_{mw} + \lambda_{ss} + \lambda_{st}) & 0 \\ 0 & 0 & 0 & 6\lambda_{mw} & -(9\lambda_{mw} + \lambda_{ss} + \lambda_{st}) \end{bmatrix}$$

Similar matrices were calculated for the following subsystems: Structures, Power, and Thermal. These matrices were then assembled into the final matrix as independent blocks. This rests on the simplifying hypothesis that no failures occur due to subsystems interaction. Although this is in partial agreement with the higher-level assumption that no loops were accounted for in the N² diagram (which would show how the different subsystems interact with one another), the subsystems teams reported no failure modes due to possible interactions among subsystems at this level of the architectural study. It is recommended that when more details become available, a more in-depth failure mode analysis be carried out and the transition matrix be updated accordingly to account for such interactions. Moreover, the Communications, Avionics, and Propulsion subsystems teams made the assumption that their subsystems never fail within the maximum time between servicing missions, 10 years, which is the worst-case scenario. Therefore, they are not part of the analysis being discussed in this section. These hypotheses rest on two factors: 1) the subsystems' component families were selected so as to meet the requirement of being functional for at least 10 years, 2) the decision was made to take specific mitigating actions which would assure such a lifetime for these subsystems. For example, extreme temperature and radiation environments in deep space require that measures be taken to avoid environment-related avionics failures. Shielding, redundancy, design/processing methods are often employed in order to protect avionics equipment.⁶⁴ Types of radiation effects include total ionizing dose, displacement damage dose, single event effects (SEE), and charging/electrostatic discharged caused by electron deposits.⁶⁵ Shielding physically mitigates radon effects on avionics through the use of materials surrounding the electronics. Redundancy involves increasing the number of components, subsystems or internal component parts. Design techniques at the component level include dopant walls, isolation trenches, and chip layout, whereas design techniques at higher levels include decoupling, spacing, and circuit corrections⁶⁴. Processing and manufacturing methods include the use of specific materials and processing techniques⁶⁴. The avionics subsystem has selected all radiation-hardened components and many space-qualified components in order to reduce avionics failures due to environmental factors. Furthermore, the avionics subsystem will also employ redundancy at the component level to mitigate the impact of avionics failures, environmental or otherwise, on the system.

The solution to the system of differential equations⁶³ provides the probability of the system being in any given state at any given time. Initial conditions are needed to solve these equations. From a purely technical perspective, there is a 100% probability to be in state 1, which is when all subsystems are functioning, and 0% probability to be in all successive states. Indeed, right before launch, everything is expected to be working properly, whereas afterwards components and

subsystems start having higher probabilities of failure due to launch vibrations, environmental factors, degradation, and so on.

In the second step, the productivity, $C(t)$, in any given state is defined as the fractions of elements that can be completed per unit time, where an element is a single unit of the subsystem metric for the given mission. Examples of elements that could be selected in this context are an image, a gigabyte of data, a measurement, etc. In the case presented here, the productivity is the utility-to-science function defined in the Trade Metrics Calculation section.

Finally, in the last step, the expected productivity, $E[Prod]$, can then be computed by the following equation:

$$E[Prod] = \int_0^{lifetime} \sum_{i=0}^n C_i(t) P_i(t) dt$$

Eq. 68

This methodology was systematically applied at the subsystem level. Namely, failure states in each subsystem were identified at the level of detail allowed by this tradespace study. While some subsystems could be characterized by component failure modes, others did not have this type of information and remained at a more general level (the subsystem level). Indeed, it is beyond the scope of this work to perform a detailed design of the telescope and all its subsystems.

Figure 47 shows the state probabilities as computed by the Markov model. In black are the states corresponding to “all instruments working” for each subsystem (the “1” nodes of the state diagrams), whose probability decreases with time, whereas in different colors all other intermediate states whose probability is 0 at the beginning of mission but increases with time.

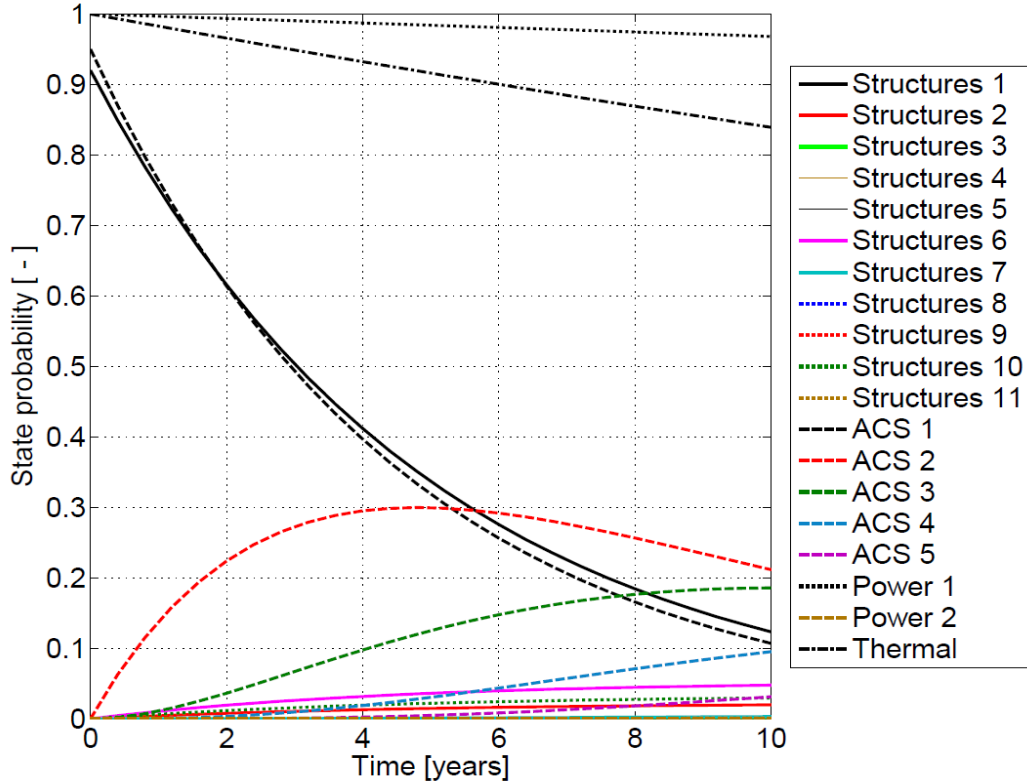


Figure 47: State probabilities as a function of time. The timespan was fixed to 10 years, as this could be the longest time interval without servicing. Since significant technology advancements may occur in such a long period of time, this type of analysis can be rerun for the remaining 30 years of the telescope’s lifetime by ensuring the failure rate values are updated.

Figure 48 illustrates the probabilities of failure of each of the subsystems previously analyzed as well as of the telescope. Such probabilities were calculated by estimating the probability that each subsystem will fail entirely due to its not being in one of the states shown in Figure 47. The same applies to the whole telescope. The equation used is the following:

$$P_{f_sub} = \prod_{i=1}^n [1 - P_i(t)] \tag{Eq. 69}$$

where P_{f_sub} represents the probability for each of the entire subsystems to be in a non-functioning state, and i varies from 1 to the total number of functioning states. By assuming that the telescope will fail if at least one of the abovementioned subsystems fails, the same equation Eq. 69 can be applied, where now $P_i(t)$ is replaced by each P_{f_sub} to yield the probability for the entire telescope to be in a non-functioning state.

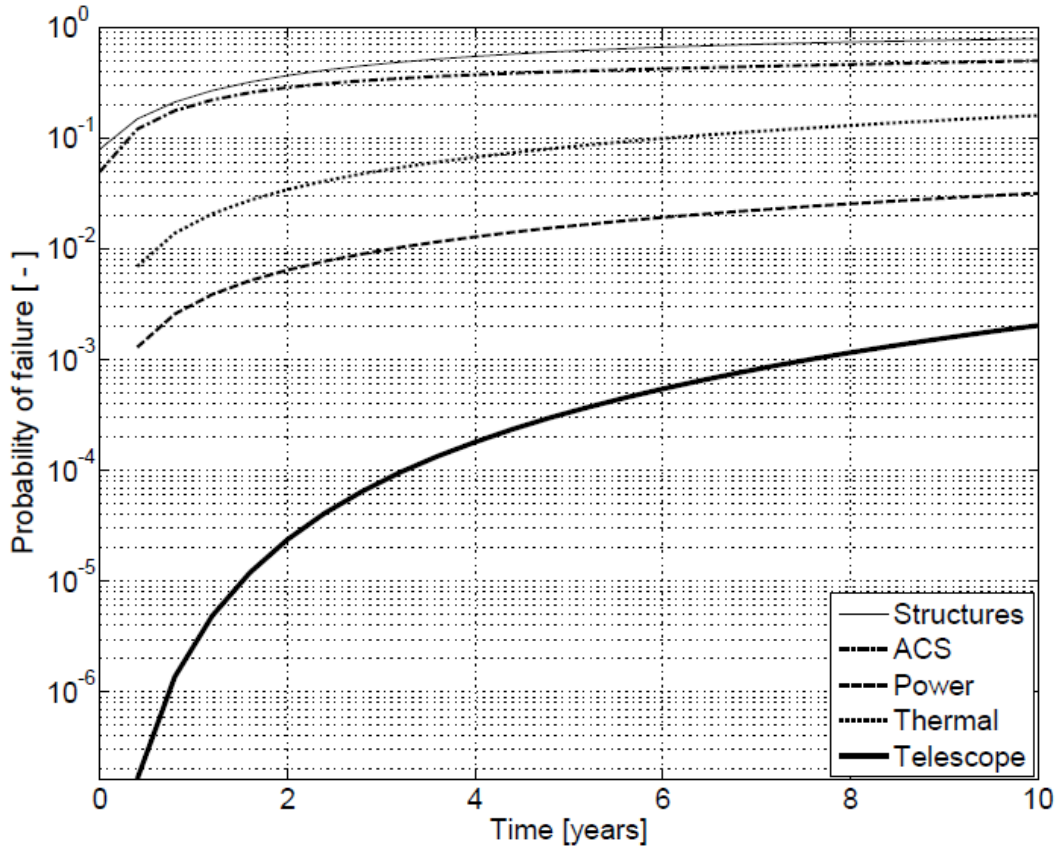


Figure 48: Probability of failure for the subsystems affected by mission risk over a time span of 10 years, which is the longest time interval that could exist between servicing missions

It can be seen the structural system is the one with higher risk, given the large number of mechanisms used. According to this model, the entire telescope could fail with a probability about 0.2% after 10 years of operations.

5.3.3.9.2.2 Implementation Risk and Schedule

As far as management failure risk is concerned, attention was paid to three factors: technology infusion, manufacturing processes, and test and verification. These are risk elements, which either decrease the probability of beginning operations in the nominal state or increase the probability that a particular subsystem will begin operations with degraded performance. These risk elements have a negative impact before launch, and thus before any utility to science is returned. In this sense, they affect the probability that a particular subsystem may be in a perfectly functioning state at $t = 0$. Such risk components result in an immediate change to the initial conditions used to find the probability of being in each state (Eq. 69). This approach enables to quantify potential schedule slippages that might occur due to the three aforementioned risk elements. However, one should remain cautious that this type of risk analysis rests on a number of assumptions made by each subsystem, which affect to some extent the uncertainty of the results discussed previously. These will be discussed separately for the subsystems involved in the remainder of this section. It will be illustrated what the technological challenges to develop

such a new large telescope array are and what their implications are on both programmatic risk and schedule.

5.3.3.9.2.2.1 Attitude and Determination Control Subsystem

In ADCS, the solar sail will require further advancements in technology and more testing before it can be qualified for flight with a TRL of 9. It is assumed today that solar sails have achieved a TRL equal to 7. It was thought to be highly likely that they will reach level 9 by 2020, but uncertainties remain which were estimated around 5%. The initial condition was therefore lowered from 1 to 0.95.

5.3.3.9.2.2.2 Communications

Free-Space Optical (FSO) solutions have been validated as viable radio-frequency (RF) communications substitutes in terrestrial systems to date. Larger bandwidth and higher data capacity capabilities for FSO, such as those needed for the communications subsystem of telescope system of study, were demonstrated in a recent NASA launch of Laser Communications Relay Demonstration (LCRD). FSO technologies for deep-space communications is a current area of development as evidenced by the NASA LCRD and other funded research activities.⁶⁶ As a consequence, FSO readiness by 2020 poses both technical and schedule risk to the telescope for FSO options.

The concept of Federated Satellite Systems (FSS) is a paradigmatic shift in how satellites share resources, e.g., processing capabilities and access time, thus impacting future satellite designs. Resource allocation is dynamic, based on the need, availability, and line of sight of participating suppliers and customers in FSS. These exchanges can be arranged by monetary or reciprocal resource sharing agreements as FSS transforms satellite resources to marketable commodities. Distributed Satellite Systems (DSS), where groups of satellites collectively perform a mission, have been demonstrated by NASA's A-Train and the Iridium satellite constellation. However, a market-based resource-allocation approach for FSS has not yet been implemented, nor has a deep-space multi-system intersatellite link (ISL) network been demonstrated. FSS is still in the conceptual phase and requires significant development of the protocols, algorithms, and technologies that would enable dynamic, secure, timely, and quality transaction. In addition, because FSS is a new paradigm for space operations based on a space market economy, there are also challenges to developing the economic, business, policy, and regulatory infrastructure necessary for FSS.

5.3.4 Operations Module

The Operations code module is a simulation of the telescope architecture's 40-year lifetime from launch to decommissioning. The simulation takes as an input a telescope architecture (defined by a component set generated by the subsystem code modules), as well as mission parameters and the architectural decision vector, and follows the process outlined in Figure 49 to produce data that are analyzed by the trade metric characterization code. Stochastic component failures are included in the simulation in order to model their impact on telescope operations and servicing; in order to account for behavior from probabilistic events, a 10-iteration Monte Carlo simulation loop was utilized for each architecture. The results of each iteration are averaged to produce the final outputs for a given architecture.

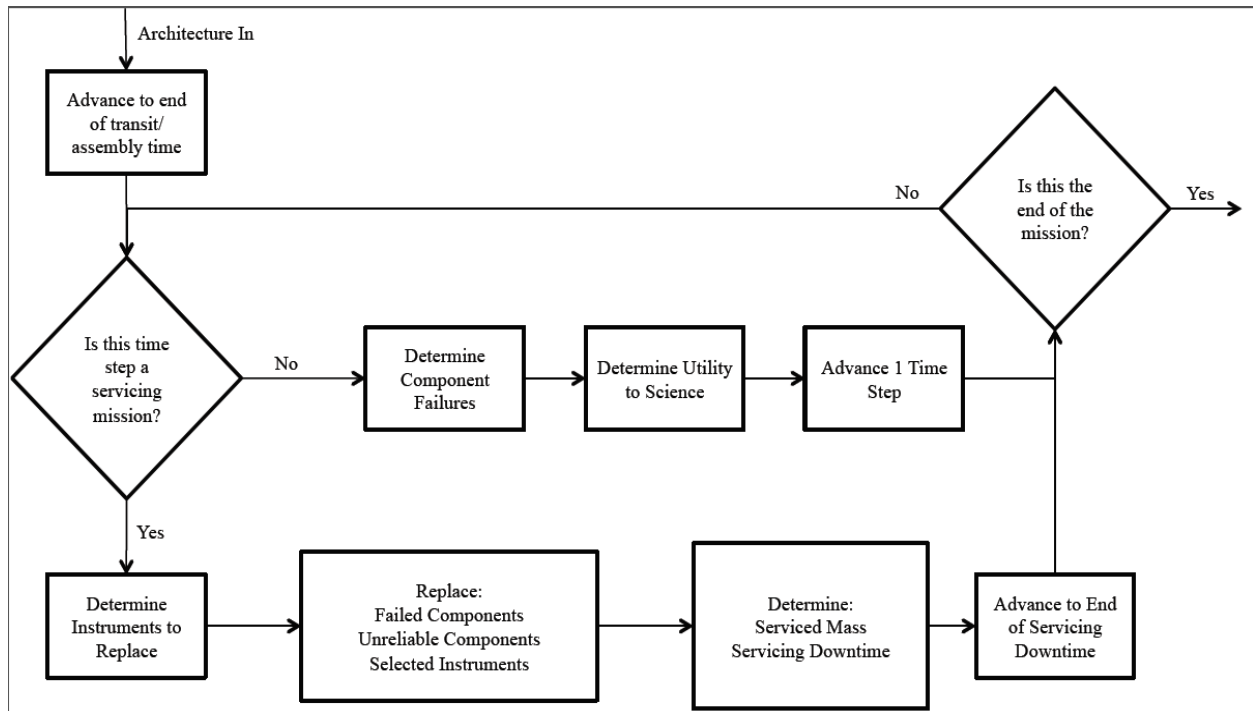


Figure 49: Code structure diagram for the operations module.

When an architecture (in the form of a MATLAB struct) is input into the Operations code module, it is translated into an architecture matrix that encodes the relevant values of the architecture into an easily accessible format. The architecture matrix is an $n \times 7$ matrix, where n is the total number of components within the architecture. Each row of the architecture matrix corresponds to a particular component, and the columns encode the relevant data for that component. In order from left to right, the columns represent:

- Components Database Row Number
- Mass (in kg)
- MTBF (in weeks)
- Module Number
- Clock
- State

The component clock is an entry that documents how long that particular component has been in operation; this entry is updated at each timestep and is reset when a component is serviced. The component state is an indication of whether the component is failed or operational at a given timestep, with 1 indicating an operational component and 0 indicating a failed component. The simulation incorporates a stochastic element that fails components based upon their reliability values to simulate component failure in the real-world telescope. When a component fails, the state flag is set to 0; when the component is serviced, the state flag is reset to 1.

This simulation uses one week as a timestep, and incorporates the three mission phases of the telescope: Assembly/Transit, Science, and Servicing. In order to minimize computational time, the timesteps can advance in jumps over sections of time that have no significant change –

specifically, the Assembly/Transit and Servicing Phases – while advancing step-by-step during science operations. The simulation begins at launch and enters the Assembly/Transit Phase. Once the Assembly/Transit Phase is complete, the telescope enters nominal operations, starting with Science. When a timestep corresponding to a servicing mission is reached (as defined by the servicing frequency architectural decision), the simulation enters the Servicing Phase. The timestep then advances to the end of the Servicing Phase and reenters the Science Phase, and the process repeats until the end of mission lifetime. Each mission phase is discussed in more detail in the following sections. The outputs of the simulation are:

- **Utility to Science Vector:** a vector indicating the utility to science of the telescope at each timestep
- **Failed Downtime Fraction:** the fraction of the mission lifetime that the telescope was not producing science because of a component failure
- **Servicing Downtime Fraction:** the fraction of the mission lifetime that the telescope was not producing science because of servicing operations
- **Serviced Mass Vector:** the vector of length n , where n is the number of servicing missions, encoding the amount of mass that was serviced during each servicing mission
- **Mean Serviced Mass:** the mean of the serviced mass vector, indicating the average mass serviced for a given servicing mission
- **Number of Servicing Missions:** the number of times that the telescope was serviced
- **Failure Matrix:** an $n \times m$ matrix, where n is the number of component families in the components database and m is the number of timesteps in the simulation, encoding the number of components of that family (row index) that are in a failed state in that timestep (column index)
- **Module Replacements Matrix:** an $n \times m$ matrix, where n is the number of modules in the telescope and m is the maximum possible number of servicing missions, encoding which module (row index) was replaced during each servicing mission (column index)

Assembly/Transit Phase

The Assembly/Transit phase begins at launch and ends when the telescope is fully assembled and is in place at SE-L2. It is assumed that assembly of the telescope takes place during transit. The transit time from LEO to SE-L2 is 63 days (or 9 weeks) and it is assumed that the telescope is fully assembled by the time it reaches SE-L2.⁶⁷ The Operations code module simulates this phase by advancing the timestep to step 9, the week where the telescope arrives at SE-L2 and begins the Science phase.

Science Phase

The Science Phase mode calculates the instantaneous utility to science of the telescope by multiplying the sum of the utilities of the four instruments on-board the telescope by the instantaneous observational efficiency. In addition, timesteps in the science phase “roll the dice” to determine which components fail, using a random number generator and the reliability of each component at that timestep; the instantaneous observational efficiency changes according to which components are failed. The utility is calculated for each week of the 40-year lifetime. The telescope enters Science Phase on all timesteps except for the beginning of the mission when it enters the Assembly/Transit Phase and at the servicing frequency when it enters the Servicing Phase.

Mirroring Baldesarra, the initial discovery efficiency of a given instrument type starts at an arbitrary value and increases in time due to technological advances that enable additional throughput or increased field of view for the same cost, mass, power, etc.¹³ Once an instrument is installed on the telescope, its discovery efficiency is assumed to slightly degrade with time due to radiation damage or similar effects. The formula for instrument utility is:

$$u_i(t) = Ae^{b(T-2028-L)} \cdot r^{t-T} \quad \text{Eq. 70}$$

where $u_i(t)$ is the utility of each instrument, A is a constant that specifies discovery efficiency at the beginning of the mission in $\text{arcmin}^2 \cdot \text{photons/second}$, T is the year the instrument was installed on the telescope, L is the latency from ground development and flight implementation of an instrument design in years, b is a constant that specifies the improvement rate of discovery efficiency over time, r is the decay factor, and t is the year of operation. Both r and b were taken from Baldesarra and are 0.99 and 0.3218 respectively.¹³ b was then adjusted off its baseline value to examine the sensitivity of utility to science to the assumed growth rate as described in Section 7.4.1.3. A was initialized to 10 for all instruments and L was assumed to be 3 years.

In order to simulate component failures, the reliability of each component at each timestep is calculated and compared to a random number in order to determine via a “dice roll” whether or not a given component fails in the given timestep. The expression used to evaluate whether or not a component has failed is

$$e^{-\frac{t_i}{MTBF_i}} \leq r \quad \text{Eq. 71}$$

where t_i the time in weeks that component i has been in operation (from the component clock entry in the architecture matrix), $MTBF_i$ is the MTBF value in weeks for component i , and r is a random number between 0 and 1. The left side of this expression represents the reliability (between 0 and 1) of component i at a given timestep; this expression evaluates as true if the reliability of component i is less than the random number. If the expression evaluates as true, the component is considered to be failed, and the state flag for the component in the architecture matrix is changed to 0. Thus, a component with a reliability of 0.8 in a given timestep has a 20% chance of failing in that timestep. Once failed, a component remains in a failed state until the next Servicing Phase occurs.

The utilities of all four instruments are then summed and multiplied by the observational efficiency. The observational efficiency will change with time as the telescope changes modes and as components on board fail. In science mode, the observational efficiency will be 90% per the requirement in Table IV. During the initial transit to the operational location and during servicing or transit to or from the servicing location, the observational efficiency will drop to 0% as the telescope is assumed to be incapable of doing science. The observational efficiency will also drop below 100% and possibly to 0% when failures aboard the telescope degrade its ability to conduct science operations. Some component failures result in degradation of the overall scientific output of the telescope (either as a geometric series or proportional to the ratio of failed to operational components for a given component family), while others result in complete loss of scientific output. The instantaneous utility to science equation therefore is:

$$US(t) = O(t) * [u_A(t) + u_B(t) + u_C(t) + u_D(t)] \quad \text{Eq. 72}$$

where $US(t)$ is the instantaneous utility to science of the telescope, $O(t)$ is the observational efficiency, and $u_i(t)$ is the utility of each instrument. The different Monte Carlo runs in Operations will capture different sets of failures that will yield slightly different instantaneous utilities to science as the set of instruments and the observational efficiency will be slightly different in each case.

Servicing Phase

The Servicing Phase begins when the timestep of the simulation coincides with a servicing mission, at which point the servicing mission counter is increased by 1. First, the model determines which instruments to replace and marks them for replacement. Instrument replacement during servicing missions is the primary means of increasing the utility to science of a given telescope architecture. As the discovery efficiency of instruments improves, the existing instruments on the telescope are replaced with newer, more capable instruments. To model real-world decision-making, instruments were marked for replacement if the discovery efficiency of the new instrument was five times greater than the discovery efficiency of the current instrument. The threshold value of five times the current discovery efficiency was chosen so that every instrument is not replaced on every timestep (as they would be if the rule were to replace any instrument that had seen a rise in discovery efficiency). The threshold creates a balance between the need to upgrade the instrument, the need to allow instruments to operate for a sufficient lifetime to generate enough utility to science to merit their cost, and the need to prevent serviced instrument mass from being the maximum value at every servicing mission.

Next, the components that are in a failed state or below a reliability threshold are marked for replacement. The rows in the architecture with a state flag of 0 indicate that that component is in a failed state, and those indices are marked for replacement. The reliability threshold is a way to enable preemptive replacement – that is, the replacement of a component that has not yet failed. If a component is still operational, but its reliability has fallen below a threshold value, then the probability of that component failing before the next servicing mission is higher than the probability for components that do not have reliabilities below the threshold value. Thus, that component is considered “unreliable” and is marked for replacement. The expression used to determine whether or not a component is below the reliability threshold is

$$e^{-\frac{t_c}{MTBF}} \leq R_{thresh} \quad \text{Eq. 73}$$

where t_c is the component time in weeks, $MTBF$ is the component Mean Time Between Failure in weeks, and R_{thresh} is the reliability threshold (unitless). For this simulation, the reliability threshold was taken to be 0.7, meaning that components with a greater than 30% probability of failure are replaced. This threshold value is an operational decision related to how far mission controllers are willing to allow components to degrade before replacing them. As such, the reliability threshold is the subject of a sensitivity analysis to a change in ± 0.05 (i.e., changing the threshold value to 0.65 or 0.75), which is described in Section 7.4 Sensitivity Analysis.

Once all components and instruments needing replacement are marked as such, the modularization of the telescope is taken into account by translating the component and instrument replacement marks into module replacement marks. If any element within a module is marked for replacement, the whole module is marked for replacement. This is due to the fact that for this model “servicing” is defined as the act of removing a module and replacing it with an identical (but potentially upgraded, if the module includes an instrument) module; the smallest unit of the telescope that can be serviced is a module. Thus, when an element is replaced all other elements in its module must be replaced as well.

Finally, all modules that are marked for replacement are replaced, meaning that all elements in that module are replaced. When a component or instrument is replaced, the component clock is reset to 0, which resets the reliability of the component to 1; in this way, the simulation represents the component as being new. In addition, the state flag is set to 1 to indicate that the replaced component is now operational. Once these replacements are complete, the mass of all modules that were replaced is summed to give the serviced mass for this servicing mission, and the value is stored in the serviced mass vector. Next, the servicing downtime is calculated.

The servicing downtime is informed by the assembly/servicing technique and the number of modules replaced. The self-assembly case is assumed to require 2 hours per module, the case using tugs is assumed to require 6 hours per module, and the case using formation flying is assumed to require 4 hours per module. These values were chosen to reflect the relationships between these three techniques. First, in the self-assembling case, the robotic arms which are incorporated directly into the telescope design have a clear and unchanging relationship between end effector location and orientation and the telescope itself; therefore, the arms may perform more complex and rapid preprogrammed motions to remove and insert modules. For this reason, self-assembly is assumed to be the fastest method. The use of a tug for servicing requires that the tug dock with the telescope, implying that there will be more uncertainty in the relative location and orientation of end effectors and telescope modules; therefore arm motions will have to be more carefully and slowly executed. For this reason the servicing by tug is the slowest technique. Finally, formation flying involves more complex movement of modules using electromagnetic (EM) coils. Since all elements are floating in free space and all forces are internal resulting from interactions between EM coils, the center of mass of the system must remain unchanged; therefore the movement of any one component will cause movement in the others. However, complex preprogrammed motion is still available for servicing operations, though it will be more complex than the simple use of robotic arms. For this reason, the formation flying assembly/servicing technique is assumed to be at a medium value, between self-assembly and tugs.

Once the time for actual servicing operations is calculated, the transit time for movement of the telescope from SE-L2 to the servicing location and back is added in to determine the total amount of time that the telescope was offline due to servicing:

$$t_d = t_{serv} + t_{transit} \quad \text{Eq. 74}$$

where t_{serv} is the servicing time, $t_{transit}$ is the transit time to and from the servicing location, and t_d is the total downtime due to servicing. In the servicing code, all of these time values were documented as days; once the value is computed, the total downtime in days is divided by seven

to convert to weeks to match the timestep length. At this point servicing is complete, the timestep is advanced to the end of servicing, and the telescope enters the Science Phase.

5.3.5 Trade Metrics Calculation

5.3.5.1 Utility to Science

The Trade Metrics module receives the instantaneous utility to science of the telescope for each week of the forty-year lifetime from the Operations module. Trade Metrics integrates this input against time to find the total utility to science for each Monte Carlo run and then averages across the Monte Carlo runs. The equation for total telescope utility to science is:

$$U = \frac{1}{N} \sum_{i=1}^N \int_0^{2080} US_i(t) dt \quad \text{Eq. 75}$$

where U is the total utility to science of the telescope, N is the number of Monte Carlo runs, i is a particular Monte Carlo run, $US_i(t)$ is the instantaneous utility to science from the Operations module, and t is the number of weeks the telescope has been operating.

5.3.5.2 Serviceability

The Servicing Phase begins when the timestep of the simulation coincides with a servicing mission, at which point the servicing mission counter is increased by 1. First, the model determines which instruments to replace and marks them for replacement. Instrument replacement during servicing missions is the primary means of increasing the utility to science of a given telescope architecture. As the discovery efficiency of instruments improves, the existing instruments on the telescope are replaced with newer, more capable instruments. To model real-world decision-making, instruments were marked for replacement if the discovery efficiency of the new instrument was five times greater than the discovery efficiency of the current instrument. The threshold value of five times the current discovery efficiency was chosen so that every instrument is not replaced on every timestep (as they would be if the rule were to replace any instrument that had seen a rise in discovery efficiency). The threshold creates a balance between the need to upgrade the instrument, the need to allow instruments to operate for a sufficient lifetime to generate enough utility to science to merit their cost, and the need to prevent serviced instrument mass from being the maximum value at every servicing mission.

Next, the components that are in a failed state or below a reliability threshold are marked for replacement. The rows in the architecture with a state flag of 0 indicate that that component is in a failed state, and those indices are marked for replacement. The reliability threshold is a way to enable preemptive replacement – that is, the replacement of a component that has not yet failed. If a component is still operational, but its reliability has fallen below a threshold value, then the probability of that component failing before the next servicing mission is higher than the probability for components that do not have reliabilities below the threshold value. Thus, that component is considered “unreliable” and is marked for replacement. The expression used to determine whether or not a component is below the reliability threshold is

$$e^{-\frac{t_c}{MTBF}} \leq R_{thresh} \quad \text{Eq. 76}$$

where t_c is the component time in weeks, $MTBF$ is the component Mean Time Between Failure in weeks, and R_{thresh} is the reliability threshold (unitless). For this simulation, the reliability threshold was taken to be 0.7, meaning that components with a greater than 30% probability of failure are replaced. This threshold value is an operational decision related to how far mission controllers are willing to allow components to degrade before replacing them. As such, the reliability threshold is the subject of a sensitivity analysis to a change in +/- 0.05 (i.e. changing the threshold value to 0.65 or 0.75), which is described in the Sensitivity Analysis section of this report.

Once all components and instruments needing replacement are marked as such, the modularization of the telescope is taken into account by translating the component and instrument replacement marks into module replacement marks. If any element within a module is marked for replacement, the whole module is marked for replacement. This is due to the fact that for this model “servicing” is defined as the act of removing a module and replacing it with an identical (but potentially upgraded, if the module includes an instrument) module; the smallest unit of the telescope that can be serviced is a module. Thus, when an element is replaced all other elements in its module must be replaced as well.

Finally, all modules that are marked for replacement are replaced, meaning that all elements in that module are replaced. When a component or instrument is replaced, the component clock is reset to 0, which resets the reliability of the component to 1 – in this way, the simulation represents the component as being new. In addition, the state flag is set to 1 to indicate that the replaced component is now operational. Once these replacements are complete, the mass of all modules that were replaced is summed to give the serviced mass for this servicing mission, and the value is stored in the serviced mass vector. Next, the servicing downtime is calculated. This value is informed by the assembly/servicing technique and the number of modules replaced. The self-assembly case is assumed to require 2 hours per module, the case using tugs is assumed to require 6 hours per module, and the case using formation flying is assumed to require 4 hours per module. These values were chosen to reflect the relationships between these three techniques. First, in the self-assembling case, the robotic arms, which are incorporated directly into the telescope design have a clear and unchanging relationship between end effector location and orientation and the telescope itself; therefore, the arms may perform more complex and rapid preprogrammed motions to remove and insert modules. For this reason self-assembly is assumed to be the fastest method. The use of a tug for servicing requires that the tug dock with the telescope, implying that there will be more uncertainty in the relative location and orientation of end effectors and telescope modules; therefore arm motions will have to be more carefully and slowly executed. For this reason the servicing by tug is the slowest technique. Finally, formation flying involves more complex movement of modules using electromagnetic (EM) coils. Since all elements are floating in free space and all forces are internal resulting from interactions between EM coils, the center of mass of the system must remain unchanged; therefore the movement of any one component will cause movement in the others. However, complex preprogrammed motion is still available for servicing operations, though it will be more complex than the simple

use of robotic arms. For this reason, the formation flying assembly/servicing technique is assumed to be at a medium value, between self-assembly and tugs.

Once the time for actual servicing operations is calculated, the transit time for movement of the telescope from SE-L2 to the servicing location and back is added in to determine the total amount of time that the telescope was offline due to servicing:

$$t_d = t_{serv} + t_{transit} \tag{Eq. 77}$$

where t_{serv} is the servicing time, $t_{transit}$ is the transit time to and from the servicing location, and t_d is the total downtime due to servicing. In the servicing code, all of these time values were documented as days; once the value is computed, the total downtime in days is divided by seven to convert to weeks to match the timestep length. At this point servicing is complete, the timestep is advanced to the end of servicing, and the telescope enters the Science Phase.

5.3.5.3 Failed Downtime

The Failed Downtime is calculated using the results of the simulation from the Operations Module. The time vector of Utility to Science, which encodes the Utility to Science of the telescope during each week of the telescope's lifetime, is analyzed to determine how many weeks show a Utility to Science of 0. This is accomplished by evaluation of the equation

$$DT_{total} = \sum(US == 0) \quad \text{Eq. 78}$$

where US is the vector of Utility to Science values for each timestep in the simulation and DT_{total} is the total downtime in weeks. By taking the sum of the number of elements in US for which the expression $US == 0$ evaluates to true (and returns a 1), the total number of timesteps for which the Utility to Science was 0 can be calculated. A Utility to Science of 0 indicates that, during that timestep, the telescope was not operational either due to component failures or servicing operations. In order to isolate the number of weeks that the telescope was down specifically for component failures, the number of weeks of downtime due to servicing is calculated by summing the servicing downtime for each servicing mission; this value is subtracted from the total downtime in order to yield the downtime due to failures:

$$DT_{fail} = DT_{total} - \sum DT_{serv} \quad \text{Eq. 79}$$

where DT_{serv} is the vector of servicing down times for each servicing mission in weeks, DT_{total} is the total downtime in weeks (from Eq. 78), and DT_{fail} is the total amount of downtime due to component failures in weeks. The Failed Downtime for each architecture is reported as a fraction of the total mission lifetime spent in a non-operational state due to component failure, therefore the output from Eq. 79 is normalized by the total mission lifetime:

$$FD = \frac{DT_{fail}}{L*52} \quad \text{Eq. 80}$$

where DT_{fail} is the number of weeks of downtime due to a component failure, L is the mission lifetime in years, and FD is the failed downtime metric, the fraction of mission lifetime spent down due to a component failure.

5.3.5.4 Cost

5.3.5.4.1 Flight System Development

As described in the Trade Metrics Descriptions section, the cost of the flight system development, which includes the design, manufacture, and testing for the entire space telescope assembly, is estimated using three models. The function that performed this calculation is called `Cost_Flight System`. This function simply summed the individual cost of each phase of the mission for each design architecture. The assumptions and characteristics of those models are presented here.

5.3.5.4.1.1 Stahl Ground-Based Telescope Cost Model

The use of the Stahl Ground-Based Telescope model implies the assumption that the costs forecasted by this model is indicative of similar space-based telescopes. The model takes into account the unique prescription segments, the number of repeated segments, the segment diameter, wavelength performance, and the overall diameter of the telescope. Notably, the model takes into account manufacturing learning curve considerations based on the number of repeated segments fabricated. This portion of the code simply outputs a cost for the optical train

of the telescope. The original model estimated this cost in year 2000 dollars, therefore an annual discount rate of 2.01% was assumed to convert these into year 2013 dollars.

The Stahl Ground-Based Telescope Model is a parametric cost model, shown as Eq. 81. It predicts the cost to produce an optical telescope assembly, which consists of the primary mirror, secondary mirror, auxiliary optics, and support structure.²⁵

$$C_{OTA} = (0.68)(SF) D^{1.8} \lambda^{-0.5} e^{0.04(Y)} \quad \text{Eq. 81}$$

where C_{OTA} is the cost of the optical telescope assembly, SF is a segmentation factor, D is the aperture diameter, λ is wavelength diffraction limited performance, and Y is the difference between the year of development and the year 2000. For segmented mirrors, SF is defined in Eq. 82 as:

$$SF = P_n R_n^{0.7} (D_s/D)^{1.8} \quad \text{Eq. 82}$$

where P_n is the number of unique prescriptions, R_n is the number of repeated segments, D_s is the diameter of the repeated segments, and D is the diameter of the primary mirror. For monolithic mirrors, the SF value is 1. The bounds implied by the data set upon which this model is based include a maximum mirror diameter of 14.142 meter and a segment diameter of 1.0-8.41 meter. The 16.8-meter assumption for the aperture violates this boundary condition. However, as discussed, the absolute cost estimate reliability is less important for this trade than the relative costs, therefore any loss in accuracy resulting from using this model is viewed as acceptable. Moreover, this model is intended for ground-based telescopes. The effects captured in this model, specifically changing cost with segmentation, learning curve considerations, and economies of scale are all expected to provide similar relative results on the optical train of a space telescope. These benefits were deemed to outweigh the loss of absolute accuracy associated with using a ground-based model for a space-based application.

5.3.5.4.1.2 NASA Instrument Cost Model (NICM)

The NASA Instrument Cost Model (NICM)²⁵ estimates the cost of instrumentation aboard a spacecraft. The specific version of the model used here is intended for interplanetary spacecraft. This was considered the most appropriate model for the mission being considered for this project. The ATLAST requirement of four science instruments was assumed to be the case for this mission, as well. The NICM outputs costs in year 2010 dollars. An annual discount rate of 2.01% was used, and the NICM outputs restated in year 2013 dollars. The model itself takes in peak power, instrument weight, and replacement frequency to determine a lifecycle cost for each of the science instruments aboard individually.

This model provides cost estimating relationships for several different types of instrumentation. The NICM predicts the development and single-unit fabrication costs without management and systems engineering “wrap” factors.²⁶

The model is defined in Eq. 83 as

$$C_{NICM} = 328 * M^{0.426} P^{0.414} DL^{0.375} \quad \text{Eq. 83}$$

where C_{NICM} is the cost of instruments, M is total instrument mass in kilograms, P is maximum instrument power in watts, and DL is design life in months.²⁶ The NICM was produced from 159 instrument cost sets and has some bounds associated with that data set to ensure reliable estimates. The bounds for the mass input are 1-75 kg. The bounds for the instrument power are 1-75 W. The bounds for total design life are 10-150 months. As with the USCM8, the NICM will allow for differentiation of the design architectures based on cost.

5.3.5.4.1.3 USCM8 Cost Model

The Unmanned Spacecraft Cost Model (USCM8) was developed by Tecolote Research for the US Air Force, Space and Missile Systems Center.²⁶ The model provides cost estimating relationships for non-recurring and recurring cost for large spacecraft buses, including the development, ground equipment, launch operations and orbital support, and communications payload. The non-recurring costs included are design and development, manufacturing, and test of one spacecraft, and acquisition of peculiar support equipment.²⁶ Recurring costs include fabrication, manufacturing, integration, assembly, and test of the spacecraft.²⁶ The full model is not presented in this document, however the inputs to the USCM8 are the weights of the various subsystems, the volume of the reaction control system (RCS) tanks, the number of communication channels, burn time to get to the final location, orbit location, and mission of the spacecraft (communications or non-communications). The USCM8 model is a set of cost estimating relationships derived from 44 satellites. Based on the data set provided by these 44 satellites, the USCM8 model has a recommended range for each input. For the entire spacecraft bus, the input range is 114–5,127 kg. Should the architectures fall outside of this or any of other input ranges, as is quite possible, the USCM8 model will be less reliable than intended. However, the relative differences in cost between architectures should still provide useful, discriminating information as discussed earlier.

5.3.5.4.1.4 Complexity

A value for structural complexity is determined in the Systems code module and is incorporated into a “complexity factor” that is used as a multiplier onto the programmatic and spacecraft bus design costs. This is intended to reflect the increased project management and systems engineering workload associated with the design of a more structurally complex system.⁶¹ The calculation of complexity is discussed in Section 5.3.3.9.1. The complexity factor (CF) is of the form

$$CF = \frac{\text{Adjusted Development Cost}}{\text{Unadjusted Development Cost}} = A \times C^{1.2} \quad \text{Eq. 84}$$

where C represents the architecture’s structural complexity and A is determined using HST as a validation point, solving the following relation:

$$\frac{\text{Hubble Actual Development Cost}}{\text{Hubble Unadjusted Development Cost}} = A \times C_H^{1.2}$$

Eq. 85

The complexity factor defined above was used to adjust the development cost predicted for HST by our model to HST's actual development cost.⁶⁸ This relationship between development cost and complexity has been adjusted from its original implementation.^{61,62} This is because only one validation point for complexity (HST) is available, and to get accurate values of β one would need several validation points. Additionally, the value of the exponent here is assumed to be 1.2 based on past space systems^{61,62}, but ideally that would also be solved for using several validation points. In light of this, complexity is only used as an adjustment onto the predicted development cost of an architecture in the model presented in this report.

5.3.5.4.2 Launch

To find the launch cost for a given telescope architecture, data was collected on various launch vehicles, either currently operational or in development, that may be potentially used for this program (Table XXX). This provided important information such as the mass that each vehicle can send to the desired Geo-Transfer Orbit (GTO), the cost charged per launch, and allowable payload volume.

Table XXX: Launch vehicle properties and cost estimates

Launch Vehicle	Cost Per Launch (FY2013 Dollars)	Payload Mass (kg) to Specified Orbit			Diameter (m)	Height (m)
		GTO	LEO	LOTUS and EM-L2		
Space Launch System ⁶⁹	500000000	23000	70000	35814.6	8.384	17
Falcon 9 ⁷⁰	56000000	5760	10454	7112.8	4.6	11.4
Falcon Heavy ⁷⁰	128000000	12000	53000	20836.2	4.6	11.4
Atlas V ⁷¹	130000000	13605	29400	17967	5	26.5
Delta IV Heavy ^{72,73}	300000000	12980	22950	15870	5	19.81

To find the total cost required for launch, the number of launches that will be necessary is also required. Determining the number of launches required for a telescope architecture involves, in some manner, packing the telescope into the launch vehicle(s) in order to ensure that the launch system can support the program. The first step in the packing process is to analyze three things: component dimensions, system mass, and system volume. The launch cost MATLAB code checks the maximum dimensions of components included in a given architecture. If the largest component dimension exceeds the payload height offered by a particular launch vehicle, that launch vehicle is immediately removed from the analysis. If the maximum component dimension does fall within the height offered by the payload fairing of the vehicle, the code checks the other dimensions to determine if the component fits within the fairing diameter, possibly in a rotated manner. In the case that it fits with rotation, or in the more common case that all dimensions fall within the payload fairing height and diameter, the vehicle remains a viable option. During this process, the code determines which launch vehicles are able to fit the particular folding/segmentation method of the primary mirror, by far the largest component in the system.

For example, based on the dimensions given in Table XXX, only the Space Launch System (SLS) is capable of fitting Segmentation of the Primary Mirror option #5, the JWST folding style mirror. However, all launch vehicles are capable of launching Segmentation option #1, the case that uses individual uncombined segments. The next step is to determine the maximum number of launches required based on mass and on volume. Total system mass is directly divided by the launch vehicles' capabilities so that there exists a step function of number of launches required for mass. The total system volume is scaled by a conservative packing efficiency of 70%⁷⁴ and divided again by the launch vehicles' capabilities. The results of the mass-based and volume-based “number of launches” calculations are compared, and the total number of launches required for a particular vehicle is taken as the larger of the two. Once the total number of required launches is known for each viable launch vehicle, these values are multiplied by the corresponding vehicle’s cost per launch (Table XXX) to determine the total launch cost.

A similar approach is used to determine cost of launches for servicing missions. In the servicing case, however, the mass capabilities of each launch vehicle vary depending on the desired servicing location. Also, because the telescope is already in orbit, and the module or component sizes for servicing are known to fit in the various payload fairings, only the mass capabilities of the launch vehicles are considered. By removing unnecessary consideration of volume or dimensional constraints, the code becomes more efficient within the servicing code module.

5.3.5.4.3 Servicing Cost

As described in the Serviceability section, this model does not estimate the cost of a servicer due to the lack of a valid servicer cost model. However, servicing operations still contribute to the overall cost of the mission in two ways. First, the cost of the development of replacement components is considered; second, the cost to launch those components to the servicing location is considered. These two cost elements sum to make up the cost to produce and launch replacement parts over the telescope lifecycle; once again, it is important to note that this cost does not include the cost of a servicer – this only includes the elements of servicing cost which can be estimated with confidence.

In order to calculate the development cost of the replacement components that were produced and used during servicing, it is assumed that the development cost per kilogram of new modules is approximately the same as the development cost per kilogram of the initial telescope. Thus, the total flight system development cost from the first build is multiplied by the ratio of total serviced mass to the system mass:

$$C_{serv}^D = C_{FS} \times \left(\frac{\sum m_{serv}}{m_{sys}} \right)$$

Eq. 86

where C_{FS} is the flight system development cost in dollars as described in the Flight System Development Cost section, $\sum m_{serv}$ is the total serviced mass in kg, m_{sys} is the mass of the telescope system in kg, and C_{serv}^D is the cost to develop replacement parts in dollars.

In order to calculate the launch cost of replacement parts, the location of servicing, the mean serviced mass per servicing mission, and the number of servicing missions are taken into account along with data for the mass-to-orbit capability as well as the launch cost of various launch

systems to various orbits, displayed in Table XXX. The servicing launch cost is determined for each servicing mission using the same algorithm as the initial launch cost, except that the lift capability of the vehicles is changed to the appropriate values for the servicing location (i.e. if the current architecture utilizes LEO as the servicing location then the launch vehicle’s mass-to-LEO capability is utilized instead of its mass-to-SE-L2 capability) and the launch mass is the serviced mass for that particular mission. The sum of the launch cost for each individual mission is the overall servicing launch cost, C_{serv}^L .

Once the development and launch costs for servicing have been calculated, the overall servicing cost is calculated by adding them together:

$$C_{serv} = C_{serv}^D + C_{serv}^L$$

Eq. 87

where C_{serv}^D is the cost to develop replacement parts in dollars, C_{serv}^L is the cost to launch the replacement parts in dollars, and C_{serv} is the overall servicing cost (not including the cost of servicers).

5.3.5.4.4 Cost Output

As a way of interpreting the outputs of the cost model, historical missions are compared to the outputs of the model. The at-launch cost of the Hubble Space Telescope was \$1.5 billion in 1990 US dollars.⁷⁵ The five servicing missions of the Hubble Space Telescope had a cost of \$9.6 billion in 2009 US dollars.⁷⁶ The James Webb Space Telescope (JWST) is estimated to cost at least \$8 billion over its lifespan. Figure 50 shows a comparison of those historical costs with the TITANS AE model cost output for both modular (Modularity Level 2-7 and non-modular (Modularity Level 1) architectures averaged over the lifetime of each mission. A breakdown of the sources of these costs is also presented. A “Hybrid Hubble” space telescope architecture was evaluated using the TITANS AE model. This architecture was intended to resemble the Hubble Space Telescope; however, due to assumptions made in the model, this Hybrid Hubble architecture is very different from the actual Hubble mission architecture (e.g., it would be stationed at SE-L2, have a 16.8-m segmented mirror, and have a lifespan of 40 years). Because of these differences, the cost of the Hybrid Hubble is not a highly accurate reflection of the actual Hubble costs. However, it is a useful comparison to make for the purposes of evaluating the output of the model. As can be seen in Figure 50, the Hubble Actual and Hybrid Hubble lifecycle costs are similar. Notably, Average of TITANS AE is slightly more expensive than Hybrid Hubble. This comparison does not reflect the other measures of performance or utility for these architectures, such as utility to science. The Hubble Actual, Hybrid Hubble, and Modular TITANS AE Architectures have lower lifecycle costs than the JWST, though the overall cost estimate of the JWST is smaller than that of the average modular TITANS AE space telescope. This is due to the much shorter lifespan of the JWST, 5 years, relative to the lifespan of the TITANS AE mission, 40 years. It can also be seen, as expected, that modular TITANS AE architectures have lower lifecycle costs (not including most servicing costs) than non-modular TITANS AE architectures. This comparison supports the notion that the cost model is giving reasonable estimates for the lifecycle costs of architectures being evaluated.

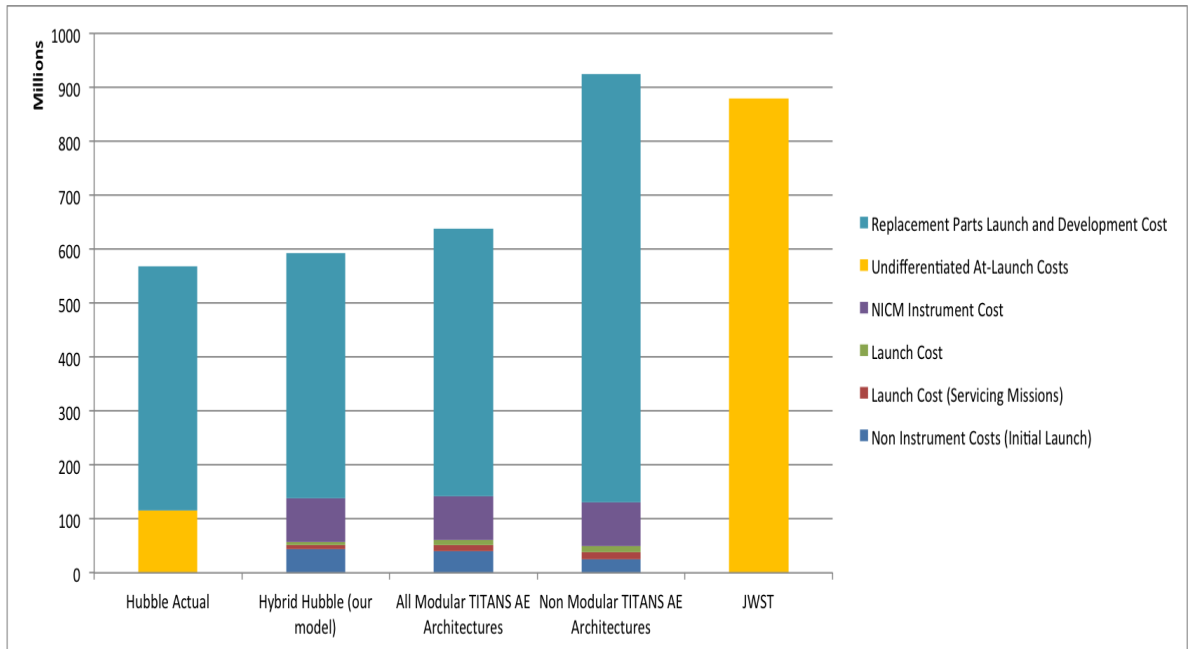


Figure 50: Comparison of cost model output to actual space telescope programs, normalized by total years of operation

6 MODEL VALIDATION

One dimension of validating the accuracy and comprehensiveness of the TITANS AE model encompasses the comparison of the actual Hubble Space Telescope (HST) and James Webb Space Telescope (JWST) mass and power values with the mass and power values of HST and JWST as predicted by the TITANS AE model given architecture decision vectors similar to the actual spacecraft. Ideally, the model predictions would be within $\pm 30\%$ of the actual HST and JWST values. Given that some of the characteristics of HST and JWST are not captured by the decision vector and the limited scope of the model, this validation was completed with as few code modifications as possible.

The following characteristics of HST and JWST were not captured in the architecture decision vector and were not accounted for in the code modifications: HST uses a monolithic mirror whereas the TITANS AE model uses only segmented mirrors, and JWST has no servicing implemented whereas the TITANS AE model does. Additionally, the model was run with a 40-year lifetime, compared to 23-and-counting for Hubble and a goal of 10 for JWST.

TITANS AE model also exhibits different modularity options; therefore, the code has been run with modularity level 6 for HST, which corresponds to the instruments being in individual modules, and the spacecraft bus is in assemblies. For JWST, the modularity level is assumed 1 (spacecraft level of modularity).

For the communication architecture: Hubble uses TDRSS, so the code has been run with the TDRSS option and JWST uses the DSN, so the JWST validation was run with the DSN option.

Another difference between the design presented here and HST is that HST is in LEO and experiences eclipses. Appropriate modifications in the code were implemented to reflect this: the power subsystem incorporated higher capacity batteries to be able to sustain the telescope consumption during eclipses and the ADCS system incorporated magnetorquers (an added mass of 180 kg). Due to technological advances, the fine guidance sensors are lighter and the batteries in the model are lighter as well.

The results of the validation are illustrated in Table XXVI.

Table XXXI: TITANS AE model validation against HST and JWST

Variable name	Model value	HST value	JWST value	Explanations
Power mass	504 kg	757.1kg ⁷⁸	-	The TITANS AE model incorporates lighter batteries (lithium) than HST (nickel metal)
Propulsion mass	0	0 ⁷⁷	-	HST does not have a propulsion system
Avionics mass	532 kg	600 kg ⁷⁸	-	12% difference, attributed to technological advances
ADCS mass	133.5 kg	1074 kg ⁷⁸	-	For HST, each fine guidance sensor weighs 220 kg and there are three of them on the HST. The HST also has 4 reaction wheels at 45 kg a piece and 4 magnetorquers at 45 kg apiece. It has an emergency system of computers and IMUs for safe mode which weighs 39 kg. It may be

				assumed that the IMUs weigh something on the order of 15 kg total. If all of these components are added up, it may be determined that the mass of HST ADCS is actually 1074 kg which leaves quite a discrepancy between the HST and the 133.5 kg shown for the TITANS AE model. However, fine guidance system mass in TITANS AE is counted under the science subsystem. Also, TITANS AE does not use any magnetorquers because it is not in LEO. The reaction wheels have less mass on TITANS AE which may cause a slower slew rate. However, this slew rate is on the right order of magnitude and is acceptable within the operational time frame of the mission. Part of the emergency system would fall under the avionics subsystem and IMUs were not accounted for in the code because TITANS AE will probably be able to have IMUs of negligibly small mass, volume, power etc. when TITANS AE is built.
Comms mass	46.79 kg	47.71kg ⁷⁸	-	1.9% difference
Optics mass	2300 kg	3860 kg ⁷⁸	-	Difference attributed to the different instruments installed on TITANS AE and HST
System mass	11473 kg	11110 kg ⁷⁸		3.2% difference, coming mainly from the optics mass difference and the ADCS subsystem
Comm average power	200 W	-	211 W ⁷⁹	5.5% difference
ADCS average power	232 W		147 W ⁷⁹	The average power is higher due to the fact that the TITANS AE model's ADCS components consume more power than the ones on JWST, thus leading to the 57.8% difference (the reaction wheels take 22W at steady-state, and there are 9 in the design)
Avionics power	200 W		187 W ⁷⁹	6.9% difference
Thermal power	207.75 W	-	250 W ⁸⁰	The difference comes from the fact that the temperature of JWST's instruments is supposed to be kept at 7K. In the code, the value is 60K, hardcoded in the optics module and was not changed for the purpose of this validation. 20% difference

Some values for JWST or HST were difficult to find on the Internet or in the available references, so the comparison could only be performed on a subset of the model outputs.

7 RESULTS AND ANALYSIS

7.1 Tradespace Exploration and Analysis

Tradespace exploration was applied to the study of the next-generation space telescope design and it facilitated the structured consideration of a large number of design alternatives for the space telescope in terms of desired trade metrics, while avoiding the premature focusing on point solutions. Instead of simply identifying “optimum” or “best” design solutions, this approach uses both graphical and quantitative means to evaluate the architectural decisions that drive the spatial distribution and orientation of all possible alternatives within the considered system design space. “Non-optimal” or “bad” designs will also be evaluated to reveal the multi-dimensional tradeoffs inherent in a complex design problem presented by the space telescope. Ultimately, tradespaces allow the comparison of point designs or sets of point designs to alternatives and accelerate the identification of both physical and preference constraints on feasible solutions.

The tradespace of the space telescope was generated by the complete enumeration of all design variables, which yielded a total of 15,120 design points. The metrics of utility to science, cost, servicing margin, and total failed downtime were previously conceptualized to help identify “good” designs. As these metrics have different units of measurement, they were normalized to facilitate effective and convenient comparison of architectural solution points on a common, quantitative basis. Hence, a solution with a normalized cost near 0 implies that it is relatively cheaper as compared to other solutions in the tradespace, and does not imply that the lifecycle cost is low in terms of absolute monetary value.

2-D and 3-D visualizations of the tradespace bounded by different combinations of metrics were then generated to analyze the interactions, tradeoffs and sensitivities of all design points. In-depth evaluation was then performed on the 2-D tradespaces bounded by cost and utility to science, where sets of design points were evaluated to determine the single or combined architectural decision that would allow one set to dominate another in the tradespace. Complete evaluation also enabled the identification of the Pareto fronts on 2-D and 3-D tradespaces, on which the Pareto Front subset solutions that offer the best tradeoffs between the metrics of interest can finally be identified and analyzed.

7.1.1 2-D visualization of tradespace: normalized Utility to Science vs. normalized Lifecycle Costs

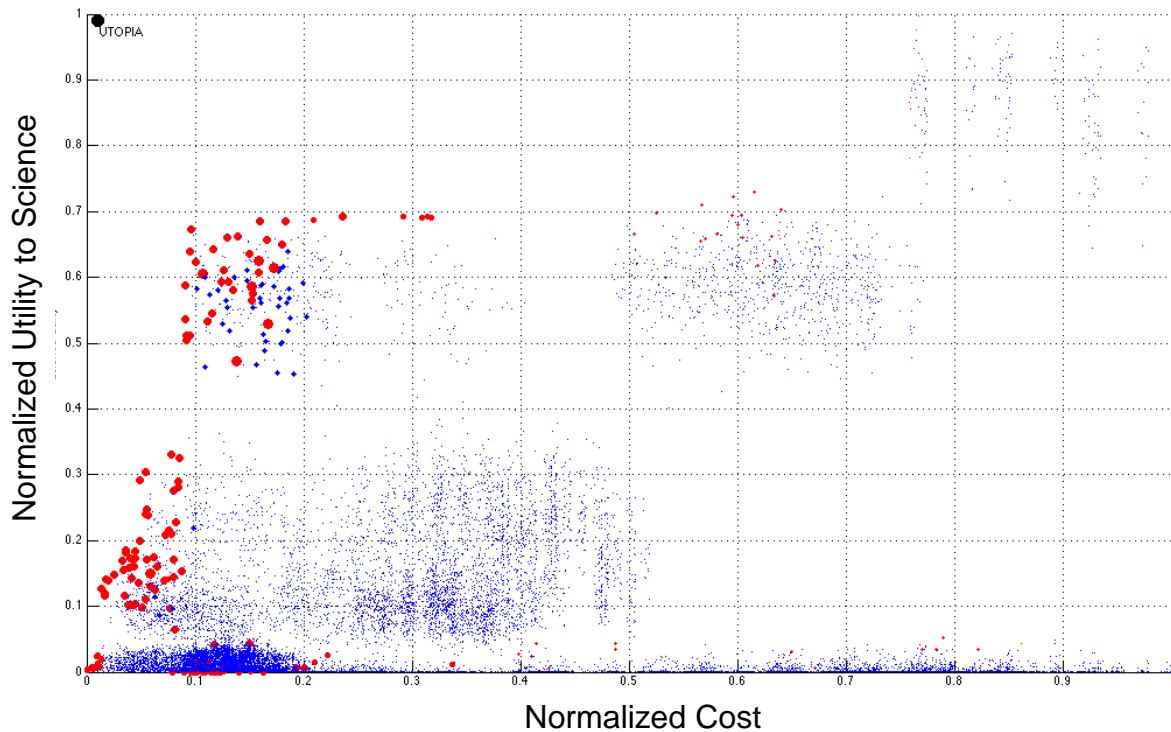


Figure 51: Pareto front solutions (in red) for tradespace bounded by cost and utility to science.

2-D visualizations of system tradespaces were first generated, and a tradespace bounded by cost and utility to science was analyzed and shown in Figure 51. An additional dimension was also reflected in the tradespace to include servicing margin as the third metric, where its value is directly proportional to the size of the point. Therefore, the 2-D tradespace representation can illustrate the interactions between three different trade metrics. The “Pareto Optimal” points were highlighted in red. They were identified using multi-objective optimization and non-dominated sorting, which were algorithms commonly used to establish the Pareto front on a set of points. Points closest to the utopia point would be considered “Pareto Optimal” and the utopia point has the lowest cost, highest utility to science, and highest servicing margin. Conversely, the so-called “bad” designs are characterized by high cost, low utility to science, and low servicing margin.

In Figure 51, clusters of architectural point solutions can clearly be seen on the tradespace, with a high concentration of points in the region with low utility to science and increasing cost. Clusters of larger points are seen closer towards the utopia point, reflective of designs with increasingly lower costs, higher utility to science, and higher servicing margin. Points on the right-hand side are generally smaller, reflecting lower servicing margin. The dominated solutions (in blue) were then removed, leaving a filtered tradespace containing only the “Pareto Optimal” solutions. This is shown in Figure 52 and a total of 8 clusters were visually and cognitively identified in the filtered tradespace for further analysis.

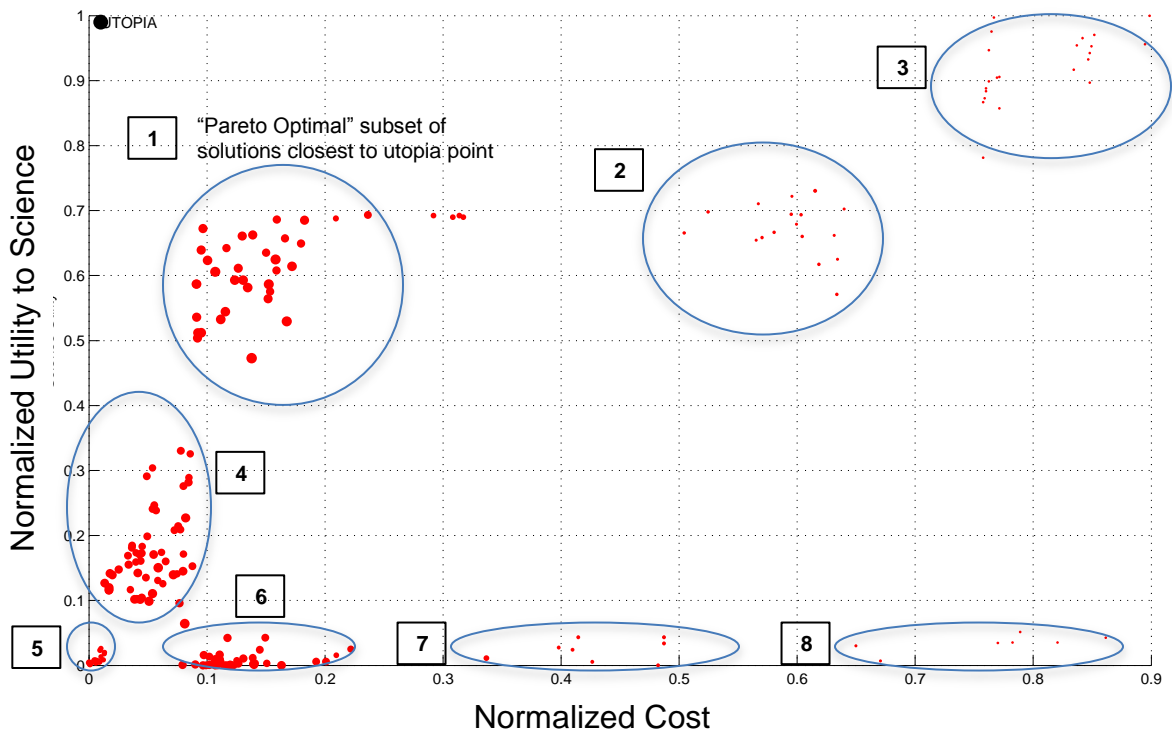
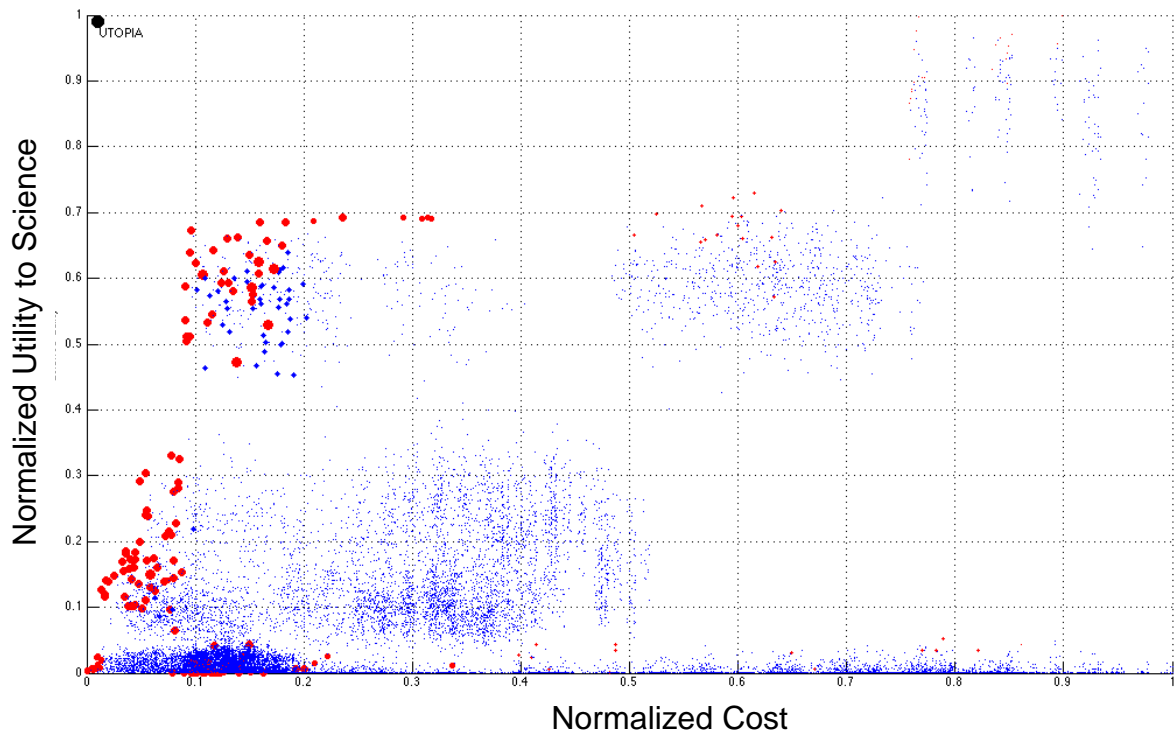


Figure 52: 2-D view of filtered 3-D tradespace of “Pareto Optimal” solutions for the space telescope bounded by utility to science and cost.

Cluster 1, which is the identified subset of “Pareto Optimal” solutions closest to the utopia point was further evaluated and each constituent design point was then labeled with its unique architectural vector to determine any commonalities that may be characteristic of the overall subset. This is shown in Figure 53 below. A brief analysis of the points directly reveals that the subset of “Pareto Optimal” solutions is dominated by the “7-1-1” architectural vector elements. “7-1-1” represents the identification numbers of the assigned alternative for the first three architectural decisions in order: the highest modularity level possible of 7, Sun-Earth L2 as the servicing location, and a servicing frequency of 3 years. The same evaluation may also be performed for the other subsets. However, the “7-1-1” subset of architectural solutions will be the focus of evaluation in this report.

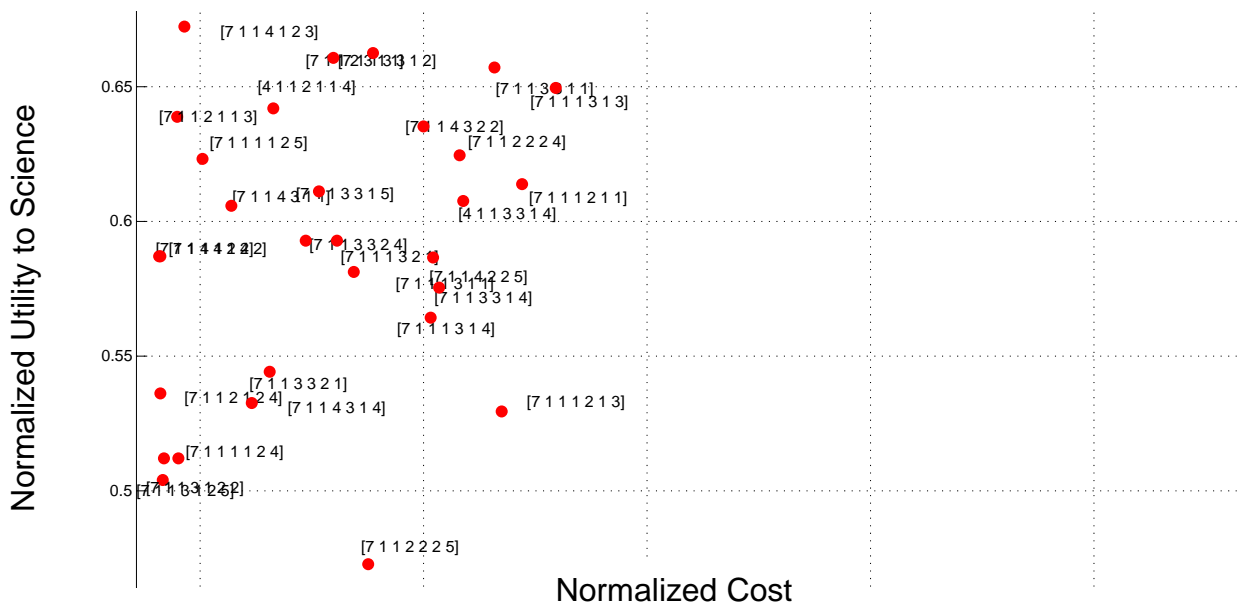


Figure 53: “Pareto Optimal” subset solutions closest to the utopia point (Cluster 1) on the filtered tradespace bounded by utility to science and cost, dominated by solutions with “7-1-1” architectural vectors.

A modularity level of 7 would constitute the combination of highest instrument modularity and spacecraft bus modularity. As explained previously, the MTBF of an assembly is equivalent to the lowest MTBF of the components within it and this drives the grouping of component families. As such, the highest level of modularity with each component family as an individual module will yield the most physically robust system with the highest MTBF values for component families and subsequently the entire system. A servicing location at SE-L2 will ensure that the space telescope never experiences downtime, thereby providing the highest utility to science. A servicing frequency of 3 years also ensures that onboard instruments and component families remain in pristine operating condition throughout their mission lifecycles. These reasons thus collectively explain why solutions with the “7-1-1” architectural vector would be dominant in the “Pareto Optimal” subset closest to the utopia point. A small number of solutions identified by the “4-1-1” architectural vector were also observed in the subset, where

‘4’ represents Modularity Level 4 and the space telescope architecture is defined by instrument packages and spacecraft bus component assemblies.

The “7-1-1” architectural vector for the visually identified “Pareto Optimal” subset of solutions closest to utopia point was reaffirmed using the Polar plot shown in Figure 54 below. The Polar plot illustrates the frequency of occurrence within the filtered Pareto set of solutions for every possible alternative in each architectural decision on a circular plane based on random sampling. Sampling from a smaller set of solution points can help identify architectural alternatives that dominate the same set. With increasing number of samples, the frequencies of occurrence for all architectural alternatives will become equal as a direct result of sampling across a large distribution. Each arrow on the circle corresponds to each alternative, and it is matched in accordance to the legend shown on the left in an anti-clockwise order. Color families distinguish the 7 key architectural decisions. The frequency of occurrence has also been normalized and it is directly proportional to the length of the arrow representing its corresponding architectural alternative. The opaque circle in the center of the plot has a radius of 1 and arrows protruding out of this circle can be easily identified as prominent architectural alternatives.

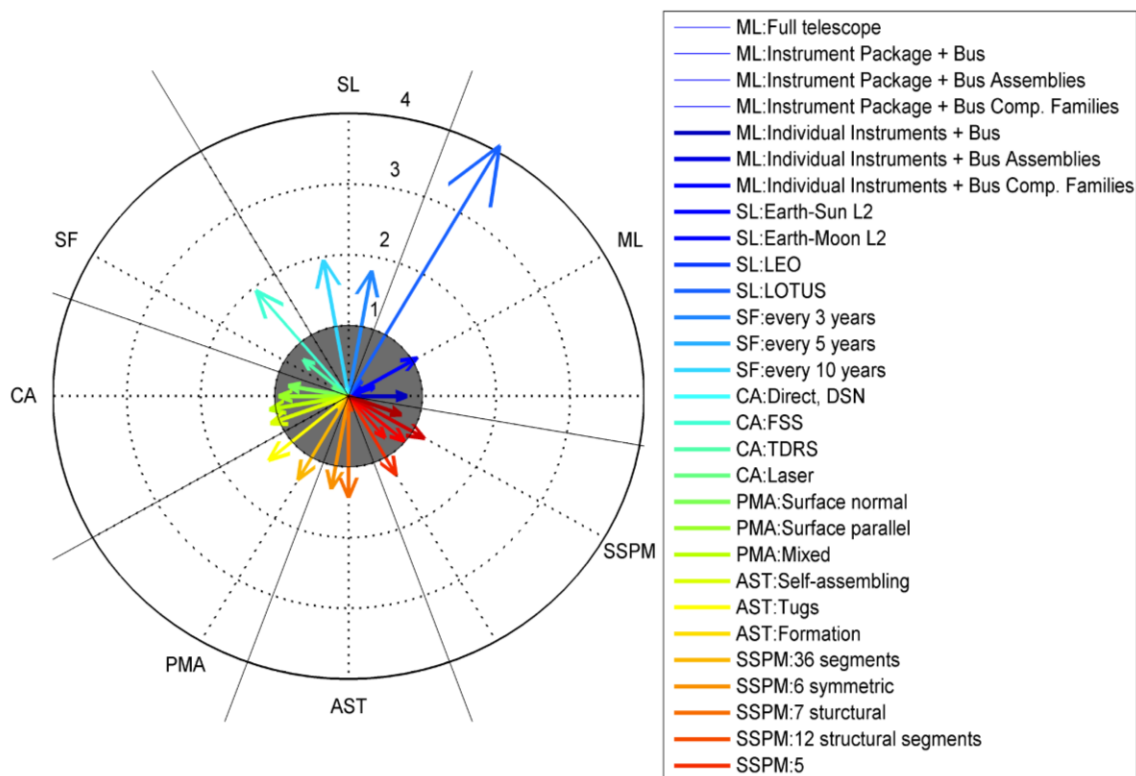


Figure 54: Polar plot indicating frequency of occurrence for every alternative in each architectural decision for Pareto Optimal solutions. ML: Modularity, SL: Servicing Location, SF: Servicing Frequency, CA: Communications Architecture, PMA: Primary Mirror Actuation, AST: Assembly/Servicing Technique, SSPM: Structural Segmentation Primary Mirror Gray circle of radius 1 represents expected radius of any architecture decision if it is not associated with Pareto solutions.

Figure 54 clearly shows that Level 7 (Individual Instruments and Bus Component families) dominates the modularity architectural decision. Both SE-L2 and LEO dominate other solutions

for the Servicing Location decision while a 3-year frequency dominates the Servicing Frequency decision. As such, the “7-1-1” subset of “Pareto Optimal” solutions comprise the dominant alternatives shown in the Polar plot, thereby verifying its close proximity to the utopia point. In other architectural decisions, laser communications is slightly dominant for communications architecture, surface-normal and hybrid assemblies are equally dominant for primary mirror actuation architectures, and space tugs and robotic self-assemblies are also distinctly dominant for assembly and servicing techniques. 36 segments and 12 structural segments are slightly dominant for the decision on mirror segmentation. The large variation in the other 4 architectural decisions thus account for the distribution of architectural solutions in the identified “Pareto Optimal” subset of solutions closest to utopia point.

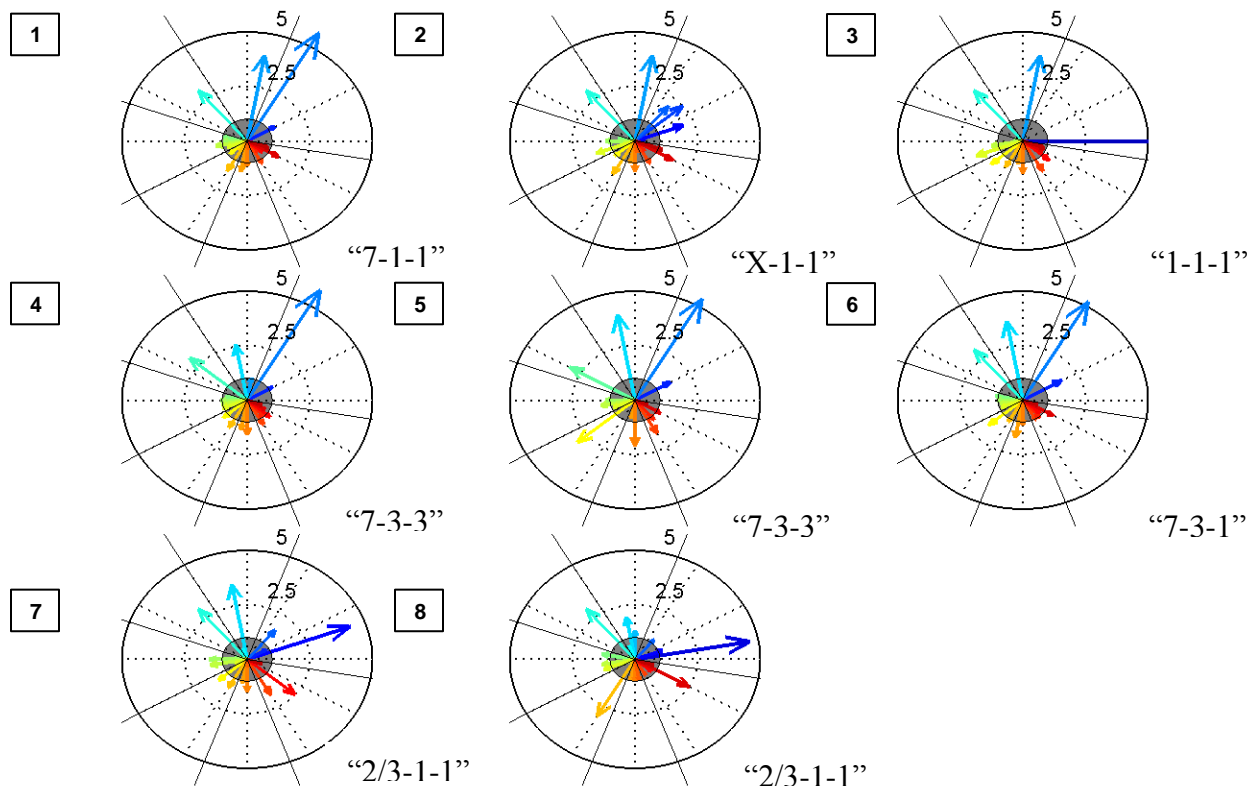


Figure 55: Polar plot array illustrating dominant architectural alternatives in every identified cluster.

The same procedure is then repeated to evaluate the dominant architectural elements in every cluster. An array of Polar plots is shown in Figure 53, where each numbered Polar plot is representative of its corresponding cluster on Figure 52. In Cluster 2, the dominant architectural alternatives are still the Sun-Earth L2 servicing location and a servicing frequency of once every 3 years (“X-1-1”). However, modularity is no longer as dominant in this cluster. In fact, lower levels of modularity become more prominent, and this results in increased cost due to higher launch costs required for high launch masses of instrument packages instead of individual components. As such, the solutions of Cluster 2 are located just to the right of Cluster 1 and in a region with higher normalized cost.

The dominant architectural alternatives in Cluster 3 are Level 1 modularity, SE-L2 servicing location and a servicing frequency of once every 3 years (“1-1-1”). This cluster is located in the top-right region of the tradespace and comprises solutions with generally high cost and high utility to science. Costs are exceptionally high for these solutions, as the lowest level of modularity and the highest frequency of servicing meant replacing the entire telescope once every 3 years. Utility to science is also highest due to regular servicing and replacement of every instrument and component onboard the spacecraft without any downtime.

The architectural alternatives of Level 7 modularity, servicing location at LEO and servicing frequency of one every 10 years dominate the solutions in Cluster 4 (“7-3-3”). Modularity Level 4 is also prominent, thus accounting for the presence of “4-3-3” solutions amongst the majority of “7-3-3” solutions. Cluster 4 is located below and to the left of Cluster 1 because servicing at LEO is a lot cheaper, but it also incurs higher downtime. Also, servicing the telescope once every 10 years means that there is a higher probability that certain instruments or components could fail without being replaced for long periods. This results in a loss of utility to science.

The Polar plot of Cluster 5 is almost similar to Cluster 4 (“7-3-3”), except that it reveals some alternatives for other architectural decisions have become more prominent. “4-3-3” points are also present in this cluster. These alternatives are laser communications architecture, surface-normal primary mirror actuation, assembly and servicing with tugs and 36 mirror segments. Normalized costs of solutions in Cluster 5 are lower than that of Cluster 4 because laser communications and the use of tugs, which are external to the space telescope system, entail lower launch mass. As such, Cluster 5 is located to the left of Cluster 4.

Cluster 6 has modularity level 7, servicing location at LEO and servicing frequency of once every 3 years as the dominant architectural alternatives (“7-3-1”). While it might be cheaper to service at LEO, a much higher frequency of servicing would result in higher total launch costs for the space telescope across its mission lifecycle. As such, the solutions in this cluster would have a higher normalized cost and they are located to the right of Clusters 4 and 5.

Finally, Clusters 7 and 8 are generally characterized by modularity levels 2 and 3, servicing location at LEO and servicing frequency of once every 3 years as the dominant architectural alternatives (“2/3-3-1”). Lower levels of modularity, near-Earth servicing location and high frequency of servicing collectively imply that large instrument packages or component families are being taken out and replaced frequently during its mission lifecycle. The high frequency of servicing drives the normalized costs up, while servicing a minimally modular spacecraft means that downtime will be a common occurrence, leading to lower utility to science. As such, these solutions are located in the region of increasing costs and low utility to science.

Through analyzing the clusters of solutions in the tradespace of “Pareto Optimal” points, it is evident that the architectural decisions of modularity, servicing location and servicing frequency have huge leverage on the spatial distribution of solutions in the utility-cost space. Higher modularity, servicing at its SE-L2 operating location, and high servicing frequency generally drive solutions towards the utopia point. Low modularity will generally drive solutions towards the high cost end while servicing at LEO or at a lower frequency will drive solutions towards the low-cost/low-utility end.

5 architectural solutions were then chosen at random from the “Pareto Optimal” subset (“7-1-1”) and plotted on a Pareto Trace plot shown in Figure 56 to demonstrate that they are always on or close to the Pareto front for all the trade metrics of interest. These points may eventually be recommended architectural solutions, but they have chosen simply for illustrative purposes. The Pareto Trace plot is a collective 3-D representation of tradespaces bounded by the fixed axis of cost and each of the remaining trade metrics to illustrate how a single architectural solution point transits across different tradespaces defined by different metrics. The x-axis defines the number of tradespaces, each defined with different metrics, to be plotted for Pareto tracing. Each tradespace in this plot can have different utopia points.

A “Pareto Optimal” point will thus move along the Pareto front for each tradespace shown in this representation. The 5 chosen points were then traced across the three different tradespaces and the traces demonstrate that these points are always on or close to the “Pareto Optimal” region in each tradespace. Therefore, these “Pareto Optimal points can be shown to have the best tradeoffs for utility to science, downtime and service margin against costs. As such, the Pareto trace plot can facilitate the illustration of the position of an architectural solution relative to other points across multiple tradespaces.

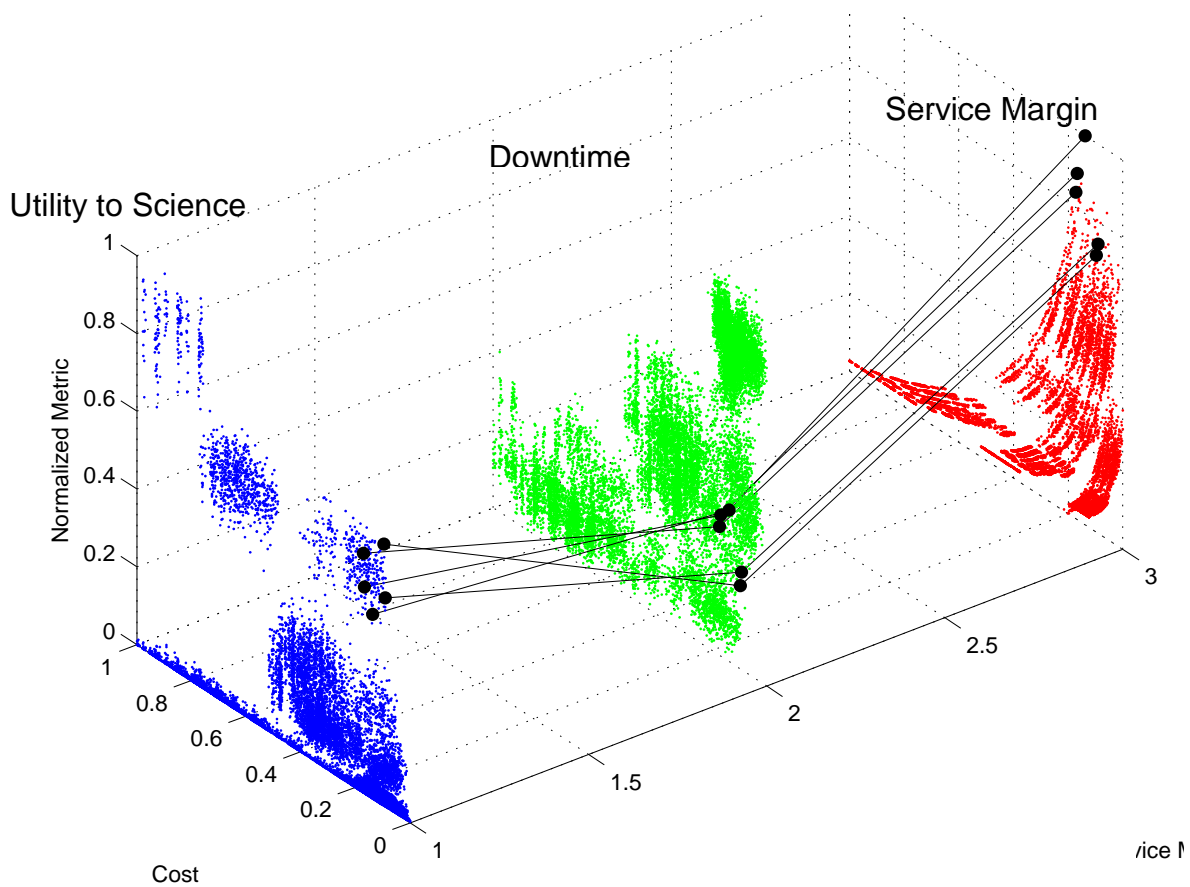


Figure 57: Pareto trace of solutions across different tradespaces defined by combinations of various trade metrics with a fixed bound of cost.

This procedure for tradespace exploration and analysis can be conducted for the other trade metrics like downtime or service margin so that further evaluations can reveal the tradeoffs that are driving the distribution and location of other architectural solutions. However, utility to science versus cost will be the focus of analysis and evaluation at this stage.

7.1.2 3-D Visualization of Tradespaces

3-D visualizations of tradespaces can also be plotted for encompassing illustrative purposes. While 3-D tradespaces are much more difficult to interpret, they are reflective of the inherent tradeoffs between the four metrics of interests. The spatial distribution of solutions within a 3-D space can thus provide new and useful insights into performing evaluation and analysis.

Two 3-D tradespace plots were generated for this illustrative, with the X-Y plane established by the dominant metrics of total lifecycle cost and utility to science. The vertical Z-axis was varied in these two plots, with Failed Downtime and Service Margin as the third metric shown in Figure 58 and Figure 59 respectively. The three metrics in each case have been normalized to compare their interactions on a common quantitative basis. A restructuring of the system design tradespace was also clearly evident with the change in third metric.

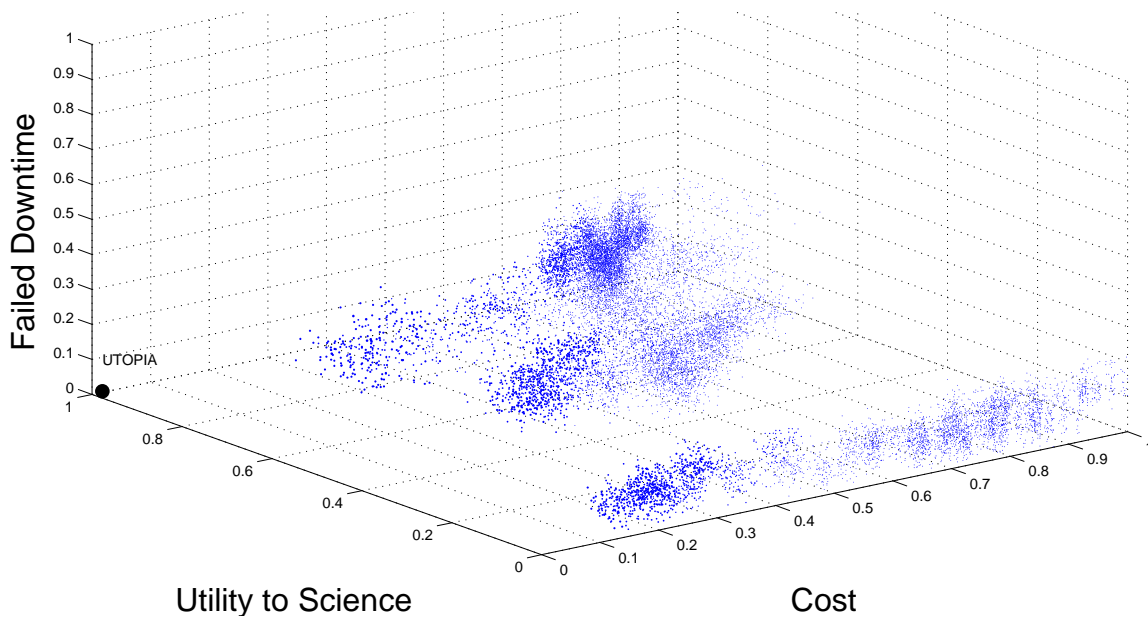


Figure 58: 3-D tradespace of the space telescope bounded by cost, utility to science and failed downtime

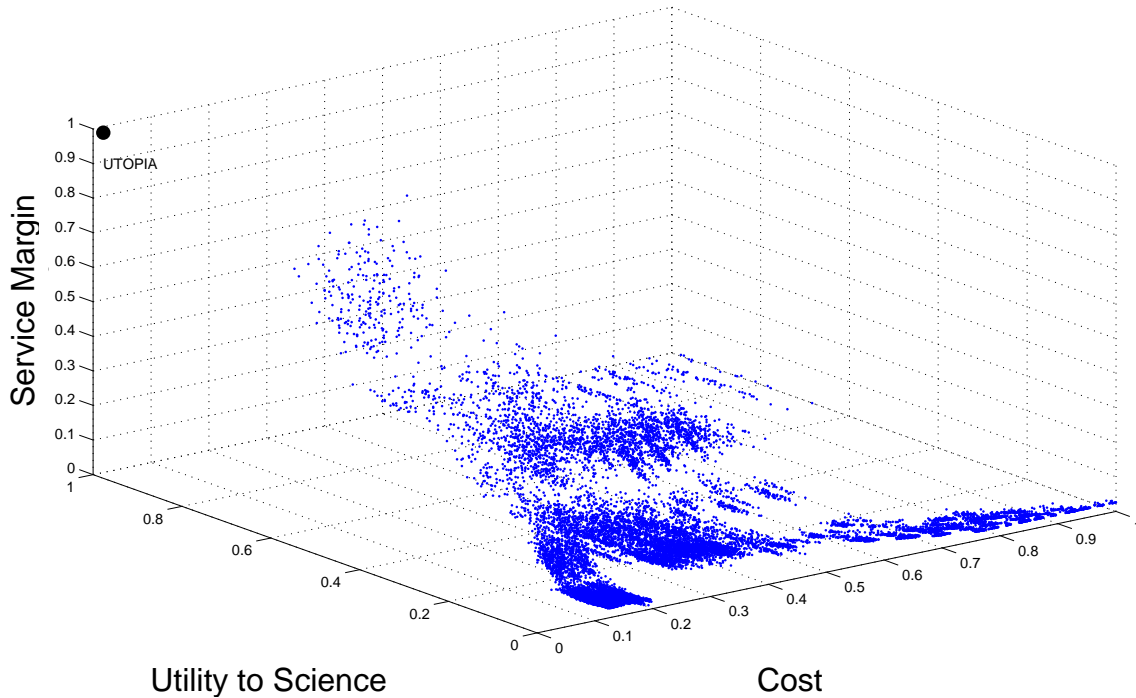


Figure 59: 3-D tradespace of the space telescope bounded by cost, utility to science, and service margin

Figure 59 shows the distribution of the same set of design points restructured by a change in the third metric from downtime to service margin. An elevated slope of design points is observed, with most points concentrated at regions with low utility to science and increasingly sparse sets of points tapering towards the utopian point with low cost, high utility to science and high service margin. This distribution can be explained with the underlying scientific principles and assumptions used to develop the trade metrics of interest in this case. The service margin is a monetary metric, quantified by the baseline cost less the development cost, launch cost and servicing cost. Clearly, the lower the costs of launching a particular service mass, the higher the service margin.

New relationships between the metrics have also been observed from these two plots. The servicing location of the space telescope has a direct impact on its downtime, where Sun-Earth L2 is the best location since there is no change in operating location and subsequently no downtime. This is followed by the Earth-Moon L2 location, the Lotus orbit, and finally LEO as determined by proximity from the designated operating location. Utility to science is generally inversely proportional to downtime. However, the cost to launch servicing mass demonstrates an inverse trend, as it entails the lowest cost for LEO owing to close proximity from Earth and the highest cost for Sun-Earth L2. Therefore, the service margin would be inversely proportional to downtime. Combining these two relationships would then imply that the service margin is directly proportional to utility to science. This implied relationship is thus evident in the upward slope observed in the tradespace of Figure 59 as “Pareto Optimal” design solutions move and taper towards the utopia point.

Instead of a Pareto front, a Pareto surface can be identified in 3D space and the “Pareto Optimal” points are highlighted in red as shown in Figure 62 below. A total of 202 solutions was found in this Pareto set. Dominated solutions can then be removed to yield the filtered tradespace shown in Figure 63. The procedures used to analyze and evaluate tradespaces in 2D can then be applied in the same manner with the added dimensionality.

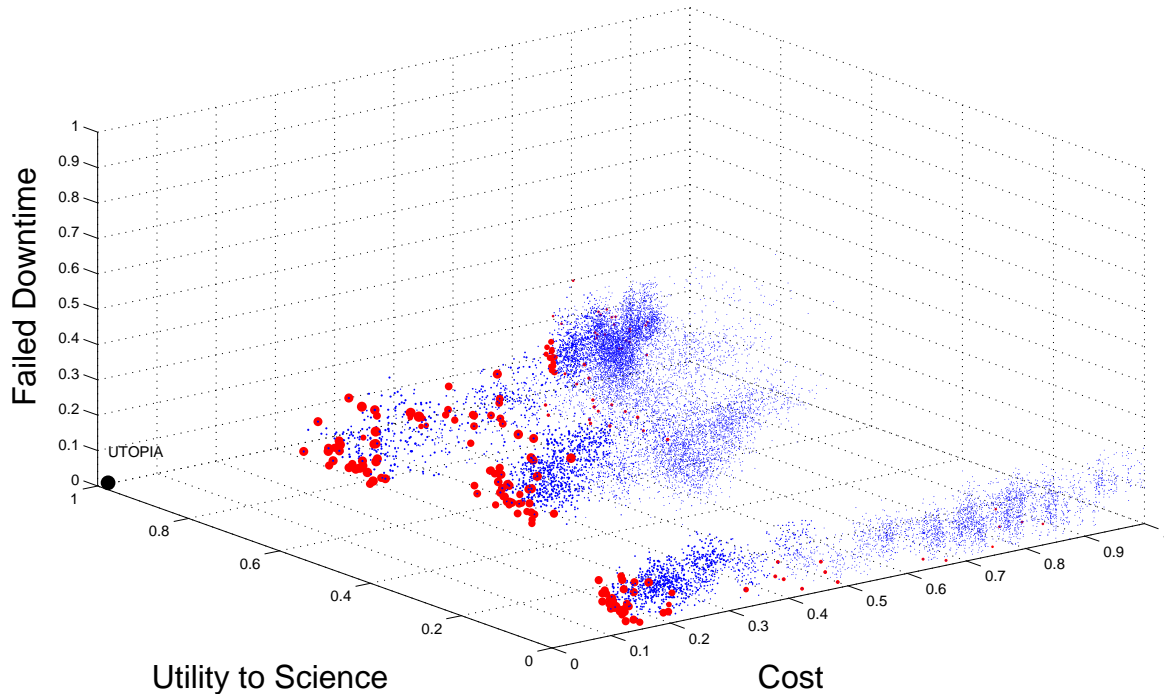


Figure 60: 3-D tradespace of the space telescope bounded by cost, utility to science and failed downtime, with “Pareto Optimal” solutions highlighted in red

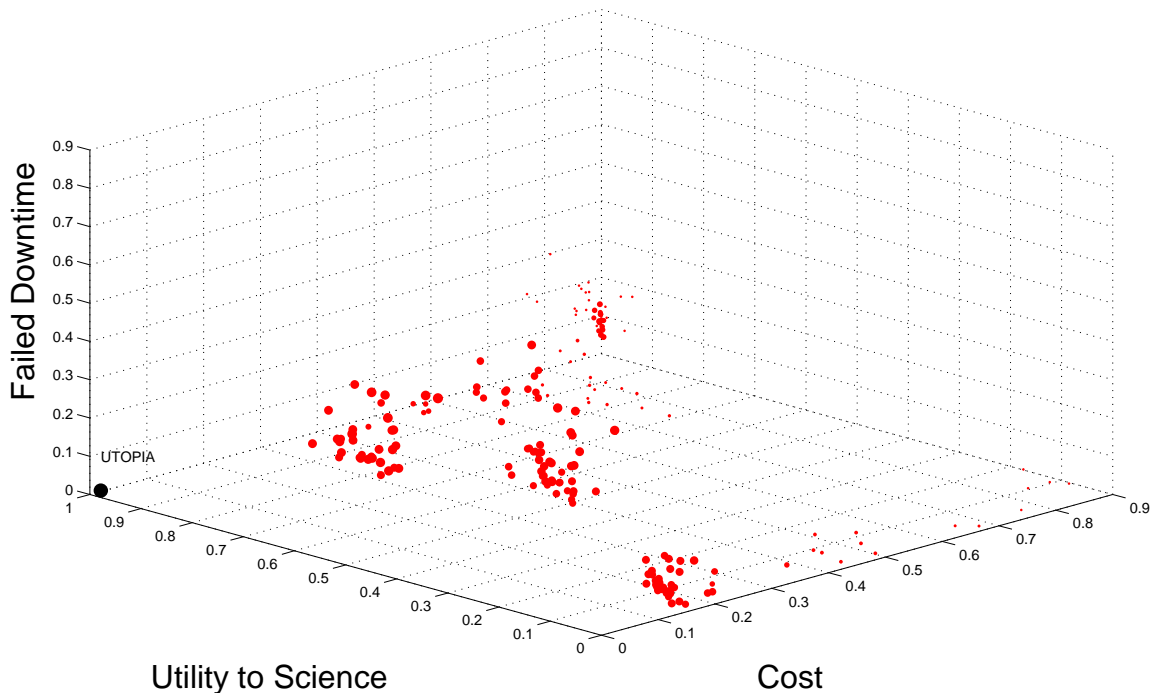


Figure 61: Filtered 3-D tradespace of “Pareto Optimal” solutions for the space telescope bounded by cost, utility to science and failed downtime

Continued exploration and analysis of tradespaces can reveal further complex interactions among trade metrics and architectural decisions. In the evaluation and analysis thus far, architectural solutions with the “7-1-1” configuration of full modularity, SE-L2 servicing location and a servicing frequency of once every 3 years, have been found to constitute the “Pareto Optimal” subset of solutions closest to utopia point. Decreasing modularity generally increases cost due to higher masses of instrument packages required to be launched during every servicing trip. Hence, solutions with lower modularity levels tend to fall on the high-cost/high-utility region of the tradespace.

Servicing locations closer to Earth generally lead to decreased utility to science, as the movement from its original operating location at SE-L2 coupled with high servicing frequency results in increased downtime. As such, solutions with servicing locations at LEO and other alternatives are found in the low-cost/low-utility region of the tradespace. The servicing frequency has a strong proportional impact on cost, but an inversely proportional effect on utility to science. Its variation thus leads to a wide distribution of solutions.

From the analysis of clusters, Polar plots and Pareto trace plots, the effects of different architectural combinations are clearly reflective in the tradespaces. Therefore, tradespace exploration motivates the process of making a priori design or architectural selections that are “Pareto Optimal” through rigorous analysis and consideration of other options.

7.2 Interactions and Main Effects

7.2.1 Science Utility

The main effects plot shows the impact that a single architectural decision has on a particular trade metric. In this case, the trade metric is science utility. Science utility is defined as the contribution of the spacecraft to the scientific community and is calculated by taking the integral of the sum of the field of view multiplied by the throughput of all the science instruments on the spacecraft.

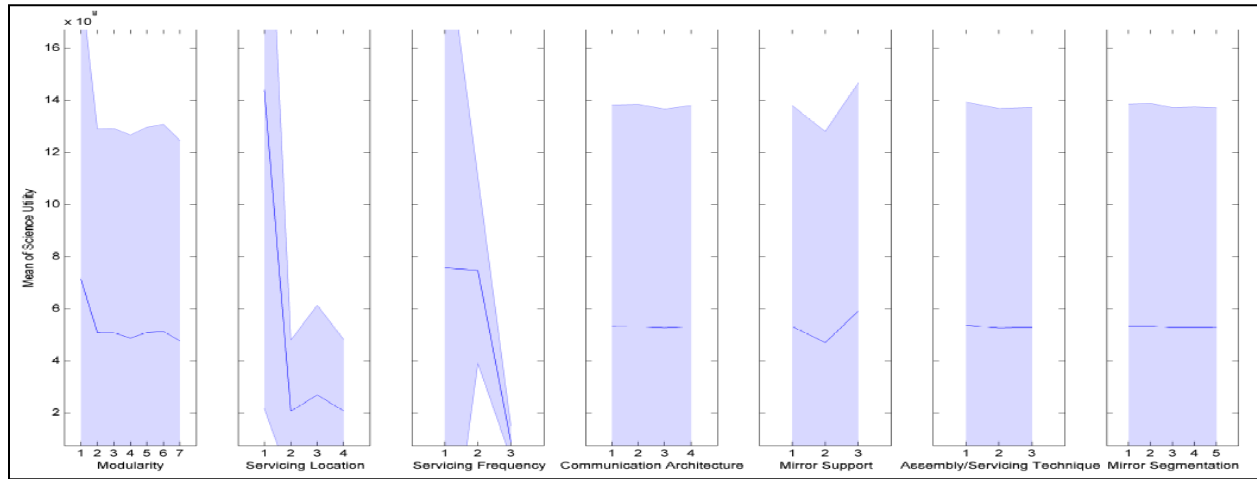


Figure 62: Main effects plot for Science Utility

With respect to modularity level, modularity level 1 is the most useful for science utility while the rest of the modularity levels exhibit approximately the same level of science utility. This occurs because modularity level 1 requires the entire satellite to be replaced, which will rapidly upgrade the science capability: 3-D tradespace of the space telescope. With respect to servicing location, SE-L2 is by far the most useful to science. This is attributed to the fact that the telescope does not have to relocate to be serviced, thus the bounded by cost, utility to science, and failed downtime value is minimized. With respect to the servicing frequency, servicing every three years provides the greatest science utility while servicing every ten years provides a drastically lower science utility. This occurs because shorter frequencies allow for the satellite to be repaired and upgraded more frequently. With respect to communication architecture, no major effects were observed. With respect to mirror support method, mixed surface-normal and parallel actuators provide the most utility to science because they allow for a more effective actuation capability. The surface-parallel option provides the lowest science utility because of the low MTBF values associated with this system. For the servicing and assembly technique, as well as the segmentation method, no major effects were observed.

An interaction plot was generated to show the effect that each architectural decision, in combination with every other architectural decision, had on the total science utility. Because there are seven architectural trades being conducted, the resulting plot was a 7-by-7 grid of graphs, with each sub-plot showing the impact that a given combination of two architectural trades have on science utility. Each row of the plot grid represents one set of architectural trades as data sets, with the number of distinct lines equal to the number of different architectures

within that tradespace. Each column of the plot grid represents the architectural decisions within that particular tradespace as distinct points along the independent axis. For all plots, science utility is represented on the dependent axis.

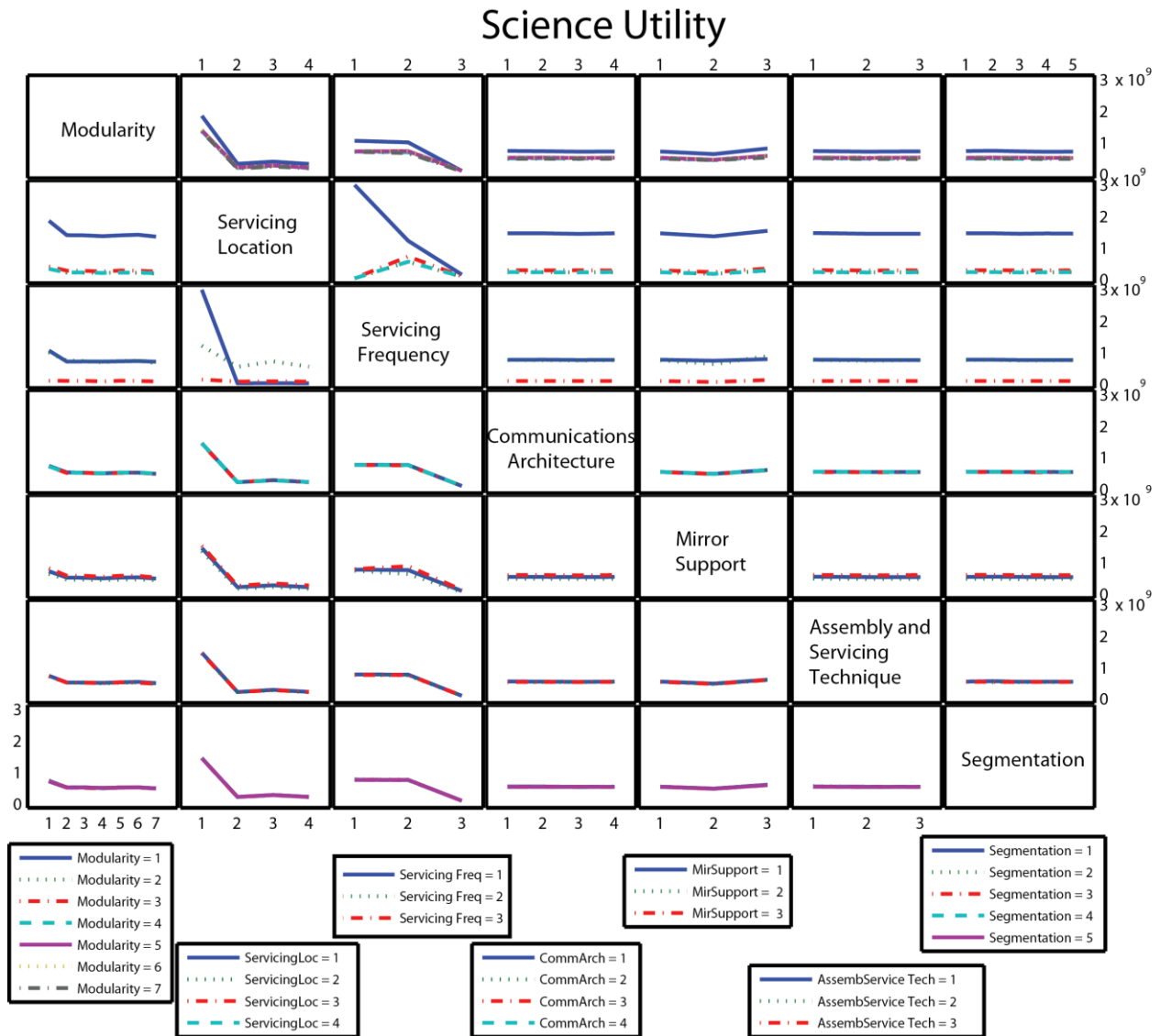


Figure 63: Interaction plot for Science Utility

The most interesting plot encompassed within the graph above shows the interaction between the servicing location and the servicing frequency. The servicing location of SE-L2 provides the greatest science utility when a servicing frequency of three years is used because SE-L2 requires no down time for transit to the servicing location. The science utility falls as the servicing frequency is decreased causing more parts of the space telescope to fail. For all of the other servicing locations, the servicing frequency of three years provides a low science utility because of the tremendous amount of time spent in transit. In these cases, the ten year servicing frequency also causes a low science utility because of the bounded by cost, utility to science, and

failed parts. The 5-year servicing time strikes an optimal balance for architectures serviced somewhere other than SE-L2.

7.2.2 Cost

The main effects plot shows the impact that a single architectural decision has on a particular trade metric. In this case, the trade metric is cost.

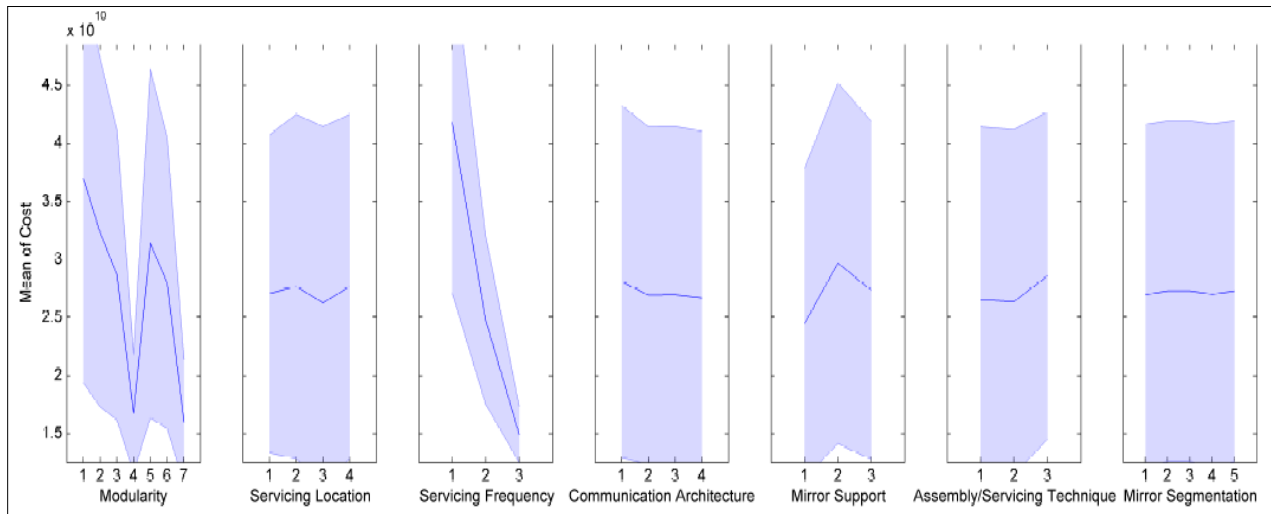


Figure 64: Main effects plot for Cost

Cost most strongly depends on servicing frequency and modularity. Servicing frequency directly affects the number of servicing missions. With each additional servicing mission, the cost will increase due to an additional launch and additional mass being added to the telescope to replace broken or unreliable components. Modularity affects the mass that is replaced in each servicing mission. When many components are grouped together in one module, the entire module must be replaced when any component in the module fails or becomes unreliable. Therefore, as modularity increases, less and less mass is replaced over the lifetime of the telescope. With less mass being replaced, fewer additional components need to be developed and lower cost launch vehicles can be used for each servicing mission. Of the remaining architectural decisions, the biggest dependency is on mirror support method and this dependency is entirely caused by the varying number of actuators involved in the mirror actuation techniques. The remaining architectural decisions (servicing location, communications architecture, Assembly/Serviceing Technique, and Mirror Segmentation) have little direct effect on cost.

These interaction plots show the same information as the interaction plots above except for the trade metric of cost.

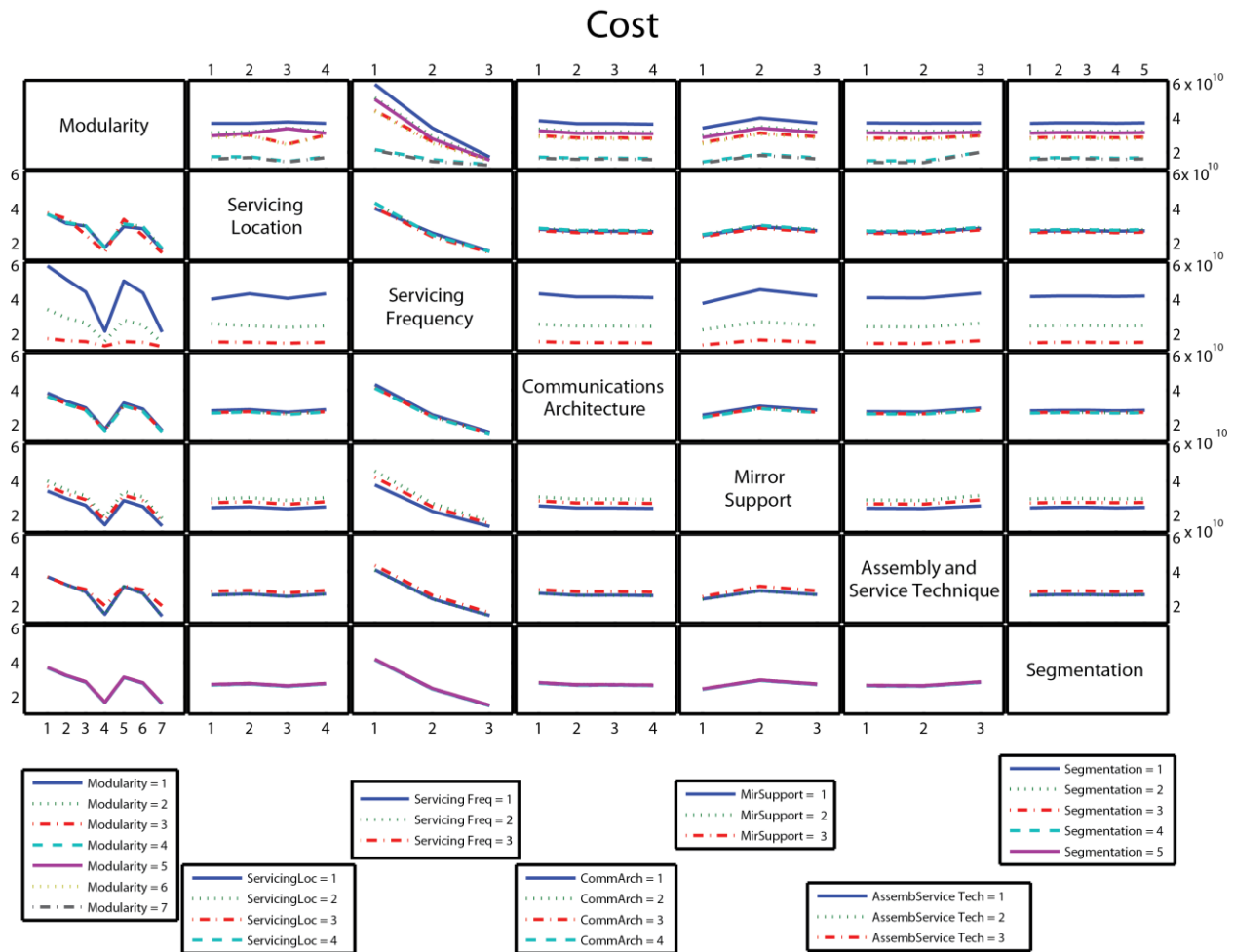


Figure 65: Interaction plot for Cost

With respect to the interaction between servicing frequency and modularity level, the higher the modularity level of the spacecraft, the less expensive that it will be. However, the cost gap between levels of modularity is greater for more frequent servicing than for less frequent servicing. This dependency on servicing frequency exists because the proportional cost of replacing large modules when only a few components within have failed is decreased with less frequent servicing because modules will tend to have more components that need servicing. Another interesting dependency is the divergence between modularity levels 3/6 and 2/5 for servicing at LEO. This divergence occurs because servicing missions using higher modularity levels and servicing at LEO are able to use smaller rockets whereas servicing missions associated with lower modularity still need to use larger more expensive rockets to move large amounts of mass into LEO and have the added cost of moving the space telescope over large distances. Lastly, there is a small dependence of cost for high modularity levels on assembly/servicing technique. The swarm assembly/servicing technique adds additional equipment necessary for assembly to each module, increasing the mass and cost.

7.2.3 Servicing Margin

The main effects plot in Figure 66 shows the impact that each architectural trade had on down time. Servicing margin was defined as cost difference between the “baseline” design for a given

set of architectural decisions – that is, the design with a monolithic bus (modularity level 1) – and an identical design with a higher level of modularity, normalized by the total mass that can be launched across all of the servicing missions.

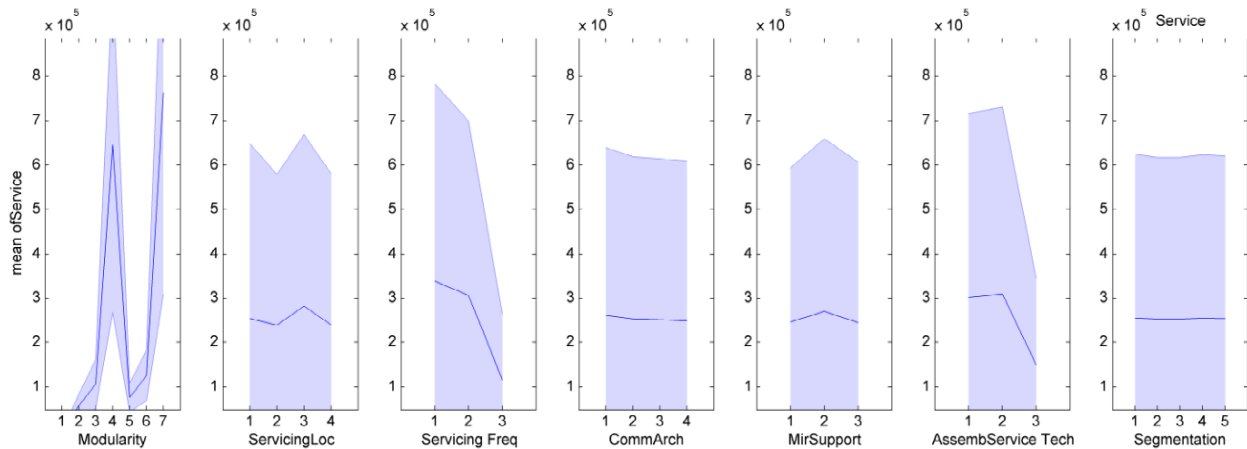


Figure 66: Main effects plot for Servicing Margin

As can be seen from the main effects plot, not all architectural trades had a significant impact on the total mission down time. In particular, Communications Architecture and Mirror Segmentation Method showed nearly flat trends across the different design decisions within those trades. Meanwhile, Modularity Level, Servicing Frequency, and Assembly/ Servicing Technique showed noticeable trends across the different design decisions within those trades.

An interaction plot was generated to show the effect that each architectural decision had on the total servicing margin. Because there are seven architectural trades being conducted, the resulting plot was a 7-by-7 grid of graphs, with each sub-plot showing the impact that a given combination of two architectural trades had on serviceability. Each row of the plot grid represented one set of architectural trades as data sets, with the number of distinct lines equal to the number of different architectures within that trade-space. Each column of the plot grid represented the architectural decisions within that particular trade-space as distinct points along the independent axis. For all plots, servicing margin was represented on the dependent axis.

7.2.3.1 Modularity

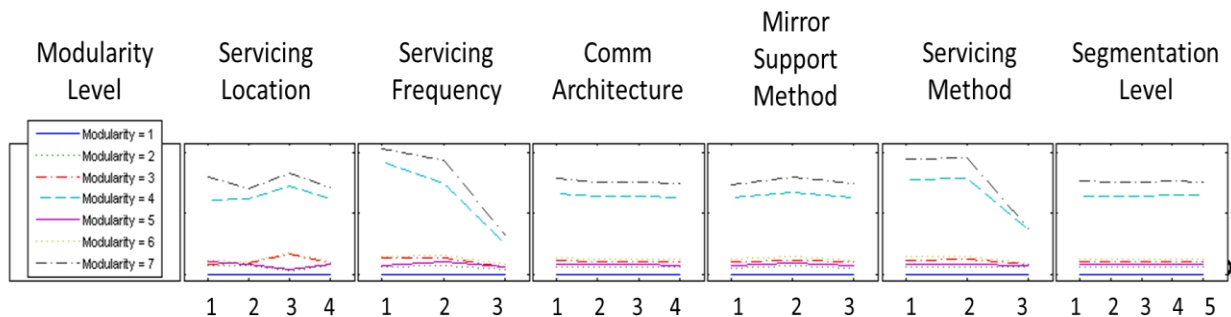


Figure 67: Service margin trends for different modularity levels

It was observed across all of the interaction plots that modularity levels 4 and 7 had the highest servicing margins. This corresponds to the two most modular design options: modularity level 4

represents a single instrument package with separate structures for each component family; modularity level 7 represents individual instruments packages with separate structures for each component family. Modularity level 7 was the most serviceable across all other design trades, since individual instruments are less costly to service/replace than a single, integrated instrument package.

7.2.3.2 Servicing Location

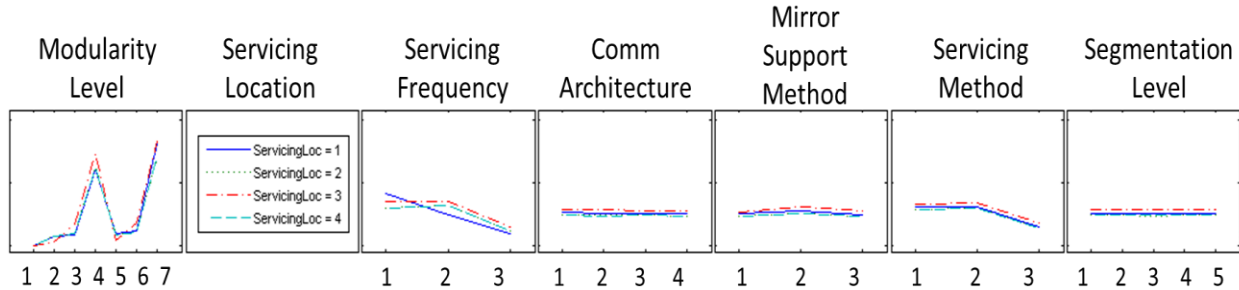


Figure 68: Service margin trends for different servicing locations

Results showed that of the four servicing locations, LEO (servicing location 3) generally provided the most servicing margin. However, interesting trends were detected when looking at both servicing location and servicing frequency. For a servicing frequency of 3 years, servicing at Sun-Earth L2 (servicing location 1) provides the most servicing margin. For servicing frequencies of 5 and 10 years, servicing in LEO provides the most servicing margin. This is thought to happen because the serviced mass at LEO is lower than the serviced mass at other locations as the telescope will use electric propulsion to get to/from LEO. That is, for a fixed payload mass launched to orbit, the mass of propellant required to refuel the telescope for its return journey to L2 is lower than the mass of chemical propellant that would be required to propel the servicing probe to any location outside of LEO. This leads to the launch cost/kg is lowest at LEO.

7.2.3.3 Servicing Frequency

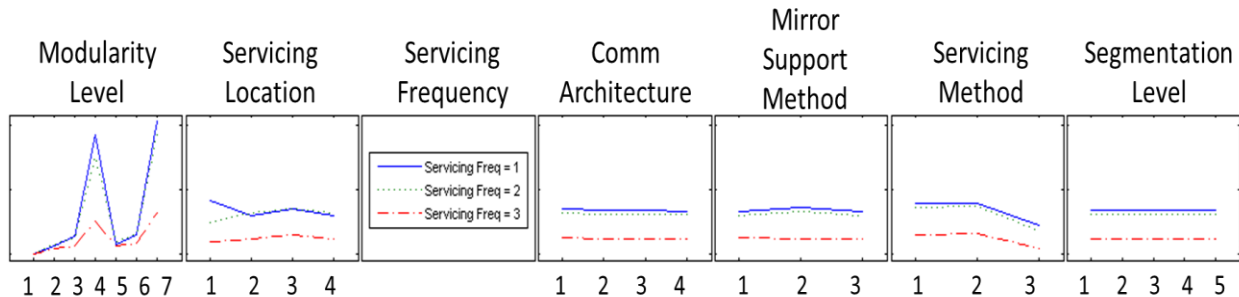


Figure 69: Service margin trends for different servicing frequencies

As can be seen in the above figure, shorter servicing frequencies lead to more servicing margin. The shortest servicing frequency – three years between servicing missions – consistently has the highest servicing margin for all architecture combinations. Likewise, the longest servicing frequency – 10 years between servicing missions – has the lowest servicing margin for all architecture combinations. This is thought to happen because having frequent servicing missions

leads to fewer components being replaced per mission, which cheaper rocket with lower payload capacities can be used. Infrequent servicing missions would be replacing more components per mission, requiring launch vehicles with larger payload capacities.

7.2.3.4 Communications Architecture

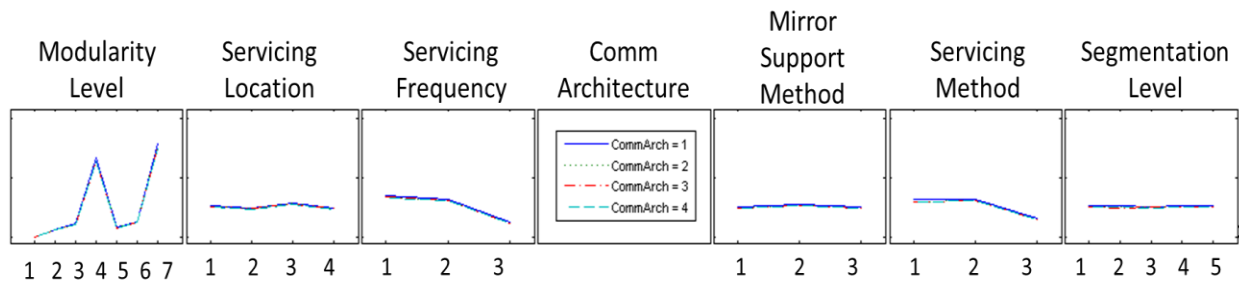


Figure 70: Service margin trends for different communications architectures

Communications architecture has little impact on servicing margin across all other design trades. Communications architecture 1 (DSN) is marginally better than the other three options, which is interesting because it the most massive and most expensive out of the four possible architectures, and therefore should have the lowest servicing margin.

7.2.3.5 Mirror Support Method

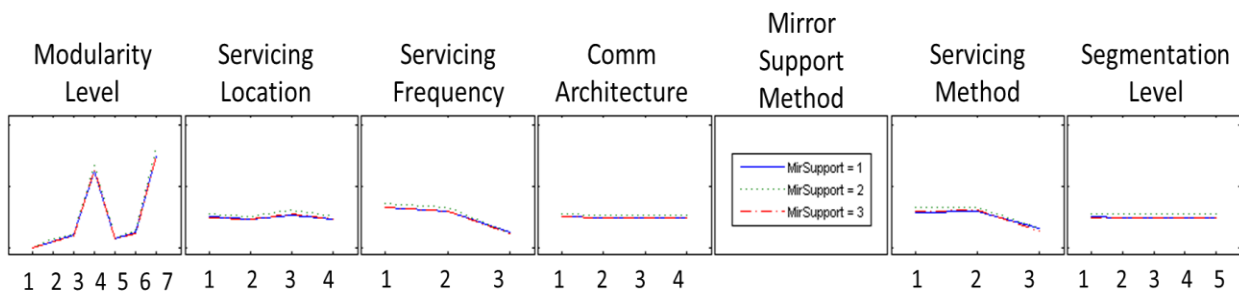


Figure 71: Service margin trends for different mirror support methods

The Mirror Support Method trade also showed little variation across the three possible architectures. Results showed that support method 2 (surface parallel) was provided a marginally higher servicing margin than the other two support methods. This is because the surface parallel support method lacks a back-structure, and therefore has the lowest mass of the three options.

7.2.3.6 Assembly/Service Technique

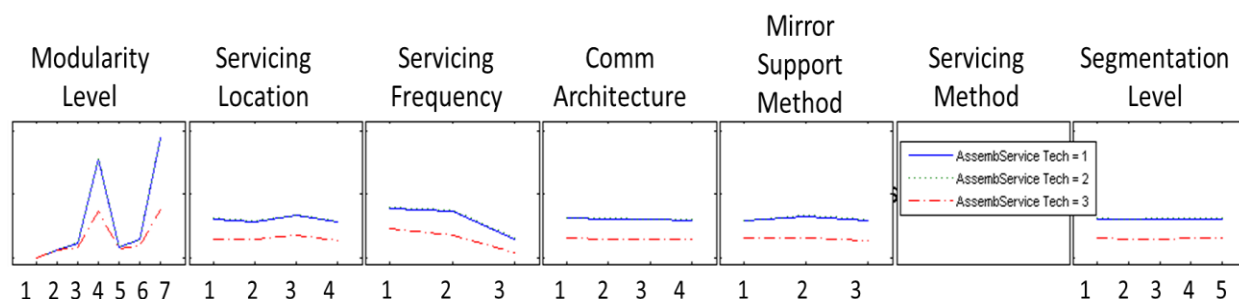


Figure 72: Service margin trends for different assembly/service techniques

Assembly/Servicing Technique had a noticeable impact on servicing margin. Techniques 1 and 2 (self-assembly and tugs, respectively) had the highest servicing margins and were nearly identical. Servicing technique 3 (formation flying individual components) had drastically lower servicing margins across all other design trades. Of the three options, servicing technique 2 had the highest servicing margin. It is believed that this is because tugs have the lowest cost.

7.2.3.7 Mirror Segmentation

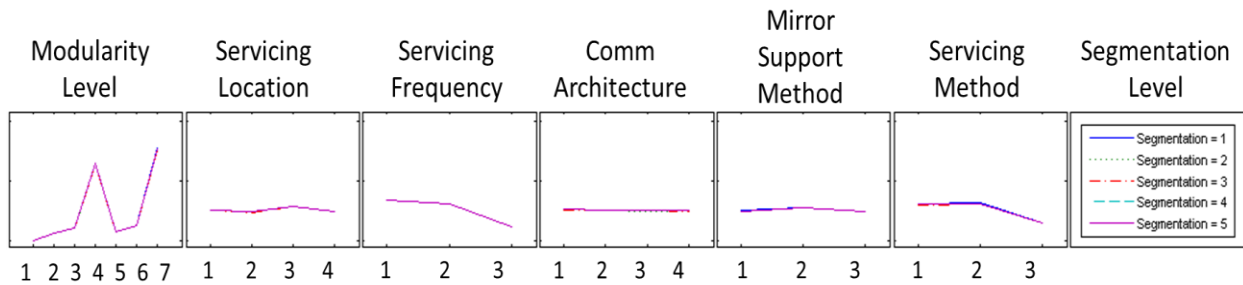


Figure 73: Service margin trends for different mirror segmentation methods

Mirror segmentation has no noticeable effect on servicing margin, as can be seen by the fact that the lines for all five segmentation types overlay each other.

7.2.4 Downtime

The main effects plot shown in Figure 74 shows the impact that each architectural trade had on downtime. Failed downtime is a combination of the time during which no science can be done due to the failure of a component and the time it takes to complete a servicing mission.

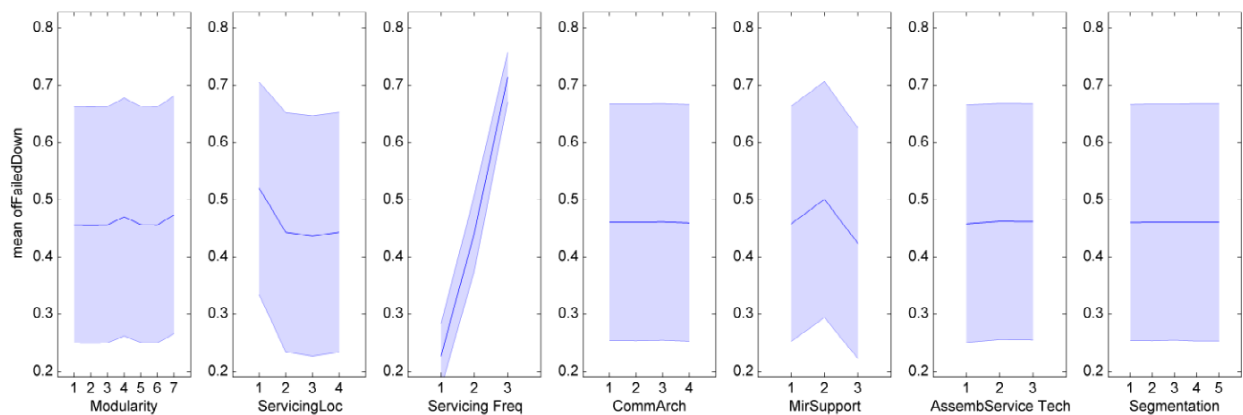


Figure 74: Main effects plot for Downtime

As can be seen from the main effects plot, not all architectural trades had a significant impact on the total mission down time. In particular, Communications Architecture, Assembly/Servicing Technique, and Mirror Segmentation Method showed nearly flat trends across the different design decisions within those trades. Meanwhile, options within the Servicing Frequency trade showed a significant variation between each other, with the most frequent servicing option (3 years between missions) having the least amount of failed down time, and the least frequent servicing options (10 years between missions) having the highest amount of failed downtime.

7.2.4.1 Modularity

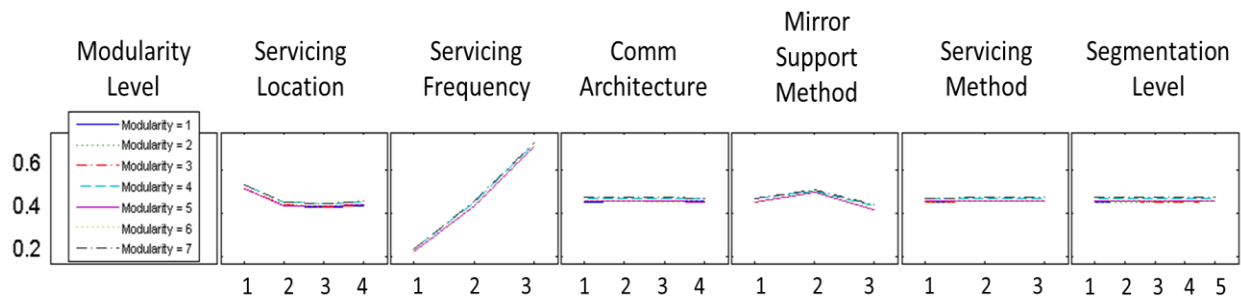


Figure 75: Downtime trends for different modularity levels

The above graphs show that there is little difference in down time between the different modularity levels. Modularity levels 4 and 7, the two most modular levels, have marginally higher down times than the other options. This is due to the fact that more modules require longer time to service.

7.2.4.2 Servicing Location

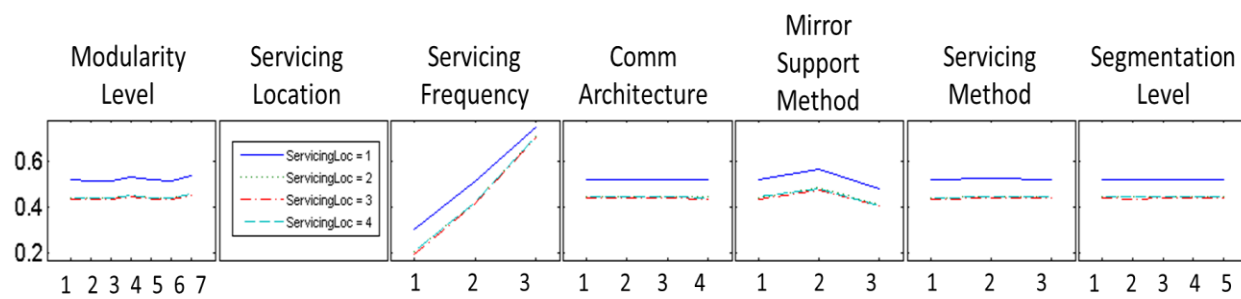


Figure 76: Downtime trends for different servicing locations

Servicing location 1 (in-situ servicing at Sun-Earth L2) has the highest amount of down time out of the four locations. This trend is interesting, considering the travel time from Earth orbit to SE-L2 is shorter than the transit time from ES-L2 back to Lunar or Earth orbit, by about 40 days. LEO, lunar, and LOTUS servicing locations all have similar down times. This makes sense, because the transit times from Earth-Sun L2 to these three locations are similar to within a few days.

7.2.4.3 Servicing Frequency

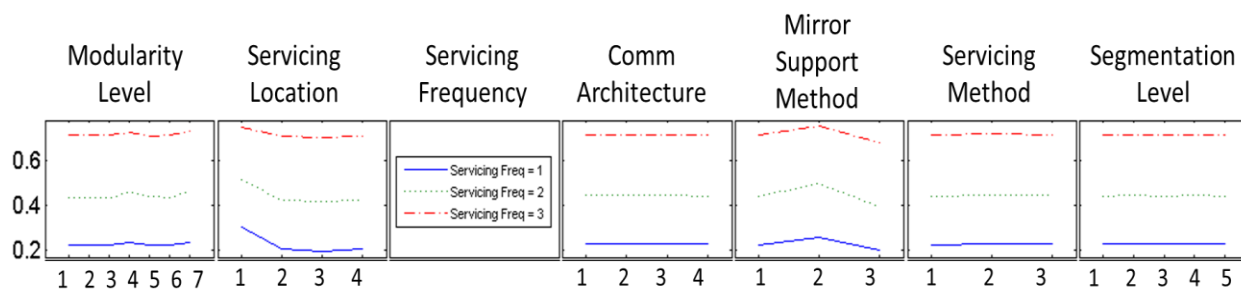


Figure 77: Downtime trends for different servicing frequencies

As mentioned in the discussion of the Main Effects plot, the total percentage of failed downtime increased with time between servicing missions. The lowest servicing frequency, 3 years between missions, has the lowest amount of failed down time. The highest servicing frequency, 10 years between servicing missions, has the highest amount of failed down time. If more time is allowed between servicing missions, more components are going to fail, leading to reduced science capacity.

7.2.4.4 Communications Architecture

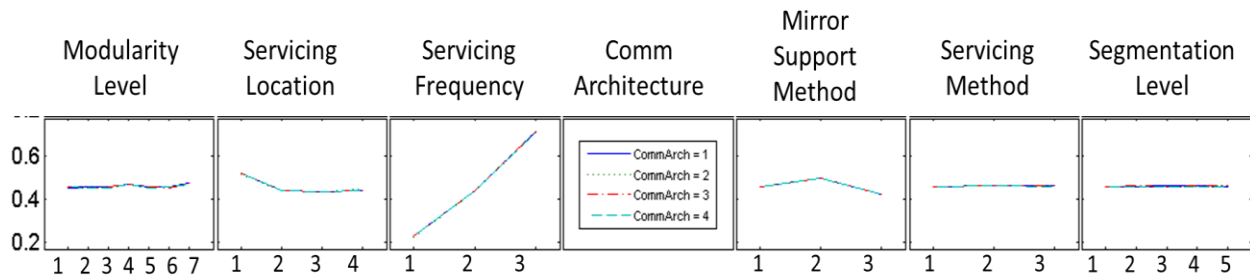


Figure 78: Downtime trends for different communications architectures

There were no noticeable differences between the downtime that resulted from different communications architectures.

7.2.4.5 Mirror Support Method

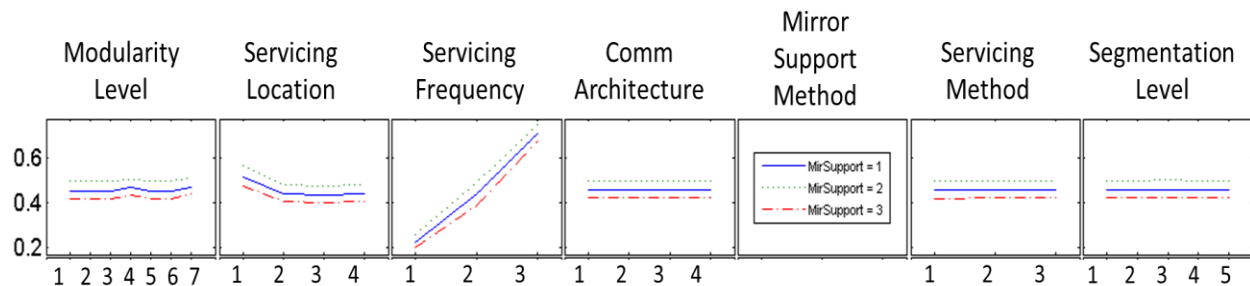


Figure 79: Downtime trends for different mirror support methods

Mirror support method 2 – surface parallel actuators – had the highest downtime out of the three options. Support method 3 – mixed surface normal and surface parallel actuators – had the lowest amount of down time.

7.2.4.6 Assembly/Service Technique

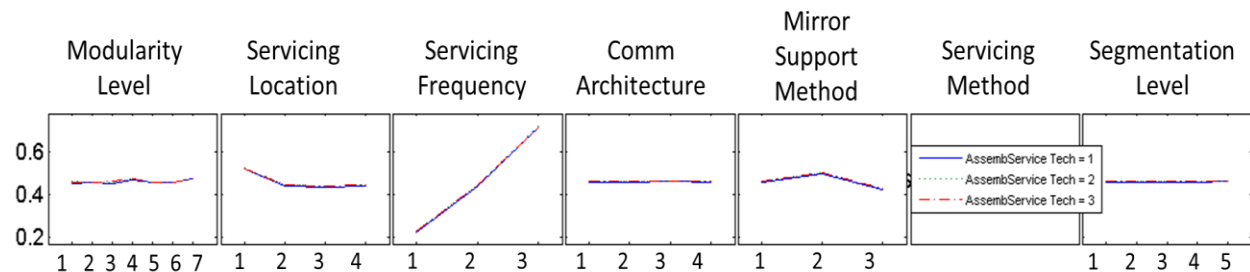


Figure 80: Downtime trends for different assembly/service techniques

There were no noticeable differences between the downtime that resulted from different assembly/servicing techniques.

7.2.4.7 Mirror Segmentation

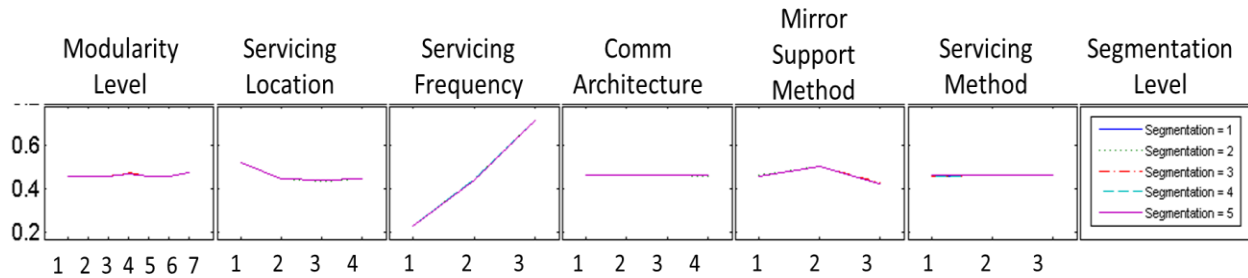


Figure 81: Downtime trends for different mirror segmentation levels

There were no noticeable differences between the downtime that resulted from different mirror segmentation levels.

7.3 Tradespace Characterization

7.3.1 Principle Component Analysis (PCA)

A principle component analysis was performed in order to determine the trade metrics that contributed the most to the overall variation. Principle component analysis decomposes a vector space into orthogonal components, the first of which maximally explains the variation in the data. Successive components explain the maximal amount of remaining variation under the constraint that they must be orthogonal to all previous components. Singular value decomposition (SVD) was used to deconstruct the trade space into principle orthogonal components and associated eigenvalues. The magnitude of the eigenvalue corresponds to the amount of variation explained by that component.

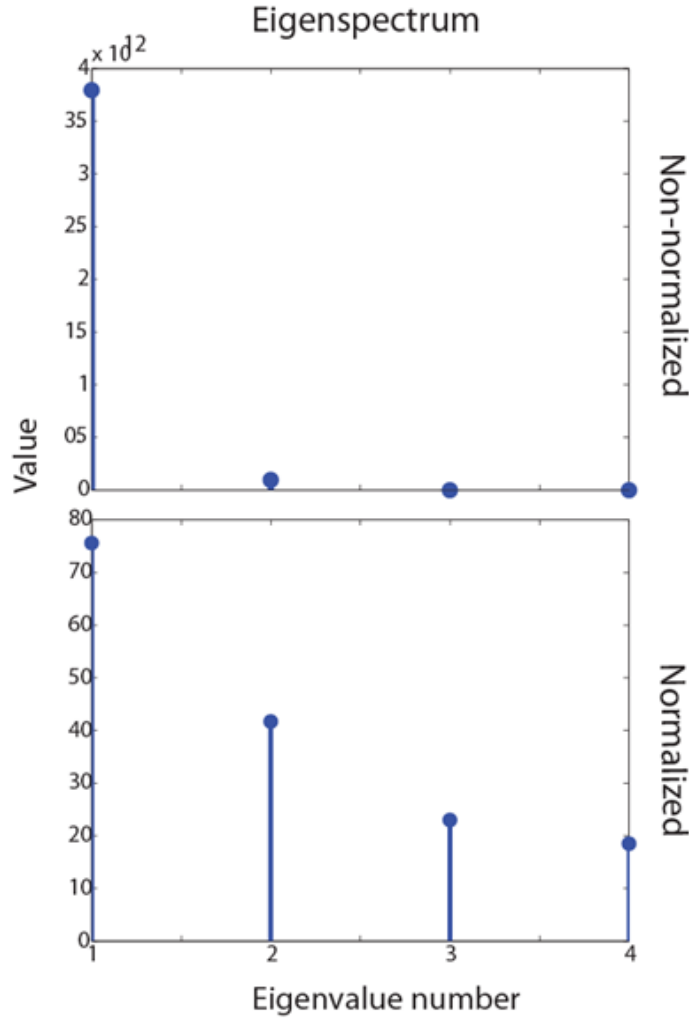


Figure 82: Eigenspectrum of non-normalized (top) and normalized trade metrics after performing PCA.

The eigenvalues corresponding to the first four principle components are shown in Figure 81. The principle component analysis was performed on the raw output trade metrics from our model. We found that the variation in certain trade metrics (particularly cost) was so large that they dominated the eigenspectrum. In order to address this large variation we performed a normalization of the trade metrics as seen in Eq. 88.

$$N_n = \frac{N_o - \min(N_o)}{\max(N_o - \min(N_o))}$$

Eq. 88

In order to assess which trade metrics contributed the most to the trade space variation, the sum over all eigenvalues for each eigenvalue multiplied by the eigenvector component corresponding to each trade metric was determined per the equation below as seen in Table XXXII.

$$\sum_{i=1}^{i=n} \lambda_i v$$

Eq. 89

Trade space analysis should be performed on trade metrics that are independent, and this analysis allows proper testing of this assumption. It is apparent that cost and failed downtime are primary drivers of tradespace variation. Complexity also appears to be an important factor in tradespace variation (Table XXXIII), but since it makes a small contribution to cost. As such it was not considered as an independent trade metric.

Table XXXII: Contributions of Each Trade Metric to Overall Variation

Trade Metric	Relative Contribution
<i>Cost</i>	47.4
<i>Science Utility</i>	23.6
<i>Service Margin</i>	23.5
<i>Failed Downtime</i>	66.8

Table XXXIII: Contributions of Trade Metrics to Overall Variation including Complexity

Trade Metric	Relative Contribution
<i>Cost</i>	45.3
<i>Science Utility</i>	23.6
<i>Complexity</i>	53.4
<i>Failed Downtime</i>	62.8

7.3.2 Hierarchical Clustering

As a next step in determining the overall structure of the tradespace, hierarchical clustering was performed on the entire tradespace as well as on the Pareto efficient architectures (Figure 82).

This hierarchical clustering was performed on the normalized trade metrics (between 0 and 1). We see two important features, clustering corresponding to similarities in trade metrics (top dendrogram) and similarities corresponding to architectural decisions (left dendrogram). It is apparent from both principal component analysis and hierarchical clustering that our four trade metrics can be reduced to two independent metrics.

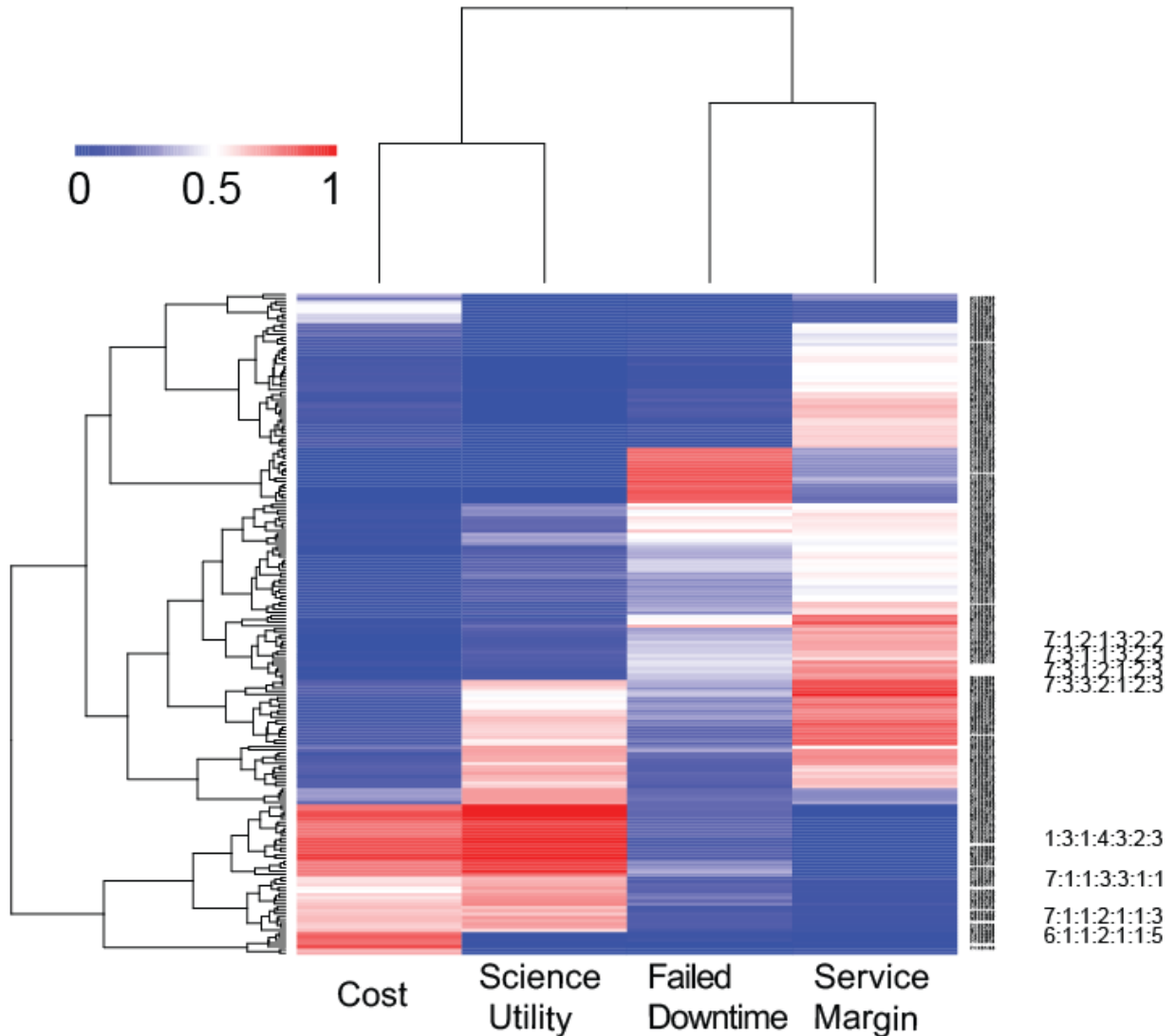


Figure 83: Hierarchical biclustering of Pareto Architectures. There are two main clusters for our trade metrics (1) cost and utility to science (2) failed downtime and service margin. There are also emergent clusters for different Pareto architectures (hierarchical branches on the left) In particular we identify the 7-1-1 set of architectures that was determined to have a high amount of science utility at relatively low cost.

Looking more globally at an assortment of trade metrics and performance metrics collected, it is apparent that there are three primary clusters of trade metrics (Figure 83). Weighting trade metrics according to their relatedness, as quantified in the dendrogram, achieves a similar function to using PCA to deconstruct maximally independent metrics. This approach has the benefit of not being constrained by an orthogonality requirement, and offers a novel means of rationally weighting the contributions of each trade metric or identifying maximally independent trade metrics from a set of performance metrics.

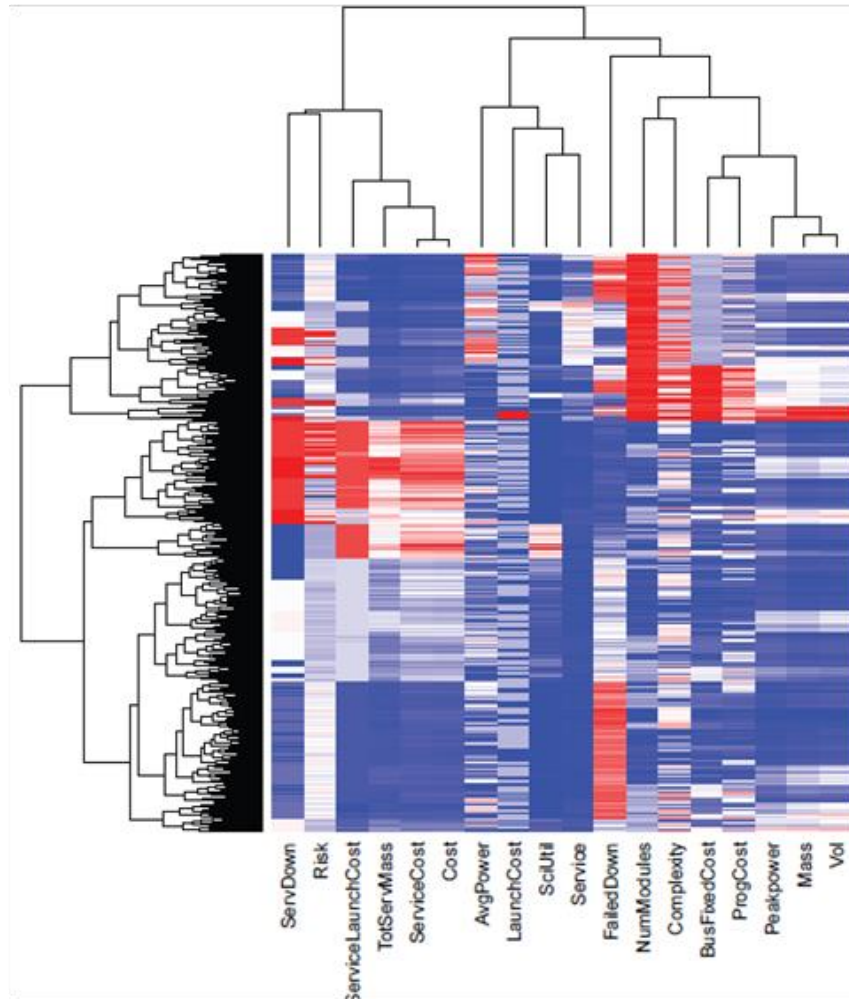


Figure 84: Hierarchical biclustering of all architectures and performance metrics. There are three main clusters for our trade metrics (1) cost and risk dominated (2) science utility and servicing dominated. (3) mass, volume, and complexity dominated. There are also emergent clusters for different architectures (hierarchical branches on the left).

7.4 Sensitivity Analysis

An analysis was conducted in order to understand the model's sensitivities to a selected number of assumptions/design parameters. Sensitivity analysis was performed on assumptions that effected many code modules that were hypothesized to directly impact trade metrics and/or were implemented in the model in such a way it was efficient to vary design parameters and run multiple iterations. These assumptions included the mean time between failure (MTBF) of all components and the Reliability Threshold at which servicing of a component will occur.

7.4.1 Assumptions

This section describes the design parameters or assumptions that were varied in order to conduct the sensitivity analysis.

7.4.1.1 Component MTBF

Component MTBF levels are provided for each component in the model, and are located in the Component Family DB; these values are based on years of lifetime and reliability values from data sheets, or estimates where data sheets are not available or where components leverage to-be developed technologies without existing MTBF analyses. Component MTBF values are used in the calculations of initial system cost and the failure rates. For the sensitivity analysis, the MTBF value for each component was increased or decreased by a certain percentage (this change is constant for all components within a single run). In order to implement this analysis, an MTBF multiplier was added into the code for each sensitivity run to increase or decrease the MTBF values of all of the components by the specified amount. The MTBF multiplier was run at values of [0.50, 0.85, 0.90, 0.95, 1.00, 1.05] to investigate a range of component MTBF values and understand how those values impact the model output.

7.4.1.2 Reliability Threshold

The Reliability Threshold is the threshold at which a decision is made to perform servicing on a non-failed component. During each servicing mission, if a component's reliability has dropped below the reliability threshold, it is replaced. This value is a representation of a program management decision of how far mission managers are willing to allow a component to degrade in reliability before replacement. This design parameter impacts serviced mass and failed downtime. For the sensitivity analysis, the Reliability Threshold was varied over the range of [0, 0.50, 0.60, 0.65, 0.70, 0.75, 0.80, 0.90, 1] in order to investigate a broad range of possible values for the Reliability Threshold. The two extreme values (0 and 1) were selected in order to examine the effect on telescope performance of the two extremes of the programmatic decision of when to service components. A reliability threshold of 0 indicates that components are never serviced due to low reliability; they are only serviced when they fail. A reliability threshold of 1, on the other hand, indicates that every component will be serviced during every mission, since any period of operational time will decrease a component's reliability below 1. The intermediate values were chosen to examine the range of reliability threshold values surrounding the nominal model value of 0.7, using two steps of 0.05 followed by a step of 0.1 in both directions.

7.4.1.3 Instrument Growth Rate Sensitivity

To examine the effect of varying rates of growth of discovery efficiency, each of the four instruments was assigned a different discovery efficiency growth rate by altering the baseline value of 0.3218 from Baldesarra¹³. Instrument A was assigned $(4/3)*0.3218$ or 0.4291. Instrument B was assigned the baseline value of 0.3218. Instrument C was assigned $(2/3)*0.3218$ or 0.2145. Instrument D was assigned $(1/3)*0.3218$ or 0.1073. By looking at the relative contributions of the different instruments to the overall utility to science, the dependence on instrument growth rate can be determined.

Figure 85 shows the utility to science of each instrument for a typical architecture. The x-axis shows time in weeks and the y-axis shows the utility to science on a logarithmic scale. The instruments are clearly sorted according to their assigned discovery efficiency growth. But most importantly, the utility of the fast-developing instruments vastly outpaces that of the slow-developing instruments. The contribution of Instruments C and D to the telescope utility to science is almost negligible. Therefore, the calculation utility to science is highly sensitive to the assumed discovery efficiency growth rate. For use in this model, this sensitivity is acceptable as utility to science is a relative metric for differentiating among architectures. But this sensitivity also illuminates the importance of investing in instrument development. Such investment has a direct payoff in terms of scientific output and a small difference in technology growth rate can greatly affect the scientific utility of a telescope.

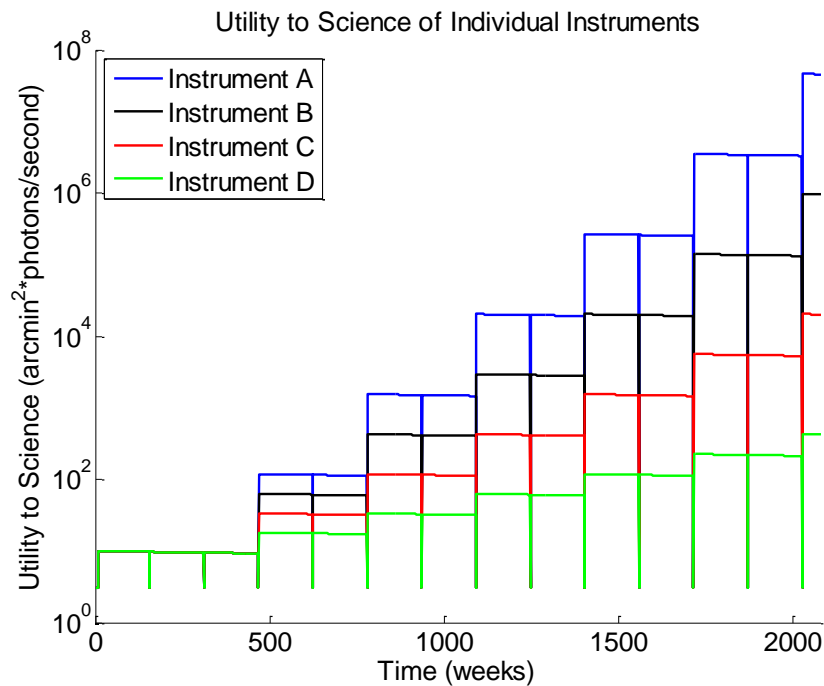


Figure 85: The utility to science of each instrument for a typical architecture. The x-axis shows time in weeks and the y-axis shows the utility to science on a logarithmic scale. The instruments are clearly sorted according to their assigned discovery efficiency growth rate.

7.4.2 Sensitivity of Trade Metrics to Assumptions

7.4.2.1 Interquartile Range of Percent Change in Trade Metrics

These charts demonstrate the spread of the differences of trade metric values between each baseline architecture (enumerated with the baseline case for the assumption) and the same architecture enumerated with a variance the assumption of interest. This method enables an examination of the effect of this parameter on an architecture-by-architecture basis, thus illuminating which metric is most affected by the parameter for a given architecture. The following plots show the effect of changing the Component MTBF and Reliability Threshold values across a certain range for all architectures. Each row of the tornado plot corresponds to a trade metric, and shows the 25th and 75th percentile values for the data set of delta values for that metric, defined as

$$T(i) = \frac{m_s(i) - m_0(i)}{m_0(i)} \times 100 \tag{Eq. 90}$$

where i is the index for a particular architecture, m is the metric under investigation (with m_s indicating the value with the changed parameter and m_0 indicating the value for the baseline case), and T is the trade metric delta value, defined as the percent change in the metric. Figure 86 represents this data for Component MTBF values changed by $\pm 10\%$. Figure 87 represents this data for Reliability Threshold changed by ± 0.05 .

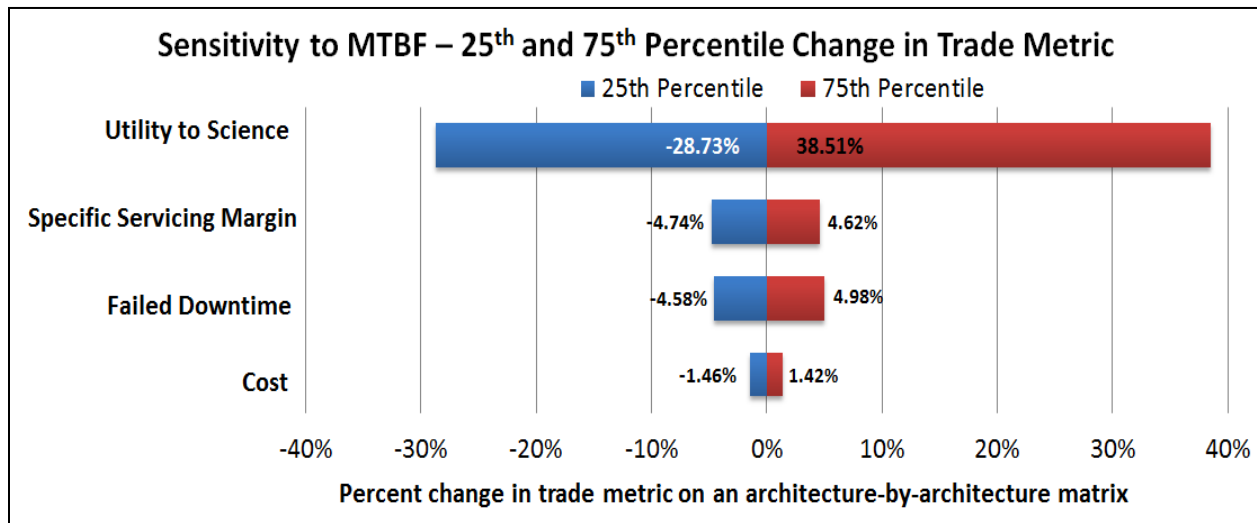


Figure 86: Tornado chart of component MTBF delta values

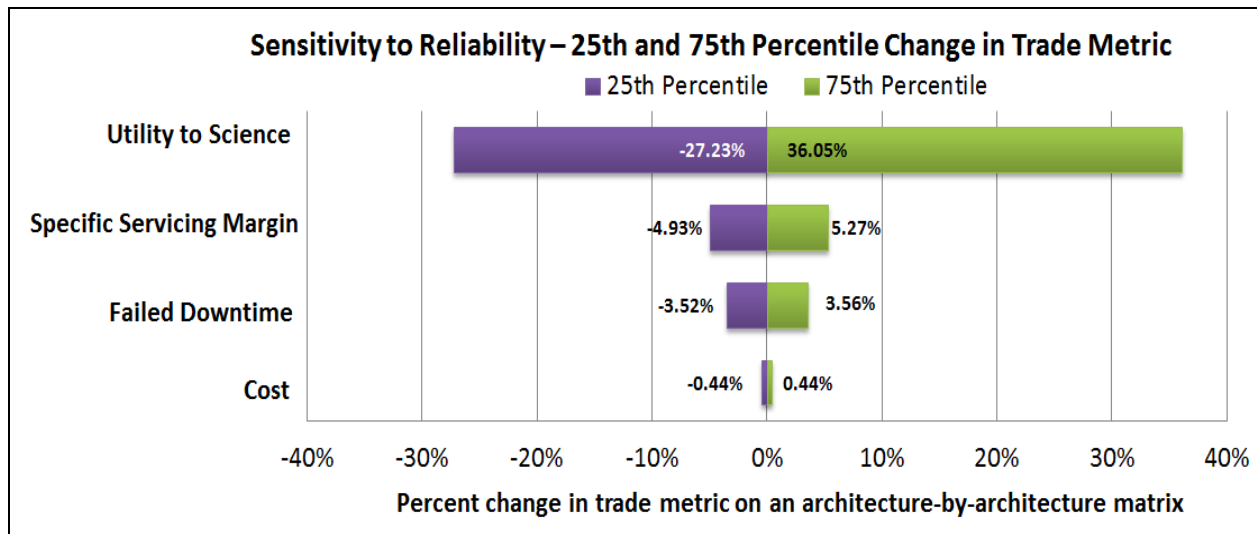


Figure 87: Tornado chart of reliability delta values

As can be seen in both sensitivity analyses, Utility to Science has the largest spread in the interquartile delta values, varying more than 30% in the positive direction, $UtS_s(x_i) > UtS_0(x_i)$, and more than 25% in the negative direction, $UtS_s(x_i) < UtS_0(x_i)$, where x_i is the i^{th} architecture, UtS_0 is Utility of Science for the baseline case and UtS_s is the Utility of Science where a design parameter was altered for the sensitivity analysis. This analysis indicates that over half of the architectures have over 25 percent change in the Utility to Science metric in the independent cases where Component MTBF is varied $\pm 10\%$ (Figure 86) and Reliability Threshold is varied ± 0.05 (Figure 87) in comparing architecture to architecture. Therefore, there are many architectures whose Utility to Science Metric is sensitive to both Component MTBF and Reliability Threshold. A closer inspection of the data shows that the Utility to Science produces high variance in values for the extremes in high and low values, making Utility to Science very sensitive to perturbations according to the percent change metric used in Figure 86 and Figure 87. The source of this variance requires further investigation.

Similarly, component family MTBF also produces delta change percentages in the $\pm 5\%$ range for Downtime and Servicing Margin and $\pm 1\%$ for Cost. Most architectures are not as sensitive in the Downtime, Servicing Margin, and Cost metrics as they are for Utility to Science when Component MTBF is varied. The same is true for the sensitivities of Downtime, Servicing Margin, and Cost metrics when the Reliability Threshold is varied (not as sensitive as Utility to Science is to varying Reliability Threshold).

7.4.2.2 Crossover

The distribution of values for per architecture percent changes reveals the percentage of the time that a specific trade metric delta was negative, i.e., $T_s(x_i) < T_0(x_i)$; this percentage will be referred to as the crossover percentage. For the metrics of Cost and Downtime, negative delta values and larger crossover percentages indicate better performance for a specific design parameter change. Note that this data is calculated with respect to the baseline case, so it is not necessary for the baseline case to be represented. For Utility to Science and Servicing Margin, positive delta values and lower crossover percentages indicate better performance with a specific design parameter change. A chart of the crossover percentages for each trade metric across

varying sensitivity levels is shown in Figure 88 for Component MTBF and Figure 90 for Reliability Threshold.

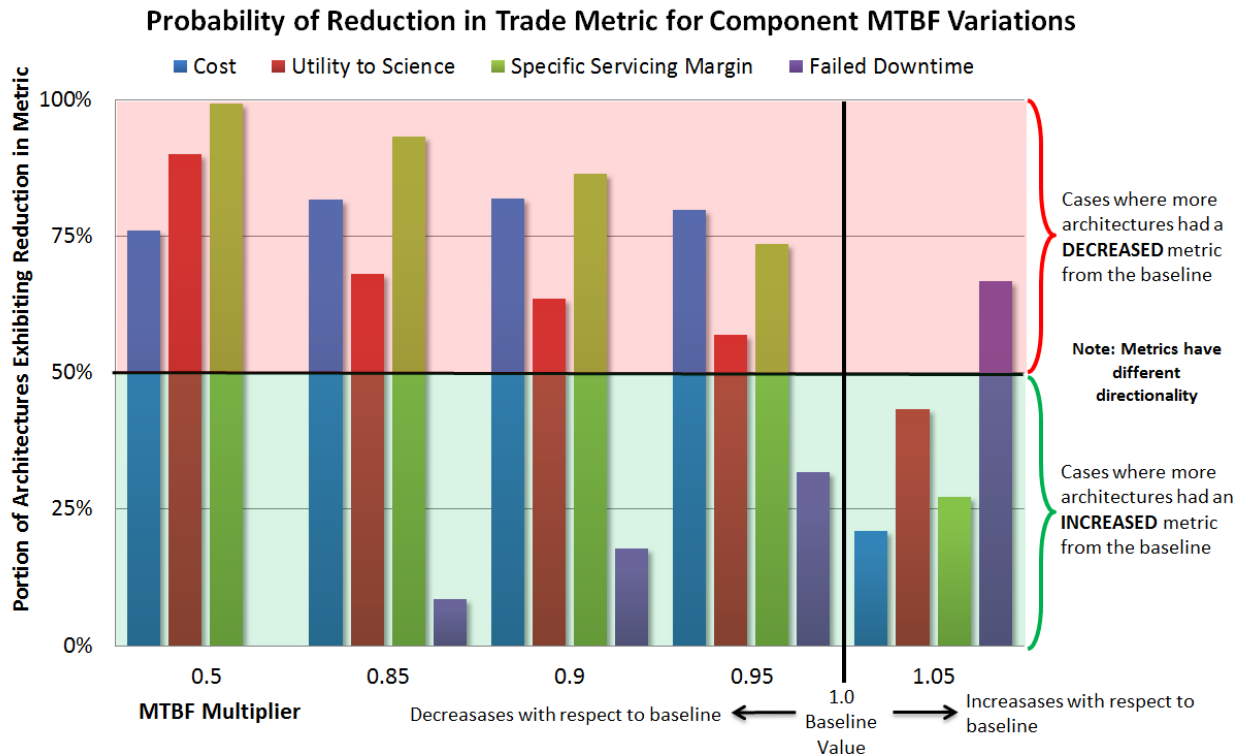


Figure 88: Crossover percentages for component MTBF variations

As expected, lowering the MTBF lowers the percentage of architectures for which $C_0(x_i) > C_s(x_i)$. Due to increased failures and increased downtime, the crossover values that exceed 50% for MTBF factors less than 100% and the greater the MTBF, the higher the crossover value (Figure 88). For the 50% MTBF case, 76% of the time the model produced a lower cost for the same architectural decision. Decreasing the MTBF values per component in the majority of architectures lowers the initial system cost. This result is because lower MTBFs correspond to less expensive components in the model; the driving assumption being components that tend to fail more often are either less expensive to make or purchase. The cost metric is determined by multiplying the initial telescope cost by the ratio of serviced mass to telescope mass. The serviced mass in the model does not fluctuate greatly with decreases in MTBF for modularity levels 1-3 and 5-6 because entire modules are replaced if at least one component has failed or is expected to fail soon, so an increase in failures does not correspond to a large increase in serviced mass. The exceptions, then, are modularity 4 and 7, where individual component families are serviced and significant increases are observed in serviced mass for increased failures (Modularity Levels with Higher Costs). For the 50% MTBF data set, the 24% of architectures for which a decreased MTBF yielded an increased cost were almost entirely composed of architectures with Modularity level 4 or 7 (Figure 89).

Modularity Level Composition of Architecture Set with Higher Costs at MTBF 50%

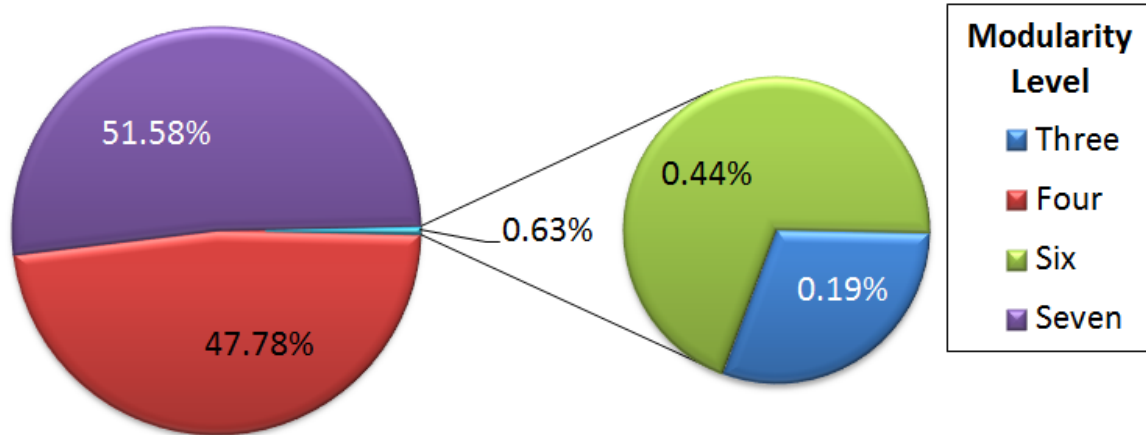


Figure 89: Modularity composition of architectures with higher costs at MTBF 50%

Servicing Margin is decreased when Component MTBF is decreased, as expected, due to the fact that serviced mass is not changed (for modularity levels 1-3 and 5-6) but servicing missions are increased. Decreasing the Component MTBF increases telescope downtime due to increased failures. A 50% decrease in Component MTBF is almost always worse than the baseline for the metric of downtime (Figure 88).

Trends in Figure 88 also show relationships between the trade metrics and the MTBF values of the components. It is important to note for this analysis that in this analysis the intervals between the MTBF multipliers are not constant, so it is not appropriate to comment directly on the rate of change of a metric with respect to the parameter without careful consideration of the variation in step size; that is the subject of future analysis. However, trends are shown and can be analyzed.

Cost shows an interesting trend. In general, lowering the MTBF values decreases the cost for 75-80% of the architectures; this makes sense, as the NICM cost model used to determine the cost of the instrument package is based in part on the MTBF values of the instruments, with lower MTBF values resulting in lower instrument costs. This also explains the cost increase for 20% of the architectures when the MTBF values are increased. However, it is interesting to point out that, while the proportion of architectures with decreased cost for decreased MTBF is steady at approximately 80% for MTBF multipliers of .85, .9, and .95, for an MTBF multiplier of .5 (the case where the MTBF values are reduced by half) the proportion of architectures with decreased cost drops to 75%. This implies that there is another effect that takes hold to increase the cost for lower MTBF values, but only when the change in MTBF values is low. This is most likely an increase in the serviced mass, which results in increased costs both in launch and development of replacement parts. While this increase in serviced mass is likely present for the other sensitivity analyses with reduced MTBF values, it is only when the magnitude of the reduction of MTBF

values is higher (reducing to 50% of the original value) that the effect of increased serviced mass overrides the effect of decreased cost.

The other trade metrics display more monotonic behavior. In general, lowering MTBF values lowers the Utility to Science with an effect proportional to the MTBF multiplier; the proportion of architectures with lower Utility to Science ranges between approximately 57% and 90% across the range of MTBF multipliers tested that were less than 1. For an increase in MTBF values, approximately 43% of the architectures exhibited increased Utility to Science. While more data from analyses with increased MTBF values would be required to verify this, these results seem to indicate that the effect of MTBF is similar for both increases and decreases, resulting in a proportional change in the percentage of architectures with increased Utility to Science.

The proportional relationship between MTBF values and Utility to Science makes sense, because the primary impact of component MTBF values on Utility to Science is in the amount of Failed Downtime; the lower the MTBF values of the components, the more often those components are expected to fail, resulting in lower downtime. To investigate this hypothesis, the Failed Downtime metric is investigated. Failed Downtime exhibits the inverse trend – the higher the MTBF values, the greater the percentage of architectures for which Failed Downtime was reduced. This supports the hypothesis. In fact, for the MTBF multiplier of 0.5, the percentage of architectures with decreased Failed Downtime is 0; for this MTBF multiplier, every architecture experienced increased downtime. This is again reflected in the fact that this MTBF multiplier experiences the highest percentage of architectures with decreased Utility to Science.

The trend in the Specific Servicing Margin shows that as the MTBF multiplier increases, the percentage of architectures with decreased Specific Servicing Margin decreases; in general, lowering the MTBF of the components in an architecture tends to decrease the Specific Servicing Margin. In fact, for an MTBF multiplier of 0.5, nearly all of the architectures experienced a decreased Specific Servicing Margin. This makes sense, as lower MTBFs result in more component failures and thus higher serviced mass. The definition of Specific Servicing Margin from Eq. 1 shows that a higher serviced mass results in a lower Specific Servicing Margin.

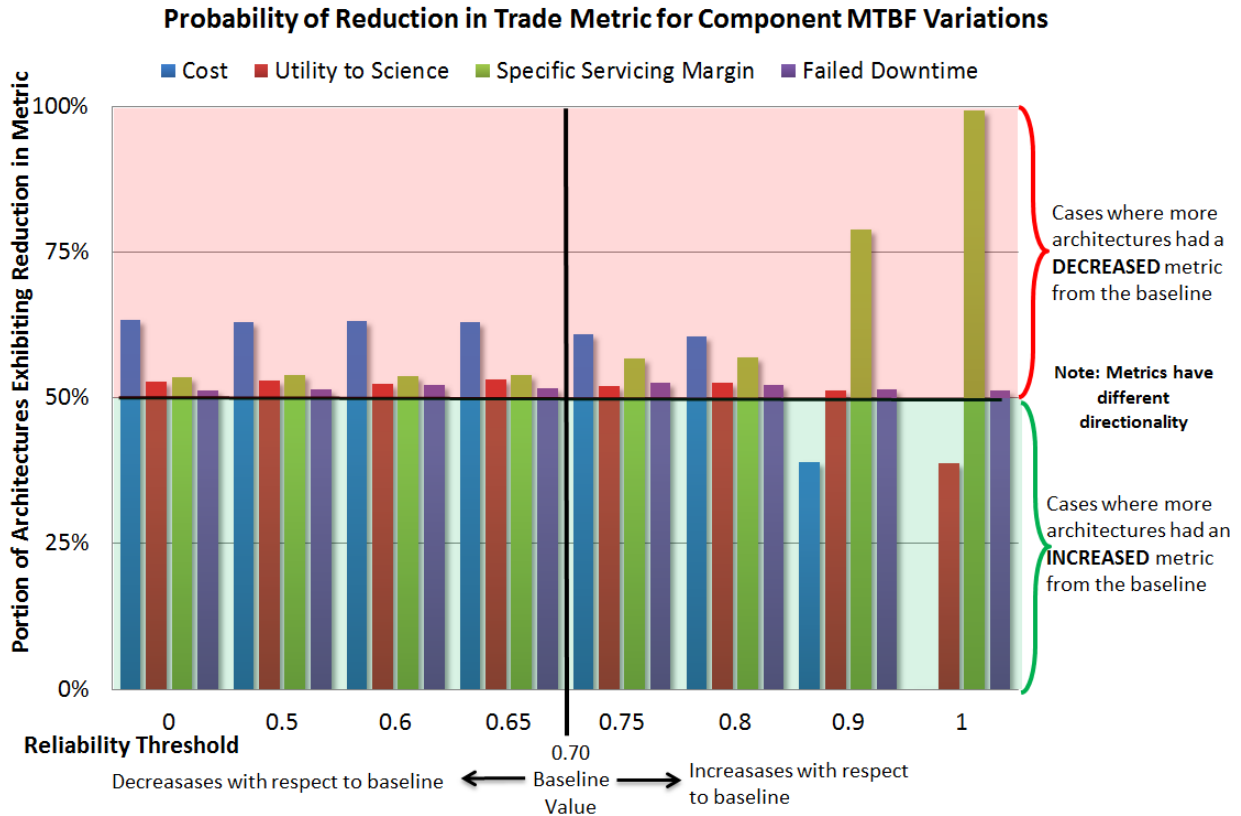


Figure 90: Crossover percentages for reliability threshold variations

The higher the Reliability Threshold, the greater the cost due to increased module servicing that increases serviced mass while not changing the initial system mass. The higher the Reliability Threshold, the greater the Utility to Science because modules are being maintained at higher reliabilities, thus decreasing downtime due to failures. On the other hand, decreasing the Reliability Threshold to values below 0.65 does not have a large impact on Utility to Science: Utility to Science is lowered but does not continue to degrade with decreasing Reliability Threshold. This trend indicates that Utility to Science is sensitive to increased changes in Reliability but not sensitive to decreases below 0.65. Similarly, Servicing Margin experiences the same sensitivities to increasing the Reliability Threshold above 0.65, but not to decreasing it.

In summary, Cost, Utility to Science, and Specific Servicing Margin are all much more sensitive to increases in the Reliability Threshold than decreases. This makes sense, as the primary interaction between these metrics and the Reliability Threshold is through the replacement of components that would not otherwise be replaced, i.e. components that are not failed but have fallen below the reliability threshold. It is expected that as the Reliability Threshold decreases the number of components serviced decreases as well, but only up to a certain point. Because random failure is also incorporated into the model, a certain number of components will be replaced regardless of the Reliability Threshold; as the Reliability Threshold decreases, the number of operational components with reliabilities below the threshold decreases due to their higher probability of having failed already. Thus, at a certain point the Reliability Threshold becomes low enough that the number of components that survive long enough for their reliability

to drop to that level is negligible, and reducing the Reliability Threshold further has no effect. Increasing the Reliability Threshold above this value, however, has a significant effect, as it significantly increases the number of components that require replacement that are not failed. Based upon this analysis, the level of Reliability Threshold at which the simulation begins replacing a significant number of components that are not failed is somewhere between 0.8 and 0.9, as this is the point where the effects in Cost and Specific Servicing Margin begin to manifest themselves.

The center of the distributions for Downtime across the varying Reliability Threshold changes is relatively constant, indicating that Downtime is not sensitive to changes in Reliability Threshold.

7.4.2.3 Cumulative Distribution Functions

For each sensitivity impact on a trade metric, Cumulative Distribution Functions (CDFs) were plotted to show the distribution of the Trade Metrics and percent change metric (Figure 91 and Figure 92). The steeper slopes in the CDFs indicate ranges for a metric for which there are many architectures. These CDFs also depict changes in center, spread, and shape of the data and regions where certain architectural sets are stochastically dominant. Though Figure 86 and Figure 87 allow conclusions to be more readily determined, the same conclusions can also be drawn from the CDF plots. Therefore, the CDF plots can provide the same conclusions, though they represent the data in a less concise manner as with the Tornado and Crossover figures. An example of each type of CDF is shown below.

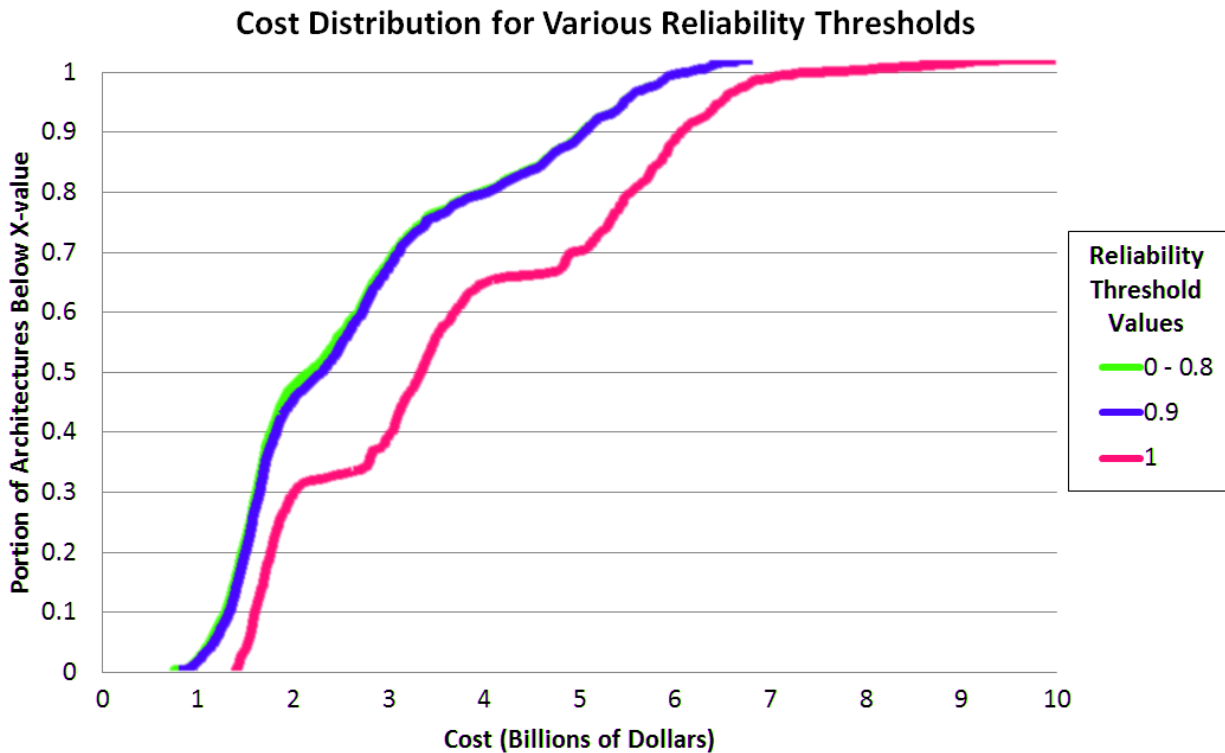


Figure 91: CDF of cost varying reliability threshold (comparing distributions)

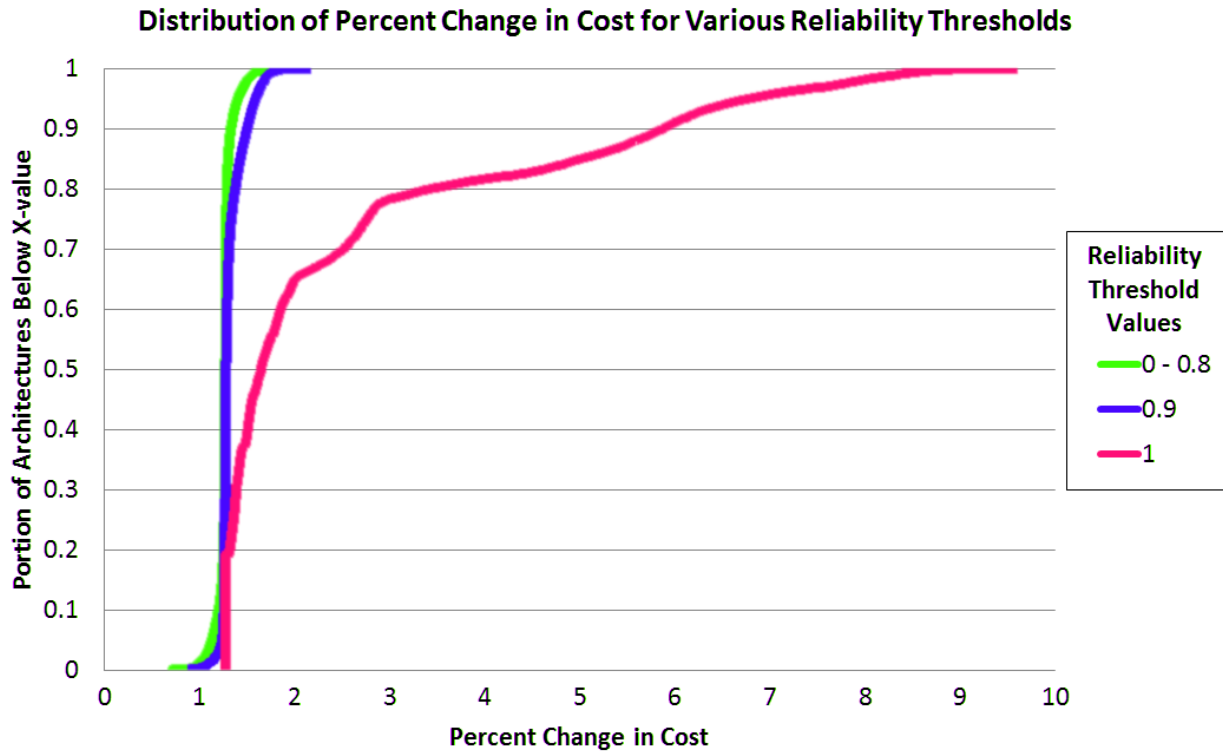


Figure 92: CDF of percent change in cost varying reliability threshold (comparing architectures)

7.4.2.4 Sensitivity of Pareto Frontier to Assumptions

In order to investigate the sensitivity of the Pareto frontier to the assumptions, a trade space exfoliation method was developed to identify layers of Pareto frontiers and the movement of architectures along the layers as a result of altering an assumption. In order to understand the results, a detailed explanation of tradespace exfoliation and Pareto layers is necessary. The following steps detail the tradespace exfoliation method:

1. For the baseline data set, identify the metrics that are traded and the number of dimensions
2. Normalize the data
3. Determine the Pareto frontier and label those architectures as Pareto layer $i=1$
4. Remove the i^{th} Pareto frontier from the data set
5. Determine the Pareto frontier of the reduced data set (the data set without the $1:i^{th}$ frontier) and label as Pareto layer $i+1$
6. Continue for $i = 1:N$, with N being the number at which the frontier is empty, i.e., until there are no points in the data set
7. Repeat steps 2-6 for the set of architectures for which an assumption was changed
8. Compare the Pareto layer numbers for each architecture in the first Pareto layer in the baseline data set to the Pareto layer in which that architecture now resides as a result of the change in the assumption/design parameter

Figure 93 depicts the cumulative distribution of the percentage of the baseline Pareto frontier that

was moved to a given Pareto layer or lower, i.e., the tradespace with the altered assumption contains y percent of the Pareto layer 1 architectures in layers 1 to x, where y is the vertical axis and x is the horizontal axis. The solid lines in Figure 93 correspond to the distributions for changes in Component MTBF of $\pm 5\%$ and the dotted lines correspond to the distributions for changes in Reliability Threshold of ± 0.05 .

With respect to change in Component MTBF values, only 10% of the Pareto-Optimal architectures of the baseline data remain in the first Pareto layer when the MTBF values are changed. Thus, the Pareto front itself is sensitive to change in Component MTBF values. However, this analysis technique allows an investigation of “Pareto zones” rather than simply fronts; the data reveal what proportion of Pareto-Optimal architectures from the baseline data moved to each Pareto layer. Approximately 60% of the Pareto-Optimal architectures remained within the first 5 Pareto layers when the parameter was changed, indicating that over half the architectures remained fairly close to the Pareto front. Given the margin for error in the calculation of model outputs, the first 5 Pareto layers represent architectures that may be considered “pseudo-Pareto-Optimal” within the accuracy of the model. The farthest that any Pareto-Optimal architecture fell is 24 Pareto layers (out of a total of approximately 40).

For change in Reliability Threshold values, approximately 20% of the Pareto-Optimal architectures remained in the first layer, and approximately 80% fell no further than 5 Pareto layers. The farthest that any Pareto-Optimal architecture fell is 14 Pareto layers. Therefore, the Pareto frontier is more sensitive to changes in Component MTBF values than changes in Threshold Reliability. The Pareto frontier itself is quite sensitive to changes in model parameters, but inclusion of the first 5 Pareto layers as “pseudo-Pareto-Optimal” shows that the Pareto zone is more robust to changes in the model parameters.

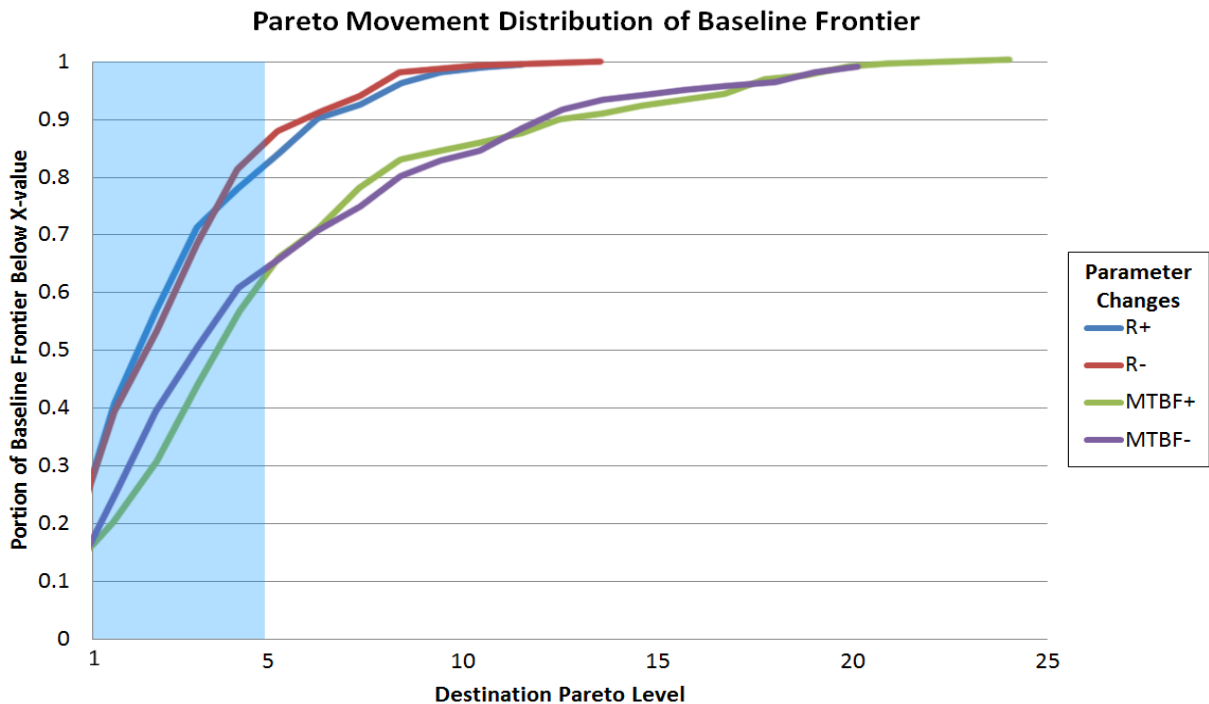


Figure 93: Pareto movement of baseline frontier

8 FUTURE WORK

There is a considerable amount of future work that can be done on this project both to increase the validity of the model and to extend the reach of conclusions achieved thus far. The main contribution of this work has been to set up a tool to evaluate possible large telescope architectures that meet the ATLAST science requirements, but many alterations should be made before the model's evaluation of architectures is to be cited confidently. As with any model and tradespace analysis, there are a great deal of points for further work and exploration; however, these are some of the immediate points that the TITANS AE team would have liked to incorporate and investigate.

8.1 Next steps to increase the validity of the model

The model serves as a tool with which the tradespace of large telescope architectures can be explored. There are many sources of uncertainty in the existing model due to, for example, low level of maturity for several considered technologies, unavailability of a full set of cost models with the appropriate ranges of validity, etc.

- *Decrease the discretization of the subsystem modules:* Because the focus of this study has been on the architecture evaluation tool, the subsystem models achieve a low level of fidelity by defining a small number of component families each subsystem can choose from. This resulted in some of the subsystem models producing only discretized architectures, which caused the trade metrics values across architectures to be less continuous than they likely are in reality.
- *Incorporate feedback loops into model:* The model does not incorporate feedback for several reasons (see Section 5.1 which talks about the N^2 and the lack of feedback). The addition of feedback into the models would decrease the number of assumptions and increase the fidelity of the subsystem architecture models.
- *Reconsider the rate of improvement in instrument discovery efficiency over the 40-year mission lifetime:* As discussed in Section 5.2.1 (utility-to-science section), the instrument improvement rate has been shown to increase exponentially, but it may not be realistic at this time to project the rate of improvement as exponential over the next 55 years.
- *Incorporate upgrades in satellite bus components:* The model incorporates advances in science instrumentation but not in engineering instrumentation. Over time, these components will only improve (i.e., become less massive, more reliable, more capable, etc.). If a model exists to obtain projected performance of engineering components, it should be implemented in order to more accurately reflect increasing engineering component capability over the telescope lifetime, which would, by extension, reflect increasing telescope capability.
- *Increase the range of validity of our architectural model so it may be further validated:* One of the biggest limitations to the model is its inability to be properly validated against even the most similar large telescope missions (i.e., JWST and HST). The assumptions made (e.g., 16.8-m-diameter primary mirror) and the way the scientific requirements

were incorporated (e.g., science data rate is a requirement for the communications system) does not make the model applicable to JWST and HST. As is natural with an ambitious study of this sort, validation is difficult and largely unattainable, but it would be useful to be able to relax the assumptions and account for requirements in a more general way so that the model can be minimally validated.

- *Track the consumption of consumables over time:* The study has assumed that the telescope will have enough consumables (e.g., propulsive fuel, coolant) to last the time between servicing missions, and that consumables are replaced during servicing missions. In the future, consumables should be considered something to be “serviced,” in the sense that they can fail by being depleted between servicing missions.
- *Account for different signal latency in servicing operations:* The differences in signal latency for various assembly/servicing locations has not been taken into account in this analysis, though it surely affects operational downtime as well as the feasibility of different types of assembly/servicing technique.

8.2 Next steps for tradespace exploration

This initial tradespace exploration should be expanded upon to increase its ability to accurately differentiate between architectures based on the four trade metrics considered. Generally, the addition of and improved implementation of architectural decisions will extend the conclusions of the trade study by allowing for a more detailed analysis of architectures’ cost and utility.

- *Estimate cost of servicing:* An estimate of servicing cost is critical to the evaluation of possible architectures for this mission. Such an estimate would be based on a currently nonexistent servicing cost model that could be developed based on further research and development effort on assembly and servicing methods for large space telescopes.
- *Improve the implementation of some architectural decisions considered in the study:* There are some architectural decisions that were implemented in a way that they did not result in interesting trades. For example, from our main effects plots, it is evident that the decisions of segmentation of the primary mirror and the communications architecture did not interface with other architectural decisions and did not significantly affect the trade metrics. Launch costs were the only thing affected by the segmentation of the primary mirror, and these are small compared to lifecycle cost. The different data transmission capabilities (i.e., data rates) of different communications architectures were not taken into account, so this choice did not change utility to science the way it likely would in reality.
- *Consider the baffle design:* The type of baffle could be made into an architectural decision or considered in a separate analysis. As a starting point, the baffle design could either be similar to the JWST baffle or Hubble baffle.
- *Consider assembly and servicing techniques separately:* Making these separate architectural decisions would allow for the consideration of different approaches to these distinct operational phases. Breaking these decisions out separately may produce

interesting results especially in distinguishing between designs with very different levels of modularity and segmentation.

- *Consider on-demand servicing:* It is assumed that servicing would be regularly scheduled to simplify the analysis. This is one of the most important architectural decisions that impact lifetime servicing cost. The implications of employing on-demand vs. scheduled servicing, or a hybrid of the two, are discussed in detail in Section 4.3.4.
- *Consider an external coronagraph:* It was assumed that the telescope system would not have a separate formation-flying coronagraph. However, such a coronagraph was proposed for ATLAST, and it this study would be remiss to explicitly not consider an external coronagraph in the future.

9 CONCLUSION

The steps outlined in this document describe the process for the tradespace analysis which was conducted in course 16.89, Space Systems Engineering, at MIT. The team investigated past designs of space telescopes and conducted a stakeholder analysis in order to determine the seven most important architectural decisions and enumerate an appropriate tradespace of alternatives associated with those decisions. The team determined the necessary system metrics (cost, utility to science, failed downtime, and servicing margin) which were used to evaluate each architecture.

The development of these metrics into a fully-functional and streamlined program enabled the team to efficiently evaluate the full set of enumerated architectures. Analysis of the outputs of the model has revealed a number of important dependencies. Utility to science depends most strongly on servicing frequency and servicing location, with the focus on upgrading the instruments often and minimizing downtime. Cost most strongly depends on modularity level and servicing frequency with architectures requiring a large serviced mass being most expensive. Failed downtime most strongly depends on servicing frequency, with the other architectural decisions contributing in minor ways. Architectures with infrequent servicing are more likely to experience failures leading to lengthy downtimes. Serviceability most strongly depends on modularity, servicing frequency, and assembly/servicing technique. Architectures with strong modularity serviced often with cheap servicing techniques exhibit the lowest cost per unit serviced mass. In the sensitivity analysis, utility to science was the sole trade metric to significantly feel the effects of the changes in MTBF and reliability threshold.

These dependencies reveal themselves in the analysis of the Pareto front. Clusters towards the higher end of the Pareto front use frequent servicing at Sun-Earth L2 and low modularity to achieve high utility to science but with high cost. Clusters near the middle of the Pareto front use high modularity to achieve lower cost by changing to high levels of modularity while losing some utility to science. Architectures near the bottom of the Pareto front use high levels of modularity and less frequent servicing at LEO to achieve very low cost with relatively little utility to science. The Pareto Optimal architectures changed with the variation of MTBF and reliability threshold. However, most of the original Pareto Optimal architectures remained close to the new Pareto fronts, indicating moderate sensitivity. While the other architectural decisions affect the trade metrics in small ways, our analysis has shown that servicing frequency, servicing location, and modularity are the most important decisions when architecting a space telescope—essential information for stakeholders in the selection of an optimal architecture for the next generation space telescope.

APPENDIX A: VARIABLE LIST

Code Module	Variable	Description	Units
Main	LTA	Structure to contain each architecture's design variables	[varies]
	res_vec	Results vector	[varies]
Sensitivity Analysis	modlevsensitivity	Sensitivity analysis variable - Multiplier of number of bus-segments needed per module	[unitless]
	MTBFsensitivity	Sensitivity analysis variable - Multiplier of MTBF column	[unitless]
	R_threshold	Sensitivity analysis variable - Required reliability of a given component family for a given servicing mission (would be pre-emptively replaced if below threshold)	[unitless]
Design Constants	reliability_req	Required reliability of a given subsystem for initial design (0.90)	[unitless]
	mirror_diam	Primary mirror diameter (16.8)	m
	mirror_temp_range	Mirror operating temperature range (20-22)	deg C
	shield_efficiency	Thermal shield efficiency (0.80)	[unitless]
	total_mass_estimate	Estimate of total spacecraft mass (15000)	kg
	R_earth2telescope	Distance from earth to the telescope (1.5 billion)	m
	acs_pointing_error	Pointing requirement taken from ATLAST reqs (1)	milli-arcsec
	unique_prescr	Number of unique prescriptions (6)	prescriptions
	num_rings	Number of mirror segment rings (3)	rings
	segment_diam	Diameter of mirror segments ($16.8/7 = 2.3$)	m
	rep_segments	Number of repeated segments (6)	segments
	lifetime_req	Requirement of mission lifetime (40)	years
Components DB and DSMs	costCol	Column of cost/unit per component family, imported from Components DB spreadsheet	\$1K US FY13
	massCol	Column of mass/unit per component family, imported from Components DB spreadsheet	kg
	dimCol	Column of mass/unit per component family, imported from Components DB spreadsheet	m
	volCol	Column of stowed-volume/unit per component family, imported from Components DB spreadsheet	m ³
	compPowerAvgCol	Column of avg-power-draw/unit per component family, imported from Components DB spreadsheet	W
	compPowerPeakCol	Column of peak-power-draw/unit per component family, imported from Components DB spreadsheet	W
	powerCol	Column of avg-power-generated/unit per component family, imported from Components DB spreadsheet	W
	TRLCol	Column of total-readiness-level/unit per component family, imported from Components DB spreadsheet	level number
	MTBFCol	Column of mean-time-between-failure/unit per component family, imported from Components DB spreadsheet	years

	lifetimeCol	Column of lifetime/unit per component family, imported from Components DB spreadsheet	years
	StructuralDSM	Design structure matrix for structural interactions between component families, imported from DSM spreadsheets	binary matrix
	ThermalDSM	Design structure matrix for thermal interactions between component families, imported from DSM spreadsheets	binary matrix
	DataDSM	Design structure matrix for data interactions between component families, imported from DSM spreadsheets	binary matrix
	PowerDSM	Design structure matrix for power interactions between component families, imported from DSM spreadsheets	binary matrix
	LTA	Structure to contain each architecture's design variables	[varies]
	OpticalDSM	Design structure matrix for optical interactions between component families, imported from DSM spreadsheets	binary matrix
Design Vector	servicing_loc	Servicing Location	selection number
	servicing_freq	Servicing Frequency	years
	comm_arch	Communications Architecture	selection number
	mirror_support	Mirror Support Method	selection number
	a_s_technique	Assembly/Servicing Technique	selection number
	mirror_segmentation	Segmentation Technique of the Primary Mirror	selection number
	modularity_level	Modularity Level	level number
Optics	optics_m	Total mass of Optics subsystem (inst. only)	kg
	optics_v	Total volume of Optics subsystem (inst. only)	m ³
	optics_avg_power_req	Average power required by Optics subsystem (inst. only)	W
	optics_temp_range	Operating temperature range of Optics subsystem (cryo inst. only)	deg C
	optics_power_diss	Average power dissipated by Optics subsystem (inst. only)	W
	inst_perf_decay_rate	Rate paramter for performance decay of an instrument over time	[unitless]
	optics_data_rate	Rate at which data is transmitted from the telescope to avionics	Mbps
	optics_components	Component family choices for Optics subsystem (inst. only)	units of comp. family
	num_segments	Total number of primary mirror segments	segments
	discovery_efficiency_inst_a	Discovery efficiency (FOV*throughput) of instrument A	arcmin ² *photons/sec
	discovery_efficiency_inst_b	Discovery efficiency (FOV*throughput) of instrument B	arcmin ² *photons/sec
	discovery_efficiency_inst_c	Discovery efficiency (FOV*throughput) of instrument C	arcmin ² *photons/sec
	discovery_efficiency_inst_d	Discovery efficiency (FOV*throughput) of instrument D	arcmin ² *photons/sec
	vol_data_to_ground	Quantity of data that needs to be transmitted to ground, largest contributor is optics/science data	Mb
Comm	comm_power_diss	Average power dissipated by Comm subsystem	W

	comm_temp_range	Operating temperature range of Comm subsystem	deg C
	comm_avg_power_req	Average power required by Comm subsystem	W
	comm_peak_power	Peak power required by Comm subsystem	W
	comm_peak_length	Time for which the peak power is needed	s
	comm_peak_frequency	How often the peak power is needed	Hz
	comm_timedelay	Transmission delay of the data	s
	comm_m	Total mass of Comm subsystem	kg
	comm_v	Total volume of Comm subsystem	m ³
	comm_MTBF	Mean time between failure (MTBF) for Comm subsystem	years
	comm_QOS_BER	Quality-of-signal / Bit-error-rate of selected Comm architecture	[unitless]
	comm_SNR	Signal-to-noise ratio of selected Comm architecture	[unitless]
	comm_components	Component family choices for Comm subsystem	units of comp. family
	comm_components_MTBF	Mean time between failure (MTBF) of individual "component families" selected for Comm subsystem	years
ADCS	acs_temp_range	Operating temperature range of ADCS subsystem	deg C
	acs_avg_power_req	Average power required by ADCS subsystem	W
	acs_m	Total mass of ADCS subsystem	kg
	acs_v	Total volume of ADCS subsystem	m ³
	acs_components	Component family choices for ADCS subsystem	units of comp. family
	acs_components_MTBF	Mean time between failure (MTBF) of individual "component families" selected for ADCS subsystem	years
	acs_MTBF	Mean time between failure (MTBF) for ADCS subsystem	years
Avionics	avionics_m	Total mass of Avionics subsystem	kg
	avionics_v	Total volume of Avionics subsystem	m ³
	avionics_avg_power_req	Average power required by Avionics subsystem	W
	avionics_power_diss	Average power dissipated by Avionics subsystem	W
	avionics_temp_range	Operating temperature range of Avionics subsystem	deg C
	avionics_components	Component family choices for Avionics subsystem	units of comp. family
	avionics_components_MTBF	Mean time between failure (MTBF) of individual "component families" selected for Avionics subsystem	years
	avionics_MTBF	Mean time between failure (MTBF) for Avionics subsystem	years
	avionics_data_rate	Avionics data rate	bps
Propulsion	prop_m_nd	Propellant mass fraction (per unit spacecraft mass)	kg/kg
	prop_v_nd	Propellant volume fraction (per unit spacecraft mass)	m ³ /kg
	prop_svc_time	One-way travel time between L2 and servicing location	days
	prop_avg_power_req	Average power required by Propulsion subsystem	W
	prop_temp_range	Operating temperature range of Propulsion subsystem	deg C
	prop_power_diss	Average power dissipated by Propulsion subsystem	W
	prop_components	Component family choices for Propulsion subsystem	units of comp. family

	prop_transit_time	One-way travel time between earth and L2	days
Power	power_m	Total mass of Power subsystem	kg
	power_v	Total volume of Power subsystem	m ³
	power_m_nd	Non-dimensionalized mass (per Watt required)	kg/W
	power_v_nd	Non-dimensionalized volume (per Watt required)	m ³ /W
	power_avg_power_diss	Average power dissipated due to power distribution inefficiencies	W
	power_array_area	Area of solar arrays	m ²
	power_temp_range	Operating temperature range of Power subsystem	deg C
	power_components	Component family choices for Power subsystem	units of comp. family
Thermal	thermal_m	Total mass of Thermal subsystem	kg
	thermal_v	Total volume of Thermal subsystem	m ³
	thermal_avg_power_req	Average power required by Thermal subsystem	W
	thermal_components	Component family choices for Thermal subsystem	units of comp. family
	thermal_components_MTBF	Mean time between failure (MTBF) of individual "component families" selected for Thermal subsystem	years
	thermal_MTBF	Mean time between failure (MTBF) for Thermal subsystem	years
Structures	structures_components	Component family choices for Structures subsystem	units of comp. family
	structures_pow_avg	Average power required by Structures subsystem	W
	structures_pow_peak	Peak power required by Structures subsystem	W
	structures_v	Total volume of Structures subsystem	m ³
	structures_m	Total mass of Structures subsystem	W
	structures_components_MTBF	Mean time between failure (MTBF) of individual "component families" selected for Structures subsystem	years
	overall_components	Compiled "component family" choices for entire spacecraft	units of comp. family
	sys_pow_avg	Total average power of entire spacecraft	W
	sys_pow_peak	Total peak power of entire spacecraft	W
	sys_mass	Total mass of entire spacecraft	kg
	prop_m	Final mass of Propulsion subsystem	kg
	sys_vol	Total volume of entire spacecraft	m ³
	prop_v	Final volume of Propulsion subsystem	m ³
	jitter	Jitter of the System (RMS)	mm
	module_definitions	Vector that captures which module each component is in	module number
Systems	sys_reliability	Total system reliability	[unitless]
	sys_complexity	Total system complexity (based on DSMs)	N/A
Operations	inst_del_rate	Rate parameter for the increase in instrument utility over time	[unitless]
	num_mod	Number of modules in spacecraft	modules
	t_end	Monte Carlo simulation variable - Time at which simulation ends	weeks passed
	dt	Monte Carlo simulation variable - Time-step of simulation	weeks

time	Monte Carlo simulation variable - Vector of evaluation times for simulation	weeks passed
architecture	Monte Carlo simulation variable - captures full spacecraft architecture's state at each servicing mission evaluation point	[varies]
inst_replaced	Monte Carlo simulation variable - captures each instrument's state of replacement at each servicing mission evaluation point	binary vector
downtime	Monte Carlo simulation variable - Downtime due to mass-servicing and transit to servicing location	days
failures	Monte Carlo simulation variable - Number of failures per servicing mission	failures
module_replacements	Monte Carlo simulation variable - Modules that were replaced per servicing mission	modules
scope_state	Monte Carlo simulation variable - State of spacecraft per servicing mission	binary vector
row_inst_a	Monte Carlo simulation variable - Row number of instrument A	row number
row_inst_b	Monte Carlo simulation variable - Row number of instrument B	row number
row_inst_c	Monte Carlo simulation variable - Row number of instrument C	row number
row_inst_d	Monte Carlo simulation variable - Row number of instrument D	row number
utility_inst_a	Monte Carlo simulation variable - Utility-to-science of instrument A at given evaluation time	arcmin ² *photons
utility_inst_b	Monte Carlo simulation variable - Utility-to-science of instrument B at given evaluation time	arcmin ² *photons
utility_inst_c	Monte Carlo simulation variable - Utility-to-science of instrument C at given evaluation time	arcmin ² *photons
utility_inst_d	Monte Carlo simulation variable - Utility-to-science of instrument D at given evaluation time	arcmin ² *photons
p_util_science_a	Monte Carlo simulation variable - Distribution of utility-to-science of instrument A over mission lifetime	arcmin ² *photons
p_util_science_b	Monte Carlo simulation variable - Distribution of utility-to-science of instrument B over mission lifetime	arcmin ² *photons
p_util_science_c	Monte Carlo simulation variable - Distribution of utility-to-science of instrument C over mission lifetime	arcmin ² *photons
p_util_science_d	Monte Carlo simulation variable - Distribution of utility-to-science of instrument D over mission lifetime	arcmin ² *photons
p_util_science	Monte Carlo simulation variable - Distribution of utility-to-science of spacecraft over mission lifetime	arcmin ² *photons
MC_results.m_serv_mat	Monte Carlo results variable - Mass serviced per servicing mission	kg
MC_results.downtime	Monte Carlo results variable - Total downtime due to failure, servicing, or transit at each servicing mission evaluation point	weeks

	MC_results.service_downtime_vec	Monte Carlo results variable - Downtime due to mass-servicing or transit per servicing mission	weeks
	MC_results.mean_m_serv_vec	Monte Carlo results variable - Avg serviced mass per servicing mission	kg
	mean_service_downtime	Total average downtime due to mass-servicing or transit time	weeks
	mean_downtime	Total average downtime due to failure, mass-servicing, or transit to servicing location	weeks
	failed_downtime	Total average downtime due to spacecraft failure	weeks
	service_downtime_frac	Fraction of intended mission lifetime used for servicing	[unitless]
	failed_downtime_frac	Fraction of intended mission lifetime when spacecraft is in failed state	[unitless]
Trade Metrics	stahl_cost1	Cost of developing the optics	USD FY13
	cost_flightsystem.program_level1	Cost of developing the spacecraft bus (NR)	USD FY13
	cost_flightsystem.program_level2	Cost of developing the spacecraft bus and infrastructure (NR)	USD FY13
	USCM8_cost1	Cost of developing the spacecraft bus and infrastructure (NR+R)	USD FY13
	NICM_cost_a	Cost of developing instrument A	USD FY13
	NICM_cost_b	Cost of developing instrument B	USD FY13
	NICM_cost_c	Cost of developing instrument C	USD FY13
	NICM_cost_d	Cost of developing instrument D	USD FY13
	NICM_cost	Cost of developing the instruments	USD FY13
	flightsyscost	Total cost of developing the flight system	USD FY13
	cost_servicing	Total cost of developing components for servicing missions	USD FY13
	cost_for_flightsystem	Total cost of flight system over mission lifetime	USD FY13
	cost_to_launch	Total cost of launching the flight system	USD FY13
	cost_servicing_launch	Total cost of launching servicing missions	USD FY13
	cost	Total cost of spacecraft over mission lifetime	USD FY13
	baseline_cost	Total cost of spacecraft assuming entire spacecraft is serviced every servicing mission (modularity level = 1)	USD FY13
	serviceability	Cost margin relative to the baseline cost per mass serviced in servicing missions	USD FY13
	utility_to_science	Total utility-to-science over mission lifetime	arcmin ² *photons
	state_probability	State probability matrix	[unitless]
	expected_productivity	Expected productivity	arcmin ² *photons

APPENDIX B: STAKEHOLDER QUESTIONS AND ANSWERS

- What ground stations will we use? DSN? How often should we assume passes occur and how long will they be?
- Is there a set of launch vehicles which we can use for making initial estimates?
- What are the mission goals? How does this telescope relate to current and future telescopes (ATLAST)?
- What is the expectation of the optical capability of the new telescope (optical bandwidth, aperture size, angular resolution, FOV, pointing stability, spectral resolution, contrast, inner working angle, wavefront error, wavefront stability, uninterrupted observation time, lifetime, operational efficiency)
- What operational orbits should we consider?
- What is the budget for this mission?
- Is there an available cost model for this mission (spacecraft, ground systems, launch vehicle)? Is there a cost model for a federated satellite system?
- When will this telescope operate? What is its expected lifetime? What other space assets will be available for utilization at that time?
- What mirror technologies should we consider?
- What detector technologies should we consider?
- What adaptive optics technologies should we consider?
- Are there specific technology insertion goals for this telescope?
- Does the data need to be secure?
- Who is going to receive the data?
- What data management system should we use?
- Is NASA interested in soliciting additional stakeholders for the project (ESA, Commercial, Hosted Payloads)?

Stakeholder Responses

Dan Lester

- What are the mission goals? How does this telescope relate to current and future telescopes (ATLAST)?

It's really up to the science community to define priority goals for a new space telescope. If the assumption is that this telescope is going to be a LARGE DIAMETER, OPTICAL telescope, then the best science case for that kind of telescope was probably made by the ATLAST team. But that's not really a consensus science case. It does seem perfectly reasonable to adopt the ATLAST goals as notional goals, which may or may not actually represent a consensus priority by the astronomical community. But there have been many other large telescopes (infrared, X-ray, ultraviolet, radio) proposed, so you pretty much have to decide which one you're interested in designing. These are YOUR goals. Not the goals of the community. So your "assumption/rationale" that the science goals/requirements for this telescope are the same as for ATLAST seems one sensible approach. There are many other sensible approaches. This exercise can then be taken as an existence proof as to whether there is an affordable strategy to build a telescope defined by the ATLAST requirements.

- What is the expectation of the optical capability of the new telescope (optical bandwidth, aperture size, angular resolution, FOV, pointing stability, spectral resolution, contrast, inner working angle, wavefront error, wavefront stability, uninterrupted observation time, lifetime, operational efficiency)

These are all expectations that depend on budget. You basically want a telescope you can afford that will do as much as possible. That being the case, you want a telescope that is at least a factor of three larger in diameter than what we virtually have now, which would be JWST. It's commonly understood that a flagship project, in order to be sellable, has to be an order of magnitude better than what you had before. In light gathering power, a factor of three in diameter would do it. So I think you need an 18+ m diameter telescope. Well, if this is really to be an optical (as in "visual wavelength" telescope, then maybe we're talking a factor of three over HST. That would be a 7-m telescope. But I think the reason that NASA chose to develop a 6m near-IR large telescope instead of a 6-m optical telescope is because that's where the best science was thought to be.

As to optical bandwidth, it's simple to have a telescope that can perform well across the reflectivity spectrum of aluminum. The would go longward from the near-UV. If the telescope is not going to be cold, there isn't much sense in having it work any farther into the infrared than 2-3 microns, as for HST. But be careful about UV requirements, as those will completely dominate the wavefront error, pointing, and cleanliness requirements for the telescope. An optimal UV-capable telescope could be enormously expensive.

Pointing stability should serve diffraction-limited performance of an 18+ m aperture telescope, on a time scale of at least hours. Same with wavefront error and stability.

Spectral resolution isn't about the telescope. It's about the focal plane instruments. If this is a serviceable telescope, where new instruments can be installed, this isn't an obviously important question. In any case, high spectral resolution isn't advantageous in wavelengths at which the Earth's atmosphere is transparent, because at such wavelengths, much larger ground-based telescopes will win every time for photon-hungry and background-tolerant applications like high spectral resolution.

As to lifetime, that's a dangerous game to play. If you go to NASA and ask them to buy into a telescope with a 40 year lifetime, for example, you're asking them to commit to 40 years of operating budgets. They simply won't do that, unless you give them a clear picture of the science those forty years will buy. We have no way of telling what that science might be. In fact, our science priorities evolve pretty dramatically on time scales of a decade or so. Ordinarily, I'd say a ten-year lifetime is defensible. Perhaps with a serviceable telescope, you could try for twenty. But you're going to pay a stiff price for long lifetime. I think the best idea is to design a telescope with fixed science capabilities that will last for ten years, and then make serviceability and servicing as extra-cost options. ROI isn't necessarily proportional to observing time, once you get past the highest priority questions.

Operational efficiency is pretty much dependent on what you're trying to accomplish. If you get outside of LEO, the operational efficiency could be quite high, in terms of the fraction of the time that data is being taken. I would assume that the planned scheduling efficiency of JWST,

which is something like 95%, should apply to this. That mainly dictates slew times and engineering time requirements.

I think the bottom line to all this is trying to come up with a concept for a huge telescope with optimum imaging performance, and see if you can do it in such a way that is affordable. Once you have that, there are many useful directions one can take.

- Is there an available cost model for this mission (spacecraft, ground systems, launch vehicle)? Is there a cost model for a federated satellite system?

There are plenty of cost models for federally funded space telescopes. In fact, a big piece of NASA develops and supports such cost modeling for space missions. Probably the most important part of a credible cost model is one that develops a clear picture of technological readiness. That is, you don't start cutting metal until you have cogently identified all technology needs, and made appropriate investments to relieve them. Identifying technology lapses late in the project is HUGELY expensive. Should assess the subsystems with regard to current TRL.

The cost curve for large space telescope development has a pretty well understood profile, and NASA SMD funding is simply incapable of supporting a peak funding rate of more than about \$500M/yr for an astronomical telescope.

That said, to the extent this mission makes any requirements on human space flight, it would be very hard to come up with a believable cost model. We don't have good cost models for human space flight outside of LEO. That being the case, maybe you should assume that the 10-year budget is <\$5B, and just make the thing optionally serviceable. Or else assume that the servicing is done robotically.

- Is there a set of launch vehicles which we can use for making initial estimates?

If you want to keep costs down, and \$/lb low, you need to be looking at Falcon Heavy. I suppose you should look at SLS, but I don't have a lot of confidence that support for that launcher will continue. It might be a dead end, as we've made no serious plans about what we'd put on it, and it's already understood to be a very expensive lift option.

- What operational orbits should we consider?

For the highest performance, in terms of thermal stability, accessibility, and field of regard, you won't do better than Sun-Earth L2. DO NOT put this telescope in LEO. A very large optical telescope will be seriously compromised by putting it in LEO, for many reasons.

- What is the budget for this mission?

I frankly don't think it's sellable if the LCC (not including servicing) is over \$5B. JWST is a bad example to follow, in terms of LCC affordability. NASA, Congress, and the science community will avoid such expensive instruments like the plague in the future. Some serious thought should be given to making such a telescope useful to other nations, with the hope that those other nations can invest in it. That's feasible only if those other nations see obvious roles for themselves in telescope development. Another country won't buy in to such a telescope scientifically unless they can exercise their technological expertise in building it. Nations largely

don't pay for space astronomy. They pay for technology development that leads to good space astronomy.

So therein lies the challenge. Can you design a very capable telescope three times the size of JWST for 50% less money?

- What ground stations will we use? DSN? How often should we assume passes occur and how long will they be?

That's not a big issue. Ground station operations are a function of data rate, comm architecture, and on-board data storage. That's not going to drive mission design. But for a mission at ES L2, you'd pretty much assume you're going to use a DSN-like comm station. If you had to build a completely new DSN station, just for this mission, it would be a small fraction of the mission budget.

- What mirror technologies should we consider?
- What detector technologies should we consider?
- What adaptive optics technologies should we consider?

These are things that come out of focused trade studies. It doesn't make a lot of sense to think about these before establishing the telescope requirements.

- Are there specific technology insertion goals for this telescope?

There are many aspects to this question. Technology insertion strategies can apply to system or technology obsolescence, and technology applicability to different stakeholder groups. I think an important one for this telescope is that technologies developed should allow for extensibility in telescope design. That is, whether I want to expand this particular telescope, or build a new much larger one after this one, I want the technologies developed for this one to be applicable to the next gen one. For example, one concept for ATLAST was putting the largest primary mirror possible in the largest launch shroud. That's not an extensible strategy, at least until someone decides to build a much bigger launcher. That is, the strategies that one develops here (construction, deployment, alignment, etc.) to make, say, an 18m telescope, should lead to envisioning a much larger one, or even expanding this one.

Another technology insertion goal is servicing. One would like a design that is not only ideally serviceable, but one that is amenable to new instruments. While one might not be sure about the prospects for servicing and instrument replacement, the telescope should not be designed in such a way to prevent that from happening.

- Why are hexagons used as the standard for mirror segments?

Because they fill space efficiently. Round segments don't. Since hexagons are roughly round, they are more symmetrically fabricatable.

- Does the data need to be secure?

Not "secure" in terms of national security. But it will be understood that preselected mission teams get first dibs on the data they've proposed to get.

- Who is going to receive the data?

Once the comm packages come down to Earth, the standard model is to have some institution (STScI for HST, or IPAC for IR data), manage, distribute, and archive the data. This is just a service you buy, and there are many with that experience,

- What data management system should we use?

That's up to the data management institution, and is not a decision for the observatory designers, nor an engineering decision. The observatory designers might like to set some specifications about what the data management system should be capable of doing. It clearly has to be one that serves a multitude of worldwide users who can't be assumed to have any engineering expertise.

- Is NASA interested in soliciting additional stakeholders for the project (ESA, Commercial, Hosted Payloads)?

I don't think "hosted payloads" has much to do with this. Commercial? That would require that industry see observatory operations as a money-making concept. I don't think that would happen. Certainly other national space agencies -- ESA, Roscosmos, JAXA, CSA, etc. could be polled about this, as per my suggestion above. But this isn't an engineering question except, as I said above, to the extent of assessing how their engineering expertise overlaps.

Lee Feinberg

I agree with almost all of your observatory requirements but I personally would advocate you go larger than 16.8-meters. I know that size was chosen for the deployed ATLAST and so there is some existing work done at that scale but once you buy into the idea of assembly and economies of scale based on identical mirrors and modules then 20+meters makes a lot more sense (I'm OK bigger than 20-meters but 16.8-meters is still at the size that you would consider deployment and not enough bang for the buck). This argument is supported by the next generation of hexagonal mirror ground telescopes which are 30 meters (TMT) and 39 meters (EELT). The argument of course is that the major costs are in the NRE of making the first modules, facilitating, and solving how to assemble - the incremental cost of additional area is not significant. For size and high contrast dynamics and pointing may actually be the limiting issue (we want to take advantage of the resolution) but the hope is active solutions can mitigate this (an area I urge you to focus on!). Conveniently, the 20-meter telescope size we chose using JWST segment size has exactly the number of hexagonal elements as the next generation deformable mirror from Boston micro-machines that the VNC group is using and which is critical to achieving high contrast. In addition, Marc Postman has done some thinking about the science for a 20-meter (and hopefully will spend more time on this issue in the future) and can comment on that aspect of things.

I'm very interested to hear what you are thinking on where and how assembly will be accomplished - that seems to be a key nut to crack. With respect to servicing, do you want to consider two key roles for human involvement: troubleshooting (if there is a major issue that robots cannot solve) and reduced latency telerobotics.

With regards to cost, TMT's model relies quite a bit on international contributions (China, India and Japan are all contributing significantly) and on economies of scale. We've studied mirror segment economies of scale from JWST and a ground telescope but a lot more needs to be done

here. I suspect there are other economies of scale arguments that would be very helpful to explaining why bigger doesn't cost that much more and I would urge you to talk to your economist colleagues at MIT to help with that. Also, I'm not sure how you cost the assembly piece so you may want to study the HST cost arguments.

Swati Mohan

- What are the mission goals? How does this telescope relate to current and future telescopes (ATLAST)?
 1. Find earth-like planets around other stars and determine if they carry the signature of life.
 2. Look at the universe as far back in time as possible and understand our origins.
 3. Look at galactic centers to understand their structure, formation, etc.
 4. STScI has a lot of information on this.
 5. We would think it relates closely to ATLAST.
- What is the expectation of the optical capability of the new telescope (optical bandwidth, aperture size, angular resolution, FOV, pointing stability, spectral resolution, contrast, inner working angle, wavefront error, wavefront stability, uninterrupted observation time, lifetime, operational efficiency).
 1. 80% Strehl ratio at 633 nm.
 2. Rules of thumb you can use for an F1 primary are:
Radius of curvature of PM = 2 * PM_diameter
Radius of curvature of SM = 0.25 * PM_diameter
PM-SM_distance = 0.9 * PM_Diameter
SM_Diameter = 0.15 * PM_Diameter
 3. You should decide the telescope operational temperature requirements based on the mission objectives. Is this UV, optical, IR or some combination?
 4. The rest of the requirements depend on the application and will be determined based on the mission objectives.
 - Is there an available cost model for this mission (spacecraft, ground systems, launch vehicle)? Is there a cost model for a federated satellite system?
 1. We don't know of any available cost model. Or a model for a federated satellite system.
 - Is there a set of launch vehicles which we can use for making initial estimates?
 1. Atlas V, Delta IV heavy, the SLS with either the Atlas V or Delta IV heavy fairing, the SLS with 8 and 10 meter fairings that are on the drawing board. Could also look at Dragon.

- What operational orbits should we consider?
 1. Fixed at ESL2.
 2. Other Lagrange points.
 3. GEO (to assemble?).
- What is the budget for this mission?
 1. \$5-10B in 2013 \$.
- What ground stations will we use? DSN? How often should we assume passes occur and how long will they be?
 1. If at SE-L2 (or L1) would use the 34 m antennas at DSN.
 2. If Earth orbiting would use TDRSS.
 3. Full coverage for critical events. One 8 hour pass a day otherwise.
- What mirror technologies should we consider?
 1. Actuated hybrid mirrors with either a nanolaminate or polished silicon carbide surface.
- What detector technologies should we consider?
 1. Suggest you pick a representative set of instruments and base the detectors on current state of the art.
- What adaptive optics technologies should we consider?
 1. Actuated hybrid mirrors with rigid body actuators for the primary.
 2. Actuated hybrid mirrors with rigid body actuators for the secondary and a primary with rigid body actuators.
- Are there specific technology insertion goals for this telescope?
 1. A great deal of technology needs to be developed to enable the telescope. Marc Postman has a chart that summarizes these. OptIX does a number of them: on-orbit assembly and servicing, actuated hybrid mirrors, laser metrology, wavefront sensing and control.
- Why are hexagons used as the standard for mirror segments?
 1. They are stackable and reasonably close to circles which makes them easier to polish. Manufacturing inertia (machines, tooling, etc. already developed) will likely keep it that way.
- Does the data need to be secure?
 1. Data security should be the same as a for a NASA science mission.

- Who is going to receive the data?

1. Assuming mission is at L2, Level 0 data will come through the DSN to the GDS at the institution operating the mission; JPL, GSFC, etc. The data will then be processed into Level 1 data and shipped to the institution(s) in charge of science; STScI, universities, etc.

- What data management system should we use?

1. We would expect the institution managing the project/mission to choose. JPL has more experience with planetary missions. GSFC with Earth orbiting. We would probably pick something at JPL since mission is at L2.

2. This shouldn't be a driver for this study.

- Is NASA interested in soliciting additional stakeholders for the project (ESA, Commercial, Hosted Payloads)?

1. Not something that we can answer other than the cost is so high that NASA will likely want partners to help defray it.

Tupper Hyde

- What ground stations will we use? DSN? How often should we assume passes occur and how long will they be?

DSN, mainly Australia site for 4 hours per day. Same as JWST.

- Is there a set of launch vehicles which we can use for making initial estimates?

Any EELV, Falcon 9, F9 Heavy, Ariane, SLS

- What are the mission goals? How does this telescope relate to current and future telescopes (ATLAST)?

UVOIR Astronomy and Earth-size exoplanets. Same science goals as ATLAST 16.8-m. Should consider servicing to enable 40+ year life.

- What is the expectation of the optical capability of the new telescope (optical bandwidth, aperture size, angular resolution, FOV, pointing stability, spectral resolution, contrast, inner working angle, wavefront error, wavefront stability, uninterrupted observation time, lifetime, operational efficiency).

Same as assumed for ATLAST 16.8-m design.

- What operational orbits should we consider?

SE-L2 for science. Any for assembly/servicing.

- What is the budget for this mission?

Cost should be an output of the trade. \$10B (of today's dollars) is not unreasonable. I bet the range will be like \$5-15B.

- Is there an available cost model for this mission (spacecraft, ground systems, launch vehicle)? Is there a cost model for a federated satellite system?

Several large telescope cost models are in the literature. I would recommend the one by Phil Stahl. NASA will provide DSN costs.

- When will this telescope operate? What is its expected lifetime? What other space assets will be available for utilization at that time?

Assume mission start in 2020 and launch by 2030. It should operate at least 10 years or up to 40 with servicing. You could assume a geo servicer such as the NASA Restore mission would be operating regularly by 2028 (ssco.gsfc.nasa.gov)

- What mirror technologies should we consider?

Glass and AHM segments. Size and number of segments is a trade.

- What detector technologies should we consider?

Same at ATLAST.

- What adaptive optics technologies should we consider?

Image and/or laser truss wavefront sensing with mirror actuation. Bandwidth (update rate) of wavefront control depends on thermal time constants. Coronagraphs will have additional deformable mirrors.

- Are there specific technology insertion goals for this telescope?

In the servicing options, upgrades for new technology in instruments should be considered.

- Does the data need to be secure?

No

- Who is going to receive the data?

A space telescope science institute (such as STScI) would archive the data and provide it to investigators

- What data management system should we use?
- Is NASA interested in soliciting additional stakeholders for the project (ESA, Commercial, Hosted Payloads)?

We expanded the stakeholder names at the meeting. I don't think adding ESA or commercial for this scope of study will be useful.

Line Number	CODE	Component Name	Installation Model/Part Number	Function Name	Mass (kg/unit)	Power (W/unit)	Power (W/unit)	Largest Dimension When Stored (m)	Volume (m ³)	Years Life (k)	Reliability (Prob. Success)	MTBF	Power Consumed (W)	Cost (\$K)	Ttl. Level	Notes/References	
1	Structures	Robotic Arm	NRL FRENQ Arm http://spoint.a2.utexas.edu/robotics/technew7_2006/robotics/2006new/10207_29_03.pdf	Robotic Arm	100	60	1.25	0.0565486	10	0.95	134.957257	0	10	7			
2	Structures	IM Coil	RINGS coil	Electromagnetic Coil	50	0	15	0.03925	10	0.95	134.957257	0	10	6			
3	Structures	UDP	Universal Docking Port	Universal Docking Port	5	0	0.02	0.000008	15	0.95	134.957257	0	15	5			
4	Structures	Primary Mirror Segment	JWST	Mirror Segment	150	0	2.28971438	11.841650	50	0.95	134.957257	0	15000	9			
5	Structures	Surface Normal Actuator	Surface Parallel Actuator	Surface Normal Actuator	1	0.5	0.05	0.000115	10	0.95	134.957257	0	10	9			
6	Structures	Surface Parallel Actuator	Surface Parallel Actuator	Surface Parallel Actuator	1	0.5	0.05	0.000115	10	0.95	134.957257	0	10	9			
7	Structures	Backframe per mirror segment	Backframe per mirror segment	Backframe per mirror segment	25	0	0.03	0.0027	50	0.95	4974.95812	0	10	9			
8	Structures	Bus structure	Structural Support	Structural Support	100	0	0.03	0.1	50	0.95	4974.95812	0	2.5	9			
9	Structures	Magnetic Isolation Device	Magnetic Isolation Device	Magnetic Isolation Device	1	0	2.5	0.000115	15	0.95	134.957257	0	10	7			
10	Structures	Viscoelastic Isolation Device	Viscoelastic Isolation Device	Viscoelastic Isolation Device	1	0	0.05	0.000115	15	0.95	134.957257	0	10	9			
11	Structures	Active Damper	Active Damping Device	Active Damping Device	1	2	2	0.05	0.000115	10	0.95	134.957257	0	10	9		
12	Structures	Deployment Device for Solar Array	Deployment Device	Deployment Device	1	3.75	3.75	0.1	0.001	50	0.95	474.561075	0	10	9		
13	Structures	Global Device	Global Device	Global Device	25	5	5	0.1	0.001	15	0.95	134.957257	0	10	9		
14	Structures	UDP	Universal Docking Port	Universal Docking Port	5	0	0	0.05	0.000115	15	0.95	134.957257	0	15	5		
15	Structures	UDP Power Interface	Universal Docking Port Power	Universal Docking Port Power	0.25	0	0	0.05	0.000115	15	0.95	134.957257	0	2.5	5		
16	Comm1	Laser Communications Box	MIT Lincoln Lab; http://spaceflightnow.com/news/n1002/technology/	Laser communications type of comm box	2.27	0.5	0.5	0.1	0.001	10	0.95	134.957257	0.1	10000	7		85-500Wb25
17	Comm2	RF for Direct Communications	Radio frequency type of comm box	Radio frequency type of comm box	2.9	7	7	0.4	0.25	10	0.95	134.957257	0	25000	9		To be removed (Redundant)
18	Comm3	Direct Download Antenna (High and Low Gain)	ATLAST	Antenna for direct downloads	40	100	1	1	1	10	0.95	134.957257	0	35000	9		
19	Comm4	Gain for Direct Communications Relay	indium NEXT (R antec Microwave Antenna)	Crosslink antenna	11.79	14	20	0.4572	0.0956	10	0.95	134.957257	0	35000	9		AnteVCo:Spacecraft Antennas and An
20	Avionics1	RAM	72d3232	Memory required to store data prior to download	3	0.165	0.165	0.1	0.001	10	0.95	134.957257	0	1700	9		
21	Avionics2	Power Converter (PCU)	PXC20	Power Converter	27	5.11	5.11	0.0508	0.0006	20	0.95	389.914514	0	2000	9		
22	Avionics3	Data Interface Unit (DIU)	Hubble	Command and Data Link Interface between other subsystems	16	5	5	0.38	0.14	20	0.95	389.914514	0	10000	7		
23	Optics1	Instrument A	Hubble References	Resolution, VIS/NIR-EXTIR, Partially coronagraphic	500	90	100	2	1.25	40	0.5412	660.07012	0	100000	8		8 M/F/V allocated based on previous prog
24	Optics2	Instrument B	Hubble References	Non-imaging, Medium/High Spectral Resolution, FUV-NUV-VIS, Non	500	90	100	2	1.82	40	0.5412	660.07012	0	100000	9		
25	Optics3	Fine Guidance Sensors	Hubble References	Orientation navigation	300	45	50	2	1.25	40	0.5412	660.07012	0	50000	9		
26	Optics4	Instrument C	Hubble References	Imaging, Low/Medium Spectral Resolution, VIS/NIR-EXTIR,	500	90	100	2	1.25	40	0.5412	660.07012	0	100000	4		
27	Optics5	Instrument D	Hubble References	Coronagraphic	500	90	100	2	1	40	0.5412	660.07012	0	100000	8		
28	Thermal1	Thermal blanket (bus)	Hubble References	Thermal insulation, Thermal isolation	30	0	0	3	0.1	15	0.94	242.42266	0	5	9		
29	Thermal2	Thermal radiator (bus)	Hubble References	Thermal reflection	30	0	0	3	0.1	15	0.94	242.42266	0	5	9		
30	Thermal3	Thermal sensor (bus) (TBC) (optics)	Hubble References	Thermal sensor	0.30	0	0	0.01	0.000001	10	0.95	134.957257	0	0.05	9		
31	Thermal4	Crosscooler (bus)	Hubble References	Cooling mechanism	5	100	100	1	1	10	0.95	137.286672	0	10	9		
32	Thermal5	Thermoelectric heater (optics)	Hubble References	Heating mechanism	0.01	5	7.5	0.01	0.000002	40	0.95	551.186650	0	0.01	9		
33	Thermal6	Hot pipe network (bus)	Hubble References	Heat transfer mechanism	1.1	0	0	1	0.01	20	0.95	389.914514	0	1	9		
34	Thermal7	Thermal sensor (optics)	Hubble References	Thermal sensing	0.005	0.01	0.015	0.001	0.000001	40	0.95	551.186650	0	0.001	9		
35	ACS 1	Nominium Wheel	Honeywell HRL6 MW(N/mz)	Attitude Control System	12	22	185	0.351	0.1712	10	0.94	503.902882	0	10	9		
36	ACS 2	Star Tracker	Star Tracker	Attitude Control System	25	200	200	0.5	0.115	10	0.94	503.902882	0	150	7		
37	ACS 3	Star Tracker	SAT CT-633 Stellar AS	Attitude Control System	2.5	2	2.0	0.1423	0.000015	10	0.94	203.925282	0	15	9		
38	Power1	Solar Array per 100 wats	Triple Junction In/GaAs cells	100 watt solar array unit (assuming 5 meter size folded)	2.25	0	0	5	0.004	15	0.93	206.695008	100	1900	9		
39	Power2	Battery per watt-hour	Lithium ion battery	1 watt-hour battery unit (assuming cube)	0.005	0	0.017657456	0.0000035	15	0.8	142.36931	0	3	9			
40	Power3	Distribution per 100 wats	VFT converters	100 watt distribution(converters) unit (assuming cube volume)	0.000225	0	0.0228823486	0.000012	40	0.85	246.125175	0	600	9			
41	Power4	Connectors and Wiring	General connector and wiring	Connectors wires needed from voltage protect the telescope optics from stray light	1	0	0	0.5	0.125	50	0.95	574.78257	0	100	9		
42	Structures	Light Shield	Hubble from Magaret	Deployment Device	500	0	2.5	1	50	0.95	4974.95812	0	10	9			
43	Structures	Deployment Device for Antenna	ATLAST 8m scaled by ratio of length to radius	Deployment Device	0.5	3.75	3.75	0.1	0.001	50	0.95	474.561075	0	10	9		
44	Structures	Primary Mirror Segment	Hubble	Primary Mirror Segment	150	0	0	0	50	0.95	134.957257	0	15000	9			
45	Structures	Primary Mirror Bath	Hubble	Primary Mirror Bath	35	0	0	0	0.1	50	0.95	4974.95812	0	1500	9		
46	Avionics4	CPU	Hubble	Avionics Central Processing Unit	50	30	30	0.48	0.066	10	0.95	134.957257	0	4200	9		
47	Avionics5	Data Management Unit (DMU)	Hubble	Process, format, code/decode messages	37	5	5	0.7	0.0714	10	0.95	134.957257	0	4000	8		
48	Thermal8	Thermoelectric heater (bus)	Hubble	Heating mechanism	0.01	5	7.5	0.01	0.000002	40	0.95	551.186650	0	0.01	9		
49	Thermal9	Thermoelectric heater (bus)	Hubble	Heating mechanism	0.01	5	7.5	0.01	0.000002	40	0.95	551.186650	0	0.01	9		
50	Thermal10	Thermal sensor (bus)	Hubble	Thermal sensing	0.005	0.01	0.015	0.001	0.000001	40	0.95	551.186650	0	0.001	9		
51	Thermal11	Thermal sensor (bus)	Hubble	Thermal sensing	0.005	0.01	0.015	0.001	0.000001	40	0.95	551.186650	0	0.001	9		
52	Thermal12	Thermal blanket (bus)	Hubble	Thermal insulation, Thermal isolation	30	0	0	3	0.1	15	0.94	242.42266	0	5	9		
53	Structures	Science Payload support structure	Hubble	Structural Support	10	0	0	0.3	0.1	50	0.95	4974.95812	0	500	9		
54	Propulsion	Monopropellant hydrazine thruster	ATLAST 8m scaled by ratio of length to radius	Thruster	5	1000	1000	0.3	0.03	40	0.8	379.648662	0	500	8		
55	Propulsion	Axial Thruster	ATLAST 8m scaled by ratio of length to radius	Thruster	6	1000	1000	0.3	0.03	40	0.8	379.648662	0	500	8		
56	Propulsion	Roller (and tank)	ATLAST 8m scaled by ratio of length to radius	Thruster	1000	0	0	10	40	0.95	779.825025	0	1000	9			

APPENDIX I: DESCRIPTION OF ATLAST REQUIREMENTS AND THEIR IMPLICATIONS

As previously referenced, the optical and instrument baselines used in the TITANS AE architectural model originate in the ATLAST requirements as developed by NASA for the proposed 16.8-m class space observatory. This baseline does not vary substantially within the tradespace explored in this project; accordingly, the relevant subsystem models have been simplified to streamline the evaluation process. However, the imposed ATLAST requirements (**Table XXXIV**) do offer substantial guidance for the design of these subsystems which may be of interest to the reader. The proposed design implementation of the ATLAST requirements for the TITANS AE set of architectures is documented here.

Table XXXIV: ATLAST Key Optical Performance Requirements and Goals⁵

Requirement Name	Requirement	Goal	Science Drivers
Optical Bandwidth	0.2 – 2.5 μm	0.11 – 2.5 μm	Solar system exploration
Aperture Size	16.8 m		
Angular Resolution	6 – 12 mas	3.5 mas	
Field of View	5 arcmin		Extragalactic star formation
Pointing Stability	1 mas		Exoplanet characterization, life detection
Spectroscopic Resolution	300	120000	Extragalactic star formation
Contrast	1e+07	1e+10	Exoplanet characterization, life detection
Inner Working Angle	50 -100 mas	40 -50 mas	Exoplanet characterization, life detection
Wavefront Error	37 nm	0.07 nm	Exoplanet characterization, life detection
Wavefront Stability	10 nm	0.07 nm	Exoplanet characterization, life detection
Uninterrupted Observation Time	2 hours		
Operational Efficiency	90%		

For the optical train, three ATLAST requirements drive design considerations relevant to TITANS AE: (1) optical bandwidth; (2) aperture size; and (3) wavefront error. The optical bandwidth indicated here stretches across the ultraviolet (UV), optical (O/VIS), and near infrared (IR/NIR) wavelength ranges and drives the selection of mirror coatings. A variety of aluminum and silver-based coatings exist which are appropriate for this range of wavelengths; however, many coatings experience a substantial reflectance fall-off in the extreme ('far') UV ranges.⁸¹ Accordingly, the use of separate channels for more and less reflection-sensitive instruments may be appropriate (see below).

As in the ATLAST case, mirror diameter has been fixed at the 16.8-meter size class. (This in turn drives the angular resolution requirements specified in Table 1). The TITANS AE design also uses the three-ring hexagonal mirror format common to the ATLAST proposal. This approach minimizes wavefront complications due to mirror segmentation while still permitting launch of the primary mirror. (The appropriate balance between segmentation and mirror size is further addressed in Appendix K.)

Finally, the wavefront error requirement of 37 nm specifies the tolerance for manufacturing errors and polishing imperfections within the optical train. Because this number specifies the total error budget for the observatory, the wavefront error contribution of each element must represent only a fraction of this value. This value represents an incremental improvement on the expected performance of the JWST optical train.⁸² More challenging, however, is the “goal” error of .07 nm. Such accuracy can only be achieved with adaptive optics. The TITANS AE design presupposes such an adaptive optics system is integrated into secondary mirror assembly, permitting fine control of wavefront across the entire FOV of the telescope.

At the instrument level, the ATLAST requirements most important for instrument design include the majority of the remaining requirements. The FOV requirement of 5 arcmin necessitates the inclusion of a wide field of view instrument. The stability requirements drive the design of the fine guidance sensors. Meeting the spectral resolution requirement (R=300) suggests an imaging spectrometer design; the higher resolution “goal” (R=12000) on the other hand necessitates a dedicated, likely slit-based spectrograph/detector approach. The contrast and inner working requirements specify the performance for coronagraphic elements. Finally, the optical bandwidth requirement imposes an additional constraint (in addition to those it imposes on the optical train): each instrument will require additional detector channels for each of the UV, VIS and NIR wavelength ranges it attempts to analyze, due to the nature of detector technologies.

ATLAST meets and exceeds the requirements specified above with the following combination of instruments (Figure I.1).

Telescope	TMA Focal Plane Instruments				Cass Focal Plane Instruments		
	Vis/NIR Wide-field Imager	Vis/NIR Multi-Object Spectrograph	Vis/NIR IFU	FGS (FOV per FGS unit)	UV IFU & Spectrograph	Starlight Suppression	Exoplanet Imager & Spectrograph
8-m, 9.2-m	8x8 arcmin	4x4 arcmin	2x2 arcmin	3x3 arcmin	30 arcsec	Internal Coronagraph or Starshade Sensor	~10 arcsec
16.8-m	4x4 arcmin	3x3 arcmin	1x1 arcmin	~1x3 arcmin	15 arcsec		~10 arcsec

Figure 94: Tentative ATLAST Science Instruments and their FOV¹⁷

The decision to include both a Three-Mirror Anastigmat (TMA) and Cassegrain focal plane helps balance the tradeoff between FOV control and throughput losses associated with the inclusion of additional mirrors and interfaces in the optical pathway. For the particularly photon-starved (reflectivity-loss-sensitive) instruments, the Cassegrain focal plane minimizes bounces, compensating for the lower reflectivity of the optics in the UV, and the general lack of photons available to be collected for exoplanet purposes. The TMA focal plane allows many instruments to “pick off” light from the observatory field of view for various scientific purposes. As suggested above, these include fine guidance sensing, WFOV imaging and lower-resolution and/or imaging (relatively wide area) spectroscopy.

Because the TITANS AE architectural model does not require the degree of specificity included in the ATLAST model, these instruments have been incorporated into four “packages” for launch, assembly and servicing purposes. This decision reflects the wide range of functionalities any instrument package may possess (including multiple modes and detector planes) while meeting the outlined scientific objectives.

APPENDIX J: FORMS AND FUNCTIONS FOR HISTORICAL MISSIONS

Structures Subsystem	Hubble	JWST	Kepler	IRIDIUM
Protecting				
Radiation Protecting	Light Shield			
Dust Protecting	Aperture door, light shield		Photometer Dust Cover	
Micrometeoroid Protecting	Aperture door, light shield	2-layer aluminum meteoroid shields	Graphite Cyanite Structure	
Stray Light Protecting	Aperture door, light shield	Sun shield, central baffle	Sun Shield	N/A
Temperature Protecting				
	Multi-layer insulation; heaters; thermal blankets	Sun shield, radiator shades, MLI	Focal Plane Radiator	
Supporting				
	Aluminum shell; graphite-epoxy frame; storage bay ring; solar arrays, high gain antennas - latches on light shield	primary mirror - backplane; secondary mirror - "tripod" booms; bus electronics - box; instruments - ISIM truss structure	Solar panels - fixed to side of telescope structure; support system electronics - honeycomb aluminum box at base of photometer	electronics - spacecraft bus; antennas - communication panel
Pointing				
Bus Pointing				
		solar pressure trim flap, reaction wheels, thrusters	Reaction Wheels; thrusters	thrusters
Articulated Pointing				
		primary mirror segments - hexapod with actuators; HG antenna - two-axis gimbal		N/A
Preventing Jitter				
		Tower structure	(operational) Reaction wheels as only moving part	N/A
Deploying				
	N/A	Extendable booms; spreader bars; stem deployers; gimballs; tension cables	N/A	N/A
Stowing				
	N/A	Unitized pallet structure; hold-downs	N/A	N/A
Interfacing				
Launch Vehicle Interfacing				
		Clamp-band	Vehicle Adapter Ring with umbilicals	
Ground System Interfacing				
		Omni antenna, high gain antenna	High gain antenna; 2x omnidirectional low gain antennas	K-band antenna panel, L-band phased array antenna x3
AIT Interfacing				
	Gas purge system	test port		test port
Access Providing				
Physical Access Providing				
	Outer doors; latches; handrails; footholds	N/A	N/A	N/A
Digital Access Providing				
		N/A	N/A	test port
On-orbit Assembling				
Manipulating				
	N/A	N/A	N/A	N/A
Integrating				
	N/A	N/A	N/A	K-band inter-satellite antenna panel
Power Subsystem				
Power Generating				
Size (Surface area or mass)	Solar Array 19 m ²		Solar Array 10.2 m ²	Solar Array
Amount	2800 W		1100 W	2000 W

Power Storing	Batteries		Battery (Lithium ion)	
Thermal Subsystem				
Insulating spacecraft	Multi-layer insulation (MLI) ; new layers (NOBL) added	5-layer sunshield	MLI	MLI and/or thermal shields
Controlling temperature of optics (ie: mirrors)	Thermostatically controlled heaters	Central baffle / radiator (cooling)	Controlled heaters; Thermal blankets (cooling)	
Controlling temperature of spacecraft bus and subsystems				Standard active and/or passive thermal designs
Cooling instrument and/or detectors	Thermoelectric coolers, Heat pipes, Capillary Pumped Loop subsystems; Cryogenic dewar	Passive radiator enclosure; Cryogenic dewar; Joule-Thomson cooler	Propane and ammonia heat pipes; External radiator	Standard active and/or passive thermal designs
Isolating instrument(s) from warm sources on spacecraft	Thermal insulation; Thermal isolation	Thermal insulation; Thermal isolation	Thermal insulation; Thermal isolation	Thermal insulation; Thermal isolation
Avionics/Comm Subsystem				
Avionics functions				
Data collecting from target	Collected by Science Instrument Control & Data Handling (SICDH)	From interface with optics subsystem	Photometer, CCD Radiator	L-band antenna
Data processing from target	Data Management System(DF-224 computers)	Moongoose 5 processor	RAD750 Processor	on-board processor
Storing of data from target	Engineering/Science Tape Recorder, Solid State Recorder	Solid state recorder (471Gbits)	16 GB Solid State Recorder	
Scheduling of tasks and resources between telescope subsystems	Data Management System(DF-224 computers)	Moongoose 5 processor	RAD750 Processor	N/A teleport network (= teleports connecting the satellites through Earth stations to a MPLS Multiprotocol Label Switching)
Scheduling of tasks and resources between FSS satellites	Data Management System(DF-224 computers)	Moongoose 5 processor	RAD750 Processor	teleport network (= teleports connecting the satellites through Earth stations to a MPLS Multiprotocol Label Switching)
Interfacing with FSS	Data Management System (Data Interface Units)	Moongoose 5 processor	RAD750 Processor	teleport network (= teleports connecting the satellites through Earth stations to a MPLS Multiprotocol Label Switching)
Processing received data from the ground station	Data Management System(DF-224 computers)	Moongoose 5 processor	RAD750 Processor	on-board processor
Storing of the received data	Engineering/Science Tape Recorder, Solid State Recorder	Moongoose 5 processor, Solid state recorder	RAD750 Processor, 16 GB SSR	on-board processor
Formatting the data for sending / receiving	Data Management System(DF-224 computers)	Moongoose 5 processor	RAD750 Processor	on-board processor
Comm functions				
Transmitting target data (image) to ground		Far omni antenna, high-gain antenna, near omni antenna		single, 48 beam TX/RX phased array antenna, one omni antenna, also two fixed and two steerable antennas
Receiving data from the ground station	Low gain and high gain antenna Communications loop between HST and Tracking and Data Relay System Satellite (TDRSS)		parabolic-dish high gain antenna, 2 TX low gain, 2 RX low gain	
Electrical power distributing between all subsystems	1 x Power Control Unit, 4 x Power Distribution Units	Electrical power unit	20 amp-hr rechargeable lithium-ion battery	Electrical power unit
Electrical power collecting / generating	Solar arrays, batteries, charge current controllers	Solar arrays, 37Ah NiH2 battery	4 non-coplanar solar panels	solar arrays, 2000W
Systems				
Launching				

Launch Vehicle	Shuttle Discovery	Ariane 5 ECA	United Launch Alliance Delta II 7925	Dnepr, Falcon 9
Launch Location	KSC	Kourou, French Guiana	Cape Canaveral Air Force Station	TBD
Launch Date	April, 1990	2018?	March, 2009	2015-2017?
Orbit	600 km	L2	Earth-trailing heliocentric	780 km
Operations				
Deploy	Single Shuttle launch	Fold-up in Ariane 5 rocket to L2	Boeing Delta II to Earth-trailing heliocentric	10 satellites, 7 launches on SpaceX Falcon 9
Control	Goddard (partial pre-program, partial real-time)	Space Telescope Science Institute	LASP (mostly auto-rolls every 6 months)	Analysis and monitoring of performance
Collect Data	Cassegrain reflector - 2.4 m mirror	6.5 m mirror	1.4 m mirror, .95 m photometer	Cross-linked architecture captures device signals (like cell towers)
Distribute Data	TDRSS	Deep Space Network	Deep Space Network	Gateway facility to telephone and internet infrastructures
Decommission	Piece-by-piece until robotically-assisted de-orbit	10 year lifespan based on fuel, unclear decommission plan	??	Atmospheric burn-up after orbital decay
Manufacturing				
Measuring light (http://www.jwst.nasa.gov/mirrors.html)	2.4-m-diameter primary mirror	6.5-m-diameter primary mirror	1.4-m-diameter primary mirror	N/A
Being lightweight	Inch-thick top and bottom plates sandwiching a honeycomb lattice	Use of beryllium (strong but light material) (1/10 of the mass of Hubble's mirror per unit area)		N/A
Mirror fitting into a rocket	N/A	18 segments on a structure that folds up	N/A	N/A
Fitting without gaps (high filling factor)	1-segment mirror	Hexagonal shape for each segment	1-segment mirror	N/A
Providing a 6-fold symmetry to reduce the number optical prescriptions	N/A	Hexagonal shape for each segment	N/A	N/A
Focusing the light into the most compact region on the detectors	Circular shape for primary mirror	Approximately circular shape for primary mirror	Circular shape for primary mirror	N/A
Focusing correctly on faraway galaxies	N/A	6 actuators attached to the back of each primary and secondary mirror segment + 1 actuator in the center to correct curvature	N/A	N/A
Keeping cold at -220°C	N/A	Cryogenic system	N/A	N/A
Shaping, smoothing, polishing	Computer-controlled machines	polishing machines	Industrial machines	N/A
Testing the change in mirror segment shape due to the exposure to cryogenic temperatures	Support the mirror on both sides with 138 rods exerting varying amounts of force	PhaseCam	Laser interferometer	N/A
Improving the mirror's reflectivity	65-nm-thick aluminum coating (+ protective 25-nm-thick magnesium fluoride coating)	Gold coating	Enhanced silver coating	N/A
Seeing newly forming stars, and faintly visible comets as well as objects in the Kuiper Belt.		MIRI (http://ircamera.as.arizona.edu/MIRI/instrument.htm)		N/A
Studying thousands of galaxies in 5 years		NIRSpec and microshutters (http://www.jwst.nasa.gov/nirspec.html)	105-square-degree field of view	N/A
Imaging in the NIR		NIRCam (http://www.jwst.nasa.gov/nircam.html)		N/A
Pointing		FGS/NIRISS (http://www.jwst.nasa.gov/fgs.html)	4 CCDs located on science focal plane	N/A
Measuring large aspheres		SSI-A (http://www.nasa.gov/topics/technology/features/web-b-spinoffs.html)		N/A
Compensating spherical aberration			Schmidt corrector	N/A
Mass-producing satellites on a gimbal	N/A	N/A	N/A	Patented technology by the engineer who set up the automated factory for Apple's Macintosh
Providing utmost reliability				Microwave inter-satellite communications links

APPENDIX K: PROPOSED METHODOLOGY FOR CALCULATING INSTRUMENT-LEVEL SCIENCE VALUE

Although detailed calculation of science utility was unnecessary for evaluation of the TITANS AE tradespace, the ability to accurately assess the relative values of various discoveries and the observatories and instruments which produce them remains a desirable capability for future comparisons between system architectures. This appendix offers a partial proposal for accomplishing this objective, with emphasis on instrument-level characterization.

For general a general set of astronomical observations, the total science utility can be expressed as a function of the value of each discovery weighted relative to the value of the given class of discoveries:

$$Total\ Science\ Utility = \sum_{i=1}^n (Discovery\ Value_i * Number\ of\ Discoveries)$$

Eq. K.1

Where i represents the class of discovery for n classes of discovery. A discovery “class” for these purposes represents a kind of observation, e.g., “faint object characterization,” where an observation is defined as the set of photons collected for the purpose. Developing relative weightings and valuations of discovery classes is difficult and inherently subjective, but may be accomplished with reference to the decadal survey or direct communication/polling of stakeholders (scientists). The decadal survey already suggests priorities for various kinds of missions and scientific efforts, which implies that a weighting schema is feasible.

Within a single class of discoveries/observations, a second set of weightings is desirable to distinguish how *useful* a given observation/set of photons is from a scientific perspective. The usefulness of a photon can be described as our ability to distinguish it (via optics and instruments) from other photons. This discrimination can come in a variety of dimensions: photometric, spatial, spectral or polarimetric, among others. For different classes of observations, certain kinds of discrimination have greater value than others; spatial discrimination is more valuable for surveys and imaging operations, while spectral characterization is arguably more valuable for exoplanet characterization. For a given weighting associated with each discrimination class z , optics and instruments can be evaluated against observation class i by referencing their discovery efficiency:

$$Discovery\ Value_i = \left[\sum_{z=1}^q (Discrimination\ Weighting_z) \right] * Discovery\ Efficiency$$

Eq. K.2

As suggested, discovery efficiency here refers to the capabilities of a given combination of instrument and optical train to discriminate between classes of photons. This equation suggests

that doubling an instrument's capacity to discriminate photons (e.g., doubling spectral resolution) only doubles discovery value if, for the current class of discoveries, such a doubling is useful (and is so reflected in the discrimination capacity weightings).

These first two equations capture the bulk of the subjective elements of utility estimation, permitting objective evaluation of optics and instrument performance in the forgoing discussion. Objective evaluation of performance is a non-trivial problem on its own, with much of the challenge lying in a determination of the appropriate units. Past efforts have suggested units such as "productivity rate" (images per unit time) or another form of "discovery efficiency" (throughput * FOV, or photons per arcmin², occasionally photons per arcmin² per unit wavelength).^{24,13} While each of these options captures some aspects of instrument performance, they collectively focus imaging operations for comparison (arguably, they are equations 'optimized' for imaging systems comparison). As the bulk of astronomical observations includes a non-imaging component, or are entirely non-imaging, a more general equation is required to fully assess such systems' performance. Such observations have only one parameter which is fundamentally comparable across all operations: the amount of time required to complete them.

At a theoretical level, for a given observation target, the amount of time required to confirm detection of the target is related to the photon flux density collected from the target and the sensitivity of the instrument/optics train. For these purposes, both sensitivity and flux density may be appropriately defined in Janskies or AB magnitude (Jansky/flux units used here for simplicity). The Jansky, defined as 10^{-26} Watts per m² per Hz, is the integral of the spectral radiance over the source solid angle, and may be applied to point or extended sources. Sensitivity, meanwhile, provides the minimum effective flux which can be extracted as signal from background noise in a given integration time and over a given wavelength range. Such values have been calculated for existing systems (Figure K.1).

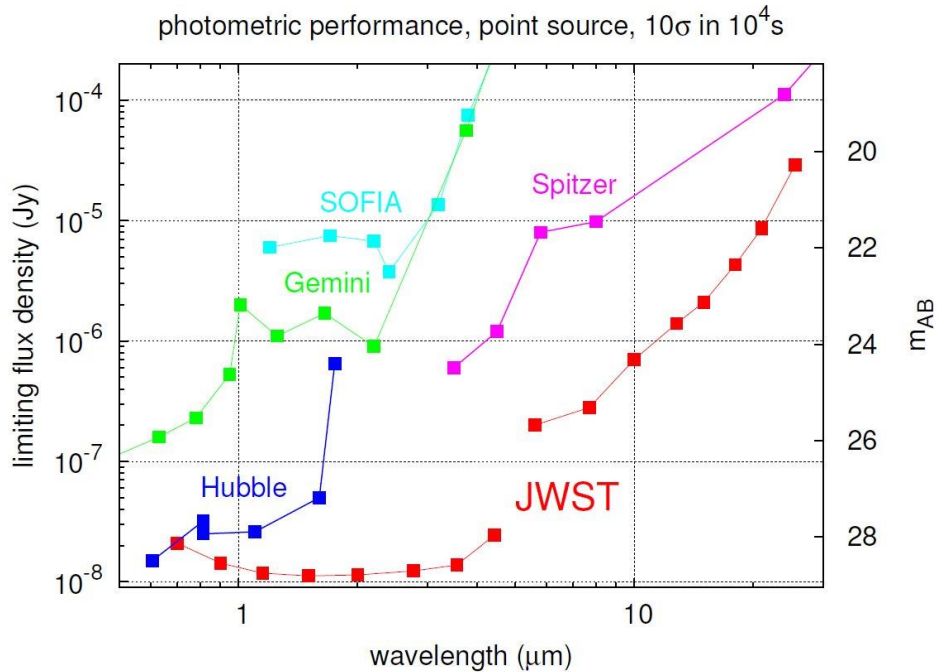


Figure K.1: The faintest flux that can be detected at 10σ in a 10^4 s integration for a variety of telescope systems.⁸³

Below the specified sensitivity threshold, any photons detected will not generate meaningful science; to make use of them, it would be necessary to increase the integration time or improve instrument performance. By contrast, sources above this threshold flux density will be observable in a smaller amount of time, or for the same time allocation, can be observed at a higher degree of discrimination/granularity. In this way, any photons collected above the sensitivity threshold can be “spent” on decreasing the integration time (allowing for more science operations), or increasing the fidelity of the current science operation (by discriminating in more detail between the kinds of photons), effectively increasing the number of unidimensional science operations.

In designing and evaluating instruments, available technologies allow for the optimization of certain science operations. At a basic level, any instrument is capable of discriminating the photons associated with a target in any dimension (spectral/spatial//photometric/polarimetric), provided that instrument is equipped with detectors, a limited set of tools and enough time. Using a one-pixel detector, a coronagraph and an adjustable slit/grating, a spatial and spectral image cube at very high contrast and high resolution over a wide field of view can be created...in a very long time. What distinguishes instruments from a scientific standpoint is how they are optimized for one or more of these discrimination tasks, and how efficiently they use the available flux density. The first of these parameters – optimization – addresses the overhead time cost associated with each science operation. An imaging instrument can be used to take spectral measurements if a filter wheel is applied. For a multispectral image, three (or more) images are taken, one at each filter wavelength range. The time required to collect enough flux to reach an SNR of 10 is directly linked to the amount of flux available (and hence, the number of ways the available flux is being subdivided). So, collecting 5 wavelength subranges takes five

times as long as collecting one panchromatic image of that target (assuming an even spectral distribution of flux in this degenerate case). Additionally, because time is required to adjust the filter wheels, an additional 5x penalty is occurred relative to the baseline panchromatic option. By comparison, the imaging aspect of the operation incurs much less penalty. Dividing a single detector into 1000 pixels over the same FOV means the image takes 1000 times as long to collect. However, no overhead cost is incurred, because all detectors collect simultaneously/in parallel. This reflects the efficient use of the available flux density per unit time associated with the two dimensional detector. In effect, less input flux is wasted as a result of parallelization. To use another example, a single spectrograph replaced by a cluster of spectrographs (as in JWST's NIRSpec) increases the parallelization and thus efficiency of collections. NIRSpec could be used for imaging operations by simply iterating the spectral collections over a large spatial area – but at a substantial time penalty².

Once photons are detected and discriminated/separated, a final step involves accounting for the actual collection capability of the optics system. The size of the primary mirror and associated resolving power determine the amount of light collected from each detection and also the degree to which that light can be resubdivided. Taken together, these factors suggest the following qualitative formula:

$$\begin{aligned} & \textit{Discovery Efficiency} \\ & = \textit{Photons Collected} * \textit{Photons Discriminated} * \textit{Photons Detected} \end{aligned}$$

Eq. 91

Where “photons collected” loosely corresponds to optical performance, “photons discriminated” accounts for the design of the instrument-level optics pathway, and “photons detected” captures the sensitivity and capability of the detectors themselves.

This conceptual framework can be made quantitative by returning to the flux density notation introduced previously. For a given class of target at a specified distance, an expected flux density profile, angular size and working area can be specified (where working area refers to the presence or absence of alternative signal sources in the vicinity). This total flux (10^{-26} W/(m²*Hz*s), when collected by an optical train with a specified mirror collection area, after experiencing differential throughput losses associated with the optical train yields the total flux collected and available for sensing at the optical bench (“photons collected”). At this point, the target is “picked off” by an instrument (in whole or in part) for analysis. (Larger targets may have an effective angular size greater than the FOV of the instrument, necessitating additional observations). The relevant photons are divided spectrally, spatially and polarimetrically by the instrument workbench, with losses associated with each discrimination accounted for (“photons discriminated”). Finally, with any extraneous signals suppressed (via coronagraphy or other methods), detectors of a given size, well depth and pixel density can record the target to a degree

² Arguably, opening all of the microshutters at once converts NIRSpec into a sort of imaging system. But assuming that only a few could be open at a time, an image could still be produced with enough time penalty.

of photometric accuracy within the limitations of the detector sensitivity (“photons detected”). These factors, when combined, yield the following equation:

$$(TFD * MCA * OTL) * \left(\frac{IFOV * SWR}{ETS * SB * NPOL} * ITL \right) * \left[\frac{(CSF * \frac{EPF}{ESF} * EDD)}{EDS} \right]$$

= *Discovery Efficiency (units: discoveries per 10⁴s @ SNR = 10*

Eq. 92

where:

- TFD* = Total (source) Flux Density (10^{-26} W/(m²*Hz)
- MCA* = Mirror Collection Area (m²)
- OTL* = Optical Train Losses (expressed as % of original remaining)
- SWR* = Spectral Wavelength Range (required wavelength coverage, Hz or λ)
- SB* = Spectral Bandwidth (number of subdivisions in wavelength range – unitless)
- IFOV* = Instrument Field of View (arcmin²)
- ETS* = Effective Target Size (arcmin²)
- NPOL* = Number of desired polarization characterizations
- ITL* = Instrument Throughput Losses (expressed as % of original remaining)
- CSF* = Contrast/Suppression Factor (ratio of intensity of target & suppressed source)
- EPF* = Effective Parallelization Factor (# of sub-observations conducted in parallel)
- ESF* = Effective Serialization Factor (# of sub-observations conducted in series)
- EDD* = Effective Detector Density (degree of sampling of diffraction limit)
- EDS* = Effective Detector Sensitivity (10^{-26} W/Hz)

This equation, while not fully characterized, captures the core logic of discovery efficiency – the amount of time it takes to make a notional discovery/observe a notional target. It appropriately penalizes complex science operations through the time mechanic. It also captures that some complexity/increased discrimination of photons is easier than other complexity for a given instrument. Finally, it captures that a given instrument may be more efficient for some discoveries than for others; a wide field instrument with a limited coronagraphic capability and set of spectral filter wheels will have a lower discovery efficiency against the exoplanet mission set (still non-zero), but a higher discovery efficiency for surveys.

Future work to on this proposed framework can leverage the rich history of existing instruments and observatories to revise and validate the model. Such efforts can leverage past efforts to evaluate new telescope proposals: the ATLAST final report includes several assessments of observatory performance phrased in similar units and terms (Figure K.2). James Webb’s resources include Exposure Time Calculators, which provide results relevant to a discovery efficiency analysis.⁸³

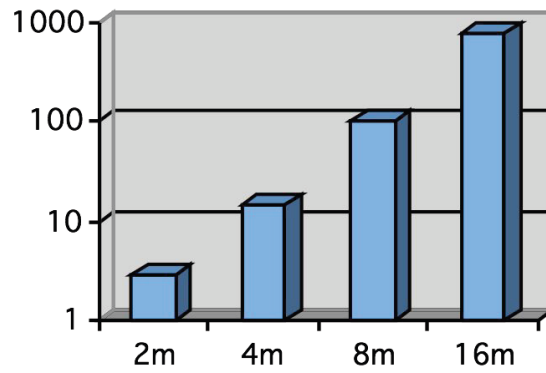


Figure 2. The average number of F, G, K stars where SNR=10 R=70 spectrum of an Earth twin could be obtained in < 500 ksec as a function of telescope aperture, D. The growth in the sample size scales as D^3 .¹⁷

Additionally, the Hubble legacy of upgrades (and historical attempts to determine discovery efficiency) offers a rich dataset for model assessment, with extensibility to other systems and wavelength regimes following thereafter.

APPENDIX L: LAUNCH MASS CAPABILITY CALCULATIONS

In order to determine the launch cost of servicing missions for the EM-L2 and LOTUS servicing locations, the launch mass capability of the various launch systems to these orbits must be determined. Due to a lack of reported data, the launch mass capability was estimated based upon known data for mass-to-LEO and mass-to-SE-L2 capabilities for each system. The rocket equation was used for this analysis:

$$\Delta V = v_e \ln \left(\frac{m_0}{m_1} \right)$$

Eq. 93

where the variables are described in **Table XXXV**.

Table XXXV: Variables of the rocket equation, with units

Variable	Description	Units
ΔV	Change in Speed	m/s
v_e	Effective Exhaust Velocity	m/s
m_0	Initial Total Mass	kg
m_1	Final Total Mass	kg

For this calculation, three assumptions are made. First, the ΔV requirement for both EM-L2 and LOTUS orbits is assumed to be approximately the ΔV requirement for Lunar orbit. Second, the final total mass m_1 is assumed to be approximately the mass of the payload, m , in kilograms. Finally, the initial total mass m_0 is assumed to be approximately the sum of the payload mass m and the mass of the rocket and propellant, p , in kilograms. Thus, the effects of staging are not encompassed in this calculation. However, this is meant to be a first-approximation value of the mass-to-orbit capability of these rockets, and thus these assumptions are considered to be valid. For final implementation of this model, actual mass-to-orbit data for each launch system for each destination orbit should be obtained from the manufacturer.

The ΔV requirement for each orbit is known, and the payload mass capability of each launch system is known for LEO and SE-L2. Therefore, the rocket equation can be rearranged and used to develop a system of two equations with two unknowns:

$$\Delta V_{LEO} = v_e \ln \left(\frac{m_{LEO}+p}{m_{LEO}} \right)$$

Eq. 94

$$\Delta V_{SEL2} = v_e \ln \left(\frac{m_{SEL2}+p}{m_{LEO}} \right)$$

Eq. 95

where ΔV and m are the change in velocity and payload mass for the orbit indicated in the subscript (known values), and v_e and p are the effective exhaust velocity and rocket/propellant mass for the launch system under consideration (unknown values). Using this set of equations, approximations for the effective exhaust velocity and the rocket/payload mass for each launch system can be calculated, and are documented in Table XXXVI.

Table XXXVI: Calculated effective exhaust velocity and rocket/payload mass for the launch systems under consideration

Launch System	Effective Exhaust Velocity v_e [m/s]	Rocket/Payload Mass p [kg]
SLS	3056	851261
Falcon 9	7659	18489
Falcon Heavy	2194	1801390
Atlas V	4904	114857
Delta IV Heavy	8425	34977

Once these parameters for each launch system have been calculated, the mass-to-lunar-orbit capability for each launch system can be calculated, again via rearrangement of the rocket equation:

$$m_{lunar} = \frac{p}{e^{\frac{\Delta V_{lunar}}{v_e}} - 1}$$

Eq. 96

The results of this calculation are documented in Table XXXVII.

Table XXXVII: Payload mass to lunar orbit capability of the launch systems under consideration

Launch System	Payload Mass to Lunar Orbit [kg]
SLS	35815
Falcon 9	7113
Falcon Heavy	20836
Atlas V	17967
Delta IV Heavy	15870

REFERENCES

- ¹ Golkar, A. (2013 April). Federated Satellite Systems (FSS): A vision Towards an Innovation in Space Systems Design. In Smith L. J. (Chair), Session 7: Special Aspects. Symposium conducted at the 9th IAA Symposium on Small Satellites for Earth Observation, Berlin, Germany.
- ² Committee for a Decadal Survey of Astronomy and Astrophysics and the National Research Council, *New Worlds, New Horizons in Astronomy and Astrophysics*, The National Academies Press, Washington, DC, 2010.
- ³ "NRO Gifts NASA Two Leftover Space Telescopes, Euclid to Cost NASA \$40-50 Million, GEMS Not Confirmed." *SpacePolicyOnline.com*. Space and Technology Policy Group, 04 June 2012. Web.
- ⁴ Postman, M., Traub, W., Krist, J., Stapelfeldt, K., Brown, R., Oegerle, W., Lo, A., Clampin, M., Soummer, R., Wiseman, J., Mountain, M., "Advanced Technology Large-Aperture Space Telescope (ATLAST): Characterizing Habitable Worlds" *ASP Conference Series, 2010*, Barcelona. 2009.
- ⁵ Redding, D.C., Hickey, G., Agnes, G., Eisenhardt, P., Green, J.J., Krist, J., Peterson L., Stapelfeldt, K., Traub, W., Unwin, S., Werner, M., "Active Optics for a 16-Meter Advanced Technology Large Aperture Space Telescope." SPIE Astronomical Instrumentation Symposium, Marseilles. 2008.
- ⁶ "The James Webb Space Telescope: About Webb's Orbit" [<http://www.jwst.nasa.gov/orbit.html>. Accessed 3/10/2012.]
- ⁷ Contract marks new generation for Deep Space Network. [Online] Retrieved from http://www.oriondeepspace.com/index.php?option=com_content&view=article&id=295:contract-marks-new-generation-for-deep-space-network&catid=41:space-science&Itemid=62
- ⁸ Iridium Satellite Constellation. [Online] Retrieved from http://spacecollaborative.com.au/2030%20Sydney/Research/Network/Iridium_Sat.html
- ⁹ Golkar, A. (2013 April). Federated Satellite Systems (FSS): A vision Towards an Innovation in Space Systems Design. In Smith L. J. (Chair), Session 7: Special Aspects. Symposium conducted at the 9th IAA Symposium on Small Satellites for Earth Observation, Berlin, Germany.
- ¹⁰ T. Tolker-Nielsen, J-C. Guillen. SILEX: The First European Optical Communication Terminal in Orbit. ESA Bulletin 96 – November 1988. Retrieved from <http://www.esa.int/esapub/bulletin/bullet96/NIELSEN.pdf>
- ¹¹ How It Works: NASA's Experimental Laser Communication System. Retrieved from <http://www.popularmechanics.com/science/space/nasa/how-it-works-nasas-experimental-laser-communication-system>
- ¹² Vincent W.S. Chan and JohnE.Kaufman. Coherent Optical Inter-satellite Crosslinks. MIT Lincoln Laboratory. Military Communications Conference, 1988. MILCOM 88, Conference Record. 21st Century Military Communications – What's Possible? 1988 IEEE.

-
- ¹³ Baldessera, M. "A Decision-Making Framework to Determine the Value of On-Orbit Servicing Compared to Replacement of Space Telescopes." S.M. Thesis, Department Of Aeronautics and Astronautics, Massachusetts Institute of Technology, Cambridge, MA, 2007.
- ¹⁴ Hastings, Daniel E., and Carole Joppin. "On-Orbit Upgrade and Repair: The Hubble Space Telescope Example." *Journal of Spacecraft and Rockets* 43.3 (2006): 614-25.
- ¹⁵ National Aeronautics and Space Administration. *On-Orbit Satellite Servicing Study: Project Report. NP-2010-08-162-GSFC Vol., 2010. Print.*
- ¹⁶ Gardner, J.P. et al. "The James Webb Space Telescope." *Space Science Reviews* 123.4 (2006): 485-606. Print.
- ¹⁷ Postman, M. et al. "Advanced Technology Large-Aperture Space Telescope (ATLAST): A Technology Roadmap For The Next Decade." Space Telescope Science Institute, May 2009.
- ¹⁸ Gralla, E., and De Weck, O., "Strategies for On-Orbit Assembly of Modular Spacecraft". *JBIS*, Vol 60, 2007. pp. 219-227.
- ¹⁹ "Phoenix." *DARPA RSS*. Web. 20 Feb. 2013.
<http://www.darpa.mil/our_work/tto/programs/phoenix.aspx>.
- ²⁰ Gettliffe, Gwendolyn. "High-Temperature Superconductors as Electromagnetic Deployment and Support Structures in Spacecraft." Masters Thesis. Massachusetts Institute of Technology. 2012.
- ²¹ Mohan, Swati. "Quantitative Selection and Design of Model Generation Architectures for On-Orbit Autonomous Assembly." PhD Thesis. Massachusetts Institute of Technology. 2010.
- ²² Stewart, A. M., "Design and Optimization of Lightweight Space Telescope Structures," S.M. Thesis, Department of Aeronautics and Astronautics, Massachusetts Institute of Technology, Cambridge, MA, 2007.
- ²³ "Primary Mirror," ESA Science & Technology, February 2004. [<http://sci.esa.int/science-e/www/object/index.cfm?fobjectid=34702>. Accessed 3/10/13.]
- ²⁴ "Hubble Space Telescope Primer for Cycle 21: 4.7 Instrument Comparisons," Space Telescope Science Institute, Maryland, December 2012. [http://www.stsci.edu/hst/proposing/documents/primer/Ch_48.html. Accessed 5/7/2013.]
- ²⁵ Stahl, P., Henrichs, T., and Dollinger, C., "Parametric Cost Models for Space Telescopes," *International Conference on Space Optics*, 2010.
- ²⁶ Wertz, J. R., Everett, D. F., Pischell, J. J., "Space Mission Engineering: The New SMAD", Microcosm Press, 2011, Ch. 24.

-
- ²⁷ Postman, Marc, et al. "Advanced Technology Large-Aperture Space Telescope (ATLAST): A Technology Roadmap for the Next Decade." NASA Astrophysics Strategic Mission Concept Study, *Space Telescope Science Institute*, (May 2009)
- ²⁸ Sirianni, Marco and Mutchler, Max. "Radiation Damage in HST Detectors." STSci Report. SDW 2005.
- ²⁹ Sirianni, Marco et al., "Radiation Damage in Hubble Space Telescope Detectors." IEEE Explore 2007.
- ³⁰ Wertz, J. R., Everett, D. F., Pischell, J. J., "*Space Mission Engineering: The New SMAD*", Microcosm Press, 2011, Ch. – Chapter 16 "Communication Payloads" page 455
- ³¹ Muriel Noca - Space system engineering, October 2010, EPFL
- ³² John Farserotu – Satellite communications class, October 2010, EPFL
- ³³ NASA DSN antennas characteristics, <http://deepspace.jpl.nasa.gov/dsn/antennas/index.html>
- ³⁴ Link budget introduction, <http://complextoreal.com/wp-content/uploads/2013/01/linkbud.pdf>
- ³⁵ NASA Optical Link Study Group (OLSG) Final Report, Interagency Operations Advisory Group - Optical Link Study Group, 5 June 2012
- ³⁶ Goddard Space Flight Center. *Hubble Facts: Hubble Space Telescope Servicing Mission 3A: New Advanced Computer.* Retrieved from http://asd.gsfc.nasa.gov/archive/hubble/a_pdf/news/facts/FS09.pdf
- ³⁷ Maxwell Technologies. *97SD3232 1Gb SDRAM.* Retrieved from http://www.maxwell.com/products/microelectronics/docs/97sd3232_rev3.pdf
- ³⁸ *Maxwell Introduces First Fully Qualified and Radiation Characterized Die-Based Memory Component for the Space Industry.* (May 1, 2003) Retrieved from <http://www.spaceref.com/news/viewpr.html?pid=11415>
- ³⁹ Lockheed Martin: Missiles and Space. *Hubble Space Telescope: Servicing Mission 3A Media Reference Guide.* Retrieved from http://asd.gsfc.nasa.gov/archive/hubble/a_pdf/news/SM3A-MediaGuide.pdf
- ⁴⁰ TDK Lambda: PXD Series. Retrieved from <http://us.tdk-lambda.com/lp/ftp/Specs/pxd.pdf>
- ⁴¹ Sonn, C. (2011). APM5003: *Exploring methodology for psychological research* [Class lecture slides]. School of Social Sciences and Psychology, Victoria University, Melbourne, Australia.
- ⁴² Cattrysse, Jill M. "Space Telescope Mission Design For L 2 Point Stationing." *54 the International Astronautical Congress of the International Astronautical Federation(IAF)*. 2003.
- ⁴³ Howell, K. C., and Kakoi, M., "Transfers Between The Earth-Moon and Sun-Earth Systems Using Manifolds and Transfer Orbits," *Acta Astronautica*, 59, 2006, pp. 367-380.

-
- ⁴⁴ Truesdale, Nick. "Using Invariant Manifolds of the Sun-Earth L2 Point for Asteroid Mining Operations." ASEN 5050 Space Flight Dynamics final report. University of Colorado. 2012.
- ⁴⁵ Sutton, George Paul., and Oscar Biblarz. *Rocket Propulsion Elements*. New York: John Wiley & Sons, 2001. Print.
- ⁴⁶ Lozano, Paulo. "Lecture 1: Missions and Thrusters". 16.522 Space Propulsion. Massachusetts Institute of Technology. 2013.
- ⁴⁷ Wertz, J. R., Everett, D. F., Pischell, J. J., "Space Mission Engineering: The New SMAD", Microcosm Press, 2011.
- ⁴⁸ Gilmore, D. G. "Space Thermal Control Handbook – Volume I: Fundamental Technologies." 2002, 2nd edition. AIAA. Reston, Virginia.
- ⁴⁹ Donabedian, M. "Space Thermal Control Handbook – Volume II: Cryogenics." 2003. AIAA. Reston, Virginia.
- ⁵⁰ Ross, Jr. R. G. "A Study of the Use of 6K ACTDP Cryocoolers for the MIRI Instrument on JWST." *Cryocoolers 13*. 2005. International Cryocooler Conference.
- ⁵¹ Kittle, P. "Cryocooler Performance Estimator." *Cryocoolers 14*. 2007. International Cryocooler Conference.
- ⁵² "eTEC HV37 Thin-Film Thermoelectric Cooler Data Sheet." Document APS0023, rev 2.0. Nextreme Thermal Solutions, Inc.
- ⁵³ Durning, J., "The James Webb Space Telescope Fast Facts," NASA/ESA/CSA. Web. 20 April 2013. <<http://www.jwst.nasa.gov/facts.html>>
- ⁵⁴ Nelson, Buddy, editor. Lockheed Martin. "Hubble Space Telescope Servicing Mission 4-Media Reference Guide. Revision 1." *United States National Aeronautics and Space Administration*. May 2009. Web. 5 May 2013. <http://www.nasa.gov/pdf/327688main_09_SM4_Media_Guide_rev1.pdf>
- ⁵⁵ Uebelhart, Scott. "Non-Deterministic Design and Analysis of Parameterized Optical Structures during Conceptual Design." PhD Thesis. Massachusetts Institute of Technology. 2006.
- ⁵⁶ Masterson, Rebecca. "Dynamic Tailoring and Tuning for Space-Based Precision Optical Structures." PhD Thesis. Massachusetts Institute of Technology. 2005.
- ⁵⁷ "Modular Optical Space Telescope (MOST) Poster." Current Programs. Space Systems Laboratory, n.d. Web. 12 May 2013. <http://ssl.mit.edu/research/Posters/MOST_Poster_2006.pdf>.
- ⁵⁸ "How to Provide High-Resolution Vision," Review of Optometry, December 2006. [<http://cms.revoptom.com/index.asp?ArticleType=SiteSpec&Page=osc/105418/lesson.htm>. Accessed 5/8/13.]

-
- ⁵⁹ Masterson, R. A. "Development and Validation of Empirical and Analytical Reaction Wheel Disturbance Models." S.M. Thesis, Department Of Aeronautics and Astronautics, Massachusetts Institute of Technology, Cambridge, MA, 1999.
- ⁶⁰ Gutierrez, H. L. "Performance Assessment and Enhancement of Precision Controlled Structures During Conceptual Design." PhD Thesis, Department Of Aeronautics and Astronautics, Massachusetts Institute of Technology, Cambridge, MA, 1999.
- ⁶¹ Sinha, K. and de Weck, O. "Structural Complexity Metric for Engineered Complex Systems and its Application," *14th International Design Structure Matrix (DSM) Conference*, 2012.
- ⁶² Sternberg, D., et al., "A Bottom-up Modeling Approach for the Profit Analysis of Cellularized Spacecraft Architectures", *IAC-13 Congress*, Beijing, China, 2013. Abstract Accepted.
- ⁶³ Wertz, J., and Miller, D., "Expected productivity-based risk analysis in conceptual design," *Acta Astronautica* 59 (2006), 420-429.
- ⁶⁴ Keys, A. et al. (2008). Radition Hardened Electronics for Space Environments (RHSE) Project Overview. [PowerPoint slides]. Retrieved from Georgia Tech website: <https://smartech.gatech.edu/bitstream/handle/1853/26381/97-168-1-PB.pdf?sequence=1>
- ⁶⁵ Jun, I. (2009). Radiation Shielding Design: Protecting Electronics from the Environment. [PowerPoint slides]. Retrieved from NASA website: <http://opfm.jpl.nasa.gov/files/N-Jun-Radiation%20Shielding1.pdf>
- ⁶⁶ Hemmati, H., Free-Space Optical Communications at JPL/HASA. Retrieved from <http://opticalcomm.jpl.nasa.gov/PAPERS/REVIEW/overview.pdf>
- ⁶⁷ Cattrysse, Jill M. "Space Telescope Mission Design For L 2 Point Stationing."54 the International Astronautical Congress of the International Astronautical Federation(IAF). 2003.
- ⁶⁸"Hubble Essentials: Quick Facts." *HubbleSite.org*. Web. 8 May 2013. <http://hubblesite.org/the_telescope/hubble_essentials/quick_facts.php>.
- ⁶⁹ Wall, Mike. "NASA's Huge New Rocket May Cost \$500 Million Per Launch." *Space.com.*, 12 Sept. 2012. Web. 08 Apr. 2013.
- ⁷⁰ "SpaceX Falcon." *SpaceX.*, 2013. Web. 08 Apr. 2013.
- ⁷¹ "Atlas V Product Card." *United Launch Alliance, LLC*. ULA, 2013. Web. 08 Apr. 2013.
- ⁷² "Delta IV Overview." *Boeing: Defense, Space & Security*. Web. 10 Apr. 2013.
- ⁷³ "Delta IV - Specifications." *Delta IV - Specifications*. Andrews Space & Technology, Web. 10 Apr. 2013.
- ⁷⁴ de Weck O.L., Nadir W.D., Wong J.G., Bounova G. and Coffee T.M., "Modular Structures for Manned Space Exploration: The Truncated Octahedron as a Building Block", AIAA-2005-2764,

1st Space Exploration Conference: Continuing the Voyage of Discovery, 30 Jan - 1 Feb 2005, Orlando, Florida

⁷⁵ Overbye, D. “Refurbishments Complete, Astronauts Let Go of Hubble.” *New York Times*

⁷⁶ Leone, D. “NASA Acknowledged James Webb Telescope Costs Will Delay Other Science Missions.” *Space News*

⁷⁷ Morgan, D. “CRS Report for Congress – Hubble Space Telescope: NASA’s Plans for Servicing Mission.” Online. <http://www.fas.org/sgp/crs/space/RS21767.pdf>

⁷⁸ Hubble_SM4_Media_Guide_rev1. Online.

http://www.nasa.gov/pdf/327688main_09_SM4_Media_Guide_rev1.pdf

⁷⁹ Stockman, P. “James Webb Space Telescope (JWST).” Online. <http://www.stsci.edu/jwst/doc-archive/presentations/JWST-STScI-000432.pdf>

⁸⁰ Zagarola, M., “Demonstration of a Two-Stage Turbo- Brayton Cryocooler for Space Applications”, International Cryocooler Conference, Boulder, CO, 2009. Online. <https://www.google.com/url?sa=t&rct=j&q=&esrc=s&source=web&cd=9&cad=rja&ved=0CJQBEBYwCA&url=http%3A%2F%2Fconferences.library.wisc.edu%2Findex.php%2Farticle%2Fdownload%2F234%2F234&ei=2YaFUevHINO54AOdkYH4Bw&usg=AFQjCNFSwKQ6AgaApwO5JttDs5sb3Ttpyg&sig2=E3SuQJtTaCNnywMKzMm1wQ&bvm=bv.45960087,d.dm>

⁸¹ CVI Melles Griot Technical Guide: Chapter 5: Optical Coatings. Online. <http://www.cvimellesgriot.com/Products/Documents/TechnicalGuide/Optical-Coatings.pdf>

⁸² James Webb Space Telescope – Image Quality. *Space Telescope Science Institute*. Online. <http://www.stsci.edu/jwst/ote/image-quality>

⁸³ “James Webb Space Telescope – JWST Sensitivity” *Space Telescope Science Institute*. Available at <http://www.stsci.edu/jwst/science/sensitivity>. Prototype ETC available at <http://jwstetc.stsci.edu/etc/>.

Appendix 5: Multi-Disciplinary Optimization of an Electromagnetic Spacecraft Boom

Multi-Disciplinary Optimization of an Electromagnetic Spacecraft Boom

Brian Cohen, Gwendolyn Gettiffe, Dave Smart

1. Introduction

1.1. Background and Motivation

Spacecraft designers have long been faced by two contradicting objectives: reduce spacecraft mass to minimize prohibitive launch costs while simultaneously making structures as dimensionally large as possible to maximize their performance. Structures that benefit from being as large as possible include primary telescope mirrors, parabolic antennas, solar arrays, solar sails, and starshades. Restrictions on spacecraft size include dimensions of launch vehicle fairings, maximum takeoff weight of launch vehicles, and the cost budget available for the mission.

The structural subsystem accounts for 20-30% of a spacecraft's dry mass [7], making it a prime target for mass reduction. The three main approaches to minimizing spacecraft mass are at the component level (reducing component mass), at the architecture level (designing a single subsystem that performs functions normally allocated to multiple subsystems), or a combination of the two. Most traditional mass reduction uses the first approach, often focusing on lightweighting the vehicle's structure because it is a large proportion of the spacecraft's dry mass. This reduction is done by reducing the density of the material used to frame and support the structure. This research will pursue the first approach as well but instead via the design and optimization of an electromagnetically-supported spacecraft boom.

Figure 1 shows how adjacent coils are tethered together (with three tethers equally spaced around the circumference of each coil) as well as a conceptual three-coil boom, attached on one end to a spacecraft bus with the electromagnetic force between the coils acting to pull the boom taut.

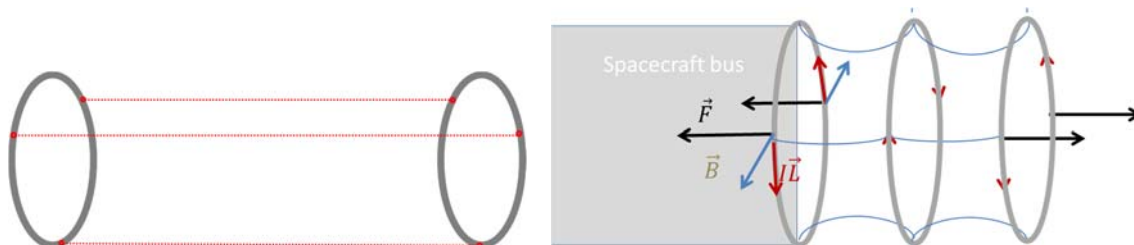


Figure 1: (a) Diagram of 3-tether spacing between two coils, (b) Three coil boom with slack tethers

Electromagnetic forces are body forces instead of surface forces, so the mass does not increase linearly with boom length as in an aluminum beam but rather in steps as coils are added along the boom. By optimizing for the minimum mass and power required for an electromagnetic boom, we hope to show that electromagnetic support of space structures is a technically feasible and viable option for spacecraft designers.

There are several reasons that electromagnetic structures are interesting:

- Depending on boom geometry, they may have less mass than a deployed/inflated boom of the same length.
- The boom can change length and is not locked into one deployed position. This is made possible by changing the current through the magnetic coils, causing a repelling or attractive force.
- They have excellent heat and vibration isolation between the two ends of the boom (due to the fact that little connective hardware is required).
- Magnetic energy in a superconducting coil provides lossless energy storage.
- Tendency of flexible electromagnetic coil to become flat and circular provides stiffening and tensioning of flexible, membranous shapes.
- Electromagnets can perform wireless power and data transfer.
- Electromagnets also provide a strong controllable magnetic field for attitude control.

Many potential configurations of electromagnetic structures exist; not all of the aforementioned are applicable to the linear boom. We focus on this boom because it is a simple, linear configuration, and there are a number of missions for which it might be used (e.g.

isolation of a nuclear element from a spacecraft bus or crew module, spacing and alignment of optics for an x-ray telescope, connection of telescopes in a sparse aperture array).

1.2. Enabling Principles and Technology

There are a number of principles and technologies that enable the design and implementation of electromagnetic booms. These principles and technologies include electromagnetic force, the microgravity environment, superconductors, and cryogenic heatpipes with cryocoolers.

1.2.1. Electromagnetic Force

A current-carrying wire produces a magnetic field. Our electromagnetic boom exploits the magnetic field and the fact that when another current-carrying wire is placed in that magnetic field, it experiences a force dependent on the orientation of the wire and of the field. The magnetic vector field at a given point is described by the Biot-Savart law

$$\vec{B}_1 = \frac{\mu I_1}{4\pi} \int_{wire} \frac{d\vec{l} \times \vec{r}}{|\vec{r}|^3}$$

where \vec{r} is the vector from the segment $d\vec{l}$ of the wire generating the field to the point where the field is being calculated (in this case, the vector from wire 1 to wire 2). I_1 is the current running through wire 1 and μ is the vacuum permeability ($4\pi * 10^{-7} N/A^2$). The Biot-Savart law integrates over the whole length of wire (or in our case, coil) to capture the contribution from every segment to the magnetic field.

The magnetic force induced on coil 2 by the magnetic field from coil 1 is described by the Laplace force law

$$\vec{F}_{EM,12} = I_2 \int_{wire} d\vec{l} \times \vec{B}_1$$

where the force from coil 1 on coil 2 is proportional to the cross product of the current through each segment of coil 2 and the field at the center of each segment, summed. The force from coil 2 on coil 1 is identical and opposite in direction. For two parallel axisymmetric coils on the same axis as in Figure 1, the net force between the two is either attractive (same direction current) or repulsive (opposite directions) along that shared axis.

Supporting a 50m+ boom just with electromagnetic forces is a virtually impossible task on the Earth's surface due to the gravity vector and quick decay magnetic fields with distance. Fortunately, two factors of our design problem make it a tenable challenge: the microgravity environment and the use of superconducting wire in the coil electromagnets.

1.2.2. Microgravity and Superconductors

In microgravity, only small forces need to be applied to a structure to move it or keep it supported. In our problem, we determine the tension required in the boom via Hill's relative motion equations for two masses to remain in their relative positions in the cross track direction.

$$F_{crosstrack} = -n^2 \left(\frac{m_{bus} m_{PL}}{m_{PL} + m_{bus}} L \right)$$

We assume that our boom is in geosynchronous orbit, so the orbital rate n is 7.29×10^{-5} rad/s. The masses of the bus (assumed 1000 kg) and payload (25 kg) as well as the length of the boom L determine the repulsive force and thus tension required in the boom.

We assume the use of SuperPower 2G HTS (high-temperature superconductor) wire, 4mm in width [6]. This HTS wire can handle up to 100A through a single turn when cooled to 77K, the boiling point of liquid nitrogen, and can handle higher currents at colder temperatures. Regular conductors are limited to one or two orders of magnitude less current density. The effective current of an electromagnet is multiplied by the number of turns in the electromagnet, so the magnets that we are modelling can easily generate the required tension in a long orbiting boom. In order to reach 77K, however, each coil requires a thermal control system to reduce it to cryogenic temperatures.

1.2.3. Thermal – Cryocoolers, Heatpipes, and MLI

The thermal control system that we assume in our model is a multi-layer insulation (MLI)-wrapped toroidal heatpipe and Stirling cryocooler on each coil in the boom. The heatpipe isothermizes the coil to the temperature of the cryocooler cold finger via capillary action; gaseous nitrogen trapped inside the heatpipe condenses at the cold finger, wicks along a mesh around the coil until it evaporates

again, and continues this cycle until the coil inside the heatpipe is brought to 77K or below. The cryocooler uses electric power to pull heat energy out of the coil and transfer it to a radiator. The MLI reduces the heat influx into the coil from external sources such as the Sun and the Earth, reducing the load on the cryocooler.

1.3. Disciplines Involved

There are three very highly coupled spacecraft subsystems involved in this multidisciplinary problem: structures and mechanisms, thermal control, and power acquisition, storage and distribution:

- **Structures:** The boom must maintain a certain tension, static stability, and a fixed end-to end distance. In the future we plan to incorporate dynamic stability conditions as constraints in this problem as well.
- **Thermal:** For a “high-temperature” superconductor (HTS) to reach its superconducting state, it has to be brought to a temperature below its critical temperature (T_c) which is usually slightly above 77K, the boiling point of nitrogen. However, cooling the coils to lower temperatures requires more massive and power hungry cryocoolers.
- **Power:** Though electromagnets draw some initial energy to initiate current in the coil, superconductors are characterized by their virtually zero resistivity when superconducting. This characteristic makes superconducting coils lossless (except for the resistivity of any joints or connective circuitry) and good for storing energy over long periods of time. The primary power draw of an electromagnetic system comes from the cryocoolers used to keep the HTS coils at a desired temperature. The number of thermal watts that need to be extracted from the system (dependent on its distance and view factor to the sun) dictate the type and power draw of requisite cryocoolers.

2. Design Problem and Models

2.1. Objectives, Design Variables, Constraints, and Parameters

Table 1 gives design variables, parameters, constraints and objectives within the scope of the electromagnetic boom design problem.

Table 1: Master table of design variables, parameters, constraints, and objectives

Design Variables	Variable	Symbol	Description	Upper Bound	Lower Bound	Nominal Initial Value	Unit
	Coil radius	R_{1-5}	Radius of the EM coils	4.5	0.1	1	meter
	# of coils	N_C	Number of coils in boom	5	2	2	-
	# of turns	$N_{T,1-5}$	Number of turns per coil	250	1	100	-
Parameters	Wire type	W	Brand of superconductor	-	-	SuperPower 2G HTS	-
	Boom length	L	End-to-end length of boom	-	-	50	meter
	Density of wire	ρ	Material density of the superconductor tape	-	-	8548.2	kg/m ³
	Solar constant	S	The flux of solar heat energy through a meter square area	-	-	1366	W/m ²
	Boom tension	t	Tension from end to end	-	-	50	μ N
	Wire width	w	Width of superconductor	-	-	4	mm
	# of tethers	N_t	Number of tethers connecting adjacent coils	-	-	3	-
	Payload mass	m_{PL}	Lump mass to be supported	-	-	25	kg
	Bus mass	m_{bus}	Lump mass at start of boom	-	-	1000	kg
Constraints	$T < T_c$	T_c, T	The temperature of each coil is less than the critical temp. of the superconductor	-	-	-	Kelvin
	$M_{cryo} \leq 50kg$	M_{cryo}	The mass of each cryocooler is less than 50kg	-	-	-	kg
Objectives	Min(mass)	M	Want to minimize the total mass of the boom and supporting hardware	-	-	-	kg
	Min(power)	P	Want to minimize the power burden of the EM boom on the spacecraft	-	-	-	W

2.2. Model Diagram and N2 Diagram

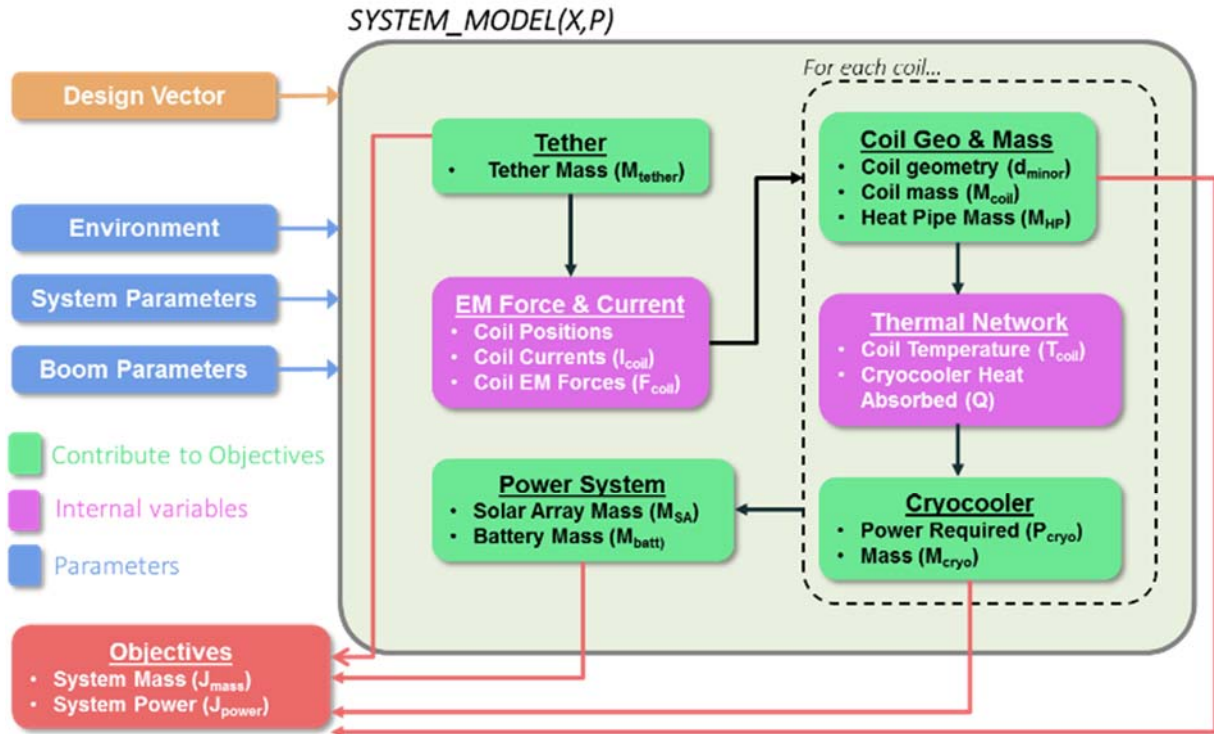


Figure 2: System block model showing design vector and parameter inputs and objective outputs

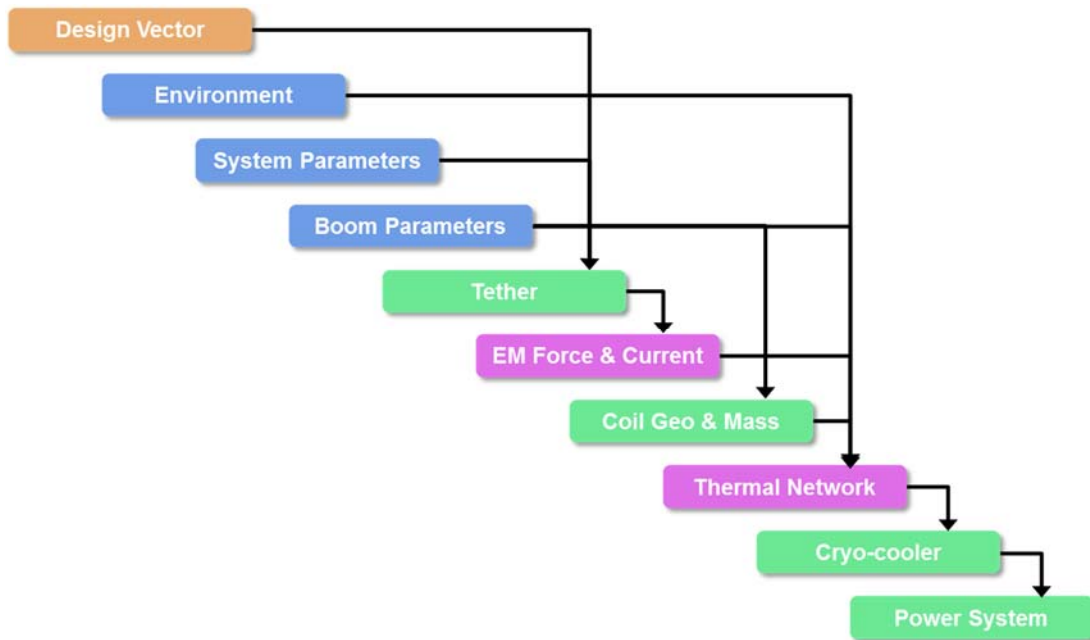


Figure 3: N² diagram showing data flows between system model blocks

2.2.1. EM Block

The electromagnetic (EM) force block distributes the given number of coils in a design along the boom length equally, then uses the required tension parameter t to dictate the necessary forces on the two end coils, with the net force on the interior coils being zero. Inter-coil EM force is a combination of coil geometry & currents, such that the EM force is:

$$\vec{F}_{EM,ij} = C_{f,ij} I_i I_j$$

$$\vec{F}_{EM,ji} = -\vec{F}_{ij}$$

where $C_{f,ij}$ is the coefficient of force and $I_i I_j$ is the product of the currents in the coils of interest (per turn).

2.2.1.1. Surrogate Model and Validation

There are two methods for calculating $C_{f,ij}$; the high-fidelity numerical approximation of the Biot-Savart Law which was mentioned in Section 1.2.1 and the low-fidelity closed-form analytical solution for force between two magnetic dipoles, written as

$$C_{f,ij} = \frac{3\pi N_i N_j R_i^2 R_j^2}{2d^4}$$

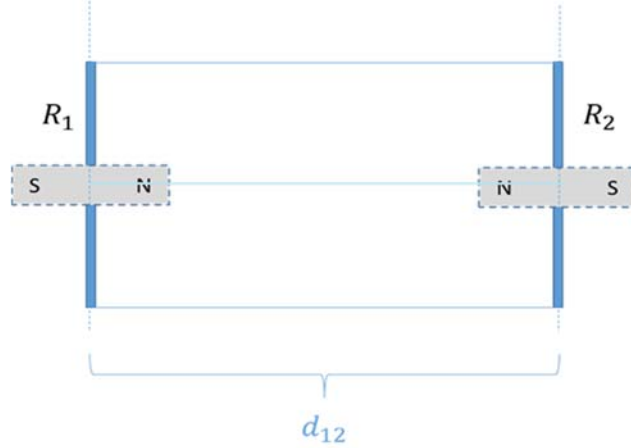


Figure 4: Magnetic dipole (bar-magnet) approximations for two coils (shown from side)

The numerical approximation is more computationally expensive because it is effectively conducting a double path integral, calculating and summing the contribution from every segment of the discretized first coil upon every segment of the discretized second coil, whereas the analytical dipole solution only requires a single calculation. Two current-carrying coils can be approximated as magnetic dipoles aligned along the axis of the coil as shown in Figure 4, but this approximation is only valid within a small degree of error (less than 5%) when the coils are at least ten coil radii apart (the smallest radii, if the coils are different sizes). We call distances greater than ten radii apart the *far-field*, and distances shorter than ten radii apart the *near-field*. Figure 5 validates the use of the dipole approximation for coils in the far-field.

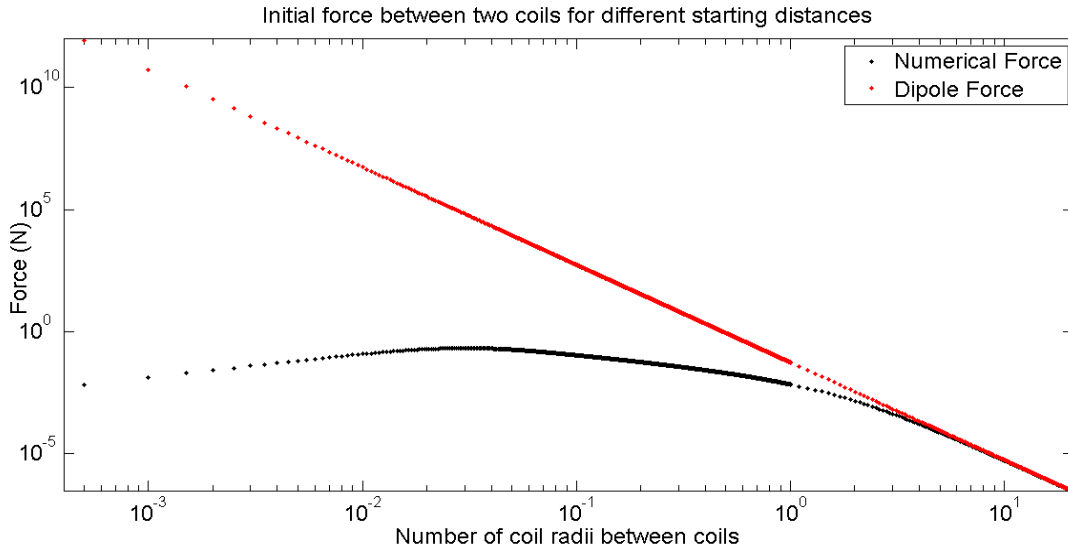


Figure 5: Comparison of numerical and dipole force approximations versus distance between coils [2]

In the interest of reducing computation time, we implement the dipole approximation as a surrogate model for calculating $C_{f,ij}$ in the far-field and the numerical approximation when the coils are in the near-field. The evaluation time after implementing the surrogate

dipole model instead of just the numerical approximation is faster by a factor of 10^4 . Since two coil models with a 50m boom length are 50m apart and the maximum coil radius allowed in our model is 5m, *all* two-coil designs (and the two end coils in any 3+ coil designs) use the surrogate dipole model to calculate $C_{f,ij}$, as well as any smaller coils that fulfill the far-field criterion for surrogate use.

2.2.1.2. Suboptimization Problem – Current Determination

For any two coils with a given force coefficient – determined either via the numerical solution of the Biot-Savart law or the magnetic dipole surrogate model – there may be many combinations of coil current values that satisfy the force equation

$$\vec{F}_{EM,ij} = C_{f,ij} I_i I_j$$

Of those multiple current configurations, the ideal solution would be that which has the smallest total system current. This is because a lower current system requires less cooling, and thus a lower mass thermodynamic system, to operate. The minimum current solution is determined by implementing a sub-optimization problem to minimize the sum of the coil currents

$$\min_x f(x) = \left(\sum_{i=1}^{nCoils} I_i \right)$$

where n is the number of coils and x is the vector of currents, $x = \{I_i, i=1:n\}$. This problem is subject to the constraints that the sum of the forces generated by each coil must add up to zero for any interior coil, and must add up to the required tension at the end coils

$$\begin{aligned} h_1(x) : I_1 \sum_{i=2}^n C_{1i} I_i + F &= 0 \\ h_k(x) : I_k \sum_{i=1}^n C_{ki} I_i &= 0 \quad k = 1, \dots, n, k \neq i \\ h_n(x) : I_n \sum_{i=1}^{n-1} C_{ni} I_i + F &= 0 \end{aligned}$$

where the coefficients c_{ij} are the force coefficients, and F is equal to the system tension.

To solve this minimization problem, the KKT system of equations which define the first order necessary conditions of optimality was constructed and solved. The KKT system is comprised of two basic relationships. First, any solution x^* must be feasible; i.e., the constraints must be satisfied

$$h_i(x^*) = 0$$

Second, the gradients of the objective function and the constraint functions must line up, in the following sense:

$$\nabla f(x^*) + \sum_{i=1}^n \lambda_i \nabla h_i(x^*) = 0$$

The set λ_i are Lagrange multipliers, and because the constraints are equality constraints there are no restrictions on their values. Because this is a convex minimization problem, the solution to this system of equations (x^*, λ) is guaranteed to be the optimal solution. In order to find the solution to this nonlinear system of equations, Newton's method was implemented, using a Jacobian-free implementation of the Generalized Conjugate Residual (GCR) algorithm at each Newton iteration to solve the following system

$$x^{k+1} = x^k - J_h|_{x^k} h(x^k)$$

The values of the coil currents $x^* = [I_1, \dots, I_n]$ represent the configuration of coil currents that satisfy the required force conditions and minimize total system current. These current values are then passed to the thermodynamic model where they are used to determine the mass of the cooling system required to support such superconducting coils.

2.2.2. Thermal Block

The thermal modeling block calculates the amount of heat that the dedicated cryocoolers have to extract from each coil, as well as the LN₂ operating temperature. These values are later used to size the cryocoolers. We first consider the thermal environment that the satellite is operating in: geostationary orbit. This orbit is represented below:

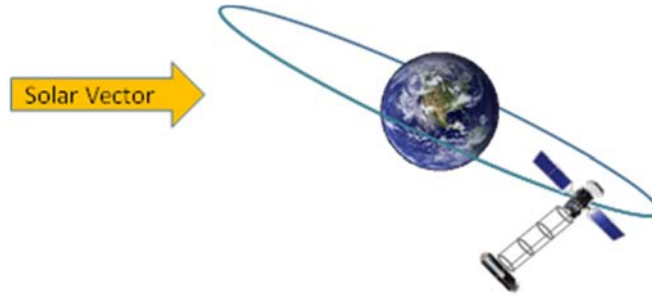


Figure 6: Boom cross-track in geostationary orbit

By selecting this orbit, we negate several important heat sources that are present in low-Earth orbiting satellites: Earth IR and Earth albedo. These two sources are negligible at geostationary altitude since the Earth is substantially far enough away and occupies only a small view factor from the satellite-boom system. Instead, we consider only solar incidence due to sunlight being absorbed through the coil exterior surfaces.

In order to reduce runtime of the model, we consider only a steady-state, one-dimensional heat conduction problem for each coil. This physical model is shown schematically below in Figure 7, as well as a mathematical representation in Figure 8:

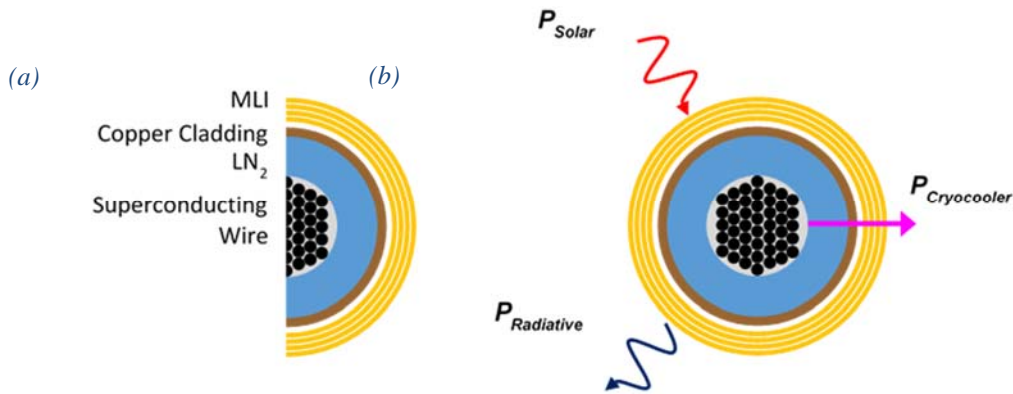


Figure 7: (a) Cross-section of coil, (b) Relevant heat fluxes for coil cross-section

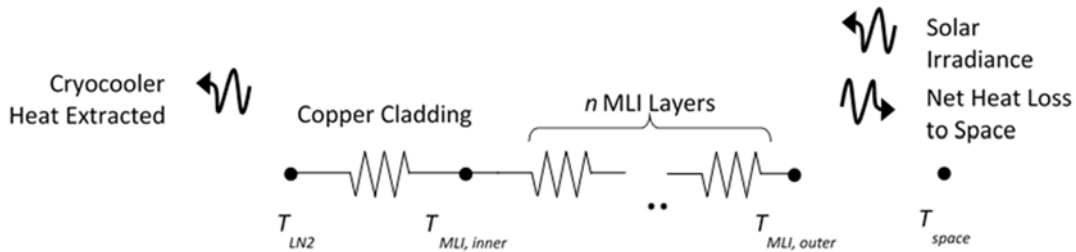


Figure 8: Mathematical representation of steady-state coil conduction problem

In order to calculate the boundary conditions for this problem (i.e. the heat fluxes due to solar incidence and radiative losses), we use several numerical techniques to arrive at the solution for the heat extracted by the cryocooler. The solar incidence requires some knowledge of the coil's illuminated and shadowed area as well as several parameter values for MLI surface properties and the solar vector (vector pointing to the Sun). We first discretize the surface of the coil, using the following transformations to represent the toroid geometry in a global Cartesian frame:

$$\begin{aligned} x &= \left[r + \left(\frac{a}{2} \right) \cos(\varphi) \right] \cos(\theta) \\ y &= \left[r + \left(\frac{a}{2} \right) \cos(\varphi) \right] \sin(\theta) \\ z &= \left(\frac{a}{2} \right) \sin(\varphi) \end{aligned}$$

Where φ and θ denote local angular coordinates, a is cross-sectional diameter, and r is the coil radius. The surface area of each element is then calculated using the relation:

$$dA = 4\pi^2 \left(\frac{a/2}{n_\theta - 1} \right) \left(\frac{r}{n_\varphi - 1} \right)$$

Where n_θ and n_φ denote the number of discrete angles in the local coordinates. An example discretization of a toroid in this global Cartesian frame is shown below:

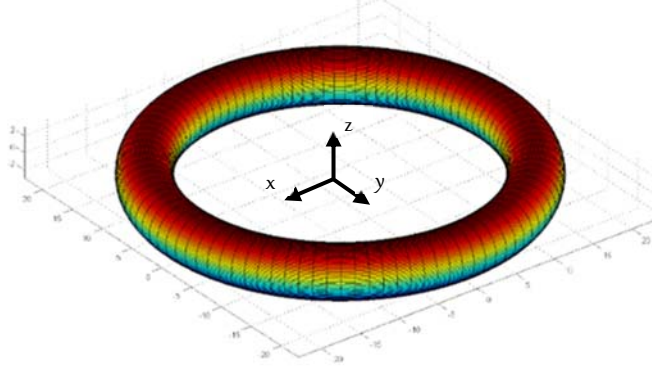


Figure 9: Toroidal discretization of coil

Next, using MATLAB's built-in function *surfnorm.m*, the surface normals are extracted for each surface element. These vectors are dotted with the solar vector and summed in order to calculate an effective illuminated area of the coils. The solar vector, however, is constantly changing during the orbit. As a first-order approximation, we calculate an orbit-averaged solar incidence by varying the relative angle between the solar vector and boom axis through an angle of -23.5° to 23.5° (the angle between the ecliptic and equatorial planes) and calculating the effective areas for each orientation. By averaging these results, the orbit-averaged approximation gives us a more valid effective area than holding the solar vector fixed. It should also be noted that we do not consider eclipse since in geostationary orbit, this phenomenon only happens for roughly 1 week out of the year. Likewise, we wish to overestimate the heat sources entering the coils since we desire colder temperatures for the superconducting wires, and thus remain conservative in our analysis.

The second boundary condition, the radiative losses, is not actually calculated explicitly, but implicitly using the Stephan-Boltzmann equation for radiation:

$$P_{radiative} = \sigma(\epsilon T_{surf}^4 - \alpha T_{space}^4)$$

Since any heat entering the surface of the coil must be extracted by the cryocooler, we can write a simple equation based on Fourier's Law for the heat passing through MLI, copper cladding and LN_2 as follows:

$$P_{cryocooler} = \frac{1}{R_{eff}}(T_{wire} - T_{surf})$$

Where R_{eff} considers the thermal resistance due to each layer of the coil, in a radial coordinate system. The temperature of the wire is determined based on the requested current by the EM Module. This current-temperature relationship was defined as a polynomial curve-fit to existing data on superconducting wire [5].

By substituting this value into the energy balance equation, we arrive at the following:

$$\frac{1}{R_{eff}}(T_{wire} - T_{surf}) = \alpha S A_{eff} - \sigma(\epsilon T_{surf}^4 - \alpha T_{space}^4)$$

which must be solved for surface temperature in order to calculate the heat extracted by the cryocooler. To do this we employ MATLAB's built-in roots finding solver *roots.m* and select the single real solution provided (other solutions are complex numbers). Once the surface temperature of the outer MLI layer is calculated, we can use the above equation to then determine the heat extracted

by the cryocooler. The heat extracted and coil wire temperature is then passes forward to the cryocooler module which sizes the cryocooler solely on these parameters.

3. Single Objective Optimization

As discussed above, mass is the most critical parameter in the design of space systems. As such, it was selected as the objective value to minimize in our effort to optimize the electromagnetic boom design over a single objective. This optimization effort began by using a Design of Experiments (DOE) to determine approximate extrema on the space of objective values. A Latin Hypercube algorithm was employed to define the set of design vectors. The Latin Hypercube takes as an input a desired number of design points (10,000 for this particular DOE) and returns that number of n-dimensional vectors (where n is the number of design variables) which evenly sample the normalized design space. Figure 10 illustrates the results of that DOE.

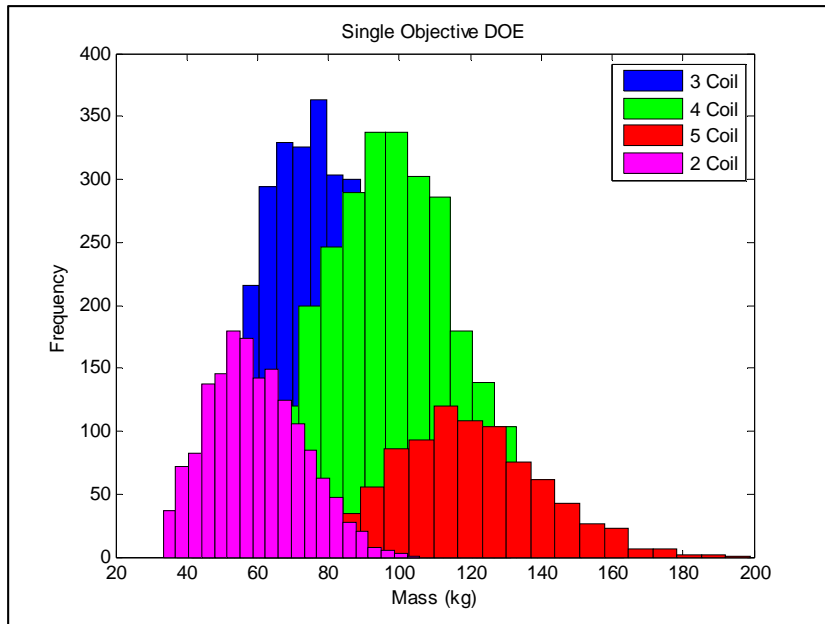


Figure 10: Single objective DOE

The frequency of objective values shown in Figure 10 are shown as a histogram and separated into families of solutions based on the number of coils in the system. The minimum objective value found in the DOE was 33.31 kg, and so the data suggest that a possible minimum mass solution for the EM boom could lie near 33 kg.

Once the DOE was complete, optimization algorithms were explored to improve upon this answer. First, a gradient-based optimization algorithm was selected – the Matlab function “fmincon”. This algorithm iteratively converges to an optimal solution by numerically computing a gradient to determine a search direction and then moving a current iterate in that direction towards a minimum value of the objective function. Numerical determination of the gradient is essential in the EM boom problem as no analytic gradient could be computed, due to the complication of the model and the fact that the design space is discontinuous (with integer-valued design variables).

A gradient-based optimization algorithm requires an initial design point x^0 from which to begin its search for a minimum of the objective function. The design point corresponding to the minimum objective value identified in the DOE was selected, on the theory that there was a reasonable chance a minimum would be located in the region, and the convergence of a gradient-based algorithm is greatly improved when the starting point is in the neighborhood of the desired solution. Table 2 shows the minimum solution identified using gradient based search.

Table 2: Solution to single objective gradient-based optimization

J	Algo	CPU Time (mm:ss)	Solution (x^*)		Performance (f^*)	
Mass	fmincon	2:35	2 coils		Mass(kg):	33.48
			Coil radii (m):	0.50, 0.50		
			No. Turns:	58, 79		

The solution found had an objective value of 33.48 kg – this value was quite close to the minimum value of the DOE, but because it was slightly larger this suggests a true global optimum was not found.

When using an optimizer, it is possible that the relative sensitivity of the objective function to the design variables may lead to difficulty converging to an optimal result. If elements of the gradient differ significantly in magnitude, then a step in a descent direction may have a great effect on the objective value due to one design variable but not another. Since both of the design variables must converge to a solution, this behavior may delay or prevent the optimizer from locating the optimum. One way to determine if this is a factor in an optimization is to examine the diagonal elements of the Hessian matrix. Ideally these numbers would be on the order of 1; if they are not, scaling the design variables so that the Hessian diagonals are roughly order 1 may help mitigate the effects of mismatched sensitivities. Scaling the design variables involves multiplying them by a constant outside of the optimizer, and then reversing that multiplication inside the system model; in this way, the sensitivity of the system response to a particular variable is altered from the optimizer’s perspective, but the results of the model execution are not affected.

In the case of the EM boom, when the Hessian was numerically computed about the optimum defined above, the diagonals of the Hessian were between 3 and 4 orders of magnitude too large. A full factorial experiment was then executed to determine which set of scaling multipliers of each of the design variable resulted in either better convergence performance or a better optimal solution (or, ideally, both). It turned out that multiplying the number of turns design variable by 10^3 and the coil radii by 10^4 improved the convergence time of the algorithm by a factor of ~15. However, the objective value of the optimal solution was not improved.

A heuristic optimization algorithm was also explored for the EM boom optimization problem. The algorithm selected was Matlab’s “ga” function (genetic algorithm, or GA). A GA searches through a design space for an optimal solution in a fundamentally different way than a gradient-based algorithm. The GA is modeled on the process of natural selection. There are many variants to this process, but the general outline presented here. It begins with a set of randomly selected points, known as a population. Some of the elements of the population “mate” to form “offspring” – meaning that the design vectors within that population are combined with other design vectors to form new possibilities in the design space. Members of the population (the design vectors) are more likely to be selected to “mate” (and pass on their design features to the next generation) according to a fitness function, which assigns a score to the design vector that assesses its relationship to an optimal solution. Mutations are also introduced – random changes to design vectors that are independent of the mating process. Over time via the selection process, the population tends towards a better and better solution, as the fittest solutions survive. The algorithm is typically terminated after it has reached a specified number of generations.

There are many parameters within a GA that can be tuned to a particular problem to improve convergence rates and/or the quality of its solutions. For the EM boom, a trade study was performed to determine the values of the GA’s population size (set to values between 5-150), the number of generations (10-100), and the number of elite individuals per generation (0-5). A series of runs of the GA were made; the best configuration of parameters was defined as the one that provided diminishing returns on reducing objective values while executing in a reasonable amount of time. The parameters selected were 100, 100, and 0. Once the GA was tuned, the optimizer was executed to determine the minimum mass EM boom system. The result of this execution is shown below in Table 3.

Table 3: Solution to genetic algorithm single objective optimization

J	Algo	CPU Time (mm:ss)	Solution (x^*)		Performance (f^*)	
Mass	GA	15:04	2 coils		Mass(kg):	31.53
			Coil radii (m):	0.276, 0.227		
			No. Turns:	152, 218		

With an objective value of 31.53 kg, the solution identified by the GA was superior to the one found by the gradient-based search scheme. However, the run time was significantly longer. After careful consideration, the 6% improvement of the GA was determined to be significant enough to justify the additional execution time, and it was selected as the underlying optimization algorithm used in all subsequent analysis.

Once the optimization was complete, a sensitivity analysis about the optimal solution was performed to determine the sensitivity of the solution to changes in the design variables. Figure 11 below shows the results of the sensitivity analysis.

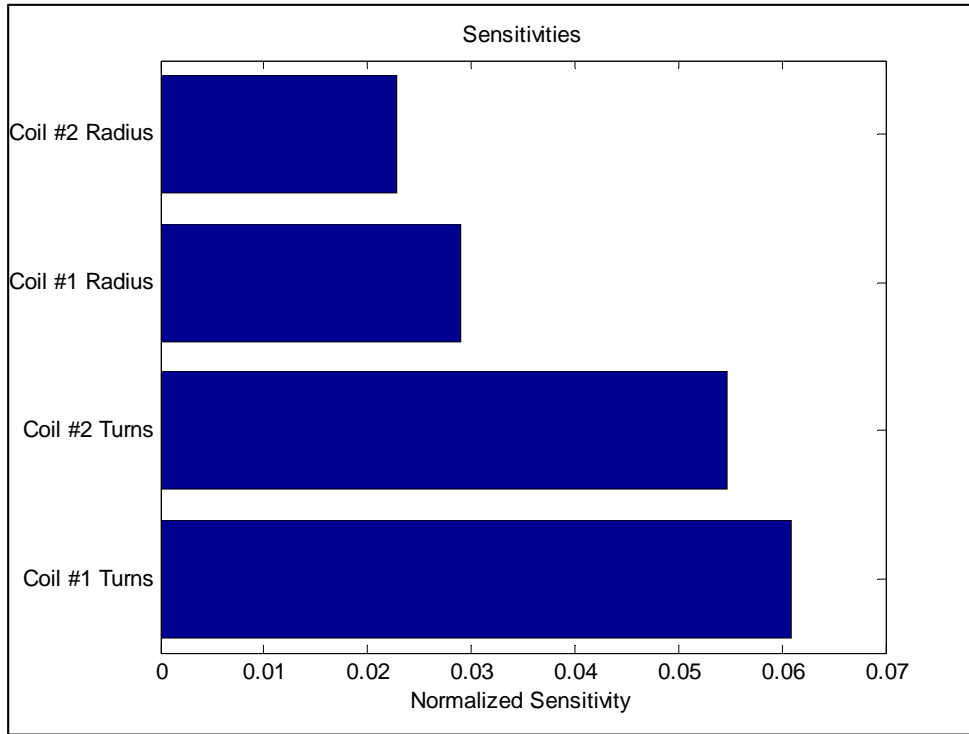


Figure 11: Sensitivity analysis

The x-axis shows the normalized sensitivity of the objective function to the design variable, defined as the percent change of the objective function value per percent change in the design variable. As Figure 11 shows, the objective function is very insensitive to design variable changes at the identified optimal solution. This is a desirable result; at an unconstrained optimum, one would expect the objective function to be completely insensitive to small design variable changes – in other words, the Jacobian would be equal to zero. The Jacobian here is not zero, but it is small, lending confidence to the identified solution as being an optimal one. The reason the Jacobian is not zero is that there is an active constraint at the optimal solution. At this solution, the temperature of the coil is equal to its lower limit, which is one of the two problem constraints. This result provides evidence that the constrained optimum of this problem may also lie near its unconstrained global optimum.

At a constrained optimum, the KKT first order necessary conditions for optimality must be satisfied. In order to determine whether the solution identified by the GA satisfies these conditions, the following system of equations must have a solution.

$$\begin{aligned} \nabla f(x^*) + \lambda_1 \nabla g_1(x^*) + \lambda_2 \nabla g_2(x^*) &= 0 \\ \lambda_1 g_1(x^*) &= 0 \\ \lambda_2 g_2(x^*) &= 0 \end{aligned}$$

Because the cryocooler mass constraint was not active, $\lambda_2 = 0$. The gradients of both the objective function f at the optimal solution x^* and the constraint function g_1 were numerically determined, and a value for λ of approximately 0.046 closely solved the KKT optimality condition. The equations above were not exactly solved; this is expected for a heuristic algorithm that does not converge arbitrarily close to an optimum. However, the residual in the least squares solution to the KKT system of equations is very small, and so the solution is very near optimal.

4. Two Objective

The power available to the cooling systems for an EM boom-equipped spacecraft may be a limited commodity, insofar as the power budget is fixed as a function of the systems' solar arrays, and energy required for coil cooling cannot be used for other essential mission functions. So, in addition to minimizing system mass, it is also desirable to minimize the required cooling power. This gives rise to a multiple-objective minimization problem where an optimal solution simultaneously minimizes mass and cooling power. As with the single objective case, the design of the EM boom with respect to the dual objectives of mass and power was started with a design of experiments. A 10,000 point Latin Hypercube DOE was performed to generate an initial exploration of the design space. Figure 12 shows a scatter plot of the values of the mass and power objectives evaluated at the DOE design points. The color of each point again identifies the number of coils in the system

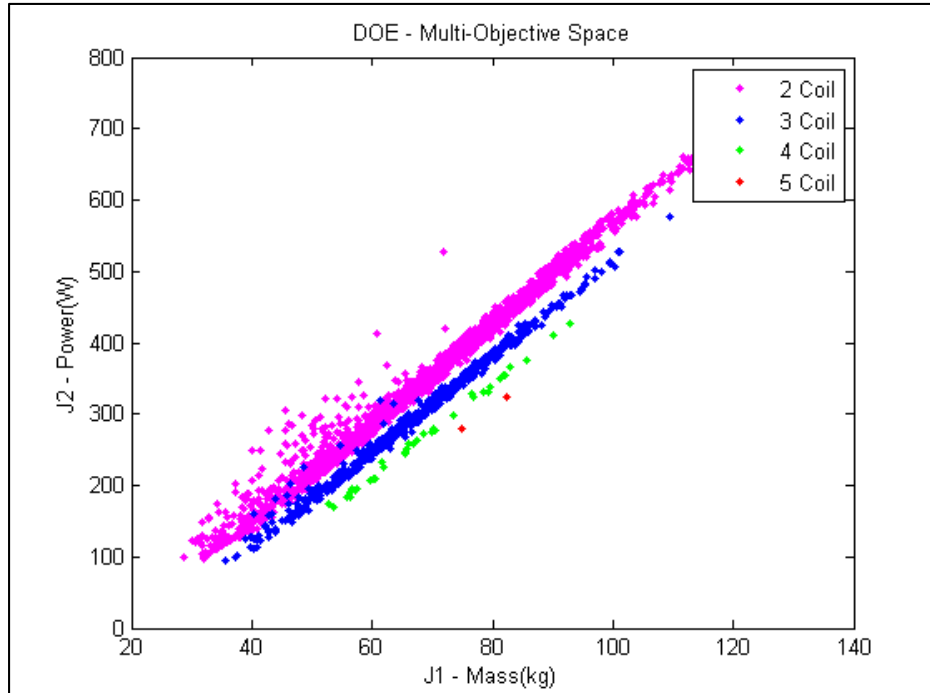


Figure 12: Multi-objective DOE

The theoretical utopia design point for the EM boom problem is at the origin. The DOE data in Figure 12 suggest that some variation of a 2-coil system is likely to be an optimal design for these two objectives. The objective function values derived from the DOE describe a reasonable approximation the boundaries of the objective space. However, it is not possible from this information alone to identify the non-dominated solutions that comprise a set of optimal designs (known as the Pareto frontier).

A technique that may be employed to locate the Pareto frontier is the Weighted Sums (WS) method. The WS method essentially turns a multiple objective problem into a single objective problem by adding the values of each objective variable, with weights on each term indicating the relative importance of that objective with respect to an optimal solution. The 2 objectives – J1 = mass and J2 = power – are combined in the following manner:

$$J_w(x) = wJ_1 + (1 - w)J_2$$

for a given value of the weighting factor w . To construct a frontier, a series of weights were used and an optimal solution to each objective function was determined using a single objective optimization routine using the GA optimizer. . 21 weights were used - varied on the range [0,1] with a 0.05 step size. The frontier points located are shown in green in Figure 13, superimposed on the DOE solutions (not to be confused with the 4 coil design points, none of which are visible in the figure):

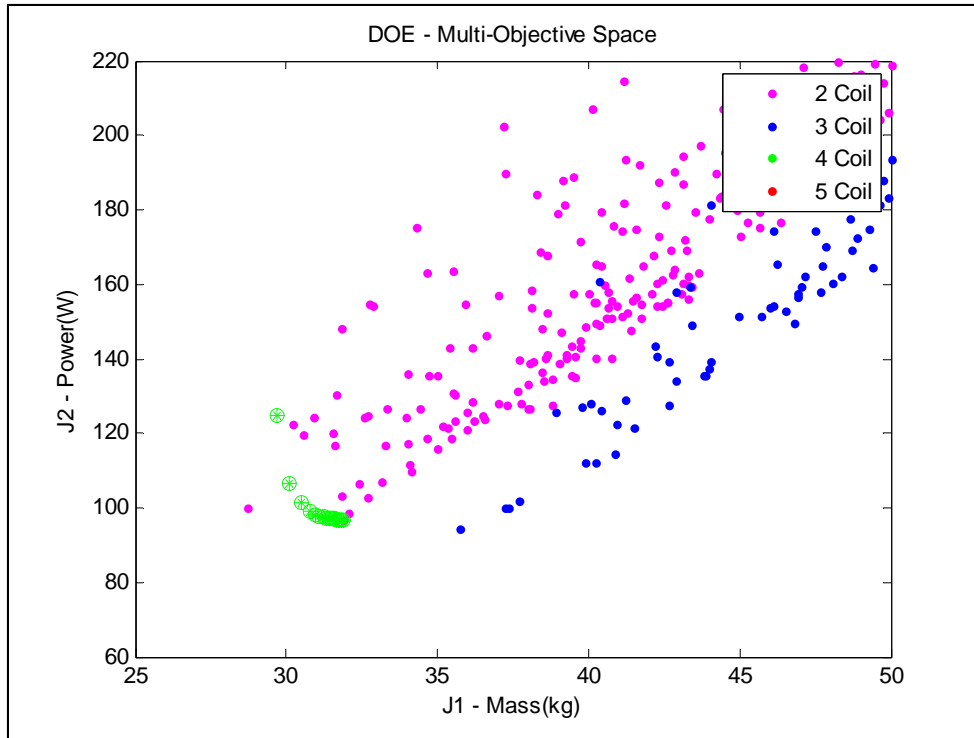


Figure 13: Weighted sum Pareto frontier

The non-dominated solutions identified by the WS method appear in an intuitive place – on what appears to be a curve containing the DOE points and lying closest to the origin. Clearly this set of points provides a better description of the Pareto frontier than the pseudo-randomly sampled data points from the DOE. However, the WS method does not provide uniformly distributed points along the Pareto front – in the regions where large gaps occur, it is possible that the locations of the non-dominated solutions are not captured. A more sophisticated technique is required to completely describe the set of Pareto optimal solutions.

To gain a complete understanding of the Pareto frontier, a version of the Adaptive Weighted Sum (AWS) algorithm was developed from descriptions of the algorithm in literature. The algorithm is based on the Weighted Sum approach, where the multiple objective values are combined into a single objective via a weighting parameter. In fact, the first step in the routine is to generate a Weighted Sum frontier. However, in this methodology additional points on the frontier are determined by applying artificial constraints on the objective values to ensure a solution is located at – or near – a desired point on the frontier. These constraints are determined as the frontier is traversed – the distance between two adjacent points is calculated, and if that distance exceeds a pre-determined threshold a weighted single-objective optimization is run to find a solution whose objective values lie on the frontier at a set distance in between, enforced via the imposed constraints. Because one of the goals of this algorithm is to generate a frontier with evenly spaced points, a filtering routine is then run to remove points that are too close together. Figure 14 illustrates the AWS Pareto frontier, superimposed in red on the DOE results.

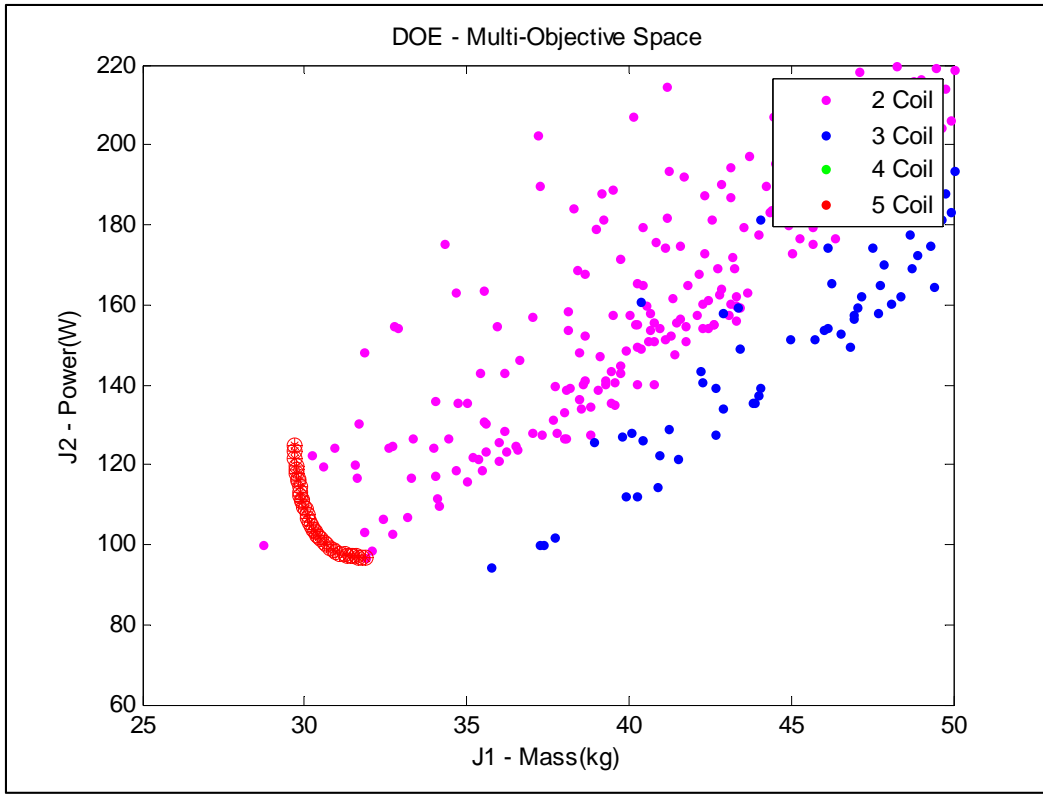


Figure 14: AWS Pareto frontier

As anticipated by analysis of the DOE points, all the solutions identified by both the WS and the AWS algorithms were 2-coil solutions.

5. Expanding the Trade Space

Given that the two-objective Pareto front shown previously explored only a narrow class of boom designs, we sought to extend the trade space exploration in search of more interesting and diverse designs. To that effect we added the length of the boom as an objective, where previously it had been defined as a parameter. There are several reasons why one may choose to maximize boom length. One possibility is that the supported payload may be radioactive (e.g. and RTG power source) and hence could damage components on the spacecraft. Another may be that the payload requires strict thermal isolation (e.g. an optics payload) and hence needs to be far in distance from the spacecraft to reduce irradiative coupling, as well as minimize conductive pathways.

In order to assign boom length as an objective, it must have some inherent relationship with the design variables. The current list of variables does not impact the boom length directly. However, we can migrate our boom tension (previously a parameter) to the design vector and write a relationship between boom length and tension required to support that length. This relationship we refer to as a stability criterion. In essence, a boom of some length will require a fixed tension in order to prevent it from failing. Without a rigorous stability criterion in hand, we use the Hill's Orbit Equations which describe the inter-satellite forces for multiple satellites in formation flight. Specifically, for a cross-track formation, we require a repulsive force of:

$$F_{cross-track} = n^2 \left(\frac{m_p m_s}{m_p + m_s} \right) L$$

Thus for a geostationary orbit and a specified payload and satellite mass, the boom length and tension are linearly related. Because the boom length is a function of only a single design variable (tension), the boom length and system mass and power will be strongly competing objectives. As the boom becomes longer and longer, the required tension will increase proportionally. Likewise, the coils along the length of the boom will be required to generate increasing magnetic forces which will require higher currents, larger coil radii and more wire turns. Thus we can expect the Pareto fronts involving system mass or payload versus boom length to be much more spread out across the objective space.

Finally, we also consider that number of MLI layers per coil as an additional design variable. Like the number of wire turns and coil radius, we allocate one design variable per coil. Thus we have a total of five additional design variables for a five coil system. Deciding

how much insulation to use on spacecraft structures, especially those housing temperature-sensitive equipment, is an important design decision that many satellite engineers encounter. Thus, by making this decision a design variable, we can better understand the tradeoff between added mass from each MLI layer versus the additional thermal insulation that ultimately lowers the amount of heat the cryocooler is extracting. Again, this only helps to diversify the Pareto optimal designs when considering multi-objective analysis.

A summary of the changes made to the objectives, design variables and parameters is listed in Table 4 below:

Table 4: Updated Objectives, Design Variables and Parameters for Trade Space Expansion

	Description	Value/Units	New Vector Size
Objectives	Boom Length	meters	3
Design Variables	Tension	μ Newtons	17
	No. MLI Layers	#	
Parameters	Satellite Mass	1000 kg	23
	Payload Mass	25 kg	

Note that having 17 design variables is somewhat cumbersome for heuristic methods. However, based on our previous experience and recommendations for optimizers from the previous model, we choose the NSGA-II algorithm as our multi-objective heuristic method. The major benefit of this decision over using the other widely known MOGA algorithm, is that the NSGA-II algorithm influences the non-dominated designs to spread out along the estimated Pareto frontier. This feature helps to avoid clusters at various regimes which can be especially disappointing as more objectives are added to the problem. The second benefit of using this algorithm is that we have access to the source code in MATLAB and thus can tune several of the parameters including mutation rate, number of generations and population size which was necessary when going from a two-objective to three-objective analysis. Our results indicate good success with this algorithm.

5.1. Single Objective Runs

Before discussing the multi-objective analysis, we first examine the single objective approach. Again we use our classical genetic algorithm as provided by MATLAB's built-in function *gam* and vary tuning parameters to speed convergence. The results of these runs, for each of the three objectives, is listed in Table 5 below:

Table 5: Single objective optimal solutions

Obj.	Algor.	CPU time (min:sec)	Solution (x^*)				Performance (f^*)	
Mass	GA	15 : 04	2 coils				Mass(kg): 31.53 Power(W): 6.67 Length(m): 51.46	
			Coil radii (m):	0.276 , 0.227				
			No. Turns:	152 , 218				
			No. MLI Layers:	29 , 30				
			Tension (μ N):	20.011				
Power	GA	22 : 36	2 coils				Mass(kg): 32.36 Power(W): 5.30 Length(m): 51.43	
			Coil radii (m):	0.268 , 0.268				
			No. Turns:	250 , 250				
			No. MLI Layers:	30 , 30				
			Tension (μ N):	20.000				
Length	GA	126 : 34	4 coils				Mass(kg): 273.54 Power(W): 409.05 Length(m): 1028.5	
			Coil radii (m):	4.903 , 4.792 , 4.823 , 4.512				
			No. Turns:	102 , 226 , 245 , 198				
			No. MLI Layers:	10 , 15 , 15 , 6				
			Tension (μ N):	399.95				

Several conclusions are evident from the above results. First, the optimal point designs for minimizing mass and minimizing power are very similar. This is intuitive from a physical standpoint since heavier cryocoolers are needed to extract more heat from the coils (and hence draw more power). Likewise, from the previous Pareto front which traded mass and power, we noticed that the set of non-dominated designs were closely related. The coupling between mass and power provides only a limited regime within the objective space to trade these two objectives. A second conclusion from the above results is that maximizing boom length requires more coils

with larger diameters. This feature is also quite intuitive if we consider much longer booms where the coils must generate even higher electromagnetic forces on one another to generate the required tension. Also, note that the time required to converge to a solution is roughly a factor of six times longer than the other two objectives. This can be reasoned by understanding that the model takes longer to execute with more coils along the boom (and hence more electromagnetic interactions to account for) as well as the fact that there are fewer feasible designs in this region of the objective space (two and three coil designs simply won't work here). As an overall conclusion, we note that maximizing boom length is completely counteractive to minimizing mass and power, as is evident in the heavy and power hungry 1 kilometer boom shown in the above single-objective run.

5.2. Two Objective Runs

We repeat the two objective run from our previous analysis, trading mass and power. As expected, this trade space is extremely limited given the close coupling between these two objectives:

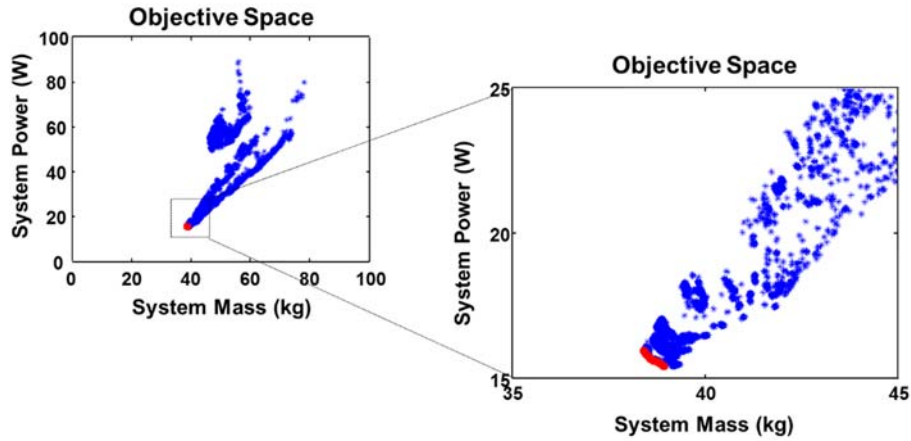


Figure 15: Objective space and non-dominated design for system mass vs. power

And as shown in the single-objective analysis, these non-dominated designs all have 2 coils with relatively small diameters of approximately 0.5 meters. The more interesting results are evident when we analyze each of the mass and power objectives with boom length. Those results are shown on the next plots:

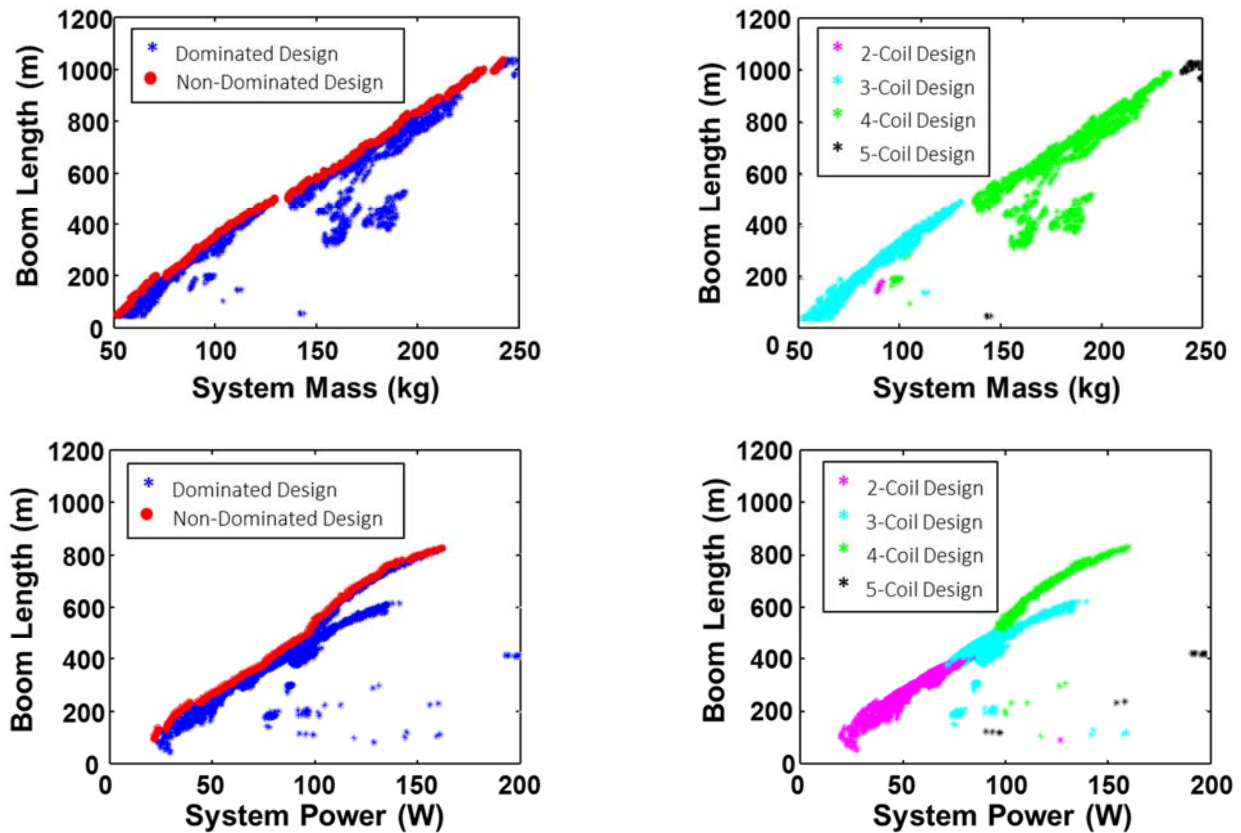


Figure 16: Two objective Pareto optimal designs using boom length

What we expected seems fairly obvious in Figure 16. The Pareto front now traverses a much larger design space with varying numbers of coils, radii, wire turns and number of MLI layers. The plots on the right illustrate the variation in number of coils used to support the

boom, and are clearly increasing with boom length. This makes intuitive sense because as the length of the boom grows, more coils are needed to support the requisite tension. However, we also note that the mass and power objectives seem to diverge at longer boom lengths than previously considered. Whereas the minimal mass booms use mainly 3-coil designs in the shorter length regime (50 – 500 meters), the minimal power booms use predominately 2-coil designs. This indicates that at larger boom lengths, the mass and power objectives start to compete with one another, as fewer coils has a much more positive impact on cryocooler power than smaller radii coils. Above 500 meters, we see that the design space begins to narrow as 4-coils architectures are exclusively selected for minimizing either mass or power.

5.3. Three Objective Runs

Finally, with three objectives now being considered, we can perform the multi-objective optimization on all three objectives and generate a Pareto surface. The competition between all three objectives will also indicate multiple design families which system engineers and managers can use to understand the real options in constructing such a system. The results from this study are illustrated in Figure 17.

Objective Space

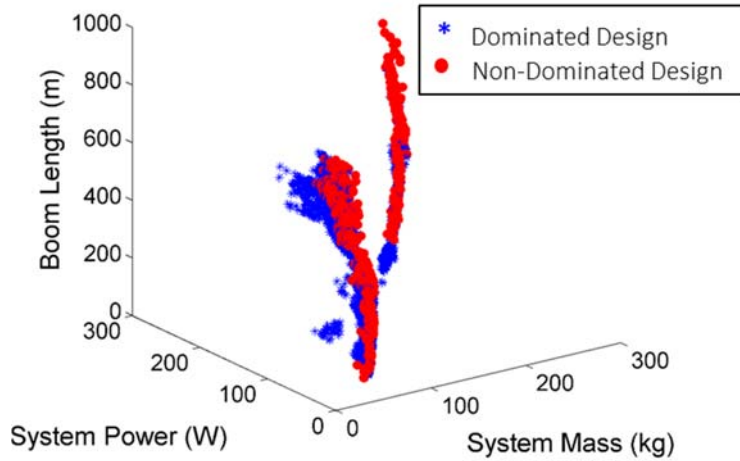


Figure 17: Three objective Pareto optimal designs

In order to generate this estimate to the true Pareto frontier, the number of population members was increased to 100 (in order survey more of the objective space) and the number of generations was also increase to 300 (since the additional objective may slow down the convergence rate). What is clear from this plot is that two design families are immediately obvious. To further explore the design architectures that have been arrived at, the non-dominated solutions are binned or categorized into families according to each major design variable: number of coils, coil radii, number of turns, and number of MLI layers. This filtering is presented in Figure 18:

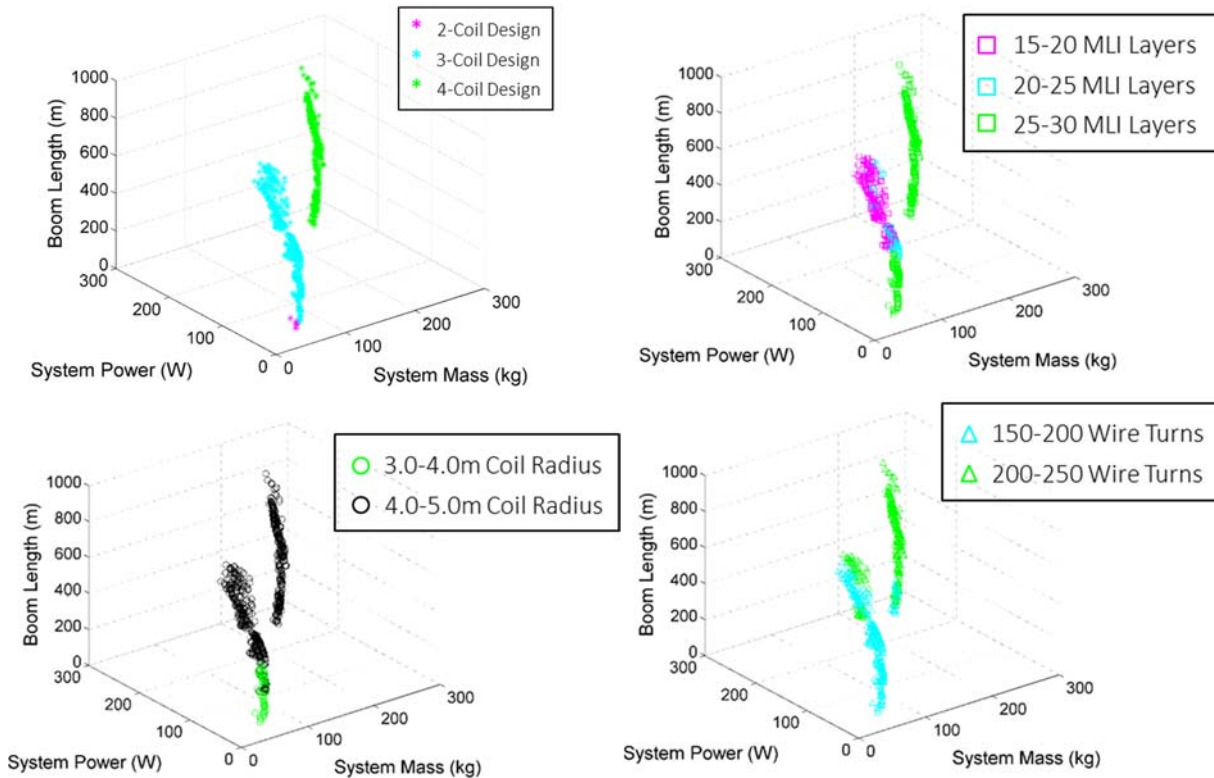


Figure 18: Two objective Pareto optimal design architectures

The 2-coil designs are limited to the very smallest mass, power and length architectures. What is predominant in this objective space are 3 and 4-coil boom designs. In addition, larger coils are typically used in the non-dominated designs (where the coil radius is that of the largest coil present). Likewise the number of MLI Layers and wire turns tends to be closer to the upper boundaries of these design variables in the optimization formulation. As a conclusion, we can say that additional MLI layers, wire turns and even radii are typically mass efficient trades to make over increasing the number of coils in the system. In other words, before adding a third, fourth or fifth coil, it is better to make the existing coils larger, use more wire turns and add insulation. From a systems perspective, this makes sense that adding a whole other element to the boom design (an additional coil) would be less attractive than simply making the existing coils more powerful and efficient. What is not intuitive is how to make these trades between the remaining design variables. However, we have shown here that an intelligent multi-objective algorithm can illustrate and aid the designer quantitatively in what these trades should be.

6. Conclusions and Future Work

We have found that the Pareto front for the two-objective optimization of min(mass) and min(power) for an electromagnetic boom of the architecture described in this paper is very small because the two single objective utopia points are very close to each other. Mass and power are very coupled objectives and we could reduce the computation involved in optimization by eliminating one of the two and optimizing for just the other.

The tradespace is significantly expanded by adding the third objective, max(length), because with greater length comes by necessity greater mass and power. The tradespace becomes more computationally expensive to produce because of its breadth, but the designs found in the Pareto front of a multiobjective problem involving length are much more diverse than the exclusively two-coil designs along the min(mass) and min(power) Pareto front.

Future work to further improve this optimization includes the incorporation of dynamic stability conditions, which depend on multiple design variables and parameters and will greater constrain the design space, resulting in islands of infeasibility where a design does not satisfy the stability constraints. A comparison of the boom optimal mass versus length with other structural technologies like deployed trusses and inflatables will provide spacecraft designers with a clear picture of the mass savings possible with an electromagnetic structure. A possible fourth objective or additional constraint is cost, though it would be difficult to capture a cost function for such a low TRL technology.

References

- 1) Donabedian, M., Gilmore, D.G., Stultz, J.W., Tsuyuki, G.T., and Lin, E.I., "Insulation," *Spacecraft Thermal Control Handbook Volume I: Fundamental Technologies*, 2nd ed., edited by D.G. Gilmore, AIAA, 2002.
- 2) Gettliffe, G.V. "High-Temperature Superconductors as Electromagnetic Deployment and Support Structures in Spacecraft," S.M. Thesis, Dept. of Aeronautics and Astronautics, Massachusetts Institute of Technology, Cambridge, MA, 2013.
- 3) Ladner, D.R., "Performance and Mass vs. Operating Temperature for Pulse Tube and Stirling Cryocoolers," *16th International Cryocooler Conference*, Atlanta, GA, 2008. Available: <https://smartech.gatech.edu/bitstream/handle/1853/39778/078.pdf>
- 4) Raab, J., Tward, E., Toma, G., and Nguyen, T., "Integrated Detector Cooler Assembly for Space Applications," *17th International Cryocooler Conference*, North Hollywood, CA, 2012.
- 5) SuperPower Inc., "Field dependence of Ic at 20 – 65K, 2011 SuperPower AP wire." Report, 2013
- 6) SuperPower Inc., "SuperPower®2G HTS Wire Specifications," [Online]. Available: http://www.superpower-inc.com/system/files/SP_2G+Wire+Spec+Sheet_for+web_2012FEC_v2_0.pdf.
- 7) Wertz, J. R., Everett, D. F., and Puschell, J. J. *Space Mission Engineering: The New SMAD*. Hawthorne, CA: Microcosm, 2011.

Appendix 6: MAGESTIC Hardware Testing

MAGNETICALLY
ENABLED
STRUCTURES
USING
INTERACTING
COILS

MAG IC



Aaron Perez & Gwen Gettliffe

SSL Seminar

MIT Space Systems Lab

August 28, 2013

[edited for inclusion in final report]



Testing Roadmap

1. Basic Deployment Tests (all using copper coils)
 - Separation Module using AirTrack
 - Hinge Unfolding Module using 3DOF Air Table
 - Inflating Module
2. High Temperature Superconductor Coil Testing
 - Expanding Module
3. Operational Demos
 - Deform
 - Reconfigure
 - Refocus
 - James Webb Telescope



Testing Roadmap

1. Basic Deployment Tests (all using copper coils)
 - Separation Module using AirTrack
 - Hinge Unfolding Module using 3DOF Air Table
 - Inflating Module

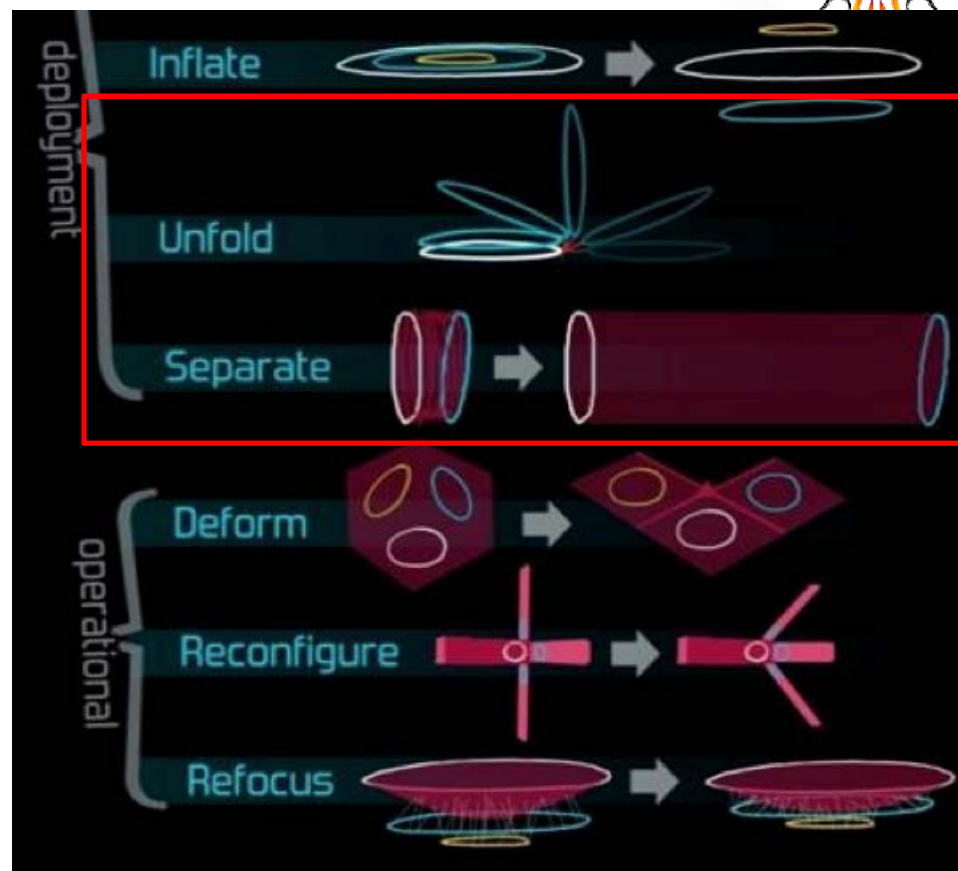
2. High Temperature Superconductor Coil Testing
 - Expanding Module

3. Operational Demos
 - Deform
 - Reconfigure
 - Refocus
 - James Webb Telescope

Basic Deployment Tests

Proposal objective: Reduce risk and validate modeling via hardware proof-of-concepts

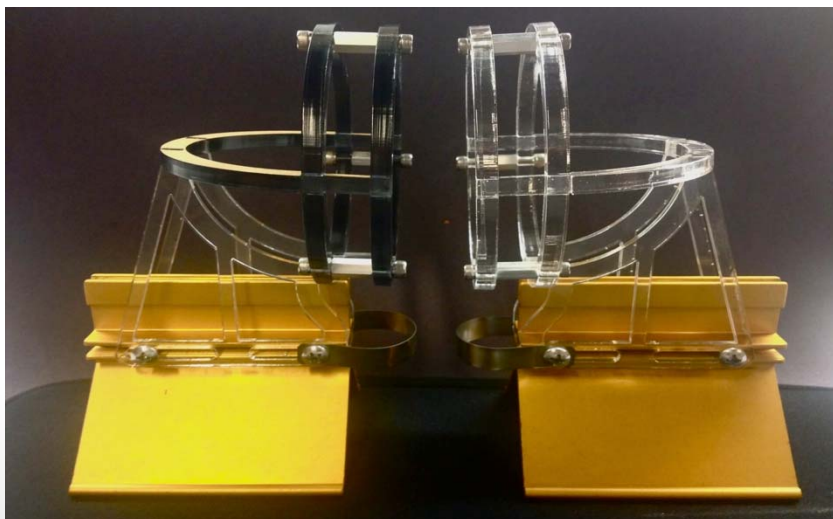
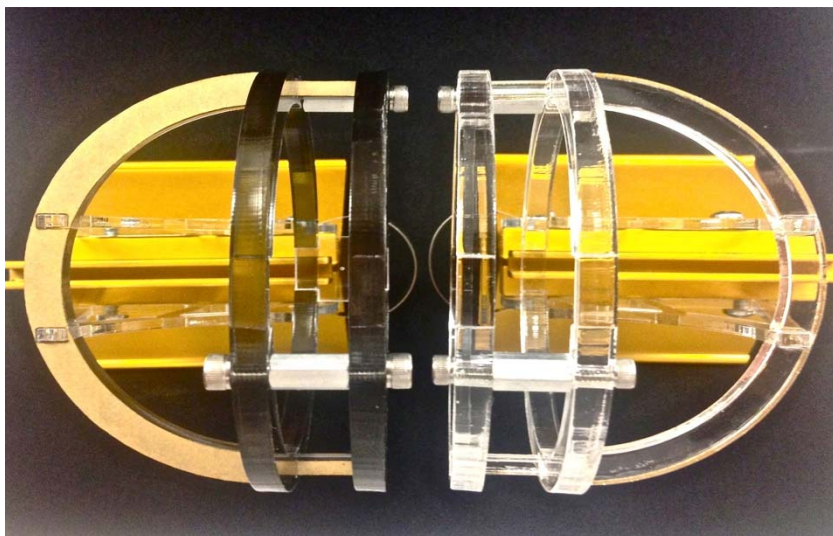
- Goal: validate findings from Phase I Separate and Unfold models
- Used regular conductors because models are scalable to low currents and different materials and wanted to see if we could validate w/out thermal hardware



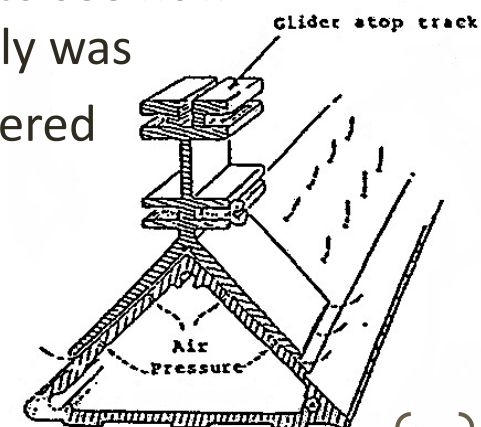
Material:	Copper magnet wire
Turns:	350
Inner Radius:	1.125 "
Outer Radius:	1.5 "
Voltage run:	~ 31.5 V
Current run:	~ 1.5 A



Separation Module



- Conducted linear air track 2DOF test (1 deg translation, 1 deg rotation per coil)
- Coils mounted in acrylic frames on air track carriages that allowed pivoting around gravity vector
 - 2DOF system reflects all relevant motion w/ axisymmetry & in frame of reference of the two coils w.r.t. each other
- First test tether free to see how frictionless track really was
- Second test was tethered



TRACK CROSS SECTION

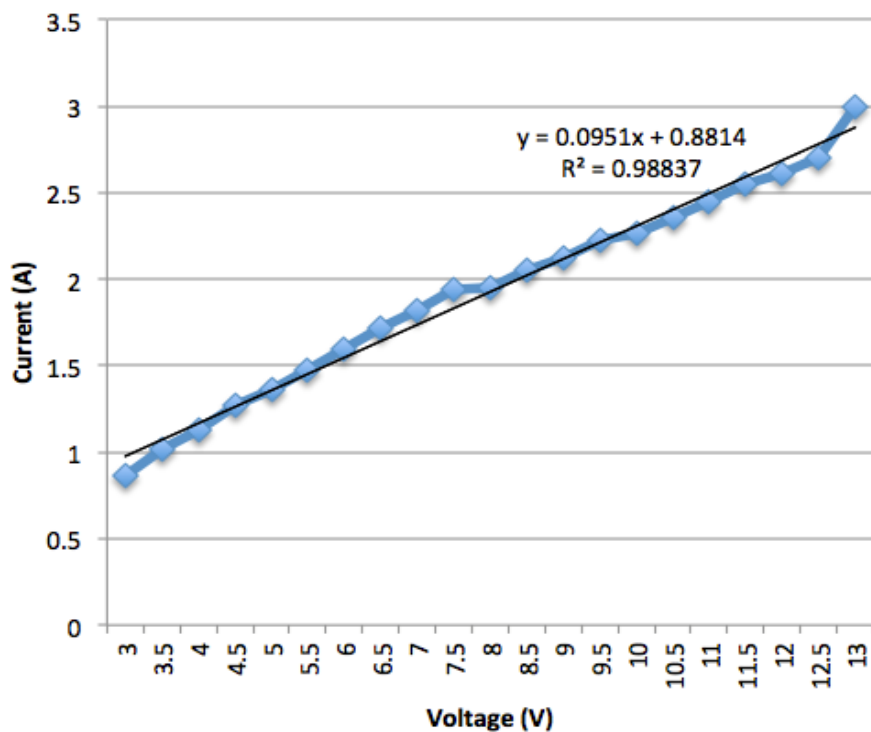
Figure 6



Track Performance

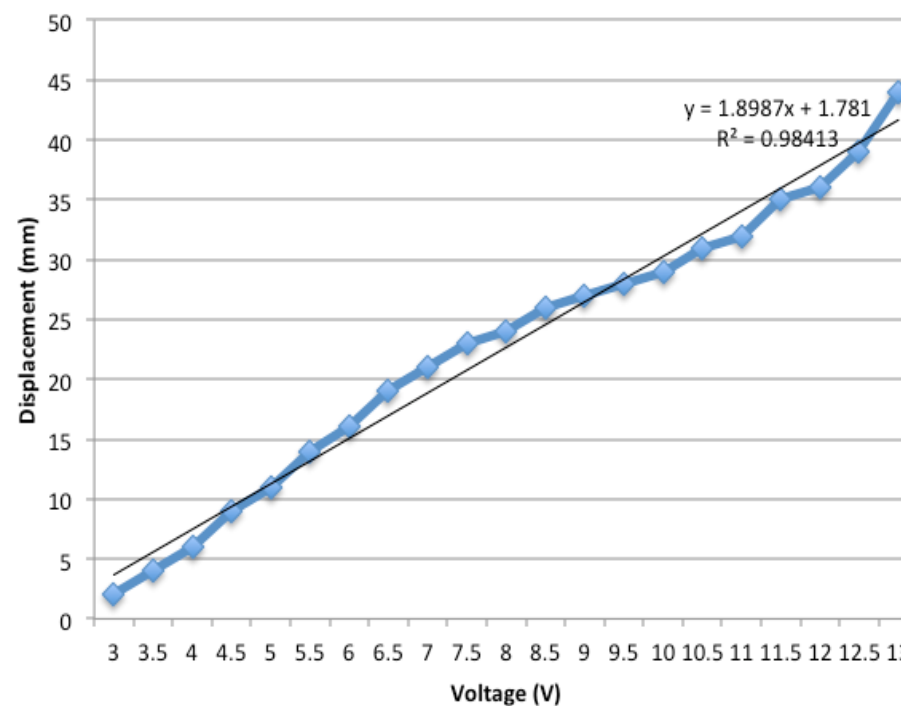
INITIAL RESULTS

I V Graph



Resistance of Coil: 10.5 Ω

D V Graph



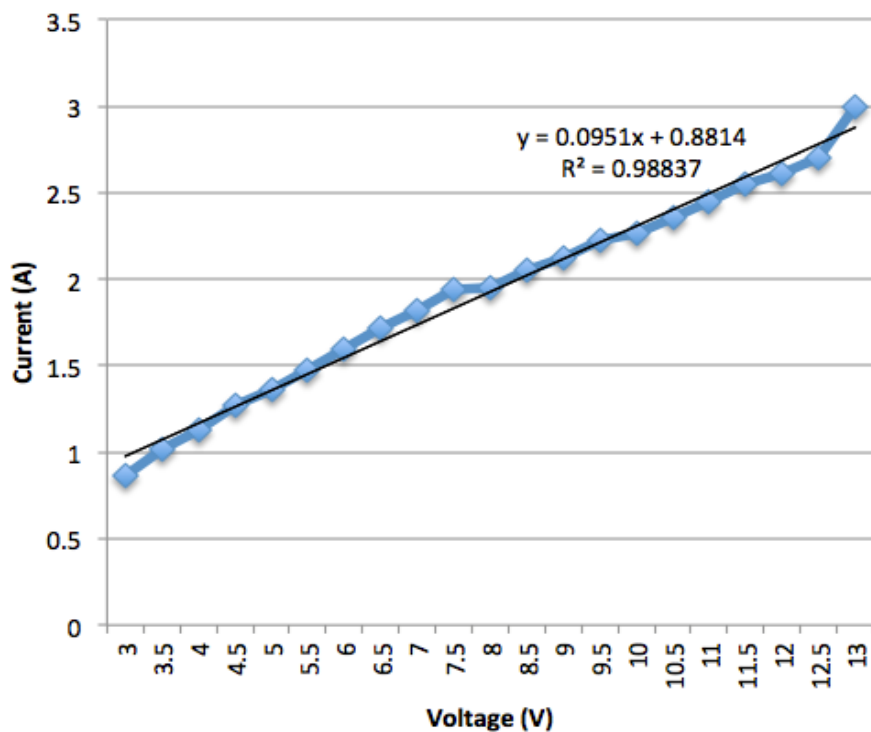
— Unexpected Curve (for D V plot)



Track Performance

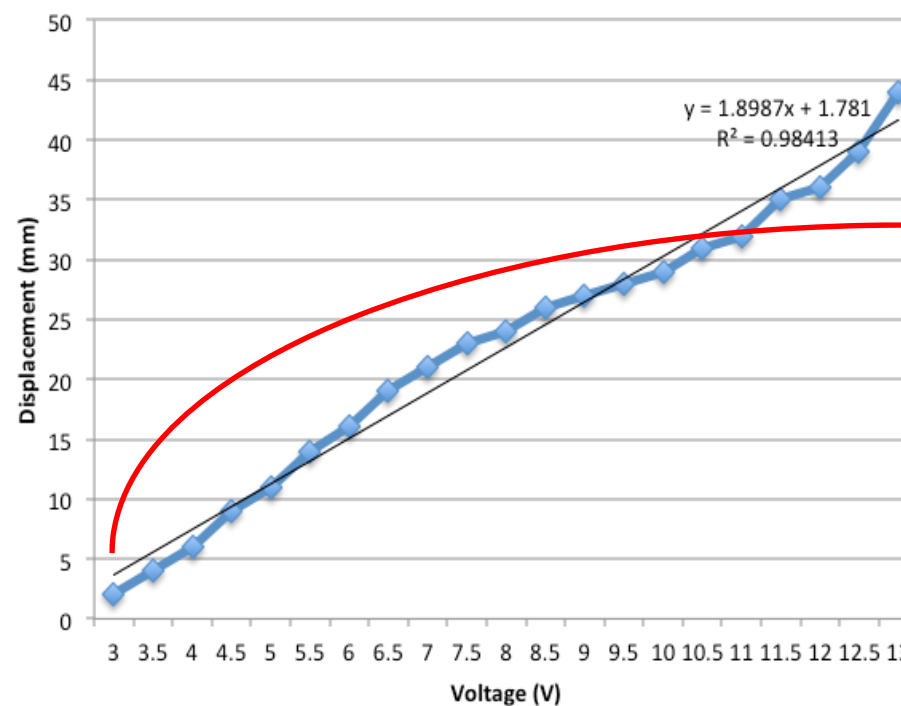
INITIAL RESULTS

I V Graph



Resistance of Coil: 10.5 Ω

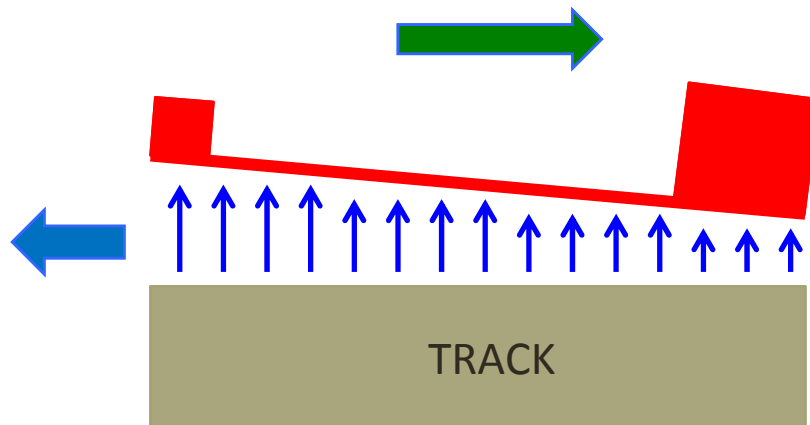
D V Graph



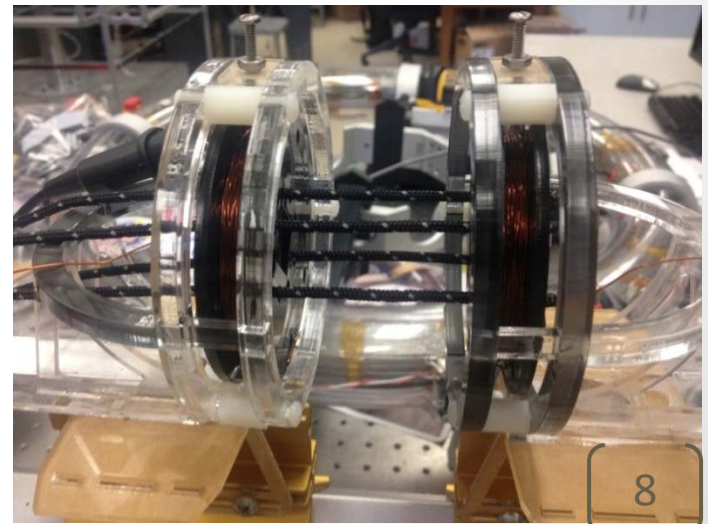
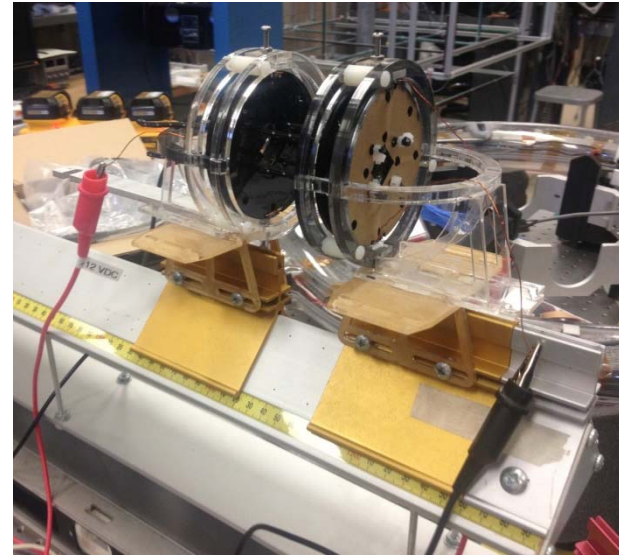
— Expected Curve

Air Track Issues

- Experienced issues with coil being not perfectly balanced on carriage and then subsequent movement due to uneven air escaping



- Experimented with different tether materials (stiff rope, fishing line) and mounting methods (knotted around edge of coil vs. slid through holes, shown right)
- Unfortunately copper coils were too weak ($\mu = NIA \approx 1.35 \text{ Am}^2$) to overcome friction forces for long, so only partial deployment

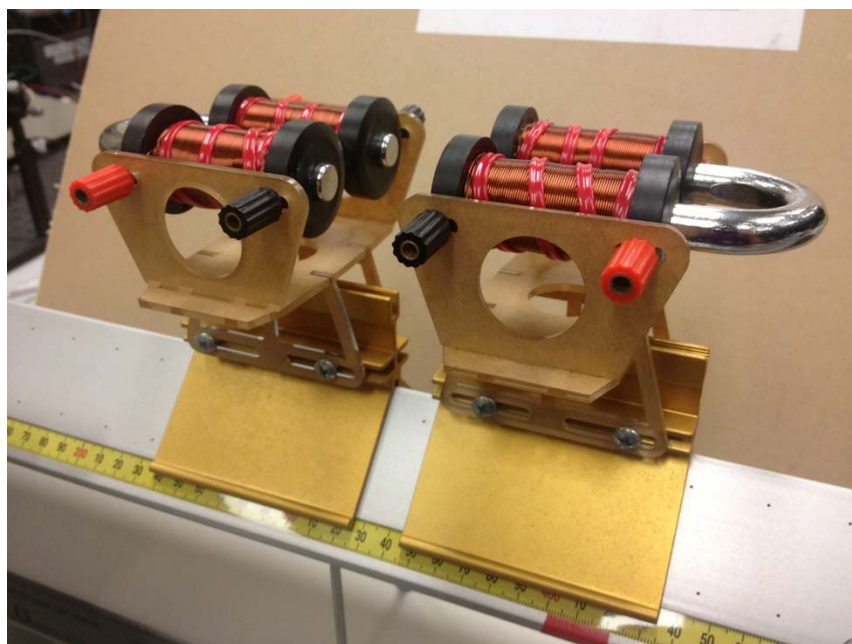




Alternate Approaches

FOR POWER:

Large Commercial Iron Core Electromagnets

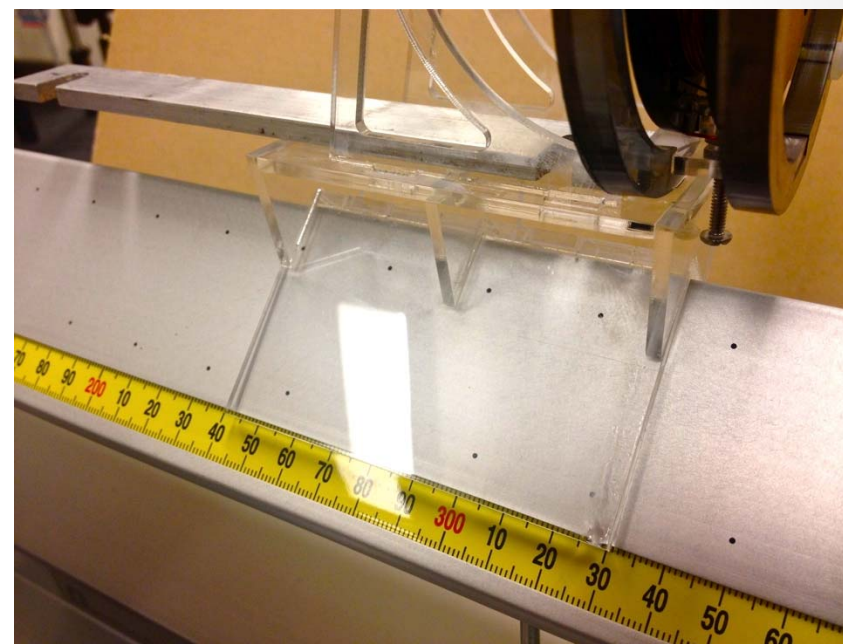


RESULTS:

Too Heavy and the model didn't consider iron core coils

FOR MAGNETIZATION:

All Acrylic Glider



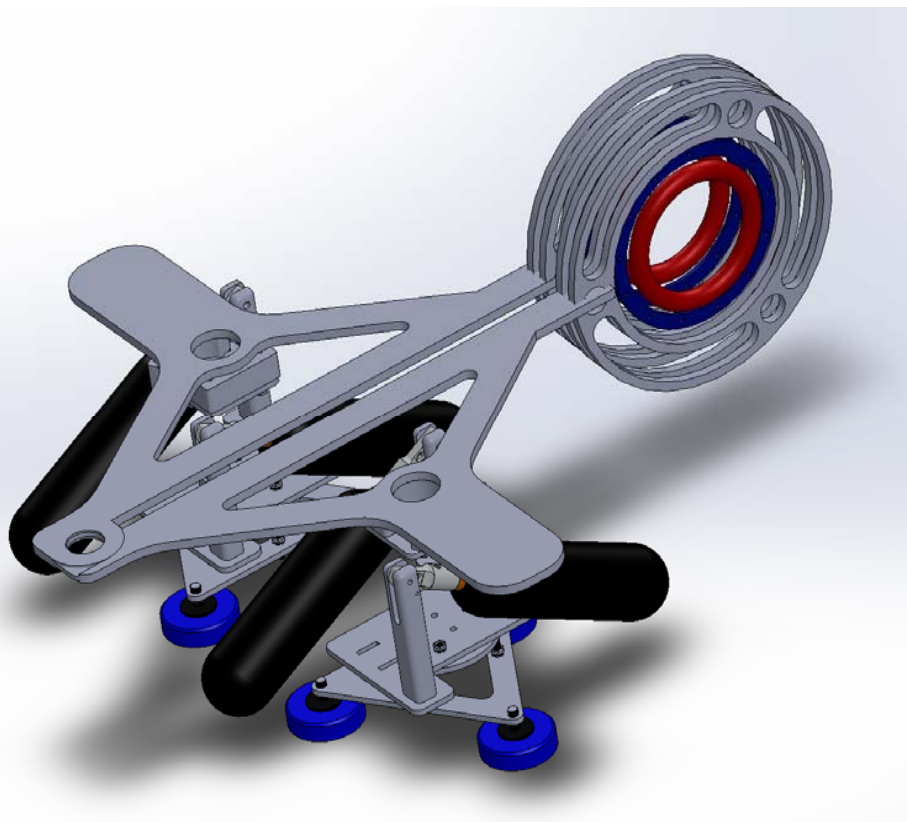
RESULTS:

Glider Angle wasn't precise enough, didn't float

VIDEO (part_1)



Hinge Unfolding Module



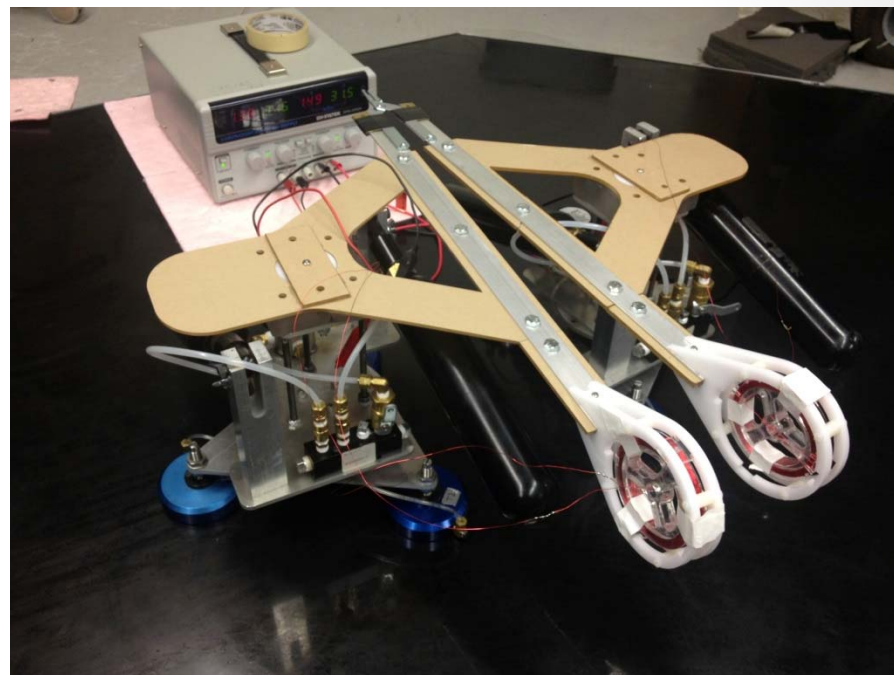
- Allow for rotation about a hinge (no spring here)
- required 2 degrees of freedom
- built around the preexisting air carriage size (very non-optimal for this application)
 - 5.68 kg carriage w/tanks, 1.02 kg hinge rig w/coils
- Tested with one carriage on (allowed to glide on air pucks) and the other off

Used Both Surfaces

3DOF Glass Table



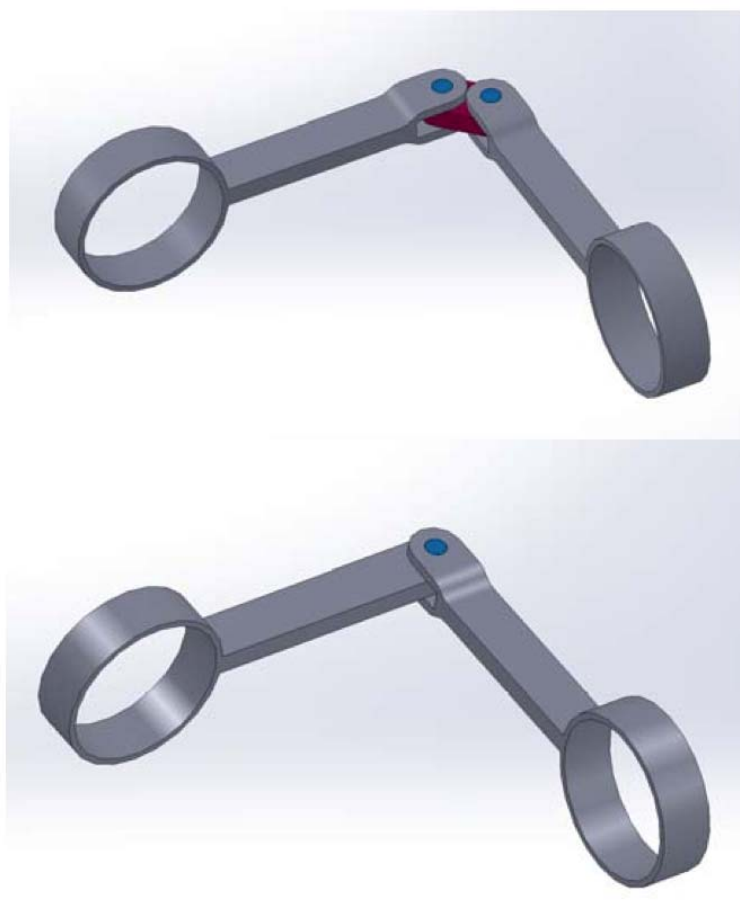
Epoxy Floor



Only saw about 3° separation due to small magnetic moment of the coils

Future Improvements

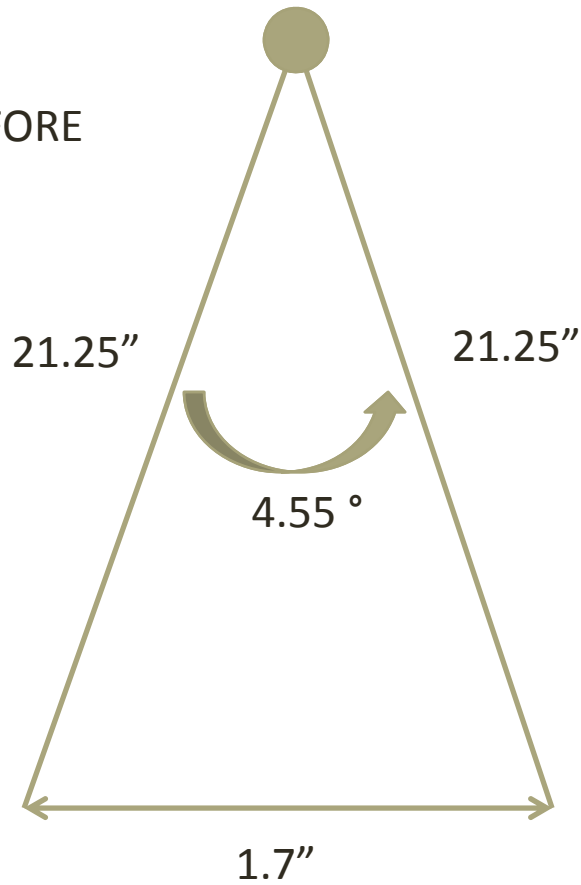
- Go smaller
- Possibly create smaller carriages for the table to reduce the inertia the coils need to overcome
- Incorporate control to reverse the current running through both coils to enable attraction and repulsion
- Use spring to better model the dynamics of such a hinge (and adequately represent the numerical model, which includes torsional springs of varying stiffness)



Initial Results



BEFORE



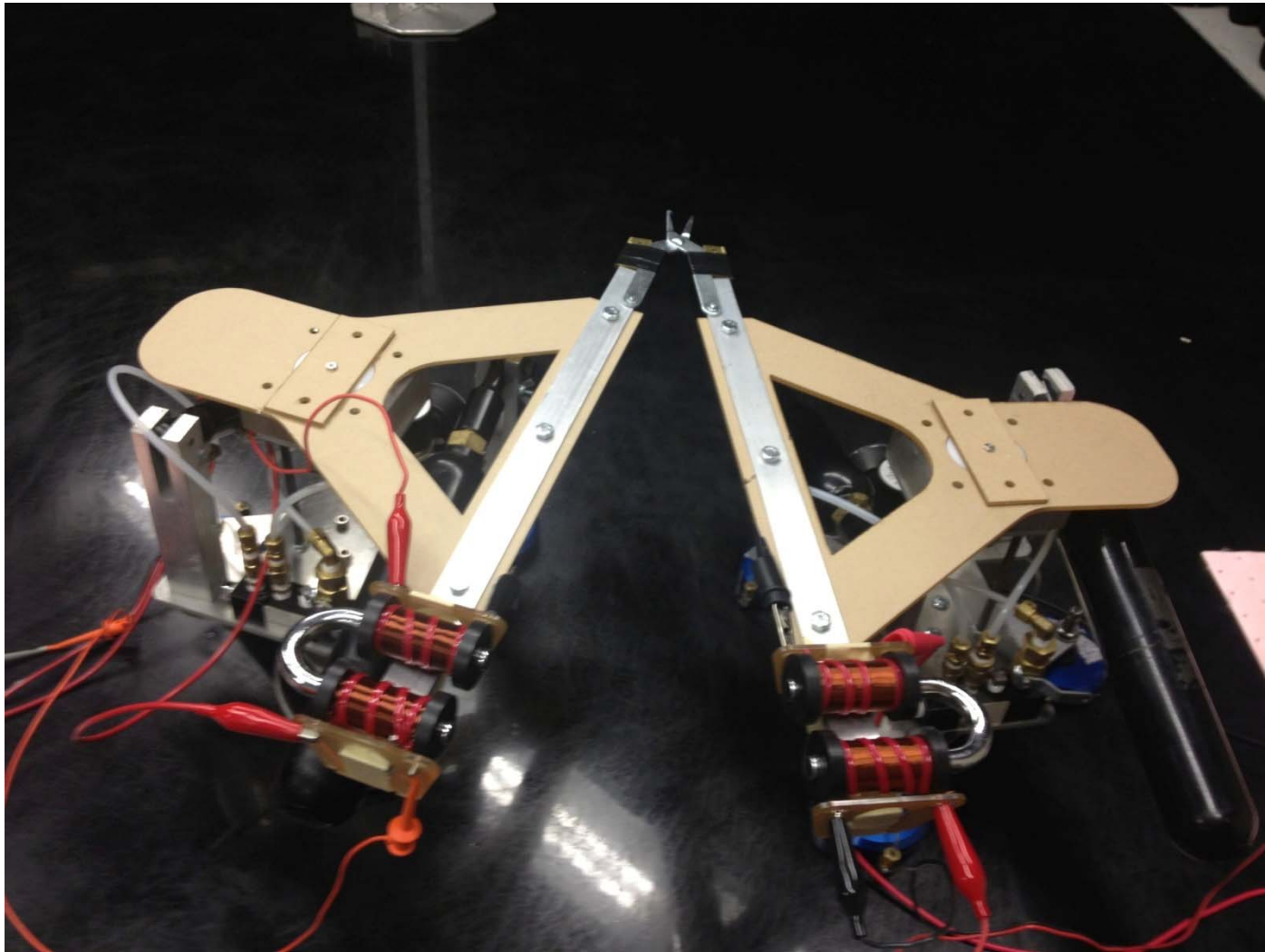
AFTER



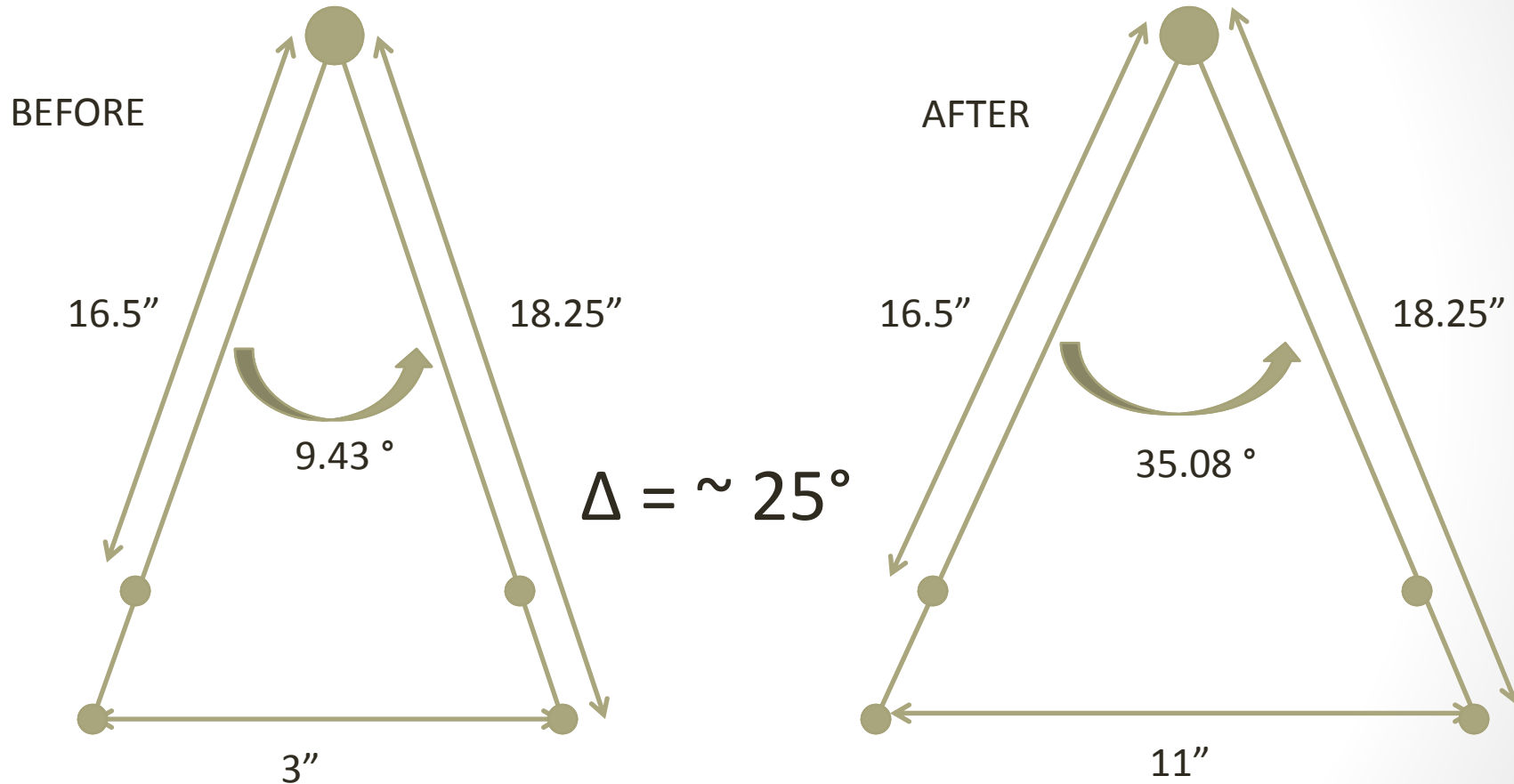
$$\Delta = \sim 3^\circ$$



Hinge with Iron Core Coils



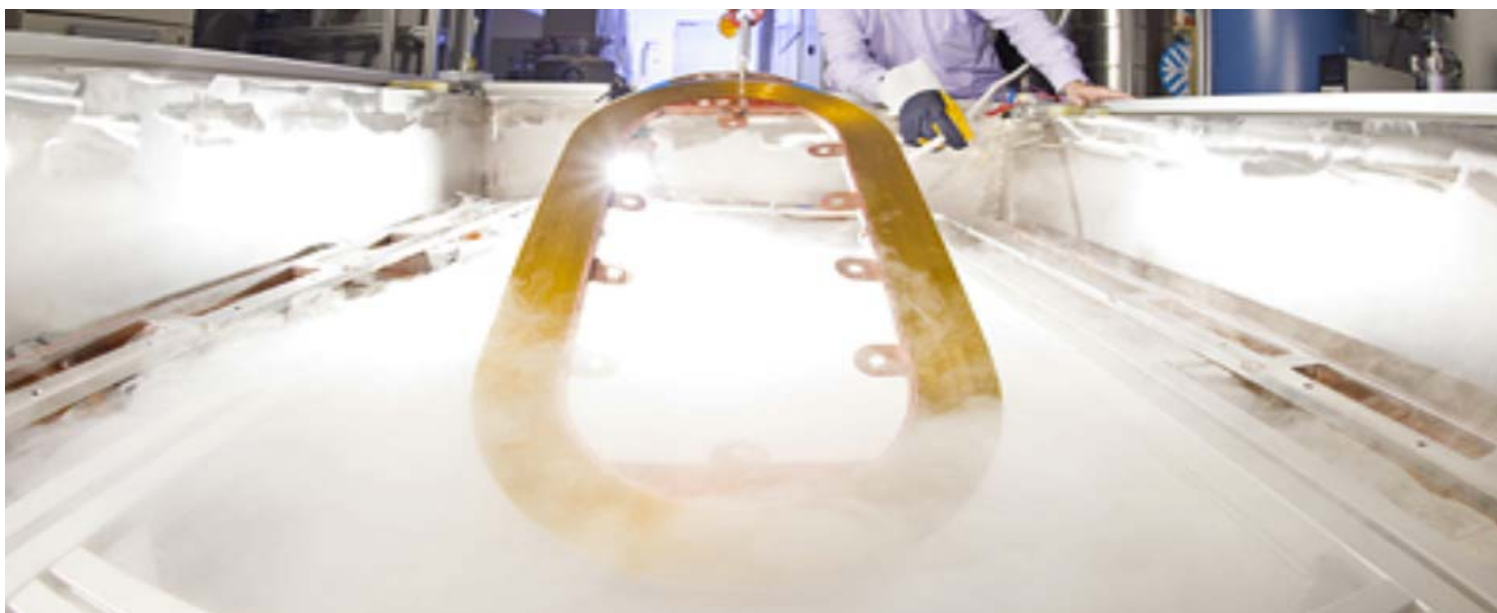
Iron Core Coil Results



- Able to achieve $\sim 25^\circ$ separation using iron-cored copper electromagnets on same carriages
- More powerful air coils needed for ground validation on air carriages
 - Considering using RINGS ground units for future validation activity

Copper Coil Drawbacks

- Energy lost to heat (melting glue in coil bobbin)
- The superconducting state will allow a much larger electric current than the ordinary copper coil creating intense magnetic fields
- The voltage was much higher in comparison to the current in the copper coils due to the resistance in the wire windings





Comparison to models?

- Nondimensionalized force and moment coefficients used to compare tether and hinge designs

$$\text{Force coefficient } \gamma = \frac{\mu I_{eff,1} I_{eff,2} \mathcal{J}^2}{4\pi m R} = 1.400 \text{ (heavy carriage) to } 2.837 \text{ (light)}$$

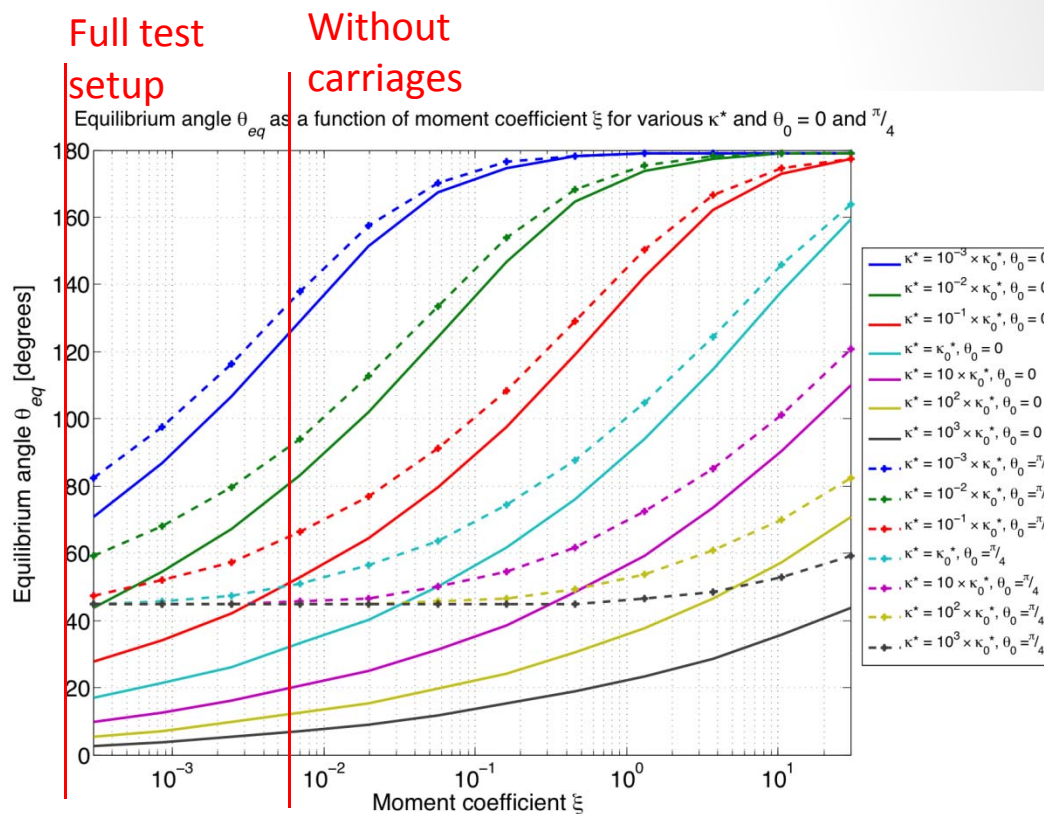
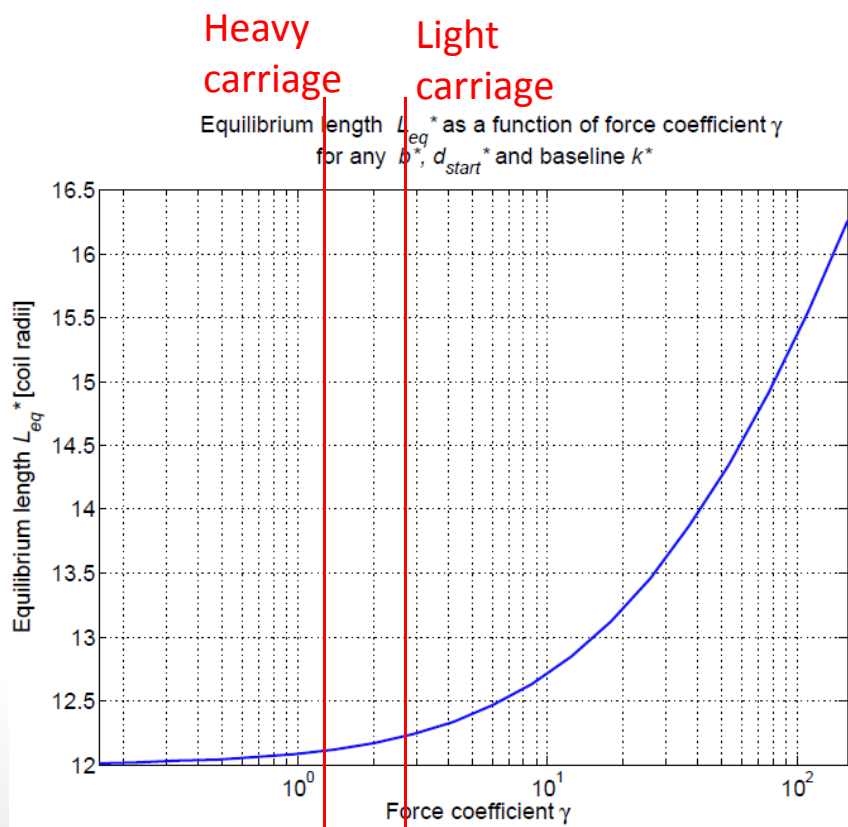
$$\text{Moment coeff } \xi = \frac{\mu I_{eff,1} I_{eff,2} \mathcal{J}^2 R}{4\pi I_{Hinge}} = 0.0049 \text{ (w/o carriages), } \sim 0.00032 \text{ (w/ carriages)}$$

- Neither test setup reflects all model assumptions so cannot yet validate
 - Need to fix balance/friction issue
 - Either remove spring from model or add spring to test setup
- Cu coils have very low γ and ξ compared to same sized HTS coils
 - 100x the current $\approx 10^4$ times bigger γ and ξ

Comparison to models?

Force coefficient $\gamma = \frac{\mu I_{eff,1} I_{eff,2} \mathcal{J}^2}{4\pi m R} = 1.400$ (heavy carriage) to 2.837 (light)

Moment coeff $\xi = \frac{\mu I_{eff,1} I_{eff,2} \mathcal{J}^2 R}{4\pi I_{Hinge}} = 0.0049$ (w/o carriages), ~ 0.00032 (w/ carriages)



Appendix 7: Introduction to Magnetic Boom Stability Analysis

Introduction to Magnetic Boom Stability Analysis

Gwendolyn V. Gettliffe [PhD dissertation to include full analysis]

Definitions of nomenclature to be used in this work

1. Types of equilibrium

There are two necessary conditions for equilibrium in a system: force balance and torque balance.¹ The vector sum of all external forces must be zero, as well as the sum of the torques from those forces around any axis. Linear and rotational momentum are conserved in the system, but they are not necessarily zero. All equilibria are either in *static* or *dynamic* equilibrium.

1.1. Static equilibrium

Static equilibrium is a subset of equilibria wherein the linear and rotational momentum of the system are zero and conserved in the reference frame being considered. In this thesis when we discuss equilibrium, we are primarily interested in static equilibrium, wherein the forces acting between coils balance and the center of mass of the system is not moving.

1.2. Dynamic equilibrium

Dynamic equilibrium refers to the subset of equilibria wherein the linear and rotational momentum of the system are constant but nonzero. We will not frequently discuss this type of equilibrium, except to say that dynamically neutral equilibrium refers to a system that has been set in motion but experiences no external forces to cease that motion.

2. Static stability of equilibrium

The first derivative of potential energy of a system in equilibrium is zero, but the second derivative determines the stability of the equilibrium, or what the system will initially do when it is perturbed from equilibrium.

2.1. Statically stable equilibrium

Statically stable equilibrium occurs when the second derivative of potential energy is positive, meaning that the system is at a local minimum in potential energy and any perturbation away from equilibrium will result in the system tending to return to that state. In systems with multiple degrees of freedom, they can be stable in one degree but unstable in others. We only refer to multidimensional systems as stable when all degrees of freedom are stable.

2.2. Statically unstable equilibrium

Statically unstable equilibrium occurs when the second derivative of potential energy is negative, meaning that the system is at a local maximum in potential energy and that any perturbation away from equilibrium will result in further divergence of the system from that equilibrium.

2.3. Statically neutral equilibrium

Statically neutral equilibrium occurs when the second derivative of potential energy is zero. In neutral equilibrium, a small perturbation doesn't tend to diverge from or converge back to the equilibrium position; the system tends to stay loosely perturbed. Statically neutral equilibrium is something we want to avoid in the systems explored in this thesis, either via model reduction to eliminate degrees of freedom with neutral equilibrium, or by constraining the system in those directions.

¹ Synge, J. L., Griffith, B.A., *Principles of Mechanics*. McGraw Hill, 1949.

3. Dynamic stability

While static stability describes the initial response of a system to a perturbation from a position of equilibrium, dynamic stability describes the response of a system to oscillations resultant from the perturbation. A system can be statically stable but dynamically unstable, for instance, if it moves back towards equilibrium from a perturbation but continues to oscillate with growing amplitude. ²

3.1. Dynamically stable

A dynamically stable system has oscillations around a static equilibrium point that decrease in amplitude over time due to damping until the system is back at its equilibrium position.

3.2. Dynamically unstable

A dynamically unstable system has oscillations around a static equilibrium point that increase in amplitude over time.

3.3. Dynamically neutrally stable

A dynamically neutrally stable system has oscillations around a static equilibrium point that neither increase nor decrease in amplitude over time. Because one of the assumptions we are making in this work is that there is no energy dissipation in the system (e.g. damping in tethers, eddy currents), if the system starts with acceleration due to a force or torque imbalance at $t=0$, the coils will oscillate without converging. They can, however, diverge. Therefore, we consider that dynamically neutral stability is a desirable form of stability and what we hope to achieve in our dynamic simulations.

² Macdonald, Sandy A. F.; Pepler, William N (2010). *From the Ground Up* (28 ed.). Ottawa, ON, Canada: Aviation Publishers Co. Ltd.

Force balances in 1 DoF spring-coil systems

In order to explore static stability in a system, we first locate equilibrium points in that system. We do that by finding where the summed vector forces (and torques) in the system equal zero, starting with simple, single-degree-of-freedom coil-spring systems. In this section, we discuss force balance with a single translational degree of freedom so that we can easily visualize the translational equilibrium points on a two-dimensional plot.

1. Force balance in a two-coil, 1 DoF (per coil) system

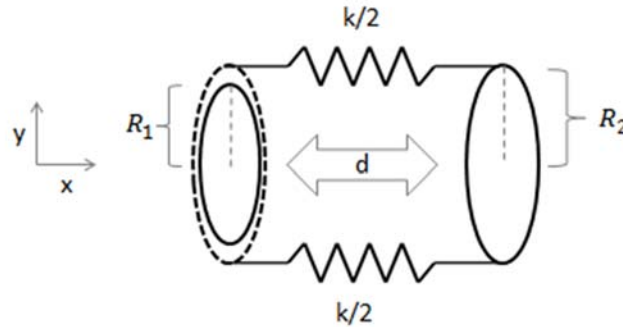


Figure 1: Two coils connected by two springs, allowed to move along the x axis

Figure 1 defines the variables and axes used in the translational one-degree-of-freedom model. Coil 1 is the left coil and coil 2 is the right coil.

Model assumptions:

- Coils are modeled as parallel and attached at their top and bottom along the y axis by two identical springs (same spring constant $k/2$) with a natural nondimensional length of $d = 2$ coil radii (such that compressive force can be provided, unlike in a tether system). Coil radii are based off of coil 1's radius.
- Coil 1 (left) has radius of 1m, coil 2 (right) has radius of 1.2m (chosen to allow coils to be coplanar at $x=0$)
- Springs are parallel to the x axis (which means they are attached to a non-electromagnetic frame of radius 1.2m around coil 1) and are modelled as being infinitely stretchable or compressible.
- The coils have the same current (80A) and number of turns (100).

1.1. Forces

The two forces acting in the system, both internal, are the electromagnetic force between the coils and the spring force between the coils. At the natural length apart, or $d = 2$ coil radii, the spring force is zero, and this is an equilibrium position if the electromagnets are not on. The spring and electromagnetic force on one coil are equal and opposite the respective forces on the other coil, so in this section, we examine the forces on coil 2 versus separation distance d . The forces all work along the x axis because the coil normal vectors and the springs stay parallel to each other and the x axis.

The spring force on coil 2 in this system is linear with a constant spring constant k , given by

$$\vec{F}_{s,2} = -k[d - 2] \hat{i}$$

where a negative $\vec{F}_{s,2}$ acts to pull the coils together and a positive $\vec{F}_{s,2}$ acts to push them apart. \hat{i} is the unit vector in the direction of the positive x axis.

There are two models for electromagnetic force between two current carrying coils. One model is the dipole approximation, which models the coils as magnetic dipoles, like bar magnets. The dipole approximation is only valid at significant distances apart wherein the coils appear much like points rather than rings (roughly 5% error in magnetic field strength from the dipole approximation at 10 coil radii apart³). The farther apart the coils are, the more accurate this

³ Gettliffe SM Thesis

assumption is, the error decreasing to zero as the distance between the coils approaches infinity. For two identical, coaxially-aligned coils with planes parallel to one another, as in this example, the dipole electromagnetic force equation for the force on coil 2 from coil 1 is:

$$\overrightarrow{F_{EM,2,dip}} = \frac{3\mu A_1 A_2 I_{eff,1} I_{eff,2}}{2\pi d^4} \hat{i}$$

where μ is the magnetic constant ($4\pi \times 10^{-7} N/A^2$), A_1 and A_2 are the areas of coil 1 and coil 2 respectively, and $I_{eff,1}$ and $I_{eff,2}$ are the effective currents in each coil, or the current I multiplied by the number of turns N (in this case, $I_{eff,1} = I_{eff,2}$). The above formula is multiplied by -1 if the currents are in the same direction, indicating an attractive force between the coils. For ease of expression, we combine the constants in this equation into

$$C_0 = \frac{3\mu A_1 A_2 I_{eff,1} I_{eff,2}}{2\pi}$$

such that

$$\overrightarrow{F_{EM,2,dip}} = \frac{C_0}{d^4} \hat{i}$$

The more precise calculation of electromagnetic force is via the combination of the Biot-Savart law and the Laplace force law, which respectively give the magnetic field amplitude at any point in space and the electromagnetic force imparted by the interaction of a current-carrying wire and a magnetic field. The Biot-Savart law gives the summed magnetic field strength at a given point a vector distance \vec{r}_{12} from each segment $d\vec{l}_1$ of current-carrying wire as follows:

$$\vec{B}_1 = \frac{\mu}{4\pi} \int_{coil\ 1} \frac{I_{eff,1} d\vec{l}_1 \times \vec{r}_{12}}{|\vec{r}_{12}|^3}$$

The Laplace force law gives the force \vec{F}_{12} on a segment of wire $d\vec{l}_2$ as a result of the magnetic field vector \vec{B}_1 at that point

$$\overrightarrow{F_{EM,2,BS}} = I_{eff,2} \int_{wire} d\vec{l}_2 \times \vec{B}_1$$

where $I_{eff,2}$ is the current through $d\vec{l}_2$ multiplied by the number of turns in coil 2.

Together, these laws give us the more precise formula for electromagnetic force from coil 1 on coil 2:

$$\vec{F}_{EM,2,BS} = \frac{\mu I_{eff,1} I_{eff,2}}{4\pi} \oint_{coil\ 2} d\vec{l}_2 \times \oint_{coil\ 1} \frac{d\vec{l}_1 \times \vec{r}_{12}}{|\vec{r}_{12}|^3}$$

It should be noted that this formulation models the system as one loop of wire through which the effective current is running; a more precise formulation would account for the individual turns of wire in the coil and their spatial locations.

Figure 2 shows how the dipole approximation of electromagnetic force converges with the more precise Biot-Savart calculation as the distance between the coils increase (using the same coil parameters and assumptions listed above). The most significant observation is that the dipole approximation massively overestimates the magnetic field when the coils are close together. The bar-magnet-like behaviour of the dipole model near $d=0$ is evident as the magnitude of the electromagnetic force sharply increases, as it does when holding two bar magnets together.

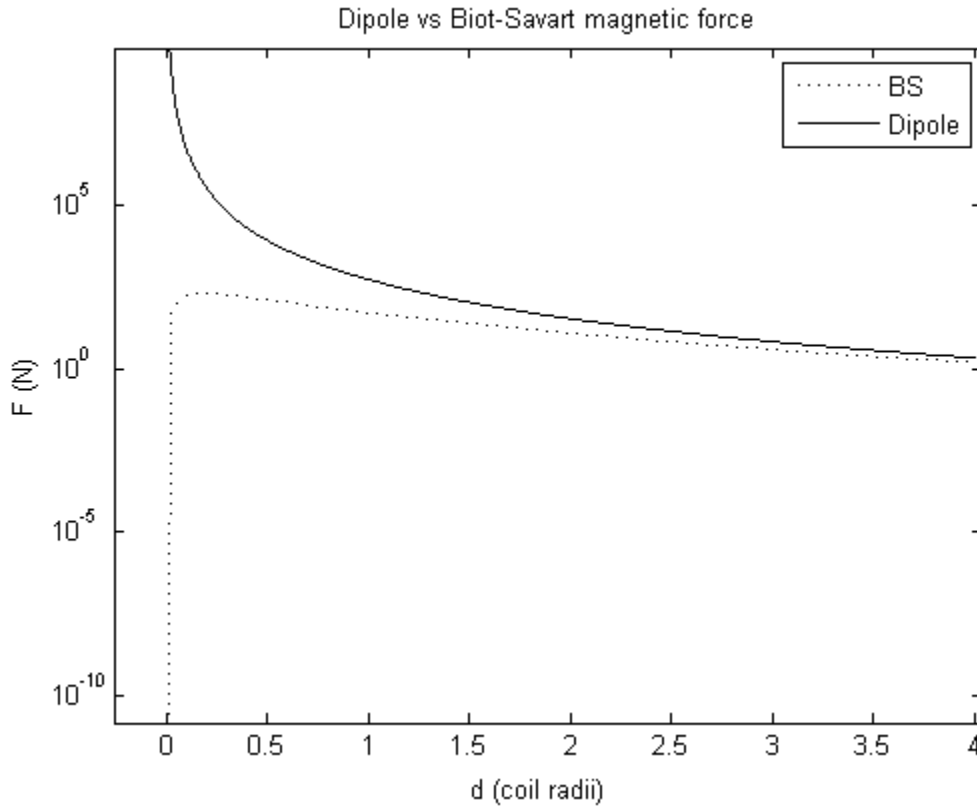


Figure 2: Comparison of Biot-Savart and dipole approximation forces versus distance between the coils

1.2. Force balance

Now that we've established what the forces in the system are, we look for where

$$\sum F = 0$$

on each coil, or in the case of our focusing on coil 2,

$$\vec{F}_{EM,2} + \vec{F}_{S,2} = 0$$

The distances apart where the forces balance will be equilibrium points. At these points,

$$|\vec{F}_{EM,2}| = |\vec{F}_{S,2}|$$

or, when using the dipole model,

$$\left| \frac{C_0}{d^4} \right| = |-k[d - 2]|$$

Because of the large range in magnitude of the electromagnetic forces in Figure 2, we plot the electromagnetic and spring forces on a semi-logarithmic plot. For this reason, the absolute value of the forces will be plotted, since negative values can't be plotted on a logarithmic axis. This also provides us the simple ability to look for where the spring forces and electromagnetic forces cross to find equilibrium points.

1.2.1. Attractive electromagnetic force

Figure 3 shows the base 10 logarithm of the magnitude of the two electromagnetic force models (Biot-Savart, or BS, and dipole) as well as six different spring forces using different constants k (represented in the legend as a ratio of magnetic coefficient C_0 , constant in this plot, over spring constant k). The base 10 logarithm is taken to condense the scale on the force axis more significantly. The coil parameters and assumptions used are the same as those given above.

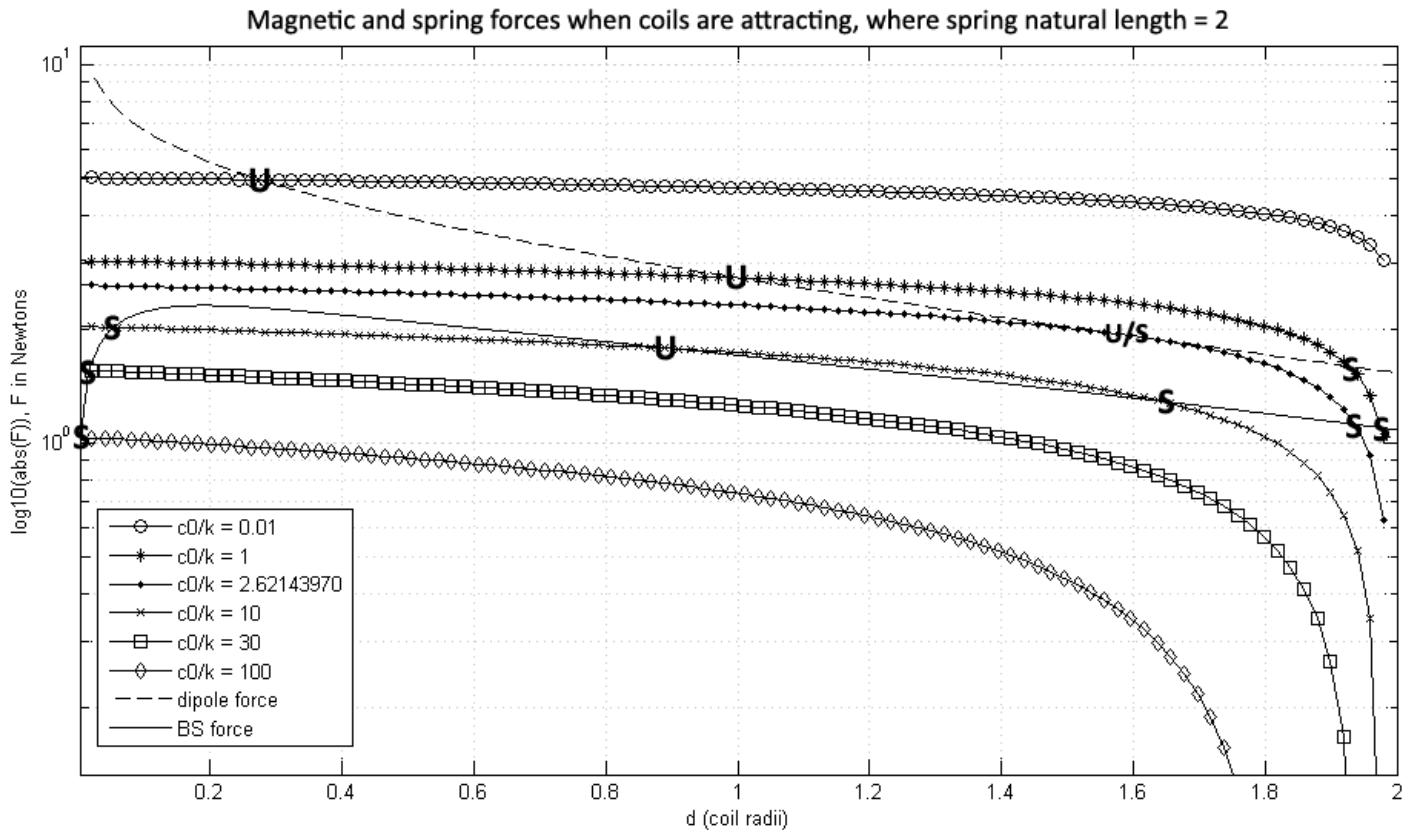


Figure 3: Electromagnetic and spring forces between two attracting coils, from $d=0$ up to the natural length of the spring, $d = 2$. C_0/k is in units of m^5 . The U's represent statically unstable equilibria, the S's statically stable equilibria, and the U/S represents layered stable and unstable equilibria.

The U and S markings in Figure 3 are located at equilibrium points where one of the spring forces balances with one of the electromagnetic forces and cross each other and signify whether or not that equilibrium is statically stable or unstable. There are several regimes in this plot, and we'll start with the dipole model equilibrium points.

Dipole model equilibrium points

We see that only three of the six spring forces intersect with the dipole (dotted) line, the three that have the largest spring constants k .

- The three spring forces with the lower spring constants *do not intersect* with the dipole force at all, indicating that the dipole force attracting the two coils always dominates the spring force acting to push the coils apart. There are no equilibria with the dipole model for the less stiff springs.
- Within the three higher spring constant forces, we see two that have two equilibrium points (the two highest k values) and one that just barely contacts the dipole force for a single equilibrium point.
 - The two spring forces with two equilibria each have one each near the natural length of the spring (the second equilibrium for $c_0/k = 0.01$ is not visible in this plot but does occur as the spring force goes to zero as d approaches 2), which makes physical sense considering that these spring forces have very stiff springs and the electromagnetic force would only be able to compress the springs slightly. These equilibrium points close to $d=2$ are *statically stable*, which can be seen by looking at which force dominates on either side of them: to the right, the magnetic, compressive force dominates, pushing the coils back towards the equilibrium point, and on the left, the spring expansion force dominates, pushing the coils back towards the equilibrium point as well.

The second intersection for each is closer to $d=0$ as the spring stiffness increases, but we note that there is a second intersection only because the dipole model starts to overestimate the electromagnetic force more significantly closer to $d=0$. These equilibria are *statically unstable*, since to the left, the electromagnetic force dominates and acts to pull the coils together, away from that equilibrium point, and to the right, the spring force dominates and acts to push the coils back out, again away from that equilibrium point.

- The spring force with only one equilibrium point is an interesting case, because the magnetic force dominates on either side of the equilibrium point, on one side pulling the coils back to the equilibrium point and on the other side pulling the coils together away from the equilibrium point. It may be more appropriate to consider this as two collocated equilibria (because for spring constants any greater than the one in this plot, there are two very close together equilibria): *one stable* (the one on the right) and *one unstable* (the one on the left), as discussed in the previous two spring forces.

The secondary, statically unstable equilibria are the ones that are nonintuitive in this system, and we will examine in the next section how using the more precise Biot-Savart calculation affects the appearance of these equilibria.

Biot-Savart model equilibrium points

Because the dipole model overestimates the magnetic force between the coils, we see a smaller force here in general, the three stiffer springs having *statically stable* intersections with the Biot-Savart (BS) force line close to $d=2$ (the stiffer the spring, the closer to $d=2$ the equilibrium point is) as they did with the dipole force line. The three less stiff springs become the interesting springs in this case.

- All three springs have *statically stable* equilibria close to $d=0$. This makes intuitive sense if you consider that these are very elastic springs that exert very little force when compressed or stretched and that the Biot-Savart force drops off as $d \rightarrow 0$.
- The most stiff of these three less stiff springs actually has three equilibria: the *statically stable* one close to $d=0$, a *statically unstable* one near $d=0.9$, and another *statically stable* one near $d=1.7$.
- A quick examination of the shape of the BS force curve and the shape of the spring curves shows that, like the spring curve that barely touched the dipole force curve, attempting to find a spring force with two equilibria using the BS model would result in the same “partially stable” equilibrium, which is essentially two separate equilibria. Because of this, all spring forces would either have one or three equilibria with the BS force model, depending on their stiffness.

1.2.2. Repulsive electromagnetic force

When the currents run through the coils in opposite directions from one another, the electromagnetic force between the coils becomes repulsive, acting to expand the distance between the coils beyond the natural length of $d=2$. Figure 4 shows the magnitudes of the magnetic and spring forces and their intersecting equilibria when the coils are repelling, rather than attracting as they are in Figure 3. Figure 4's x axis shows distances greater than the natural spring length of 2, since the electromagnetic force acts to force the coils apart from the natural length at which it rests when there is no current running through the coils.

Magnetic and spring forces when coils are repelling, where spring natural length = 2

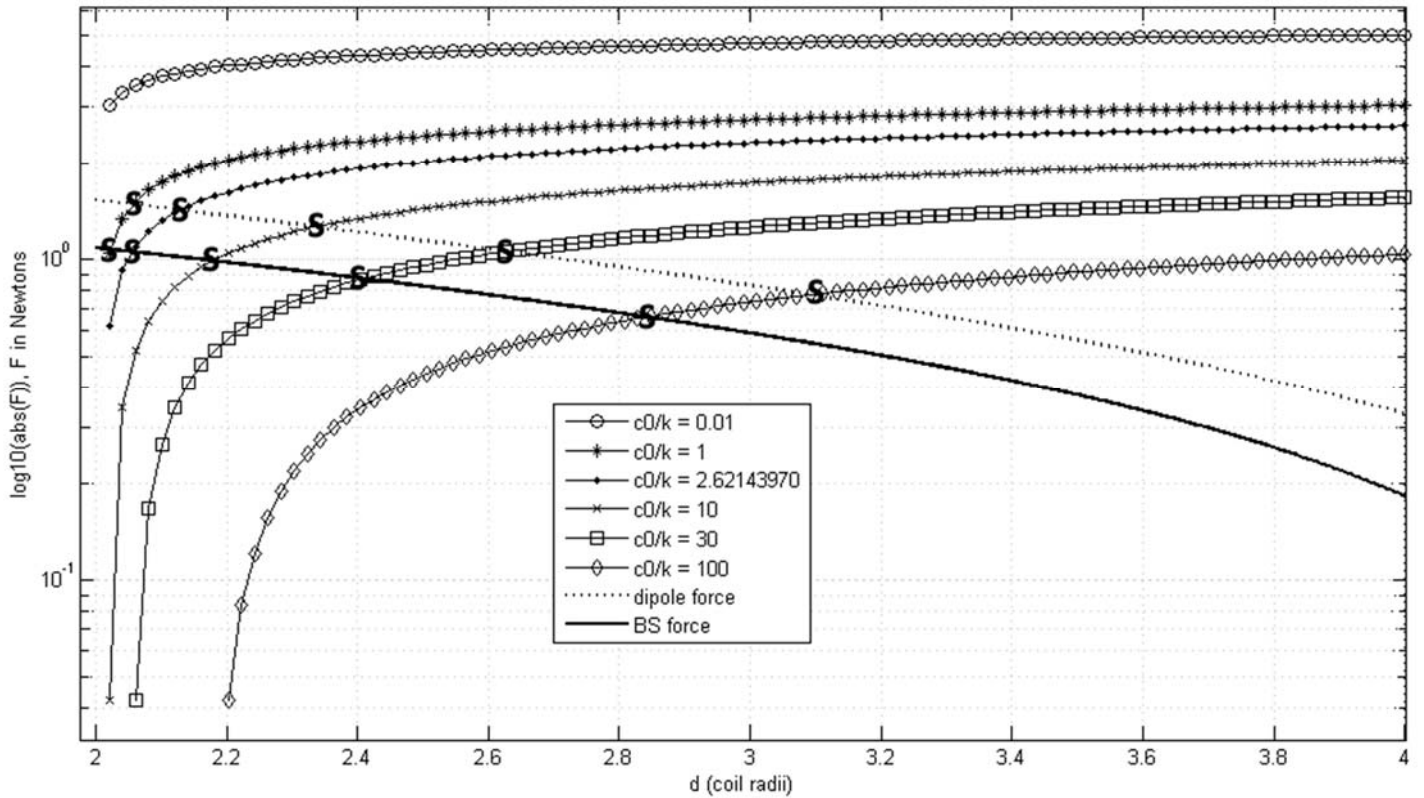


Figure 4: Electromagnetic and spring forces between two repelling coils, from $d=0$ up to the natural length of the spring, $d = 2$. C_0/k is in units of m^5 . The U's represent statically unstable equilibria, the S's statically stable equilibria, and the U/S represents layered stable and unstable equilibria.

There are a few significant differences between Figure 4 and Figure 3. First, because the axis spans $d=2$ to $d=4$, the two electromagnetic force models are not significantly different from one another in anything but magnitude. Second, all of the equilibria/intersections depicted are statically stable. Finally, each spring force plotted only has one equilibrium point with each electromagnetic model, those with the dipole model appearing at larger separations because the dipole model overestimates the magnetic field strength.

1.3. Dynamic stability and model reduction

Locating the equilibrium points in the system allows us to determine the static stability of those points, but more work is required to determine the dynamic stability. We must first write the equations of motion for the system.

Let the coils be modelled as two masses, m_1 and m_2 , for coil 1 and 2 respectively, the system viewed side-on in Figure 5.

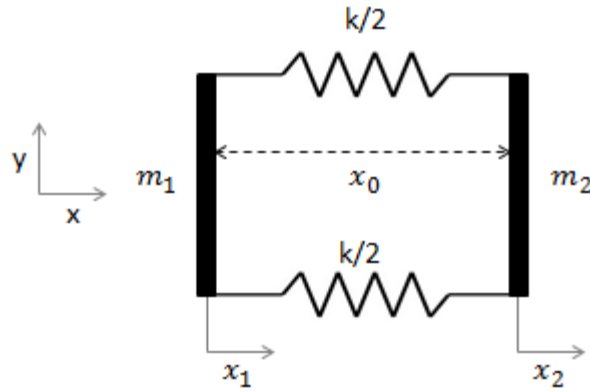


Figure 5: Two coil, single translational degree-of-freedom system

As in the static system, we have two forces working on each mass, the spring force and the electromagnetic force, which we know act both equal and opposite on one coil versus the other. x_1 and x_2 describe the amount each of the coils moves from its starting position of x_0 apart.

Attractive electromagnetic force model reduction

If we model the system in Figure 5 with an attractive electromagnetic force, assuming dipole force in order to have an analytical formulation, then

$$\vec{F}_{EM,1,attr} = \frac{C_0}{[x_0 + x_2 - x_1]^4} \hat{i}$$

$$\vec{F}_{EM,2,attr} = \frac{-C_0}{[x_0 + x_2 - x_1]^4} \hat{i}$$

$$\vec{F}_{S,1} = k[x_2 - x_1] \hat{i}$$

$$\vec{F}_{S,2} = -k[x_2 - x_1] \hat{i}$$

Because we have two masses allowed to move along the x axis, we have two equations of motion. The equations of motion for each of the masses (in the direction of the x axis) are

$$m_1 \ddot{x}_1 = k[x_2 - x_1] + \frac{C_0}{[x_0 + x_2 - x_1]^4}$$

$$m_2 \ddot{x}_2 = -k[x_2 - x_1] - \frac{C_0}{[x_0 + x_2 - x_1]^4}$$

However, since the system starts at a rest and forces are all relative and internal to the system, meaning that the center of mass of the system will remain fixed in inertial space, we would like to reduce this system to a single, relative equation of motion by discarding the trivial absolute degree of freedom. One way to do this is to define two new variables in terms of x_1 and x_2 to represent the relative and absolute variables of interest along the x axis.

$$\bar{x} = [x_1 + x_2]/2$$

$$\Delta x = x_2 - x_1$$

\bar{x} is a variable describing the amount that the linear center of the two coil system has moved along the x axis. In a system where the coils have the same radius and number of turns (and thus the same mass), \bar{x} is the amount that the center of mass of the system has moved along the x axis. \bar{x} is thus a variable that describes absolute motion of the system in inertial space.

Δx is a variable describing the change in the distance between the coils. When the coils are x_0 apart, $\Delta x = 0$. If Δx is positive, then the distance between the coils has increased and the springs are exerting a force to pull the coils together. If Δx is negative, then the distance has decreased and the springs are exerting a force to push the coils apart. Δx is thus a variable that describes the relative motion of the coils.

Let's first assume that $m_1 = m_2$.

Solving the above system of equations for x_1 and x_2 in terms of Δx and \bar{x} gives us

$$x_1 = \bar{x} - \frac{\Delta x}{2}$$

$$x_2 = \bar{x} + \frac{\Delta x}{2}$$

Inserting these definitions back into the original equations of motion, we get

$$m_1 \left[\ddot{\bar{x}} - \frac{\ddot{\Delta x}}{2} \right] = k\Delta x + \frac{C_0}{[x_0 + \Delta x]^4}$$

$$m_2 \left[\ddot{\bar{x}} + \frac{\ddot{\Delta x}}{2} \right] = -k\Delta x - \frac{C_0}{[x_0 + \Delta x]^4}$$

Adding and subtracting these equations, we are left with

$$2m\ddot{\bar{x}} = 0 \text{ (trivial)}$$

And

$$-m\ddot{\Delta x} = 2k\Delta x + \frac{2C_0}{[x_0 + \Delta x]^4} \text{ (nontrivial)}$$

The first equation expresses that there is no acceleration of the center of mass of the system and therefore no force acting to accelerate it (as we expected in a system with only internal forces), and so we are left with a single equation of motion regarding the relative motion of the coils.

It should be noted that the definitions of Δx and \bar{x} are easier to surmise in a symmetrical single degree of freedom system such as the one above. If we use the previous section's coil parameters rather than making the coils identical, then $R_2 = 1.2R_1$ and $m_2 = 1.2m_1$ and summing the equations of motion gives us the following instead of a trivial equation.

$$[m_1 + 1.2m_1]\ddot{\bar{x}} + \frac{\ddot{\Delta x}}{2}[1.2m_1 - m_1] = 0$$

$$2.2m_1\ddot{\bar{x}} + \ddot{\Delta x}[0.4m_1] = 0$$

$$5.5\ddot{\bar{x}} + \ddot{\Delta x} = 0 \text{ (nontrivial)}$$

This may be remedied by better selection of our Δx and \bar{x} definitions.

Repulsive electromagnetic force model reduction

Assuming coils of the same mass, we get similar equation of motion by following the process above, but with the sign of the electromagnetic force flipped in the nontrivial equation:

$$2m\ddot{x} = 0 \text{ (trivial)}$$

And

$$-m\ddot{\Delta x} = 2k\Delta x - \frac{2C_0}{[x_0 + \Delta x]^4} \text{ (nontrivial)}$$

Appendix 8: Thermal Enclosure Design and Testing Report

Final Report
for
NIAC NNX12AQ59G

Prepared by: Allison Porter

Inquiries to:
Raymond Sedwick
University of Maryland
3146 Glenn L. Martin Hall
College Park, MD 20742

Fax: 301-314-9001
Office: 301-405-0111
Email: sedwick@umd.edu

List of Figures

Figure 2.1 Axial spring force testing configuration.....	4
Figure 2.2 Enclosure deployment force at different rates of axial motion.....	5
Figure 2.3 Deployment force test a) at the start of compression, b) near full compression.....	6
Figure 2.4 Schematic showing spring-damper acting in parallel.....	6
Figure 2.5 Damping coefficient for straight segment enclosure.....	8
Figure 2.6 HTS superconducting wire a) Generation 1 made by American Superconductor, b) Generation 2 made by SuperPower.....	9
Figure 2.7 Proof of concept of ribbon wire when a) stowed and b) deployed.....	10
Figure 2.8 Structure of full lab-scale enclosure.....	11
Figure 3.1 Fraction of heat flux due to radiation and conduction between cold wall at 123 K and warm wall of 273 K [3].....	14
Figure 3.2 Total heat flux for a) fixed number of layers, b) fixed thickness [5].....	16
Figure 3.4 Overlap configurations for MLI [11].....	18
Figure 3.5 Mass and input power for recent cryocoolers compared to trend by Ladner [21].....	22
Figure 3.6 Orientation of torus in orbit around Earth and Sun (not to scale).....	24
Figure 3.7 View factor numbering designation where surface 1 is a sphere, surface 2 is a flat disc (not including surface 3 as a hole).....	25
Figure 3.8 Energy balance at outer surface of thermal enclosure where a) is the Sun-facing surface and b) is the Earth-facing surface.....	28
Figure 3.9 Cross-section of enclosure minor diameter.....	28
Figure 3.10 Thermal loading on the vapor core for varying torus sizes for fixed MLI thickness of 2 cm.....	30
Figure 3.11 Thermal loading for varying insulation thickness with a vapor core radius of 10 cm 31	
Figure 3.12 Close-up of toroidal enclosure segment with a) inner core, b) fiberglass sleeve over core, c) thermal blanket.....	33
Figure 3.13 Conceptual cross-section showing stack of MLI.....	34
Figure 3.14 a) Deployed straight thermal enclosure, b) partially compressed.....	35
Figure 3.15 Initial concept for accordion-inspired MLI folding.....	36
Figure 3.16 a) Butting of MLI panel short edges.....	36
Figure 3.17 Vapor containment end caps and closed cell foam.....	37
Figure 3.18 End caps with ends of plastic and fiberglass secured.....	38
Figure 3.19 Vacuum chamber used for thermal testing.....	39
Figure 3.20 Chamber port configuration, view from above.....	40
Figure 3.21 Thermocouple locations around MLI blanket layers.....	41
Figure 3.22 Lab-scale thermal enclosure sitting in open vacuum chamber.....	41
Figure 3.23 Effective thermal conductivity dependence on temperature using empirical function given by Hoffman [29].....	48
Figure 3.24 Comparison of heat transfer to thermal conductivity during Test Run #18.....	49
Figure 4.1 Nitrogen temperature at different circumferential locations for Test Run #19.....	50
Figure 4.2 Proof of concept prototype for alternating flow direction testing.....	51
Figure 4.3 Schematic of directional flow control scheme.....	52
Figure 4.4 Thermal test for proof of concept of alternating flow direction.....	53

List of Tables

Table 2.1 Summary of spring specifications.....	2
Table 2.2 Summary of deployment force for straight enclosure segment	7
Table 3.1 Summary of cryocooler state of the art suitable for HTS applications.....	21
Table 3.2 Summary of thermal loading variables	29
Table 3.3 Dimensions of torus for thermal and deployment testing.....	38
Table 3.4 Summary of MLI Effective Thermal Conductivity	46

Table of Contents

1	Summary	1
2	Deployment of Inflatable Torus Design	2
2.1	Deployment of straight section assembly.....	2
2.1.1	Test article fabrication.....	2
2.1.2	Test setup	3
2.1.3	Results and discussion.....	4
2.2	Deployment of lab-scale toroidal thermal enclosure.....	8
3	Vapor Cooled Thermal Design	12
3.1	Methods of thermal management for cryogenic systems	12
3.1.1	Heat pipe	12
3.1.2	Multilayer insulation blanket	13
3.1.3	Cryocoolers	19
3.2	Theoretical thermal loads	23
3.2.1	Governing heat transfer equations.....	23
3.2.2	Analytical model using only MLI.....	27
3.3	Laboratory thermal testing	31
3.3.1	Fabrication of test article.....	32
3.3.2	Equipment setup in laboratory	38
3.3.3	Testing Procedure.....	42
3.3.4	Results and discussion.....	43
4	Integration of deployment and thermal design	50
4.1	Integrated design based on results.....	50
4.2	Future considerations for fully integrated system	53
5	Conclusions	55
	Appendix A: Thermal Data for Full Torus Lab Test	56
	References	69

1 Summary

This report covers an investigation of delivering a thermal enclosure capable of deploying in space for the operation of a large superconducting coil. The investigation was broken up into two primary components. The first part was an examination of the structure and deployment method. The second part was an examination of the thermal performance for evaluating the ability to maintain a superconducting coil at temperatures below the critical temperature of the material. After investigating different thermal management technologies, the use of a cryocooler to chill liquid nitrogen circulated as a vapor in a thin walled structure was chosen. The thin walled structure would house the superconducting coil in the core and be thermally insulated from incident radiation using a multi-layer insulation blanket.

For each portion, a combination of an analytical approach and experimental results were found. Multiple test articles including a straight cylindrical segment for deployment force testing and toroids of varying major radii for development of the deployment concept and thermal testing. The majority of the thermal testing involved the cooling of a torus with a major diameter of 1.85 m in a custom vacuum chamber.

2 Deployment of Inflatable Torus Design

In order to deliver a large diameter superconducting coil contained within an enclosure for structural support and thermal management, the enclosure must be capable of being stowed inside a launch vehicle fairing. For many applications, the desired coil diameter would far exceed the dimensions inside the envelope payload of the fairing. The enclosure and the coil need to be structurally integrated in such a way to permit a large ratio of the deployed to stowed size.

2.1 Deployment of straight section assembly

Due to the size and shape of the full toroidal enclosure used for thermal testing (discussed in Section 3.3), a segment identical in composition was fabricated for preliminary deployment force testing. The design consisted of a single spring. The same spring was also used in the full torus, laboratory test article.

2.1.1 Test article fabrication

The main structural component was the spring custom fabricated by Murphy & Read Spring Mfg. with the following specifications listed in Table 2.1. The folding of the plastic double layer that acted as primary containment of the nitrogen vapor in the core coupled with the thermal insulation blankets also supplied axial force during deployment.

Table 2.1 Summary of spring specifications

Wire material	Carbon steel (music wire)
Wire diameter	2.997 mm (0.1180 in.)
Outer coil diameter	10.46 cm (4.120 in.)
Length	75.52 cm (2.478 ft)
Total coil turns	20
Active coil turns	18
Mass (Weight)	0.3542 kg (0.780961 lbf)

Spring constant	0.35 N/cm (0.2 lb/in.)
-----------------	------------------------

The ends of the spring were secured using zip ties to PVC rings of similar diameter to match the PVC joints used to join segments in the full enclosure. This also provided a rigid structure and flat surface for adhering the thermal insulation blanket pieces. Four identical long panels of insulation were applied due to the thermal design discussed in detail in Section 3.3. Only the short edges of the blanket pieces were attached to the PVC cuffs, allowing the long edges to be free for bowing radially outward when compressed into the stowed configuration. An image of the test article can be seen in Figure 2.3.

2.1.2 Test setup

The axial force was measured using the Tinius Olsen H25KT Universal Testing Machine. The force was measured by a load cell that moved at a constant rate during the course of the test. The test article was fixed to 1-inch thick aluminum base plates at the ends using L-brackets attached to the outer surface the PVC cuffs. The plates were attached to the testing machine base and load cell using large machine screws. The testing configuration is shown in Figure 2.1.

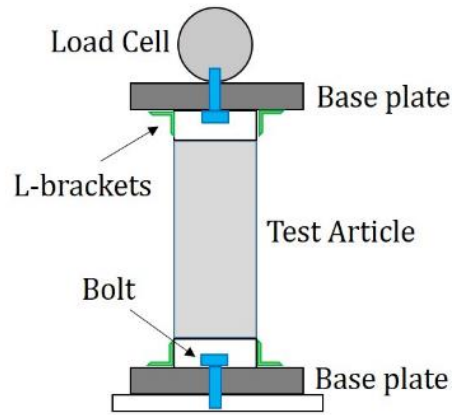


Figure 2.1 Axial spring force testing configuration

Three rates of motion were observed: 100 mm/minute, 150 mm/minute, and 200 mm/minute. The initial position of the load cell held the assembly close to the deployed, zero-forces state before compressing the spring the minimum allowable length. The position of maximum compression was held for 10 seconds before the load cell retracted and measured the deployment force while moving at the same rate as the compression.

2.1.3 Results and discussion

The test results are shown in Figure 2.2. The force was negative when the load cell moved the beyond the zero-force point of the spring deformation. The stair-stepping of the data was due to the resolution of the universal testing machine.

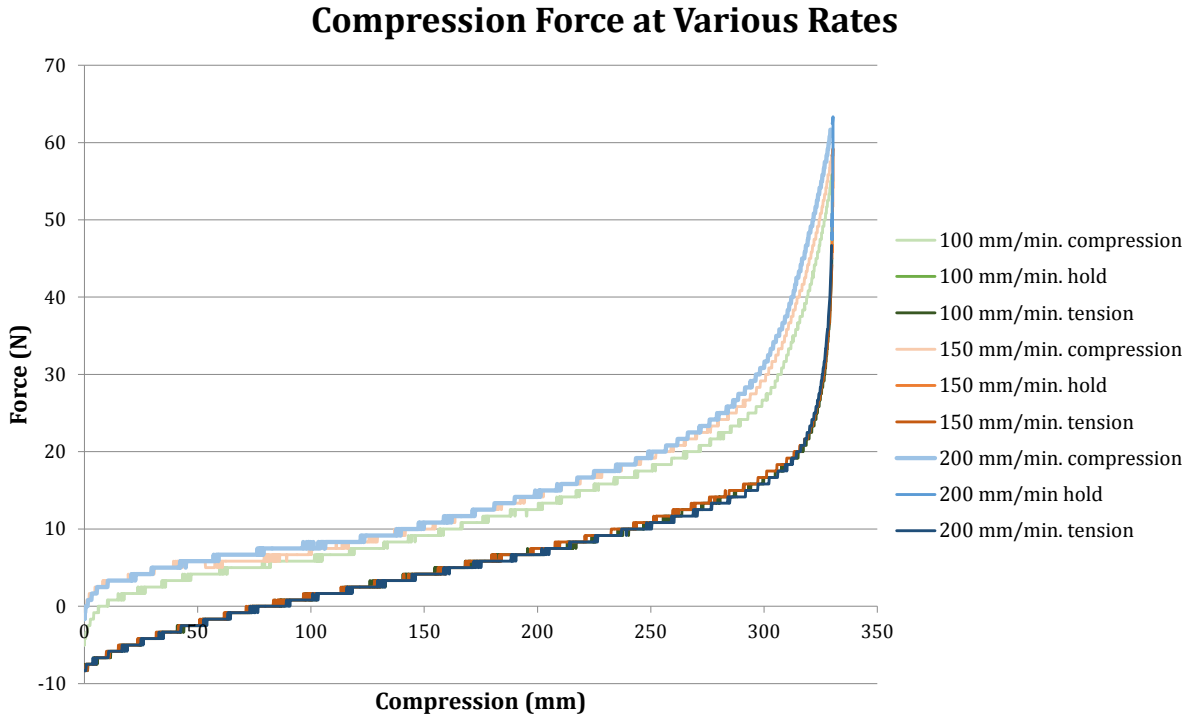


Figure 2.2 Enclosure deployment force at different rates of axial motion

The compression distance was relative to the initial position of the spring in a near fully deployed state with the force close to zero. Positive compressive motion correlated to the load cell moving downward at a constant speed as shown in Figure 2.3, reducing the axial distance between the base plates. The difference in the zero force crossing compared to compression distance between the compression and deployment motion was due to an imperfect recovery of the spring potential energy.

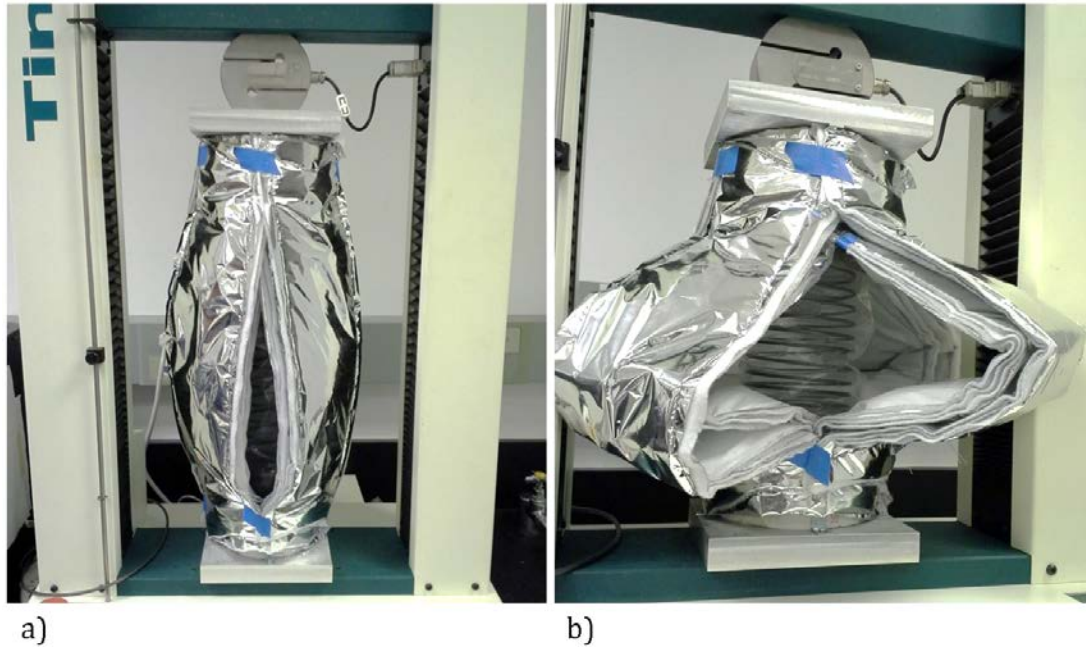


Figure 2.3 Deployment force test a) at the start of compression, b) near full compression

Looking at the test article as a combination of a pure spring and pure damper elements, the displacement and velocity of the pure spring element was the same as the damper element so the components were treated as if connected in parallel as shown by the schematic in Figure 2.4. The velocity of the mass was constant in time so the acceleration was approximately zero, meaning the forces exerted on the mass element from the load cell, $f(t)$, was balanced by the force contributions of the spring element, k , and damper, c .

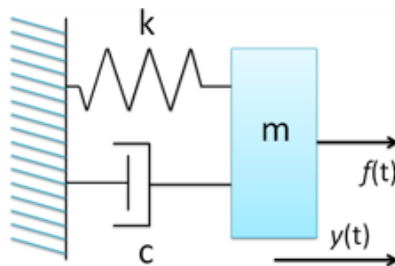


Figure 2.4 Schematic showing spring-damper acting in parallel

The data from a compression distance of 45 mm to 275 mm was selected to for a linear fit. The non-linear behave outside of the lower bound was contributed to the spring not having uniform turns for the entire length. The first and last turns on the ends of the spring do not cover the same axial distance as the other turns to create an outer face of the spring cylinder that was perpendicular to the axis. The non-linear behave outside of the upper bound was due to the spring reaching the fully compressed state such that there was no more space between turns of the spring turns. It was assumed that the spring constant contributed to the linear force on the assembly. By doing a linear fit, the spring constant was extracted. The calculated spring constant for each compression rate is given in Table 2.2, and the average spring constant was found to be 0.688 N/cm. This value was almost double the manufactured specification of 0.35 N/cm listed in Table 2.1. The difference can be possibly due to the resistance of the plastic and thermal blankets folding during compression and elongation of the test article.

Table 2.2 Summary of deployment force for straight enclosure segment

<u>Case</u>	<u>Spring constant (N/cm)</u>
Compression at 100 mm/min.	0.723
Deployment at 100 mm/min.	0.635
Compression at 150 mm/min.	0.755
Deployment at 150 mm/min.	0.654
Compression at 200 mm/min.	0.731
Deployment at 200 mm/min.	0.628

The dampening coefficient accounted for any curvature away from a linear relationship between the force and compression distance. The dampening coefficient for the different compression rates are shown in Figure 2.5. When compared to the force

contribution, it was found the spring force dominates. This meant the force exerted on the load cell was close to linear with the displacement distance during the test.

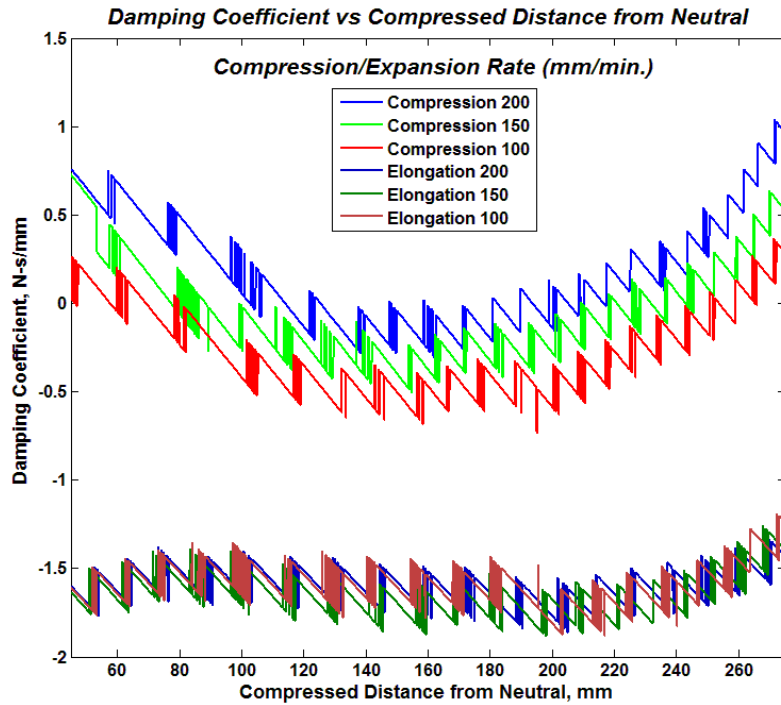


Figure 2.5 Damping coefficient for straight segment enclosure

2.2 Deployment of lab-scale toroidal thermal enclosure

The deployment force was not the only consideration for the structural design of the enclosure. The enclosure must also support the superconducting coil and allow for it to be stowed in a compact configuration. Recent development in Type-II superconductors, also known as high temperature superconductors, have resulted in wire shaped in a thin ribbon form. The thin superconducting materials was supported by substrates that allowed for the ribbon wire to bend at a smaller radius of curvature (2.5 cm) than the older Type-II superconductors that were made of thin filaments encased in silver with a minimum

curvature radius of 10 cm. The internal structure of the wire for both are depicted in Figure 2.6.

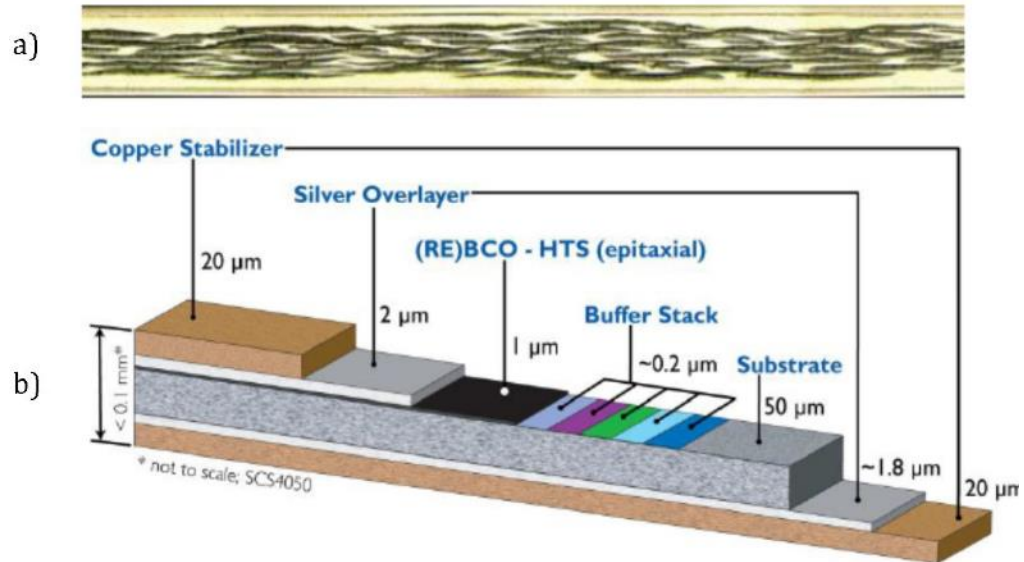


Figure 2.6 HTS superconducting wire a) Generation 1 made by American Superconductor, b) Generation 2 made by SuperPower

The small bend radius of the thin ribbon wire was utilized in the enclosure design as shown in a concept model in Figure 2.7. The red line in Figure 2.7a traces over the curved path of a plastic ribbon used as stand-in material for the superconducting coil. The image in Figure 2.7b shows how the ribbon uncurls to form a nearly circular shape while suspended within the volume of the spring coil. For this proof of concept four springs (identical to the one used in straight assembly testing and segments of the large lab-scale test article for thermal testing) were connected to form a torus of a smaller major diameter. The plastic ribbon that represented the superconducting coil was held in place by threading it through washers connected to the spring coils using zip ties. Twists in the zip ties encouraged the exaggerated S-curving of the ribbon when the springs were compressed into the stowed configuration.

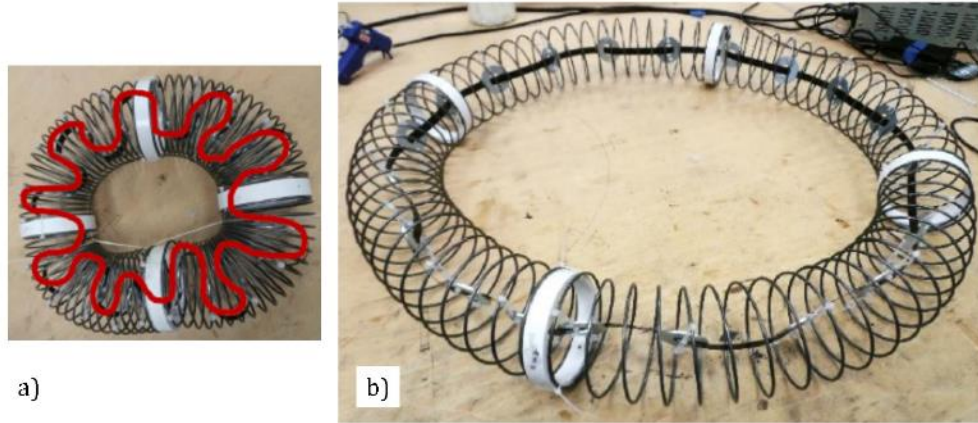


Figure 2.7 Proof of concept of ribbon wire when a) stowed and b) deployed

In order for the springs to compress to close to their minimum distance, the additional enclosure layers for containment of the nitrogen vapor and thermal management had to be designed for high collapsibility. Other space missions that used superconducting material such as Cryogenic Flexible Diode Heat Pipe (CRYOFD) which is further discussed in Section 3.1.1 used a stiff stainless steel bellow. Stowing a metal bellow of this kind would not yield a high deployment ratio. For this reason and the benefit of a reduced structure mass, a thin walled structure was considered for containment of the nitrogen vapor. The containment and thermally insulative layers of the enclosure are described in Section 3.3.1. An image of the structure full lab-scale torus is shown in Figure 2.8 which was built using 11 springs held in place using zip ties connected to the larger diameter polyvinyl chloride (PVC) cuffs.

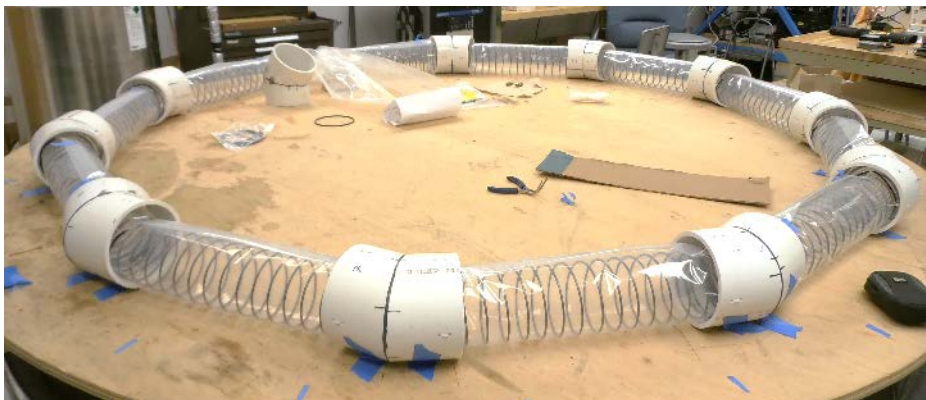


Figure 2.8 Structure of full lab-scale enclosure

The PVC joints were cut from 5-inch, schedule 80 pipe. The pipe was cut at an angle so that a closed path was created at the major diameter matching the toroidal vacuum chamber. The angled edges of the PVC were glued together using a cryogenically rated, two-part epoxy. The angled joints of the PVC allowed for the spring axis to remain straight in the deployed and stowed configuration. In turn, this allowed for the blanket pieces to lie flat when spanning from one joint surface to an adjacent surface. If the springs bowed out in an irregular manner it could cause gaps in the insulation blanket coverage.

3 Vapor Cooled Thermal Design

3.1 Methods of thermal management for cryogenic systems

By reviewing recent advances in cryogenic systems under consideration for cooling a HTS coil, a set of thermal management technologies were selected that fit the goals of this work. Selecting a technology to implement depends on comparative feasibility of integration to an inflatable structure and high volume expansion ratio for deployment.

3.1.1 Heat pipe

Heat pipes were an appealing thermal management tool in space because they passively extract heat and the working fluid would not be a consumable so the lifespan would be relatively high. There have been extensive research in heat pipes in general, but few advances have directly been applied to cryogenic temperatures within the range of HTS material, scalable for a large coil, and flexible for stowage during launch and deployment upon delivery. While no previous research investigations satisfy all of these needs, related work has been done.

The Cryogenic Flexible Diode Heat Pipe (CRYOFD) demonstrated by the Air Force Research Laboratory during the Space Shuttle missions STS-83 and STS-94 in 1997 used oxygen and methane working fluids contained by stainless steel bellow of 3/8 inch outer diameter to bend a radius of 2.7 inches to maintain temperatures between 60 and 145 K (for oxygen), and between 95 and 175 K (for methane) [1]. This showed that a flexible heat pipe could be achieved at the cryogenic temperatures necessary for operation of a HTS coil. However, complications with scaling this demonstration for cooling a large coil, and not using a closed path would make implementing a similar design for a superconducting

coil difficult. In contrast, a toroidal cryogenic heat pipe with nitrogen as the working fluid has been demonstrated with intended applications for large HTS coils [2]. The path of the heat pipe followed a closed circular loop with a major diameter of 2 m, significantly closer to the size of a potential space operated HTS coil. The HTS coil was enclosed in the vapor space of the heat pipe, rather than an external thermal connection like conventional heat pipes. However, the toroidal heat pipe was rigidly constructed using copper tubing as the outer envelope.

Given the current state of cryogenic heat pipes, it did not seem feasible to develop a heat pipe flexible enough to compactly stow a coil capable of the missions and a deployed diameter of 5 meters or larger. The required structure of a heat pipe was unfavorable for a light weight structure capable of compact stowage. By shifting to a vapor cooled system using nitrogen as the cryogen, it seemed more reasonable to develop an inflatable enclosure for the HTS coil with a high stowed to deployed volume expansion ratio.

3.1.2 Multilayer insulation blanket

Multilayer insulations blankets (MLI) were a key technology to the success of the human space exploration and lunar missions. The blankets were an effective method of passive radiation shielding, using highly reflective surfaces separated by insulative materials with low surface contact to reduce thermal conductivity. The resultant product typically consisted of many thin layers of the reflective material (often deposited on plastic film) alternated with insulation to produce a light weight blanket with a low effective thermal conductivity. This was due to the domination in the radiative mode of heat transfer compared to conduction and convection. Figure 3.1 shows the percentage of total heat flux for radiation compared to conduction through the solid insulation material and the gas

between layers for 1D heat transfer through slabs of material with the cold bounded wall at 123 K and the warm bounded wall at 273 K [3].

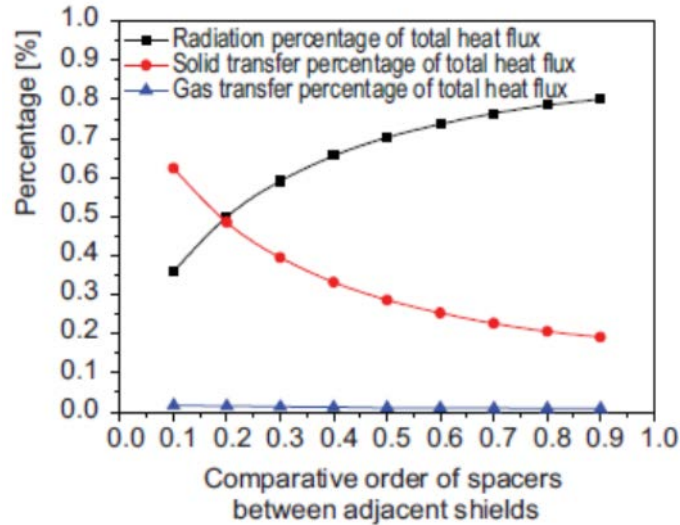


Figure 3.1 Fraction of heat flux due to radiation and conduction between cold wall at 123 K and warm wall of 273 K [3]

The convection due to the gas between layers was neglected. The spacers was the insulative material between reflective surface layers, shields, to prevent direct thermal contact. The shield was a thin deposition of aluminum (0.03 and 0.05 micrometers) on a sheet of polyester film (6 to 12 micrometers) with polyester netting acting as the spacer material. The insulative material conducted thermally in parallel with the conduction through gas. However, as the ratio of shield contact area for gas over insulation, spacer material, increased beyond 0.2, the radiation heat flux dominated as the primary mode of heat transfer [3].

The performance of MLI changes with environmental factors such as temperature and pressure, and also with variation in construction which makes predicting the effective thermal conductivity very difficult. For this reason, there is significant experimental tests

to measure the effectiveness of blocking radiation heat transfer. One such study examined the heat transfer rate of between two fixed temperature boundaries for two sets of boundary conditions and multiple materials. The materials tested were thin aluminum foil separated by nylon mesh, aluminum foil coated with zirconia for insulation, 3M™ brand aluminum adhesive tape, and a polyester film aluminized on both sides. For cold wall boundary of 77 K and warm wall boundary of 248 K, it was found that performance increased substantially with increased number of layers up to 5 to 10 layers for all of the MLI types [4]. For more than 10 layers, the performance return was not substantial for the increased amount of material.

According to a study early in the development of MLI for space applications, an optimum was found for the layering configuration necessary to minimizing heat flux that was dependent on the fixed temperature boundary walls [5]. The shield material, aluminum, was assumed to be at uniform temperature due to the small thickness compared to the plastic film, Mylar® and Kapton®. The effects from radiation tunneling were assumed to be negligible since the reflective layers were sufficiently large and temperatures were much higher than 10 K [6]. Radiation tunneling is when radiation propagates through a thin medium despite the incident angle being larger than the critical angle for total reflection [7]. Gas conduction between layers was also considered negligible. Analytical predictions for double-sided aluminized Kapton® insulated with glass fiber and double-sided aluminized Mylar® insulated with silk netting were compared with experimental results. Figure 3.2b shows that for a fixed blanket thickness, in this study it was 2.54 cm, there is a minimum heat flux for each temperature curve. However, for a fixed number of layers, no minimum existed so the heat flux was reduced with increased layer spacing [5].

This was an undesirable design point since the thickness of the MLI blanket would become unmanageably large. This result agreed with a later study of multilayer insulation by Bapat in 1990 that showed heat flow decreased with decreased layer density for a fixed number of layers, and heat flow also decreased with increased number of layers for a fixed density [8].

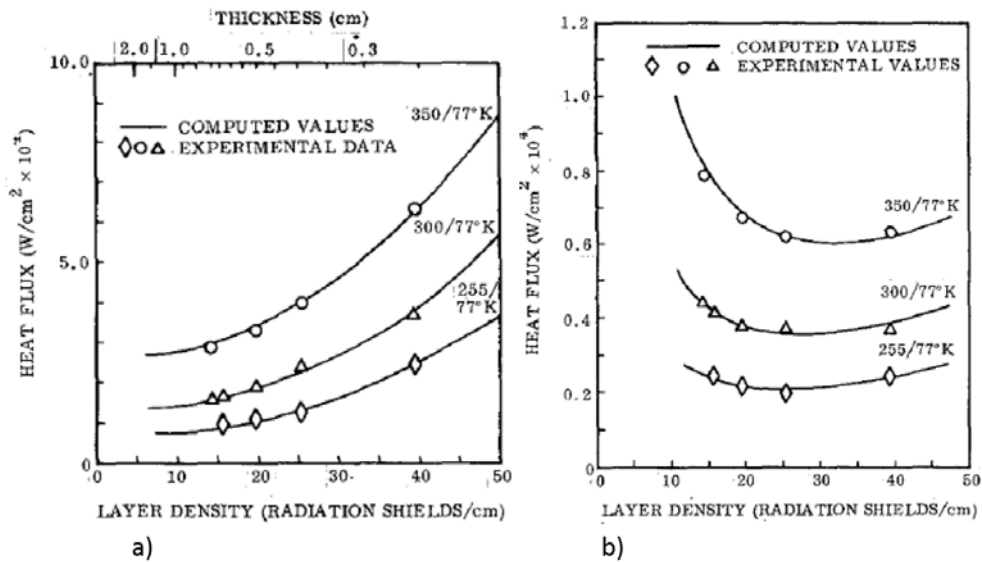


Figure 3.2 Total heat flux for a) fixed number of layers, b) fixed thickness [5]

The construction of a multi-layer insulation blanket is not simply comprised of just the shielding reflective layers and the insulative spacer material. An official guideline document for construction of flight multi-layer insulation blankets by NASA asserts that an outer cover and other layers are necessary in addition to the alternating reflective and spacer layers. The outer layer, with a possible reflective backing, protects the blanket from “shedding, flaking, and other forms of particulate generation” [9]. Materials listed as suitable for NASA missions included beta cloth, Teflon®, Tedlar®, and Kapton® with various material properties such as solar absorptivity and infrared emissivity. These

surface properties were necessary for determined the overall heat transfer capability of the blanket.

For applying multilayer insulation, the design required many seams to follow the curved geometry of a torus enclosure. Experimental data seams created thermal shorts due to conduction through the thread material and increased contact caused by the stitch at the seam location [10,11,12]. In an experiment conducted by Lin et al, it was found that the temperature difference between the inner and outer blanket layers was reduced near the seams, resulting in a larger heat flux in the vicinity of the seams [12]. The MLI blanket used to thermally protect components on the Cassini spacecraft. The stitching at the seam caused the inner layer (warm side) to decrease and the outer layer to increase (cold side). While the main purpose of this blanket was to keep components warm by reflecting radiated heat back on to the spacecraft, the temperature difference observed between the warm and cold sides at the seam compared to the center of the blanket is applicable for a blanket that radiates incident heat away from the spacecraft.

Another practical feature often required during MLI blanket fabrication is the overlapping of two adjacent blanket edges which are also a source of heat leaking [10,11]. The simple overlap (Figure 3.4a) is often undesirable despite being the easiest to implement because the cold inner layer of the top blanket would come in contact with the warm outer layer of the bottom blanket, leading to large thermal conduction across the seam boundary. In contrast, the interleaved overlap (Figure 3.4a) keeps the corresponding layers of the two blanket edges in contact with each other to prevent thermal shorting across the seam boundary, but this method is much more difficult to implement. The butted and outward overlap (Figure 3.4c) offers a middle ground by mating the two cold inner layers with the

seam edge pointing outward to prevent thermal shorting of the warm side from the cold side. However, this configuration exposes the edge to the warm surroundings.

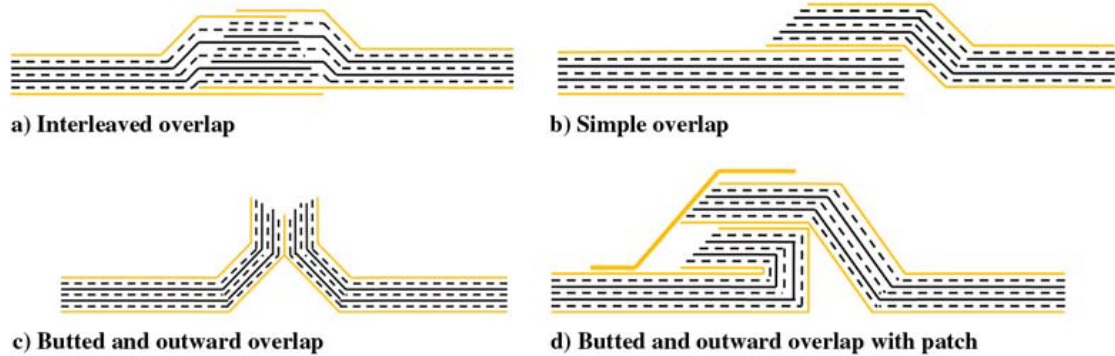


Figure 3.3 Overlap configurations for MLI [10]

A study by Okazaki et al. experimentally measures the effect of a patch that covers a folded over, butted outward overlap (configuration shown in Figure 3.4d) compared to a simple overlap or a butted outward overlap with no seam [10]. The heat flux due to radiation was assumed constant for all three overlap configurations and determined using analytical methods. The radiation was then subtracted from the total heat flux to determine the combined heat flux due to solid and gas conduction. As expected, the simple overlap allowed the highest heat flux through the seam. The butted and outward overlap without a patch reduces the heat flux to 0.412 W/m^2 at the location of the overlap [10]. The overlap region was 30 mm wide for all three configurations. This is a reduction of over 63% compared to the simple overlap. By adding the thermal control tape as patch on top of the overlap region, the heat flux at the location of the overlap was further reduced to 0.096 W/m^2 (reduction of 91.5% compared to the simple overlap) [10].

The use of multilayer insulation blankets is very common for spacecraft thermal management. Previous studies related to blanket features, fabrication, and material

selection will influence the thermal management system for maintaining the deployable torus enclosure.

3.1.3 Cryocoolers

Cryocoolers are a popular method in laboratory and space applications for obtaining cryogenic operation temperatures, typically consisting of a regenerator stage and heat exchanger stage. The first NASA mission to use a cryocooler in space was the Upper Atmospheric Research Satellite (UARS) in 1991 [13]. There are several types of cryocoolers with different advantages and disadvantages. Selection was typically dependent on the refrigeration power required and the operation temperature, but efficiency and mass should also be considered.

A literature survey was conducted to examine the state of the art cryocoolers that have cold tips near the critical temperature of HTS wire. A summary of the results are presented in Table 3.1. The cooling power of the cryocoolers listed range from values as low as 0.7 W [14] to 300 W [15]. For better comparison of cryocooler performance across a wide range of refrigeration power, it was useful to examine the efficiency as a percent of the coefficient of performance. The coefficient of performance is the efficiency of the Carnot refrigeration cycle, or reverse Carnot cycle as given by

$$COP = \frac{T_{refr}}{T_{rej} - T_{refr}} \quad (3-1)$$

As expected, the coefficient of performance is a function only the cold tip temperature (T_{refr}) and the rejection temperature (T_{rej}). This ideal efficiency was compared to actual refrigeration efficiency, given by

$$\eta_{refr} = \frac{P_{refr}}{P_{comp}} = \frac{1}{SP_{refr}} \quad (3-2)$$

Where the efficiency was the ratio of the refrigeration power (P_{refr}) over the compressor or electrical input power (P_{comp}). Some literature refers to the inverse of this ratio as the specific power. The ratio of the refrigeration efficiency, η_{refr} , over the coefficient of performance, COP , gives the percentage of actual efficiency compared to the ideal. This was sometimes referred to as the percentage of Carnot efficiency, and served as way of comparing the performance of different cryocoolers that may have different operating temperatures and different cooling capabilities. Table 3.1 lists the percentage of COP which ranges from a low of 3.9% for TRW pulse tube cryocooler developed by Northrop Grumman with a cooling power of 1.5 W at 56 K [16] to CryoTel® CT Stirling cryocooler developed by Sunpower, Inc. with a cooling power of 11 W at 77 K [17]. For the thermal loading predicted in Section 3.2, the two cryocoolers with cooling power of 15 W should be considered. Interestingly, the mass of the LPT 9710, a pulse tube type developed by THALES Cryogenics [18], was five times heavier compared to the CryoTel® GT, a Stirling type developed by Sunpower, Inc [17], despite the CryoTel® GT achieving a higher percentage of Carnot.

Table 3.1 Summary of cryocooler state of the art suitable for HTS applications

Model #	Type	Cooling Power (W)	Cold Tip (K)	Input Power (W)	Hot Side (K)	% of COP	Mass (kg)	Manufacturer	Source
Ricor K508	Stirling	0.7	77	12	233	12.3	0.45	CheMin & Ricor	[14]
	pulse tube	1.2	80	42	300	7.9	0.9	Northrop	[19]
TRW	pulse tube	1.5	56	92	190	3.9	8.2*	Northrop	[16]
MPTC	pulse tube	1.6	70	50	288	10.0	2.8	Air Liquide	[21]
RS1	Stirling	3.3	58	108	300	12.7	14	Raytheon	[24]
CryoTel MT	Stirling	5.0	77	80	296	17.8	2.1	Sunpower	[17]
	pulse tube	6.5	67	165	300	13.7	5.0	Northrop	[22]
	turbo Brayton	7.1	73	375	278	5.3	18*		[23]
CryoTel CT	Stirling	11.0	77	160	296	19.6	3.1	Sunpower	[17]
LPT 9710	pulse tube	15.0	80	300	296	13.5	16	THALES Cryogenics	[18]
CryoTel GT	Stirling	15.0	77	240	296	17.8	3.1	Sunpower	[17]
	pulse tube	200.0	70	8600	300	7.6	190*		[25]
HTS-3	pulse tube	300.0	80	4300	300	19.2	114*	Praxair Inc	[15]

*Calculated using Equation (3-3) [20]

The cryocooler with the smallest mass listed in Table 3.1 was a pulse tube type developed by Northrop Grumman with a modest cooling capacity of 1.2 W and achieved 7.9% of the Carnot [19]. The cryocooler mass was not available for all of the cryocoolers examined in Table 3.1; however, a relationship proposed by Ladner gives the relationship of cryocooler total mass in kilograms as a function of input power for single stage pulse tube and Stirling cryocoolers as

$$M_{cryo} = 10^{-5.5260E(-02)(\log(P_{comp}))^3 + 5.565E(-01)(\log(P_{comp}))^2 - 1.0931 \log(P_{comp}) + 1.3315} \quad (3-3)$$

which can be used to estimate an expected mass for input powers between 50 W and 200 kW [20] as shown by the blue line in Figure 3.5. The mass and input power for several cryocoolers are indicated by red circles also in Figure 3.5 which showed a close correlation between the data and the trend line Equation (3-3) given by Ladner. This allowed for a

prediction of cryocooler mass for coolers where the mass was not readily available. They are marked with an asterisk in the table to indicate that the mass was a calculated value.

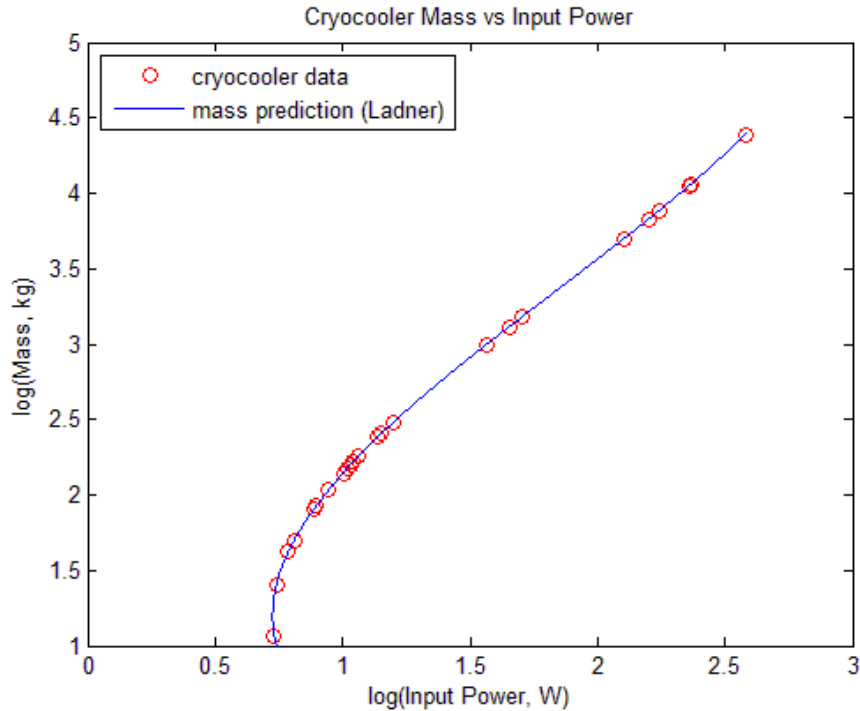


Figure 3.4 Mass and input power for recent cryocoolers compared to trend by Ladner [20]

Only five of the cryocoolers included in Table 3.1 were developed for space applications or have been successfully operated on a space mission. Research regarding state of the art cryocoolers primarily focuses on delivering cooling power of less than 1 W to maintain temperatures of 4 K which is a different operation range than what is necessary for an HTS coil. The TRW pulse tube was developed to provide cooling to the Atmospheric Infrared Sound (AIRS) instrument on the NASA Aqua spacecraft which launched in 2002 with over six years of operation in space [16]. The Miniature Pulse Tube Cooler (MPTC) developed by Air Liquide was a component on the ESA Sentinel-3 mission

with 5260 operating hours as of April 2008 [21]. Northrop Grumman demonstrated that a coaxial pulse tube cryocooler similar to the coolers that flew as part of the Japanese Advanced Meteorological Imager (JAMI) in 2005 and the Thermal and Near Infrared Sensor for Carbon Observations (TANSO) payload on the GOSAT in 2009 could achieve 6.5 W cooling at 65 K [22]. The cryocooler with the highest cooling capacity for space applications listed in Table 3.1 was the turbo-Brayton capable of 7.1 W at 73 K while achieving 5.3% of the Carnot for the Near Infrared Camera and Multi-Object Spectrograph (NICMOS) installed on the Hubble Space Telescope during a service mission in March 2002 [23]. Though not developed for a spacecraft, the Ricor K508 Stirling cryocooler was included in the Mars Space Laboratory design for cooling the Chemistry Mineralogy (CheMin) instrument [14]. While other cryocoolers may not be space qualified, the operational ranges round out the survey such as the Stirling RS-1 developed by Raytheon [24] and the pulse tube capable of 200 W cooling at 70 K tested by Dietrich, et al [25].

3.2 Theoretical thermal loads

In order to select thermal management system components using the technologies surveyed in Section 3, the expected thermal loading of the system must be determined. For this analysis, it is assumed that the a cryocooler will be used to supply the system with cooling power and a multi-layer insulation blanket will be used to shield the vapor core from incident energy sources.

3.2.1 Governing heat transfer equations

The goal was to approximate the heat rate into the vapor core. For this analysis, it was assumed that the mission under consideration is as in low-Earth orbit (LEO) at an

altitude of 400 km. The energy input to the system were the incident radiation from the Sun, Earth, and the background radiation of space. A worse-case scenario placed the spacecraft orbiting around Earth when the Earth was at the perihelion location, resulting in the highest solar radiation. Assuming the spacecraft was in LEO also agreed with the conditions for a worst-case scenario since the spacecraft would be close to Earth for higher albedo and Earth emitted radiation. The only component of the spacecraft considered was a single torus that encloses the HTS coil. By examining the torus with the major axis aligned with the radial path from the Sun to Earth as shown in Figure 3.6, the plane of the torus was normal to major incident radiation components which resulted in higher heat flow into the system than other orientations.

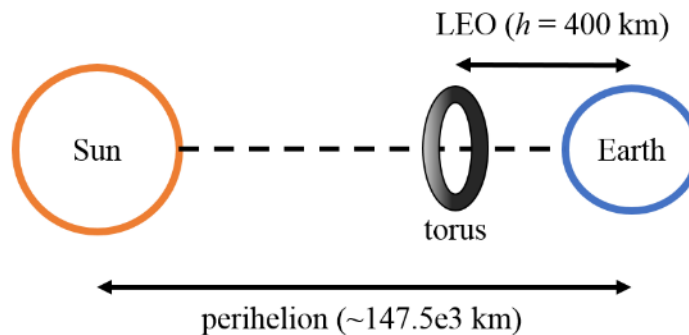


Figure 3.5 Orientation of torus in orbit around Earth and Sun (not to scale)

The solar flux, G_s , assumed at perihelion was approximately 1422 W/m^2 . The Earth albedo at winter solstice which accounted for the amount of solar radiation that was reflected off the Earth's surface is 0.35 [26]. While winter solstice and the position of Earth at perihelion would not be aligned on the same day, they would be close to each other for approximating worst-case incident thermal loads. The albedo heat flux incident on the torus is given by

$$q_a = G_s a F_{21} \quad (3-4)$$

Where F_{21} is the radiation view factor from the torus enclosure, surface 2, to Earth, surface 1, as indicated in Figure 3.6. Since the torus would be far from the surface of the Earth and small in comparison, the torus can be approximated as a 2D projection normal to the incident energy. The view factor of the flat ring with a radial thickness that matched the minor diameter of the torus to Earth as shown in Figure 3.7 was calculated using the summation condition and then the reciprocity relation where

$$F_{12} = F_{1 \rightarrow 2,3} - F_{13}$$

$$F_{21} = F_{12} \frac{A_1}{A_2} \quad (3-5)$$



Figure 3.6 View factor numbering designation where surface 1 is a sphere, surface 2 is a flat disc (not including surface 3 as a hole)

The view factors $F_{1 \rightarrow 2,3}$ and F_{13} were found using a common view factor relation for a flat disc and a sphere [27]

$$F_{1 \rightarrow 2,3} = \frac{1}{2} \left(1 - \frac{1}{\sqrt{1 + \left(\frac{R_c + r_h}{R_E + h} \right)^2}} \right) \quad (3-6)$$

$$F_{1 \rightarrow 2,3} = \frac{1}{2} \left(1 - \frac{1}{\sqrt{1 + \left(\frac{R_c - r_h}{R_E + h} \right)^2}} \right)$$

where R_c was the major radius and r_h was the minor radius of the torus enclosure (including the thickness of radiation shielding material), R_E was the radius of the Earth, and h was the altitude. The areas A_1 and A_2 in Equation (3-5) were the surface of Earth and the 2D projected area of the torus, respectively. The emitted infrared radiation flux from the Earth is given by

$$q_a = \sigma T_E^4 F_{21} \quad (3-7)$$

where the average temperature of Earth as 262 K. The background space radiation was assumed to behave under blackbody radiation conditions, and, therefore, is given by

$$q_b = \sigma T_b^4 \quad (3-8)$$

The heat absorbed at the outer surface of the thermal enclosure must either be conducted to the vapor core where heat was extracted using the cooling management system or emitted as radiation into space by the enclosure surface. Without taking into account convection heat transfer from the enclosure core walls to the cold vapor flowing inside, the heat flowing into the vapor core could be represented using solid conduction. The heat conduction equation for concentric tori was quite complicated due to the changing surface in two dimensions. A simplification that was applied treated the concentric tori as

concentric cylinders such that the only the minor radius changes for the separate temperature walls. The length of the cylinder was given by the circumference of the torus as

$$L = 2\pi R_c \quad (3-9)$$

$$Q_{cond} = 2\pi kL \frac{T_h - T_c}{\ln(r_h/r_c)} \quad (3-10)$$

$$Q_{emit} = \sigma \epsilon T_h^4 \quad (3-11)$$

The conduction depended on the outer enclosure wall radius and the inner vapor core radius, as well as the surface temperatures at those radii locations. Similarly, the heat leaving surface as emitted radiation depends on the surface temperature of the enclosure, and also depended on the surface properties of the outer enclosure. To solve the governing equations, a model connecting the relationship between all of the contributing heat sources and sinks was be established.

3.2.2 Analytical model using only MLI

To establish a baseline of the rate of heat flow into the vapor core, some assumptions were made about the radiation shielding. Without any shielding the heat loading on the vapor core of the torus would much higher than the desired design point of the system. For that reason, it was assumed that a single blanket of undetermined thickness consisting of multi-layer insulation must be wrapped in direct contact with the circular cross-section of the vapor core enclosure. The heat loading on the vapor inside the torus were determined using an energy balance at the outer surface of the torus to calculate the input energy and solve for the conduction from surface to the vapor core. A radial, 1D

cylinder case simplified the analysis where the length of the cylinder was the circumference of the torus.

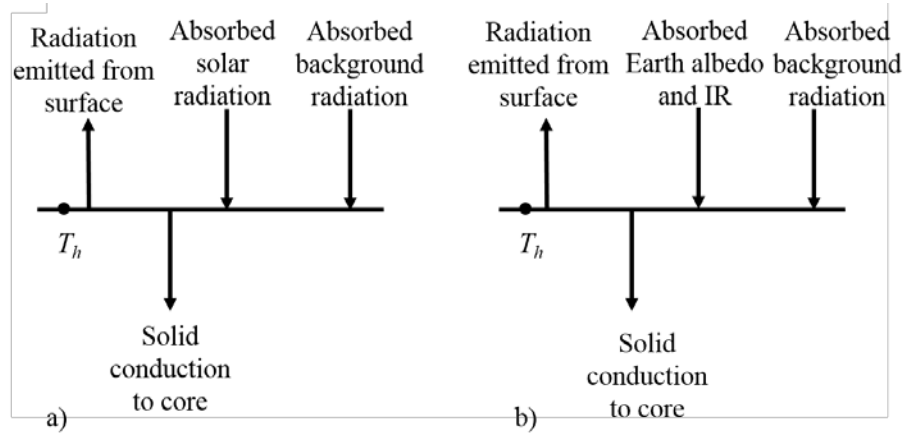


Figure 3.7 Energy balance at outer surface of thermal enclosure where a) is the Sun-facing surface and b) is the Earth-facing surface

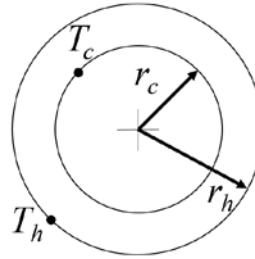


Figure 3.8 Cross-section of enclosure minor diameter

The energy balance at the surface shown in Figure 3.8 for temperatures and enclosure dimension shown in Figure 3.9 is given by

$$0 = \sigma \epsilon T_h^4 A_h + 2\pi k L \frac{T_h - T_c}{\ln(r_h/r_c)} - \alpha A_h G_s - \alpha A_h q_b \quad (3-12a)$$

$$0 = \sigma \epsilon T_h^4 A_h + 2\pi k L \frac{T_h - T_c}{\ln(r_h/r_c)} - \alpha A_h (q_a + q_E) - \alpha A_h q_b \quad (3-12b)$$

The equations were separately solved to find the outer surface temperature of the torus and the heat conducted to the core is given by the second term. This assumed the heat loading

for each equation was symmetrical about the plane of the torus and the temperature of the vapor core was fixed at T_c . To find the total heat flow into the vapor core was found by taking half of the value for the heat flow contribution from each equation and adding them together. Equation (3-12a) accounts for the heat flow from the sun facing side of the torus while Equation (3-12b) accounts for the Earth facing side.

Table 3.2 Summary of thermal loading variables

Quantity	Symbol	Value
Stefan-Boltzmann constant	σ	$5.67e-8 \text{ W(m}^2\text{-K}^4\text{)}$
Radius of Earth	R_E	6378 km
Torus altitude	h	400 km
Solar flux	G_s	1422 W/m^2
Earth albedo [26]	a	0.35
Background space temperature	T_b	4 K
MLI effective thermal conductivity [8]	k	$5e-5 \text{ W/(m-K)}$
MLI absorptivity [9]	α	0.10
MLI emissivity [9]	ϵ	0.85
Vapor core temperature	T_c	77 K

The surface properties of the MLI assumed an outer cover of FEP Teflon with vacuum deposited silver and Inconel backing [9]. The effective thermal conductivity value was based on the previous experimental results by Bapat, et al. for a layer density of 20 layers per cm [8].

The thermal loading for a tori varying in vapor core radius and major radius is shown in Figure 3.10. These results assumed a blanket thickness of 2 cm.

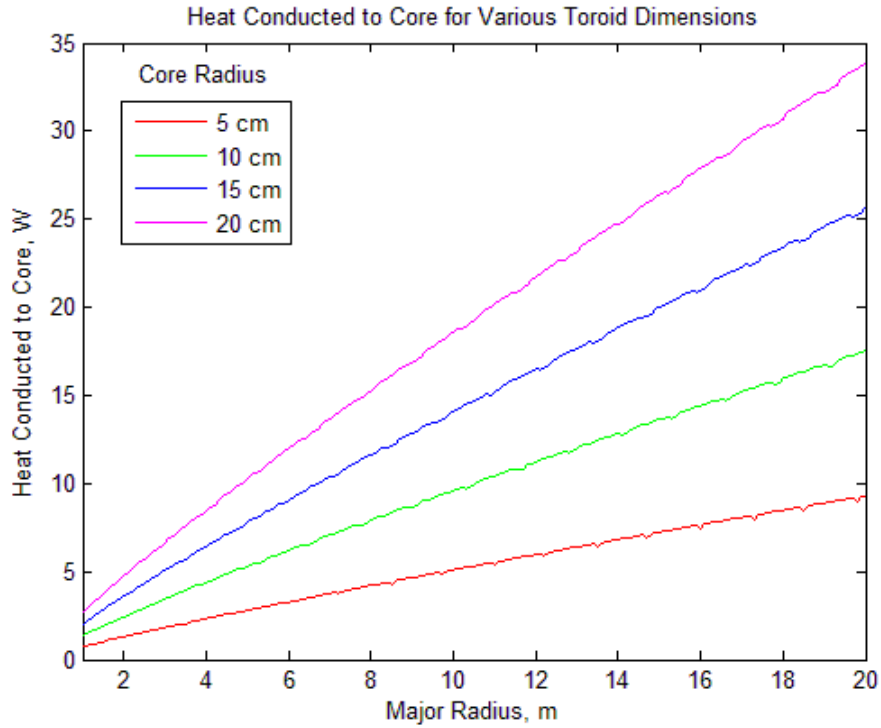


Figure 3.9 Thermal loading on the vapor core for varying torus sizes for fixed MLI thickness of 2 cm

To examine the effect of different insulation blanket thicknesses, a major radius of 5 m and a core radius of 10 cm was chosen as a baseline or “average” case. The results are shown in Figure 3.11. The rate of heat flow into the vapor core of the enclosure increased greatly as the thickness goes to zero at an outer minor radius of 10 cm. With a multi-layer blanket insulation thickness of 1 cm (11 cm outer minor radius), the rate of heat flow was already below 10 W and below 5 W at an insulation thickness of 2 cm.

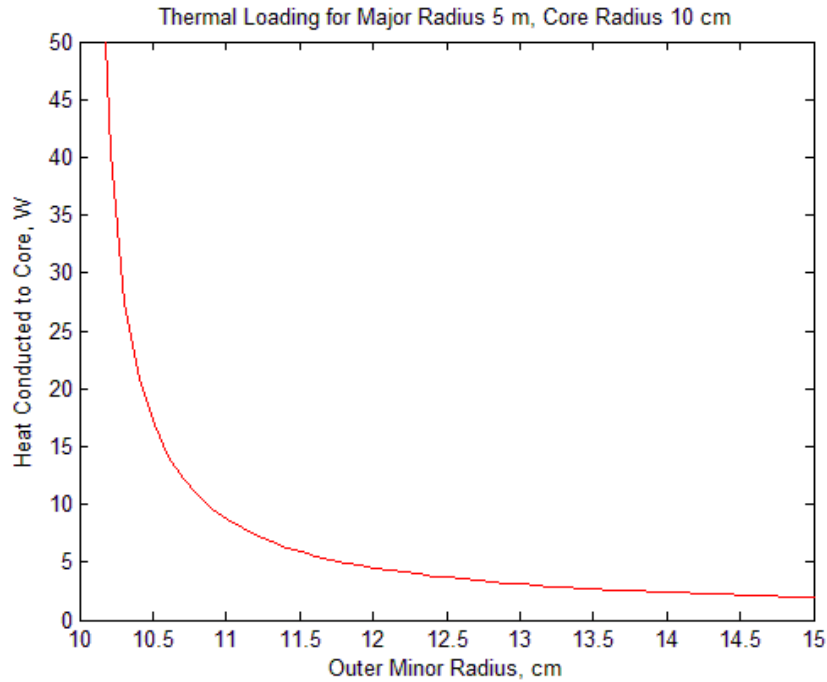


Figure 3.10 Thermal loading for varying insulation thickness with a vapor core radius of 10 cm

3.3 Laboratory thermal testing

To better estimate the thermal performance of the inflatable thermal enclosure during on-orbit operations, laboratory thermal tests were conducted to measure the heat transfer into the system and characterize effect of thermal insulation. The purpose of the testing was to show that it would be feasible to maintain operational temperatures below the critical temperature of the superconducting material using nitrogen vapor from a liquid reservoir. A full toroidal test article was fabricated for the testing and analysis was performed using the temperature measurements taken at various locations along the circumference of vapor core and across the thermal insulation layers. The results of the test were used to elevate the conclusions about the analysis used for on-orbit performance predictions.

3.3.1 Fabrication of test article

The full toroidal enclosure was fabricated for thermal testing with the intent to use a pre-existing custom low-vacuum, torus-shaped chamber at the University of Maryland Space Power and Propulsion Laboratory (UMD-SPPL) [2]. The vacuum chamber was previously used for toroidal heat pipe testing so the dimensions of the vapor cooled thermal enclosure were primarily governed by the vacuum chamber dimensions. The central core of the thermal enclosure circulated chilled nitrogen vapor confined a double layer of polyethylene plastic. The minimum core diameter was defined by the linear compression springs used to aid in deployment (previously discussed in Section 2) while the maximum core diameter was constrained by a biaxial fiberglass sleeve as shown in Figure 3.12(a & b). The plastic layers were a larger diameter than the maximum allowable diameter of the fiberglass sleeve, allowing for the fiberglass to bear the majority of pressure forces while inflated.



Figure 3.11 Close-up of toroidal enclosure segment with a) inner core, b) fiberglass sleeve over core, c) thermal blanket

Angled joints made from schedule-80, 5-inch diameter PVC pipe served as the mounting structure for the thermal insulation and vapor containment assembly. The joints were sized such that the majority of the spring length was not contained inside the PVC so that the spring can compress nearly the full allowable distance when the enclosure was in the stowed configuration. Zip ties were tightened around the circumference of the spring near the ends with the fiberglass and plastic layers constrained underneath. Smaller zip ties were looped through the large zip ties, extending axially and looping through holes in the PVC. This allowed the vapor containment assembly to be suspended inside the PVC

and created a gap between the fiberglass and the inner most surface of the thermal insulation, reducing heat conduction to the nitrogen vapor.

Flight quality multi-layer insulation was not commercially available since most thermal blankets are uniquely fabricated for each space mission. Custom thermal blankets were made in-house using alternating layers of low density nylon felt and single-sided aluminized polyester film. Each blanket piece was sewn together along the edges. For each joint-to-joint span covered by a single spring length there were four panels of blanket shown in Figure 3.12c. Each panel needed to split into an inner and outer stack due to the sewing machine unable to pass material at the full thickness shown in Figure 3.13. The inner stack consisted of three reflective film layers separated by two layers of felt cloth. The outer stack also consisted of three reflective film layers alternated with three layers of felt cloth so that the bottom felt pieces was in contact with the top reflective film layer of the inner stack. This prevented thermal shorting between the inner and outer stacks of MLI.

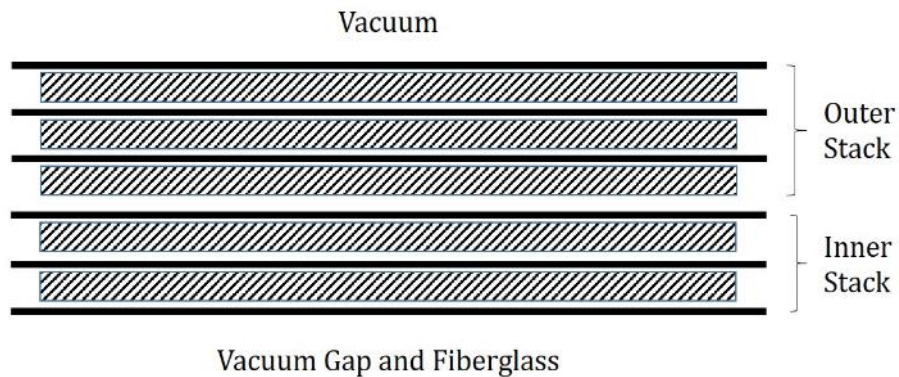


Figure 3.12 Conceptual cross-section showing stack of MLI

Spray adhesive was used to attach the four panels of MLI to the outer surface of the PVC joints. The long edges of the panels slightly overlap to prevent any gaps when fully

deployed. In the stowed configuration, the center of the panels push out radially from the compressed spring. This prevents the thickness of the blanket layers from restricting the ability of the spring to fully compress. A sample of the enclosure assembly (Figure 3.14) was constructed using a single spring and material layers of the same specifications as the full-sized torus. The partial compression of the spring shown in Figure 3.14b demonstrated how the blanket panels bowed out in four radial directions. Slight overlap (conceptual depicted by the gray regions in Figure 3.21) of the panels provided thermal insulation without the need for the long edges of the panels to be attached to the adjacent panel. The top panel in Figure 3.14a was slightly lifted up to show how the edges of the panel was not restrained by the edge of the front facing panel.

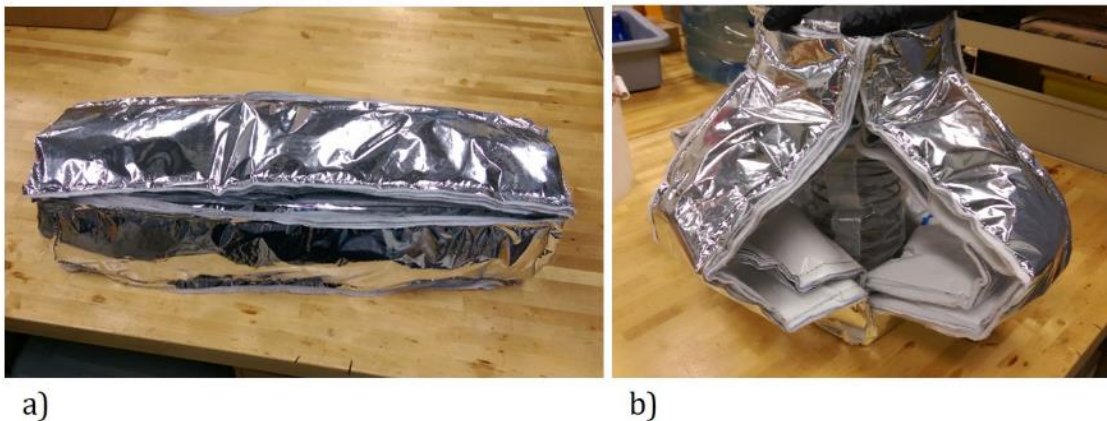


Figure 3.13 a) Deployed straight thermal enclosure, b) partially compressed

Other design concepts were investigated such as an accordion-inspired folding concept (Figure 3.15), but the four panel design was appealing because it also minimized the labor in constructing the blanket pieces and stitching which created thermal leaking through the MLI. The short edges of the blanket pieces were butted together (Figure 3.16a) so that the common bottom layers of the stack were touching and then folded over in the

same manner as Figure 3.4d. The fold was then covered over using aluminum tape Figure 3.16b. The short edges of the inner and outer stacks were matted together separately.



Figure 3.14 Initial concept for accordion-inspired MLI folding

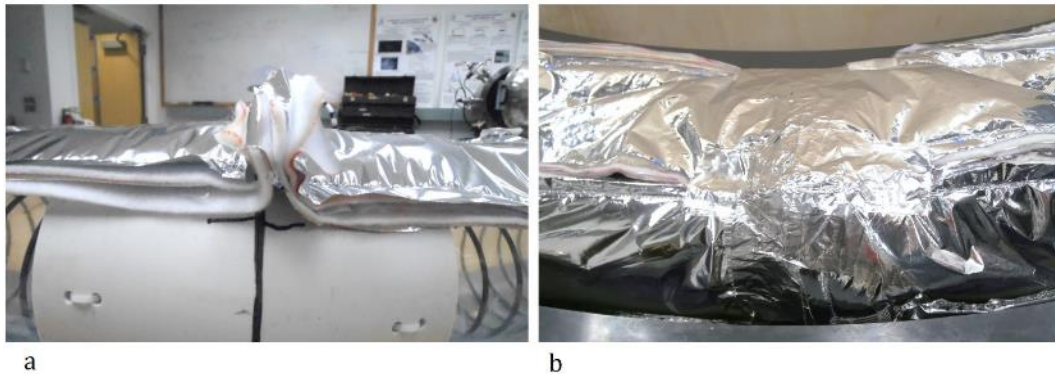


Figure 3.15 a) Butting of MLI panel short edges

The two nested plastic layers and fiberglass sleeve were a continuous piece around the circumference of the enclosure. The edges of the plastic layers were sealed using fiberglass reinforced packaging tape with the air extracted from between the layers using a laboratory low-vacuum line. This was necessary to prevent undesirable bulging due to air pressure between layers in the time during the pump down of the vacuum chamber and

when the start of pressurized nitrogen vapor began to flow through the enclosure. The ends of the plastic and fiberglass were strapped to aluminum caps shown in Figure 3.17 and Figure 3.18 using closed cell foam and hose clamps. The end caps also served as the connection point for the inlet and outlet tubing for the nitrogen. The flat bottoms of the ends caps were separated using some foam insulation to reduce thermal conduction from the outlet side to the inlet side of the enclosure. A small c-clamp was used to maintain the shape of the enclosure while inflated. Without the clamp, the pressure from nitrogen would push the ends of the enclosure out radially.



Figure 3.16 Vapor containment end caps and closed cell foam



Figure 3.17 End caps with ends of plastic and fiberglass secured

The final dimensions of the full torus used for thermal and deployment laboratory testing are given in Table 3.3.

Table 3.3 Dimensions of torus for thermal and deployment testing

Major diameter	185 cm
PVC minor OD	140.9 mm
PVC minor ID	126.mm
Single plastic layer thickness	0.13 mm
MLI total thickness	~ 17 mm (+/- 2 mm)
Fiberglass sleeve thickness	0.6 mm

3.3.2 Equipment setup in laboratory

The enclosure was placed in the vacuum chamber shown in Figure 3.19 for thermal testing. As previously mentioned, the chamber was custom fabricated for a previous investigation of a toroidal heat pipe [2]. The chamber walls were constructed using 10-inch schedule 80 PVC pipe segments. The top and bottom halves separated in the plane of the major circle of the torus. The flanges and ports were also constructed using PVC material. The port feedthroughs were configured as shown in Figure 3.20. Two ports were

dedicated to the thermocouple feedthroughs which passed through five channels per port. The pressure inside the chamber was measured using a cold cathode vacuum transducer made by MKS (P/N: 972B-20134). The nitrogen flow was measured using an Omega flow meter (P/N: FMA 1609A) connected downstream of the outlet using 1/4-inch nylon tubing. Temperature, pressure, mass flow rate, and volumetric flow rate were reported at 1.0153 seconds per sample. The flow meter had a low temperature operating bound of $-10\text{ }^{\circ}\text{C}$ so extra tubing was used to allow more heat to warm up the nitrogen before passing through the flow meter. For this reason, the flow meter measurements for temperature and pressure did not match the conditions directly at the outlet of the enclosure.



Figure 3.18 Vacuum chamber used for thermal testing

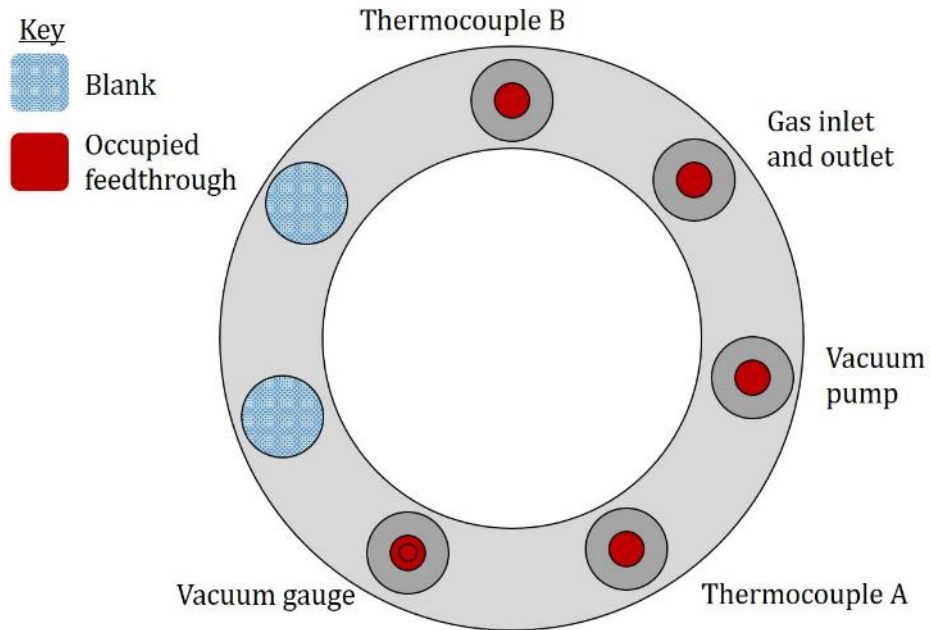


Figure 3.19 Chamber port configuration, view from above

Temperature of the outer plastic surface was measured at four different locations on the enclosure as a representation of the vapor core temperature: near the inlet ($x = 0$) and outlet ($x = L$), $x = L/2$, and $x = 3L/4$ where L is the circumference length of the torus. Additionally, temperature at three different insulation layers were measured at $x = L/2$. To reduce the effect of thermal conduction along the thermocouple wire causing erroneous measurements, the thermocouple wire was wrapped around the surface of interest several times as indicated by the dashed lines in Figure 3.21. The wire wrapping was done for the thermocouples measuring the core locations and the blanket layers. The last thermocouple measured the vacuum chamber wall in the vicinity of the ‘Thermocouple B’ feedthrough.

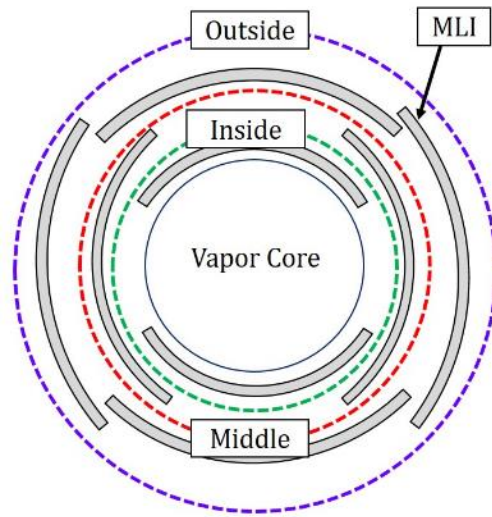


Figure 3.20 Thermocouple locations around MLI blanket layers

To reduce thermal conduction to the chamber walls, 1.5 cm diameter G10 rods were placed underneath each joint to reduce contact between the MLI and the chamber. There was still some contact with the MLI and the inner surface of the chamber as shown in Figure 3.22.

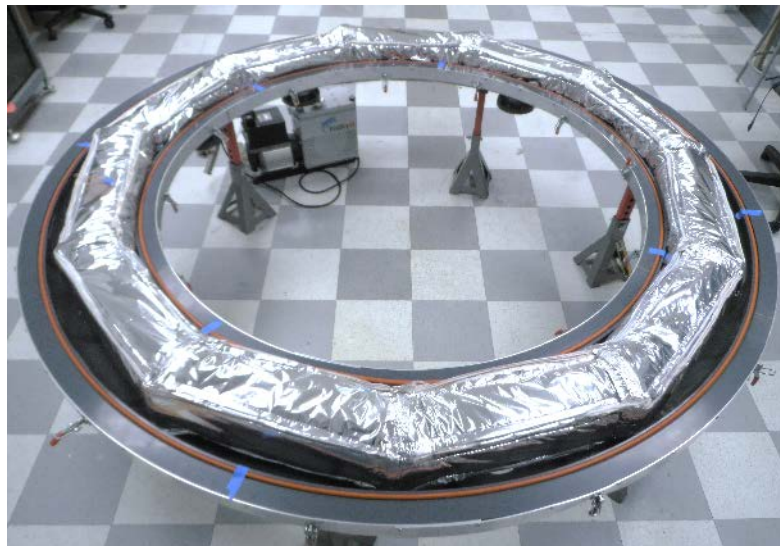


Figure 3.21 Lab-scale thermal enclosure sitting in open vacuum chamber

The temperature measurements were reported using an Omega data logger (P/N: HH309). The data logger could only measure four channels at a time. Each data logger communicated with a separate laptop through an RS-232 communication port. Due to limited resources, only two computers were used for data recording. This meant that one channel at each thermocouple feedthrough port was unused. One of the laptops was simultaneously also reading in data from the flow meter. The vacuum chamber pressure measurements were recorded by hand at irregular intervals.

The chamber vacuum was achieved using a roughing pump. The seams connecting the segments of vacuum chamber PVC and out of plane deformation of the large flange mating surfaces prevented the chamber pressure from reaching below 30 mbar for any of the test runs. For this reason, the turbo pump connected to the system could not be turned on and instead acted as an intermediate connection between the roughing pump and the chamber port.

The nitrogen was supplied using a high-pressure liquid nitrogen cylinder. The dewar was pressure limited to 230 psi. The gas line on the dewar was connected to the inlet side of the gas feedthrough port of the chamber using a thermally insulated metal bellow and ¼-inch nylon tubing. It was found that the pressure gauge on the tank on the gas line was unable to read the pressure under cold conditions.

3.3.3 Testing Procedure

First, the roughing pump was turned on to allow the vacuum chamber to reach a starting pressure of around 70 mbar. The data recording programs had to be started manually. The flow meter does not print out time stamp information so the script that polls the flow meter for data had to be started simultaneously with start of the thermocouple

recording on the other laptop so that the data start time of the flow meter was known. The second set of thermocouple readings were started on the same laptop as the flow meter at a set known interval of time after.

The liquid nitrogen tank was opened, but not connected to the gas feedthrough for several minutes to allow for a high flow rate while the outer gas line coils inside the dewar cool down as liquid nitrogen was drawn out of the central volume. Once the tank was outputting nitrogen vapor at temperatures colder than $-40\text{ }^{\circ}\text{C}$, the tank was temporarily closed while the hose was connected to the vacuum chamber gas feedthrough. The gas valve on the tank was then opened again and chilled nitrogen vapor flow inside the enclosure was initiated. Due to the inability to regulate the flow rate or the pressure output of the dewar, the flow conditions and cool down rate of the enclosure varied from test to test.

The procedure for ending of a test was initiated by the closing of the nitrogen tank. The data continued to record while the enclosure slowly warmed up for several of the tests to monitor the heat rate into the system with the flow rate at a minimum. Lastly, the data recording and roughing pumps were shut off to conclude the test.

3.3.4 Results and discussion

There were 13 full test runs conducted. Despite following the same general operating procedure, each test had a unique set of operation conditions that were adjusted as the test ran. This was due to controllable factors such as contraction of the aluminum end caps compared to the plastic and closed cell foam created substantial leaking of nitrogen vapor into the vacuum chamber as the inlet temperature decreased substantially. Additionally, the roughing pump was unable to maintain the vacuum pressure achieved at

the beginning of the tests. This raised the need to record the vacuum chamber pressure by hand due to a lack of resources to record the values automatically. During a test, if the pressure in the vacuum chamber raised above 500 mbar, the flow rate of the nitrogen tank had to be reduced to decrease the amount of nitrogen leaking into the chamber. As a result, the temperatures achieved during some tests did not fully reach a steady state either from the test ending due inoperable vacuum chamber pressures or the nitrogen reservoir becoming empty. The foam pieces between the flat faces of the enclosure end caps were added to reduce thermal conduction between the outlet and inlet of the enclosure. Even with the foam, thermal conduction between the end caps and perhaps from the gas in the vacuum chamber in the vicinity of the inlet since the outlet temperature was sometimes observed to be lower than the temperature at the $x = 3L/4$ location upstream.

To examine the thermal performance based on the data collected, a simple energy balance was conducted to determine the thermal conductivity of MLI. The heat rate into the system assuming constant heat rate per circumferential distance of the toroidal enclosure and constant heat extraction per circumferential distance due to forced nitrogen vapor flow. The heat rate into the system was calculated using cylindrical conduction heat transfer relations for the layers of material that make up the cross-section of the enclosure assembly. At the $x = L/2$ location, measurements of the temperature around the outside of the plastic were compared to the temperature on the outer most surface of the MLI with the radial distances of these locations known and all of the material properties except the MLI thermal conductivity to also be known values. The rate of heat extracted was calculated using the mass flow rate measured by the flow meter and the temperature rise between the inlet and the $x = 3L/4$ location. Due to conduction driving down the outlet temperature,

the $x = 3L/4$ location was used for the heat extraction calculation instead. The energy balance for cylindrical heat transfer per unit length of the enclosure was as follows

$$Q'_{out} = \frac{\dot{m}c_p(T_{3L/4} - T_{inlet})}{3L/4} \quad (3-13)$$

$$Q'_{in} = \frac{2\pi k_{MLI}(T_{bl,o} - T_{L/2})}{\ln(r_{bl,o}/r_{bl,i})} \quad (3-14)$$

where c_p was the specific heat at constant pressure for nitrogen gas, L was the circumferential length of the torus, and \dot{m} was the mass flow rate. The temperatures $T_{L/2}$, $T_{3L/4}$, and T_{inlet} referred to core at the $L/2$, $3L/4$, and inlet locations, respectively, while $T_{bl,o}$ referred to temperature of the outermost surface of MLI. Similarly, $r_{bl,o}$ and $r_{bl,i}$ referred to the radius from the center of the vapor to the outer and inner surfaces of the MLI, respectively. Equation (3-14) is simply Equation (3-10) divided by length. In this case, the lower temperature is at $x = 3L/4$ instead of L so the length that the total heat Q is divided by is also $3L/4$.

The thermal conductivity was then found for each time step. The initial values of the thermal conductivity were large and quickly dropped down due to the highly transient nature of the system when the nitrogen vapor was first circulated in the enclosure. The energy balance assumed steady state since the heat rate was set equal to the heat rate extracted. During the tests, the flow rate often fluctuated dramatically, but the inlet temperature tended to progressively cool down, reach a minimum value, and then increase as the nitrogen supply was reduced or shut off. For this reason, the optimum thermal conductivity of the MLI was best determined by performing the energy balance at the inlet temperature minimum for each test. The results were listed in Table 3.4 and all the graphs

from the data recorded were included in Appendix A: Thermal Data for Full Torus Lab Test. The first set of graphs showed the temperature of the outer surface of the plastic containment layers, referred to as the core locations. Additionally, the vacuum chamber wall temperature was also shown. The second set of graphs showed the temperature profile of the MLI at the $x = L/2$ location. The last set of graphs showed the calculated thermal conductivity using the energy balance compared to the core temperature at location $x = L/2$. The values on these graphs were plotted at a time step of 1 minute.

Table 3.4 Summary of MLI Effective Thermal Conductivity

<u>Test Run</u>	<u>Effective Thermal Conductivity (W/m-K)</u>	<u>Lowest Inlet Temperature (K)</u>	<u>Lowest $x = L/2$ Temperature (K)</u>
7	0.0071	192.4	285.0
8	0.0017	162.9	240.0
9	5.99e-5	119.0	245.0
10	1.48e-4	130.7	244.5
11	3.74e-5	153.6	238.3
12	0.0154	231.6	281.4
13	0.0035	167.3	172.5
14	0.0013	166.0	157.0
15	0.0012	178.1	154.0
17	1.94e-4	154.9	193.0
18	0.0012	151.3	166.0
19	0.0020	169.3	212.8
20	0.0039	165.9	218.2

The median thermal conductivity was 0.0013 W/(m-K). Test Run #16 was stopped prematurely due to substantial leak in the gas feedthrough so it was not included in the table summary. The average thermal conductivity was 0.0029 W/(m-K) with a standard deviation of 0.0043 W/(m-K). The thermal conductivity of air at atmospheric pressure is 0.024 W/(m-K) and about 0.002 W/(m-K) at 50 mbar. Assuming that the thermal

conductivity of pure nitrogen gas was similar to air at low pressures, then the median thermal conductivity of the MLI performed slightly better than two layers of material separated by the residual gas of the chamber alone.

The thermocouple measuring the vapor containment surface at the inlet location was replaced after observing non-physical jumps in the data for Test Runs #9-11. After the thermocouple replacement, the lowest temperature achieved at the inlet location was 151.3 K during Test Run #18. The lowest temperature for the $x = L/2$ location of the core was observed during Test Run #15 at a value of 154.0 K. At these low temperatures, conduction dominated as the primary mode of heat transfer due to the substantial leaking of nitrogen vapor into the vacuum chamber, resulting in high chamber pressures. Using materials with more similar thermal contraction rates with temperature changes would significantly increase the performance of the enclosure, allowing for the primary mode of heat transfer to remain radiative. Even without nitrogen vapor circulating in the enclosure the vacuum chamber was unable to pump down to pressures low enough for the turbo pump to be used. In the vacuum of the space environment and space mission-grade MLI, the heat transfer to the nitrogen vapor core would be reduced significantly.

An investigation by Hoffman [28] gave an empirical function for thermal conductivity as a function of temperature for multi-layer insulation of 40 layers spanning a total thickness of 40 mm. The equation was as follows

$$k_{MLI} = a + bT^c \quad (3-15)$$

where $a = 1.6918e-5$, $b = 1.2268e-13$, and $c = 3.6457$. The pressure for this relationship needs to be less than 0.01 Pa. A graphical depiction is shown in Figure 3.23.

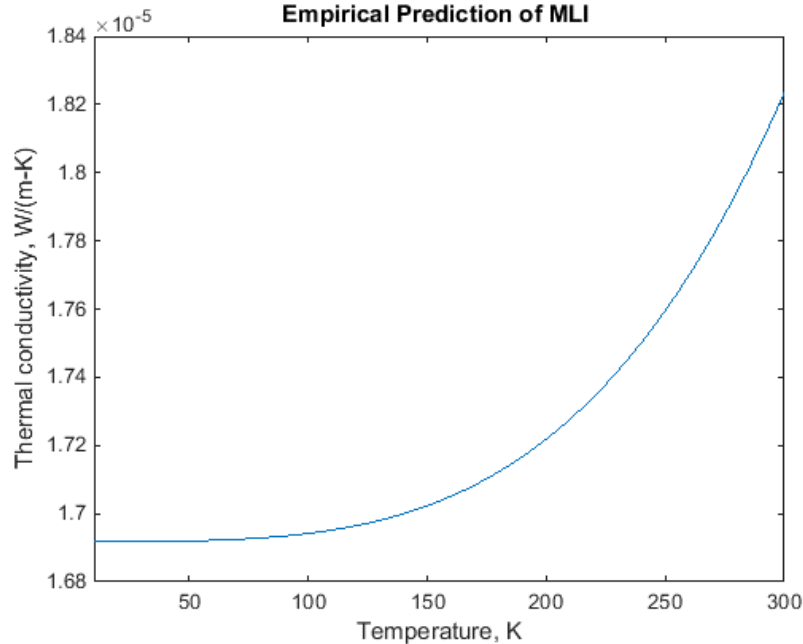


Figure 3.22 Effective thermal conductivity dependence on temperature using empirical function given by Hoffman [28]

Assuming the enclosure in a space environment where the pressure requirement would be met, the thermal conductivity at 150 K would be approximately 1.702×10^{-5} W/(m-K) which would be two orders of magnitude (approximately factor of 76) improvement over the observed performance of the six-layer MLI tested in the laboratory for toroidal enclosure. As an example of how this would reduce the heat transfer to the system can be seen by looking heat transfer per unit length calculated from the thermal data for Test Run #18 shown in Figure 3.24. This test had a thermal conductivity at the $x = L/2$ minimum core temperature near the median of the test results. The heat transfer at the time of the minimum temperature for the $x = L/2$ location was 13.5 W/m. According to Equation (3-14), the heat rate per unit length into the system is proportional to thermal conductivity. If the thermal conductivity performance was approved by a factor of 76 using the improved value given by Equation (3-15), the heat transfer per unit length would be reduced to 0.178

Section 3: Vapor Cooled Thermal Design

W/m and a total of 1.04 W for the entire enclosure. For an enclosure with an increased major radius of 5 m the heat transfer into the system would be 5.58 W, within the range of a commercially available cryocooler listed in Table 3.1.

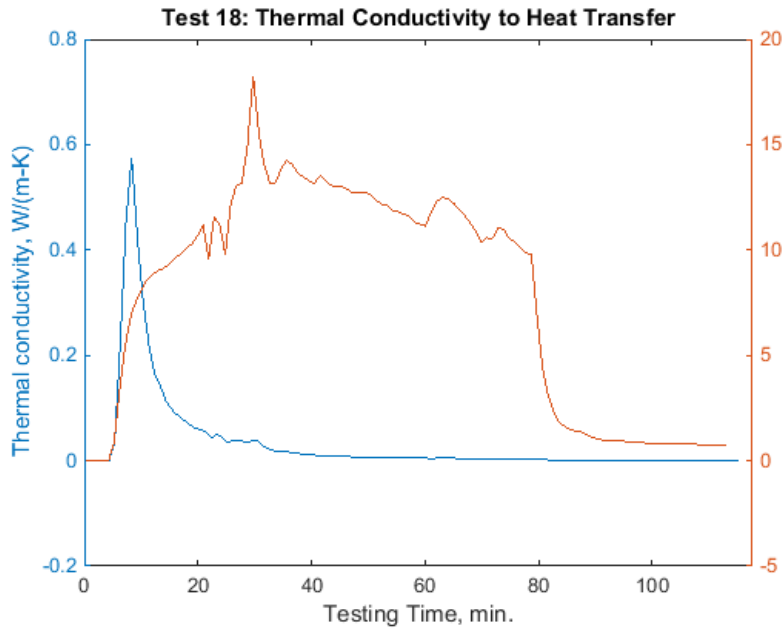


Figure 3.23 Comparison of heat transfer to thermal conductivity during Test Run #18

4 Integration of deployment and thermal design

4.1 Integrated design based on results

The thermal testing showed a large temperature differential along the flow path of the nitrogen, exemplified by Test Run #19 in Figure 4.1.

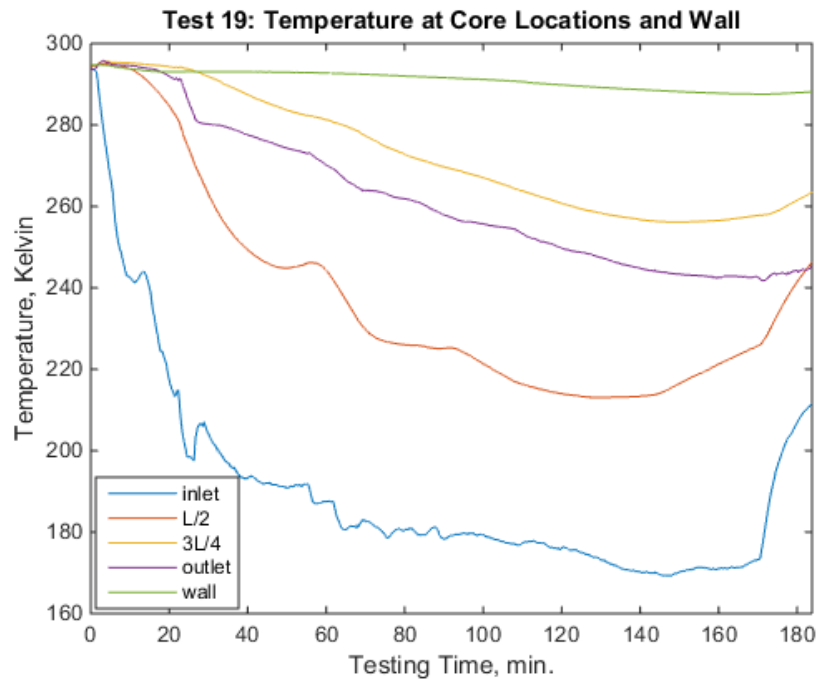


Figure 4.1 Nitrogen temperature at different circumferential locations for Test Run #19

As previously stated, the vapor core at the outlet reached lower temperatures than the $x = 3L/4$ location due to conduction from chamber walls and end caps. The temperature differential between the inlet and the $x = 3L/4$ location was 75.5 K at the minimum $x = L/2$ core temperature. To maintain a more uniform temperature profile along the length of the enclosure, an alternating flow direction system was investigated. Using the smaller prototype shown in Figure 4.2 was constructed from flexible air duct wrapped foam for

insulation, chilled nitrogen vapor was circulated where the direction of the flow alternated using cryogenically rated normally-open (NO) valves.



Figure 4.2 Proof of concept prototype for alternating flow direction testing

The schematic shown in Figure 4.3 shows the configuration of the valves. In order to use the same vacuum chamber feedthrough for the inlet and outlet, four valves were required to switch the flow direction. The valves operated in pairs indicated by the V# with T-joints in the flow path labeled as J#. The valves in yellow (V1 and V2) were paired together and the valves in blue (V3 and V4). A pressure relief valve was installed upstream of the valves to protect the hardware from the high pressure of the liquid nitrogen reservoir. The pressure and flow rate were measure downstream of junction J4.

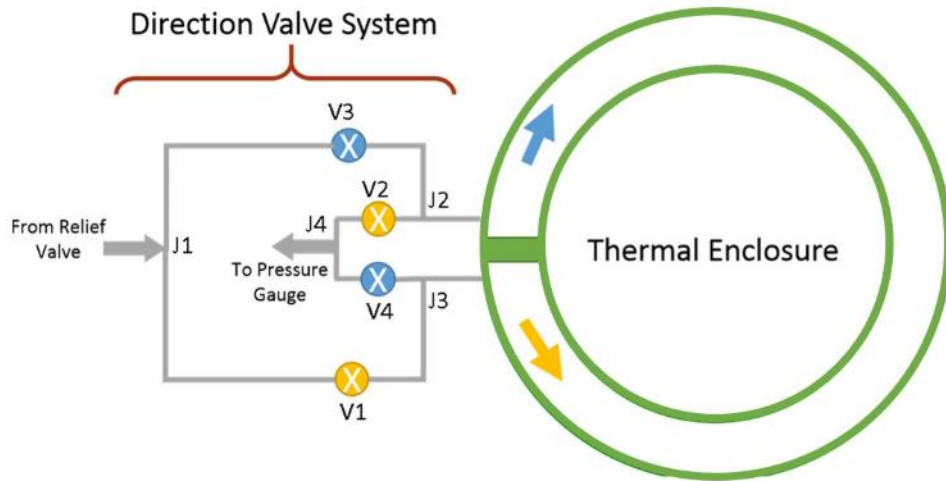


Figure 4.3 Schematic of directional flow control scheme

The results of a test using the same liquid nitrogen reservoir as the full scale lab test can be seen in Figure 4.4. Thermocouple T1 was located near the inlet of the enclosure, followed by T2 at $x = L/2$, and T3 at the outlet. The valves switched from one pair to the other at an interval of 2 minutes, controlled using an Arduino Uno and OPA541 operational amplifiers. Even though the flow path of the nitrogen was significantly shorter than the full lab-scale enclosure, it was shown that the temperature difference between the small prototype locations at any point of the time were maintained close together for long durations. The data is shown in Figure 4.4.

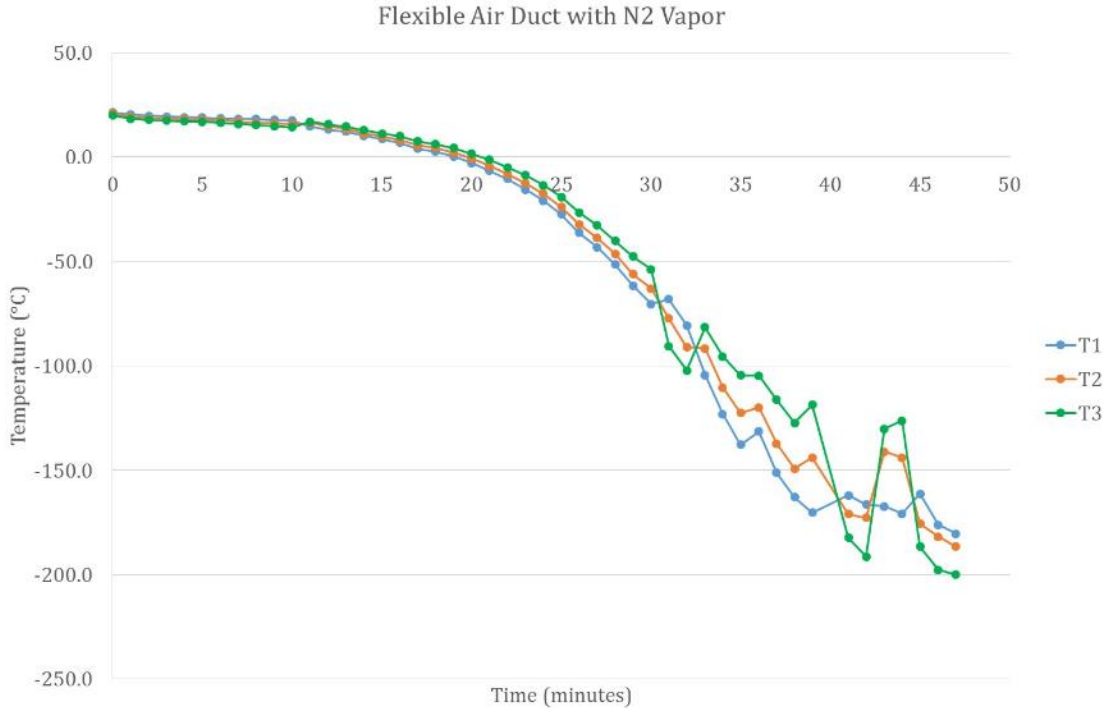


Figure 4.4 Thermal test for proof of concept of alternating flow direction

This same method could be applied to larger test article if the flow path from the tank through the valve system is properly insulated so that vapor delivered to the inlet side of the enclosure is lower than the critical temperature of the superconducting wire.

4.2 Future considerations for fully integrated system

In addition to implementing a more advanced thermal management system to control the temperature profile of the enclosure along the axial length, other system design considerations should be explored before a design capable of an on-orbit demonstration would be possible. Since the enclosure relied on the circulation of nitrogen vapor, protection of the containment layers against debris and other minor impacts would be important. This problem has been thoroughly investigated for space applications such as inflatable support structures and habitats. Technology development ranges from

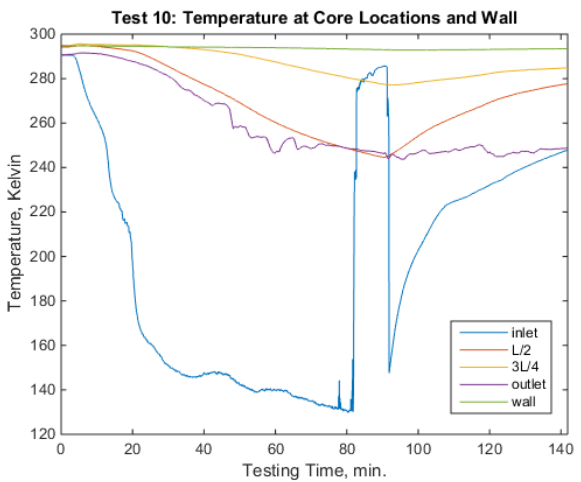
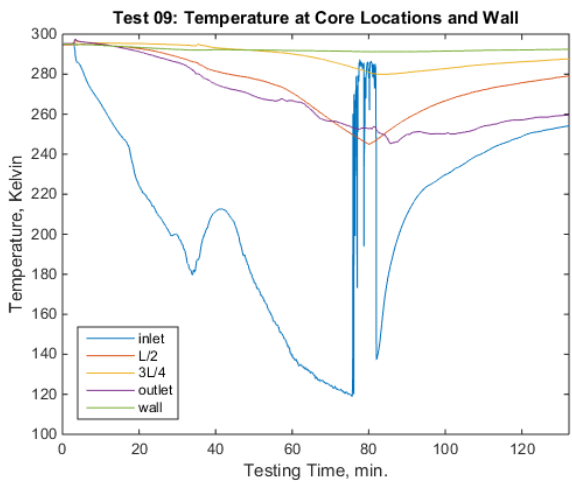
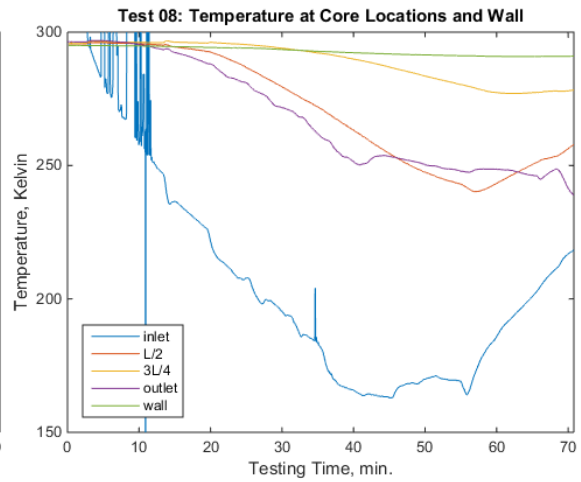
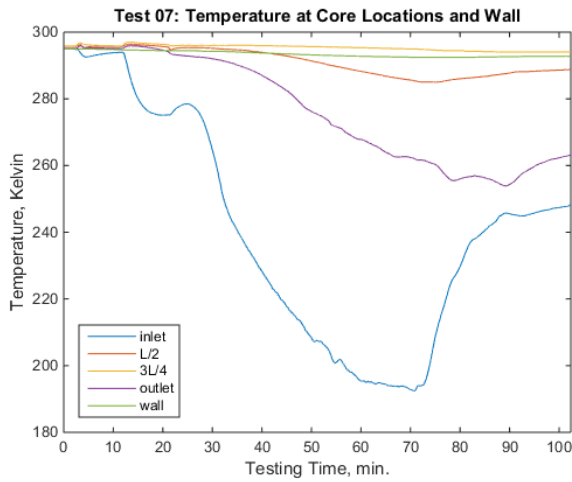
rigidizable structures using UV activated epoxy to self-healing materials. The enclosure becoming rigid after deployment would be possible since the joints of the enclosure do not need to move relative to each other after initial deployment. Self-healing and other passive methods of repairing any punctures that are sustained during operation would also be advantageous.

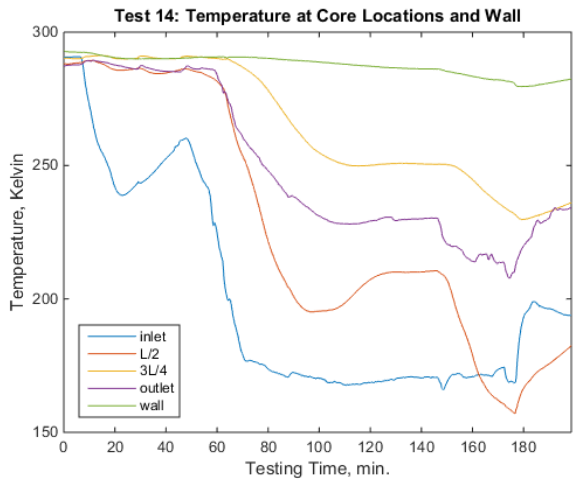
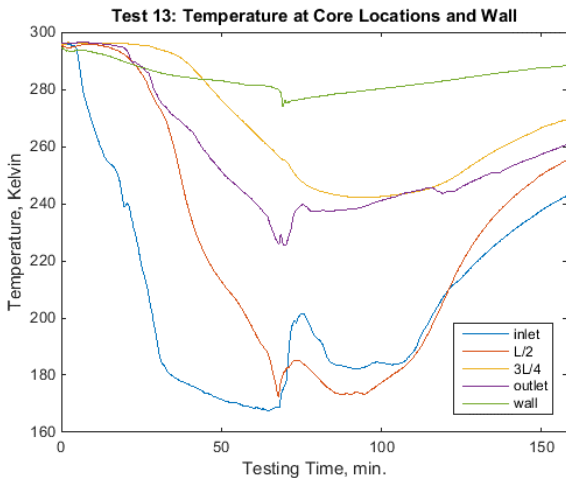
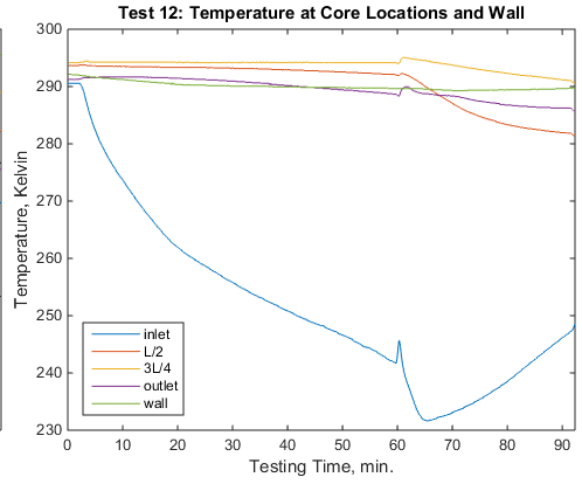
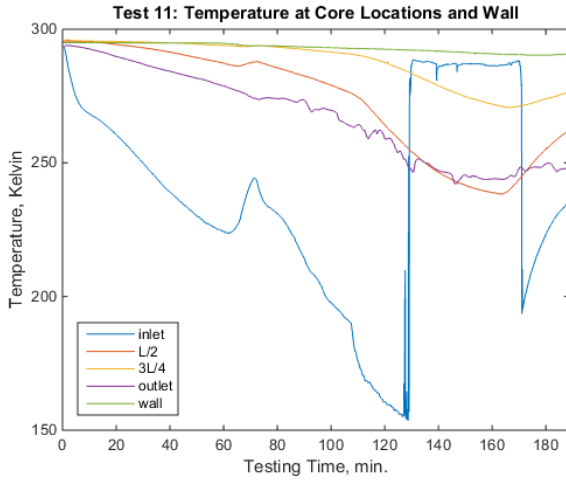
During deployment, the structure may experience modal structural motion between the joints. This motion would dampen before filling the enclosure with nitrogen vapor for operation of the superconducting coil, however; if the enclosure remains attached to another structure, the modal vibration may be undesirable. In this case, an advanced deployment control method may be necessary.

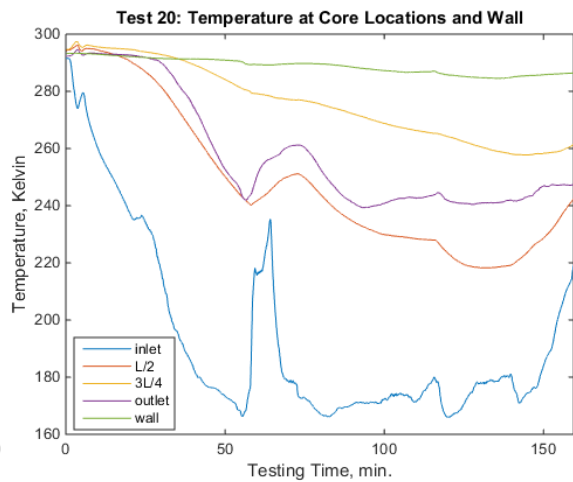
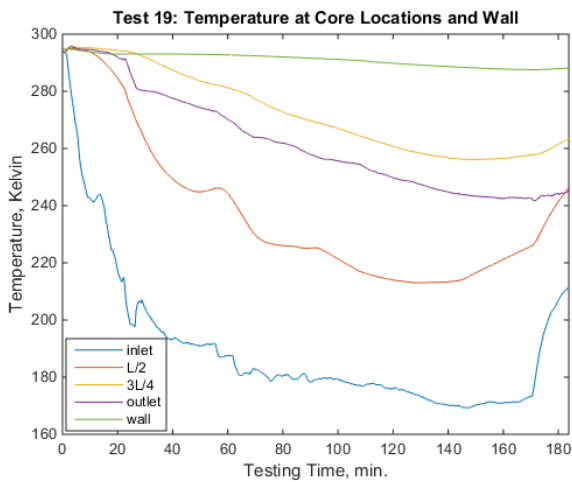
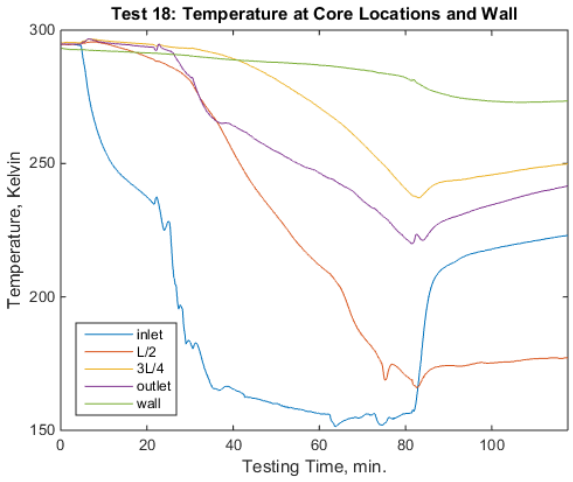
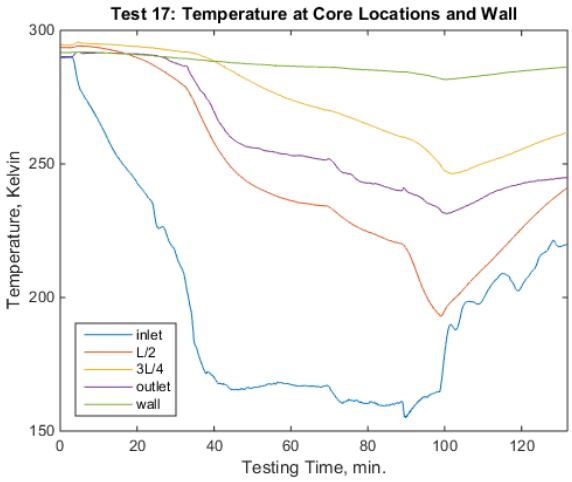
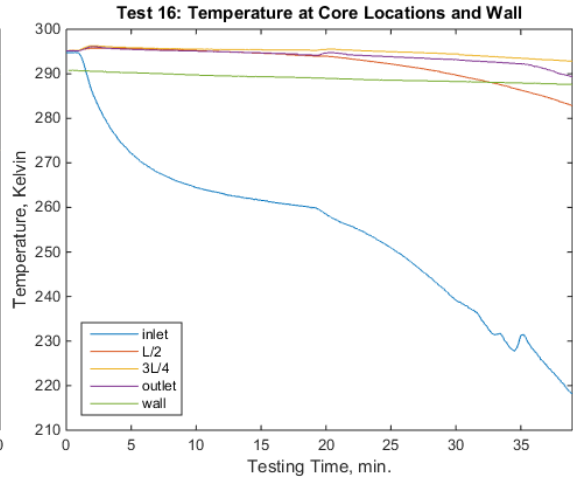
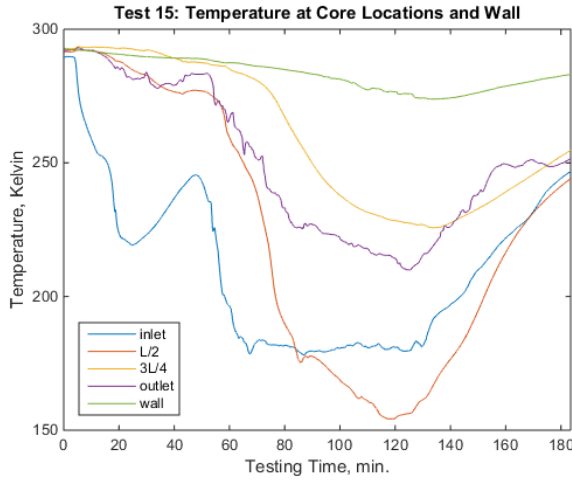
5 Conclusions

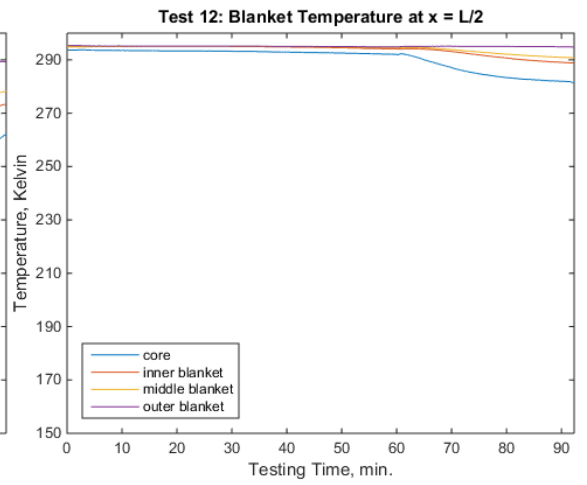
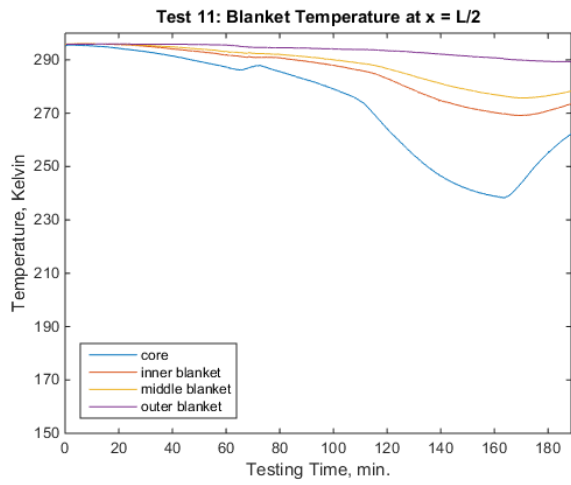
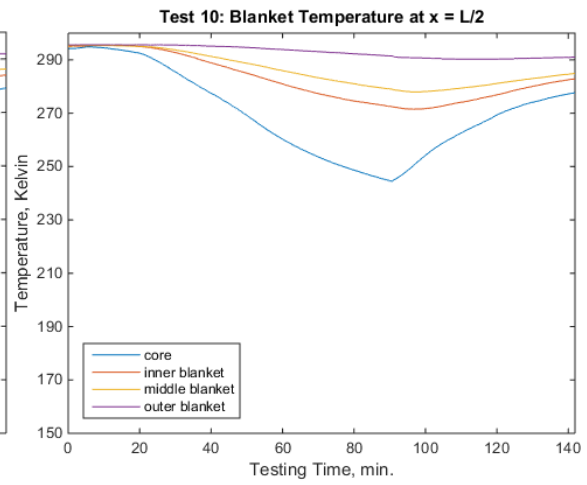
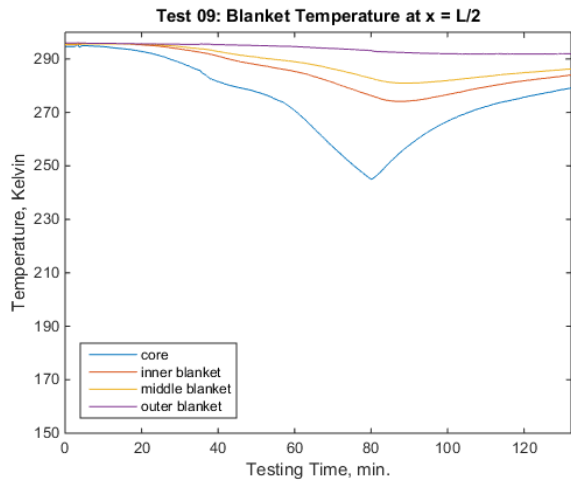
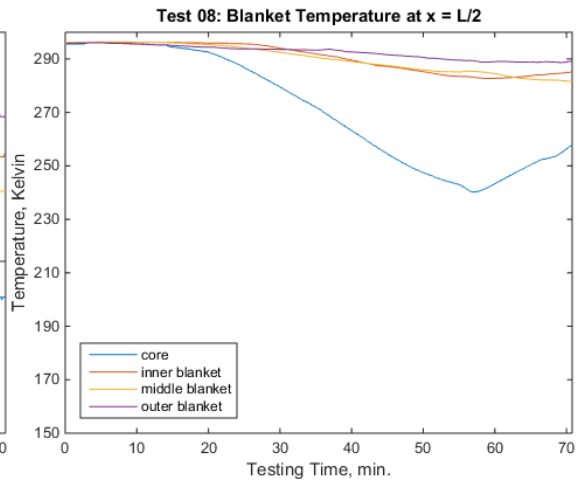
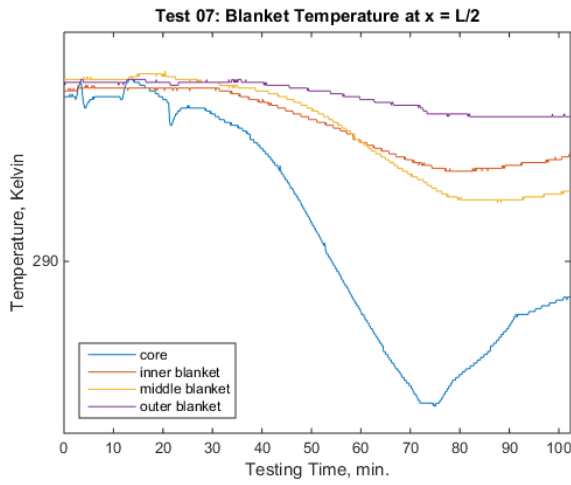
The force for deployment was found to be dominated by the spring with some contribution from the MLI and plastic layers. The motion of the straight segment was primarily linear for slow deployment rates. The same structure and material layers included in a full torus enclosure and thermally test in a vacuum chamber to investigate the ability to obtain sufficiently low temperatures for superconducting coil operation. The poor performance of the insulative material and high vacuum chamber pressure resulted in much higher temperatures and heat transfer rates than what an expected on-orbit system would experience. However, since analysis has shown that if the insulative material properties matched empirically derived values for conditions in high vacuum, the rate of heat extraction using forced nitrogen vapor flow would be sufficient given the capabilities of commercially available cryocoolers. The thin walled structure would be capable of stowing compactly for delivery to orbit and deployed prior to operation using primarily spring force.

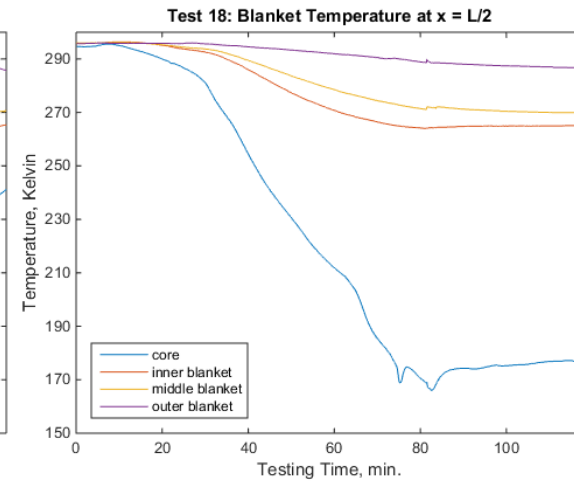
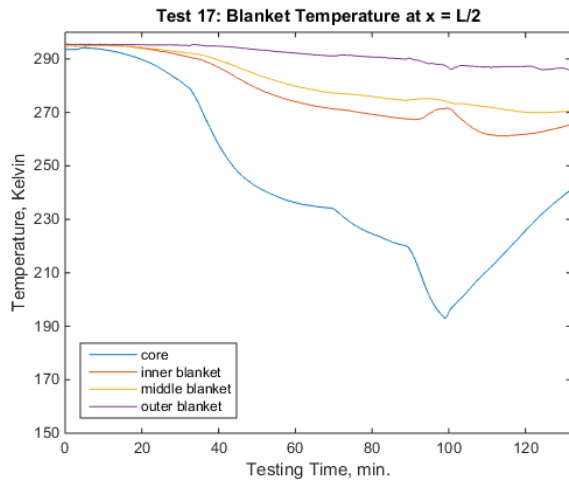
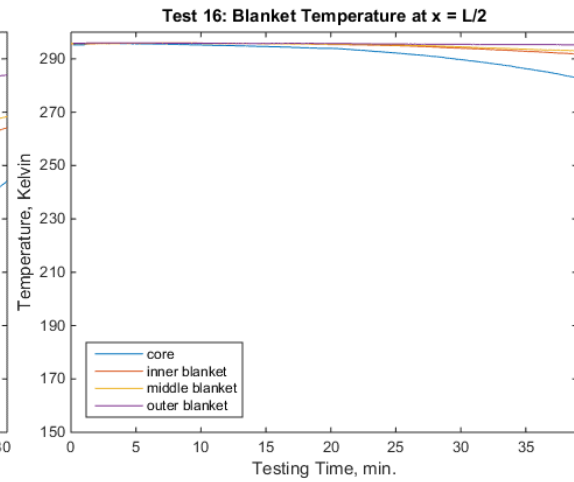
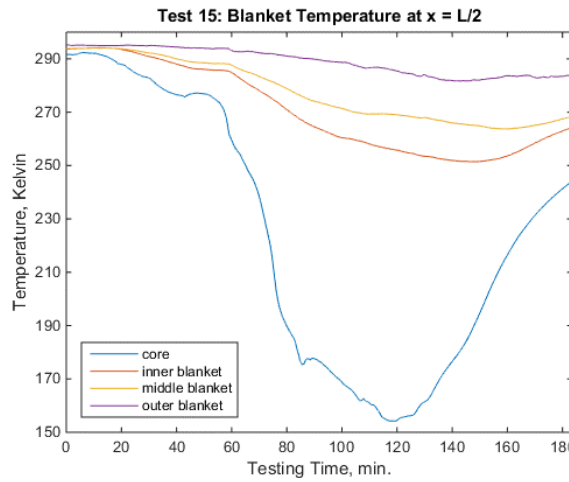
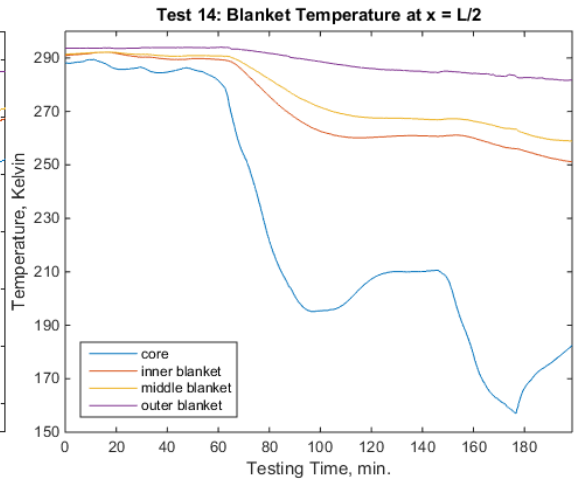
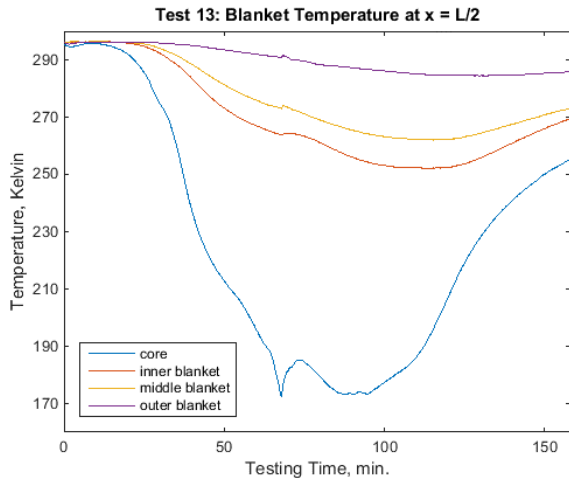
Appendix A: Thermal Data for Full Torus Lab Test

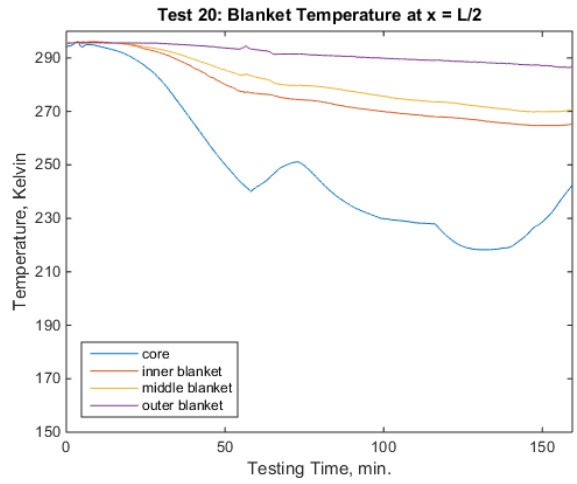
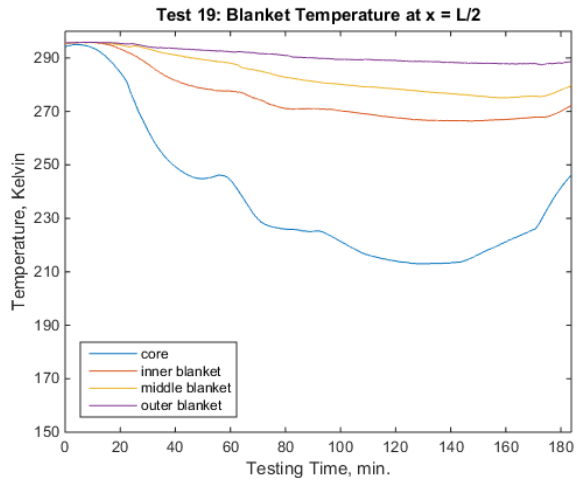


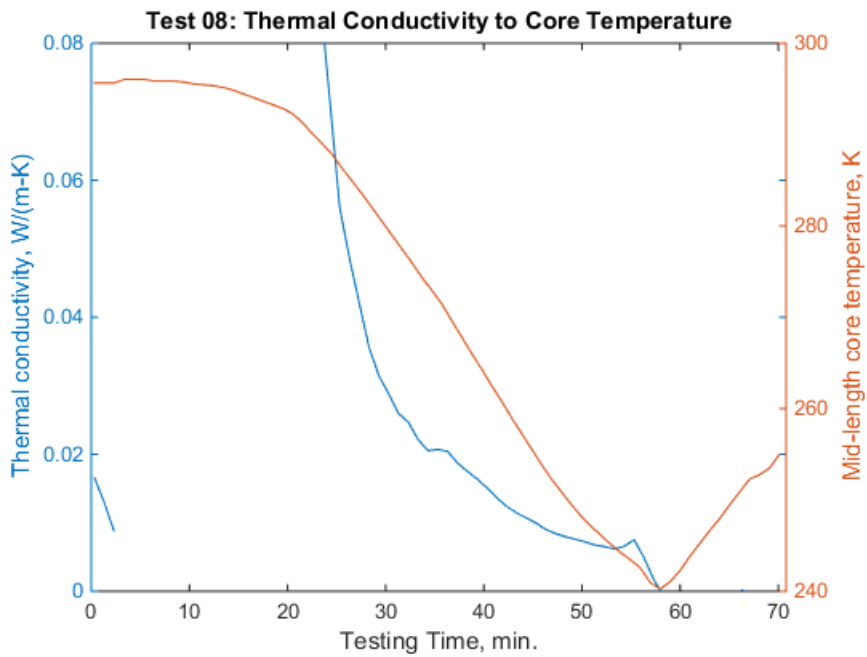
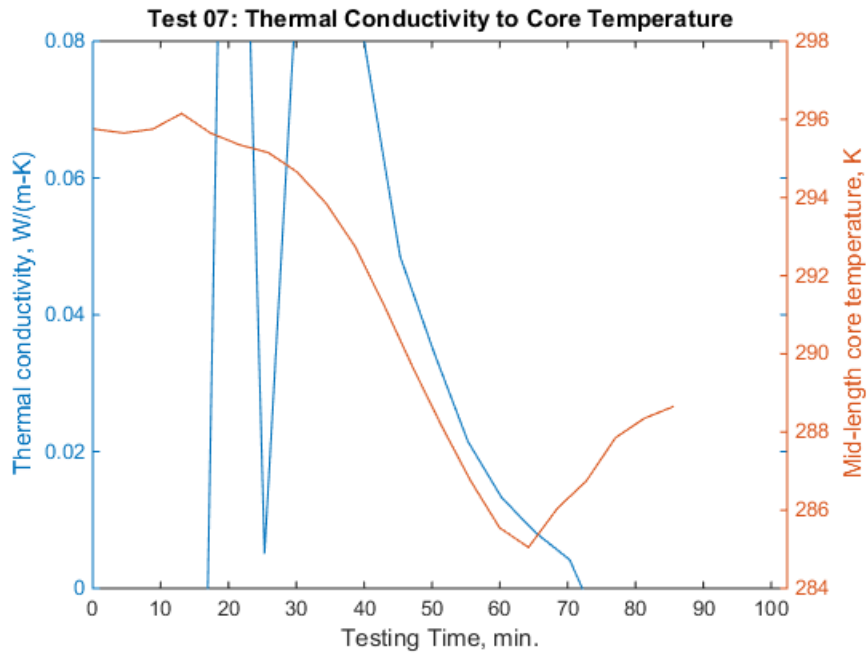


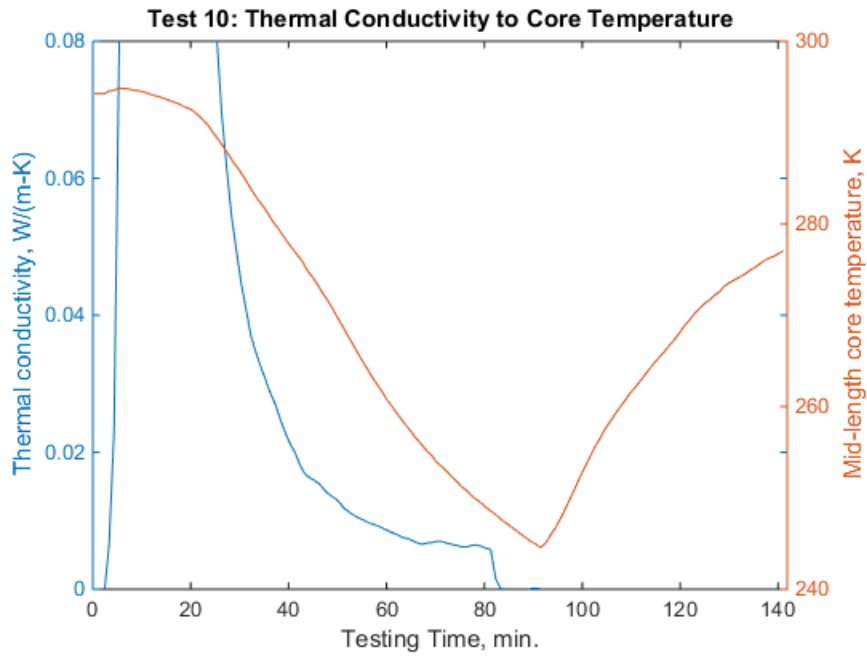
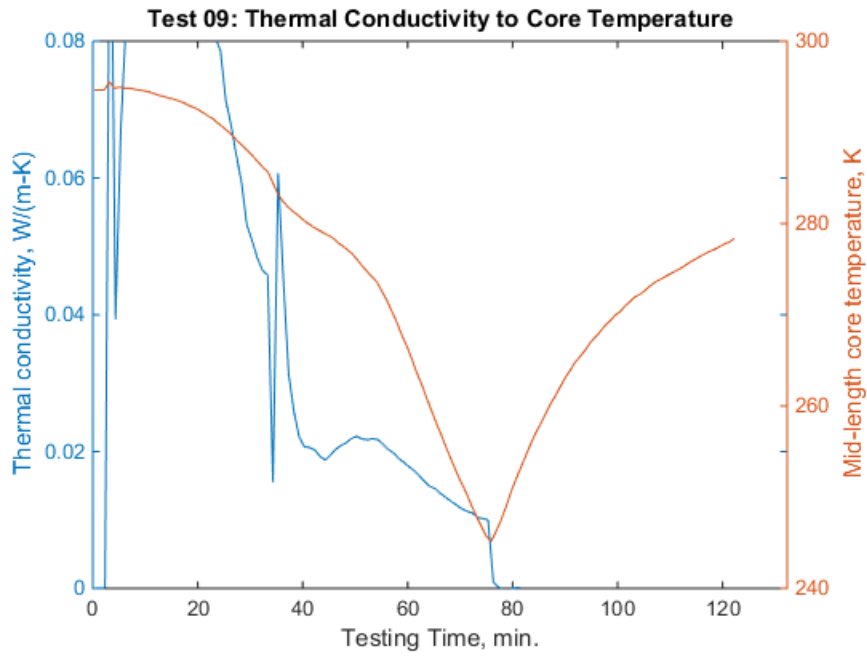


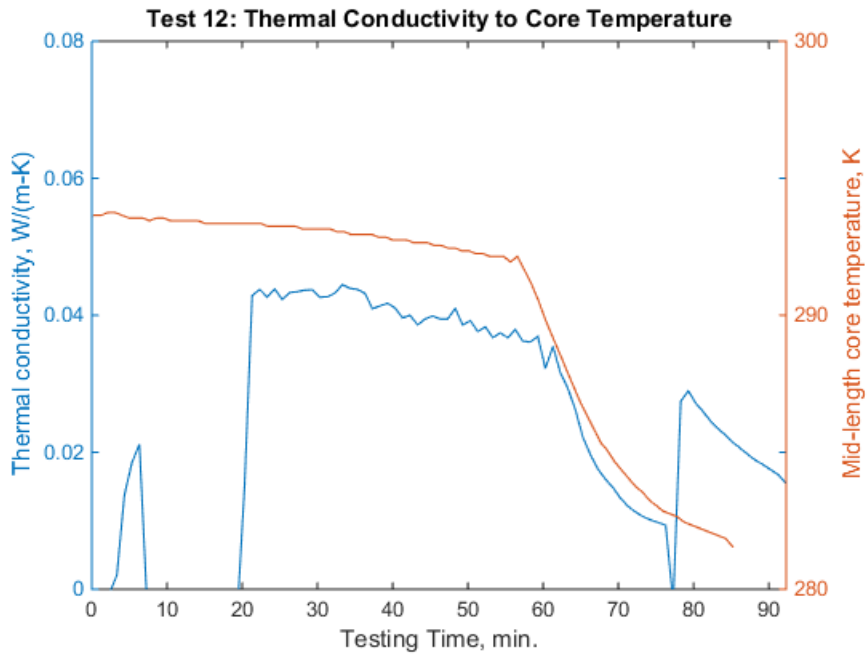
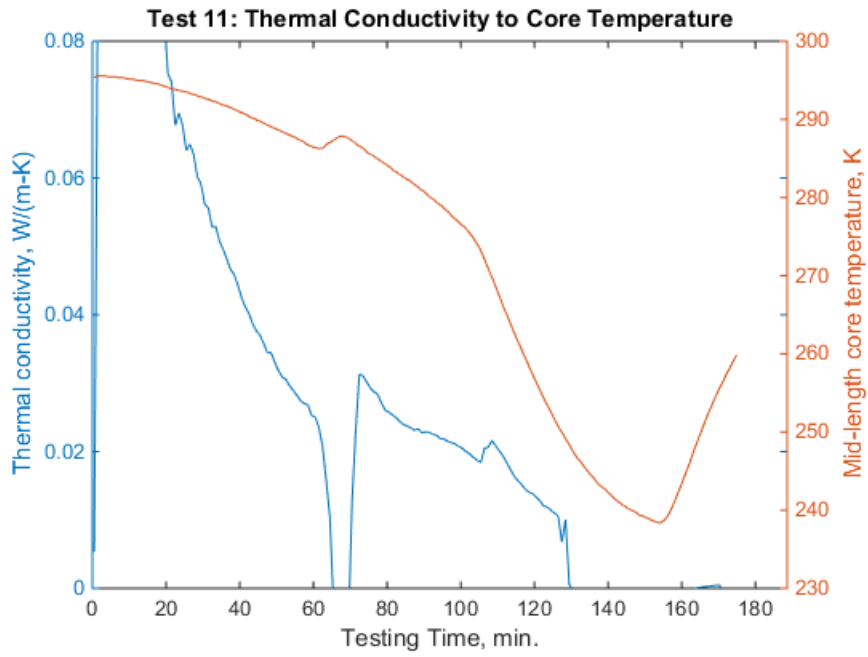


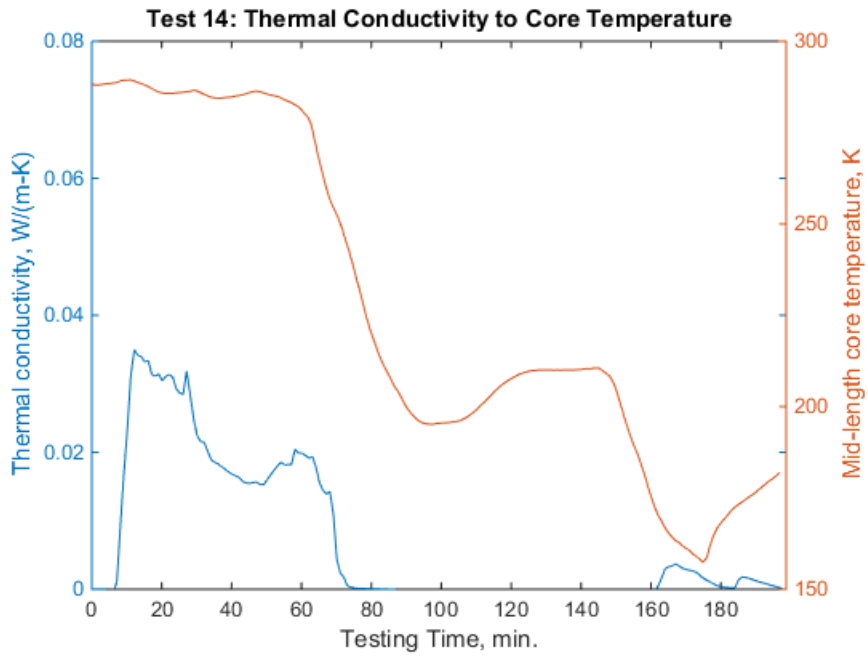
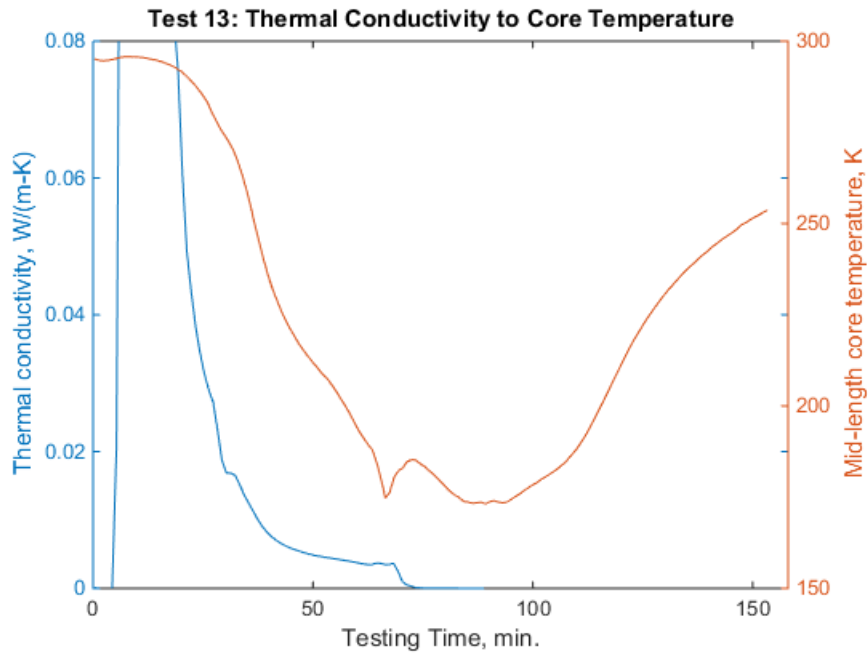


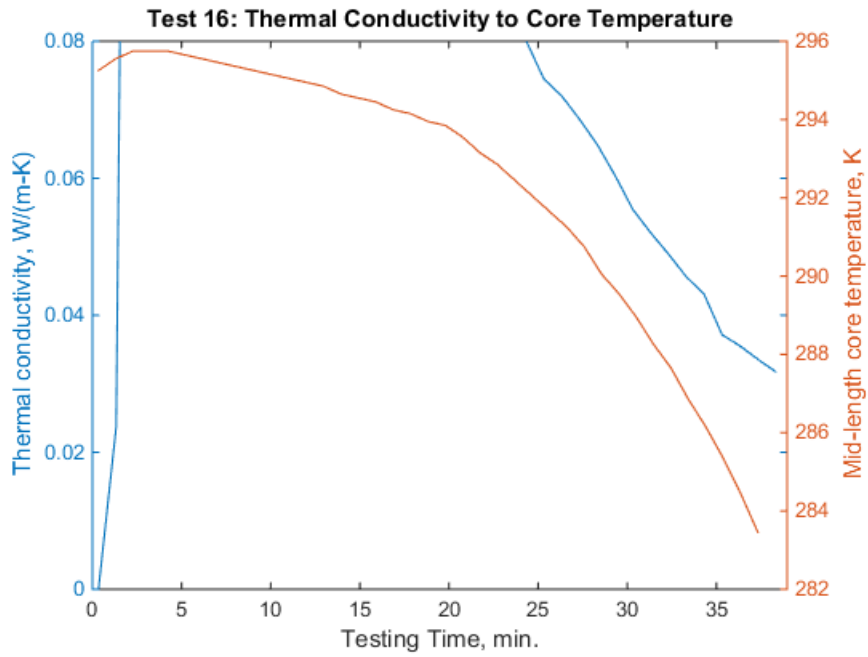
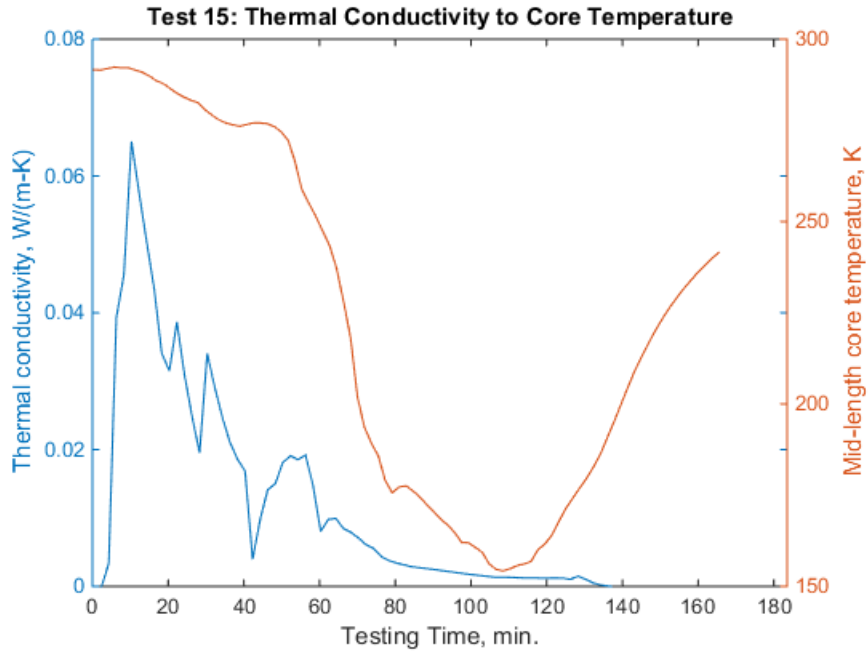


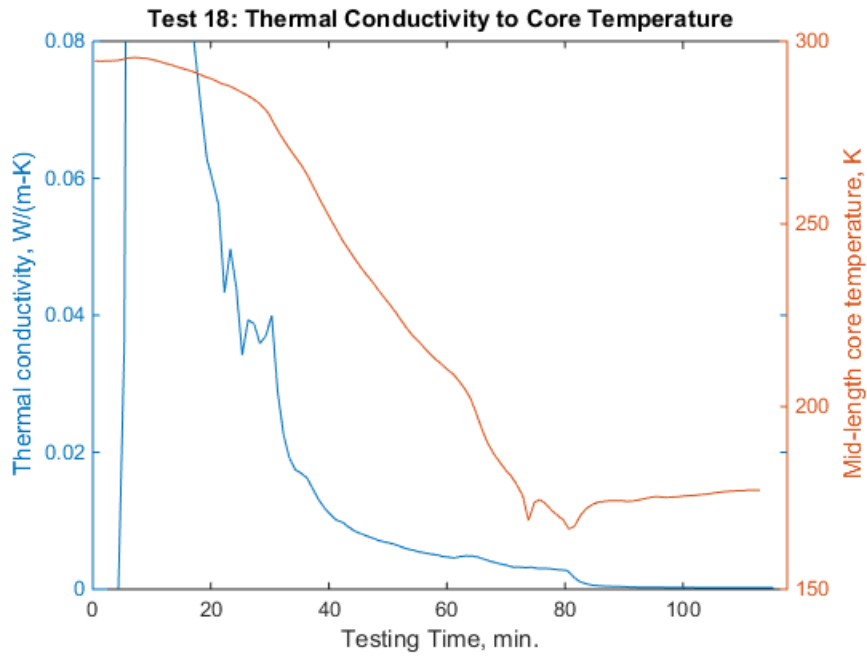
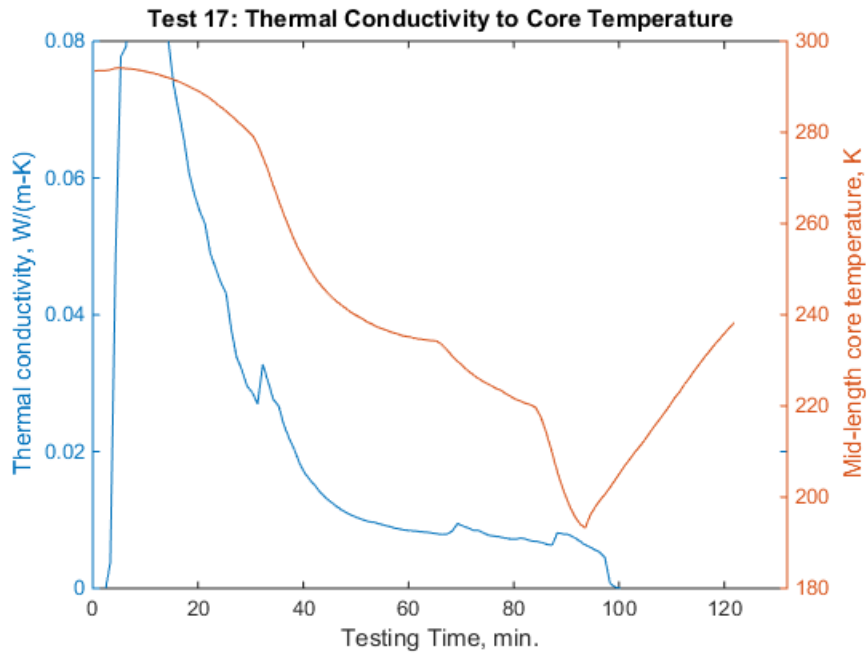


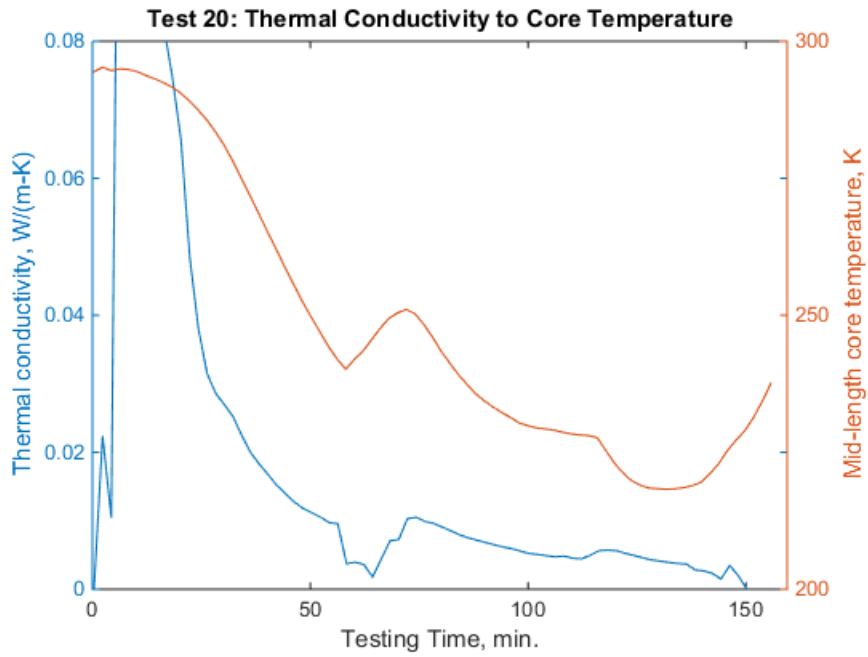
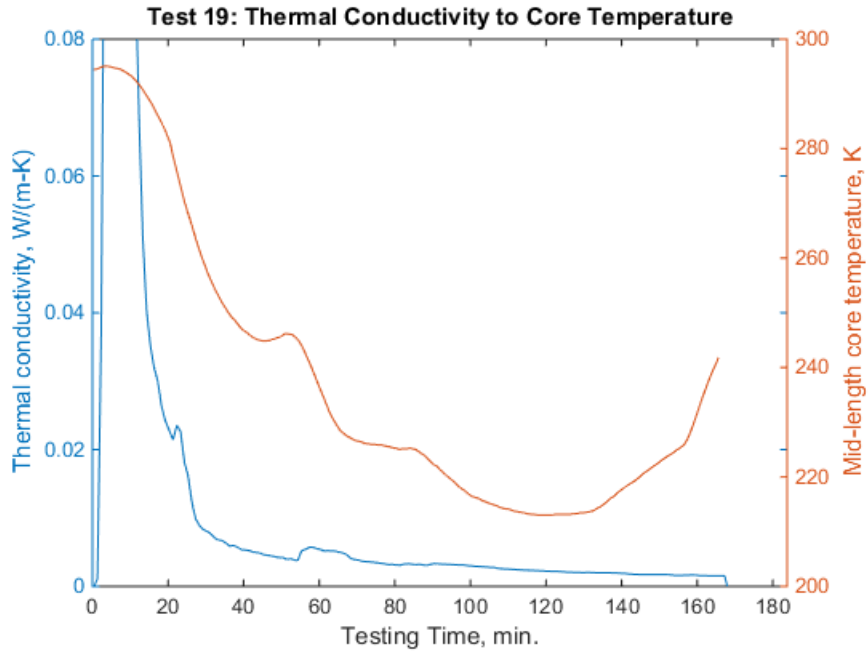












References

- [1] Thienel, L., Lewis, M.R., Brennan, P.J., Buchko, M., Glaister, D., Stoyanof, M., “Design and Performance of the Cryogenic Flexible Diode Heat Pipe (CRYOFD) Flight Experiment,” Air Force Research Laboratory, Society of Automotive Engineers, Inc, 1998.
- [2] Kwon, D.W., Sedwick, R.J., “Cryogenic Heat Pipe for Cooling High-Temperature Superconducting Coils,” *Journal of Thermophysics and Heat Transfer*, Vol. 23, No. 4, 2009, pp. 732-740. DOI: 10.2514/1.43728
- [3] Chen, J., Guo, Z., Yu, W., “Heat Transfer Analysis of Insulation Materials with Flexible Multilayers,” *Thermal Science*, Vol. 17, No. 5, 2013, pp. 1415-1420.
- [4] Gathright, T.R., Reeve, P.A., “Effect of Multilayer Insulation on Radiation Heat Transfer at Cryogenic Temperatures,” *IEEE Transactions on Magnetics*, Vol. 24, No. 2, 1988, pp. 1105-1108.
- [5] Cunnington, G.R., Tien, C.L., “A Study of Heat-transfer Processes in Multilayer Insulations,” *AIAA 4th Thermophysics Conference*, San Francisco, CA, June 16-18, 1969.
- [6] Siegel, R., Howell, J.R., Thermal Radiation Heat Transfer, 2nd ed., Hemisphere Publishing Corporation, Washington, 1981, pp. 291.
- [7] Cravalho, E.G., Tien, C.L., Caren, R.P., “Effect of Small Spacings on Radiative Transfer Between Two Dielectrics,” *Journal of Heat Transfer*, Vol, 84, No. 4, 1967, pp. 351-358.
- [8] Bapat, S.L., Narayankhedkar, K.G., Lukose, T.P., “Experimental Investigations of Multilayer Insulation,” *Cryogenics*, Vol. 30, Iss. 8, 1990, pp. 711-719.
- [9] Finckenor, M.M., Dooling, D., NASA Multilayer Insulation Material Guidelines, 1999
- [10] Okazaki, S., Kawasaki, H., Murakami, M., Sugita, H., Kanamori, Y., “Influence of Processing on Thermal Performance of Space Use Multilayer Insulation,” *Journal of Thermophysics and Heat Transfer*, Vol. 28, No. 2, 2014, pp. 334-342. DOI: 10.2514/1.T4163
- [11] Donabedian, M., Gilmore, D.G., Stultz, J.W., Tsuyuki, G.T., Lin, E.I., “Insulation”, *Spacecraft Thermal Control Handbook: Volume 1: Fundamental Technologies*, The Aerospace Press, El Segundo, 2002, pp. 161-205.
- [12] Lin, E.I., Stultz, J.W., Reeve, R.T., “Effective Emittance for Cassini Multilayer Insulation Blankets and Heat Loss near Seams,” *Journal of Thermophysics and Heat Transfer*, Vol. 10, No. 2, 1996, pp. 357-363. DOI: 10.2514/3.795
- [13] Ross, R.G., Boyle, R.F., “An Overview of NASA Space Cryocooler Programs – 2006,” *Cryocoolers 14*, International Cryocooler Conference, Boulder, CO, 2006, pp. 1-10.
- [14] Johnson, D.L., Carroll, B.C., Leland, R.S., “MSL/CheCheMin Cryocooler System Requirements and Characterization Tests,” *Cryocoolers 15*, International Cryocoolers Conference, Boulder, CO, 2009, pp. 621-630.

-
- [15] Zia, J.H., “A Pulse Tube Cryocooler with 300 W Refrigeration at 80 K and an Operating Efficiency of 19% Carnot” *Cryocoolers 14*, International Cryocooler Conference, Boulder, CO, 2007, pp. 141-147.
- [16] Ross, R.G Jr., Johnson, D.L., Elliott, D., Licata, S.J., Overoye, K., “AIRS Pulse Tube Coolers Performance Update – Six Years in Space,” *Cryocoolers 15*, International Cryocooler Conference, Boulder, CO, 2009, pp. 613-620.
- [17] Sunpower, Inc., “CryoTel® Family,” URL: <http://sunpowerinc.net/cryocoolers/cryotel> [cited: 27 March 2014].
- [18] van de Groep, W.L., Mullié, J.C., Willems, W.J., Benschop, T., “Development of a 15W Coaxial Pulse Tube Cooler,” *Cryocoolers 15*, International Cryocooler Conference, Boulder, CO, 2009, pp. 157-165.
- [19] Nguyen, T., Petach, M., Michaelian, M., Raab, J., Tward, E., “Space Micro Pulse Tube Cooler,” *Cryocoolers 16*, International Cryocooler Conference, Boulder, CO, 2011, pp. 97-101.
- [20] Ladner, D.R., “Performance and Mass vs. Operating Temperature for Pulse Tube and Stirling Cryocoolers,” *Cryocoolers 16*, International Cryocooler Conference, Boulder, CO, 2011, pp. 633-644.
- [21] Trollier, T., Tanchon, J., Buquet, J., Ravex, A., “Status of Air Liquide Space Pulse Tube Cryocoolers,” *Cryocoolers 15*, International Cryocooler Conference, Boulder, CO, 2009, pp. 115-123.
- [22] Nguyen, T., Toma, G., Jaco, C., Michaelian, M., Raab, J., “HEC Pulse Tube Coaxial Cold Head Coolers,” *Cryocoolers 16*, International Cryocooler Conference, Boulder, CO, 2011, pp. 143-148.
- [23] Swift, W.L., McCormack, J.A., Zagarola, M.V., Dolan, F.X., Sixsmith, H., “The NICMOS Turbo-Brayton Cryocooler – Two Years in Orbit,” *Cryocoolers 13*, Springer Science+Business Media, Inc., New York, 2004, pp. 633-639.
- [24] Barr, M.C., Price, K.D., Pruitt, G.R., “Raytheon RS1 Cryocooler Performance,” *Cryocoolers 13*, Springer Science+Business Media, Inc., New York, 2004, pp. 59-63.
- [25] Dietrich, M., Yang, L.W., Thummes, G., “High-power Stirling-type pulse tube cryocooler: Observation and reduction of regenerator temperature-inhomogeneities,” *Cryogenics*, Vol. 47, 2007, pp. 306-314.
- [26] Wertz, J. R., and Larson, W. J., “Space Mission Analysis and Design”, 3rd ed., Microcosm Press, 1999
- [27] Brewster, M.Q., Thermal Radiative Transfer and Properties, John Wiley & Sons, Inc, New York, 1992, pp. 501.
- [28] Hofmann, A., “The Thermal Conductivity of Cryogenic Insulation Materials and Its Temperature Dependence,” *Cryogenics*, Vol. 46, (2006), pp. 815-824. DOI: 10.1016/j.cryogenics.2006.08.001